DOE/ID-10460
VOLUME 1
October 1996

IN-VESSEL COOLABILITY AND RETENTION OF A CORE MELT

T. G. Theofanous, C. Liu, S. Additon,
S. Angelini, O. Kymäläinen, T. Salmassi

Advanced
Reactor
Severe
Accident
Program

Department of Energy

DOE/ID-10460
VOLUME 1

IN-VESSEL COOLABILITY AND RETENTION OF A CORE MELT

T.G. Theofanous, C. Liu, S. Additon,
S. Angelini, O. Kymäläinen, T. Salmassi

contributed appendices by:
F.J. Asfia and V.K. Dhir (UCLA)
T.Y. Chu et al. (SNL), J. Rashid (ANATECH)
L. Baker, Jr., C.C. Chu & J.J. Sienicki (ANL)

First Draft: September 1993
Final Draft: November 1993
Peer Review Version: November 1994
Peer Re-Review Version: July 1995
Final: October 1996

Center for Risk Studies and Safety
Departments of Chemical and Mechanical Engineering
University of California, Santa Barbara
Santa Barbara, CA 93106

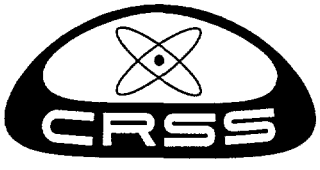

Prepared for the
U. S. Department of Energy
Idaho Operations Office
Under ANL Subcontract No. 23572401

PREFACE

These two volumes of the *In-Vessel Coolability and Retention of a Core Melt* report document a comprehensive assessment and review effort aimed at addressing in-vessel retention (IVR), by external cooling, as a severe accident management strategy. The assessment is contained in volume 1, which first appeared in November 1994. The review, which occurred in the intervening two years and involved 17 internationally known experts (in areas covering the subject matter) in two iterations with the authors, is documented in volume 2. Special procedures to maintain scrutability will reference to the reviewer's comments, and for keeping track of new material, developed by the authors during the review process, are described in the Preface to the July 1995 version (see next page).

Closure has been achieved, as evidenced in Appendix V. This appendix also includes results from the recently-built ACOPO experiment (Appendix V-2), and some new and interesting information from the ULPU experiment on the boiling crisis mechanisms (Appendix V-3). The ACOPO results are confirmatory of the authors' treatment of natural convection in the oxidic pool, while the identification of the boiling crisis mechanism opens up the way to the prediction of critical heat flux from basic considerations.

The experts were requested to examine this work as to its validity and applicability in the licensing arena, and the selection was made such as to include all key persons in the area, internationally, and to ensure that all key sub-areas were covered. The specific evaluation was for the AP600, and having achieved closure, this work is used in the certification of this design, presently under NRC review. More broadly, however, we expect that the methodology and base technology developed in this effort will be of value for other designs and at least for some of the operating reactors both domestically and internationally.

Sterling Franks, III
Associate Director for Engineering
and Technology development
U.S. Department of Energy
19901 Germantown Road
Germantown, Maryland 20874-1290
(301) 907-3456

PREFACE TO THE JULY 1995 VERSION

This is intended as the final version of DOE/ID-10460, addressing in-vessel retention as an accident management strategy for an AP600-like reactor design. The first volume is a revision of the peer review version first issued in November 1994. The second volume consists primarily of the peer review comments and our responses. Both volumes contain new technical material in the form of addenda (in the first volume) and new appendices (in the second). Some explanations are offered as follows:

- To maintain scrutability with reference to the reviewer's comments, the original material in DOE/ID-10460, including page numbering, was left untouched, except for a few typos.
- Revisions were made either by means of minor addenda incorporated into the text without affecting page numbering, or by major addenda provided at the end of preexisting chapters or appendices in Volume I. All such addenda are clearly marked by being enclosed in double brackets, i.e., [[...]]. A listing of the major addenda is provided at the end of this Preface.
- Further additions were made in the form of new appendices in Volume II. They are marked by the double bracket notation, also, and a listing is provided at the end of this Preface.
- The as-received review comments are collected in Appendix S. Point-by-point responses are provided in Appendix T. For convenience, this material is also presented in a topic-by-topic form collated in Appendix U. Both appendices (T and U) also contain overview statements (General Comment and Highlights) on each reviewer's comments.
- The new round of review comments received, and any responses, if warranted, will make up Appendix V in the final document.

LISTING OF MAJOR ADDENDA AND NEW APPENDICES

Chapter 3.	Summary of New ULPU Runs
Chapter 4.	Consideration of Ductile Tearing
Chapter 5.	Flux Shape Effects over the Metal Layer
Chapter 7.	Summary of New System Effects Results and Parametric Studies
Appendix E.3.	New ULPU Results on Flux Shape and Flow Rate Effects
Appendix E.4.	ULPU Configuration III Results
Appendix J.	Further Results on Long Term Eutectic Interactions
Appendix K.	Thermal Insulation Design
Appendix M.	Updated Cavity Flooding Considerations
Appendix O.	Consideration of "Other" Proposed Scenarios
Appendix P.	Additional Parametric and Sensitivity Studies
Appendix Q.	Detailed Results from Selected Cases
Appendix R.	Decay Heat Generation In the Metallic Layer

ABSTRACT

The efficacy of external flooding of a reactor vessel as a severe accident management strategy is assessed for an AP600-like reactor design. The overall approach is based on the Risk Oriented Accident Analysis Methodology (ROAAM), and the assessment includes consideration of bounding scenarios and sensitivity studies, as well as arbitrary parametric evaluations that allow the delineation of the failure boundaries. The technical treatment in this assessment includes:

(a) new data on energy flow from either volumetrically heated pools or non-heated layers on top, boiling and critical heat flux in inverted, curved geometries, emissivity of molten (superheated) samples of steel, and chemical reactivity proof tests,

(b) a simple but accurate mathematical formulation that allows prediction of thermal loads by means of convenient hand calculations,

(c) a detailed model programmed on the computer to sample input parameters over the uncertainty ranges, and to produce probability distributions of thermal loads and margins for departure from nucleate boiling at each angular position on the lower head, and

(d) detailed structural evaluations that demonstrate that departure from nucleate boiling is a necessary and sufficient criterion for failure.

Quantification of the input parameters is carried out for an AP600-like design, and the results of the assessment demonstrate that lower head failure is "physically unreasonable." Use of this conclusion for any specific application is subject to verifying the required reliability of the depressurization and cavity-flooding systems, and to showing the appropriateness (in relation to the database presented here, or by further testing as necessary) of the thermal insulation design and of the external surface properties of the lower head, including any applicable coatings.

The AP600 is particularly favorable to "in-vessel retention." Some ideas to enhance the assessment basis as well as performance in this respect, for applications to larger and/or higher power density reactors are also provided.

CONTENTS

NOMENCLATURE

A	property group evaluated at "film" temperature, $\equiv 0.15k\left\{(g\beta)/(\alpha\nu)\right\}^{1/3}$
c_p	heat capacity
D	diameter
Da	Dammköhler number, $\equiv \dot{Q}H^2/k(T_{max}-T_i)$
E	Young's modulus of elasticity
Gr	Grashof number, $\equiv g\beta(T_{max}-T_i)H^3/\nu^2$
g	acceleration of gravity
H	depth of oxidic pool
h	heat transfer coefficient
I	Impulse
k	thermal conductivity
Nu	Nusselt number, $\equiv (qH)/k(T_{max}-T_i)$
P	pressure
Pr	Prandtl number, $\equiv \nu/\alpha$
$\dot{Q}$	volumetric heat generation rate
q	average heat flux at pool boundaries
$\tilde{q}$	characteristic heat flux, $\equiv \epsilon\sigma\tilde{T}^4$
q^*	dimensionless heat flux, $\equiv q/\tilde{q}$
q_{CHF}	critical heat flux
$q_{\ell,w}$	heat flux at vessel wall in contact with metal layer
$q_w(\theta)$	local heat flux across the vessel wall, at angular position θ
R	reactor vessel, hemisphere radius
Ra	Rayleigh number, $\equiv \{g\beta(T_{max}-T_i)H^3\}/(\alpha\nu)$
Ra′	Rayleigh number (internal), $\equiv (g\beta\dot{Q}H^5)/(k\nu\alpha)$
Re	Reynolds number, $\equiv (UD)/(\nu)$
r	radial coordinate
S	surface area
T	temperature
T^*	dimensionless temperature, $\equiv T/\tilde{T}$
T^{**}	water saturation temperature
$\tilde{T}$	characteristic temperature, $\equiv (A/\epsilon\sigma)^{3/8}$
T_m	oxidic pool liquidus
T_{max}	maximum (or "bulk," if uniform) pool temperature
U	velocity
V	volume of oxidic pool
Z_τ	total thickness of ablated wall following a relocation event
$\dot{Z}$	wall ablation rate

Greek

α	thermal diffusivity
β	thermal expansion coefficient
β'	linear thermal expansion coefficient
δ	thickness
ϵ	emmisivity
θ	polar angle on the lower head (see Fig. 2.1)
θ_ℓ	polar angle of metal layer top
θ_p	polar angle of oxidic layer top
λ	latent head of fusion
ν	kinematic viscosity
ν'	Poisson Ratio
ρ	density
σ	stress or Stefan–Boltzman constant
τ	duration of main relocation event

Subscripts

b	bulk value
CHF	critical heat flux
cr	crust value
dn	downward (over the hemispherical boundary)
F	failure condition
i	boundary value
j	based on jet properties
ℓ	metal layer
ℓ, i	inner metal layer boundary value
ℓ, m	liquidus of the vessel wall in contact with metal layer
ℓ, o	outer metal layer boundary value
ℓ, w	at vessel wall in contact with metal layer
m	liquidus
r	core relocation quantity, or radial coordinate
s	radiative sink value
s, i	inner radiative sink surface value
s, o	outer radiative sink surface value
up	upward (over the flat boundary of the oxidic pool)
v	inner vessel wall (upper vessel only)
w	vessel wall value
z	axial coordinate
0	initial value
θ	azimuthal coordinate

LIST OF ACRONYMS

ANATECH	ANATECH Research Corporation
ANL	Argonne National Laboratory
BC	boiling crisis
CEN	Centre d'Etudes Nucleaires de Grenoble
CHF	critical heat flux
CRSS	Center for Risk Studies and Safety (at UCSB)
CSNI	Committee on the Safety of Nuclear Installations (under OECD)
DOE	Department of Energy
EPRI	Electric Power Research Institute
FAI	Fauske & Associates, Inc.
FCI	fuel-coolant interaction
KfK	Kernforschungszentrum Karlsruhe GmbH
NRC	Nuclear Regulatory Commission
OECD	Organization for Economic Cooperation and Development
PWR	Pressurized Water Reactor
ROAAM	Risk Oriented Accident Assessment Methodology
SNL	Sandia National Laboratories
TMI-2	Three Mile Island, Unit II
UCLA	University of California, Los Angeles
UCSB	University of California, Santa Barbara

ACKNOWLEDGEMENTS

This work was supported under the ROAAM program carried out for the US DOE's Advanced Reactor Severe Accident Program (ARSAP), under ANL subcontract No. 23572401 to UCSB. The program was initiated in 1991 and managed by Mr. W. Pasedag (DOE, Headquarters) and Mr. S. Sorrell (DOE, Idaho Operations Office). The authors are grateful for the support, cooperation, and advice received from these individuals throughout the performance of this work, including the preparation of this document. For ANL the contract was managed by Dr. L. Baker, and his cooperation significantly facilitated the authors' focusing on the technical aspects of the work.

This has been a multifaceted technical effort that was enriched significantly by interactions with several individuals in other organizations outside UCSB. These include: J. Scobel (Westinghouse), J. Sienicki (ANL), J. Rashid (ANATECH), V.K. Dhir (UCLA), T.Y. Chu (SNL), C. Chu (ANL), and R. Hammersley (FAI). Thanks are also due to the following individuals affiliated with UCSB: M. Frye, J. Smith and G. Wang.

Last but not least we wish to acknowledge Ms. Eileen Horton, Administrative Assistant of CRSS, for her unhesitating devotion to this project, from contractual matters to budgeting and accounting to the preparation of this report, often under very tight schedules.

[[The work was brought to a fruitful conclusion thanks to the participation of 17 experts, engaged independently through Argonne National Laboratory. They contributed not only by setting forth an in-depth record of scrutiny on essentially all aspects of the work, but also by providing further insights and otherwise enriching the technical bases of the work. The authors are grateful for their diligence and cooperation.]]

1 INTRODUCTION

This document addresses a severe accident management concept known as "in-vessel retention," and it has been put together with two purposes in mind: one, to demonstrate the effectiveness of the concept for an AP600-like design; and two, to provide a readily adaptable path for its consideration for other designs.

The accident management strategy is to flood the reactor cavity, submerging the reactor vessel. The concept is based on the idea that the lower head, cooled externally, will be able to arrest the downward relocation of a degraded (melting) core. The related issue before us, then, is whether lower head integrity can be maintained subject to the thermo-mechanical loads created during such a situation.

These loads are created because of the presence of the high temperature melt ($\sim$3000 K for the oxidic, $\sim$1800 K for the metallic) on the inside. The mechanisms leading to such melts can span a wide range of behavior, from that associated with the initial portion of the relocation, through a series of intermediate states, to a final quasi-steady state, where essentially all the core materials have been relocated and are found on the lower head. Correspondingly, the process is initially dominated by forced convection, eventually reverting through a series of mixed regimes, to a purely natural convection one. Lower head integrity can be compromised by meltthrough, or by a combination of wall thinning and mechanical loading (including any internal pressure and/or thermal stresses developed as a result of the heating on the inside and cooling on the outside) that can cause structural failure.

In addition, mechanical loads can be created due to thermal interactions of the melt with any coolant present in the lower head. Such contact can arise either during the core relocation process, or later on if, upon regaining injection capability, water was to be supplied on top of the molten pool in the lower head. Of particular concern in this respect are energetic interactions, also known as steam explosions, especially in the relocation regime as it is capable of setting up conditions for "premixed" explosions.

The overall problem, as described above, is depicted in Figure 1.1. This figure also introduces the terminology to be used for the various loads, failure criteria, and corresponding loading "regimes." There are three such regimes. The "thermal regime" constitutes the subject of this report, and this portion of Figure 1.1 will be taken up again in the next chapter. For now, suffice it to say that: (a) $q_w(\theta)$ and $\delta_w(\theta)$ denote the heat flux through, and wall thickness of, the lower head at any angular position θ (see Figure 1.2); and (b) integrity is to be assessed by comparing these "load" values with corresponding failure criteria; that is, the critical heat flux, $q_{CHF}(\theta)$, and the minimum wall thickness, δ_F needed to ensure structural integrity. The other

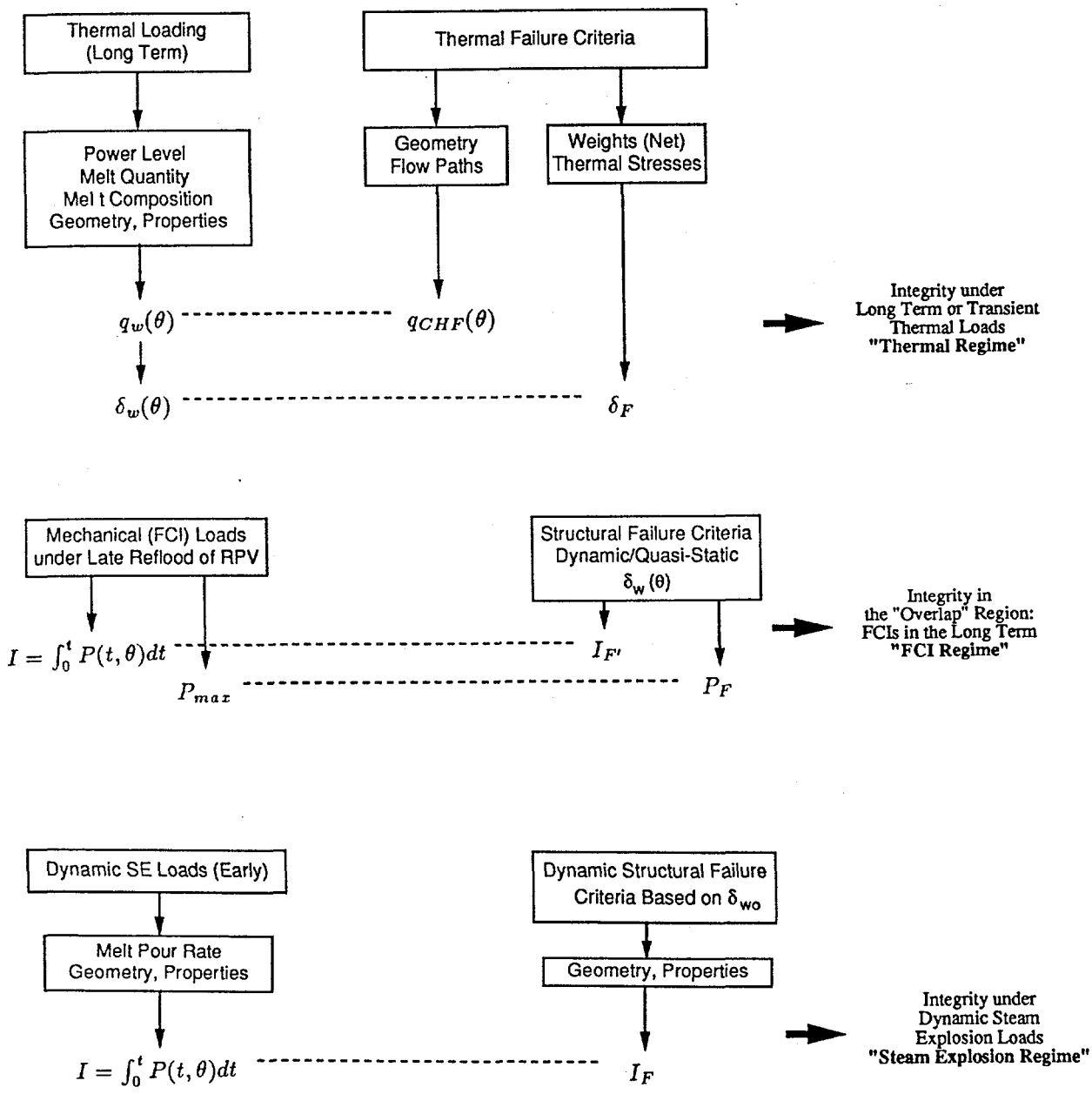

Figure 1.1. An overall view of the in-vessel retention issue.

two regimes in Figure 1.1 refer to the consequences of melt-coolant interactions, and they are addressed in a separate report (Theofanous et al., 1996).

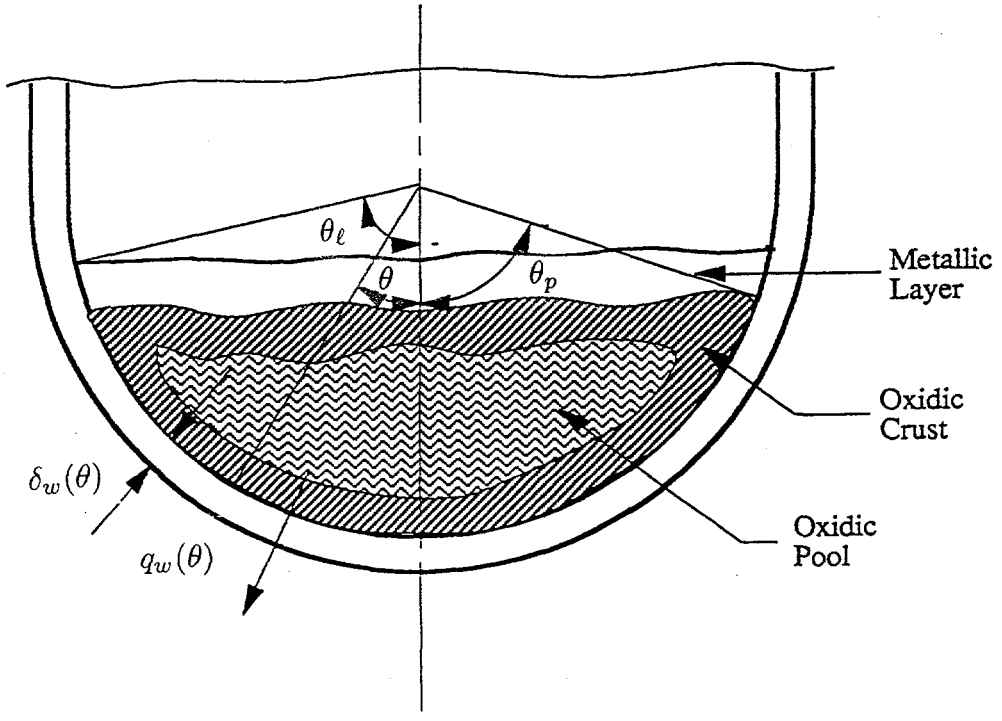

Figure 1.2. The basic geometry and nomenclature of in-vessel retention in the long-term, natural convection-dominated, thermal regime.

Briefly however, a key distinction (that gives rise to the subdivision of melt-coolant interactions into two regimes) with some bearing on the present effort needs to be made at this time. Namely, that energetic interactions can be of concern mainly in premixed explosions, (melt and water intermixed at coarse scales) as they might arise, for example, during the early stages of the core relocation, while interactions in a stratified configuration, concerning late water injection, are relatively benign. The key implication then is that integrity in the potentially energetic "Steam Explosion Regime" can be assessed against the full lower head capability (normal wall thickness), while in the benign "FCI Regime" any wall thinning, as a result of the thermal loads considered in the present report, must be taken into account. The other point made in Figure 1.1 is that due to the reduced wall structural capability in the FCI Regime, the static (or quasi-static) primary system pressure rise (to a peak pressure P_{max}) as a result of the steam produced, but not immediately vented, in the melt-coolant interaction might also have to be considered against a failure level, P_F, consistent with wall thickness, $\delta_w(\theta)$, and prevalent thermal stresses. Finally, in both melt-coolant interaction regimes, the main structural consideration is indicated

in Figure 1.1 in terms of the delivered impulse, I, against the failure criteria I_F and $I_{F'}$. This is illustrative only of the key global consideration; the actual assessment is likely to require additional details, such as the space-time distribution character of the loads.

So far, the subject has been approached only from the standpoint of the Thermal Regime in the long term, and all this work is relatively recent. The technical feasibility of the idea was first demonstrated for the Loviisa nuclear power plant, a Russian VVER-440 in Finland (Theofanous, 1989). This reactor is equipped with a Westinghouse ice condenser containment, and the cavity design happens to be, both in size and location, subject to flooding by the ice melting during the course of any severe accident. Thus, in-vessel retention formed the cornerstone of severe accident management in Loviisa (Tuomisto and Theofanous, 1994), and a related research program has been going on for the past several years (Kymäläinen et al., 1992; Kymäläinen et al., 1993). The complete assessment, representing the culmination of these efforts, has been submitted recently to the Finnish regulatory authority, STUK, (Kymäläinen, 1994). [[Approval was obtained in November 1995.]]. The present effort for an AP600-like design evolved in close relation to this Finnish work, including the sharing of some facilities and personnel (Theofanous et al., 1994a; Theofanous et al., 1994b). More recently this informal bilateral effort has been expanded to a formal agreement to include the Italian utility ENEL and the Electric Power Research Institute (EPRI) for the purpose of furthering the confirmatory basis of the current assessments and extending the application to larger reactor designs.

Independently, the idea of in-vessel retention has been pursued also by Henry and co-workers (Henry et al., 1991; Henry and Fauske, 1993), by Hodge (1991), and it has been critically examined by Park and Dhir (1991), Park et al. (1992), and Hawkes and O'Brien (1991). Interest around the world developed rapidly; a number of new research programs are in place; and a CSNI-sponsored specialists meeting on the subject took place recently in Grenoble, France. The summary of this meeting, prepared for the CSNI by the participating experts, provides the most recent and comprehensive status report on the subject (CSNI, 1994). More detailed reviews of the technical issues involved, and of the various experimental programs worldwide, also have been prepared by groups of experts for the CSNI (Okkonen, 1993; Rougé and Seiler, 1994). By virtue of this large, international activity the problem can now be considered to be ripe for decisive steps, such as those needed in the regulatory context, toward resolution. This is the intent of the present document. It is important to emphasize, however, that such a task must be approached on a reactor-specific basis—the design of interest here is that of the Westinghouse advanced passive design: the AP600.

This report consists of six main technical chapters and a large number of supporting appendices. Two chapters (3 and 4) address the failure criteria: the q_{CHF} and δ_F, as identified in Figure 1.1 already, while the remaining four contain the development of the thermal loads.

Namely, Chapters 5, 6, and 7 address the long-term natural-convection-dominated regime, while Chapter 8 is devoted to the consideration of forced convection effects. The overall aim of these chapters and their interrelations are explained as a part of the overall approach and methodology in Chapter 2. The report comes to an end with the conclusions and recommendations presented in Chapter 9.

2 PROBLEM DEFINITION AND OVERALL APPROACH

We begin with the basic assumptions that if core degradation takes place, the primary system will be depressurized and the lower head will be fully submerged in cavity water prior to the arrival of core debris on the lower head. Further, we assume that the water level in the cavity would be maintained indefinitely. Detailed consideration of these inherent aspects of the AP600 design are beyond the scope of this report, but the design attention given to the assurance of their validity is summarized in Appendix M. Their consequences can be listed as follows:

(a) Prior to being exposed to the melt the lower head is quenched down to the saturation temperature of water at ~1 bar: ~100 °C.

(b) In the absence of significant primary pressures, only a very small fraction of the lower head thickness is needed to support the dead-weight loads—thermal stresses and creep are the primary failure mechanisms to be considered instead.

(c) With the lower head fully submerged, the outside surface will remain in nucleate boiling (at ~100 °C) provided the critical heat flux is not exceeded at any point on it—a significant aspect of this requirement is that the thermal insulation allows sufficient flow paths for water to flow in and vapor to escape. The design of the thermal insulation for the AP600 has not been finalized yet, but as discussed in Appendix K, no difficulties in principle are anticipated.

Additional attractive features of the AP600, relative to this accident management strategy, are that its lower head is free of any penetrations, and its core power density is rather low.

To predict the thermal loadings on the lower head in all their detail, one would need the complete sequence of thermal states of the core and other internal structures throughout the core degradation and melt relocation processes. Rather than getting immersed, and perhaps lost, in such details, our approach is based on the identification of certain dominant features of these complex scenarios, and the detailed study of the loads in certain well-defined material and thermal state configurations. Our aim is to thus envelop the behavior, with regard to loads, and we will argue that this indeed has been achieved. Quantification of uncertainties will be emphasized in the detailed analysis carried out for each of these representative, enveloping configurations. The overall philosophical/methodological approach follows the risk oriented accident analysis methodology (ROAAM), which is described in Appendix A (see also Appendix A of DOE/ID-10541 by Theofanous et al., 1996). The scenario-independence stated above, and explained below, will be recognized as a Grade B approach, which is desirable in realizing the high confidence assessment sought here. This approach is conservative, but not unduly so, and it is consistent with the existence of a wide range of bifurcating behavior possible in such phenomenologically complex situations.

In the same vein we restrict our attention to scenarios in which failure to supply coolant into the reactor vessel persists indefinitely.[a] This is clearly a limiting case, especially in light of the recovery that took place in Three Mile Island, Unit II (TMI-2). The unexpected arrest of lower head heatup and eventual quenching was key to the survival of the vessel (Strickler et al., 1994; Turland et al., 1993), and it is currently pursued mechanistically as yet another potentially important approach to arresting a severe accident in-vessel (Henry and Dube, 1994). [[Still, for another perspective on the likelihood of passive reflood in AP600, and its effect on the accident scenarios and failure margins, see Section 4.4 of DOE/ID-10541.]]

The basic geometry can be represented in rather general terms in the manner shown in Figure 2.1. It consists of the lower head with some of the core debris on it, the rest of the reactor pressure vessel not in direct contact with core debris, and the core barrel, the reflector, and the core support plate, with any remaining core debris on it, as the key internal components. This figure also indicates the various pathways for the flow of thermal energy generated by radioactive decay processes within the core debris. These energy flows occur in accordance with the driving potential (temperature differences) and corresponding resistances. We have a strongly coupled problem here in that any imbalance between production and dissipation [[heat input and heat loss]] is accommodated by an increase in the driving potential which, in turn, gives rise to phase change (heat sinks) and convective losses either by relocation or by enhanced natural convection.

Considering the natural convection process, in this context, first, the thermal load to the lower head is maximized when:

(a) The debris pool has reached a steady thermal state,

(b) The heat generating (fuel) debris volume has been maximized, and

(c) The thermal resistance along the upward thermal radiation path has been maximized.

Indeed, for any given volumetric heat source, steady state implies that all internal heat sinks have been eliminated (melt-out of steel structures in the lower plenum), and that the pool temperature reached the highest value, as needed to exactly balance production by natural convection to the boundaries (see also Chapter 6). What occasionally has been mentioned as a slow approach to steady state is really attributable to the thermal capacitance of the pool rather than to unsteadiness in the natural convection process. In particular, in Appendix D we demonstrate that boundary layer effects dominate, so that the behavior of such pools is readily predictable even under non-stationary conditions. What this means is that thermal loads to the pool boundaries throughout the time period of a heat-up transient are bounded by the thermal loads in the final steady state.[b] The effect of debris volume (item (b) above) is due primarily to the reduction in surface-to-volume

---

[a] However, the structural loading implications of coolant supply, late in the retention scenario, is considered in the "FCI Regime," as noted above (Figure 1.1).

[b] [[But as discussed in Chapters 5 and 7 and Appendices O and P, the focusing effect due to a "thin" metal layer on top must be considered separately.]]

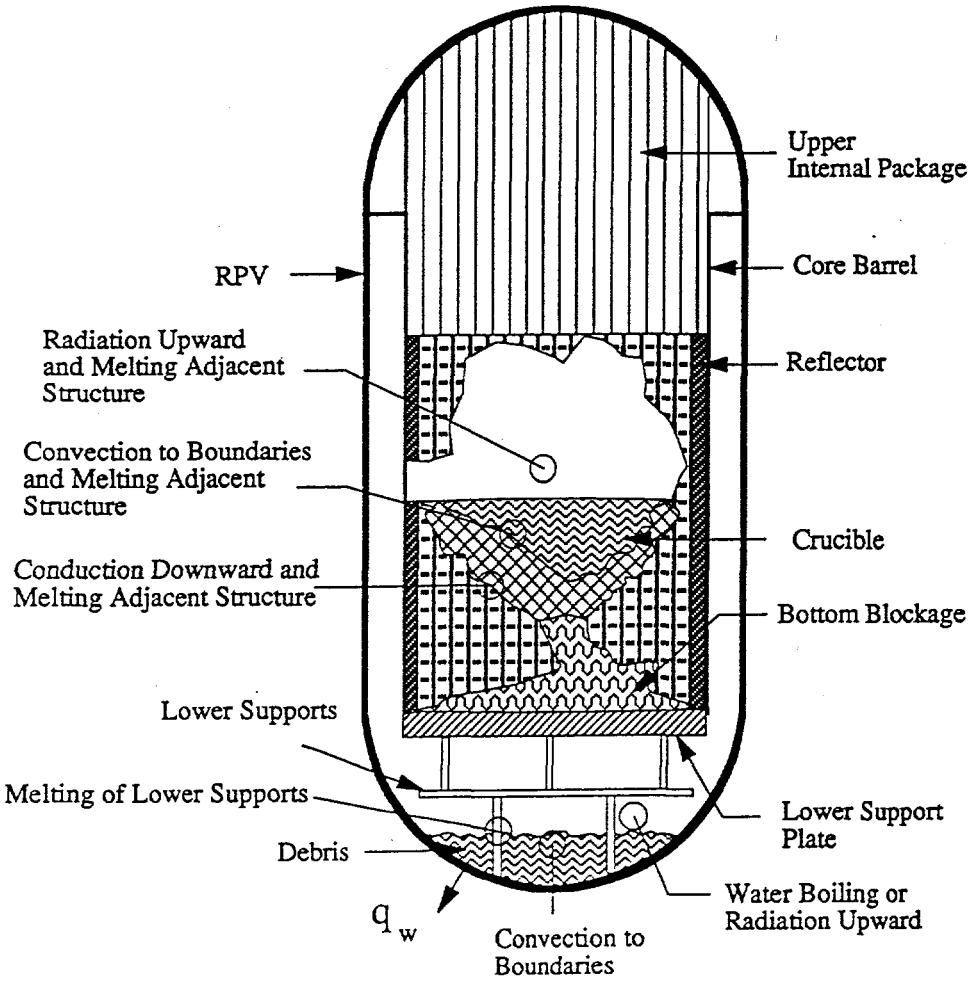

Figure 2.1. Material configuration and heat transfer processes at an intermediate state of the melt progression—after the initial, major relocation event, and before the attainment of a final steady state.

ratio as the pool level rises in a hemispherical geometry. Finally, the effect of the thermal resistance along the radiation path is straightforward—as the resistance increases the metal layer must reach a higher temperature to reject the same amount of heat, which causes an increase in the thermal loading to the vessel walls.

Thus we arrive at the first configuration appropriate for detailed examination and quantification. It is schematically illustrated in Figure 2.2, and its key elements can be listed as follows:

(a) All the core debris is contained, as either a solid oxidic crust or a molten oxidic pool, at steady state in the lower head.

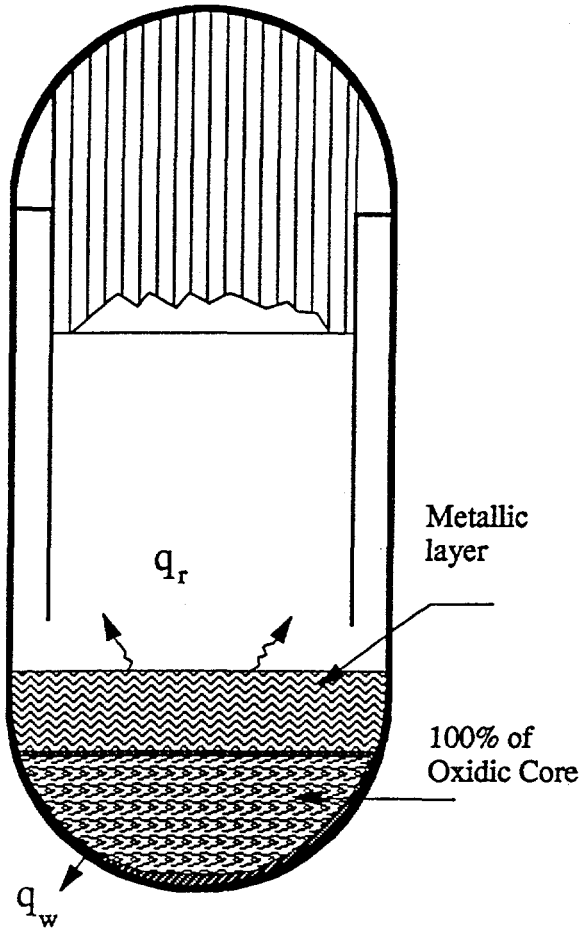

Figure 2.2. Materials configuration in the natural convection, steady state, extreme.

(b) A molten steel layer on top of the crust of the oxidic pool, made up of all the "light" components of the core region, the reflector and core support plate, at least a portion of the core barrel, as well as all lower (plenum) internal structures.

In Chapter 7 we will demonstrate that the incorporation of the structural elements listed under item (b) above into the molten steel layer is a necessary consequence of the existence of a molten pool of significant size in the lower plenum.

This configuration is of fundamental significance in assessing the problem at hand, not only because it bounds all intermediate states, but also because it represents the final state that would actually be realized in any in-vessel retention scenario. [[See also Appendix O.]]

The bounding nature of the configuration described above could be violated only in the presence of significant forced convection effects. Such effects can arise as core debris relocates

into the lower plenum, throughout the core degradation sequence, and most notably so during the major, initial discharge. This discharge would be expected to occur upon failure of a core-internal crucible that forms as a consequence of the melting–freezing phenomena—melting in the inner, higher power density region, and freezing as the melt relocates in the outer, colder boundaries. As it happened in TMI-2, the tight PWR bundle geometry favors the formation of such internal crucibles and the accumulation of significant melt quantities in them prior to their failure. [[The explanation for this TMI-2 behavior was first given by Epstein and Fauske (1989).]] In the AP600 such behavior is further favored by the bundle inlet geometry and the solid zirconium slug in each pin in the entrance region—an additional heat sink—and by the substantial steel reflector component that surrounds the core inside the core barrel. These, together with the thermal load distribution at the boundaries of a volumetrically heated pool, as discussed in Chapter 5, guarantee that in the AP600 failure will occur at the core side and that the initial discharge will involve a sizeable fraction of the core [[something like 30%]] (Sienicki and Theofanous, 1995). [[See also Chapter 4 of DOE/ID-10541.]]

Clearly, then, this is the second configuration of major interest for thermally loading the lower head. It is illustrated in Figure 2.3, and involves a "wall jet" released from near the top of the molten core pool, through the downcomer, and into the lower plenum. Subsequent to this initial release, melting and relocation occur in a much more gradual fashion, and melt and crusts already on the lower head further reduce the impact of these forced convective effects. Thus we can see that this second configuration provides an appropriate bound for all convective effects as they are found in the intermediate core degradation states.

To summarize, we have identified two specific configurations (as described by debris mass and thermal state), one dominated by natural convection and the other by forced convection and impingement effects. We take the position that these configurations bound the thermal loads on the lower head with respect to any other intermediate state that can reasonably be expected in the time interval between, and including, the initial major relocation event and the final steady state where all debris is contained in the lower head. The terms "natural convection" and "impingement" will be used to describe these two extreme thermal loading configurations. They are covered in Chapters 5 through 7 and Chapter 8, respectively.

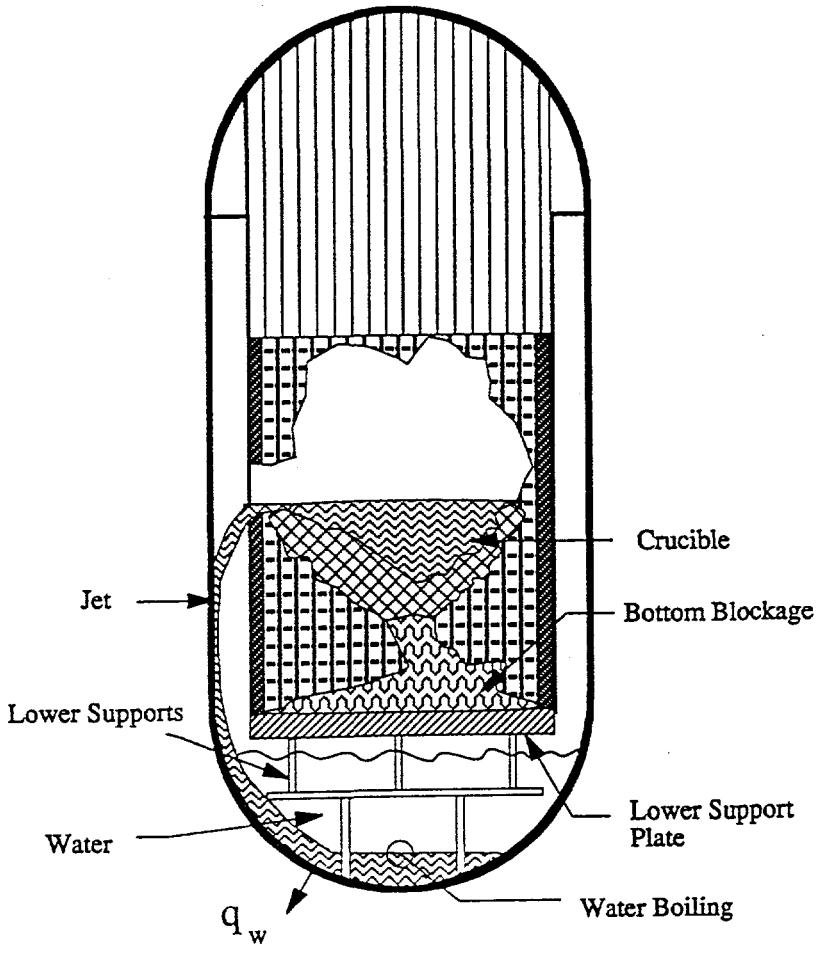

Figure 2.3. Materials configuration, in the forced convection, jet impingement extreme, associated with the major core relocation event.

3 THERMAL FAILURE CRITERIA

The principal and, as we will show in the next chapter, most limiting failure mechanism of the lower head is the boiling crisis (BC). It occurs when the heat flux through it exceeds the critical heat flux (CHF) at the same location, and it results in a sudden transition of the flow regime from nucleate to film boiling. Film boiling is characterized by considerably lower heat transfer coefficients, and as a consequence the surface temperature rises to considerably higher values in order to accommodate the imposed thermal load from the inside. For example, for a heat flux of 400 kW/m^2 the surface temperature must rise to $\sim$1200 °C in saturated water, while subcooling can only modestly moderate this rise (i.e., $\sim$1100 °C for 20 °C subcooling). At such temperatures the steel loses essentially all of its strength, and it becomes susceptible to creep, and structural instability, even under the modest mechanical loads of interest to this problem. Moreover, the thermal gradient in the wall at the same flux level is 160 °C/cm which, considering a wall liquidus of 1300 °C (see Chapter 7) indicates a wall thickness of only 6.0 mm. As we will see in Chapter 6, heat fluxes on the lower head can considerably exceed the 400 kW/m^2 level considered in the above example. By contrast, nucleate boiling heat transfer coefficients are so high that any flux level, up to the CHF (but prior to BC), can be accommodated with only a few "tens" of degrees in wall superheat (temperature above the coolant saturation temperature). Nominally, therefore, in nucleate boiling the outer surface of the lower head is at $\sim$100 °C.[a] This is very significant for the structural stability of the lower head, and it is taken up again in the next chapter. In the remainder of the present chapter our task is to discuss the boiling crisis and come up with reliable estimates of the heat fluxes necessary to cause its occurrence.

The key features of the problem can be seen with the help of Figure 3.1. Considering first the "local" aspects, we will note that the downward-facing geometry lends itself to the formation of a two-phase boundary layer that is "squeezed" upon the heating surface by gravity forces. This "squeeze" is moderated by turbulent mixing (including interfacial instabilities and entrainment) as buoyancy drives the steam past the heating surface and the surrounding water. The balance between these two mechanisms is quite different in the various regions around the lower head. This gives rise to widely different two-phase flow regimes, and as a consequence, we can expect significant variations of the critical heat flux and perhaps even of the underlying mechanism(s) for it. For example, in the vicinity of the stagnation point ($\theta \sim 0°$) the vapor velocities are very low and the surface orientation, relative to the gravity vector, drives the maximum phase separation with the vapor "squeezed" up against the wall. We expect periodic formation of relatively large bubbles, growth, and escape. Under such flow conditions we can expect that boiling crisis will occur if the underlying thin liquid film dries out, within one such period, **and if** the surface temperature rises to high enough levels to prevent

[a] [[Note that the vessel wall will cool from the inside during depressurization of the reactor coolant system, so that nucleate boiling will occur without any delay when the lower head comes in contact with cavity water on the outside.]]

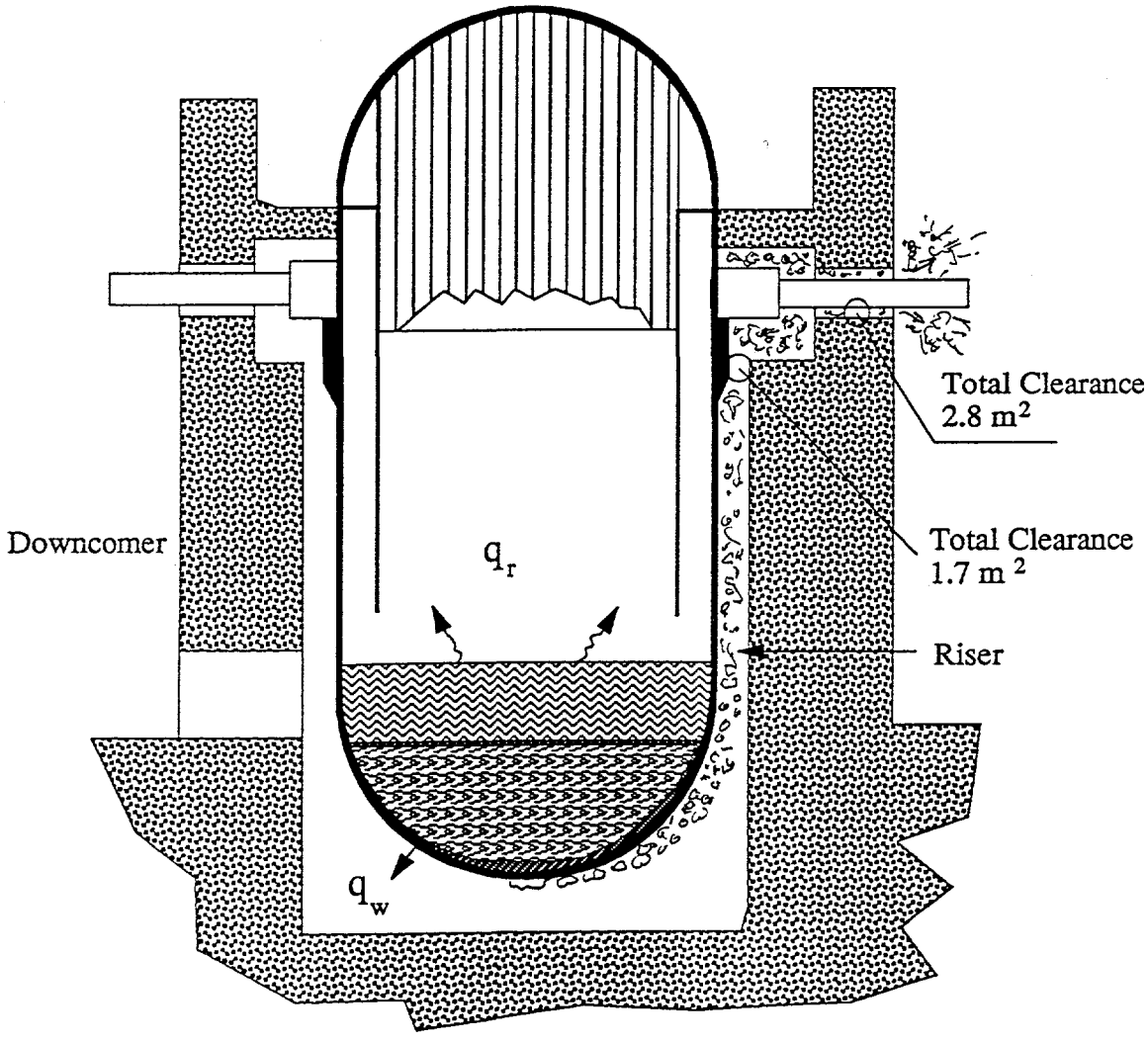

Figure 3.1. Key geometric features of cavity flooding and venting paths. Illustration of the two-phase boundary layer on the lower head. Thermal insulation not shown.

rewetting when the liquid rushes back-in following bubble escape. As a consequence, surface wetability (controlling the behavior of the thin film) and wall thickness (controlling the rate of heatup following the dryout of this film) should be important. Aspects that could affect the behavior of these bubbles, including any convection in the free-stream water (see global

behavior discussed below) and its subcooling, should also be important. On the other hand, near the equator of the lower head hemisphere ($\theta \sim 90°$), we expect that cumulative vapor generation from all the upstream positions will give rise to high vapor, and entrained liquid, flow velocities, and in addition, the vapor "squeeze" effect described above would be minimal in the near-parallel orientation of the surface to the gravity vector. As a consequence, we expect a highly turbulent two-phase flow within a relatively "diffuse" boundary layer. Correspondingly, the BC mechanism would be convection-dominated. However, phase separation and perhaps even capillarity may continue to have some bearing on the mechanism in this regime, as well. Evidently, intermediate (or mixed) mechanisms can be envisioned as we go from the stagnation region to the equator with the details of this transition region being strongly dependent upon the power (input) shape.

Let us turn next to the global aspects. In a fully-flooded cavity, as indicated in Figure 3.1, the gravity head would be ~7 meters, which corresponds to ~14 °C subcooling with saturated water at the top. The supply of this subcooled water to the cavity depends on any flow restrictions on the flow path, and on the gravity head developed due to the two-phase flow in the riser. Moreover, the availability of any subcooled water in the immediate vicinity of the heating surface would depend on the **local** mixing and flow patterns as described above. This coupling of the local to the global behavior is quite important in that it indicates a truly conjugate behavior. The situation is less so at a flooding level low enough to interrupt the natural circulation flow path; still, level swell is important in determining the extent of the cooled portion of the reactor vessel. Such partially flooded conditions are of limited interest only, as discussed in Appendix M; however, as demonstrated later on, the resulting "pool boiling" provides a low (conservative) estimate of the critical heat flux under fully flooded conditions. Back to a fully flooded condition, the key mechanism is void drift in the riser, and the void fraction distribution depends on the power input (including shape), the subcooling, and on the flow losses along the natural circulation path—especially on any inlet or outlet restrictions. The following clarifications need to be made: (a) power is also supplied along the riser section, it being the radiative heat flow conducted through the side wall of the reactor vessel; (b) in the AP600, as indicated in Figure 3.1, the flow path into the reactor cavity is wide open; and (c) key aspects of the flow geometry would be dictated by the thermal insulation design (and response in a severe accident) as discussed in Appendix K. In addition, the dynamics of the natural circulation loop, such as flow and pressure oscillations may be important (i.e., loop elasticity), especially on the bubble regime discussed above.

Mechanistically, these are behaviors unlike any CHF situations considered previously. Considering also the status of fundamental understanding in the extensively investigated problem of BC on a horizontal, upwards facing plate (Lienhard, 1994), we chose to pursue an experi-

mental approach **that faithfully simulates the reactor in all the key aspects of the phenomena involved.** Based on the above discussion, these key aspects include:

1. **Heater length scale and shape.** To properly represent the two-phase boundary layer behavior, especially in the intermediate region, we need a full-length geometry, including the correct curvature.

2. **Heating surface thermal inertia.** In the reactor, the lower head thickness could vary from its initial value of 15 cm (for most of the region), to a low value of a few centimeters due to thinning by melt attack near the equator (see Chapter 7). Therefore, a minimum of a few centimeters in heated thickness is needed to properly represent the thermal inertia.

3. **Power shape.** In conjunction with the above item 1, a correct power history in the upstream region is necessary to represent the two-phase boundary layer conditions in the reactor. In addition, the total power shape, including that in the riser, must be represented to simulate void distribution and natural circulation flow behavior.

4. **Heating surface wetability.** The reactor lower head is designed to be made of forged carbon steel (SA 508), machined to 200 r.m.s. mean roughness. Even though it is to be painted in situ, the paint might be expected to flake off in boiling water, and the exposed steel surface to be well-wetted. This surface condition must be confirmed and matched experimentally.

5. **Loop length scale and hydraulic diameter.** To properly represent subcooling due to gravity head we need a full-length loop ($\sim$7 m). The annular gap in the reactor is $\sim$20 cm, and a similarly large cross sectional length scale (diameter) is needed in a one-dimensional geometry to allow proper simulation of the vapor drift.

The ULPU facility was built to embody all of the above key characteristics, allowing, therefore, a full-scale simulation capability. The facility, experimental program, and results obtained are described in detail in Appendix E. One key aspect[b] discussed but not listed above concerns the detailed representation of the thermal insulation geometry, especially the inflow and outflow paths and hence of the loop flow and dynamic response. As discussed in Appendix K, this is because the design has not actually focused yet on this aspect of the thermal insulation performance under severe accidents. Our approach in this respect, therefore, has been to study a rather broad range of conditions (Configurations I, II, and III, as described in Appendix E). **Clearly, however, this is one restriction imposed on the conclusions of the report that will have to be revisited once the design is finalized.** The other qualification on the results available to date from the ULPU facility is that they were obtained in the well-wetting condition of an aged copper surface. We expect to confirm these results

[b] [[Both the thermal insulation design and a representative AP600 vessel wall material and finish, discussed in the remainder of this paragraph, are now covered in Appendices E.3 and E.4, as described in the addendum at the end of this chapter.]]

with a test section made to order, according to AP600 specifications, from one of the potential suppliers of the reactor pressure vessel—The Japan Steel Works plant in Hokkaido, Japan. This piece of steel is expected to be delivered for installation in the ULPU facility by November 15, 1994. It will be shipped and handled in a manner very similar to that normally used for reactor vessels, and we expect to have test results from it prior to the completion of the peer review of this report.

The ULPU experiments confirmed the flow regimes and the general point of view taken in our experimental approach as expressed above. Details can be found in Appendix E. Here, we present the main results as summarized in Figures 3.2 and 3.3. The results in Figure 3.2 were obtained in experiments carried out with a limited submergence and absence of natural circulation (pool boiling). As noted above, these conditions are of limited, if any, significance to the problem at hand, but the results provide interesting perspectives in comparison to those of Figure 3.3 obtained under almost full submergence (~6 m) and natural circulation. This Figure 3.3 is the result appropriate for quantifying the thermal failure criteria. From an evaluation of uncertainties, as discussed in Appendix E, we expect this result to be good within a few percent, so that CHF can be excluded outside a rather narrow range around it. In Chapter 7 we will see that the margins to failure are so significant that they totally dwarf this uncertainty in this failure criterion.

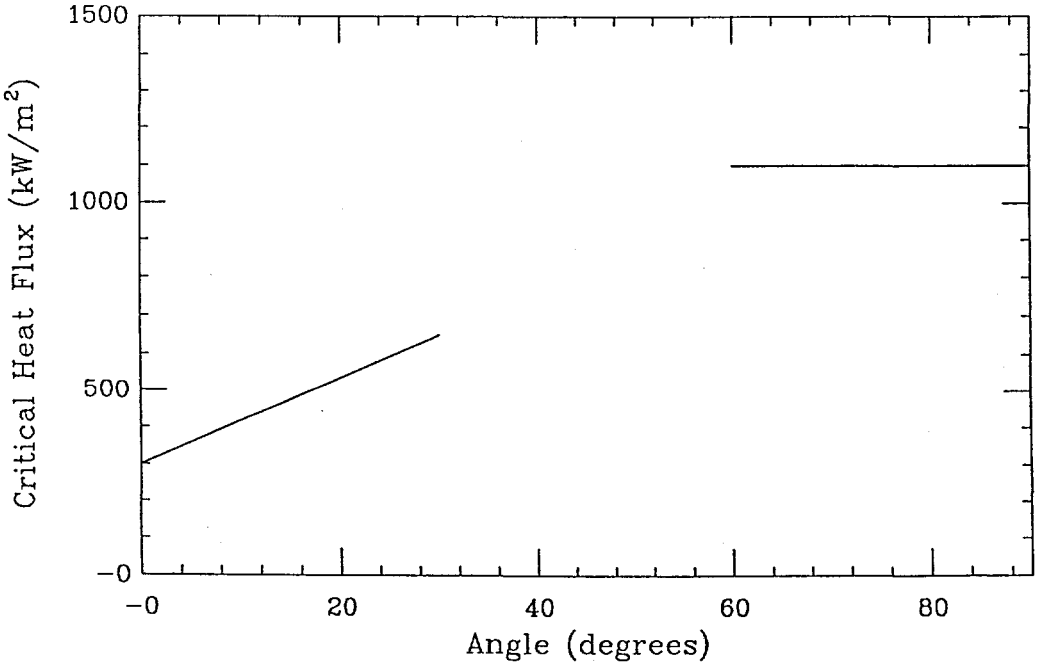

Figre 3.2. Critical heat flux as function of position on the lower head; from ULPU, in pool boiling.

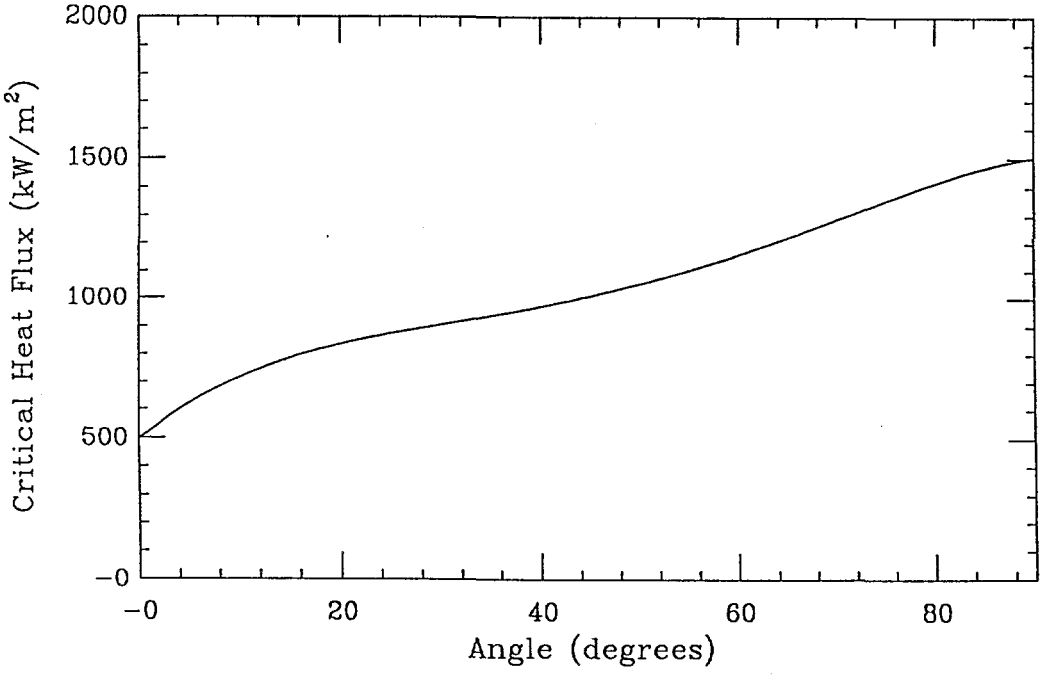

Figure 3.3. Critical heat flux as function of position on the lower head; from ULPU under full submergence and natural convection.

In concluding this chapter we would like to mention certain others' past and on-going efforts addressing CHF in relation to lower head integrity.

1. The CYBL experiment (SNL). A full-sized, stainless steel vessel with torospherical lower head of 1 cm thickness. Radiant heating applied internally (to the lower head) with peak flux capability of about 200 kW/m^2. Experiments showed persistent nucleate boiling up to this level of heat flux. This work was carried out for the DOE's Advanced Reactor Severe Accident Program as a complement to that in ULPU. For more details see Appendix F. It is interesting to note that the periodic bubble formation and departure observed in CYBL was found also in ULPU—about 2 Hz at 200 kW/m^2.

2. The FAI experiments (Henry et al., 1991; Henry and Fauske, 1993). These were carried out in a 32 cm diameter (outer) pipe cap, with thermite as the heat source, in a transient mode. Peak fluxes of $\sim$1 MW/m^2 were measured. The effect of reflective thermal insulation was assessed, both experimentally and analytically, and it was found to introduce no important limitation to coolability.

3. The SULTAN experiments (CEN, Grenoble). The test section consists of a long, straight channel in an adjustable orientation relative to the gravity vector. Experiments are in progress (Bonnet et al., 1994).

4. The Penn State experiments. These NRC-sponsored experiments involve steel hemispheres up to 30 cm in diameter (1/24- to 1/10-scale) and are on-going.

5. Other small scale work. This involves quite a few experiments with centimeter-scale heating surfaces, or very narrow channels, carried out primarily in connection with cooling of electronic components. This work is not relevant to the present problem and thus is not mentioned explicitly.

[[ADDENDUM TO CHAPTER 3]]

The experimental basis for the main result of this chapter—Figure 3.3 and Eq. (3.1), below—is now supplemented by two addenda to Appendix E, prepared simultaneously, and as a part of the responses to the first round of the reviewers' comments. The first addendum is provided as Appendix E.3. It covers the results of an extended experimental matrix in Configuration II with flux shapes that include those found in the sensitivity/parametric studies as well as variations thereof, and arbitrary variations of recirculation flow rates, obtained by throttling the inlet, to 50% of the normal ($\sim$130 gpm) flow rate, and to full stagnation. The results indicate that Eq. (3.1) is a robust conservative estimate appropriate for the evaluations performed in this report. The second addendum is provided as Appendix E.4. It covers Configuration III ULPU experiments, built in accordance with the thermal insulation design just completed by Westinghouse (see Appendix K). In addition, this set of experiments included the effect of a prototypic heating surface, i.e., reactor vessel grade steel with and without the normally employed paint. The results once more demonstrate the robustness of Eq. (3.1) and its applicatility for our purposes.

$$q_{cr}(\theta) = 490 + 30.2\ \theta - 8.88 \cdot 10^{-1}\theta^2 + 1.35 \cdot 10^{-2}\theta^3 - 6.65 \cdot 10^{-5}\theta^4 \quad \text{kW/m}^2 \qquad (3.1)$$

4 STRUCTURAL FAILURE CRITERIA

In this chapter we examine the behavior of the lower head under thermal loads severe enough to cause extensive wall thinning, and we show that structural failure cannot occur unless there is boiling crisis. In other words, we will endeavor to demonstrate that the thermal failure criteria discussed in the previous chapter are both necessary and sufficient for assessing lower head integrity. Under the low pressure conditions of interest here there are sufficient margins in the consideration to allow a basic-principles approach while avoiding the actual determination of structural failure. Other situations involving higher pressures may require detailed numerical simulations of the type illustrated in Appendix G, and for them, the so-derived structural failure criteria may become more limiting (than CHF). The purpose of including Appendix G is, in addition to this illustration, to provide further perspectives confirmative of the basic-principles approach pursued in this chapter.

We have already shown in the previous chapter that boiling crisis is a sufficient condition for lower head failure. Now, we wish to demonstrate that this is also the necessary condition; that is, unless BC occurs, there can be no failure. For this purpose it is adequate to demonstrate that a CHF-limited wall thickness is sufficient to support the lower head and its contents. The CHF-limited wall thickness can be readily obtained from Figure 3.3, using the steel thermal conductivity referenced together with other useful properties in Appendix L, and a steel liquidus temperature (see Chapter 7) of 1300 °C (1573 K). The result is shown in Figure 4.1. The critical region is around $\theta \sim 90°$, and the integrity of this region must now be examined in detail. Interestingly enough, this is the region revealed to be the most limiting from the thermal margins point of view as well (see Chapter 7).

The physical situation is illustrated in Figure 4.2, and the following key points can be made regarding the state of stress in the segment shown.

1. Deadweight and Buoyancy. These two forces nearly cancel each other out. Take, for example, a melt layer 2 m deep, in the lower head, and a vessel submerged up to the hot leg nozzle elevation (~7 m from the bottom of the lower head). With a melt density of 8000 kg/m^3 we have a melt weight of 134 tons, a lower head weight of 29 tons, and a buoyancy force of 92 tons due to the effective hydrostatic head of 6.33 m on the lower head outer surface. The net force of 71 tons ($7 \cdot 10^5$ N) would require a wall thickness of 0.15 mm to reach the yield stress of this steel at full strength (355 MPa). In Figure 4.2 we can see that this region of full strength (i.e., below 900 K), under the heat flux condition of interest is 1.1 cm, and thus able to comfortably carry the applied stress.

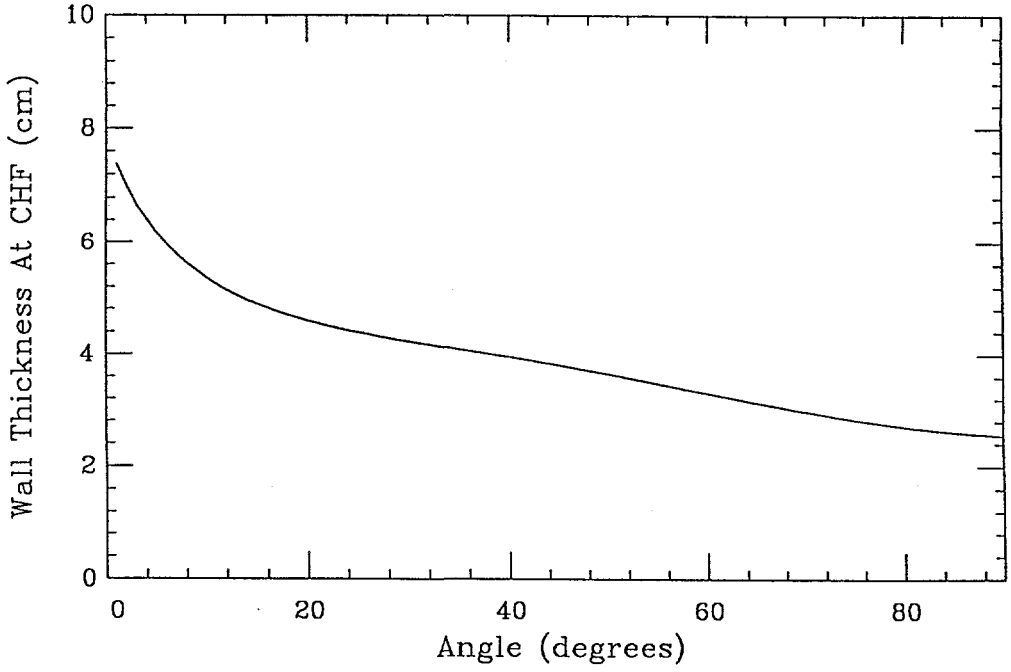

Figure 4.1. Maximum wall thicknesses allowed to accommodate the critical heat fluxes at various angular positions around the lower head, subject to 400 K and 1573 K temperature boundary conditions at the outside and inside boundaries respectively.

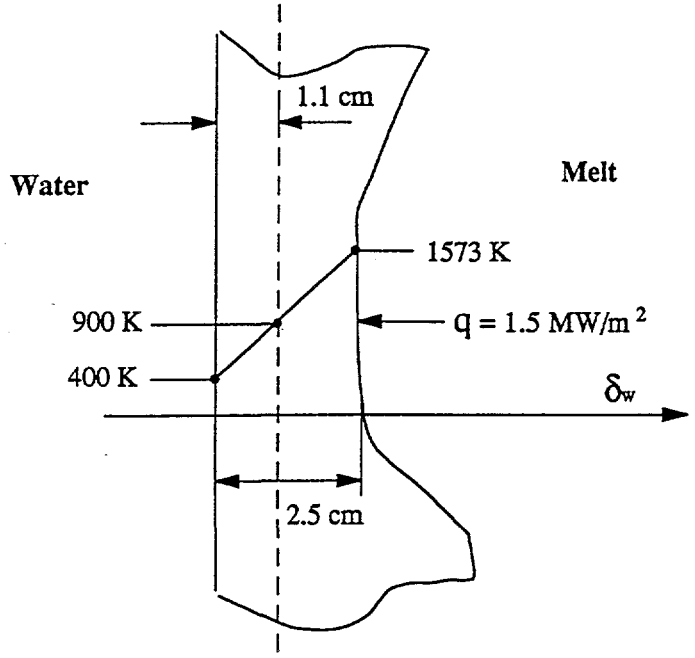

Figure 4.2. Illustration of conduction-limited wall thickness, and of the full-strength outer region ($T < 900$ K), under an imposed heat flux of 1.5 MW/m^2.

2. Thermal Stress. As a result of the steep temperature gradient, the inner region is in compression, and the outer region is subject to tension at levels that, on an elastic basis, would significantly exceed the yield stress. A basic characteristic of thermal stresses is that they are self-equilibrating, i.e., in the absence of other stresses, thermal stresses must integrate to a net zero force on any freebody section of the structure. Material plasticity would cause the temperature stresses to relax and redistribute to a profile that is bounded by the temperature-dependent tensile strength of the materials. In order to satisfy the self-equilibrating property, the thermal stress must redistribute to a profile that exhibits high tensile stress over a relatively narrow external (colder) portion of the vessel wall and a low compressive stress on the remainder of the wall. This thermal stress redistribution, when superimposed on stresses from other sources such as the differential internal pressure discussed under item 1 above, would result in the enhancement of the tensile stresses with the final stress distribution remaining at or below the temperature dependent flow stress of the material. Thus, the load carrying capacity of the vessel will be governed by the outer thickness of the wall that is under tension. Below, we will show that for the conditions of this problem, this outer region has a thickness of about one-fifth the wall thickness; that is, it is ~5 mm thick for the limiting case considered in Figure 4.2. It is easy to see that this elastically stressed portion of the wall is more than sufficient to carry the stress levels due to the externally imposed forces (as discussed under item 1).

In carrying out the quantitative demonstrations indicated above, we take a three-step approach. The first is idealized enough to allow an analytical result showing the basic features and extent of the tensile-stress region. We assume a linear dependence of the yield stress on temperature and a perfectly plastic behavior. The second step makes use of a simple numerical model to show the relief mechanism described above and the load carrying capability of the outer tensile region. In Appendix G—finally, the third step—we can find that incorporation of creep confirms these results and that structural integrity is assured even under relatively significant primary system pressure. [[A detailed evaluation of ductile tearing has also been made, as described at the end of this chapter.]]

To illustrate the first step let us consider the thermal stresses in a cylindrical wall subject to a linear temperature distribution with a total temperature difference across it of magnitude ΔT. For a wall thickness, δ_w, small compared to the vessel radius, the analytical solution for the stress distribution (the azimuthal, σ_θ, axial, σ_z, and radial, σ_r, stresses) in the elastic region can be simplified to:

$$\sigma_\theta = \sigma_z \sim \frac{\beta' E \Delta T}{2(1-\nu')} \left\{ 1 - 2\frac{r}{\delta_w} \right\} \qquad \sigma_r \sim 0 \tag{4.1}$$

where β', E, and ν' are the linear thermal expansion coefficient, Young's modulus of elasticity, and the Poisson ratio, respectively, and r is the distance from the outer boundary. The resulting

equivalent (von Mises) stress is shown in Figure 4.3. Note that because the response is still elastic the midpoint is at zero stress and a region around it is subject to a low stress level. As T and ΔT increase the stresses in the extreme outer and inner regions reach yield, and assuming a perfectly plastic behavior, the situations obtained would be as illustrated in Figure 4.4. Clearly, the size of the elastic core decreases as the applied T and ΔT increase, and the elastic stress gradient increases with it.

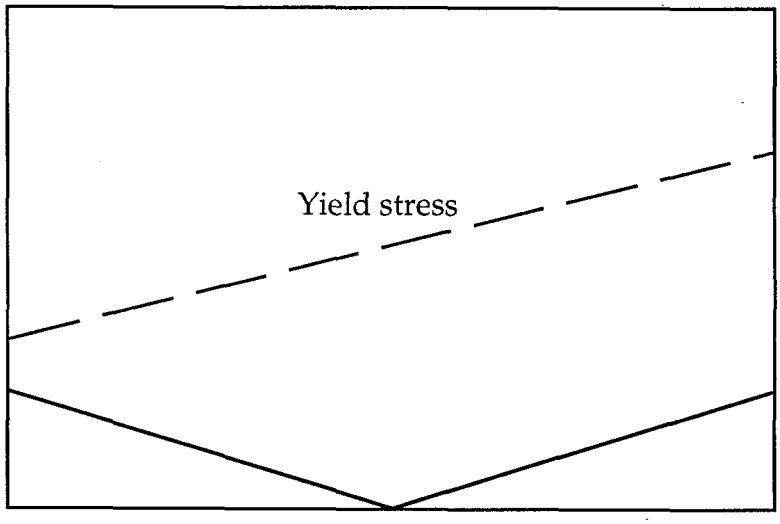

Figure 4.3. Equivalent (von Mises) stress distribution due to temperature gradient across the thickness of a vessel wall. Note that the yield stress is assumed to be linear with temperature.

For the second step, we make use of a finite element model of the whole reactor vessel (see Figure 4.5) Calculations were carried out with the code ABAQUS (version 5.2) and material properties accounting for the variation of the yield stress with temperature according to the recent data of Chavez et al. (1994). These data (for steel SA 106B, which is quite similar to that specified for the AP600) extend to 1150 K, and they were extrapolated linearly to zero at the steel liquidus (~1500 K). A wall thickness of 5 cm was taken in the calculation. The result is shown in Figure 4.6. Again, the tensile zone, which consists of an elastic core and a plastic outer region add up to about one-fifth of the wall thickness. The effect of yield variation with temperature is to shift this tensile zone toward the outside while much of the inside is seen to have relaxed to a near stress-free level.

In concluding this chapter we emphasize again that boiling crisis is the limiting failure criterion only at primary systems pressures near ambient (containment atmosphere). In fact, at

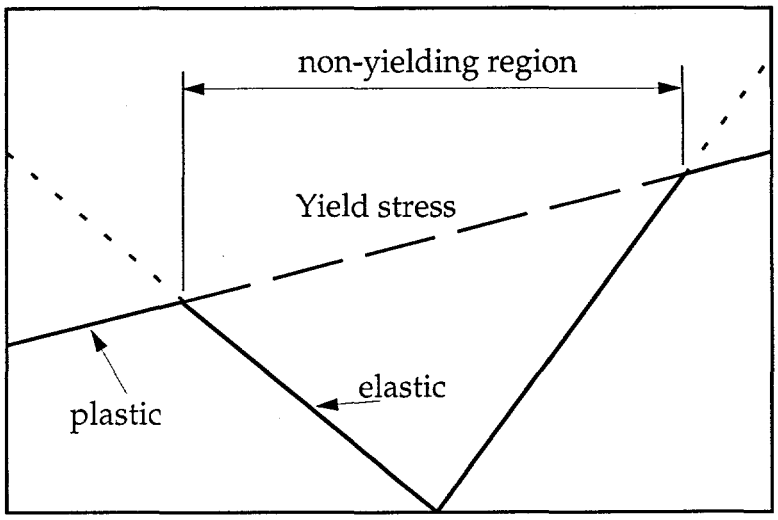

Figure 4.4. Equivalent stress distribution due to temperature gradient across the thickness of a vessel wall. The continuous line represents the stress distribution for elastic plastic behavior.

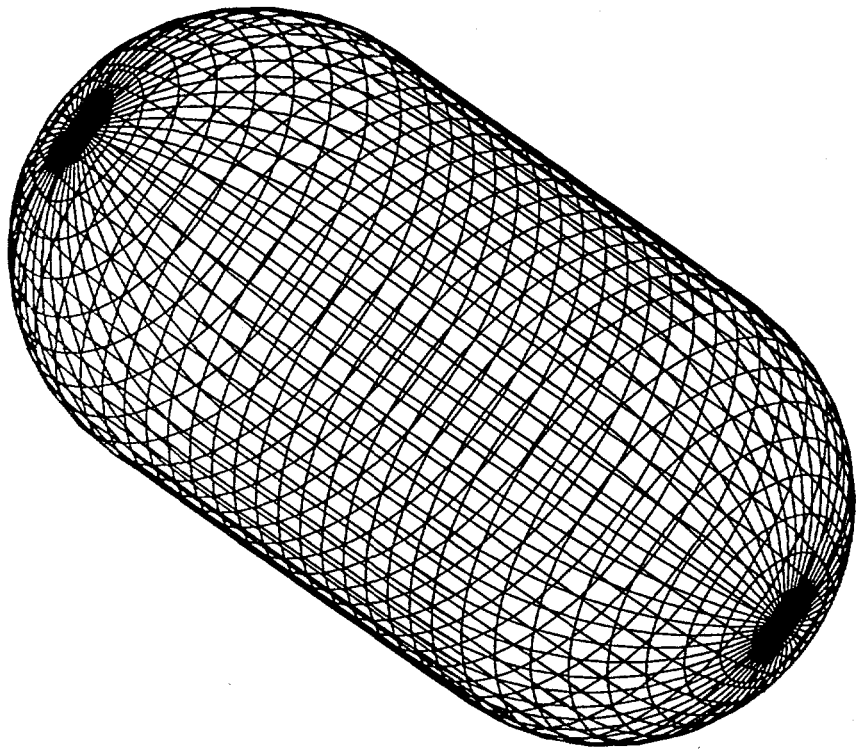

Figure 4.5. The finite element model utilized in the computations.

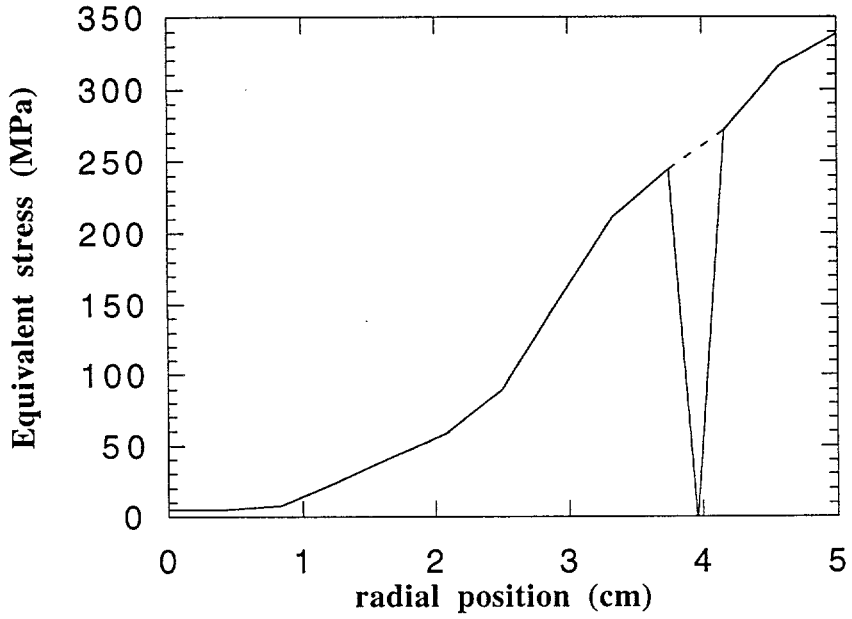

Figure 4.6. Equivalent stress distribution in the most critical section of the vessel from an ABAQUS calculation. Dashed line represents yield data at the temperatures corresponding to the various positions along the wall (from Chavez et al., 1994).

some higher pressure level we would expect that control passes over to structural failure criteria, for which the computational approach of Appendix G is appropriate and should be applied (with due consideration of uncertainties). Note that in this respect (of uncertainties) the present case is rather straightforward: boiling crisis is a conservatively limiting structural failure criterion. That is, structural failure margins are larger than margins to boiling crisis, which in turn are very large compared to uncertainties in this criterion (see Chapters 3 and 7).

[[ADDENDUM TO CHAPTER 4]]

CONSIDERATION OF DUCTILE TEARING

The purpose of this addendum is to address a question brought up by one of the reviewers (Nickell) about "ductile tearing" as a failure mode. The concern is about large, *local* deformations, and strains sufficient to cause tearing, brought about by the combination of the highly non-uniform loads (hydrostatically induced both internally and externally), wall thicknesses, and temperature distributions. As correctly noted by the reviewer, much more detailed nodalization

(than that utilized previously) would be needed to properly consider such local behavior. This was done here for the most extreme parametric case considered in Chapter 7 (the one illustrated in Figure 7.16). This does push the problem to the limit of thermal failure, and as we will see below, in terms of mechanisms, it has the greatest potential for the local deformations that are of concern here. The results show that a core of strong (below yield) material remains in the manner described previously in the report, leading to the conclusion that ductile tearing is not a feasible failure mode, in our case. Also the local maximum strains in the direction along the wall meridian (longitudinal bending) are below 7%, indicating margins to tearing everywhere.

Rather than the shell elements used previously, we now use "bricks" (which give more flexibility in the specification of the geometry) and rather than a full-vessel 3D model, we use an axisymmetric model of the lower portion (extending by 0.35 m into the cylindrical segment). Because the main part of this cylindrical segment remains cool and strong, it provides an effective isolation from the remainder of the vessel that is not modelled (this was tested by calculations). Also, this time we use the actual hydrostatic load distributions (of the melt pool on the inside and of the water pool on the outside), but numerical experiments demonstrated that their effect, compared to the thermal stresses, is negligible. The internal temperature and wall thickness profiles, as functions of the angular position, are shown in Figure 4.7. The temperature at the outside boundary was specified as 130 °C (nucleate boiling). The finite element model is shown in Figure 4.8. The grid is made of 31 nodes across the wall thickness at all angular positions. In the meridian plane, nodes are 0.1^o apart in the region of major interest (that of varying thickness plus segments of the thick parts connecting to it) and 2^o elsewhere. This corresponds to bricks that are 3.5 mm long and 1 mm thick in the highly-eroded portion of the wall, and 7 cm long, 5 mm thick in the intact portion. In the straight cylinder section, nodes are 5 cm apart in the vertical direction and the wall thickness is again divided into 30 elements. Change in elastic properties of the material with temperature is included, but perfect plasticity is assumed (strain hardening present in the actual material makes this a conservative assumption).

The results are depicted in Figures 4.9 through 4.14, focusing on the region of interest. The predicted deformation pattern, alongside with the undeformed grid, is shown in Figure 4.9, and it is as expected, forcing a longitudinal bending in the narrow region driven by the cumulative expansion of the lower part, while confined by the upper cylindrical portion. This bending subjects the outer wall material, at the "junction" between hot and thin segment to the upper cold and thick segment, to compression (see Figure 4.10), which in part compensates for the tension driven by the local thermal stresses. The axial stress component is thus strongly reduced, in turn lowering the equivalent (von Mises) stress. Consequently, the non-yielding region which under unconstrained thermal loading is *within* the wall, is now located on the outside. This

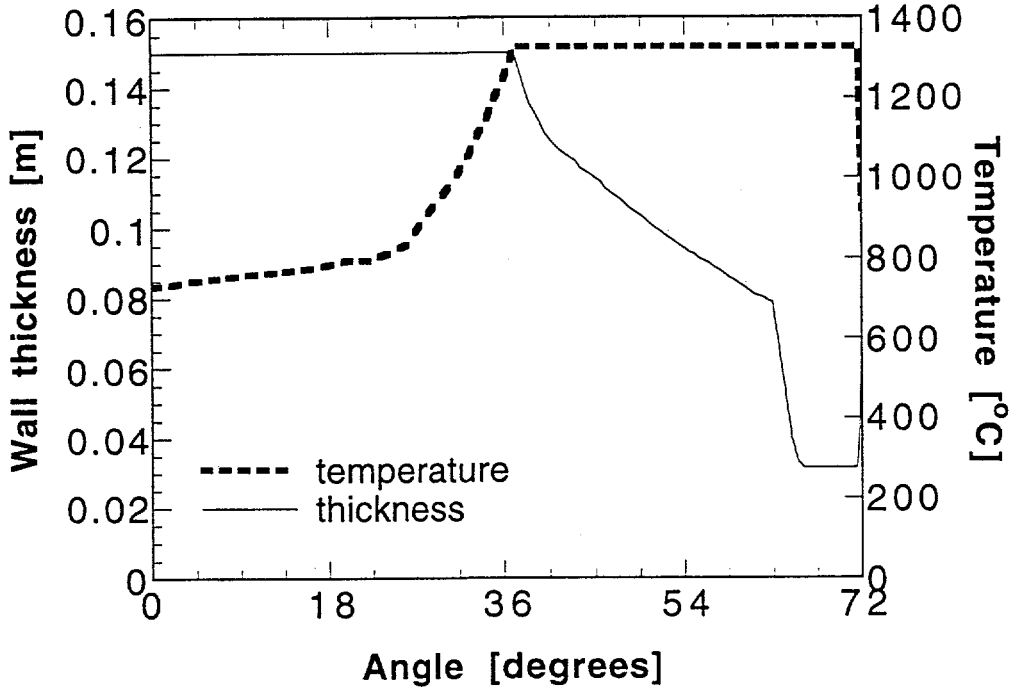

Figure 4.7. Inner temperature and wall thickness profiles used in the ABAQUS calculation.

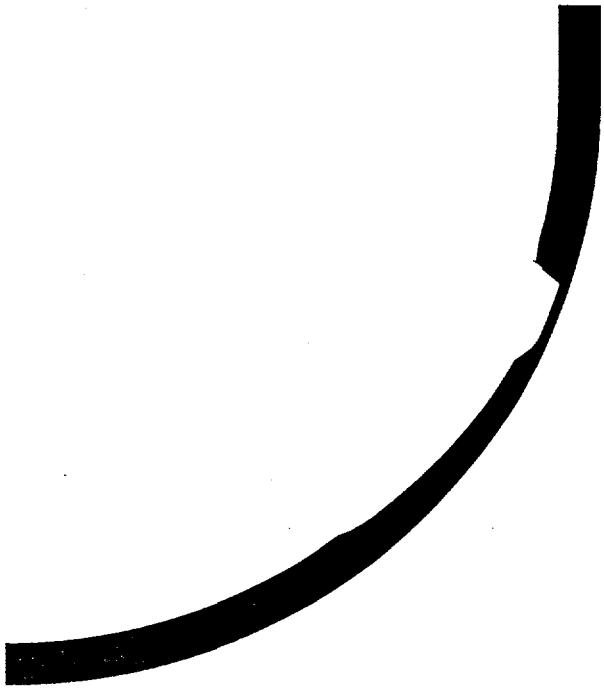

Figure 4.8. Finite element model used in the ABAQUS simulation.

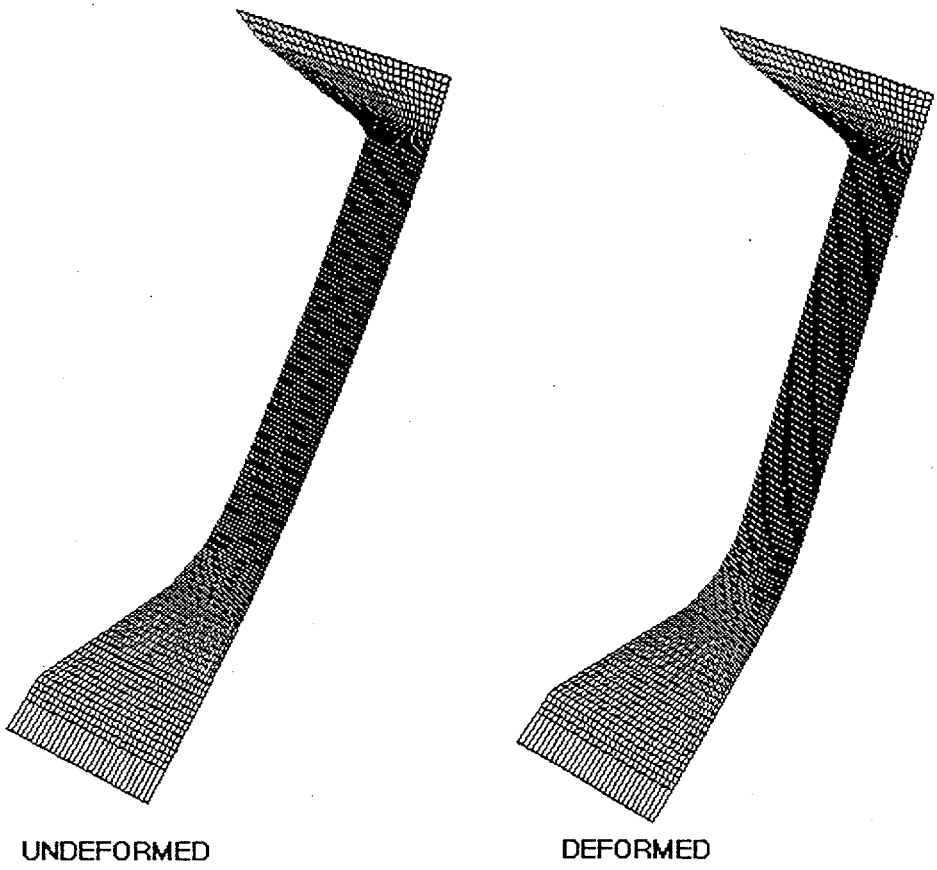

Figure 4.9. Undeformed grid (left) and deformation pattern after loading (right) in the region of interest.

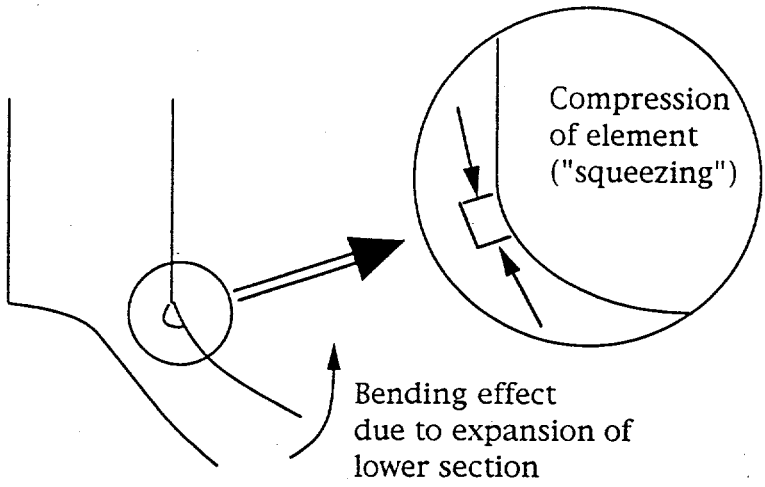

Figure 4.10. Axial stress relaxation due to longitudinal bending.

can be identified in Figure 4.11, depicting the map of the von Mises stress. In this figure, we can see that a relatively low stress zone (the green region) exists throughout. Strains are below 1% everywhere, aside around the lower junction between the thin and the thick part. Here the maximum principal strain reaches values of about 7% and 18% at the outer and inner layers respectively, as illustrated in the map of Figure 4.12. Figure 4.13 shows the distribution of the principal strains at these inner and outer layers in the region of interest. On the inside, the maximum principal strain (ϵ_{p3}) is in the local radial direction, while the minimum principal strain (ϵ_{p1}) is in the local meridian direction; that is, the elements in that area are very compressed and of no concern for tearing. On the outside, the maximum principal strain is in the local meridian direction while the minimum principal strain is in the local radial direction: the elements in this area are stretching, although far from what is needed to cause tearing. Finally, in both inside and outside layers the intermediate principal strain (ϵ_{p2}, in the azimuthal –hoop– direction) is not affected strongly by the displacements and remains always at values below 1%. The existence of the unstretched "core" material mentioned before is illustrated in Figure 4.14, showing the profiles of the two principal strains discussed above over the local radial direction.

The localized strains are due to the fact that the thin section represents the "weak" transition between the cold, strong and not-displacing part at the top and the expanding lower shell. The latter wants to "open up" to accommodate the thermal loading. These "external" forcings subject the "weaker" thinner region to a reverse bending (as already shown in Figure 4.9), which nevertheless is able to accommodate the situation with longitudinal strains far lower than needed to cause tearing (on the outside of the lower junction), and a strong core of non-yielding material throughout. In fact we found this "accommodating" quality of the thin region to prevent failure in trial calculations even under much higher temperature gradients.

A concluding note about this calculation: a linear temperature gradient through the wall has been assumed. The wall actually must go through a transient, during which the gradient is steeper on the inside than on the outside. However, the heat transfer analysis presented in the addendum to Chapter 5 shows that for the imposed heat fluxes, the gradient becomes almost linear before the inside temperature reaches 1000°C, which takes place within about 4 minutes. To investigate the effect of this non-linear temperature distribution through the wall thickness, we have carried out computations in which we forced a very steep gradient in the first quarter of the section, relaxing it slowly to the outside temperature over the remainder. This calculation has shown additional margins, due to a greater portion of the wall that remains cold and thus can better resist to the imposed loads. This, together with the assumption of perfect plasticity, adds to the conservatism of our analysis.

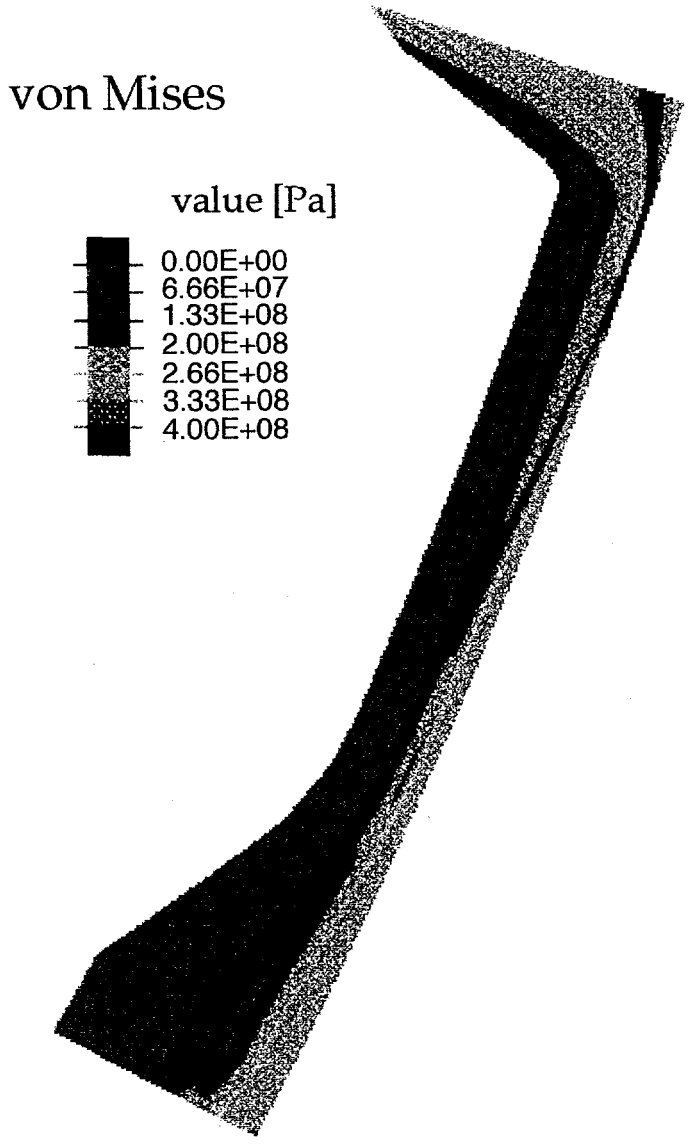

Figure 4.11. Map of equivalent (von Mises) stress distribution.

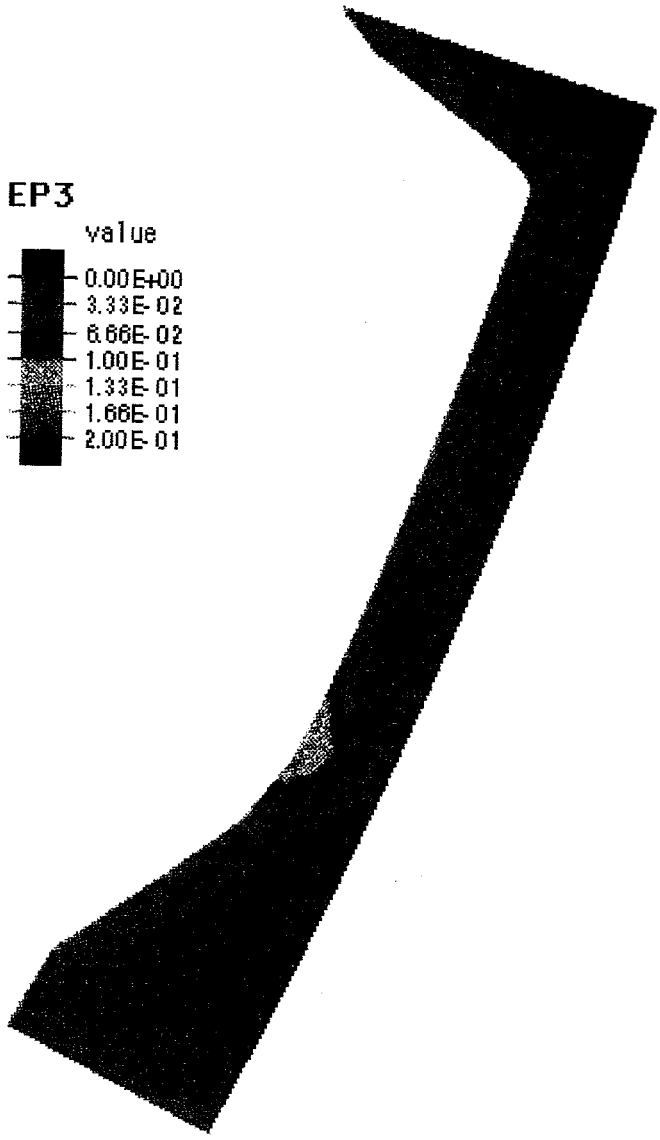

Figure 4.12. Map of maximum principal strain distribution.

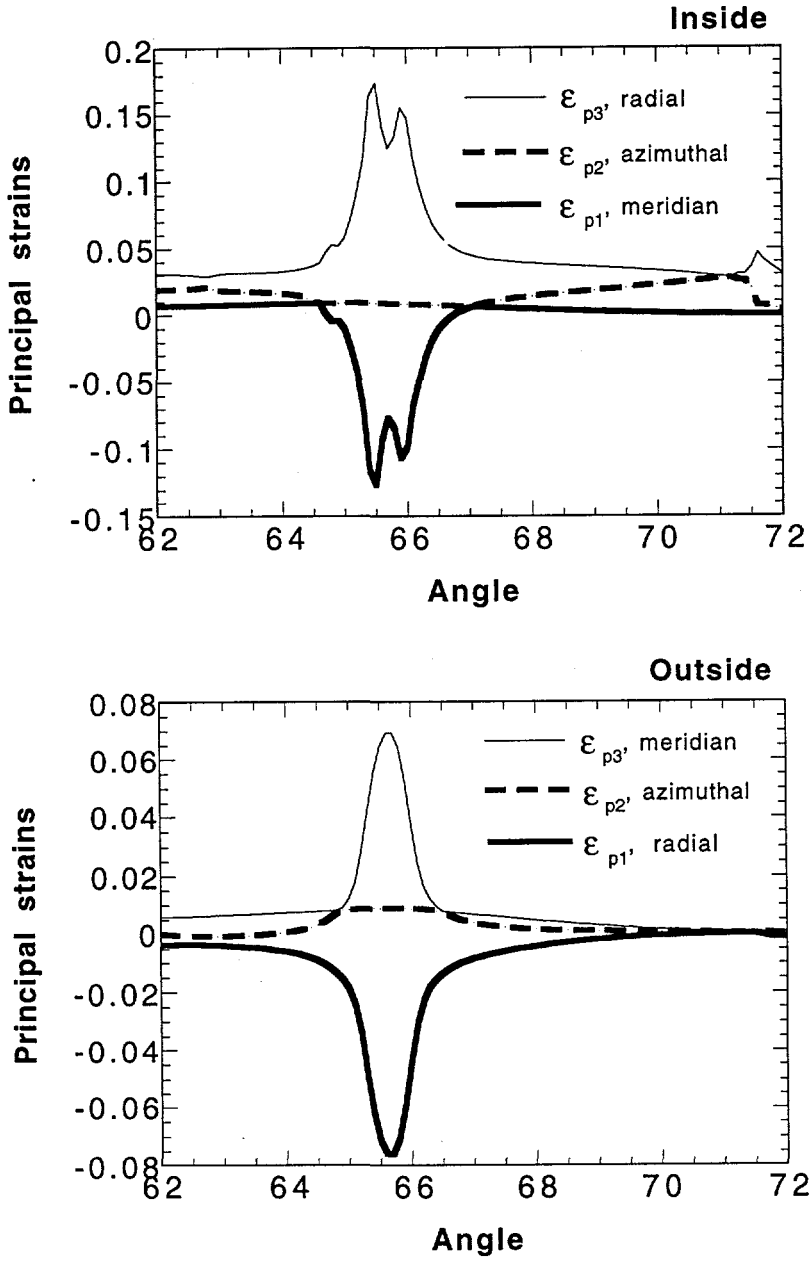

Figure 4.13. Maximum and minimum principal strain distributions along the inside (top) and outside (bottom) walls.

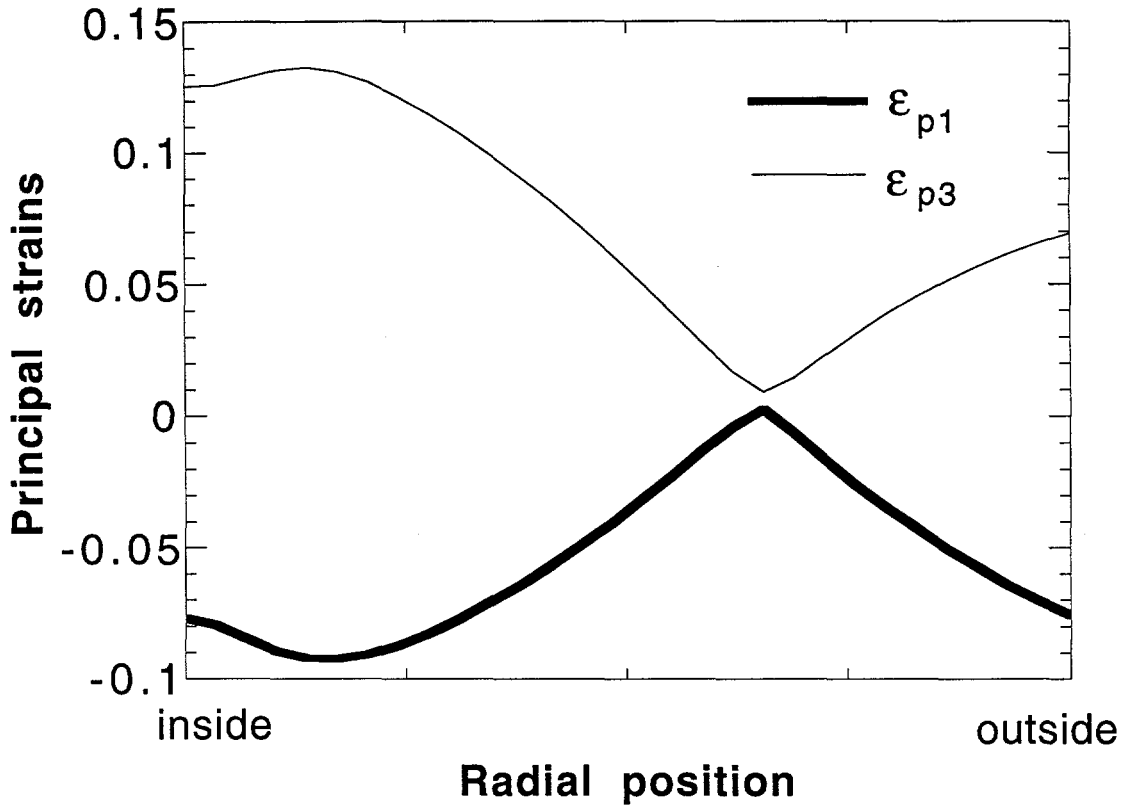

Figure 4.14. Maximum and minimum principal strain distribution across the wall thickness at the element with the largest positive strain on the outside.

5 PARTITION OF THERMAL ENERGY FLOW BY NATURAL CONVECTION

In this chapter we consider the configuration dominated by natural convection phenomena and seek to determine the heat flow distribution at the boundaries of the volumetrically heated pool and of the steel layer. This is the key aspect of the overall model described in the next chapter, and therefore it is treated here separately. The physical situation is depicted in Figure 5.1, and its main characteristics can be listed as follows:

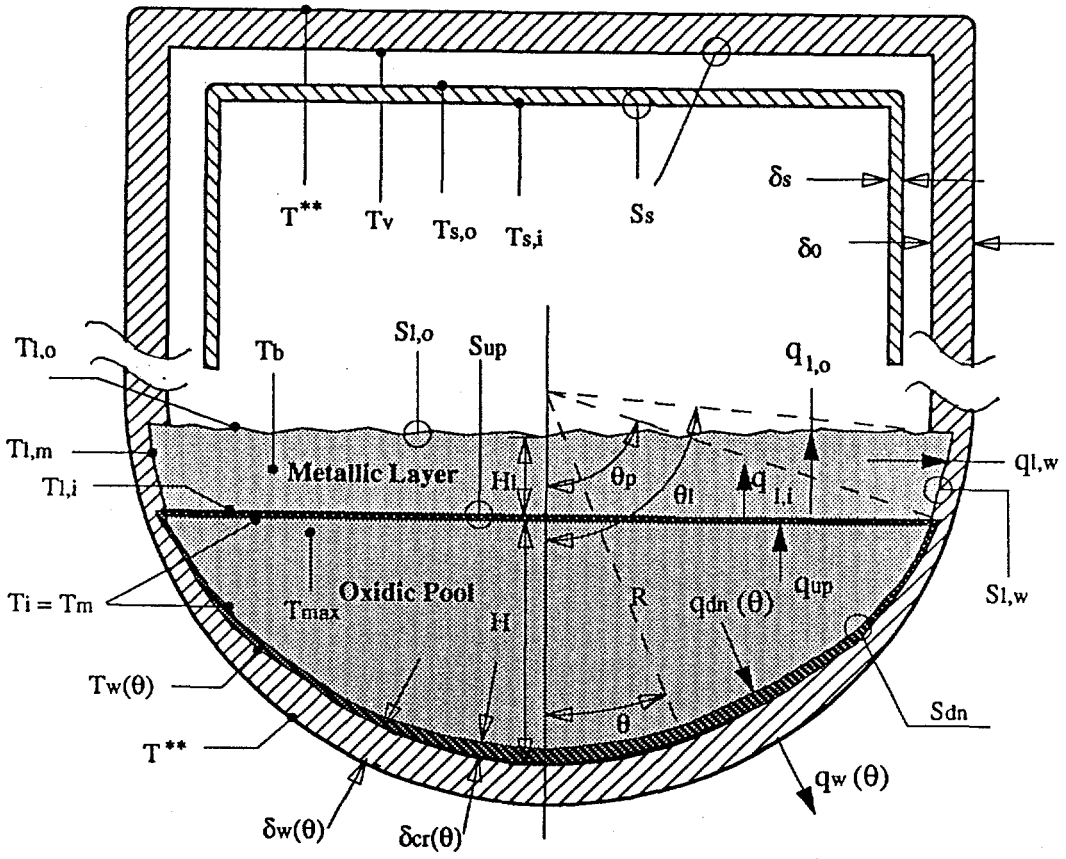

Figure 5.1. Schematic of the physical model used to quantify energy partition, and thermal loads in the long-term, natural convection thermal regime. Also shown is the nomenclature used in the formulation of the mathematical model.

1. The hemisphere is almost full (θ_p ~75°) with the oxide pool and the metal layer on top (θ_ℓ ~90°). This means that the effect of the "fill level" can be considered negligible for our purposes.

2. The oxide pool contains the oxidic components of the core melt (mainly UO_2 and ZrO_2), with a liquidus of ~2973 K. Because of this very high liquidus relative to the cooling capability at all boundaries (see Chapter 6) this pool is surrounded completely by crusts.

3. The crusts are thin enough not to appreciably alter the shape of the enclosure, and they impose a uniform temperature boundary condition—the melt liquidus. As a consequence, the pool-internal heat transfer problem is uncoupled from what goes on outside, (as long as the crusts do not vanish from any part of the boundary). This means that the internally imposed heat flux, together with thermal resistances and sink temperatures, determine the crust thickness distribution all around the pool boundary.

4. The metallic layer is of a large aspect ratio (thin compared to its diameter) and with its sidewalls almost vertical. It is heated from below and cooled from above and its sides. Again, natural convection drives the heat flow distribution, but now only the side boundary temperature is fixed—at the liquidus of the metal layer of ~1300 °C (see Chapter 6).

The nomenclature to be employed is as follows: From the oxide pool we have an "up" to "down" energy flow split. These two heat flows will be characterized by the average heat fluxes over the horizontal and hemispherical boundaries of the pool (q_{up} and q_{dn}) respectively. Local values on the hemisphere will be defined by the angular position as indicated in Figure 5.1. Note that $q_w(\theta)$ contains $q_{dn}(\theta)$ plus the contribution of the heat generated in the crust at angular position θ. The heat flows "into" and "out" of the horizontal boundaries of the steel layer will be characterized by the average fluxes $q_{\ell,i}$ and $q_{\ell,o}$, respectively. The average heat flux through the side boundary of the steel layer will be denoted by $q_{\ell,w}$. The quantities of primary interest to the task of this chapter are those that directly affect lower head integrity; that is, $q_w(\theta)$ and $q_{\ell,w}$. However, these quantities can only be obtained from an integral analysis (presented in the next chapter) which makes use of all the heat fluxes defined above. The formulation necessary for this purpose is provided below.

Natural convection phenomena can be scaled in terms of the Grashof, Gr, and Prandtl, Pr, numbers, and in the presence of volumetric heating the Dammköhler, Da, number is also needed. These numbers are expressed as (Mayinger et al., 1975)

$$\mathrm{Gr} = \frac{g\beta(T_{max} - T_i)H^3}{\nu^2} \quad \mathrm{Pr} = \frac{\nu}{\alpha} \quad \mathrm{Da} = \frac{\dot{Q}H^2}{k(T_{max} - T_i)} \tag{5.1}$$

where $\dot{Q}$ is the volumetric heat generation rate, H is a characteristic dimension of the region in the vertical direction (i.e., pool depth), and β, k, ν, and α are the fluid thermal expansion coefficient, thermal conductivity, kinematic viscosity, and thermal diffusivity, respectively. The

overall heat transfer phenomenon is characterized by the Nusselt number, Nu, defined by

$$\text{Nu} = \frac{qH}{k(T_{max} - T_i)} \tag{5.2}$$

where q is the average heat flux over a boundary of interest kept at uniform temperature T_i, and T_{max} is the maximum temperature in the pool. (In the absence of volumetric heating the "bulk" temperature (T_b) is used in place of T_{max}.) That is, the behavior can be characterized by correlations in the form

$$\text{Nu} = \mathcal{F}\,(\text{Gr, Pr}) \qquad \text{no volumetric heating} \tag{5.3}$$

$$\text{Nu} = \mathcal{G}\,(\text{Gr, Pr, Da}) \qquad \text{with volumetric heating} \tag{5.4}$$

which can be obtained from model experiments or numerical simulations. Experience indicates that most, if not all of the effect of the Prandtl number is to be found in combination with the other dimensionless groups in the form of the Rayleigh, Ra, or "internal" Rayleigh, Ra′, numbers given by

$$\text{Ra} = \text{Gr Pr} \qquad \text{Ra}' = \text{Gr Pr Da} \tag{5.5}$$

such that

$$\text{Nu} = \mathcal{F}\,(\text{Ra, Pr}^m) \tag{5.6}$$

$$\text{Nu} = \mathcal{G}\,(\text{Ra}', \text{Pr}^n) \tag{5.7}$$

where m and n indicate a small (or zero) dependance. Our task, then, is to determine the functions $\mathcal{G}$ and $\mathcal{F}$ (and the exponents m and n) for the oxidic pool and metal layer, respectively. A key point, of course, is "similarity"—that is, these functions should be appropriate for the Ra, Ra′, and Pr number ranges of interest in the reactor. For the present application these ranges are:

$$\text{Oxidic Pool}: \quad 10^{15} < \text{Ra}' < 6 \cdot 10^{15} \qquad \text{Pr} \sim 0.6 \tag{5.8}$$

$$\text{Metallic Layer}: \quad 5 \cdot 10^{9} < \text{Ra} < 2 \cdot 10^{10} \qquad \text{Pr} \sim 0.1 \tag{5.9}$$

Another key point regarding similarity is the relationship of the final, truly steady state, to the sequence of transient states leading up to it. Finally, any correlation scheme has to be explicit on the "effective" temperature at which the various thermophysical properties are to be evaluated—normally the "film" temperature, i.e., the average value between the bulk and wall, is used, but because experiments so far related to Eq. (5.7), have been carried out with relatively small $(T_{max} - T_i)$, this is still an open question. [[Molecular diffusion considerations indicate that multicomponent effects on density and resulting natural convection cannot provide any sustainable influence, especially at high Rayleigh numbers. This was demonstrated experimentally by Schneider and Turland (1994).]]

5.1 The Oxidic Pool

The basic features of the flow regime in the oxidic pool are indicated in Figure 5.2. They consist of steep boundary layer regions adjacent to the isothermal boundary, a well-mixed upper pool volume, and a broadly stratified lower pool portion. These regions can be expected from consideration of basic principles of natural convection and have been demonstrated by the interferograms of Jahn and Reineke (1974) in a slice (semicircular) geometry. The upper mixed region is created by the cold "plumes" detaching continuously from the upper boundary layer, and the lower stratified region is the result of the downflowing boundary layers along the curved boundary and the induced bulk motion; that is, a combination of entrainment all along the outer edge of the boundary layer, and a turnover process in the bulk (due to the wall-plume penetration). The transition from the well-mixed to the stratified region is controlled by the interplay between the mixing process from above and the bulk-convection (turnover) from below. The Ra' numbers of interest are high enough to ensure turbulent motions for which we generally expect little or no effect of the length scale. This means correlations of the form

$$Nu \sim Ra'^{0.2} \tag{5.10}$$

from which the length scale just cancels out. As a consequence, regarding the behavior at the upper (flat) boundary we can also bring to bear results from fluid geometries enclosed between two horizontal boundaries, with at least the upper one held isothermal (i.e., the lower boundary can be isothermal or adiabatic). This is fortunate because this geometry has received wider attention than the hemispherical one, and available data for it extend to higher values of the Ra' number. The following material in this section is arranged in three segments. In the first two we consider the upper (flat) and lower (curved) boundaries, respectively, while in the third we pursue certain interesting deductions from their interrelationship.

The best known correlations for the upper boundary have derived from the experiments of Kulacki and Emara (1975) and Steinberner and Reineke (1978). The correlations and respective ranges of the experimental variables can be summarized as follows:

$$\text{Kulacki–Emara}^{a} \qquad Nu_{up} = 0.34\, Ra'^{0.226} \tag{5.11}$$
$$2 \cdot 10^4 < Ra' < 4.4 \cdot 10^{12} \qquad Pr \sim 7$$

$$\text{Steinberner–Reineke} \qquad Nu_{up} = 0.345\, Ra'^{0.233} \tag{5.12}$$
$$10^7 < Ra' < 3 \cdot 10^{13} \qquad Pr \sim 7$$

[a] [[Recast to the present definition of Ra' number]]

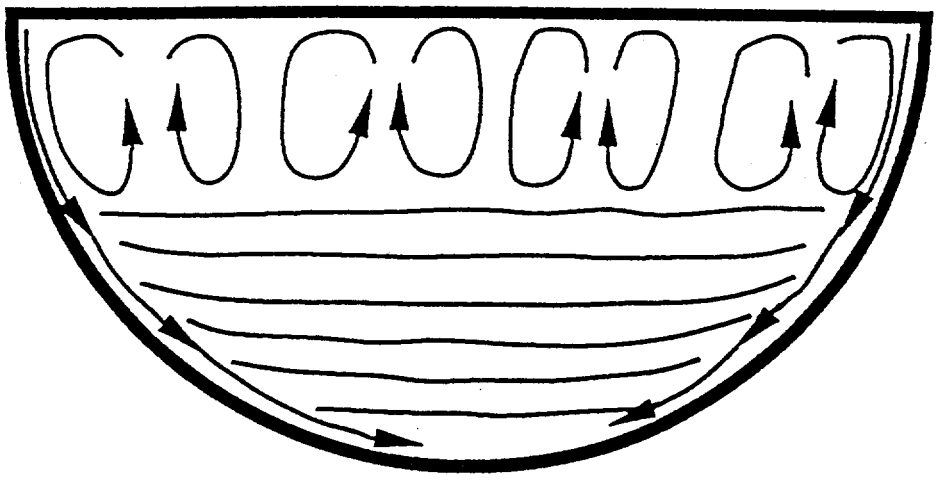

Figure 5.2. Illustration of the natural convection flow and stratification patterns in the oxidic pool.

The experiments were carried out in rectangular geometries, under relatively small temperature differences. Kulacki and Emara also attempted to identify an independent Prandtl number effect (the n in Eq. 5.7) and wrote:

$$\mathrm{Nu}_{up} = 0.2\ \mathrm{Pr}^{0.239}\ \mathrm{Ra}'^{0.233} \tag{5.13}$$

which, interestingly enough, gives the same Ra′ number dependance as Eq. (5.12). However, it has been recognized that the data base was inadequate to support the Pr number dependance. Using a Pr number of 7 in Eq. (5.13), we obtain

$$\mathrm{Nu}_{up} = 0.32\ \mathrm{Ra}'^{0.233} \tag{5.14}$$

which can only be seen as an independent confirmation of the correlation by Steinberner and Reineke (1978).

More recently, the COPO experiments (see Appendix B) extended the Rayleigh number range to $1.5 \cdot 10^{15}$. The COPO data were obtained with hot water (Pr ~2.5), in a large-scale facility ($H = 0.8$ m), and were found to be in excellent agreement with Eq. (5.12) up to a Ra′ of $6 \cdot 10^{14}$. However, an apparent rapid transition occurred at this value of Ra′ number that produced a relatively consistent ~30% underprediction at the upper end of the range investigated. The authors of Appendix B express some caution that such a transition is not understood and that its

existence needs further investigation. The UCLA data (Appendix C) were obtained with Freon (Pr ~8) in a medium-sized hemispherical test section ($R = 0.4$ m). Both data points are below Eq. (5.12), one by 37% and the other, at $Ra' = 9 \cdot 10^{13}$, by 17%. It should be noted, however, that due to the experimental arrangement the values reported pertain only to the outer position of the upper boundary.

Finally, the subject has been approached theoretically by Cheung (1980), who concluded that the asymptotic dependance for large Ra' numbers is to the 1/4 power, and that at low Pr numbers there is a separate dependance (on Pr) to the 1/4 power as well. For the intermediate Pr number range (which is of interest here) he found that

$$Nu = \frac{Ra'^{1/4}}{B_1 \Delta - B_2 \, Pr^{-1/3} \, Ra'^{-1/12}} \tag{5.15}$$

where B_1, B_2, and Δ are all functions of the Pr number. He then used the data of Kulacki and Emara to show that the above formulation is consistent with "fitting" correlations of the form of Eq. (5.12) to data over limited ranges of the Rayleigh number, and that the exponent would be expected to increase asymptotically to the 0.25 value. In particular, he proposed that

$$Nu_{up} \sim Ra'^{0.227} \qquad \text{for} \quad Ra' < 10^{11} \tag{5.16}$$

$$Nu_{up} \sim Ra'^{0.245} \qquad \text{for} \quad 10^{12} < Ra' < 10^{22} \tag{5.17}$$

Note that this is consistent with Eq. (5.12), and its potential applicability up to the range of our interest ($Ra' \sim 10^{16}$). However, he did not consider the Kulacki-Emara data adequate for extracting the Pr number dependance.

In light of the above, the basic issues regarding our present needs can be summarized as follows:

1. Validity of Eq. (5.12) to a Ra' numbers range extended by 3 orders of magnitude. Besides the basic requirement for data support, we have the doubt cast on it by the COPO data and even (to a much lesser extent, however) by the UCLA data. It should be noted here that due to the importance of q_{up} on the behavior of the steel layer (see the next section), even a 30% discrepancy could be potentially rather significant to our conclusions.

2. Independent Prandtl number effect. Since our case requires an extrapolation (of the main data base) by about one order of magnitude (from ~7 to ~0.6) even a small dependance could produce a significant effect. For example, the dependance in Eq. (5.13) would produce a reduction by almost a factor of 2! Now, the COPO data indicate that such a strong effect

is unlikely, since a Pr $\sim$3 could have produced a 20% effect, rather than the excellent agreement found for $Ra' < 6 \cdot 10^{14}$. However, the discrepancy found for $Ra' > 6 \cdot 10^{14}$ prevents this issue from being considered closed.

The mini-ACOPO experiments, described in Appendix D, have been carried out for the purpose of addressing these issues. They were carried out in a medium-scale (R $\sim$0.4 m) hemispherical geometry, using water or freon as the working fluids. The experimental ranges covered were

$$10^{12} < Ra' < 7 \cdot 10^{14} \qquad 2.6 < Pr < 10.8 \tag{5.18}$$

and pool-to-wall temperature differences ranged up to 70 K. The main results for the upper boundary are summarized in Figures 5.3 and 5.4. Figure 5.3 shows the comparison with the Steinberner–Reineke correlation.[b] The agreement in the region of overlap with their data ($10^{12} < Ra' < 3 \cdot 10^{13}$) is excellent, which confirms the experimental approach in the mini-ACOPO. The agreement of the extended correlation with the data for Ra′ numbers that reach up toward prototypic values is also excellent. In Figure 5.4 we show the same data in a form suitable for detecting any Prandtl number effect. None can be seen, and we can thus see no problem for using this correlation under a small extrapolation down to Pr $\sim$0.6.

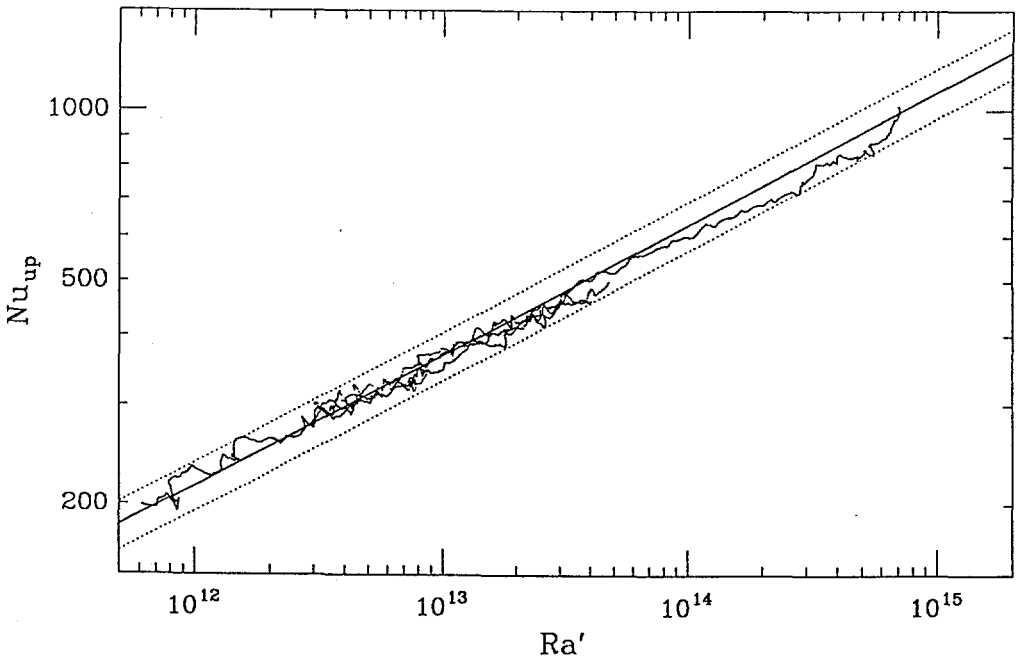

Figure 5.3. The mini-ACOPO results for upward heat transfer against the Steinberner and Reineke (1978) correlation. Data in the range $3 \cdot 10^{13} < Ra' < 7 \cdot 10^{14}$ are from run A16, the last Freon run, and the rest of the data are from runs B1, B2 and B3, carried out with water at various temperature ranges. Properties evaluated at "film" temperature.

[b] [[For the latest information on this subject, see Appendix V-2.]]

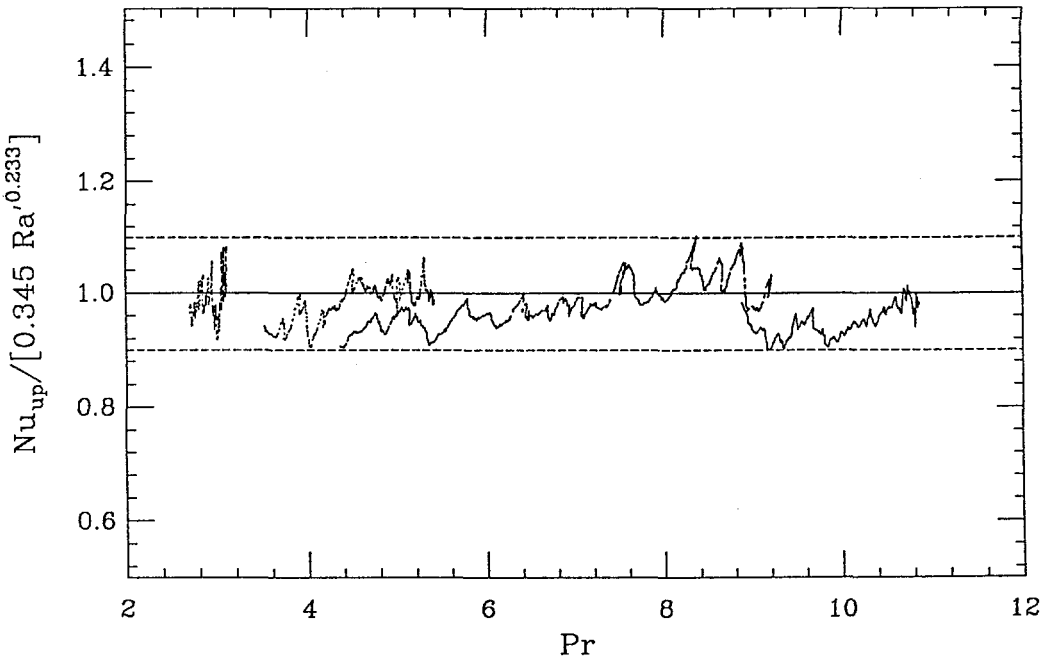

Figure 5.4. Mini-ACOPO data normalized according to the correlation in Figure 5.3, shown against the applicable Prandtl numbers.

Finally, it is worth mentioning the numerical simulations of Mayinger et al. (1975) and of Kelkar et al. (1993), mainly because they appear to have actually produced correct **predictions** for the **downward** heat flux (see below). Both calculations were carried out for a hemisphere. Mayinger et al. covered the range $7 \cdot 10^6 < \mathrm{Ra}' < 5 \cdot 10^{14}$, using a Prandtl number of 0.5 and fitted the results (for the upward heat flux) by

$$\mathrm{Nu}_{up} = 0.4\ \mathrm{Ra}'^{0.2} \tag{5.19}$$

It can be readily seen that this result at a Ra′ of 10^{15} would under-predict Eq. (5.12) by a factor of 3. The numerical simulations of Kelkar et al., were run with the low Reynolds number turbulence model of Jones and Laurder and included a "wall correction" due to Yap. Results were given for $10^8 < \mathrm{Ra}' < 10^{16}$ and a Prandtl number 1. They can be well fit by

$$\mathrm{Nu}_{up} = 0.18\ \mathrm{Ra}'^{0.237} \tag{5.20}$$

which can be seen to be essentially parallel to Eq. (5.12), but to provide a consistent under-prediction by almost a factor of 2.

Experiments for the hemispherical boundary [[downwards heat transfer]] have been problematic because of the difficulty in producing uniform heating. Thus, a slice (semicircular)

geometry has been favored, even though it cannot reproduce the converging effect of the boundary layers present in the full geometry. The experiments of Jahn and Reineke (1974) were run with water (Pr ~7), covered the range $10^7 < \mathrm{Ra}' < 5 \cdot 10^{10}$, and produced

$$\mathrm{Nu}_{dn} = 0.54\ \mathrm{Ra}'^{0.18} \left(\frac{H}{R}\right)^{0.26} \tag{5.21}$$

The measurement also provided local heat fluxes and an indication of the peaking at higher polar angles. Equation (5.21) was confirmed by the COPO experiments and thus extended to $4 \cdot 10^{12} < \mathrm{Ra}' < 1.8 \cdot 10^{13}$ and Pr ~3. Data were also provided for the local heat fluxes on the vertical and lower boundaries. Mayinger et al. (1975) were able to reproduce Eq. (5.21) using the Navier–Stokes equations with an eddy diffusivity model, which was then applied to an axisymmetric geometry to produce

$$\mathrm{Nu}_{dn} = 0.55\ \mathrm{Ra}'^{0.2} \tag{5.22}$$

for $7 \cdot 10^6 < \mathrm{Ra}' < 5 \cdot 10^{14}$ and Pr = 0.5. These as well as the COPO data were also interpreted by means of a turbulence model, incorporating an empirical modification of the eddy diffusivity via the Richardson number (Dinh and Nourgaliev, 1994). Kelkar et al., (1993) in the calculations mentioned above provided predictions for Pr = 1 and Ra′ numbers up to 10^{16} which can be fit by

$$\mathrm{Nu}_{dn} = 0.1\ \mathrm{Ra}'^{0.25} \tag{5.23}$$

This is a quite different trend than that in Eq. (5.22), but interestingly enough, at a Ra′ number of 10^{15} a discrepancy between these two equations is only ~2%!

The UCLA experiments mentioned above, and described in Appendix C, also provided data for the lower boundary of the hemisphere. Two data points on the average fluxes obtained at Ra′ numbers of $3 \cdot 10^{13}$ and $9 \cdot 10^{13}$ are in good agreement (15% higher) with Eq. (5.22), and the local fluxes were correlated by

$$\frac{h(\theta)}{h} = c_1\ sin\ \Theta - c_2\ cos\ \Theta \qquad \text{for } 0.75 < \frac{\theta}{\phi} \leq 1 \tag{5.24}$$

where

$$c_1 = -1.25\ cos\ \phi + 2.6$$

$$c_2 = -2.65\ cos\ \phi + 3.6$$

and

$$\frac{h(\theta)}{h} = 1.17\ sin^4\ \Theta + 0.23 \qquad \text{for } 0 < \frac{\theta}{\phi} < 0.75 \tag{5.25}$$

where ϕ is the polar angle at the pool surface, and $\Theta = \frac{\theta}{\phi}\frac{\pi}{2}$. These experiments are encouraging in tying in with Eqs. (5.22) and (5.23); however, there are several aspects in relation to the present application that require further clarification. They can be summarized as follows:

1. Based on the highest UCLA data point, the present use would require an extrapolation on the Ra′ number by nearly two orders of magnitude. The higher trend in Eq. (5.23) than from Eq. (5.22) (with Ra′ number) then becomes of concern, especially as Kelkar et al. noted that (due to this trend) the downward heat flux approaches the upward flux at the high Ra′ number range of interest here. As noted previously, their upward fluxes are underestimated by a factor of 2, which weakens this conclusion but does not eliminate the concern.

2. Although there is adequate experimental basis now (as explained above) that any independent Pr number effect is slight enough to be negligible at the upper (flat) boundary, indicating a high likelihood that the same is true for the curved boundary, this is still tentative and subject to experimental verification. (Both UCLA data points were obtained at Pr = 8.2.)

3. The microwave radiation heating technique employed in the UCLA experiments requires a slightly coupling medium (freon) in order to obtain uniformity over the scale of the experiment. This low heating rate forced operation at rather low temperature differences ($T_{max} - T_i$), while conduction resistance through the glass wall produced a non-uniformity in T_i of similar magnitude as the ($T_{max} - T_i$) itself. For example, the run at Ra′ $\sim 9 \cdot 10^{13}$ involved a ($T_{max} - T_i$) of 1.9 K at the top and a ($T_{max} - T_i$) of 5.8 K at the bottom of the pool, while the T_i varied by 4.5 K from the equator to the bottom of the hemisphere (Asfia, 1994). This could raise concerns about the appropriateness of the comparison with Eq. (5.22), or the validity of Eq. (5.24) to an isothermal boundary situation. (However, current efforts at UCLA are directed at obtaining freezing at the boundaries which would ensure an isothermal boundary—in this case the flux distribution can be obtained from the variation of crust thickness.)

4. Transient effects. While heat transfer at steady state occurs with a stable stratification pattern as indicated in Figure 5.2, consideration of transient behavior, besides pool thermal inertia effects, also needs to be concerned with timewise variation of this stratification pattern. In particular, starting from a uniform pool, this final pattern would be approached from a sequence of more uniform (than the final) states, and one might ask how this would affect the up-to-down energy flow split and the flux distribution over the curved boundary. Clearly, there is a potential here for significantly higher (than at steady state) thermal loads at lower positions on the lower head. Given the shape of the critical heat flux (Figure 3.3), it is immediately obvious that this topic constitutes a major open issue.

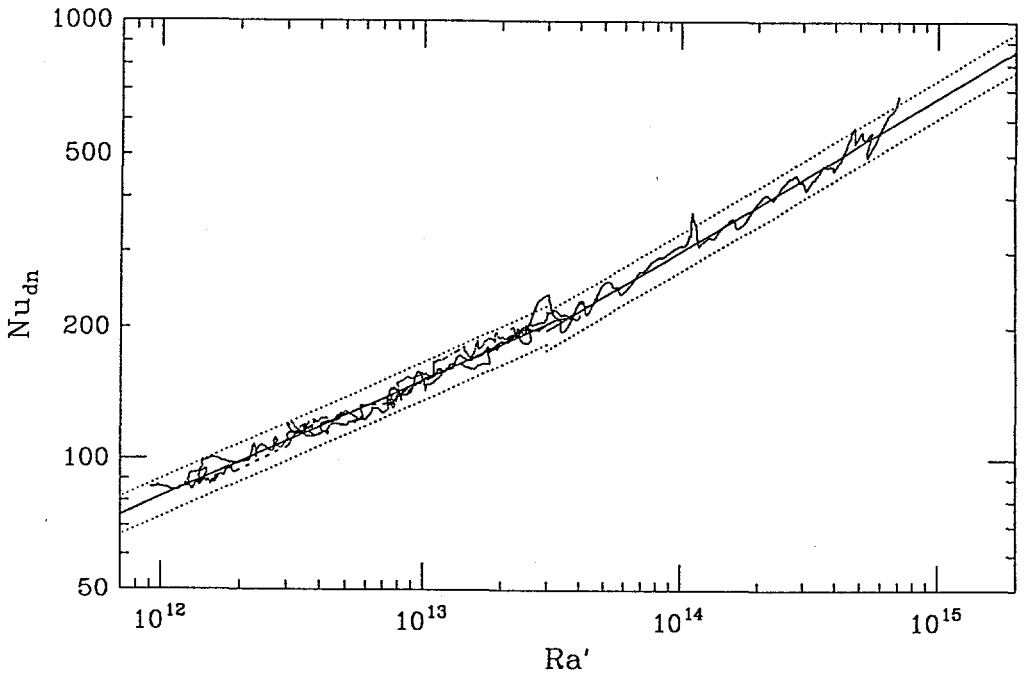

Figure 5.5. The mini-ACOPO results for downward heat transfer against Eqs. (5.27) and (5.28). Shown are: run A16, the last Freon run, and runs B1, B2 and B3 carried out with water at various temperature ranges. Properties evaluated at "film" temperature.

The mini-ACOPO experiment mentioned above (and described in detail in Appendix D) was built and operated to address this different set of issues as well. Again, the experimental ranges covered were

$$10^{12} < \mathrm{Ra}' < 7 \cdot 10^{14} \qquad 2.6 < \mathrm{Pr} < 10.8 \tag{5.26}$$

and the pool-to-wall temperature differences ranged up to 70 K. The main results for the downward heat transfer are summarized in Figures 5.5 and 5.6. As seen in Figure 5.5, the data are tightly correlated by

$$\mathrm{Nu}_{dn} = 0.048\ \mathrm{Ra}'^{0.27} \qquad 10^{12} < \mathrm{Ra}' < 3 \cdot 10^{13} \tag{5.27}$$

$$\mathrm{Nu}_{dn} = 0.0038\ \mathrm{Ra}'^{0.35} \qquad 3 \cdot 10^{13} < \mathrm{Ra}' < 7 \cdot 10^{14} \tag{5.28}$$

Even though an overall correlation

$$\mathrm{Nu}_{dn} = 0.02\ \mathrm{Ra}'^{0.3} \qquad 10^{12} < \mathrm{Ra}' < 7 \cdot 10^{14} \tag{5.29}$$

would still fit quite well, the use of the upper branch (Eq. (5.28)) is deemed preferable for this application. In Figure 5.6 we show the data in a form suitable for detecting any independent Pr number effect. None can be seen, and we can thus conclude that Eq. (5.28) is applicable under the modest extrapolation to a Pr number of 0.6.

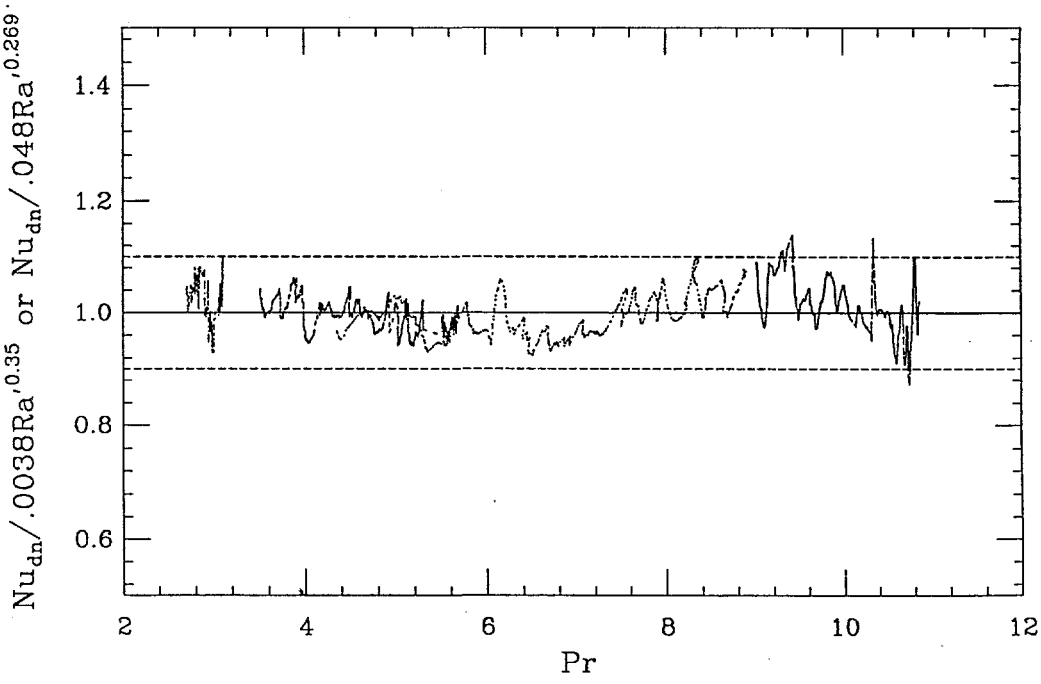

Figure 5.6. Mini-ACOPO data normalized according to the correlations in Figure 5.5, shown against the applicable Prandtl numbers.

Another interesting perspective can be obtained from Figure 5.7, containing the present data and correlations, Mayinger's correlation (Eq. 5.22), the numerical results of Kelkar et al., and the UCLA data. We can see that all of these results are mutually reinforcing. While in the range expected to dominate the thermal loads in this application ($10^{15} < \mathrm{Ra}' < 5 \cdot 10^{15}$), the Mayinger correlation provides a lower bound, the present correlation provides an upper one (the trends of the UCLA data and Kelkar et al. simulations indicating an intermediate behavior). The effect of using the lower bound in the analysis is examined in a sensitivity study in Chapter 7.

Now, revisiting the four issues being addressed here, the mini-ACOPO data show that even under the most extreme transient conditions (as in run A16), the boundary layers and overall stratification patterns develop quickly enough to exhibit an average behavior quite consistent with steady-state behavior. However, these data also show a finer structure of stratification pattern adjustment, as a result of the transient, that produces some variation of the heat flux distribution. This is illustrated in Figure 5.8, containing all the mini-ACOPO data, and including for comparison the UCLA correlation and the shape found by Jahn (Mayinger et al., 1975) in a slice geometry at an Ra′ number of $1.2 \cdot 10^{10}$. This figure also shows that

$$\frac{\mathrm{Nu}_{dn}(\theta)}{\mathrm{Nu}_{dn}} = 0.1 + 1.08\left(\frac{\theta}{\theta_p}\right) - 4.5\left(\frac{\theta}{\theta_p}\right)^2 + 8.6\left(\frac{\theta}{\theta_p}\right)^3, \qquad 0.1 \le \frac{\theta}{\theta_p} \le 0.6 \qquad (5.30a)$$

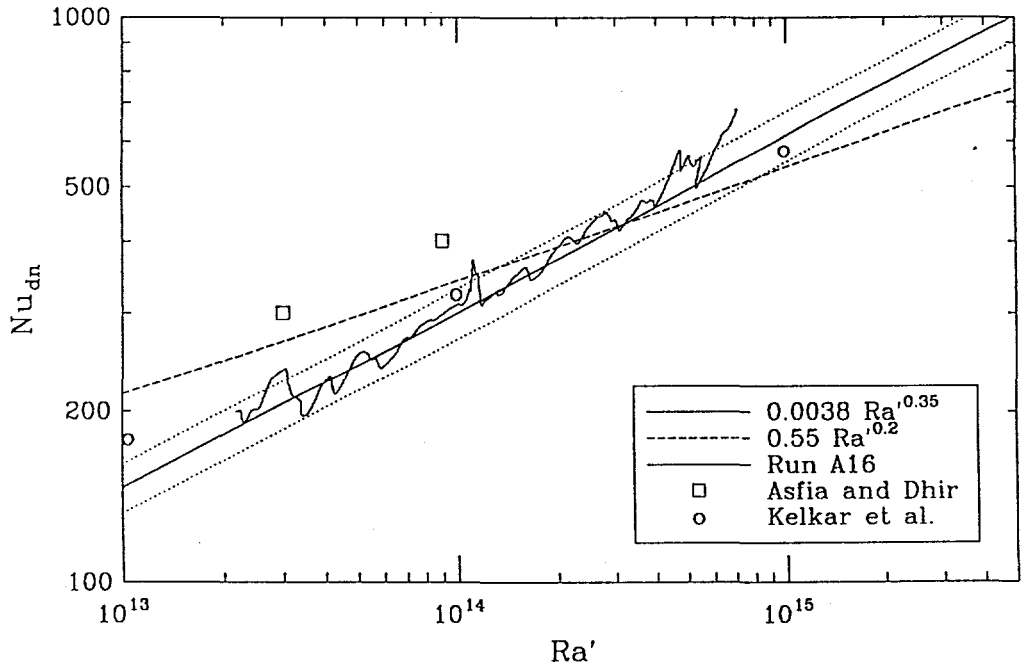

Figure 5.7. The mini-ACOPO data (downward heat transfer) and correlation obtained from them (Eq. (5.28)), shown against the Mayinger et al. (1975) correlation, the UCLA data, and the results of the numerical simulations by Kelkar et al. (1993).

$$\frac{\mathrm{Nu}_{dn}(\theta)}{\mathrm{Nu}_{dn}} = 0.41 + 0.35\left(\frac{\theta}{\theta_p}\right) + \left(\frac{\theta}{\theta_p}\right)^2, \qquad 0.6 < \frac{\theta}{\theta_p} \leq 1 \tag{5.30b}$$

reasonably represents the mini-ACOPO data. Although this correlation was derived with full hemisphere, it remains adequately normalized, and we expect it to be reasonably valid for $60° < \theta_p < 90°$. The UCLA correlation exhibits a somewhat more peaked distribution, and it will be used in a sensitivity study in Chapter 7. Also shown in Figure 5.8 is the result of the numerical simulations ($\mathrm{Ra}' = 10^{14}$ and 10^{16}) of Kelkar et al. (1993). It exhibits a trend more uniform than any of the experiments and, in fact, in the important upper regions it provides a lower bound.

Further confirmation of the treatment proposed here will be obtained with the ACOPO experiment which is presently under construction [[see Appendix V-2]]. Operating at a 4 times larger scale than the mini-ACOPO it will afford a much longer "internal time scale" and hence full exploration of the stratification adjustment effects discussed above. The key characteristics of this experiment have been summarized in Table 5.1, and put into perspective with the mini-ACOPO, and the other ongoing experiments at UCLA (currently efforts to obtain freezing at the boundaries), and at IVO (currently directed to a semicircular slice geometry, with freezing at the boundaries). In addition, the BALI experiment at CEN, Grenoble (similar in concept and scale to the COPO,

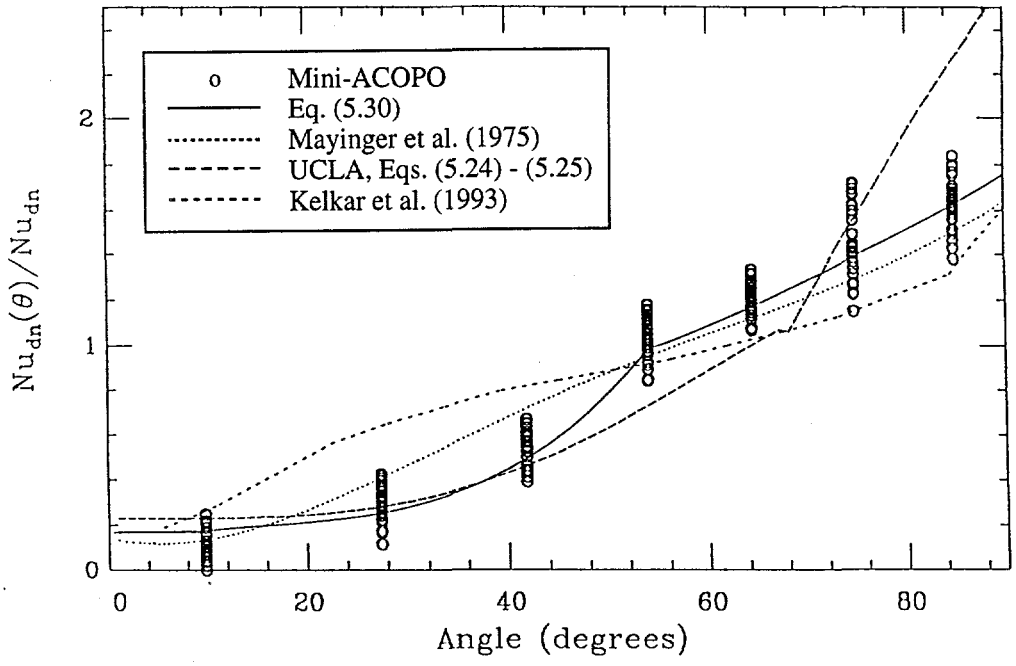

Figure 5.8. The mini-ACOPO data and the correlation obtained from them (Eq. (5.30)), for heat flux distribution as function of the angular position, shown against the UCLA correlation. Also shown is a line through the data obtained by Jahn (Mayinger et al., 1975), for $Ra' \sim 2 \cdot 10^{10}$, renormalized (by area averaging) to an axisymmetric geometry, and the result of numerical simulations by Kelkar et al. (1993), for $10^{14} < Ra' < 10^{16}$.

but including additional capabilities, such as gas or liquid injection at the boundaries), expected to be operational in the near future, should be mentioned (Bonnet et al., 1994).

Table 5.1. An Overall View of Recent Work with Volumetrically Heated Pools

Experiment Concept	Scale/Shape Dimensionality	Working Fluid	$T_{max} - T_i$ (K)	Pr	Ra'
COPO Joule Heating	1/2 Torospherical 2-D slice	Water	10	$2 < Pr < 3$	$1 \cdot 10^{14} < Ra' < 8 \cdot 10^{15}$
UCLA Microwave Heating	1/8 Semispherical Axisymmetric	Freon-113	2 to 8	$8.2 < Pr < 9.5$	$4 \cdot 10^{11} < Ra' < 1 \cdot 10^{14}$
Mini-ACOPO Cooldown	1/8 Semispherical Axisymmetric	Freon-113 Water	40 100	$7 < Pr < 11$ $2 < Pr < 10$	$2 \cdot 10^{13} < Ra' < 7 \cdot 10^{14}$ $1 \cdot 10^{11} < Ra' < 3 \cdot 10^{12}$
ACOPO Cooldown	1/2 Semispherical Axisymmetric	Freon-113 Water	40 100	$7 < Pr < 11$ $2 < Pr < 10$	$1 \cdot 10^{16} < Ra' < 2 \cdot 10^{17}$ $4 \cdot 10^{13} < Ra' < 2 \cdot 10^{16}$

Finally, it is instructive to consider what can be learned from Eqs. (5.12), (5.28), and (5.30), regarding energy partition from the oxidic pool, and resulting local thermal loads at the curved boundary. First, the ratio of the up-to-down heat fluxes can be obtained from:

$$R' \equiv \frac{\mathrm{Nu}_{up}}{\mathrm{Nu}_{dn}} = 90\ \mathrm{Ra}'^{-0.117} \tag{5.31}$$

which for $\mathrm{Ra}' \sim 5 \cdot 10^{15}$ gives a ratio of 1.31. Using Eq. (5.22) in place of Eq. (5.28), on the other hand, we obtain

$$R' \equiv \frac{\mathrm{Nu}_{up}}{\mathrm{Nu}_{dn}} = 0.63\ \mathrm{Ra}'^{0.033} \tag{5.32}$$

which for the same Ra' yields a ratio of 2.1. Now, from an overall energy balance on the oxidic pool (of volume V) we have

$$\dot{Q}V = S_{up}q_{up} + S_{dn}q_{dn} \tag{5.33}$$

which for an hemisphere can be written as

$$q_{dn} = \dot{Q}V\left\{2\pi R^2(1+0.5R')\right\}^{-1} \qquad [[(5.33')]]$$

where R' is the ratio defined above (Eq. (5.31) or (5.32)). This allows a simple estimate of q_{dn}, for Ra' numbers around the $5 \cdot 10^{15}$ value utilized in the derivation, and using it to estimate the flux shape (from Eq. (5.30)), and q_{up} (from the value of the Ra'). In the next section we will show how the complete solution for the steel layer can be obtained after q_{up} is known. [For cases where the Ra' is significantly different than $5 \cdot 10^{15}$, the same procedure can be utilized, after solving Eq. (5.33) for the Ra' number, as discussed in Chapter 6.] For example, supposing that $\dot{Q} = 1.3$ MW/m^3 and $V = 10$ m^3 (typical values for the AP600), and with $R = 2$ m, we obtain q_{dn} as 313 kW/m^2 or 252 kW/m^2 depending on whether the R' is obtained from Eq. (5.31) or (5.32), respectively. We can see that the sensitivity is only ~25%. We can also see that even with a bounding peak-to-average value of 2 (see Figure 5.8) we cannot expect local values much in excess of 626 kW/m^2 at $\theta \sim 90°$, which shows a margin of safety by over a factor of 2 (see Figure 3.3). [[The 10 m^3 do not quite fill the hemisphere and use of Eq. (5.33') is only approximate. Using Eq. (5.33), we obtain $q_{dn} = 391$ kW/m^2, as compared to the 313 kW/m^2 quoted above. On the other hand, using the complete numerical solution according to Chapter 6, we have $q_{dn} = 357$ kW/m^2.]]

5.2 The Metallic Layer

Available work in this area has considered only situations without side wall cooling; that is, liquid layers heated from below and cooled on the top. Our approach is to make use of this work in conjunction with heat transfer to a vertical wall, in a manner that conservatively represents this most important, for our purposes, component. The discussion proceeds in three steps. In the first we summarize available results for natural convection through liquid layers. In the second we consider natural convection to a vertical, cooled wall from an ambient fluid.

Finally, in the third step, we explain how the previous two components can be put together to treat conservatively the role of the metal layer in the model that integrates the heat transfer behavior. This third step is also supported by a simple simulant experiment, run specifically for this purpose.

On the first step, let us begin with the widely used Globe and Dropkin (1959) correlation,

$$\mathrm{Nu} = 0.069\,\mathrm{Ra}^{1/3}\,\mathrm{Pr}^{0.074} \tag{5.34}$$

incorporating data with various fluids ($0.02 < \mathrm{Pr} < 8750$) at Rayleigh numbers in the range $3 \cdot 10^5 < \mathrm{Ra} < 7 \cdot 10^9$. For the relevant Prandtl number ($\sim$0.13) the above correlation reduces to:

$$\mathrm{Nu} = 0.059\,\mathrm{Ra}^{1/3} \tag{5.35}$$

On the other hand, there is considerable evidence in the literature that for turbulent flow (high Ra) the Rayleigh number exponent should be less than 1/3. In fact, works by Silveston (1958) and O'Toole and Silveston (1961) recommend, respectively,

$$\mathrm{Nu} = 0.1\,\mathrm{Ra}^{0.31}\,\mathrm{Pr}^{0.05} \quad \text{and} \quad \mathrm{Nu} = 0.104\,\mathrm{Ra}^{0.305}\,\mathrm{Pr}^{0.084} \tag{5.36}$$

while Goldstein and Chu (1969) determined an exponent of 0.294 for air (Pr$\sim$1). For Pr = 0.13 Eqs. (5.36) reduce to

$$\mathrm{Nu} = 0.09\,\mathrm{Ra}^{0.31} \quad \text{and} \quad \mathrm{Nu} = 0.088\,\mathrm{Ra}^{0.305} \tag{5.37}$$

which are in apparent difference with Eq. (5.35). In fact, at the range of Rayleigh numbers of interest here, Ra $\sim 10^{10}$, these results are quite close, as can be seen by forcing Eq. (5.35) to a 0.31-type dependence on the Rayleigh number; that is,

$$\mathrm{Nu} = 0.1\,\mathrm{Ra}^{0.31} \tag{5.38}$$

Based on these considerations we can be quite confident in using Eq. (5.35), which is therefore selected for the analysis carried out in the next chapter.

For the second step, the situation is one of heat transfer to an isothermal vertical plate, and the appropriate driving force is **the bulk liquid temperature minus the plate temperature.** The heat transfer coefficient can be obtained according to Churchill and Chu (1975) from

$$\mathrm{Nu}^{1/2} = 0.825 + \frac{0.387\,\mathrm{Ra}^{1/6}}{\left\{1 + (0.492/\mathrm{Pr})^{9/16}\right\}^{8/27}} \tag{5.39}$$

which is valid for any Prandtl number and Ra $< 10^{12}$. Again, the properties are to be evaluated at the "film" temperature. For Pr = 0.13, the reduced form of the above equation is

$$\mathrm{Nu} = 0.076\,\mathrm{Ra}^{1/3} \tag{5.40}$$

Note the similarity of this to Eq. (5.35) above; however, also note that Eq. (5.35) is based on a ΔT that involves two, rather than one, boundary layers.

As we proceed now onto the third step it is appropriate to first consider the role of the metal layer qualitatively. For a given thermal load at the lower boundary of this layer (note that this is determined solely from the natural convection processes within the oxidic pool) the behavior is controlled by the thickness of this layer and the radiative emission properties of the upper boundary. The basic trend is easy to see: as the thickness and/or the emissivity decrease, the layer temperatures must reach higher and higher levels, and since the thermal boundary conditions at the vessel wall must remain fixed (at the melt liquidus), the heat fluxes into it must increase correspondingly. This "focusing" effect can be counteracted only by one mechanism, owing to the rather large aspect ratio (layer diameter to height) at which this focusing effect begins to become important. That is, eddy diffusion limitations in the bulk, and the development as a consequence of a significant lateral temperature gradient. This mechanism has been confirmed in the experiment discussed at the end of this chapter and in Appendix N, and we expect to quantify it in the large ACOPO experiment in the near future. For now, we will make the conservative assumption that the layer is well mixed in the bulk.

In addition, recognizing that the situation described by the Globe-Dropkin correlation is symmetrical (two boundary layers of equal magnitude in temperature drop), we can "specialize" Eq. (5.35) to either of the two boundaries as

$$h = 0.15\,k\left\{\frac{g\beta}{\alpha\nu}\Delta T'\right\}^{1/3} \tag{5.41}$$

where $\Delta T' = T_{\ell,i} - T_b$ or $\Delta T' = T_b - T_{\ell,o}$, and T_b is the "bulk" temperature, and where properties are evaluated at the "film" temperature of the respective boundary layers. In Chapter 6 this equation is used in conjunction with Eq. (5.40) to describe the metal layer. That this formulation is appropriate and conservative has been demonstrated experimentally, as discussed in Appendix N.

To gain some general perspectives here on the role of this metallic layer, we make use of these equations together with the following simplifying assumptions (to eliminate second order effects):

1. The property group in Eqs. (5.40) and (5.41) has the same value at all three boundaries.
2. The upper and lower boundaries of the layer have the same area (thin layer, at ~90°).
3. The crust between the oxidic pool and metallic layer is thin.
4. The energy radiated from the surrounding cavity to the layer is negligible.

From energy balance considerations and for a nearly full hemisphere ($H \sim R$),[c] we then have (see Figure 5.1 for nomenclature):

$$(T_{\ell,i} - T_b)^{4/3} = (T_b - T_{\ell,o})^{4/3} + \frac{H_\ell}{R}(T_b - T_{\ell,m})^{4/3} \tag{5.42}$$

$$0.15k\left\{\frac{g\beta}{\alpha\nu}\right\}^{1/3}(T_b - T_{\ell,o})^{4/3} = \epsilon\sigma T_{\ell,o}^4 \tag{5.43}$$

$$q_{up} = 0.15k\left\{\frac{g\beta}{\alpha\nu}\right\}^{1/3}(T_{\ell,i} - T_b)^{4/3} \tag{5.44}$$

that is, three equations in the three unknowns T_b, $T_{\ell,i}$, and $T_{\ell,o}$. The $T_{\ell,i}$ can be eliminated by substitution from Eq. (5.44), and the T_b can be solved explicitly in terms of $T_{\ell,o}$ from Eq. (5.43) to obtain:

$$T_b = T_{\ell,o} + \left(\frac{\epsilon\sigma}{A}\right)^{3/4} T_{\ell,o}^3 \tag{5.45}$$

and

$$q_{up} = (\epsilon\sigma)T_{\ell,o}^4 + A\left(\frac{H_\ell}{R}\right)\left\{(T_{\ell,o} - T_{\ell,m}) + \left(\frac{\epsilon\sigma}{A}\right)^{3/4} T_{\ell,o}^3\right\}^{4/3} \tag{5.46}$$

where

$$A = 0.15k\left(\frac{g\beta}{\alpha\nu}\right)^{1/3} \tag{5.47}$$

This system of equations reveals a characteristic temperature for this problem given by

$$\tilde{T} = \left(\frac{A}{\epsilon\sigma}\right)^{3/8} \tag{5.48}$$

from which we can also define a characteristic heat flux,

$$\tilde{q} = \epsilon\sigma\tilde{T}^4 \tag{5.49}$$

Based on these quantities we can define the dimensionless variables:

$$T_b^* = \frac{T_b}{\tilde{T}} \quad T_{\ell,o}^* = \frac{T_{\ell,o}}{\tilde{T}} \quad T_{\ell,m}^* = \frac{T_{\ell,m}}{\tilde{T}} \quad q_{up}^* = \frac{q_{up}}{\tilde{q}} \tag{5.50}$$

[c] For $R/2 < H < R$, the ratio H_ℓ/R in Eq. (5.42) can be approximated well by H_ℓ/R_c, where R_c is the radius of the circular segment at position H.

and the above system becomes:

$$T_b^* = T_{\ell,o}^* + T_{\ell,o}^{*3} \tag{5.51}$$

$$q_{up}^* = T_{\ell,o}^{*4} + \left(\frac{H_\ell}{R}\right)\left\{T_{\ell,o}^* + T_{\ell,o}^{*3} - T_{\ell,m}^*\right\}^{4/3} \tag{5.52}$$

and the heat flux to the sidewall can then be written as:

$$q_{\ell,w}^* = \frac{1}{2}(T_b^* - T_{\ell,m}^*)^{4/3} \tag{5.53}$$

where the independent parameters of the problem, A, ϵ, $T_{\ell,m}$, and q_{up}, have been recast in terms of q_{up}^* and $T_{\ell,m}^*$ only. The other independent parameter, H_ℓ/R, remains the same.

The solution of the above system of equations can be obtained numerically, once and for all, and it is shown in Figures 5.9 and 5.10. From these, the sidewall heat flux can be obtained using Eq. (5.53), and the result is shown in Figure 5.11. When q_{up} is less than the value at which $T_{\ell,o}^* = T_{\ell,m}^*$ freezing of the upper boundary is predicted, and a closed form solution for the sidewall heat flux can then be simply obtained as:

$$q_{\ell,w} = \frac{1}{2} q_{up}\left\{1 + \frac{H_\ell}{R}\right\}^{-1} \tag{5.54}$$

As an example of using these solutions, consider the following typical values of the parameters: $A = 2764$ W/m$^2\cdot$ K$^{4/3}$, $\epsilon = 0.45$, $T_{\ell,m} = 1600$ K, $q_{up} = 600$ kW/m^2, and suppose that $H_\ell/R = 0.4$. From Eqs. (5.48) and (5.49) we obtain $\tilde{T} = 1.37 \cdot 10^4$ K, and $\tilde{q} = 9.1 \cdot 10^5$ kW/m^2, from Eq. (5.50) we obtain $T_{\ell,m}^* = 0.116$ and $q_{up}^* = 0.66 \cdot 10^{-3}$, and from Figures 5.9 and 5.10 we read $T_b^* = 0.12254$ and $T_{\ell,o}^* = 0.12078$. Then, from Eq. (5.53) we calculate $q_{\ell,w}^* = 5.58 \cdot 10^{-4}$, which finally gives $q_{\ell,w} = 508$ kW/m^2 (this can also be read directly off Figure 5.11). Moreover, from Figure 5.10 we find that freezing of the upper boundary will occur for an H_ℓ/R value of 0.3, if $q_{up} = 220$ kW/m^2 ($q_{up}^* = 0.24 \cdot 10^{-3}$); in this case the sidewall heat flux would be (from Eq. (5.54)) 85 kW/m^2, and for any larger value of H_ℓ/R the side heat flux could be obtained from

$$q_{\ell,w} = 110\left\{1 + \frac{H_\ell}{R}\right\}^{-1} \text{ kW/m}^2 \qquad \text{for} \quad \frac{H_\ell}{R} > 0.3 \tag{5.55}$$

Finally, the above results can be used to determine in a rather general way the metal layer thickness below which the sidewall heat flux will exceed the peak heat flux from the oxidic pool boundary (at the uppermost end of it). Again, the above typical values of A, ϵ, and $T_{\ell,m}$ can be used, so that we have only one "free" parameter—the q_{up}. A given value of q_{up} implies a pool

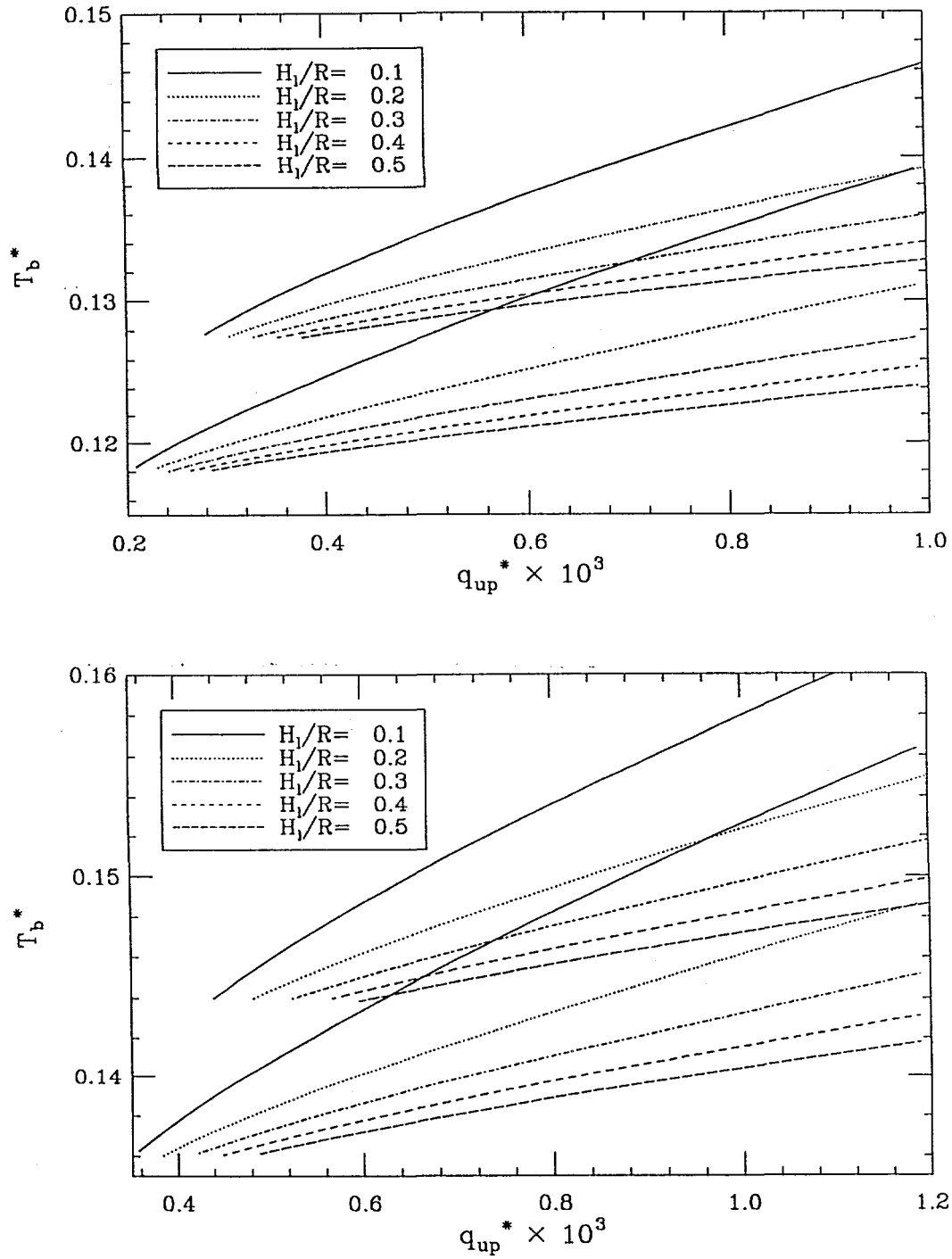

Figure 5.9. Solution to the system of Eqs. (5.51) and (5.52) for T_b^*, with H_ℓ/R and $T_{\ell,m}^*$ as the parameters. Each group of H_ℓ/R lines is for one value of $T_{\ell,m}^*$. [[Before using these figures first identify the $T_{\ell,m}^*$ values for each of the four groups of lines in Figure 5.10, and then proceed to Figure 5.9, recognizing that the four groups are similarly placed. Also note that corresponding lines (same $T_{\ell,m}^*$) start at the same value of the coordinate (q_{up}^*).]]

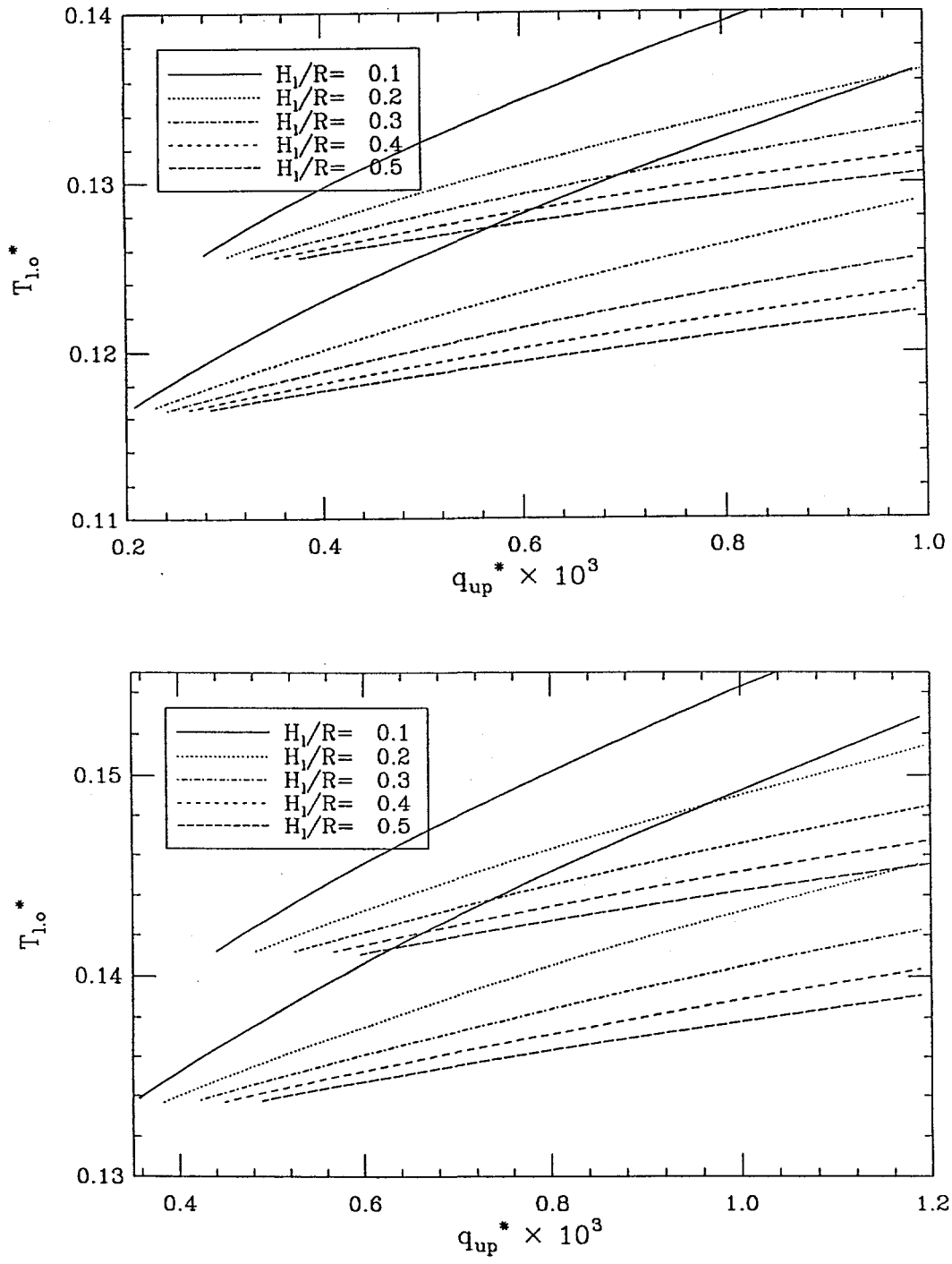

Figure 5.10. Solution to the system of Eqs. (5.51) and (5.52) for $T^*_{\ell,o}$, with H_ℓ/R and $T^*_{\ell,m}$ as the parameters. Each group of H_ℓ/R lines is for one value of $T^*_{\ell,m}$. [[It can be read from the position at which the lines stop.]] As noted in the text, the lines stop when there is freezing at the upper boundary, that is, when $T^*_{\ell,o} = T^*_{\ell,m}$. There are four such groups.

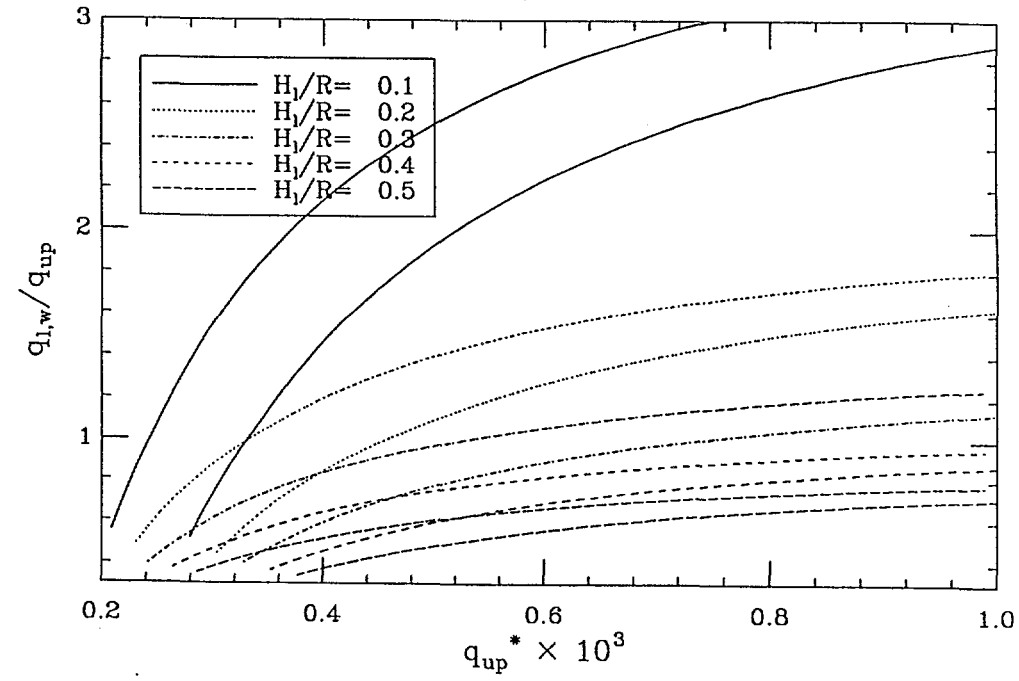

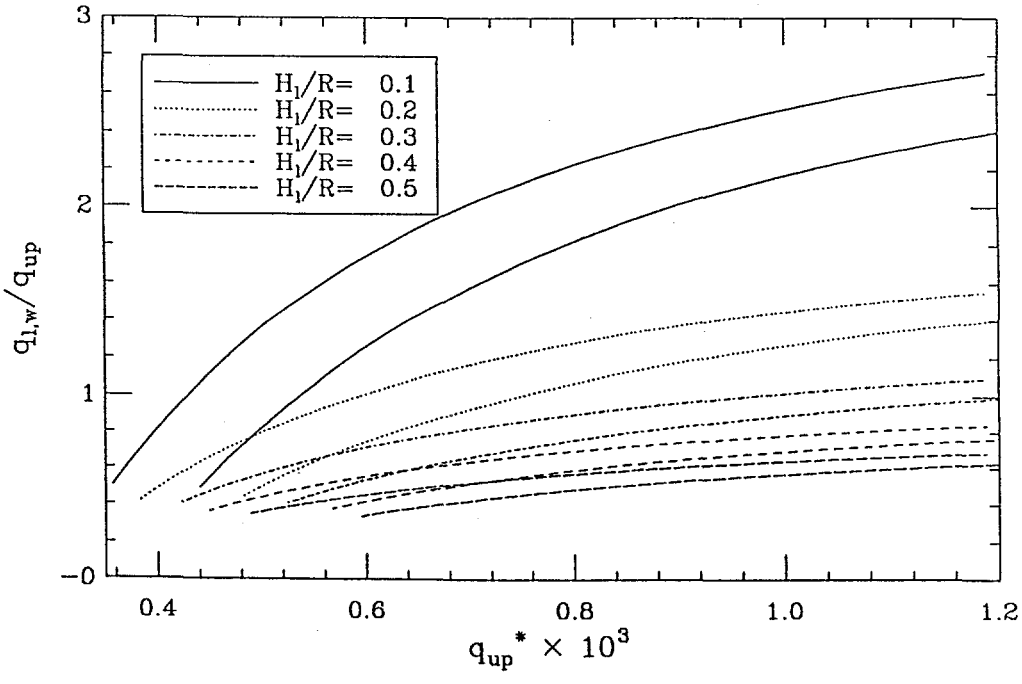

Figure 5.11. The heat flux to the sidewall, in contact with the metallic layer, obtained from the solutions in Figure 5.10 and Eq. (5.53). Again, each group of H_ℓ/R lines corresponds to one value of $T^*_{\ell,m}$. Note that the $T^*_{\ell,m}$ can be found in each case with the help of Figure 5.10 (by locating the corresponding minimum value of q^*_{up})

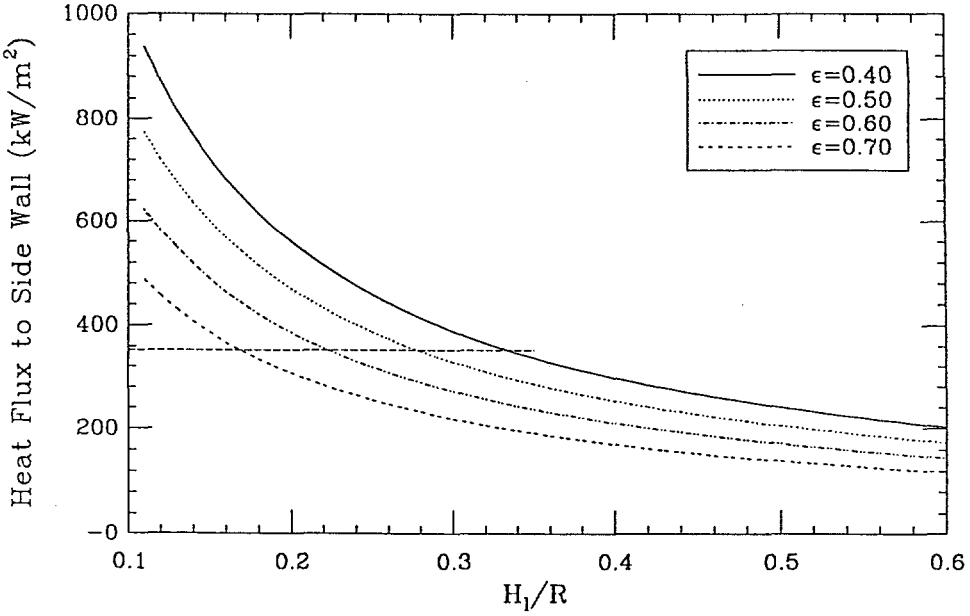

Figure 5.12. Solution to the system of Eqs. (5.51) and (5.52) in physical variables, with the emissivity as the parameter. q_{up} = 400 kW/m^2, and A = 2764 W/m^2· K$^{4/3}$. For the chosen value of q_{up}, the peak heat flux at the edge of the oxidic pool is 350 kW/m^2, and the intersections shown represent the threshold values of H_ℓ/R for the various emissivities.

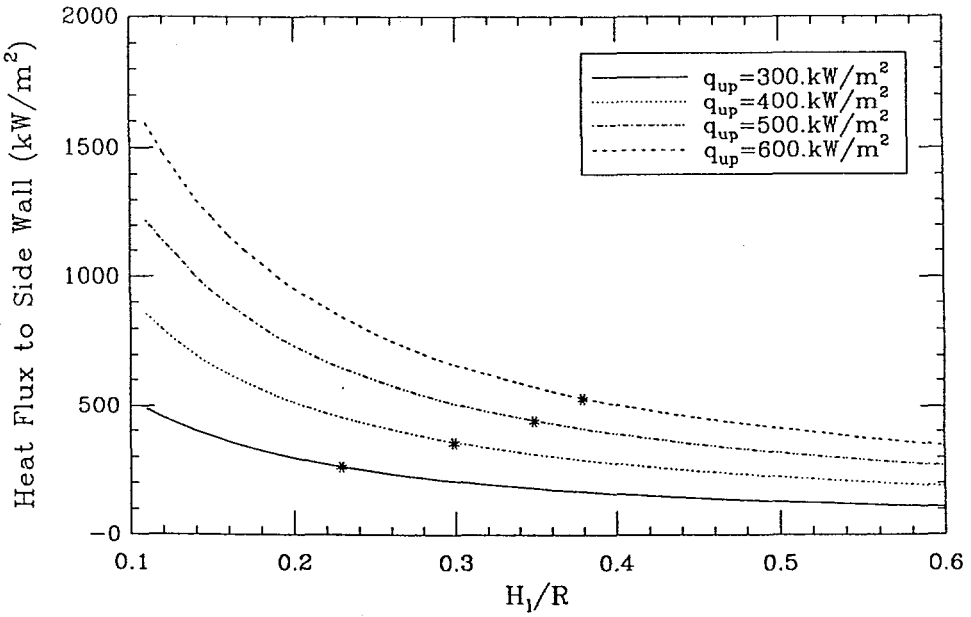

Figure 5.13. Solution to the system of Eqs. (5.51) and (5.52) in physical variables, with the imposed upward heat flux as the parameter. ϵ = 0.45, A = 2764 W/m^2· K$^{4/3}$. The threshold values of H_ℓ/R, obtained as in Figure 5.12, are shown by the $*$'s.

Rayleigh number (from Eq. 5.12), which in turn gives q_{dn} (from Eq. 5.28), and the peak flux at $\theta \sim 90°$, from Eq. (5.30). This value is then set equal to $q_{\ell,w}$ and making use of the procedure in the previous paragraph, in reverse, we can determine the corresponding value of H_ℓ/R. That is, calculate $\tilde{T}$, $T^*_{\ell,m}$, and $\tilde{q}$, use q_{up} and $q_{\ell,w}$ to get q^*_{up} and $q^*_{\ell,w}$, use Eq. (5.53) to get T^*_b, and from Figure 5.10 read (or interpolate) the H_ℓ/R value that satisfies this solution. A graphical depiction of the solution in dimensional variables, and including the just-discussed "threshold" values of H_ℓ/R (the "threshold" marks the transition from oxidic pool to melt layer heat flux dominance) is provided in Figures 5.12 and 5.13.

[[ADDENDUM TO CHAPTER 5]]

FLUX SHAPE EFFECTS OVER THE METAL LAYER

It is well established that in natural convection from a vertical, flat plate, under turbulent flow conditions, the Nu number is proportional to the one-third power of the Ra number, which leads to a length-scale independence of the heat transfer coefficient. In particular, this is true for Eq. (5.39) utilized in the present work.

Now, transition to turbulence occurs at a local Gr_x number (based on the length from the initiation of the boundary layer) of $\sim 10^8$, which for a Pr number fluid of 0.13 translates to a local Ra_x of $\sim 10^7$. For our base case the Ra based on the whole metal layer thickness is $\sim 10^{10}$, and noting that

$$\frac{\mathrm{Ra}_x}{\mathrm{Ra}} = \left(\frac{x}{H_\ell}\right)^3 \tag{5.56}$$

we find that transition occurs at an x/H_ℓ value of 0.1. For the 80 cm pool, therefore, we can expect a uniform heat transfer coefficient for the lower 90% of the height (or 72 cm) and a short, 8-cm long, region at the top, where the flow may be laminar and/or transitional. For the extreme parametric case (Figure 7.16) the Ra number is $\sim 5 \cdot 10^8$, and transition is obtained at an x/H_ℓ value of 0.27, or 6 cm. These represent the two extremes for the problem at hand, and the insensitivity in the physical dimension of the laminar region is due to the cubic dependence in Eq. (5.56).

In the laminar region the heat flux varies with position in the manner derived by Squire (1938):

$$Nu_x = 0.508\ \mathrm{Pr}^{1/4}(1+\mathrm{Pr})^{-1/4}\ \mathrm{Ra}_x^{1/4} \tag{5.57}$$

For $Pr = 0.13$, this becomes

$$Nu_x = 0.30\, Ra_x^{1/4} \tag{5.58}$$

and the flux (heat transfer coefficient) shape relative to that in the turbulent region can be obtained by dividing through Eq. (5.40), as

$$\frac{h_x}{h} = \frac{Nu_x}{Nu}\left(\frac{H_\ell}{x}\right) = 3.95\frac{Ra_x^{1/4}}{Ra^{1/3}}\left(\frac{H_\ell}{x}\right) \quad Ra_x < 10^7 \tag{5.59}$$

The result for the two extreme cases considered above is shown in graphical form in Figure 5.14. Note that the high fluxes are confined to such a small region that we can expect 2D conduction effects to more than compensate for them. This is demonstrated below for the more limiting, extreme parametric case.

The heat transfer model is illustrated in Figure 5.15. The convective heat fluxes over the segment of the wall in contact with the oxidic pool were obtained from the analysis that led to Figure 7.16. The radiative flux at the upper exposed segment was obtained from the radiation emitted from the top of the metallic pool, again according to the integral analysis. The wall shape was obtained from an iterative process. Starting with a uniform temperature defined by the outer boundary, the wall in its original thickness is subjected to the expected heat fluxes in a steady state heat transfer calculation. This determines a temperature distribution through the thickness, at steady state, which exceeds the melting temperature in several points. The shape is changed to reflect this melting process and the calculation is repeated, yielding new temperature profiles through the wall. The iteration ends when an internal isothermal boundary at the specified melting point (1600 K) is obtained.

The results of the calculation are shown in Figure 5.16. In the upper portion we find that 2D conduction is able to just about compensate for the enhanced heat transfer in the entrance region. In the lower portion we find that 2D conduction can provide some relief of heat flow and hence allow a locally smoother transition in the wall thickness. These are generic, bounding results.

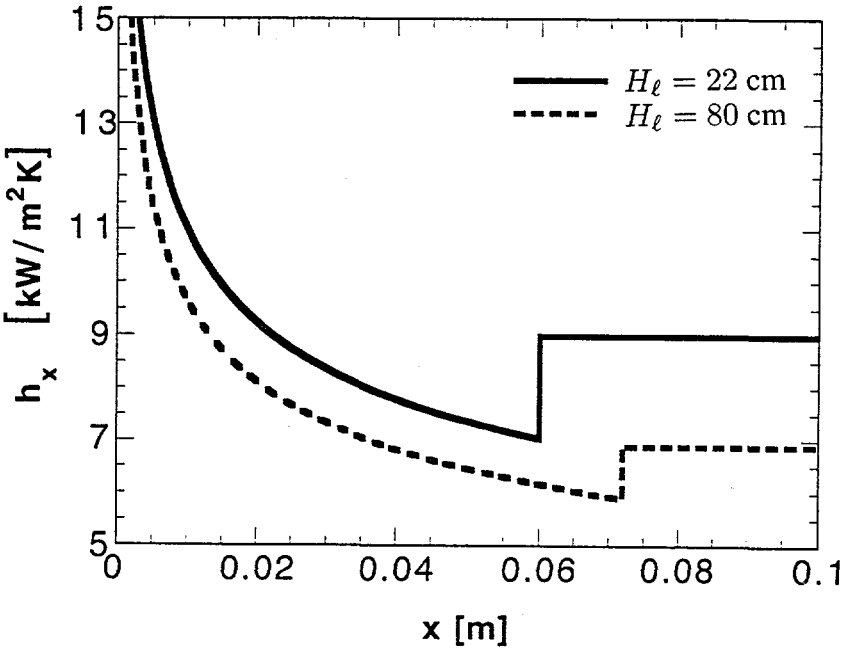

Figure 5.14. Heat flux shape in the entrance, laminar boundary layer, region for the two extreme cases considered in Chapter 7. The $H_\ell = 80$ cm is for the Base Case, and the $H_\ell = 22$ cm is for the Extreme Parametric (see Figure 7.16 in Chapter 7).

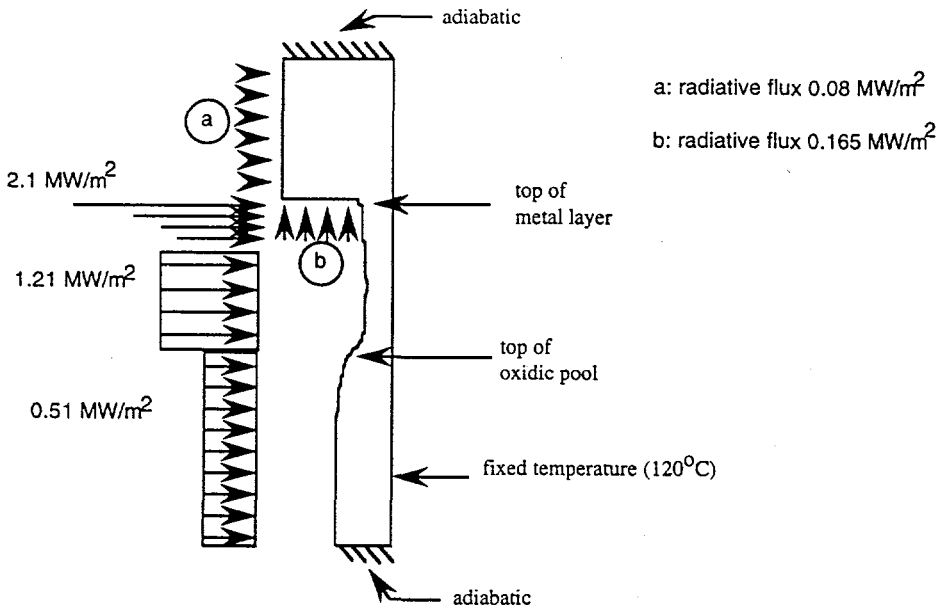

Figure 5.15. The heat transfer model employed to evaluate entrance region effects in conjunction with 2D conduction. Wall dimensions are to scale, the upper portion being the full wall thickness of 15 cm.

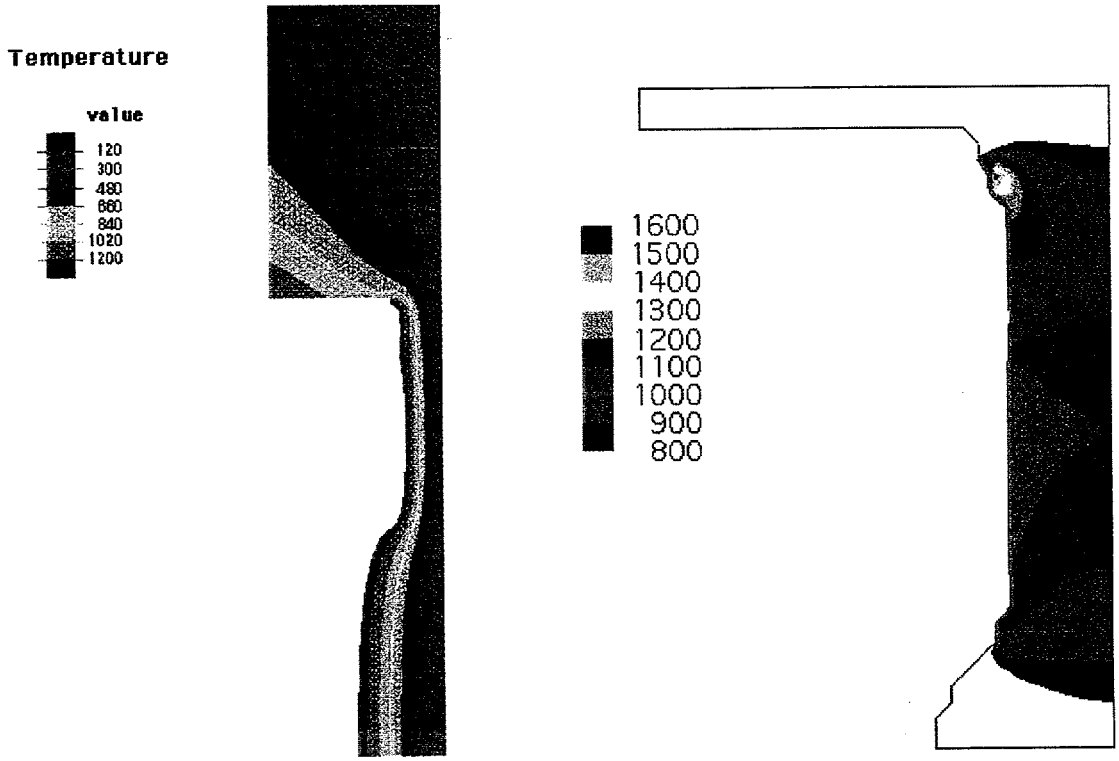

Figure 5.16. Calculated temperature (left; in degrees Celsius), and normal (to the wall outer boundary) heat fluxes (right, only the region at the metallic layer is shown; in kW/m^2) for the model of Figure 5.15.

6 FORMULATION OF THERMAL LOADS UNDER NATURAL CONVECTION

The purpose of this chapter is to explain how the key transport processes discussed in the previous chapter are integrated into an overall computational scheme. In addition to these processes, the thermal radiation/conduction path to and through the core barrel and vessel wall to the water outside is considered explicitly. Since the model and the computer programming work are straightforward, we took a special purpose approach; that is, emphasizing simplicity of presentation through approximations quite acceptable in this application, rather than generality. Checks in the calculations, as described below, ensured that the error due to these approximations is less than a few percent and always on the conservative side.

We are given the volumes V and V_ℓ of the oxidic pool and the metallic layer respectively, their compositions, and the volumetric heat generation rate, $\dot{Q}$, and we seek to find $q_w(\theta)$ as a function of position all around the lower head. From the volumes we can calculate the heights, H and H_ℓ, and polar angles, θ_p and θ_ℓ, using:

$$V = \frac{1}{3}\pi H^2(3R - H) \quad \text{for} \quad V \leq \frac{2}{3}\pi R^3 \tag{6.1}$$

$$V + V_\ell = \frac{1}{3}\pi(H + H_\ell)^2(3R - H - H_\ell) \quad \text{for} \quad V + V_\ell \leq \frac{2}{3}\pi R^3 \tag{6.2}$$

and

$$cos\,\theta_p = \frac{R - H}{R}, \quad cos\,\theta_\ell = \frac{R - H - H_\ell}{R} \tag{6.3}$$

The above apply for volumes less than that of the hemisphere ($\frac{2}{3}\pi R^3$), which is always true for V. When this is violated for $V + V_\ell$ all that is needed is H_ℓ, which can be obtained by adding the height in the cylindrical portion of the vessel to the metal height in the hemisphere (i.e., $R - H$).Using the compositions we can obtain the thermophysical properties from Appendix L and the liquidi from the phase diagrams in Figures 6.1 and 6.2. The heat generation rate is assumed to be uniformly distributed throughout the oxidic pool (including crusts). In reality, some of this decay energy will escape the pool as gammas, to be deposited in the vessel wall or the metallic layer, while some will escape the system altogether. Scoping and sensitivity calculations have indicated that such effects are quite negligible. We now proceed to solve for the pool, the metal layer, and the radiative/conduction path, in that order.

The oxidic pool maximum temperature (T_{max}) is obtained from an energy balance, which, ignoring the crusts, can be written as:

$$\dot{Q}V = q_{up}S_{up} + q_{dn}S_{dn} \tag{6.4}$$

where S_{up} and S_{dn} are the flat and curved areas respectively of the surface of the hemispherical segment.

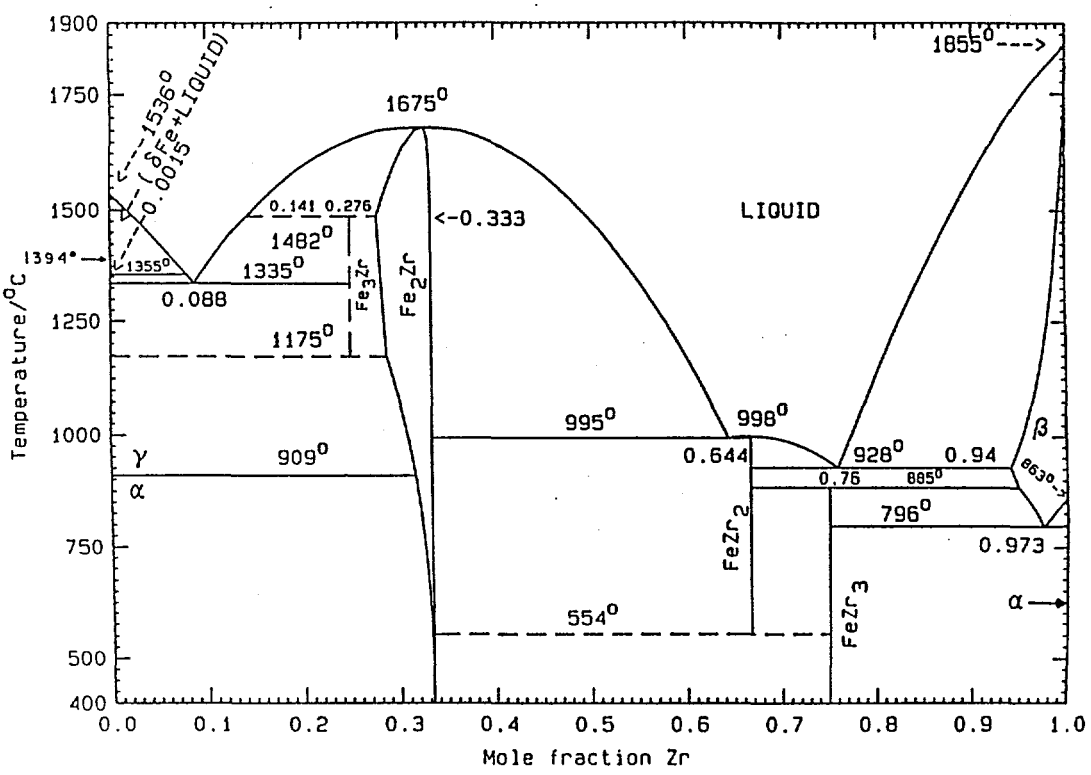

Figure 6.1. The iron-zirconium phase diagram (Pelton et al. 1994).

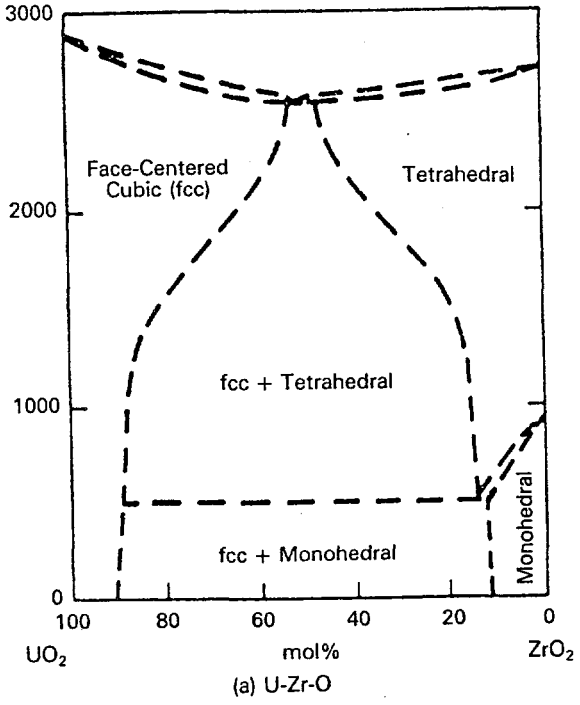

Figure 6.2. The UO_2–ZrO_2 phase diagram (Butterman and Foster, 1967).

The q_{up} and q_{dn} are obtained from:

$$q_{up} = h_{up}(T_{max} - T_m) \quad \text{and} \quad q_{dn} = h_{dn}(T_{max} - T_m) \tag{6.5}$$

with h_{up} and h_{dn} given by Eqs. (5.12) and (5.28) respectively. As we will see in the next chapter, the H/R is greater than 0.8, which makes the factor $(H/R)^{0.25}$ (see Eq. 5.21) greater than 0.95, indicating that it can be ignored—however, it is accounted for in parametric cases with lower H/R values. T_m is the oxidic material liquidus temperature. Once T_{max} is found the fluxes are also known from Eqs. (6.5). The q_{up} will be used (further below) as an input to the treatment of the metallic layer, while q_{dn} is now used to obtain the crust thickness, $\delta_{cr}(\theta)$, and the heat flux into the vessel wall, $q_w(\theta)$, as functions of θ.

This can be done by means of a local energy balance as:

$$q_w(\theta) \equiv q_{dn}(\theta) + \dot{Q}\delta_{cr}(\theta) = k_w \frac{T_w(\theta) - T^{**}}{\delta_w(\theta)} \tag{6.6}$$

[[k_w is the effective thermal conductivity of the steel wall, accounting for the temperature dependence as given in Appendix L]] and consideration of conduction within the crust [[we mean here an "effective" crust that includes the slush layer that allows the transition from the liquidus to the solidus temperature—see also responses to Henry (item #2) and Tuomisto (item #2)]]:

$$T_m - T_w(\theta) = \frac{\dot{Q}\delta_{cr}^2(\theta)}{2k_{cr}} + \frac{\delta_{cr}(\theta)}{k_{cr}} q_{dn}(\theta) \tag{6.7}$$

where $q_{dn}(\theta)$ is obtained from q_{dn} and the shape function given by Eq. (5.30) as discussed in Chapter 5. In the above, $T_w(\theta)$ is set equal to the wall liquidus temperature, $T_{w,m}$, if it is found to be above it. Thus, Eqs. (6.6) and (6.7) constitute a system of two equations in two unknowns, $\delta_{cr}(\theta)$ and $T_w(\theta)$ or $\delta_w(\theta)$, depending on whether there is wall melting. At the conclusion of this calculation we compute

$$\int_0^\theta \delta_{cr}(\theta') 2\pi R \cos\theta d\theta \tag{6.8}$$

and have thus ensured that it is always less than a few percent of V (the oxidic pool volume) in this application.

Now, having q_{up}, the metallic layer is treated in the manner described by Eqs. (5.42) to (5.44) except for three additions: (a) accounting for the area difference between the upper and lower boundaries, (b) accounting for variations of thermophysical properties with temperature, and (c) representing the radiation/conduction path. Thus, we have:

$$sin^2(\theta_p) A_{\ell,i}(T_{\ell,i} - T_b)^{4/3} = sin^2(\theta_\ell) A_{\ell,o}(T_b - T_{\ell,o})^{4/3} + \frac{2H_\ell}{R} A_{\ell,m}(T_b - T_{\ell,m})^{4/3} \tag{6.9}$$

$$A_{\ell,o}(T_b - T_{\ell,o})^{4/3} = \sigma(T_{\ell,o}^4 - T_{s,i}^4) \left\{ \frac{1}{\epsilon} + \frac{1-\epsilon_s}{\epsilon_s} \frac{S_{\ell,o}}{S_s} \right\}^{-1} \tag{6.10}$$

$$q_{up} = A_{\ell,i}(T_{\ell,i} - T_b)^{4/3} \tag{6.11}$$

where

$$A_{\ell,j} = \mathcal{F}(\mathrm{Pr}_{\ell,j})k \left\{ \frac{g\beta}{\alpha\nu} \right\}_{\ell,j}^{1/3} \qquad j = i,\ o,\ \text{or}\ m$$

the index indicating the boundary layer at whose "film" temperature the properties are to be evaluated, [[the function $\mathcal{F}(\mathrm{Pr}_{\ell,j})$ indicating the Prandtl number dependence in Eqs. (5.34) and (5.39) for $j = i$ or o and $j = m$ respectively]], and

$$\sigma(T_{\ell,o}^4 - T_{s,i}^4) \left\{ \frac{1}{\epsilon_s} \frac{S_s}{S_{\ell,o}} + \frac{1-\epsilon_s}{\epsilon_s} \right\}^{-1} = k_s \frac{T_{s,i} - T_{s,o}}{\delta_s} = \epsilon\sigma(T_{s,o}^4 - T_v^4) = k_w \frac{T_v - T^{**}}{\delta_o} \tag{6.12}$$

This system of equations is solved by using T_s as an iteration parameter. That is, with a value of T_s assumed, Eqs. (6.9) to (6.11) are solved; with the $T_{\ell,o}$ thus found, $T_{s,i}$ and $T_{s,o}$ are computed from the first two equations in Eq. (6.12); with these values the third equation is checked to determine whether it is satisfied, and the procedure is repeated until this is so. Once the temperatures are known the heat flux to the sidewall, $q_{\ell,w}$, can be computed by

$$q_{\ell,w} = A_{\ell,m}(T_b - T_{\ell,m})^{4/3} \tag{6.13}$$

and the existence of an oxidic crust between the pool and the metallic layer is verified by the conditions that the quadratic

$$T_m - T_{\ell,i} = \frac{\dot{Q}\delta_{cr}^2}{2k_{cr}} + \frac{\delta_{cr}}{k_{cr}} q_{up} \tag{6.14}$$

has one positive root as long as $(T_m - T_{\ell,i}) > 0$. That this crust is thin is verified by the condition:

$$0 < \frac{\delta_{cr}\dot{Q}}{q_{up}} < 0.03 \tag{6.15}$$

Finally, at the conclusion of a computation the Rayleigh numbers are computed at the appropriate film temperature properties to ensure that the correlations have been applied within their designated ranges.

Before carrying out the detailed quantification with this model it is interesting to determine the effect of the additional effects included in the treatment of the metallic layer, in relation to the simpler model described at the end of Chapter 5. For this purpose, we have carried out a series of calculations, spanning relevant ranges of the parameters for this application, and plotted the results in the manner of Figures 5.12 and 5.13. As seen in Figures 6.3 and 6.4, the results are essentially indistinguishable for $0.4 < \epsilon < 0.5$, which constitutes the main range of interest to this study. Some difference appears for higher values of the emissivity, but it remains less than 12% even for the extreme case of $\epsilon = 0.7$, $H_\ell = 0.1$. Note that on this basis the whole problem

can be reduced to a hand calculation. Specifically, once Eq. (6.4) is solved for $(T_{max} - T_m)$, the q_{up} and q_{dn} can be found via Eqs. (6.5), and then the solution for the metal layer can be simply read off Figures 5.9 through 5.11. This may be convenient for the reader, in exploring thermal loads under any specific conditions of interest. Our calculations in the next chapter are carried out with the full model put into a relatively straightforward computer program.

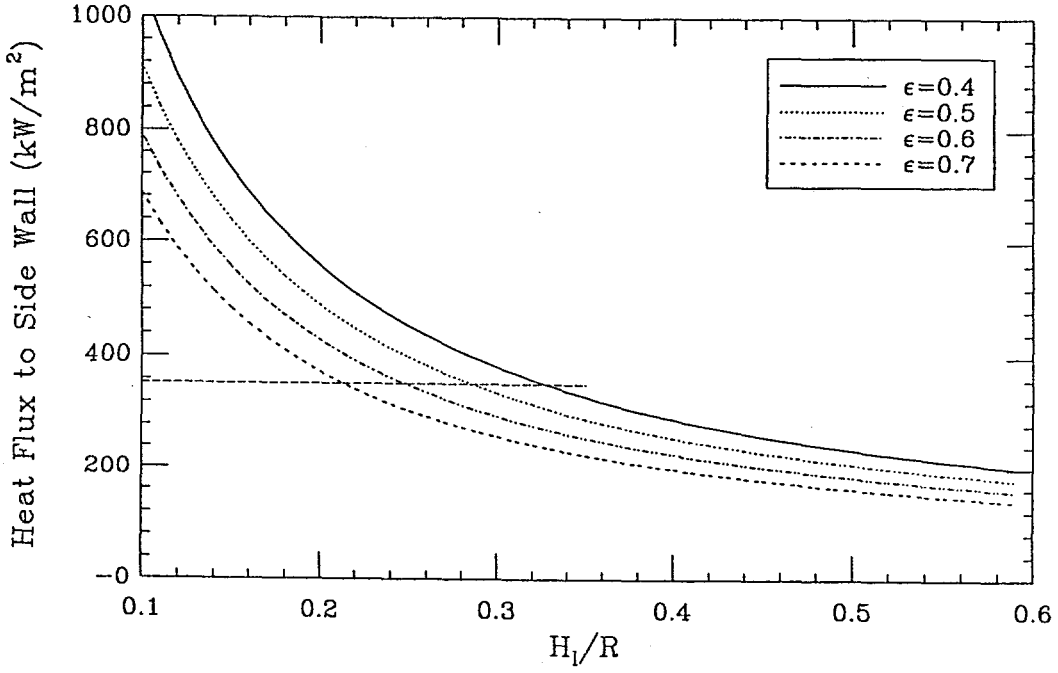

Figure 6.3. Solution to the system of Eqs. (6.9) through (6.13), with the emissivity as the parameter. $q_{up} = 400$ kW/m^2, and $A \sim 2764$ W/m$^2 \cdot$ K$^{4/3}$ (property variations with temperature properly accounted for). For the chosen value of q_{up}, the peak heat flux at the edge of the oxidic pool is 350 kW/m^2, and the intersections shown represent the threshold values of H_ℓ/R for the various emissivities.

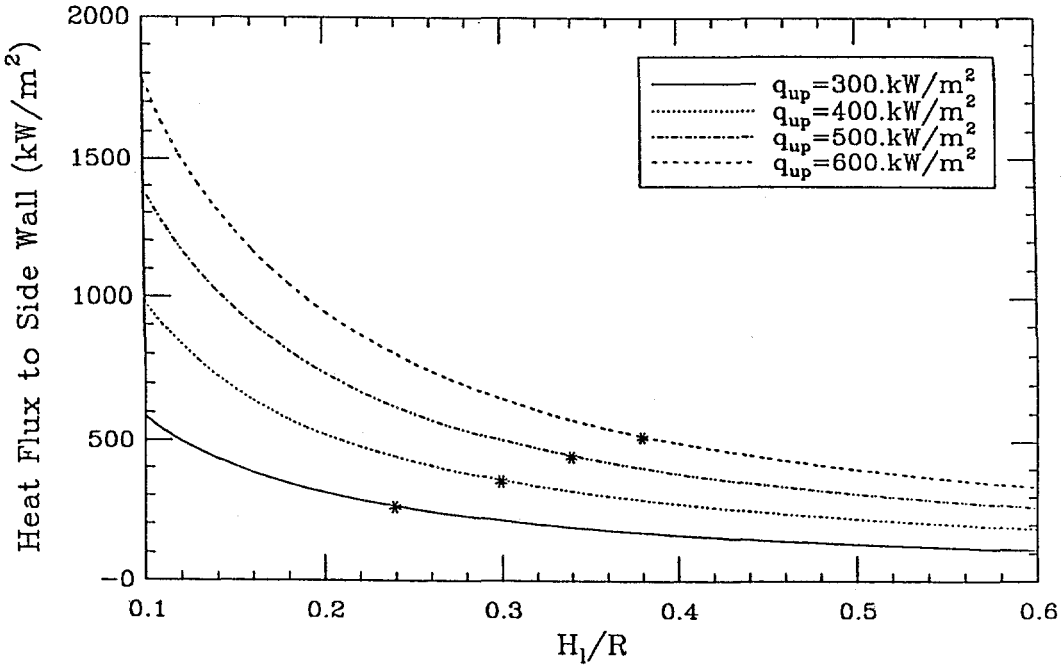

Figure 6.4. Solution to the system of Eqs. (6.9) through (6.13), with the imposed upward heat flux on the parameter. $\epsilon = 0.45$, $A \sim 2764$ W/m$^2 \cdot$ K$^{4/3}$. The threshold values of H_ℓ/R, obtained as in Figure 6.3, are shown by the $*$'s.

7 QUANTIFICATION AND ASSESSMENT OF THERMAL LOADS UNDER NATURAL CONVECTION

7.1 Quantification of Input Parameters

In this chapter we take on the numerical implementation of the formulation provided in Chapter 6. But first it is appropriate to briefly discuss some methodological aspects, and this is done with reference to Appendix A. We recognize that we have a deterministic model, fully supported by experiments and scaling considerations, and therefore modelling uncertainty can be considered negligible in relation to the margins inherent in the definition of this one bounding configuration. Also, we have seen that there is no scenario dependence. Thus, the model is appropriate for a Grade B assessment (as defined in Appendix A).

The parameters are basically deterministic, except for the decay power, the quantity of zirconium oxidized (this affects the volumes and compositions in the metallic layer and oxidic pools), and the quantity of steel in the metallic layer (this affects the depth). All three quantities are to some (minor) degree intangible and, therefore, their values and uncertainties will be considered very carefully. Our approach is to provide reasonably bounding distributions in the ROAAM sense using Table A.1 as a guide. More of an intangible is the possibility of an oxidic "film" on top of the metallic layer, a film that is thick enough to make the conduction resistance overtake the improved radiation emissivity due to it. This is approached by means of a sensitivity study. Also approached by sensitivity studies is the use of Mayinger's correlation instead of Eq. (5.28), and of the UCLA flux shape correlation instead of Eq. (5.30). Finally, we have uncertainties on thermophysical properties, as described in Appendix L; they are of minor significance, but included anyway by means of Gaussian distributions with two standard deviations at the uncertainty intervals quoted in Appendix L. These parameters, their mean values, and their 2σ values, are summarized in Table 7.1. In this table is included also the emissivity value used for the steel layer, as measured in the laboratory (see Appendix I). While any small amount of oxides and/or impurities would tend to produce higher values, such effects are difficult to judge, and the conservatively bounding value for a perfectly clear surface is preferred for these calculations. The emissivity of the "sink" surface (upper reactor inner boundaries), ϵ_s, is taken as 0.8, as is appropriate for high temperature (oxidized) solid stainless steel. Because of the very large areas involved, the effect of any reasonable variation in this parameter is negligible.

The decrease of the radioactive decay power with time is shown in Figure 7.1. From this we have to subtract the volatile component; however, this cannot be done as a constant fraction because the volatiles are decaying faster. Thus, in Figure 7.2 we show how the volatile component fraction changes with time (Schnitzler, 1981), and in combination with Figure 7.1, we obtain

Table 7.1. Property Values and Uncertainty Intervals Used in the Computations		
Property	Oxide Phase	Metallic Phase
Melting Point (K)	2973	1600
Density (kg/m^3)	Volume Averaged $\rho_{UO_2} = 8740$ $\rho_{ZrO_2} = 5990$	Volume Averaged $\rho_{Fe} = 7020$ $\rho_{Zr} = 6130$
Thermal Conductivity (W/k·m)	5.3 ± 1.6 ($\pm 30\%$)	25 ± 6.3 ($\pm 25\%$)
Viscosity (Pa·s) $\times 10^{-3}$	$\frac{5.3}{33.4}\ exp\left(\frac{10430}{T}\right) \pm 2.5$	$\frac{4.1}{37.0}\ exp\left(\frac{5776}{T}\right) \pm 1.1$
Specific Heat (J/kg·K)	Mass Averaged $c_{p,UO_2} = 485$ $c_{p,ZrO_2} = 815$	Mass Averaged $c_{p,Fe} = 835$ $c_{p,Zr} = 458$
Volume Thermal Expansion Coefficient (1/K) $\times 10^{-4}$	1.05 ± 0.12 ($\pm 11\%$)	1.1 ± 0.18 ($\pm 16\%$)
Effective Thermal Conductivity (W/k·m)	2.8 ± 0.4 ($\pm 14\%$) Crust	32.0 Vessel Wall
Emissivity	Crust 0.8	Molten State 0.45

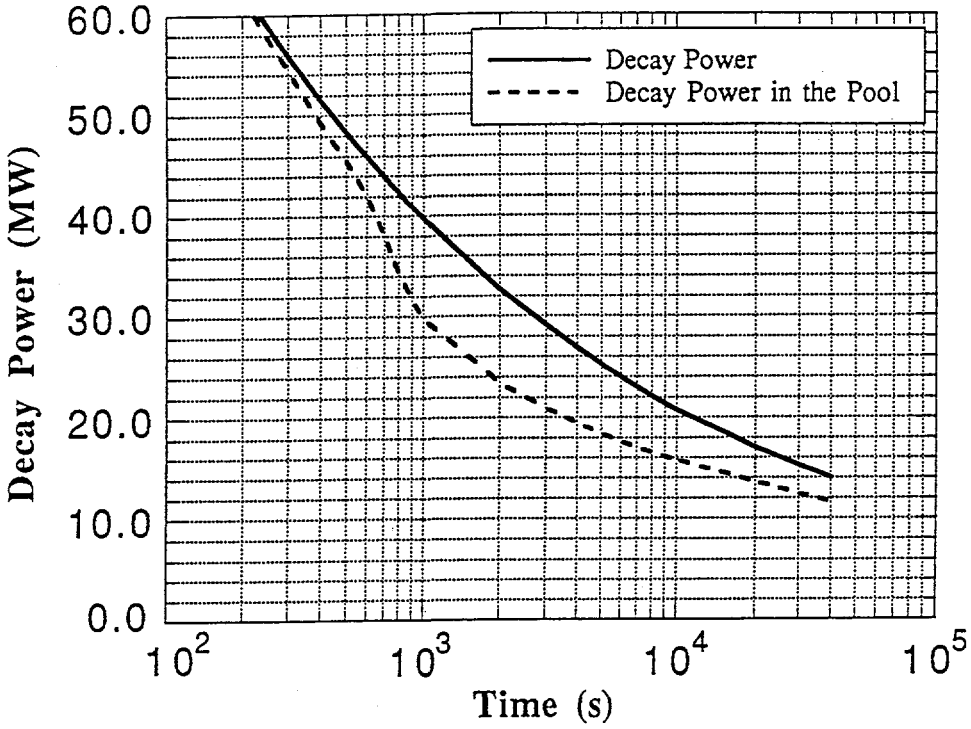

Figure 7.1. The decay power as a function of time after shutdown (AP600, 1994). The "in pool" curve accounts for loss of volatiles, their contribution being as in Figure 7.2. The rated power of the AP600 is 1933 MW.

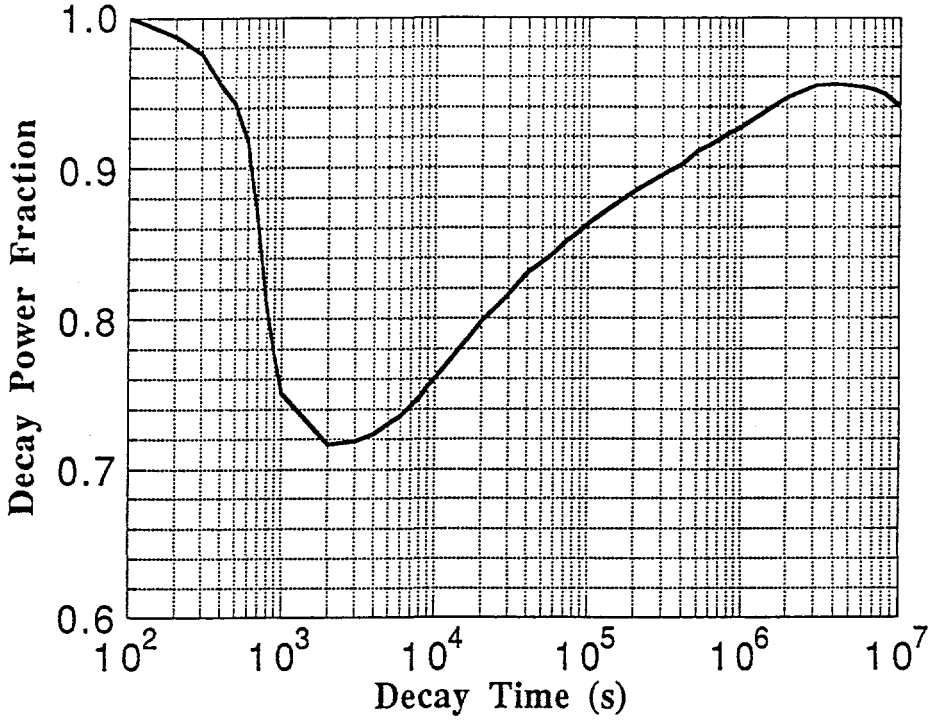

Figure 7.2. Fraction of total decay power remaining in pool, accounting for volatile fission product release as a function of time after shutdown.

the decay power for the non-volatile components as a function of time (also shown in this figure). We now proceed to quantify the fraction of the zirconium oxidized and, with this plus all the above information, to arrive at probability distributions that characterize the volumes (and heights) of the oxidic pool and metallic layer, and the volumetric heat generation rate. The various materials inventories within the reactor vessel are listed in Table 7.2.

Table 7.2. Material Inventories in the Reactor Vessel

Component	Material	Mass (kg) $\times 10^{-3}$	Volume[1] (m^3)
Fuel	UO_2	75.9	8.68
Core Cladding	Zircalloy	15.8	2.58
Peripheral Cladding[2]	Zircalloy	3.4	0.56
Control Rods	Silver/Indium/Cadmium	2.9	0.43
Lower Internals Package (LIP) — Estimated			
Core Barrel	Stainless	40	5.70
Lower Support Plate[†]	Stainless	25	3.56
Lower Supports	Stainless	2	0.29
Reflector	Stainless	40	5.70
Upper Internals Package (UIP) — Estimated			
Upper Support Plate	Stainless	23	3.38
Support Columns	Stainless	4	0.57
Rod Guides	Stainless	8	1.14
Lower Guide Tubes	Stainless	8	1.14
Upper Core Plate	Stainless	3.5	0.5

[1] In liquid state

[2] Mostly at the core entrance, as 7.5 cm-long pellets, at the lower end of the fuel rods

[3] Including inlet nozzles

Available information on zirconium oxidation in a severe accident includes: the TMI-II accident, a large number of out-of-pile experiments such as those in the CORA facility in KfK, and a large number of special purpose models and code calculations. All this evidence points strongly to a heavy zirconium oxidation, and this is easy to see especially because of the open core geometry in a PWR. Thus, we assign a most likely expected value, for the fraction oxidized, in the range 40 to 60%, one unlikely range (the 10^{-1} level) in the 10% interval immediately above this range, and one highly unlikely (10^{-2}) in the 20% interval beyond. Higher values may be appropriate with recovery, but our interest here, obviously, is for unrecovered cases. [Also, higher values would reduce the decay power density, and hence the thermal loads.] This quantification is shown in Figure 7.3 in the form of a probability density function.

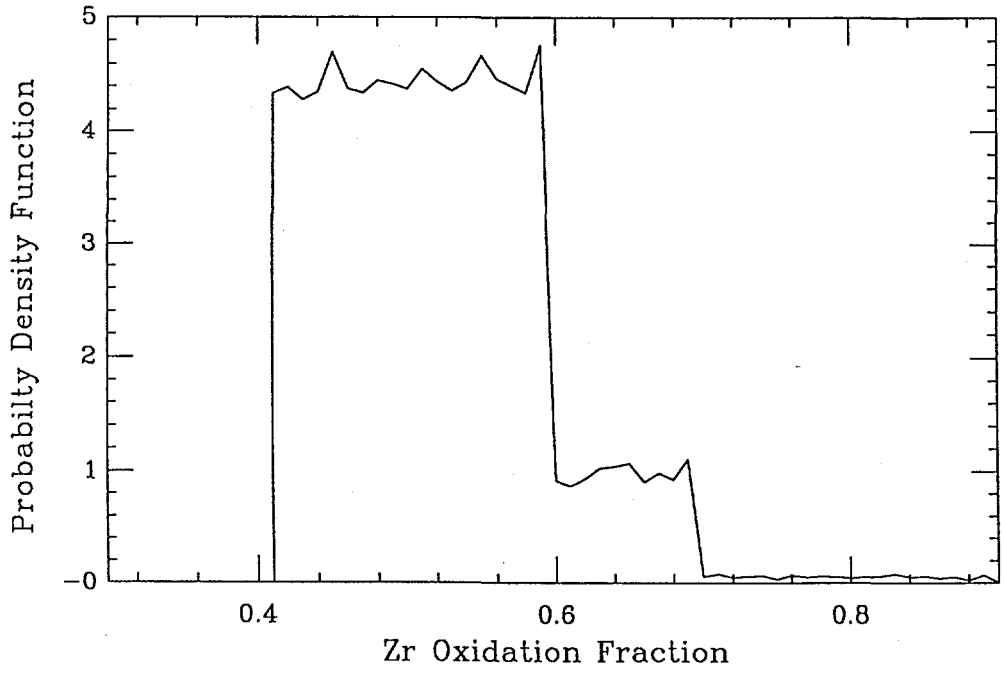

Figure 7.3. Specification of the fraction of zirconium oxidized, as a probability density function.

Using these fractions and the total quantity of zirconium present we can obtain the quantities of ZrO_2 to be mixed with UO_2 in the oxidic pool, and the quantity of Zr metal to be mixed with steel in the metallic layer. For the UO_2 we use the whole inventory which leads directly to the probability distribution of the oxidic pool height, shown in Figure 7.4. Since the radius of the vessel is 2 m, these heights correspond to polar angles in the range $75° < \theta < 81°$; that is, a nearly full hemisphere, as mentioned already.

For the metallic layer, we note that the lower (or core) support plate is positioned at a height of 1.5 m (its bottom face), and according to the above, it would be in contact with the oxidic pool. This implies that the metallic layer cannot form until this plate (25 tons) melts in, which would also release any remaining (not yet melted) portions of the reflector (40 tons), and the lowest portions of the core barrel (a total of 40 tons). The metallic layer should also have to include all the lower internal structures (2 tons). Thus, the only intangible aspect is the extent of involvement of the upper internal structures, and the probability assignments are made as follows: a likely range ($\sim$10°) for 67 to 72 tons (to include 1 m of core barrel), an unlikely range ($\sim 10^{-1}$) for 72 to 77 tons (to include 2 m of core barrel), and a very unlikely range ($\sim 10^{-2}$) for 77 to 87 tons (to include a small portion of the upper internals). The probability density function corresponding to this specification is shown in Figure 7.5. With these values added to the amounts of unoxidized zirconium, we can obtain the probability distribution of the

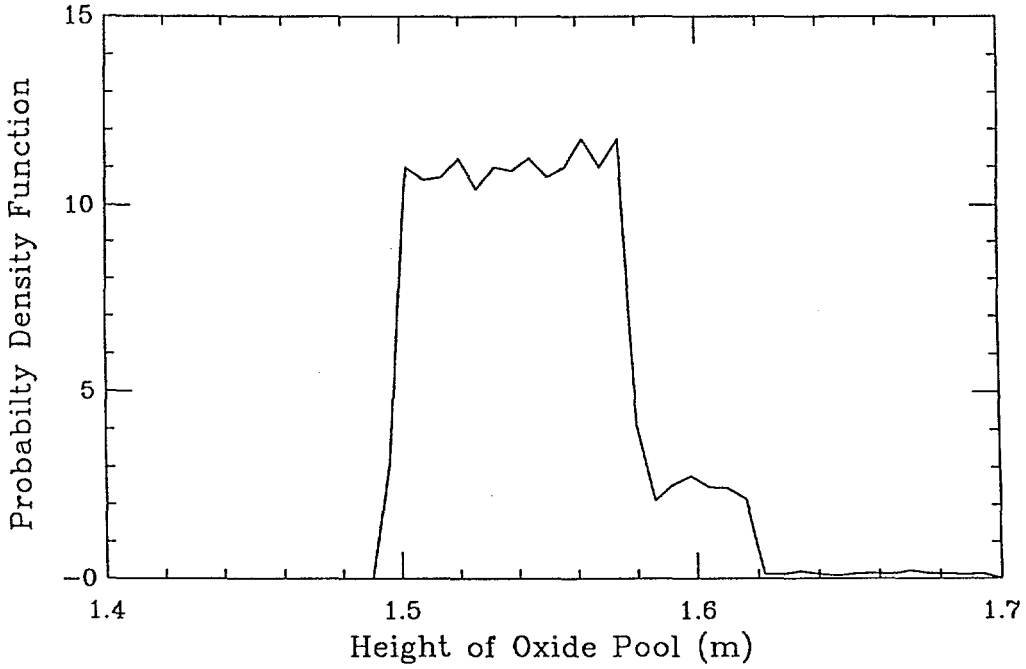

Figure 7.4. The oxide pool height probability distribution resulting from a UO_2 volume of 8.68 m^3, a hemisphere radius of 2 m, and the specification of Figure 7.3.

metallic volume, and hence the layer height, as shown in Figure 7.6. Note that in constructing this figure we had to combine also Figure 7.4, to account for the actual position of the layer's lower boundary.

Finally, for the volumetric heat generation rate, besides the volume of the oxidic pool (Figure 7.4), we must consider the timing for the formation of the configuration under investigation. We wish to do so in a manner that is generally conservative (i.e., minimizing this timing), and not relying on detailed aspects of code calculations (to maintain the Grade B rating). Rather, we proceed from a general perspective of severe accident initiators, as provided by the level 1 PRA for AP600, to a selection of bounding, from the point of view of timing, scenarios of interest here, and finally to an understanding of what controls this timing. All non-negligible contributors to severe core damage, found in the AP600 PRA (submitted to the NRC) are listed in Table 7.3. This table also lists the time for the first relocation event into the lower head (as calculated with the MAAP code) and includes comments on each case relevant to the present usage. The term "Not Relevant to IVR" was applied to cases 1AC, 1APC, 3BRC and 3C on the following basis:

- Case 3BRC. This variant of a large break LOCA accident leads to recovery and arrest prior to any debris relocation.
- Case 3C. This is clearly outside the scope of IVR, and subject to meeting a screening frequency criterion.

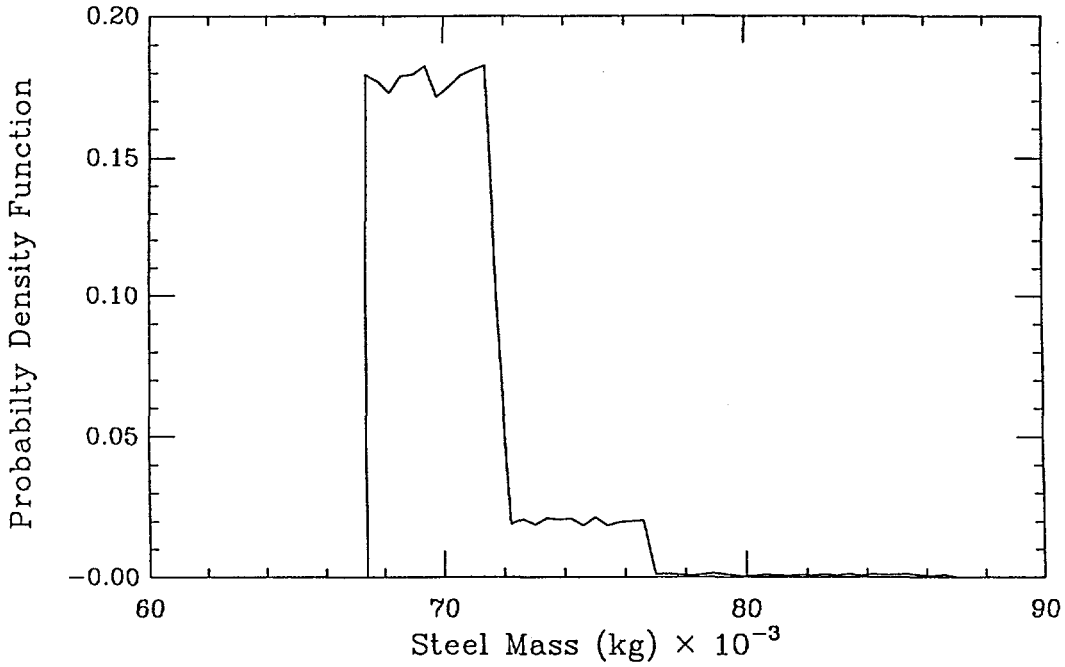

Figure 7.5. Specification of the steel mass in the metallic layer, as a probability density function.

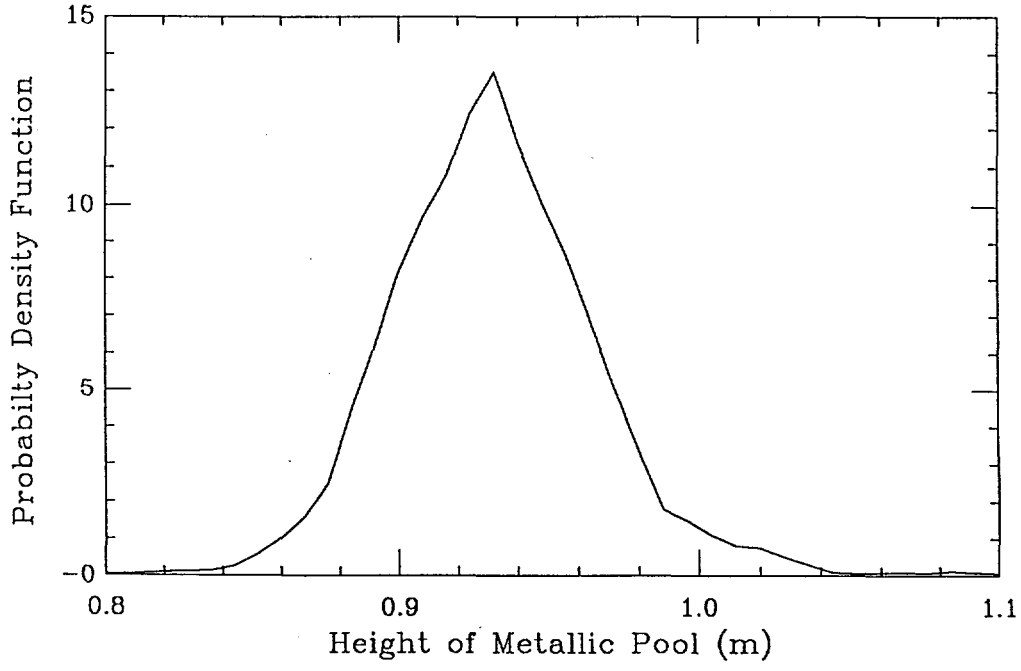

Figure 7.6. The metallic layer height probability distribution resulting from the specifications in Figures 7.3 and 7.5.

Table 7.3.[c] Accidents Contributing to the Core Damage Frequency (CDF) of the AP600 as Developed in the Level 1 PRA (AP600, 1994)

Case I.D.	% of CDF[1]	Timing of First Relocation (hr)	Accident Description and Comments
1AC	18	~5.5	• Transient or small LOCA[2] at high pressure; manual ADS[3] failure. • Not Relevant to IVR.
1APC	0.5	~10.5	• Like 1A, but PRHR operating. • Not Relevant to IVR.[4]
3BE	30	~4+	• Large or medium LOCA with full depressurization. Injection failure. • Of Main Interest to IVR.
3BRC	22	N/A	• Early accumulator and CMT[5] failures but manual depressurization leads to IRWST[6] availability and reflood. Recovered accident. • Not Relevant to IVR
3C	23	N/A	• Vessel rupture. • Not Relevant to IVR.
3DC	2.7	~22+	• Non large LOCA with partial depressurization. • Of some Interest to IVR
6E	3.3	~22+	• Core damage after SG[7] tube rupture • Of Some Interest to IVR

[1] CDF = Core Damage Frequency
[2] LOCA = Loss of Coolant Accident
[3] ADS = Automatic Depressurization System
[4] IVR = In-Vessel Retention
[5] CMT = Core Makeup Tank
[6] IRWST = In-Containment Refueling Water Storage Tank
[7] SG = Steam Generator

[c][[This table has been revised on the basis of design updates and a revised PRA. For the revision and a discussion on IVR scenarios see addendum at the end of this chapter.]]

- Cases 1AC and 1APC. Such high pressure accidents are expected to fail the hot leg nozzle and depressurize in any case. For the passive AP600 it is expected that failure to depressurize will meet the screening frequency criteria, such as to be negligible. It is inherent in these accidents to proceed at a slower rate (due to lower rate of coolant loss) as compared to large LOCAs—see Table 7.3—thus a depressurization too late to recover the accident still can be covered, conservatively, under case 3DC. [As one can see in Figure 7.1, the decay power at 10 hrs is only 80% of that at 4 hrs.]

The term "of Some Interest to IVR" was applied to cases 3DC and 6E in recognition that even though small contributors to CDF, these cases could be readily accommodateable in the IVR. The long term evolution is inherent of coolant availability and passive cooling design feature in these accidents; at 22 hrs the decay heat is only 67% of that at 4 hrs, and the so-reduced thermal loads are expected to accommodate structurally at least part (if not all) of such higher pressure scenarios—with a fourth stage ADS failure the pressure would be under 100 psi— (see Appendix G). Finally, and in light of the above, we are left primarily with case 3BE, which therefore has been termed "of Main Interest to IVR." It is the simplest, and fastest, scenario, thus it is of good bounding quality for timing the decay power. Both the core makeup tanks and the accumulator will passively inject to quench the core down to ~400 K and leave the primary system essentially full of water. A severe accident from this condition requires failure of the gravity-driven injection system, depletion of the in-vessel coolant inventory, and core heatup. Material relocation to the lower head in addition requires core melting with significant melt accumulation to cause side failure(s) through the reflector (minimum thickness 13 cm) and core barrel (minimum thickness 5 cm). An independent assessment of the timing of all these phenomena (Sienicki and Theofanous, 1995) are in general agreement with the MAAP result, in Table 7.3, of 4+ hours. Thus, we assign the main probability interval (~10°) between 4 and 5 hours, an unlikely range (~ 10^{-1}) between 5 and 6 hours, and a very unlikely range (10^{-2}) between 6 and 7 hours. As a perspective on the insensitive nature of this quantification, note, from Figure 7.1, that from 3 to 5 hours' shutdown time the decay power changes from 15 to 14 MW, that is, by less than 7%. The resulting probability density function from the above specification of the shutdown time is shown in Figure 7.7. The probability density function for the decay power density is then obtained by combining Figures 7.1, 7.3 and 7.7. The result is shown in Figure 7.8.

Note that the primary quantification carried out above is contained in Figures 7.3, 7.5, and 7.7, and they are independent of each other, as will be explained in the next paragraph. The quantities H, H_ℓ, and $\dot{Q}$ (Figures 7.4, 7.6, and 7.8) were derived using a Monte Carlo sampling program from these primary quantifications. These are **not** independent of each other, thus they

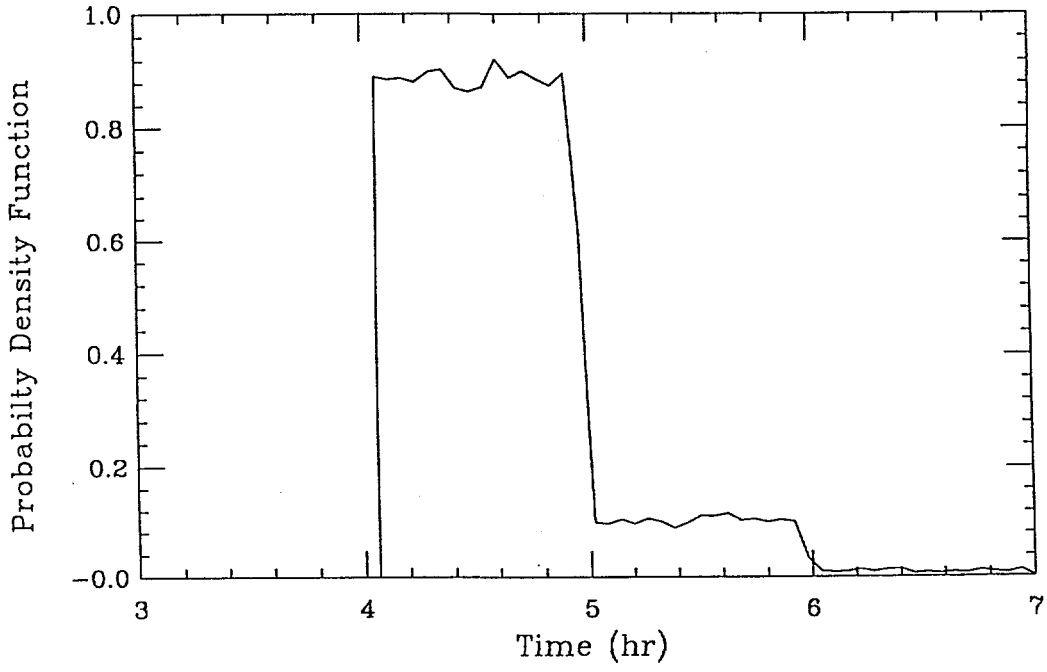

Figure 7.7. Specification of the shutdown time (for use in estimating decay power), as probability density function.

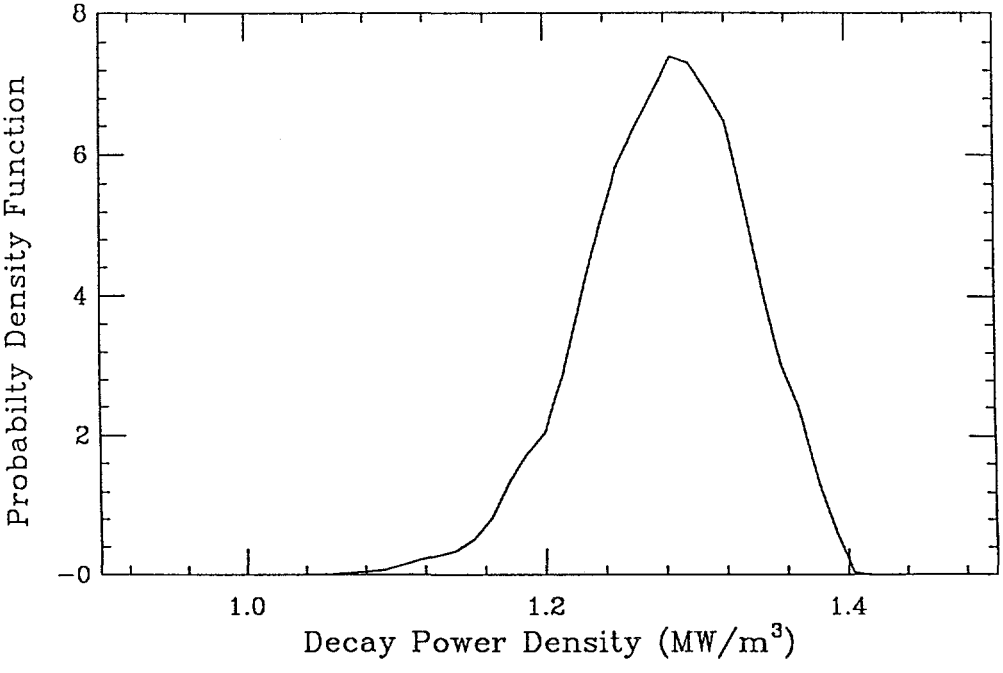

Figure 7.8. The decay power density probability distribution resulting from combination of Figures 7.1, 7.3, and 7.7.

are not convenient as inputs to the main calculation; rather, they were derived to provide some transparency of the quantification since any values from these figures can be used to directly read off the answers (heat fluxes) as described already in Chapter 5. In carrying out the calculations with the model we use the primary quantifications as above, but each sample is carried through the model to calculations of the heat flux distribution at the outer boundary of the lower head. Thus, the result is the probability distributions of the thermal loads at all angular positions in contact with the oxidic pool and the steel layer. As noted already, the distributions of property values are also sampled simultaneously.

Before displaying the results of these calculations, let us address the question of independence between quantities shown in Figures 7.3, 7.5 and 7.7. They are independent because each quantity is governed by completely different aspects of the melt progression sequence. Starting with the timing τ, the primary consideration is in the early portion of the sequences (as discussed above), prior to core uncovery, and the starting of degradation, which draws heavily on the likelihoods of various accidents **leading** to core melt, and thermal-hydraulic assessments (and systems codes) that operate in relatively "well-charted' space. The zirconium oxidation is related primarily to the early portion of severe accident sequences—during core uncovery—and it is clearly quite independent of τ. Finally, the quantities of upper internals melted, **at low pressure** as in the case here, would be rather limited, depending primarily on the phenomenology of the late phases of the core melt scenario, timing of core relocation, and heat transfer processes (radiation/conduction, primarily) between the upper core and the upper internal structures.

7.2 The Main Results

The results of the calculations are summarized in Figures 7.9 and 7.10. [[The detailed results are given in Appendix Q.]] Figure 7.9 shows the cumulative probability distributions of the heat fluxes at various angular positions around the lower head, while in Figure 7.10, the same results are presented as probability density functions of the heat fluxes at selected positions, divided by the corresponding critical heat flux value at the same position. This second manner of presentation makes the margins to failure immediately evident, and it is interesting to note that contrary to popular opinion these margins are greatest at the lower positions ($\theta \sim 0°$) of the lower head. However, even at the high positions the margins-to-failure are sufficiently comfortable to lead to the conclusion that failure is "physically unreasonable." This conclusion is further buttressed by the numerous sensitivity and parametric calculations presented immediately below.

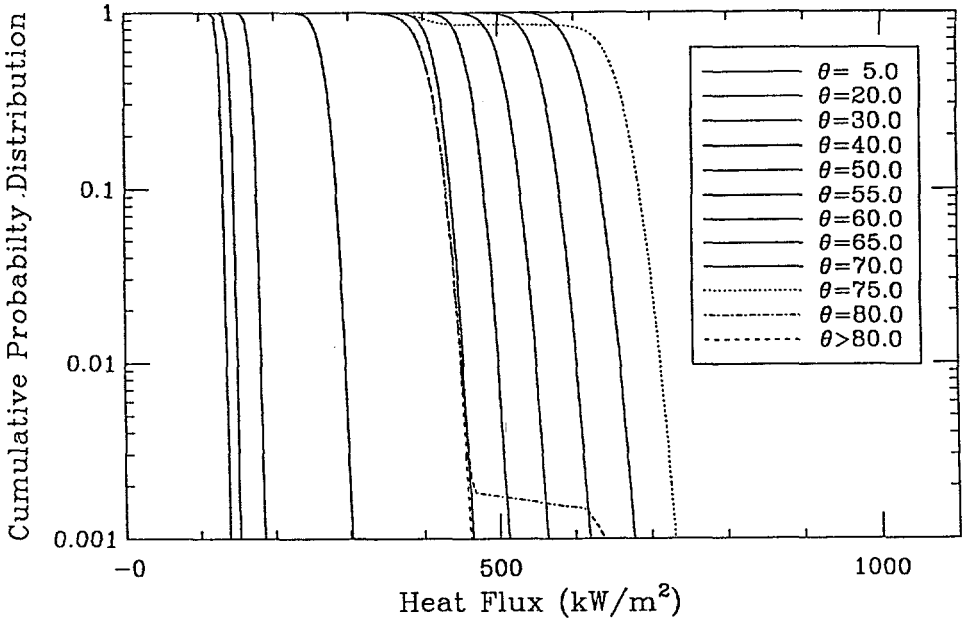

Figure 7.9. Probability distributions of the heat fluxes at various angular positions around the lower head. Over the region of the oxidic pool, fluxes increase monotonically with angle (all solid lines). The lines corresponding to the metallic layer are identified separately. The stepwise behavior at positions $\theta = 75°$ and $80°$ arises because of "sharing" the oxidic pool and metallic layer contact.

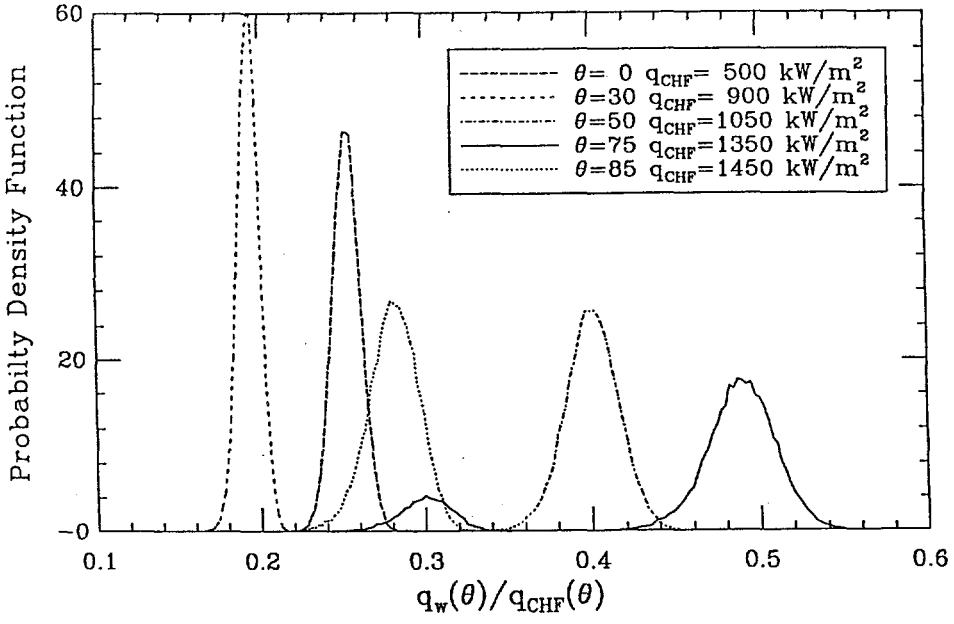

Figure 7.10. Probability distribution of the heat fluxes normalized by the local critical heat fluxes, for selected positions around the lower head. The position $\theta = 85°$ corresponds to the metallic layer. The double-hump behavior at position $\theta = 75°$, arises because of "sharing" the oxidic pool and metallic layer contact.

7.3 Sensitivity and Parametric Studies

One group of sensitivity and two groups of parametric studies have been performed to make apparent:

(a) The effect of shifts in the input distributions, namely:

- Fraction of Zr oxidized: Shift the distribution of Figure 7.3 to the right by 0.1
- Time: Shift the distribution in Figure 7.7 to the left by 1 hr.

(b) The effect of using different correlations for:

- Downward heat transfer: Eq. (5.12) instead of Eq. (5.28)
- Flux shape: Eqs. (5.24) and (5.25) instead of Eq. (5.30).

both done in conjunction with assuming a 1 cm-thick oxide crust on top of the metal layer, or an adiabatic upper boundary.

(c) The extreme specification necessary to approach failure:

- Assuming that the lower support plate is intact,

Each group is presented and discussed, in turn, in the following.

The distribution shifts are straightforward, and the results are displayed in Figures 7.11 and 7.12. We see no significant effect on the margins understood from the base case results. Note that the double-hump is not present in Figure 7.11 because, with the oxide volume increase (due to added ZrO_2), the metal layer shifted higher, while the slight shift to higher q/q_{CHF} values is due to the correspondingly thinner metallic layer. As additional sensitivity on the base case, we also considered the effect of dividing the coefficient in the Globe–Dropkin correlation by a factor of 2, and of reducing the wall melt temperature by 100 K (i.e., 1500 K instead of 1600 K). The effect of both of these variations was slight.

The calculations using the various correlation options were carried out with $H = 1.6$ m, $H_\ell = 0.8$ m, and $\dot{Q} = 1.4$ MW/m^3. The results are displayed in Figures 7.13 through 7.15. In Figure 7.13 we see that even with an adiabatic upper boundary the metallic layer is quite sufficient to dissipate the heat load over its side boundary, still leaving significant margins to failure. In Figure 7.14 we see that use of the UCLA flux shape produces a 20% more peaking at $\theta \sim 80°$, but still a significant margin to failure remains. Finally, in Figure 7.15 we see that the use of Mayinger's correlation biases the flux upward over the steel layer portion of the boundary by ~15% only. This rather low sensitivity was predicted already in Chapter 5.

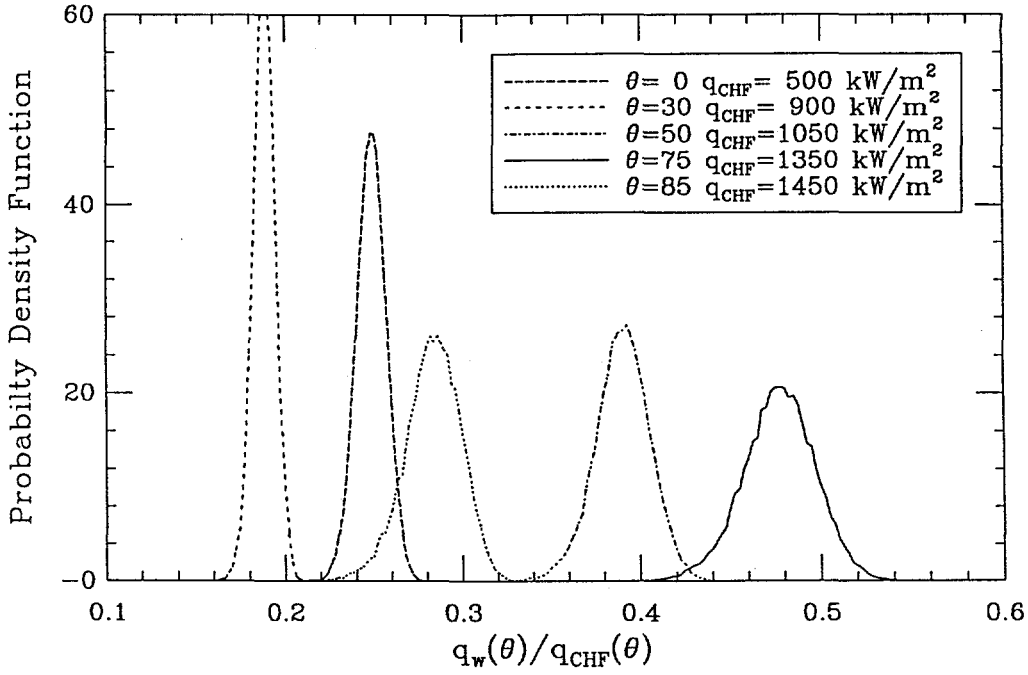

Figure 7.11 The results of a sensitivity study, specified by shifting the distribution for the zirconium fraction oxidized to higher values by 10%. All other inputs as in base case.

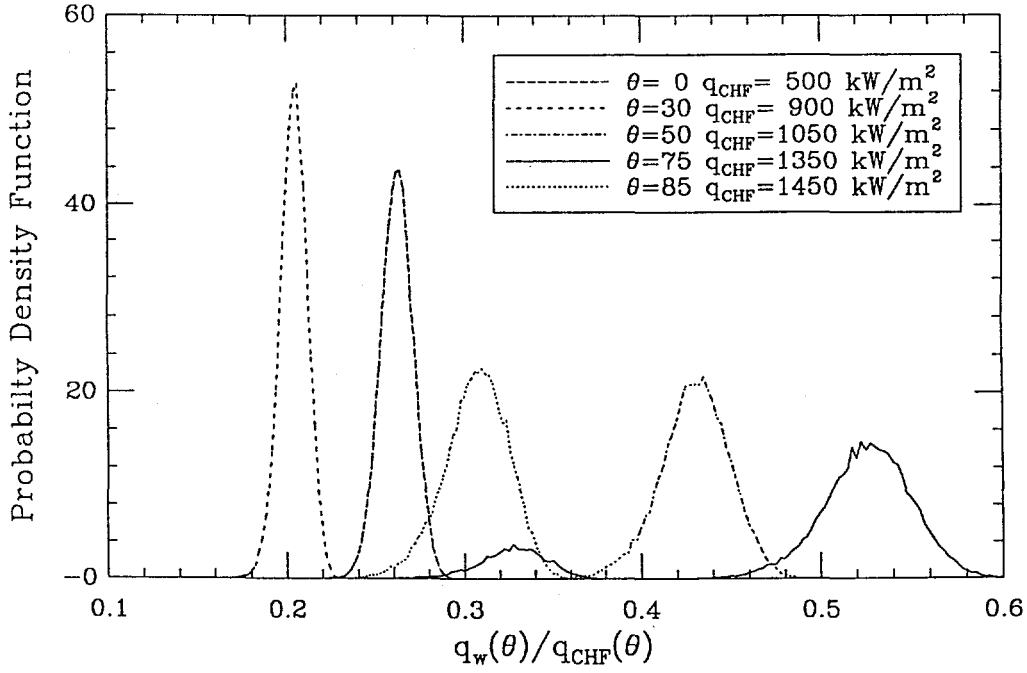

Figure 7.12. The results of a sensitivity study, specified by shifting the distribution of the shutdown time to lower values by 1 hr. All other inputs as in base case.

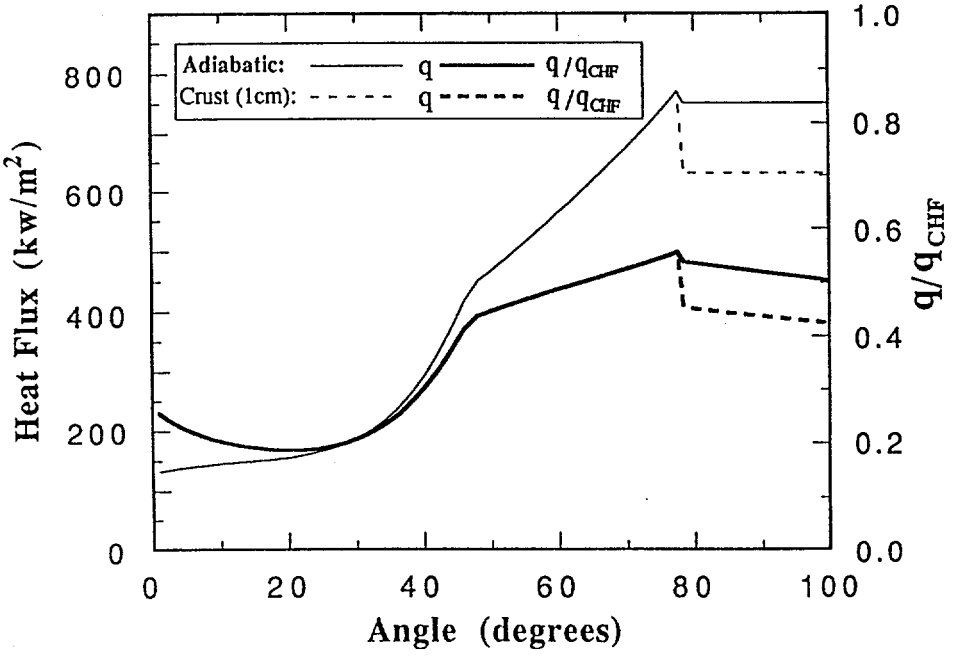

Figure 7.13. Results of a parametric study using an "adiabatic" boundary or a 1-cm-thick oxidic crust on top of the metallic layer. Values for H, H_ℓ, and $\dot{Q}$ were fixed at 1.6 m, 0.8 m, and 1.4 MW/m^3, respectively.

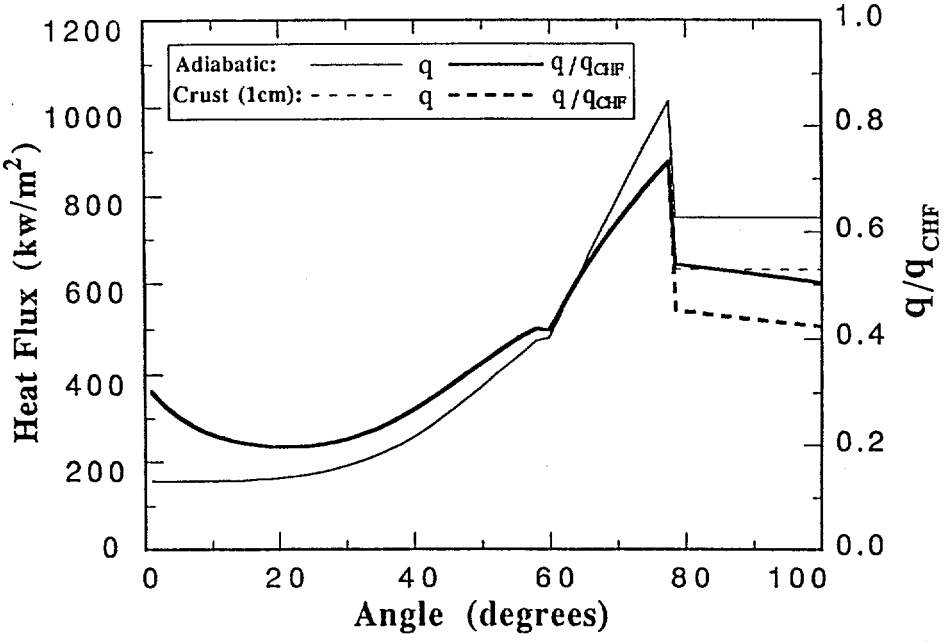

Figure 7.14. Results of a parametric study specified as in Figure 7.13 but using the UCLA flux shape (Eq. 5.24) in place of Eq. (5.30).

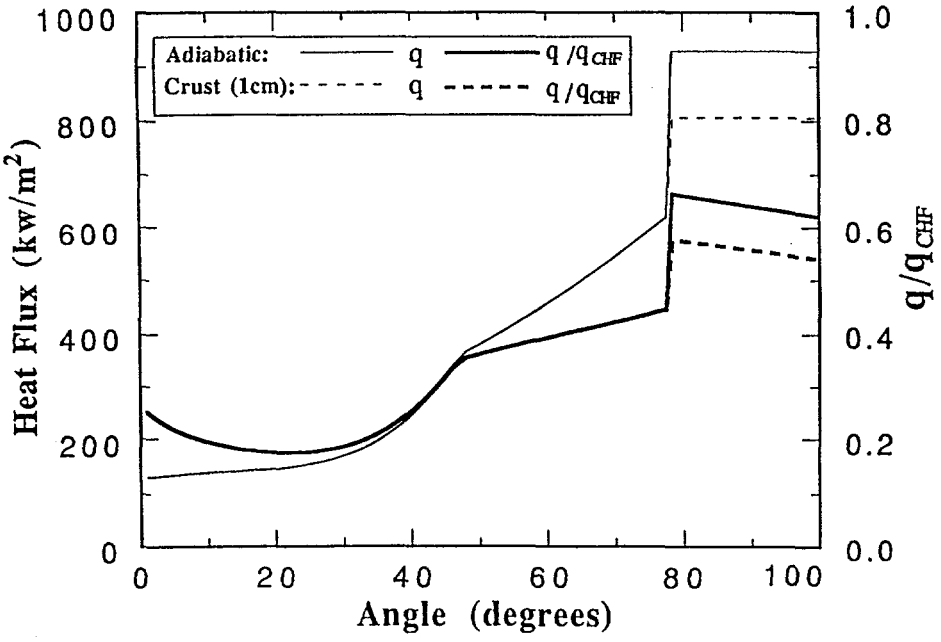

Figure 7.15. Results of a parametric study specified as in Figure 7.13 but using the Mayinger et al. (1975) correlation (Eq. 5.22) in place of Eq. (5.28).

From all the above we can conclude that there is no way to cause failure over the oxidic pool boundary. Thus, as we are left to seek "the limits to failure," in an arbitrary parametric study using the "focusing" mechanism due to the steel layer, described in Chapter 5. For this to occur, the top of the metal layer must be below the lower support plate. The metallic layer will then consist of only the lower support structures and the molten metals that relocated together with the fuel. To create a significant thermal load this fuel must be in excess of 70% of the core, which implies a rather extensive melt attack on the reflector and the core barrel. (Note that failure of both of these boundaries (see Figure 2.2) is required for the relocation of molten core materials to the lower plenum.) The reflector will supply ~10 tons of steel per axial meter melted, and the core barrel similarly ~5 tons per meter. One axial meter corresponds to 25% of the core height, and it can be considered (together with the 2 tons from the lower support structures) as a reasonable lower bound of the metallics available to form a layer on top of the oxidic pool. That is, a total of 17 tons, which if made to just touch the bottom face of the lower support plate (1.4 m from the bottom of the lower plenum) would produce a depth of 22 cm, and would allow a maximum oxidic pool depth of 1.18 m. (Note that these are conservative limits in that no account was taken of the metallic zirconium that participated in the relocation, nor of the thermal expansion and creep in the core barrel—[[see also Appendix O.]]) Using these depths together with the

upper bound in the decay power, which from Figure 7.8 is seen to be 1.4 MW/m^3, we obtain the results shown in Figure 7.16. Marginal failure is indicated; however, it is doubtful that even this extreme specification could in reality produce failure. This is because in addition to ignoring zirconium in the metal layer and elongation (and possible failure) of the core barrel, as just mentioned, this calculation has ignored 2-D effects due to (a) eddy diffusion in the bulk of the metal layer, and (b) conduction in the vessel wall. In addition, the effect of the highly localized thermal loads on the critical heat flux, also expected to be mitigative, has been ignored.

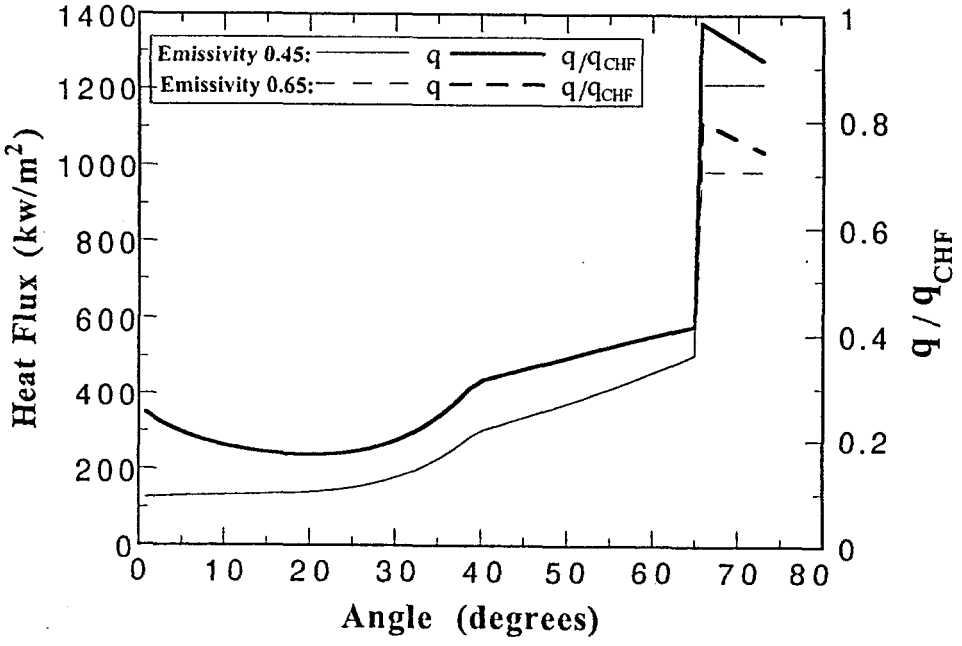

Figure 7.16. Results of an extreme parametric study carried out to "test the failure boundaries." $H = 1.18$ m, $H_\ell = 0.22$ m, and $\dot{Q} = 1.4$ MW/m^3. **See text for explanation.**

7.4 Discussion

As stated in Chapter 6, all these calculations were checked to verify that the conditions expressed by Eqs. (6.8) and (6.15) are satisfied. In addition, to check the applicability of the heat transfer correlations we computed the Ra and Ra$'$ numbers in the metal layer and oxidic pool respectively. The results from the base case calculation, shown in Figure 7.17 and 7.18, respectively, indicate that for the AP600 the relevant ranges are

$$5 \cdot 10^9 < \mathrm{Ra} < 2 \cdot 10^{10} \qquad 10^{15} < \mathrm{Ra}' < 6 \cdot 10^{15}$$

These also encompass the cases considered in the sensitivity and parametric studies:

$$\mathrm{Ra} = 1.1 \cdot 10^{10} \qquad \mathrm{Ra}' = 4 \cdot 10^{15}, \qquad \mathrm{Ra} = 2 \cdot 10^{8} \qquad \mathrm{Ra}' = 10^{15}$$

and are to be compared to the experimental ranges, which for convenience are repeated here again:

Globe–Dropkin:	$3 \cdot 10^5 < \mathrm{Ra} < 7 \cdot 10^9$
Chu–Churchill:	$\mathrm{Ra} < 10^{12}$
Present (mini-ACOPO):	$10^{12} < \mathrm{Ra}' < 7 \cdot 10^{14}$

We can see that in all three cases we are essentially where we need to be. There is a less than one order of magnitude extrapolation of the Globe–Dropkin correlation which besides being modest, it pertains to the thickest range of metal layers, which is uninteresting from a thermal loads point of view. On the simulation of the oxidic pools the mini-ACOPO revealed no significant surprises, and hence the extrapolation by about one order of magnitude can be considered modest also. This conclusion is to be confirmed by the main ACOPO experiment, scheduled for operation in the next few months, which will afford Ra′ numbers up to 10^{16} (or 10^{17} using Freon). Moreover, we expect that with its widely different transient response, the ACOPO will further demonstrate the adequacy of our present approach in bounding the behavior due to adjustments in the internal stratification patterns.

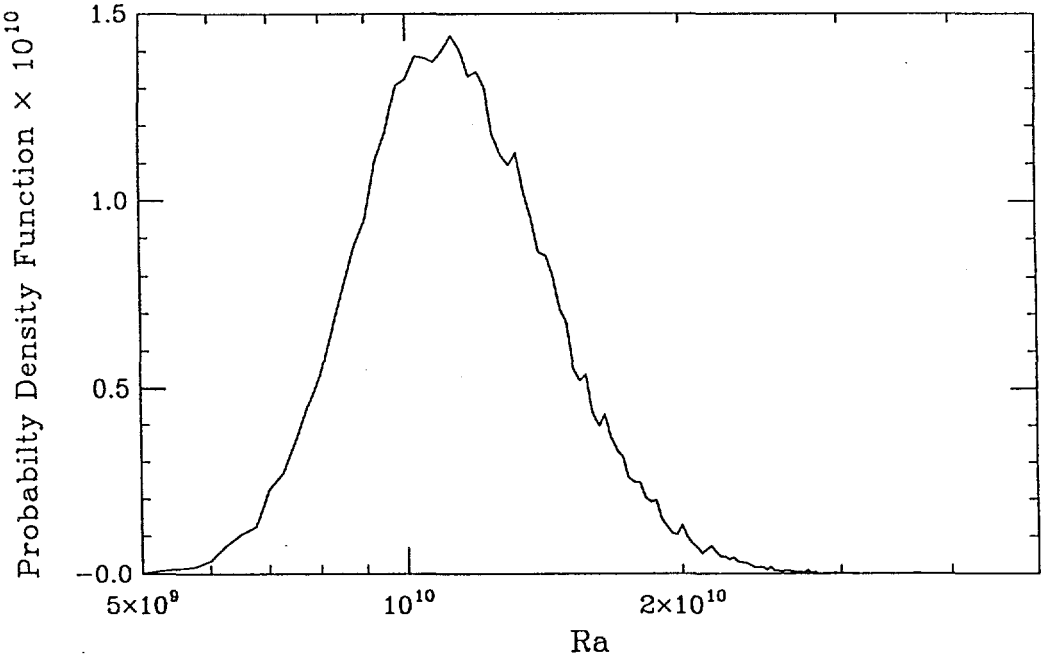

Figure 7.17. The Ra number distribution found in the calculations of the base case.

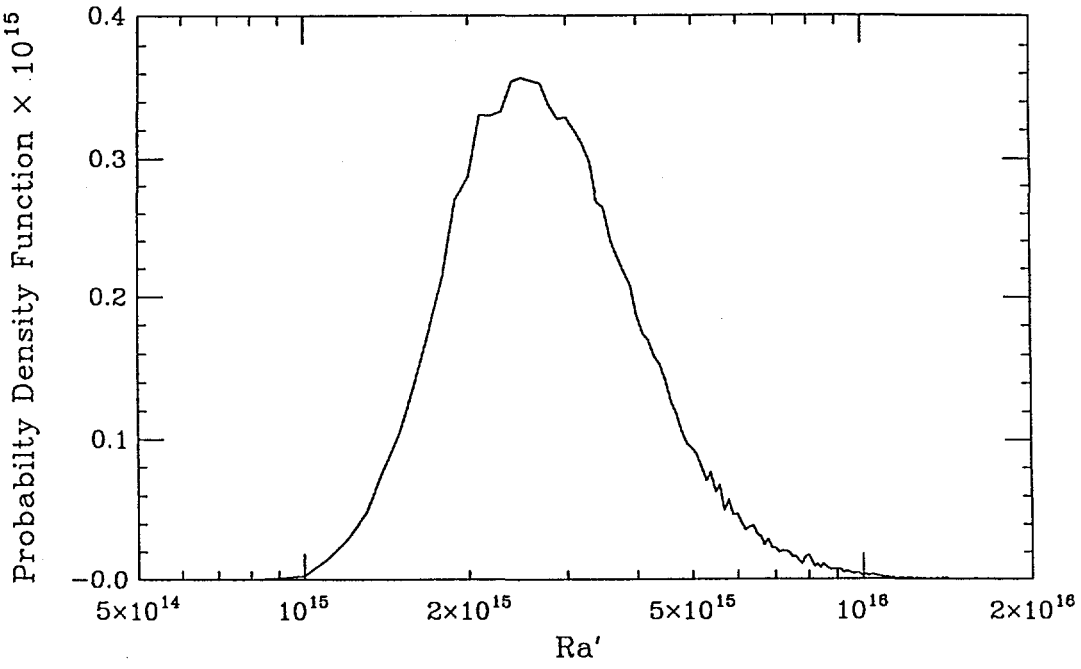

Figure 7.18. The Ra′ number distribution found in the calculations of the base case.

[[ADDENDUM TO CHAPTER 7]]

The purpose of this addendum is to summarize and refer the reader to certain new material presented in addenda to Appendices K and M and in the new Appendices O and P. As separate items, we summarize here also certain systems effects, including an update to Table 7.3 according to the revised PRA Level 1 for the AP600, and the position of the designer regarding thermal shock.

The addendum to Appendix K describes the thermal insulation design recently completed by Westinghouse, and with specific reference to the present work. The key features include a passively made available (upon flooding) large opening for water inflow opposite to the pole of the lower head, a minimum clearance of 23 cm at an angular position of ~30°, an annular gap between the vessel and insulation of 15 cm, and exit flow paths at the top with two successive restrictions (from the 1.88 m^2 available in the annulus) of a total flow area of 0.7 m^2. Configuration III of ULPU was assembled to represent this geometry, and the test results, as reported at the end of Chapter 3 and in Appendix E-4, demonstrate the robustness of Eq. (3.1) and its applicability of our purposes.

The addendum to Appendix M contains the newly revised design of the cavity flooding system (now consisting of two 6" lines), and reliability considerations (including human factors) for it. Procedures call for the operators to start cavity flooding upon reaching core exit temperatures of $\sim$2000 °F (just prior to the rapid oxidation phase). The lower head is immersed in less than 10 to 20 minutes for 2 or 1 drain line(s) operating respectively, and the vessel is effectively submerged (2 phase level with average void fraction of 50%) by 35 to 70 minutes respectively. As explained in Appendix O, these times are well within the timing of the first relocation to the lower head. The unreliability of the cavity flooding system, conditional on demand, is estimated at less than 10^{-2}. This includes as a major contributor, human unreliability conservatively estimated at $3.4 \cdot 10^{-3}$ for each flow path. We believe that with the importance attached to this accident management scheme, operator training, and comfortable time intervals available for action (hours), the actual unreliability would be low enough that, together with the very low frequency of any core melt sequence relevant to IVR, it renders an unflooded situation below screening frequency levels of $\sim 10^{-7}$ per year.

The new Appendix P provides a whole new set of parametric calculations, many requested by the reviewers, others taken up at the authors' initiative. These have to be examined in their entirety in Appendix P, but perhaps the most instructive result is about how quickly the margin to failure increases as the oxidic pool height decreases from its maximum value used in the Extreme Parametric case examined previously (see Figure P.4).

The new Appendix O is an attempt to get somewhat deeper into the potential intermediate states described in Chapter 2. This is done through some key timing considerations in the melt-down/relocation sequence, and it provides a perspective against which the scenarios proposed by several reviewers can be considered. This consideration is also made in Appendix O. Additional perspectives on what might be required to cause failure are provided by a parametric study on the $H_\ell \times H$ combination, where we see that shallower oxidic pools can accommodate thinner metal layers without danger of failure.

In 1995, a revised Level 2 PRA for the AP600 was submitted to the NRC that also included an update to the Level 1 quantification. On this basis our Table 7.3 was revised as shown in Table 7.4. The new core damage frequency estimate is $2.5 \cdot 10^{-7}$ per year. The most important differences are in sequences 3C (vessel rupture), whose contribution to CDF decreased from 23% to 4.1%, 3BRC (in-vessel recovery, no interest to IVR), 3BE (LOCAs of main interest to IVR) which increased

Table 7.4 Accidents Contributing to Core Damage Frequency (CDF) of the AP600 as Developed in the Level 2 PRA with Update Level 1 Quantification (AP600, 1995)

Case I.D.	% of CDF[1]	Timing of First Debris Relocation (hr)	Accident Description and Comments
1AC	1.9	~5.5 hr	• Core damage following transient or small LOCA[2] at high pressure; manual ADS[3] failure. • Some relevance to IVR[4] if hot leg nozzle ruptures and depressurizes system.
1APC	0.4	~10.5 hr	• Like 1AC, except PRHR operating. • Some relevance to IVR; less decay heat than 3BE; partially pressurized (<5 a.).
3BE	50	~4+ hr	• Core damage following large LOCA or other event with full depressurization (injection failure); may reflood through break as cavity floods. • Of main interest to IVR.
3BRC	~29	N/A	• Core damage following LOCA with early accumulator and CMT[5] failures or any other sequences where manual depressurization leads to reflood from IRWST[6] and recovery in-vessel. • Typically, not relevant to IVR
3C	4.1	N/A	• Vessel rupture. • Not relevant to IVR.
3DC	13	~22+ hr	• Non-large LOCA with partial depressurization. • Of interest to IVR, but less decay heat than 3BE.
6E	2.3	~22+ hr	• Core damage after steam generator tube rupture. • Of interest to IVR, but less decay heat than 3BE
3BE.cc0	N/A	~3 hr	• Sensitivity case for 3BE without cavity flooding. • Bounds IVR timing uncertainty

[1] CDF = Core Damage Frequency
[2] LOCA = Loss of Coolant Accident
[3] ADS = Automatic Depressurization System
[4] IVR = In-Vessel Retention
[5] CMT = Core Makeup Tank
[6] IRWST = In-Containment Refueling Water Storage Tank

by 7% and 20% respectively, and 3DC (low decay heat) which increased by ~10%. Also, sequence 1AC (transient or small LOCA with core damage at high pressure) decreased from 18% down to ~2%; the designation of this sequence as "of no interest to IVR" was changed to "of some interest to IVR" because at least a fraction of them would lead to hot leg nozzle failure and depressurization. These changes are all favorable to the IVR management concept. It is also important to note that the two potentially damaging sequences (1AC and 3C) have been reduced to only *"a few percent"* placing them at the margins, if not outside, the severe accident management window of interest. Note, however, that even accounting for potential uncertainties in these values as well as in the total CDF estimate, their likelihood is so low as to be considered below a reasonable choice ($\sim 10^{-7}$) of a screening frequency criterion (see Appendix A).

Finally, since several reviewers asked questions related to thermal shock performance of the reactor vessel material, hereby we summarize some key aspects. Regarding the pressurized condition, Westinghouse has a design requirement that the vessel accommodate one inadvertent flooding during normal operation. The analysis to demonstrate that this requirement can be met will include the effect of fluence on the lower head as a possible embrittlement mechanism, and will be ready later this summer. Regarding general low pressure performance as during IVR, it is noted that the reactor vessel manufacturer can meet initial RTNDT specifications of -10 °F and -20 °F for the beltline forging and weld respectively, and a maximum end-of-life value of 23 °F for both. The temperature range in the containment is specified as 50 to 120 °F, and 50 °F is, therefore, the lowest possible temperature for IRWST water. This being significantly higher than the end-of-life RTNDT value, is sufficient to establish absence of brittle behavior during IVR.

8 QUANTIFICATION AND ASSESSMENT OF THERMAL LOADS UNDER JET IMPINGEMENT

In this chapter we examine the potential extent of local thermal attack on the lower head during the initial core relocation event. This is the second bounding configuration discussed in Chapter 2. In this consideration we ignore the cooling and dispersive effect of water on the relocating melt—ignoring both effects is clearly conservative and useful in obtaining the simple, yet bounding argument sought here. Further, we assume jet impingement occurs even though TMI vessel inspection found no evidence of such impingement (i.e., no wall attack). A complementary perspective on this problem, including consideration of these effects, is provided in Appendix H.

The situation then can be described as one involving a superheated oxidic melt of diameter D_j impinging on the lower head with the velocity U_j. The fundamental consideration is that molten oxide cannot exist next to a steel boundary even under strongly convective conditions; accordingly, the potential driving steel melting is the jet superheat. This idea was originally established by Epstein and co-workers (Epstein et al., 1980). More recently it was further validated and refined by Saito et al. (1990). In particular, they demonstrated experimentally the important effect of turbulence (in high Reynolds number jets) in enhancing the ablation rate significantly above that obtained in the laminar regime considered by Epstein et al. The experiments were carried out with molten salt ($NaC\ell$) at temperatures up to 1140 °C (Pr $\sim$1) impinging on tin plates; the condition covered jet velocities up to 5 m/s, diameters up to 3 cm and Reynolds numbers up to $\sim 3 \times 10^5$. Two runs were also carried out with $A\ell_2O_3$ at 2200 °C impinging on a steel plate at room temperature. In this case the Prandtl number is 5.46 and the Reynolds numbers were around 2×10^3. The data yielded a heat transfer correlation indicative of turbulent convection

$$\mathrm{Nu}_j = 0.0033\ \mathrm{Re}_j\ \mathrm{Pr}_j \tag{8.1}$$

and from it an ablation rate

$$\dot{Z} = 0.0033 \frac{\rho_j c_{pj}(T_j - T_m)}{\rho_w[\lambda + c_{pw}(T_{w,m} - T_{so})]} U_j \tag{8.2}$$

agreeing well with all the data that could be obtained. According to Eq. (8.1) the minimum required UO_2 temperature to prevent crust formation on steel is $\sim$4400 K (Saito et al., 1990). This is significantly lower than the 6400 K obtained for laminar flow, but still well above any temperature of interest in the present application. We make use of Eq. (8.2), therefore, directly.

Using the material properties and a melt superheat of 200 K, Eq. (8.2) can be written as:

$$\dot{Z} = 4 \times 10^{-4} U_j \tag{8.3}$$

which can be integrated, assuming U_j is constant, over the duration of the relocation, τ, to yield the total ablation depth

$$Z_\tau = 4 \times 10^{-4} U_j \tau \tag{8.4}$$

The U_j and τ quantities are related by the total volume of relocated material and an effective jet diameter by

$$V_r = \frac{\pi}{4} D_j^2 U_j \tau \tag{8.5}$$

and if the principal variables are V_r and D_j Eq. (8.4) becomes

$$Z_\tau = 5.1 \times 10^{-4} \frac{V_r}{D_j^2} \tag{8.6}$$

This result, for a relocated volume of 2.5 m^3 ($\sim$ 1/3 of the fuel volume), as a function of D_j is shown in Figure 8.1.

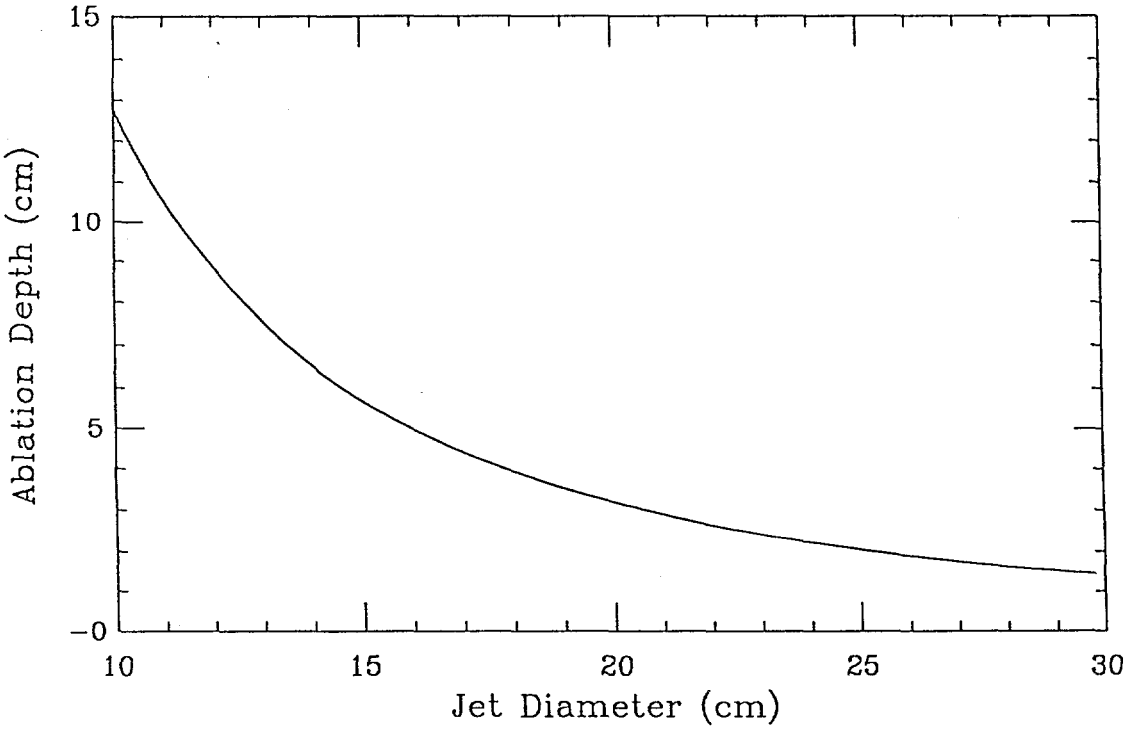

Figure 8.1. Wall ablation depth as function of jet diameter, for a melt pour of 2.5 m^3 ($\sim$1/3 of the fuel volume).

An equivalent pour (jet) diameter of 10 cm is considered to be an extreme lower bound for such massive pours; still, it is seen to be unable to produce lower head penetration. Actually, we would expect the pour rate to increase with time as the breech on the core side boundary is enlarged by ablation (i.e., Sienicki and Theofanous, 1995).

These numbers are indicative of the rather intense and prolonged thermal loading required to produce local failures, and provide important perspectives on the even greater margins present in considering other transient phenomena, such as subsequent relocations into an existing corium pool. Such relocations would be expected to create "sinking" (cold) plumes, and in fact, Mayinger et al. (1980) measured the heat transfer rates in the impinging region of such plumes. Clearly, however, even ignoring the effects of crusts, momentum interactions in the corium pool, and turbulence would produce cooling and deceleration effects, thus making the wall interactions much more benign than those considered above.

Based on the above, we can conclude that under no circumstance of a physically meaningful relocation scenario can we see local wall failures due to jet impingement. Under some extremely prolonged pours there may be some local attack and perhaps even a temporary CHF, if the ablation exceeds $\sim$3 cm at $\theta \sim 0°$, or $\sim$9 cm at $\theta \sim 30°$. However, due to the local nature of the thermal load, the dried out region would be expected to quench quickly after the temporary thermal load terminates.

Turland (1994) also concluded that jet attack does not provide a viable mechanism for lower head penetration, even for pours as large as 1/2 the core inventory.

9 CONCLUSIONS AND RECOMMENDATIONS

The major conclusion of this study is that thermally-induced failure of an externally flooded, AP600-like reactor vessel is "**physically unreasonable.**" Methodologically (see Appendix A for definitions), the assessment approach is of Grade B type (involving a single but complex physical process, slight scenario dependence, fully supported by scaled experiments, minimal intangibles treated in a reasonably bounding manner) which affords a high confidence level on this conclusion. Upon completion of the peer review of this report, the Phase of Development of this problem reached the maturation status (Phase IV) which is appropriate for use in licensing activities. Phase V (extension) will follow shortly as various on-going programs internationally produce their own assessments. The breadth to be achieved by these efforts, oriented to the more challenging task of larger reactors, is expected to further enhance the depth of the present assessment in a confirmatory sense.

In making use of these results for a specific AP600-like reactor, it is important to ascertain, or verify if appropriate, the following key system's features:

- Reliability of the depressurization and cavity flooding systems (valves) to ensure that failures can be classified in the "below-screening-frequency" category.
- Thermal insulation design that allows sufficient access of water to the bottom of the lower head [[and not subject to clogging]], and venting of a steam/water mixture on the top. Further, based on this geometry (and available clearances), the dynamic behavior of the two-phase natural circulation flow should be assessed, and experimentally tested if necessary (i.e., if significantly different than the cases considered already in this study).
- Lower head external surface characteristics (finish, coatings, oxidation) that do not impair critical heat flux performance.

We believe that with appropriate attention in the design, none of these key features present serious difficulty in realizing this "in-vessel retention" concept.

The key mechanistic features for this favorable conclusion in AP600-like reactor designs can be listed as follows:

- A low power density core. In fact it is easy to see from the results of this study that at the decay power levels appropriate to this reactor it is virtually impossible for the oxidic pool to impose threatening thermal loads on the lower head, under **any** circumstances.
- A periodic bubble formation and detachment mechanism at the position of horizontal tangency ($\theta \sim 0°$) on the lower head, that, in combination with the large thermal inertia of it, allows very significant margins to critical heat flux. At higher positions, the thermal loads increase faster than the critical heat flux and, depending on the thickness of the metal layer,

there may be locally even an essentially discontinuous further increase in the thermal load. That is, the margins to CHF decrease monotonically as we move from the center to the equator; however, they remain comfortable under all practically conceivable circumstances.

- Reactor vessel internals design that virtually prohibits the formation of superheated, thin, metallic layers on top of the oxidic pool. (Such layers would provide the only mechanism—a"focusing" in energy flow—that could conceivably compromise lower heat integrity.) This design includes:

  (a) a core inlet geometry (with large heat sinks) that would arrest downward relocation, allowing the formation of a core-wide crucible, and sideward failure through the reflector and core barrel,

  (b) massive reflector and core barrel components, extensively ablated and incorporated in the melt—that is, a significant metallic constituent with the relocating melt and

  (c) a massive lower (or core) support plate positioned such as to be subsummed in a large molten pool contained in the lower head.

Presently, this "focusing" mechanism has been conservatively treated by ignoring internal transport limitations (2D effects) due to the exceedingly large aspect ratio (~20) in such thin layers [[i.e., less than 20 cm]]. Eliminating the conservatism may provide important (needed) relief in assessing larger, and/or higher power density reactors.

Other ideas to improve the assessment basis, or the in-vessel retention performance for large and/or higher power density reactors can be listed as follows:

- Extend the database for heat transfer in volumetrically heated pools up to Rayleigh numbers of $\sim 10^{17}$. This is presently underway in the COPO (IVO) and the ACOPO (UCSB) experiments, which will also investigate thin metallic layers.

- Extend the CHF database to include reactor-specific thermal insulation, and relief path designs. This is ongoing in the ULPU experiment. Also under investigation (in ULPU) are surface treatment and structural modification to enhance CHF performance. The treatment is more germaine to the region $\theta \sim 0°$, and the structural modification (such as "fins") are oriented more to the upper region ($50° < \theta < 90°$ and including the vertical wall).

- Design reactor internals that effectively prohibit the formation of thin, superheated metallic layers on the top of a molten oxidic pool of significant size. The desired trend refers to availability of steel around the core and position of the lower support plate in the lower plenum, as discussed above.

- [[Examine the potential for fouling effects on CHF under long term operation.]]

Needless to say, slow accident progression to allow decreasing of the decay power to very low levels, comfortable times for primary system depressurization and cavity flooding, and a water return flow path would continue to be important.

10 REFERENCES

1. AP600 (1994) "AP600 Probabilistic Risk Assessment," Prepared for U.S. Department of Energy, DE-AC03-90 SF18495, Rev. 1, July 22, 1994.

2. Asfia, J. (1994) Personal Communication.

3. Bonnet, J.M., S. Rougé and J.M. Seiler (1994) "Large Scale Experiments for Core Melt Retention — BALI: Corium Pool Thermalhydraulics SULTAN: Boiling Under Natural Convection," Proceedings, OECD/CSNI/NEA Workshop on Large Molten Pool Heat Transfer, Nuclear Research Centre, Grenoble, France, March, 9–11.

4. Butterman, W.C. and W.R. Foster (1967) *Am. Minerologist*, **52**, 884.

5. Chavez, S.A., G.E. Korth, D.M. Harper and T.J. Walker (1994) "High-Temperature Tensile and Creep Data for Inconel 600, 304 Stainless Steel and SA106B Carbon Steel," *Nuclear Engineering and Design* **148**, 351-363.

6. Cheung, F.B. (1980) "Heat-Source-Driven Thermal Convection at Arbitrary Prandtl Number," *J. Fluid Mech. 97*, part 4, p. 743.

7. Churchill, S.W. and H.H.S. Chu (1975) "Correlating Equations for Laminar and Turbulent Free Convection from a Vertical Plate *Int. J. Heat Mass Transfer* Vol. 18, 1323-1329.

8. CSNI (1994) Proceedings of the Workshop on Large Molten Pool Heat Transfer. Organized by OECD Nuclear Energy Agency in collaboration with Centre d'Etudes Nucleaires de Grenoble (France), 9-11 March, NEA/CSNI/R(94)11.

9. Dinh, T.N. and R.R. Nourgaliev (1994) "Numerical Analysis of Two-Dimensional Natural Convection under High Ra Number Conditions in Volumetrically Heated Corium Pool," Proceedings, OECD/CSNI/NEA Workshop on Large Molten Pool Heat Transfer, Nuclear Research Centre, Grenoble, France, March, 9–11.

10. Epstein, M., et al. (1980) "Simultaneous Melting and Freezing in the Impingement Region of a Liquid Jet," AIChE **26**, 5, p. 743.

11. Epstein, M. and H. Fauske (1989) *Nuclear Technology* **87**, 1021–1035.

12. Globe, S. and D. Dropkin (1959) *J. Heat Transfer* **81**, 24.

13. Goldstein, R.J. and T.Y. Chu (1969) "Thermal Convection in a Horizontal Layer of Air," *Prog. Heat Mass Transfer* **2**, 55.

14. Hawkes, G.L. and J.E. O'Brien (1991) "ARSAP AP600 In-Vessel Coolability Thermal Analysis Final Report," DOE/ID-10369, December.

15. Henry, R.E., J.P. Burelback, R.J. Hammersley, C.E. Henry, and G.T. Klopp (1991) "Cooling of Core Debris Within the Reactor Pressure Vessel Lower Head," ANS Summer Meeting, Orlando, Florida.

16. Henry, R.E. and H.K. Fauske (1993) "External Cooling of a Reactor Vessel Under Severe Accident Conditions," *Nuclear Engineering and Desing* **139**, 31.

17. Henry, R.E. and D.A. Dube (1994) "Water in RPV: A Mechanism for Cooling Debris in the RPV Lower Head," OECD-CSNI Severe Accident Management Specialists Meeting, Stockholm, June 1994.

18. Hodge, S.A. (1991) "Identification and Assessment of BWR In-Vessel Accident Management Strategies," ANS Trans. **64**, 367.

19. Jahn, M. and H.H. Reineke (1974) "Free Convection Heat Transfer with Internal Heat Sources," Proceedings of the Fifth International Heat Transfer Conference, Vol. 3, p.74.

20. Kelkar, K.M., K.K. Khankari, and S.V. Patankar (1993) "Computational Modelling of Turbulent Natural Convection in Flows Simulating reactor Core Melt," Innovative Research Inc. Report submitted to Sandia National Laboratories.

21. Kulacki, F.A., and A.A. Emara (1975) "High Rayleigh Number Convection in Enclosed Fluid Layers with Internal Heat Sources," U.S. Nuclear Regulatory Commission Report NUREG-75/065.

22. Kymäläinen, O., H. Tuomisto and T.G. Theofanous (1992) "Critical Heat Flux on Thick Walls of Large, Naturally Convecting Loops," ANS Proceedings1992 National Heat Transfer Conference, San Diego, CA, Aug. 9-12, 1992, Vol. 6, 44–50.

23. Kymäläinen, O., H. Tuomisto, O. Hongisto and T.G. Theofanous (1993) "Heat Flux Distribution from a Volumetrically Heated Pool with High Rayleigh Number," Proceedings NURETH-6, Grenoble, October 5-8. [or *Nuclear Engineering & Design* **149**, 401-408, 1994.]

24. Kymäläinen, O. (1994) "Loviisa 1 & 2, In-Vessel Retention of Corium During a Severe Accident," IVO Int'l, Ltd. Report L01-GT1-64.

25. Lienhard, J.H. (1994) "Snares of Pool Boiling Research: Putting our History House," Proceedings of International Heat Transfer Conference, UK.

26. Mayinger, F., M. Jahn, H. Reineke, and U. Steinberner (1975) "Examination of Thermohydraulic Processes and Heat Transfer in a Core Melt," Final Report BMFT RS 48/1.

Technical University, Hannover, W. Germany. As reviewed by F.A. Kulacki, Ohio State University, for the US NRC, march 31, 1976.

27. Mayinger, F., et al. (1980) "Theretische und Experimentelle Untersuchung des Verhaltenseines Geschmolzenen Kerns im Reaktorbehälter und auf dem Betonfundament," BMFT RS 166-79-05, Band V.

28. Okkonen, T. (1993) "In-Vessel Core Debris Cooling Through External Flooding of Reactor Pressure Vessel," Report by Group of Experts, Final Draft. To be published by CSNI.

29. O'Toole, J.L. and P.L. Silveston (1961) AIChE Chem. Eng. Prog. Symp. Ser. 57(32), 81.

30. Park, H. and V.K. Dhir (1991) "Steady State Thermal Analysis of External Cooling of a PWR Vessel Lower Head," AIChE Symp. Series, No. 283, Vol. 87, p.1.

31. Park, H., J. Lee, V.K. Dhir and A.K. Mal (1992) "Thermal Stresses and Creep Rupture Analysis for a PWR Vessel Lower Head During External Flooding," Proceedings 1992 National Heat Transference Conference, San Diego, CA, Aug. 9-12.

32. Pelton, A.D., L. Leibowitz and R.A. Blomquist (1994) *J. Nucl. Matter* (in press).

33. Rougé, S. and J.M. Seiler (1994) "Core Debris Cooling with Flooded Vessel or Core-Catcher: Heat Exchange Coefficient under Natural Convection," OECD/CSNI/PWG4, October 1994.

34. Saito, M., et al. (1990) "Melting Attack on Solid Plates by a High Temperature Liquid Jet – Effect of Crust Formation," *Nuclear Engineering and Design* **121**, 11-23.

35. Schneider, S.B. and B.D. Turland (1994) "Experiments on Convection and Solidification in a Binary System," Proceedings, OECD/CSNI/NEA Workshop on Large Molten Pool Heat Transfer, Nuclear Research Centre, Grenoble, France, March, 9–11.

36. Schnitzler, B.G. (1981) "Fission Product Decay Heat Modelling for Disrupted Fuel Regions (FRECAY)," EG& G Report EGG-PHYS-5698, Dec. 1981.

37. Sienicki, J.J. and T.G. Theofanous (1995) Draft material for Appendix O of this report made available in the July 1995 version.

38. Silveston, P.L. (1958) Forsch. Ingenieurwes **24**, 29, 59.

39. Squire, H.B. (1938) in **Modern Developments in Fluid Dynamics**, S. Goldstein, Ed., Oxford University Press, London, Vol. II, p. 641.

40. Steinberner, U. and H.-H. Reineke (1978) "Turbulent buoyancy convection heat tansfer with internal heat sources," Proc. Sixth International Heat Transfer Conf., Toronto, Canada, Aug 1978.

41. Stickler, L.A., et al. (1994) "Calculations to Estimate the Margin of Failure in the TMI-2 Vessel," NUREG/CR-6196, U.S. Nuclear Regulatory Commission.

42. Theofanous, T.G. (1989) "Some Considerations on Severe Accidents at Loviisa," Theofanous & Co., Inc. January 1989, IVO Proprietary Report.

43. Theofanous, T.G., S. Syri, T. Salmassi, O. Kymäläinen and H. Tuomisto (1994a) "Critical Heat Flux Through Curved, Downward Facing, Thick Walls," OECD/CSNI/NEA Workshop on Large Molten Pool Heat Transfer, Nuclear Research Centre, Grenoble, France, March, 9–11 [or *Nuclear Engineering and Design* **151** No. 3].

44. Theofanous, T.G., C. Liu, S. Angelini, O. Kymäläinen, H. Tuomisto and S. Additon (1994b) "Experience From the First Two Integrated Approaches to In-Vessel Retention Through External Cooling," OECD/CSNI/NEA Workshop on Large Molten Pool Heat Transfer, Nuclear Research Centre, Grenoble, France, March, 9–11.

45. Theofanous, T.G., W.W. Yuen, S. Angelini, J.J. Sienicki, K. Freeman, X. Chen and T. Salmassi (1996) "Lower Head Integrity Under In-Vessel Steam Explosion Loads," DOE/ID-10541, June 1996.

46. Turland, B.D., N.A. Johns and M.P. Owens (1993) "The Implications of the TMI-2 Vessel Investigation Project for Lower Head/Melt Interactions," AEA Technology Final Report AEA RS 7771, October 1993.

47. Turland, B.D. (1994) "In-Vessel Phenomena Relevant to the Achievement of Debris Coolability by Ex-Vessel Flooding for a PWR," Proceedings, OECD/CSNI/NEA Workshop on Large Molten Pool Heat Transfer, Nuclear Research Centre, Grenoble, France, March, 9–11.

48. Tuomisto, H. and T.G. Theofanous (1994) "A Consistent Approach to Severe Accident Management," *Nuclear Engineering and Design*, **148** 171-183 (1994). [see also Proceedings Specialist Meeting of Severe Accident Management Programme Development, ENEA/DISP, Rome, Italy, Sept. 23-25, 1991, 133-151.]

APPENDIX A

THE ROAAM AND PROCEDURES

Dealing with Phenomenological Uncertainty in Risk Analysis

Plenary Lecture in Workshop I in Advanced Topics in Reliability and Risk Analysis
Annapolis, MD, October 20-22, 1993
NUREG/CP-0138, October 1994

APPENDIX A

DEALING WITH PHENOMENOLOGICAL UNCERTAINTY IN RISK ANALYSIS

T.G. Theofanous

Department of Chemical and Nuclear Engineering
Center for Risk Studies and Safety
University of California, Santa Barbara, CA 93106

ABSTRACT

The Risk-Oriented Accident Analysis Methodology (ROAAM) is summarized and developed further towards a formal definition. The key ideas behind the methodology and these more formal aspects are also presented and discussed.

A.1 INTRODUCTION

The assessment of risks in very low probability, high consequence situations entails an intellectual challenge of unparalleled dimensions in science and technology. The principal reason for this is that "by definition" these assessments must be made on the basis of more-or-less incomplete information. By this, we mean a lack of firsthand information on the behavior of the system under the postulated extreme (another way of saying, rare) conditions involving the manifestation of hazard! We need, of course, reliable estimates; normally there is a tendency to aim for reliably conservative estimates, while at the same time consideration of competing risks do not afford us the luxury of the more handily obtainable highly conservative, or "bounding estimates." We believe much of what is required to address this challenge is methodological and much of the thrust in this methodology is in communications and synergism among independent workers. We have developed the Risk-Oriented Accident Analysis Methodology (ROAAM) for this purpose. The germinal stages of it can be found in Theofanous and Bell (1986) and Theofanous et al. (1987); a full demonstration is given in Theofanous et al. (1991) and brought to completion in Theofanous et al. (1993); another application is currently underway in Pilch et al. (1993); and a couple of new applications are presently in the offing (Theofanous et al., 1994; Additon et al., 1994). We take the opportunity of this invitation to translate this experience into a somewhat more formal definition of ROAAM, especially including important classification aspects. Still, the best way to appreciate ROAAM is through its application to specific problems, such as those mentioned above, and this paper is written as a complement rather than a substitute

of them in this respect. In particular, aiming for an efficient presentation of the main ideas here, we do not get into elaborations with particular examples. These can best be deduced from the applications already available.

A.2 PROBABILISTIC FRAMEWORK

Given a "system" and "operating conditions" we seek to quantify "likelihood" of a certain set of "damage" outcomes due to a set of externally imposed or internal perturbations. For each damage component D_i we have:

$$L(D_i) = \mathcal{F}(p_1, p_2, \ldots p_n) \qquad (A.1)$$

where the p's are parameters needed to completely characterize the response of the system. The function $\mathcal{F}$ is a "model" that is, in general, very complex and with many degrees of freedom. The model can be deterministic, or stochastic, or some combination thereof.

Definition. A "probabilistic framework" represents a decomposition of the model into one or more "cause–effect" relationships and the assignment of p's into one of the following three categories:

$d_1, d_2, \ldots d_n$	a set of deterministic parameters
$r_1, r_2, \ldots r_\ell$	a set of random parameters
$i_1, i_2, \ldots i_m$	a set of intangible parameters

subject to the following requirements:

Requirement 1. The decomposition should be such that each "cause–effect" relationship represents a well-defined physical problem. A key aspect of "well-posedness" is absence of unquantifiable bifurcation or other sudden transitions in behavior — that is, continuity on initial data. In this case, we have a *deterministic model* which, however, may admit, beyond deterministic parameters, random or intangible ones also.

Requirement 2. The random parameters should be supported by statistical bases, or at least be amenable to statistical inference — this means that developing an appropriate data base should be a practical task. In this case we have a *stochastic model.*

Requirement 3. The set of intangible parameters is to include those that do not fall into either of the above two categories — that is, they cannot be related to other, known, parameters through either deterministic or stochastic models.

By way of explanation, the following additional remarks can be made on the above:

1. The specific construction of a probabilistic framework cannot be prescribed (or automated). As a key element, it involves the identification of the controlling physics/mechanism), which often involved *ad hoc* creative elements. Thus, the central element of a probabilistic framework is one or more causal relationships (CRs).

2. A similarly important decision is involved in allocating the key parameters in the three categories. To some extent this depends on the state-of-the-art, but it must also anticipate, *or guide*, the future developments. In any case, the identification of intangible parameters must be explicit, and thorough enough that it can be considered complete.

3. Both random and intangible parameters are quantified by means of probability density functions (pdf's) — in the former case by means of stochastic models (SMs) and in the latter case by means of engineering judgments (EJs) guided by whatever evidence is available.

4. All three quantifications, CRs, SMs and EJs, are subject to errors which, however, are of qualitatively different natures and which become progressively, in the above order, more and more ill-defined. This can be understood by the conditions of "applicability"; in the CR case it is based on relatively well-established scientific/engineering tools of scaling and experimentation; in the case of the SM it depends on the "similarity" of the circumstances prevalent in the data base; and in the case of EJs it can only be judged on a case-by-case basis. *On the other hand, the assessment of errors in all three cases involves judgment, and as such, an irreducible component that can be approached only qualitatively. The key aim of the methodology is to provide the necessary procedures and safeguards so as to recover from this subjective element sufficiently to assure robustness of the results.* [That is, to counterbalance the "loss" due to the subjective element by rigor in the assessment process.] This is the unique intellectual challenge mentioned in the introduction.

5. To this end, beyond what has been described above, we have introduced the idea of enveloping the behavior by means of "splinter scenarios" and conservatively-biased quantifications of the intangible uncertainties (as noted above, these include errors in the intangible parameters as well as model errors in the CRs and SMs). Splinter scenarios give rise to multiple quantifications and, therefore, multiple results which by definition are indistinguishable (in terms of likelihood) from each other. These results thus provide a conservative envelope of the behavior that could actually be obtained. As new knowledge becomes available, some of those splinter scenarios become irrelevant and the envelope of results narrows correspondingly.

6. The other key idea is that the quantification is considered to be "*a process*," involving a wide range of experts, aiming for "refinement" and "enrichment" of the quantification bases, while explicitly recognizing "position on the learning curve" for the CRs and the SMs, and "quality of quantification" for the probabilistic framework (and the intangibles). These are described further below.

A.3 QUANTIFICATION

By "quantification," we mean assigning probability distributions to the various components of the probabilistic framework. To deal with the irreducible, qualitative, component discussed above, we introduce a probability scale, as indicated in Table A.1.[a] The scale itself is arbitrary, except for requiring that the third level is equal to the product of the first two which, in fact, gives our definition of "physically unreasonable" (that is, a consequence of two independent steps, events, or processes of likelihood equal to the first two levels, respectively). The scale is used temporarily only, as a device of synthesizing through the framework an overall result, which is to be converted using the same scale to the corresponding qualitative meaning. *An important consequence of this line of thinking is that in the presence of intangibles we can have no numerically expressed safety goals.* Or conversely, such numerical goals are quite meaningless unless they are accompanied by an explicit definition of how they are to be computed.

Table A.1. Definition of Probability Levels

Process Likelihood[a]	Process Characteristics
1/10	Behavior is within known trends but obtainable only at the edge-of-spectrum parameters.
1/100	Behavior cannot be positively excluded, but it is outside the spectrum of reason.
1/1000	Behavior is physically unreasonable and violates well-known reality. Its occurrence can be argued against positively.

[a] A probability distribution is constructed by joining piewise uniform segments and normalizing the total probability to unity. That is, the ~90% segment represents the expected range.

Another key questions is: What scenarios are to be quantified? This depends, to a large extent, on the reliability of the various active components of the system (including the human component), and is appropriate, and convenient, to consider it again in an enveloping manner by means of a "cut-off" frequency in admissible system damage states. This requires a safety goal, which must also be explicit in the consideration of "uncertainties" satisfying it. Thus the concept of scenario, under which Eq. (A.1) is to be evaluated, is seen to consist of two separate aspects: the culling of potential scenarios to select those worthy of detailed examination and the identification of physical laws which govern the ones to be studied. The first entails the "cut-off" frequency intending to establish an envelope of system behavior, while the second involves the progression of physical events being enveloped by means of a set of splinter scenarios and the quantification of a probabilistic framework.

The quantification is initiated by an integrated document that contains the framework, detailed explanations of all quantifications and their bases, synthesis of results, and a set of *arbitrary* sensitivity studies — the latter have been found handy in anticipating "what if" questions that invariably arise during the review. For the process to work, this must be a highly cohesive document and a largely valid first step in the quantification, containing a clear point of view, that the authors have thought enough about to be willing and able to defend. Although we have not tried it, our own experience indicates that the initiating document could not be successfully developed in a "committee" setting. Rather, most effective in this regard is a closely-knit group of individuals who can interact freely and with reasonable flexibility in carrying out support activities or seeking outside help as necessary. There has been a criticism that this may bias the process to "converge" to a wrong solution. To this, we respond as follows: (a) once convergence has been achieved, in the manner described below, the solution cannot be wrong; (b) quite clearly, such complex problems are amenable to a variety of quantifications yielding correspondingly a variety of conclusions, thus it is only reasonable that one aims at *an effective* solution; and (c) the effectiveness of a solution can be judged only after it is actually obtained — this depends very much on the inherent merits of the probabilistic framework and the validity of the quantifications rather than on whether these, in the initial step, are a product of diverse committee or the closely-knit group which we advocate. Experience shows that diverse committees tend to diverge, and so far, we have no example of an issue resolved by such committee work.

The ROAAM peer-review process is to involve, to the extent possible, all key experts with established credentials (i.e., having worked) in the various aspects addressed in the quantification. This allows experts at the generic level which is beneficial in both broadening the cadre of individuals involved, but more importantly in allowing the review to take on a strongly fundamental component. The review comments are to be published (signed) together with point-by-point

responses by the authors, together with the originating, called "peer-review version," document. The reviewers are encouraged to provide alternative quantifications together, of course, with the bases for them, and the authors' responses may make use of these inputs in synthesizing updated results as appropriate. Alternatively, the authors may elect to ignore any of these inputs by providing appropriate rebuttals. In any case, decomposition affords a focusing on narrow technical issues that can be resolved sooner or later by means of either subgroup workshops, independent research or audit activities or more likely by appropriate combinations. Experience has demonstrated that very often initial disagreements are because of communications and/or difficulty to appreciate another way of thinking on a particular problem. Interactions are useful in overcoming these difficulties, but more importantly, these activities can add to the substantive aspects of the quantification by including consideration of alternative scenarios and enriching the quantification bases of the more controversial components.

The aim is to achieve sufficient enrichment and eventually convergence *on each* of the components of the probabilistic framework. Such by-parts convergence assures agreement on the results of the synthesis, and this is defined as "resolution."

A.4 SOME QUALITY ATTRIBUTES

Even before final resolution is achieved, during the ROAAM peer-review process, the results can be useful as the basis for tentative decisions and for allocating research resources. Following resolution, and depending on the problem, it may still be prudent that aspects of it continue to be pursued in what might be called "defense in depth in assessment." To aid those responsible for making these decisions, we believe it is appropriate that the results of such analyses be transmitted with certain "higher level" quality indicators explicitly discussed. They are a "Quality Grade" on the framework, especially with regards to handling the intangibles, and a "Development Phase" on the various key models (the CRs and the SMs). Each is discussed in turn below.

We define three quality grades. The highest, Grade A, is assigned to an assessment (framework) carried out by means of a single, limiting process, evaluated on basic physical laws, with appropriately bounding inputs. Here there is no scenario dependence, any intangible parameters are bounded, there is no need for experimental verification, and the assessment can be considered of extremely high reliability. The next, Grade B, is for an assessment involving a single but complex physical process evaluated at a high confidence level. Here there may be slight scenario dependence (within each splinter scenario), there is need for solid experimental support and scaling, and any significant intangibles are treated in a reasonably bounding sense. Finally, we have Grade C, reserved for strongly, and clearly, coupled sequences of processes, each one

quantified with support from scaled/applicable experiments. Here there may be some scenario dependence (and system's effects), counter-balanced by appropriately conservative quantification of the intangibles. In all of these cases the emphasis is on controlling physics. Also note that we do not assign a grade, nor do we consider acceptable, *in the present frame*, an approach that relies heavily on the use of system's codes as the primary means of quantification.

The phases of development are introduced to explicitly denote a position on a learning curve, thus safeguarding against premature abandonment of the assessment process, and hence against inadequately verified results. We define six development phases, as indicated in Table A.2. As noted already, the examination of any problem normally begins with a scoping phase. It involves simple, and usually parametric models to check out the magnitude of the various effects. As the issues are understood better, we can expect the development of detailed models, while at the same time we see various attempts at experimentation. By and large, however, this is still a pre-experimental phase. The quantitative phase is obtained when analyses and experiments converge sufficiently to obtain a mutually beneficial feedback, especially in identifying the important phenomenological regimes and especially in addressing scaling and applicability. This phase is consummated with the first arguably valid model comparison with scaled experiments. Further refinement and enrichment of both analytical and experiment tools is obtained in the next phase, as results are verified, refined, or even corrected as further results arrive from multiple origins. Hence this is called the "maturation" phase. Invariably, the maturation phase will be "driven" by related applications, and depending on the variability involved (from the initiating study), there may be a significant extension aspect and hence the "extension" phase. Finally, and depending on the problem, we may need a long-term activity to provide what we have described as "defense-in-depth in assessment." It is to further explore the intangibles. It will be recognized that the initiating ROAAM document will normally span phases II and III, while the ROAAM peer-review process can take on a significant portion of phase IV. It is understood that the actual completion of phase IV would take place outside and after resolution has been achieved, while at the same time being reinforced by other related applications in phase V. Finally, the need for phase VI can only be judged on a case-by-case basis, and in a broader programmatic context as well.

In the above, the phases of development have been discussed from the point of view of CRs, as physical models are central to the ROAAM. These same phases, however, can also be defined for stochastic modelling, the emphasis here being on any physics with potential bearing on the applicability of the data base, and on the necessary statistical tests to verify the model. Phase VI in this context would be concerned with any unaccounted for or unforeseen factors that could affect the results.

Table A.2. Definition of "Phases of Development" for Causal Relations

Phase I	Scoping	Simple Models, Parametric Results
Phase II	Analytical	Detailed Models, Pre-experimental
Phase III	Quantitative	Experiments, Scaling, Model Comparisons
Phase IV	Maturation	Verified Results from Multiple Origins
Phase V	Extension	Other Related Applications
Phase VI	Defense-in-Depth	Further Exploration of Intangibles

In both cases the long-term activity of phase VI is aimed at addressing the open-ended issue of "completeness." However, this is only in a defense-in-depth sense, since for the most part this has been addressed by the ROAAM peer-review process and the followup portion of phases IV and V.

A.5 CONCLUDING REMARKS

Parametric propagations of uncertainty can only explore a subregion of the true uncertainty space. The magnitude of the fraction thus explored is a strong function of the validity of the model, thus model uncertainty is related to this limitation. There is no way to *a priori predict* this limitation, since a given model either captures the basic physics or not. Thus, rather than seeking a "theory" approaching this prediction task generally, there is much to be gained in focusing efforts on specific issues of great importance. We have outlined a methodology for such an applications-oriented, or product-oriented approach, and we now have a significant amount of experience with it in real-life applications. We found in all cases that the answers lie in the depth afforded by this specificity, and that once an adequate understanding has been found and communicated that synergism and convergence among the experts is possible. This is fundamental since agreement among experts is a necessary condition for a rational approach to decision making.

The ROAAM avoids the arbitrariness of the so-called deterministic approaches (a true Grade A approach, which is, in effect, commonly found to be impractical), and the divergence of the so-called expert elicitation process (as well as other pitfalls) in level II PRAs. It is neither of these two, and in applications it must be followed in its entirety. It can be applied equally well to assessing risk (likelihood-damage pairs) in existing facilities, as well as to guide the design and/or accident management options when improvements are deemed worthwhile.

A.6 ACKNOWLEDGEMENT

The development of the ideas that led to ROAAM took place over many years of work in various NRC programs, and more recently under the DOE's ARSAP program. The author is grateful to Mr. S. Additon (TENERA) for incisive comments during the preparation of this presentation and also on an early draft of the manuscript.

A.7 REFERENCES

1. Additon, S.L., W.L. Pasedag and T.G. Theofanous (1994) "The Risk Oriented Accident Analysis Methodology (ROAAM) Applied to Passive ALWRS," ARS–94 – International Topical Meeting, Advanced Reactors Safety, Pittsburgh, PA, April 17–21, 1994.

2. Pilch, M.M., H. Yan and T.G. Theofanous, "The Probability of Containment Failure by Direct Containment Heating in Zion," Draft NUREG/CR-6075, SAND93-1535, June 1993.

3. Theofanous,T.G., W.H. Amarasooriya, H. Yan and U. Ratnam (1991) "The Probability of Liner Failure in a Mark-I Containment, NUREG/CR-5423, August 1991.

4. Theofanous, T.G. and C.R. Bell (1986) "An Assessment of Clinch River Breeder Reactor Core Disruptive Accident Energetics," *Nuclear Science and Engineering* **93**, 215-228.

5. Theofanous, T.G., C. Liu, S. Angelini, O. Kymäläinen, H. Tuomisto and S. Additon (1994) "Experience From the First Two Integrated Approaches to In-Vessel Retention Through External Cooling," OECD/CSNI/NEA Workshop on Large Molten Pool Heat Transfer, Grenoble, France, March 9–11.

6. Theofanous, T.G., B. Najafi and E. Rumble (1987) "An Assessment of Steam-Explosion-Induced Containment Failure. Part I: Probabilistic Aspects," *Nuclear Science and Engineering*, **97**, 259-281.

7. Theofanous, T.G., H. Yan/UCSB; M.Z. Podowski, C.S. Cho/RPI; D.A. Powers, T.J. Heames/SNL; J.J. Sienicki, C.C. Chu, B.W. Spencer/ANL; J.C. Castro, Y.R. Rashid, R.A. Dameron, J.S. Maxwell, D.A. Powers/ANATECH (1993) "The Probability of Mark-I Containment Failure by Melt-Attack of the Liner," NUREG/CR-6025, November 1993.

APPENDIX B

THE COPO EXPERIMENTS

Heat Flux Distribution from a Volumetrically Heated Pool with High Rayleigh Number

Proceedings, NURETH-6, Grenoble, October 5-8, 1993

or

Nuclear Engineering and Design **149**, 401-408, 1994

APPENDIX B

HEAT FLUX DISTRIBUTION FROM A VOLUMETRICALLY HEATED POOL WITH HIGH RAYLEIGH NUMBER

O. Kymäläinen,[a] H. Tuomisto,[a] O. Hongisto,[b] T.G. Theofanous[c]

[a]Nuclear Power Engineering
[b]Process Laboratory
IVO International Ltd, SF-01019 IVO, Finland

[c]Department of Chemical and Nuclear Engineering
University of California, Santa Barbara, CA 93106

ABSTRACT

Experimental results are presented on the heat flux distribution at the boundaries of volumetrically heated pools at high enough Rayleigh numbers to be directly relevant to the problem of retention of a molten corium pool inside the lower head of a reactor pressure vessel. The experimental facility, named COPO, is 2-dimensional ("slice"), Joule-heated and geometrically similar in shape (torospherical at 1/2-scale) to the lower head of a VVER-440 reactor. The results show that

- the heat flux on the side wall (vertical portion) is essentially uniform,
- the downward heat flux strongly depends on position along the curved wall, and
- average fluxes on the side and downward direction are in agreement with existing correlations, but somewhat underestimated in the upward direction.

For the shape considered, the heat flux along the lower curved wall seems to be independent of the presence and extent of the liquid pool (contained by the vertical sidewalls) portion above it.

B.1 INTRODUCTION

This study is motivated by an interest in arresting the progression of a hypothetical severe accident in the reactor pressure vessel by submerging it in a pool of water (i.e., flooding the reactor cavity). This is expected to occur in all risk-significant severe accident scenarios in the Loviisa plant, because it is equipped with an ice condenser containment; thus, it has formed the cornerstone of the severe accident management approach for it (Tuomisto and Theofanous [1]).

The basic requirement in this accident management concept is that the thermal loads from the volumetrically heated, naturally convecting corium pool are dissipated through the lower head of the reactor vessel without jeopardizing its integrity. For this, it is sufficient to show that *nowhere* is the heat flux high enough to cause significant local wall thinning (by melting and/or chemical attack), and that *everywhere* the local fluxes are below the local critical heat flux limits on the outside. The first condition is interesting because existing data and numerical simulations indicate the possibility of strong heat flux peaking near the top of the vertical boundaries of such pools (e.g., Steinberner and Reineke [2]). The second condition arises because of the "inverted" boiling regime, expected to promote critical heat flux by forcing the two-phase layer to flow (while vapor accumulates) along the surface. Clearly, both processes (buoyancy driven) depend on the shape of the boundary and the radial position along it and knowledge of respective distributions are a crucial part of the argument. In addition, total heat flows (or average fluxes) in the upward, sideways, and downward directions are important because through them one can conveniently estimate the maximum pool temperatures required to dissipate the volumetric heat source (decay power). This, then, establishes the maximum driving force for the local evaluations.

In the original assessment (Theofanous [3]) existing correlations were used in conjunction with parametrics on local peaking to broadly scope out the problem. For a decay power level of 9 MW and a maximum pool height of 1.2 m, a Rayleigh number of $\sim 3 \cdot 10^{14}$ and a maximum pool superheat (relative to the boundaries) of ~100 K were estimated. By comparison, existing data were limited to Rayleigh numbers smaller by at lease one order of magnitude, than the 10^{14} order deemed relevant. Moreover, the Loviisa lowerhead is "dished" (torispherical) and the pool extends significantly into the cylindrical portion of the vessel, while previous studies were limited to rectangular, hemispherical, or semicircular shapes only. Thence was initiated the present experimental program. A parallel experimental program on the critical heat flux aspects of this problem is also in progress (Kymäläinen et al. [4]).

Similar calculations and limitations of the existing data base were also noted recently by O'Brien and Hawkes [5] and Frantz and Dhir [6]. For power reactors of the 1000 MWe class employing hemispherical lower heads, the pool depth is 67% of the lower head radius and the Rayleigh numbers are of the order 10^{17}. Frantz and Dhir [6] presented three data points obtained with hemispherical pools (adiabatic top boundary) at $Ra \sim 5 \cdot 10^{13}$ and "fill ratios," H/R_e, of 0.4, 0.6 and 1.0, where H is the maximum pool height and R_e is the equivalent radius corresponding to the pool volume. These data were only slightly lower than a numerically predicted result due to Mayinger et al. [7]

$$Nu_{dn} = 0.55 \ Ra^{0.2} \qquad (B.1)$$

who used the data of Jahn and Reineke [8], obtained with semicircular pools, to benchmark the analysis. A related experimental correlation for circular segments by Mayinger et al. [7] is

$$Nu_{dn} = 0.54\ Ra^{0.18} \left(\frac{H}{R}\right)^{0.26} \qquad (B.2)$$

where H is the pool depth and R is the radius of curvature of the segment. The experimental conditions for this correlation cover the ranges $0.3 < H/R < 1.0$ and $10^7 < Ra < 5 \cdot 10^{10}$. Note that in Eq. (B.1) the length scale cancels. This is also approximately true in Eq. (B.2) when $H/R = 1$, and in any case the length scale dependency is rather small.

For the upward and sideways heat fluxes the most pertinent are correlations obtained in a rectangular (slice) geometry by Steinberner and Reineke [2],

$$Nu_{up} = 0.345\ Ra^{0.233} \qquad (B.3)$$

$$Nu_{hr} = 0.85\ Ra^{0.19} \qquad (B.4)$$

The data range for these correlations was $8 \cdot 10^{12} < Ra < 4 \cdot 10^{13}$. Note, again, that the length scale very nearly cancels from both correlations, so the application of them is not sensitive to the exact definition of pool height in cases of a curved lower boundary, as is the case here.

Regarding the flux shapes, the data, and the theoretical interpretations of them, are even more limited. On the vertical wall of a rectangular pool with aspect ratio of ~1, Steinberner and Reineke [2] found a peak-to-average value of ~2. On a hemispherical boundary, Frantz and Dhir [6]measured peak-to-average values of ~2 also, with a strong bias of strongly increasing flux with radial positions (away from the centerline). On the other hand, O'Brien and Hawkes [5] from a numerical study (k-ϵ model) noted the possibility, at high Rayleigh numbers, of a more uniform behavior, i.e., higher fluxes to the more downward facing parts of the lower head. No data exist for torispherical shapes.

In this work we present data for the particular range of Rayleigh numbers, O (10^{15}) and pool shapes (torispherical) of interest to the Loviisa case. However, comparisons with existing correlations (obtained at lower Rayleigh numbers) provide interesting insights of a more general nature, and the local flux distributions on the lower torispherical shape in conjunction with data from hemispherical shapes (obtained elsewhere) can be of value for a more fundamental understanding in numerical modelling efforts.

B.2 EXPERIMENTAL FACILITY

The experimental approach is based on using a two-dimensional "slice" of the Loviisa lower head, including a portion of the cylindrical vessel wall. This allows well-controlled, uniform heating (using the flats as the electrodes) and is convenient for achieving large characteristic length scale and thus large Rayleigh numbers. The test section of the facility (called COPO) is illustrated in Figure B.1, and the shape is shown in more detail in Figure B.2. It is at half-scale, geometrically similar to Loviisa, it measures a span of 1.77 m and allows a maximum pool depth of 0.8 m. The thickness of the slice is 0.1 m.

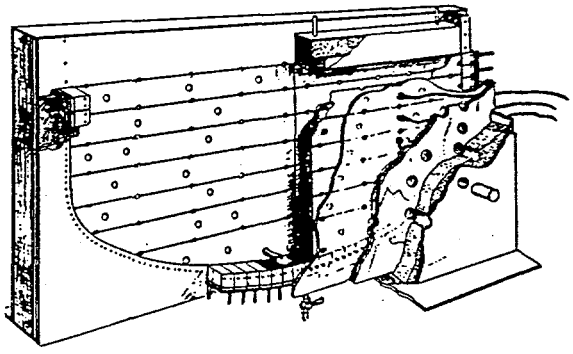

Figure B.1. Schematic of the COPO facility.

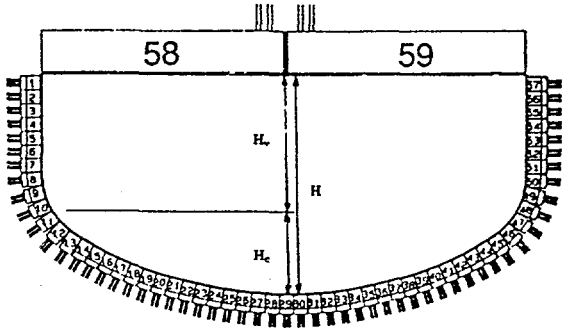

Figure B.2. The shape of the COPO test section and identification of the cooling units on it.

The flats of the test section are built from polycarbonate plates and are heavily insulated as shown. On the inside the plates are lined by seven pairs of electrode strips. At selected locations both electrodes and insulation have 20 mm holes to gain visual access to the fluid. The pool is a conducting $ZnSO_4$–H_2O solution and the current through each electrode can be individually adjusted, if necessary, in order to produce uniform volumetric heating.

The side and bottom walls consist of 57 separate cooling units, as illustrated in Figure B.2. Each cooling unit consists of a 50 mm thick brass wall electrically insulated from the pool by a 0.1 mm thick teflon tape. Coolant water is circulated on the back side of the brass walls. The units are grouped into three groups (Group 1: 1–8 and 50–57 units; Group 2: 9–18 and 40–49 units; and Group 3: 19–28 and 30–39 units) and the flow is adjusted evenly among the units of each group to obtain a nearly isothermal boundary. The top surface cooling is provided by two units (58 and 59). They are constructed out of aluminum sheet and are electrically insulated from the pool by a thin aluminum-oxide coating. The cooling water passes through heat exchangers and its flow rate is measured by an electromagnetic flow meter.

The fluid and pool boundary temperatures are comprehensively mapped by 140 thermocouples. Power input is deduced from electric current and voltage measurements. The local heat fluxes are obtained from energy balances on the coolant circulating through each cooling unit. The overall energy balance was found accurate within 10%.

B.3 EXPERIMENTAL RESULTS

The conditions for all experimental runs performed are summarized in Table B.1. The two pool heights employed were chosen to provide a significant variation in the H/H_C ratio (see Figure B.2), that is, in the "curved" portion to the total pool volume. The table also gives the maximum pool temperature, T_{pmax}, and Rayleigh numbers achieved in each experiment. The average temperatures at the top (cooling units 58 and 59), vertical (cooling units 1 to 10 and 48 to 57), and lower (cooling units 11 to 28 and 30 to 47) pool boundaries, $\overline{T}_{up}$, $\overline{T}_{sd}$, and $\overline{T}_{dn}$, respectively, are also reported as an indication of the degree of isothermality achieved. This degree can also be expressed by the parameter τ defined by

$$\tau = \frac{\overline{T}_{up} - \overline{T}_{sd}}{T_{pmax} - \overline{T}_{sd}} \qquad (B.5)$$

such that as τ increases from 0 to 1 the upper surface condition changes from isothermal to adiabatic. In certain runs the conditions were purposely selected to yield τ's in the 0.1 to 0.3 range, to test the effect of the degree of partial cooling of the upper surface on the heat transfer phenomena studied. This may be of interest to some special conditions in reactor applications. For runs in which $\tau << 1$, any deviations from zero are due to limitations in controlling the surface temperatures by handling the cooling units in three groups as discussed in section B.2. A more complete view of this control limitation in the present experiment can be obtained from Table 1 by comparing the differences in all pool boundary temperatures to the overall difference from the maximum pool temperature. In some cases the deviations seem to be excessive; however, no distinction could be made on the data trends of these (including runs in which the τ was set as high as 0.3) as compared to runs in which the condition of isothermality was more adequately observed. In all present runs, even those with τ's up to 0.2 or 0.3, the pools appeared to be well mixed and all temperature non-uniformities were confined within narrow layers near the boundaries. This is not at all the case for pools with adiabatic boundaries (as in the case considered by Frantz and Dhir [6]), in which the bulk is strongly stratified.

B.3.1 Average Heat Fluxes

The experimentally measured local heat fluxes were grouped and averaged over the pool top boundary (cooling units 58 and 59), the vertical pool boundary (cooling units 1 to 10

Table B.1. Main Parameters of the COPO Tests

Run No.	H (m)	T_{pmax} (°C)	$\overline{T}_{up}$ (°C)	$\overline{T}_{sd}$ (°C)	$\overline{T}_{dn}$ (°C)	τ	Ra
29a	0.8	79.3	66.7	65.3	60.8	0.10	$1.61 \cdot 10^{15}$
29b	0.8	81.0	68.4	66.1	61.4	0.15	$1.53 \cdot 10^{15}$
30a	0.8	64.4	55.5	55.4	53.2	0.01	$6.79 \cdot 10^{14}$
30b	0.8	64.5	56.1	53.0	48.6	0.27	$7.24 \cdot 10^{14}$
30c	0.8	65.6	57.7	53.5	48.8	0.35	$6.79 \cdot 10^{14}$
30d	0.8	75.6	62.8	61.6	57.6	0.09	$1.52 \cdot 10^{15}$
30e	0.8	75.8	63.1	61.3	56.6	0.12	$1.54 \cdot 10^{15}$
32a	0.8	74.8	61.6	62.7	60.3	-0.09	$1.43 \cdot 10^{15}$
32b	0.8	77.9	66.3	64.2	59.7	0.15	$1.59 \cdot 10^{15}$
32c	0.8	79.9	68.3	65.5	60.1	0.19	$1.66 \cdot 10^{15}$
32e	0.8	80.4	68.1	65.7	56.8	0.16	$1.62 \cdot 10^{15}$
32f	0.8	70.5	59.7	59.1	56.5	0.05	$8.76 \cdot 10^{14}$
33a	0.8	70.8	60.4	59.5	56.8	0.08	$9.89 \cdot 10^{14}$
33b	0.8	69.9	60.0	57.5	53.3	0.20	$9.87 \cdot 10^{14}$
33c	0.8	70.9	62.2	58.1	53.6	0.32	$9.60 \cdot 10^{14}$
40a	0.6	82.8	67.6	66.6	58.4	0.06	$5.23 \cdot 10^{14}$
40b	0.6	83.7	68.4	66.5	58.5	0.11	$5.70 \cdot 10^{14}$
40c	0.6	82.5	67.9	64.9	55.5	0.17	$5.57 \cdot 10^{14}$
40d	0.6	81.8	66.9	63.8	55.8	0.17	$5.34 \cdot 10^{14}$
41a	0.6	71.4	60.2	60.2	56.7	0.00	$2.65 \cdot 10^{14}$
41b	0.6	72.3	61.9	60.2	55.6	0.14	$2.70 \cdot 10^{14}$
41c	0.6	72.7	62.4	61.2	56.3	0.10	$2.70 \cdot 10^{14}$
41d	0.6	72.8	61.9	61.1	56.4	0.07	$2.70 \cdot 10^{14}$
42a	0.6	61.3	52.7	54.6	54.7	-0.28	$1.38 \cdot 10^{14}$
42b	0.6	61.4	53.8	54.2	53.7	-0.06	$1.26 \cdot 10^{14}$
42c	0.6	62.9	55.4	55.5	54.1	-0.01	$1.24 \cdot 10^{14}$
42d	0.6	63.1	55.5	54.8	52.5	0.08	$1.34 \cdot 10^{14}$

and 48 to 57), and the lower, curved pool boundary (cooling units 11 to 47). Thus we have the "upwards," "horizontal" and "downwards" heat transfer coefficients and Nusselt numbers, respectively, denoted by Nu_{up}, Nu_{hr} and Nu_{dn}. They are considered in turn, below, in relation to the correlations quoted in the introduction. The plots are given in linear coordinates to make more evident the quantitative comparisons.

For the upwards heat flux the data are shown in Figure B.3, together with Eq. (B.3) for comparison. While Eq. (B.3) is seen to be in reasonable agreement at the low end of the Rayleigh number range studied, we observe increasing deviations at the higher end. At $Ra = 1.6 \cdot 10^{15}$ the maximum deviation of the prediction from the data is ~30%. As mentioned already, Eq. (3) is very nearly independent of the length scale; in plotting the data the maximum pool depth was utilized; if one could visualize a somewhat smaller equivalent pool depth (because of the curved lower boundary), the deviation from the correlation would be somewhat larger. It is noted that for reactor assessments this trend is conservative since the upwards flux radiates to the vessel side walls from which it is easily dissipated—a lower upwards flux means higher thermal loads on the lower head.

For the horizontal heat flux the data are shown in Figure B.4 along with predictions from Eq. (B.4). We see that the use of the maximum pool depth works well considering the wide variation between the H/H_C covered by the two pool depths utilized in the experiments.

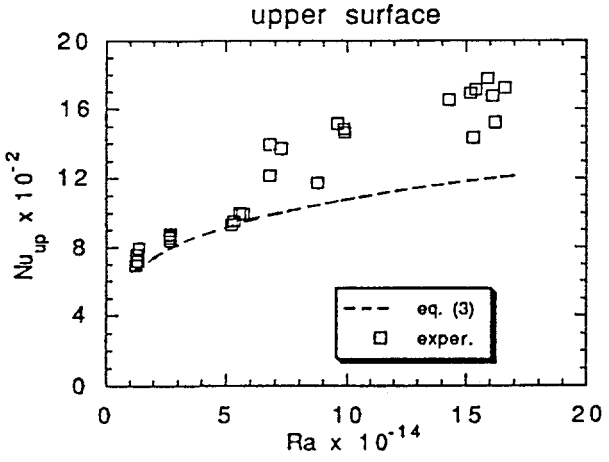

Figure B.3. Variation of upwards heat fluxes with Rayleigh number.

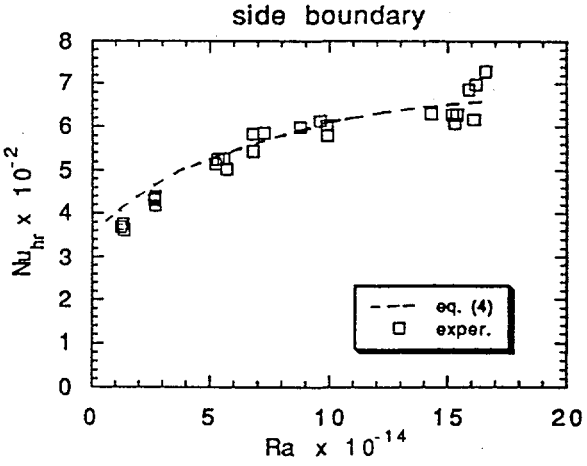

Figure B.4. Variation of the heat fluxes on the vertical boundary of the pool with the Rayleigh number.

For the downwards heat flux the data are shown in Figure B.5, in comparison with Eq. (B.2). In this case Eq. (B.2) was evaluated in terms of the height of the curved position of the pool, H_C, and the agreement is seen to be rather good. The radius of curvature, R, was taken as that of the major portion of the lower boundary, i.e., excluding the more highly curved two ends. Including these ends, in some fashion, would produce a somewhat smaller "equivalent" radius of curvature and probably an even better agreement with Eq. (B.2). However, it is more straightforward for our present purposes (i.e., the Loviisa shape and Ra number ranges) to account for slightly higher data trends by increasing the Rayleigh number exponent slightly to 0.182. Figure B.5

also shows that for $H > H_C$ the downwards heat flux is independent of the total pool height. This is an interesting and not unexpected result. On the other hand, recognizing that besides the significantly different shape the present data are at Rayleigh numbers (based on H_C) 3 orders of magnitude greater than the upper end of the data base used in deriving Eq. (B.2), the agreement is remarkable.

B.3.2 Heat Flux Distributions

For horizontal heat fluxes, measured local values from six typical runs (3 for each pool depth) are shown in Figures B.6a and B.6b. It is clear that there is no systematic tendency for peaking in the upper portion of the pool boundary. This is in contrast to the significant peaking reported by Steinberner and Reineke [2], but it could well be expected by almost two orders of magnitude spread in Rayleigh numbers between the two experiments, and, perhaps more importantly, by the wide difference in aspect ratio (width to depth) i.e., 1 vs 3.4 or 5.6 for the 0.8 and 0.6 m pools, respectively (pool depth based on the rectangular portion of the pool only, i.e., $H - H_C$) in the present experiment. Both these aspects would tend to produce unsteady and "broken" recirculation flow patterns favoring uniformity of heat flux on the vertical boundary.

The data for the lower, curved boundary for the same six runs are summarized in Figures B.7a and B.7b. The decrease as the test section centerline is approached is much more gradual (essentially linear) than observed on a hemispherical shape (Frantz and Dhir [6]), and this could be indicative of the strong flow convergence not present in the slice geometry. However, this could also be the consequence of the strong thermal stratification present in the Frantz-Dhir experiments because of the adiabatic upper boundary in them. It is also remarkable that the flux shape seems to be largely independent of pool depth and Rayleigh number variations within the range covered in Table B.1.

B.4 DISCUSSION

Having achieved the proper range in Rayleigh number, applicability of the results of these experiments depends primarily on the relation of the slice geometry to the "full" reactor geometry. This is the question addressed here.

As noted in the previous section, at these high Rayleigh numbers the pool is highly turbulent in the bulk and basically at uniform temperature. This certainly would be in the case of full geometry also. Now, the thermal transport processes at the upper and vertical boundaries would be controlled by thin, turbulent boundary layers and the 10 cm gap in the experiment is certainly large enough to have no effect whatsoever. This is supported further by the agreement of the present results with the results of Steinberner and Reineke [2] obtained with a 3.5 cm gap.

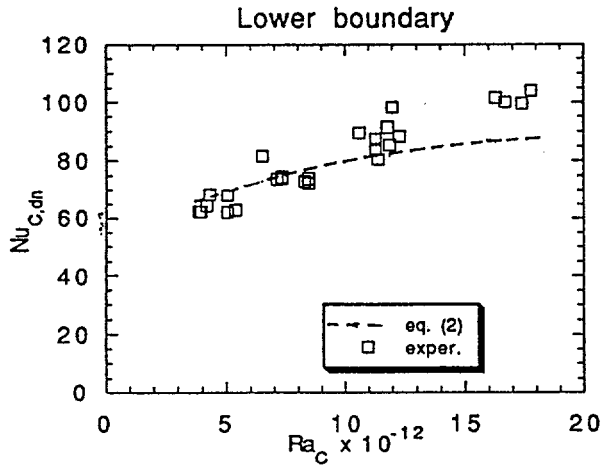

Figure B.5. Variation of the downwards heat fluxes with the Rayleigh number.

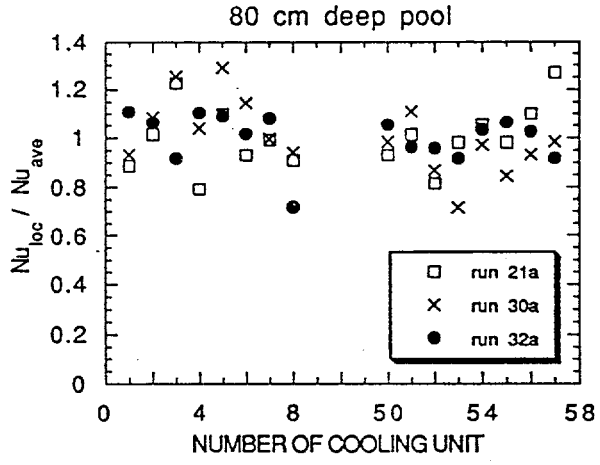

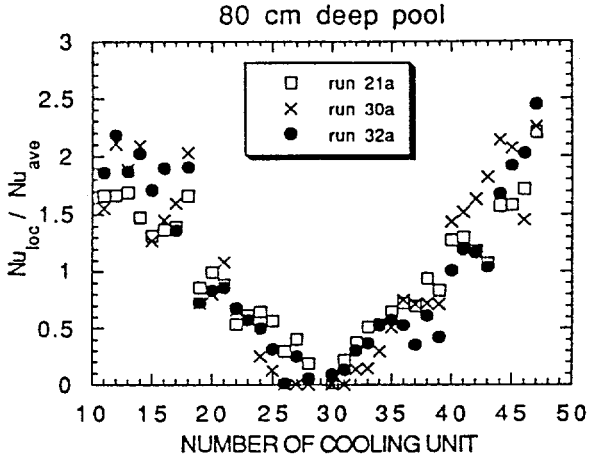

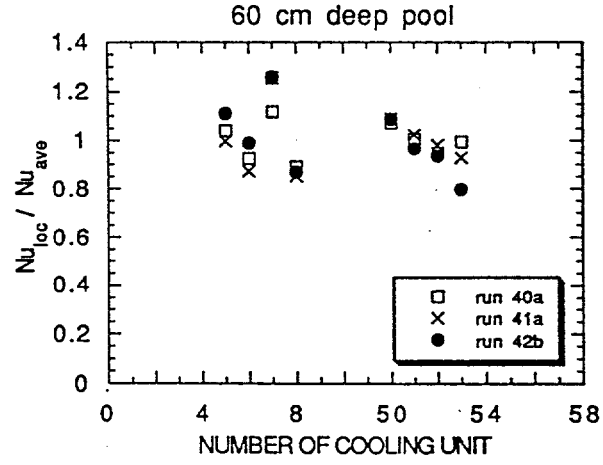

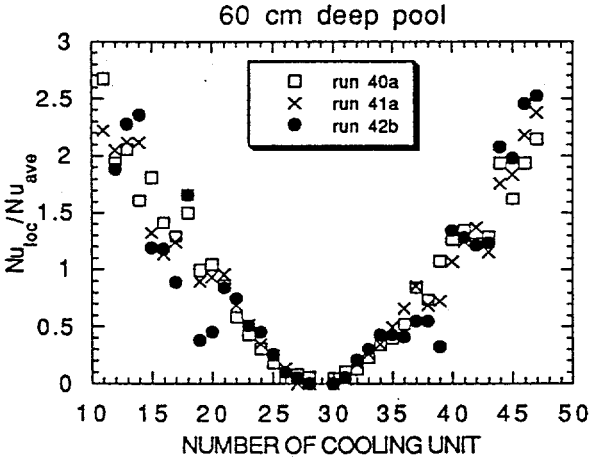

Figure B.6a,b. Distribution of heat flux on the vertical pool boundary for three typical runs.

Figure B.7a,b. Distribution of heat flux on the lower, curved pool boundary for three typical runs.

For the downward heat transfer controlled by descending boundary layers we do expect some difference because of the converging flow found in the full geometry, which is absent in the slice geometry. We would expect that this would produce more progressive "thickening" of the thermal boundary layer as the vessel centerline is approached and, thus, correspondingly lower heat transfer coefficients, as compared to the slice geometry. If this is correct, the flux shape obtained from the present experiments can be used to conservatively bound the behavior. We plan to further investigate this issue by a numerical modelling approach, benchmarked for the turbulence treatment to the present data. On the other hand, it is probably interesting to note that the agreement of the present data to Eq. (B.2), which is closely related to Eq. (B.1) obtained for a full hemispherical geometry, offer two other possibilities: (a) the flux shape from the slice geometry may turn out to be reasonably applicable, or (b) the average downwards flux, as obtained from the slice geometry and predicted by Eq. (B.2), is realistic for the full geometry. In case (b) the calculated fluxes for Loviisa are low enough ($\sim$200 kw/m^2) to expect that absence of CHF could be demonstrated for a uniform heat flux of this magnitude. Recognizing that the flatest portion of the lower head is controlling, this approach would be conservative.

B.5 CONCLUSIONS

Experimental results are presented on the heat flux distribution at the (isothermal) boundaries of volumetrically heated pools at high enough Rayleigh numbers to be directly relevant to the problem of retention of a molten corium pool inside the lower head of a reactor pressure vessel. The results show that

1. The heat flux on the side wall (vertical portion) is essentially uniform and predicted well by Eq. (B.4),

2. The downward heat flux strongly depends on position along the curved wall, and for the shape considered it seems to be independent of the presence and extent of the liquid pool (contained by the vertical sidewalls) portion above it, and

3. The heat flux to the top boundary is somewhat underestimated by Eq. (B.3), but the deviation makes use of Eq. (B.3) conservative.

The use of the heat flux distribution along the lower curved boundary requires some further consideration along the lines mentioned in the discussion.

B.6 ACKNOWLEDGEMENTS

The experiments were carried out in the Hydraulic Laboratory of IVO. Thanks are due to the staff of the laboratory for their contribution and help. The efforts by Mr. E. Pessa in designing the instrumentation are gratefully acknowledged.

B.7 NOMENCLATURE

g = gravitational acceleration (m/s^2)
H = height of the pool (m)
H_C = height of the curved part of the pool (m)
Nu_H = $\frac{qH}{\Delta T \lambda}$
Nu_C = $\frac{qH_C}{\Delta T \lambda}$
q = heat flux (W/m^2)
Q = volumetric heat generation (W/m^2)
R = radius of curvature of a semicircular cavity (m)
Ra_H = $\frac{gQ\beta H^5}{\alpha \upsilon \lambda}$
Ra_C = $\frac{gQ\beta H_C^5}{\alpha \upsilon \lambda}$
T = temperature
$\overline{T}$ = average temperature

Greek

α = thermal diffusivity (m^2/s)
β = thermal expansion coefficient (a/K)
ΔT = difference between the maximum temperature of the pool and the wall surface temperature (K)
λ = thermal conductivity (W/m K)
υ = kinematic viscosity (m^2/s)
τ = relative difference between upper surface temperature and the side wall temperature

subscripts

ave = average
C = curved part of the pool
dn = downward or bottom boundary
H = height of the pool
hr = horizontal, sideward direction
loc = local
$pmax$ = maximum in the pool
sd = side wall, vertical portion of the boundary
up = upward or upper boundary

B.8 REFERENCES

[1] H. Tuomisto and T.G. Theofanous, A consistent approach to severe accident management. Proc. Specialist Meeting on Severe Accident Management Programme Development. OECD/ CSNI/SESAM. Rome, Italy, September 23–25, 1991.

[2] U. Steinberner and H.-H. Reineke, Turbulent buoyancy convection heat tansfer with internal heat sources. Proc. Sixth International Heat Transfer Conf. Toronto, Canada. Aug 1978.

[3] T.G. Theofanous, Some considerations on severe accidents at Loviisa, TcI-891, Theofanous & Co., Inc., January 1989.

[4] O. Kymäläinen, H. Tuomisto and T.G. Theofanous, Critical heat flux on thick walls of large naturally convecting loops. ANS Proc. 1992 National Heat Transfer Conf. San Diego, CA, August 9–12, 1992. ANS HTC, Vol 6, pp 44–50.

[5] J.E. O'Brien and G.L. Hawkes, Thermal analysis of a reactor lower head with core relocation and external boiling heat transfer, AIChE Symposium Series, Heat Transfer-Minneapolis, MN, 1991, 159-168.

[6] B. Frantz and V.K. Dhir, Experimental investigation of natural convection in spherical segments of volumetrically heated pools. ASME Proc. 1992 National Heat Transfer Conference. San Diego, CA, August 9–12, 1992. HTD Vol 192, pp 69–76.

[7] F. Mayinger, M. Jahn, H.H. Reineke and U. Steinbrenner, Examination of thermalhydraulic processes and heat transfer in a core melt, BMFT R8 48/1, 1976. Institut für Verfahrenstechnik der T.U. Hannover.

[8] M. Jahn and H.H. Reineke, Free convection heat transfer with internal heat sources, calculations and measurements, Proc. Fifth In. Heat Trans. Conf., Tokyo, September 1974, Paper NC2.8.

APPENDIX C

THE UCLA EXPERIMENTS

An Experimental Study of Natural Convection in a Volumetrically Heated Spherical Pool Bounded on Top with a Rigid Wall

Proceedings of the Workshop on Large Molten Pool Heat Transfer
Grenoble, France, 9-11 March, 1994

APPENDIX C

AN EXPERIMENTAL STUDY OF NATURAL CONVECTION IN A VOLUMETRICALLY HEATED SPHERICAL POOL BOUNDED ON TOP WITH A RIGID WALL[a]

F.J. Asfia and V.K. Dhir

Mechanical, Aerospace and Nuclear Engineering Department
School of Engineering and Applied Science
University of California, Los Angeles
Los Angeles, CA 90024

ABSTRACT

Flooding of the reactor cavity is being considered as a cooling strategy to prevent vessel thermal failure in the case of severe core damage accidents in which relocation of core material into lower vessel head occurs. A recent study carried out at UCLA showed that the flooding of cavity could indeed be a viable option. However, one important factor contributing to uncertainty in that study was internal natural convection heat transfer coefficient. In the present work, experiments were conducted to examine natural convection heat transfer in internally heated hemispherical pools with external cooling. In the experiments, Freon-113 contained in a Pyrex bell jar, was used as a test liquid and the vessel was cooled from the outside with water. The pool was bounded with a rigid wall at the top, and was heated with a 750 Watt magnetron taken from a conventional microwave. A series of chromel alumel thermocouples was used to measure the pool and wall temperatures at different locations.

Experiments were performed for pools with both nearly insulated and cold rigid walls at the top. The depth of the pool was varied parametrically. Both local and average heat transfer coefficients based on maximum pool temperature were obtained. The results have been compared with the correlations obtained for pools with free surface.

C.1 INTRODUCTION

The study of natural convection in volumetrically heated pools is of interest in many engineering applications, especially in nuclear reactor safety analysis. In the case of a severe core damage accident, it is possible that molten fuel and structures relocate into the reactor vessel

[a] This work received support from EPRI and DOE.

lower head. After the core relocation in the vessel, a pool of molten core material which is internally heated by fission product decay heat is formed. If the pool is not successfully cooled, it could lead to reactor vessel failure. One strategy for preventing vessel wall from melting is to flood the cavity of a Pressurized Water Reactor (PWR) or drywell of a Boiling Water Reactor (BWR).

Since the temperature of vessel inner wall is below the freezing temperature of the relocated core material, a crust of core material forms on the inner wall of the vessel and possibly on the free surface of the pool. However, interior of the pool remains molten and decay heat induces natural convection in the pool. A recent study carried out by Park and Dhir (1991), showed that significant deviations in the predicted temperatures of the vessel head containing molten material can occur because of uncertainties in the reported natural convection correlations.

The earliest study on natural convection in volumetrically heated horizontal layers is that of Kulacki and Goldstein (1971). In their experiments, an interferometer was used to measure the temperature distribution within a layer of dilute aqueous silver nitrate solution which was bounded with two isothermal upper and lower plates. Rayleigh numbers covered a range of $200 \leq Ra \leq 1.27 \times 10^6$ which included laminar and turbulent regimes of natural convection. Upon examination of the temperature field data, they discovered the existence of cellular structures in the upper region of the laminar regime ($Ra \leq 10^4$). The area occupied by the cells decreased with increasing Rayleigh numbers until the cells were nonexistent in the turbulent regime. In this regime, the temperature field consisted of an isothermal central region bounded by a thin, unstable upper boundary layer and a wider, more stable lower boundary layer. The energy transport at the upper bounding surface was found to be much higher than that on the lower surface.

Later, Jahn and Reineke (1974) performed an experimental and numerical study of natural convection in internally heated pools contained in rectangular and semicircular cavities. In the experiments, holographic interferometry was used to measure the temperature field. The Rayleigh number range examined was $5 \times 10^5 \leq Ra \leq 5 \times 10^8$. Similar to Kulacki and Goldstein experiments, for rectangular cavity the fluid layer was bounded by two isothermal upper and lower flat plates. Jahn and Reineke found the existence of a series of non-uniform fluctuations in the temperature field in the upper region of the pool with a stable and calm liquid layer in the lower region. They concluded that for rectangular cavity, heat was transferred more effectively in the upper region as opposed to the bottom. For the semicircular cavity, the fluid layer was bounded by an isothermal spherical segment at the bottom and an isothermal flat plate at the top. The results were similar to those for the rectangular container in that the temperature field in the upper and lower regions exhibited the same type of behavior. The isotherm patterns

for this curved region resembled those characteristic of a cooled vertical wall. This pattern led to the conclusion that the Nusselt number varies greatly along the cooled surface. Nusselt number was highest at the equator and lowest at the bottom. Numerical results were found to be in a good agreement with the experimental data.

Subsequently, a series of natural convection experiments in a horizontal fluid layer bounded from above with a plate maintained at constant temperature and from below by an insulated plate was conducted by Kulacki and Emara (1975). For this set of boundary conditions, average heat transfer coefficient were obtained for Rayleigh numbers up to about 2.17×10^{12}. For Prandtl numbers varying from 2.75 to 6.85 a correlation for Nusselt number dependence on Rayleigh number for the upper surface was developed. This correlation was expressed as

$$Nu_{upper\,surface} = 0.403\ \mathrm{Ra}^{0.226} \qquad (C.1)$$

However, when explicit dependence of Nusselt number on Prandtl number was considered, the data were correlated as

$$Nu_{upper\,surface} = 0.233\ \mathrm{Ra}^{0.233}\ \mathrm{Pr}^{0.239} \qquad (C.2)$$

In these equations Nusselt and Rayleigh numbers were defined based on the thickness of the layer, H, as

$$Nu = \frac{h_{av}H}{k_p} \qquad (C.3)$$

$$\mathrm{Ra} = \frac{g\beta Q_v H^5}{2k_p\nu_p\alpha_p} \qquad (C.4)$$

Suo-Anttila and Catton (1976) conducted an experimental study of a horizontal fluid layer with volumetric heating. The layer was bounded by two flat plates maintained at different temperatures. Data were obtained for Rayleigh numbers up to 10^{12}. Similar to the previous studies, they showed that the flow was unstable and turbulent in the upper portions and stable and calm in the lower portions of the layer. They also concluded that the heat transfer would be affected by a stabilizing or destabilizing temperature gradient. By imposing a stabilizing temperature difference, downward heat transfer could be increased.

Later, Min and Kulacki (1978) performed the same type of experiment, with the exception that the fluid layer was bounded from below by a spherical segment with a polar angle of 60 degrees rather than by a horizontal plate. They showed that aspect ratio, defined as L/D, where L is the depth of the fluid layer and D is the sphere diameter, has an important role in determining the relationship between Nusselt number and Rayleigh numbers for the upper surface. At low

aspect ratios, the plot of Nusselt versus Rayleigh numbers is much flatter, which corresponds to the theory that conduction is the primary mode of heat transfer. However, when they increased the aspect ratio, the Nusselt versus Rayleigh number results approached those for a horizontal fluid layer. This is due to the fact that as the volume of fluid increases, the effects of the spherical boundary diminish.

Mayinger et al. (1976) numerically and experimentally obtained the average heat transfer coefficient on the wall of a rectangular and a semicircular cavity. They also used numerical analysis to determine the average heat transfer coefficient on the wall of a hemispherical and a vertical cylinder cavity. In their calculations, the wall temperatures were kept constant. According to their work, the average heat transfer coefficients on the upper surface and the lower curved surface for a filled hemisphere were found to be

$$Nu_{upper\,surface} = 0.4\ \mathrm{Ra}^{0.2} \qquad (C.5)$$

$$Nu_{lower\,surface} = 0.55\ \mathrm{Ra}^{0.2} \qquad (C.6)$$

Very recently, Sonnenkalb (1994) has presented a report on previous German research activities on natural convection in volumetrically heated fluids. According to this report, Reineke (1979) used numerical analysis to determine the average heat transfer coefficient on the wall of a partially filled hemispherical cavity with constant wall temperatures and he found the following correlations.

$$Nu_{lower\,surface} = 0.49\ \mathrm{Ra}^{0.18}(H/R)^{0.29} \qquad H/R > 0.2 \qquad (C.7)$$

$$Nu_{lower\,surface} = 0.64\ \mathrm{Ra}^{0.18}(H/R)^{0.29} \qquad H/R < 0.2 \qquad (C.8)$$

where $10^7 \leq \mathrm{Ra} \leq 10^{10}$. Both Nusselt and Rayleigh numbers were defined in terms of maximum fluid level. It should be noted that when for $H/R = 1.0$ Eq. (C.7) is extrapolated to $\mathrm{Ra} = 10^{17}$ (Rayleigh number of interest in nuclear reactor applications), Nusselt numbers calculated from Eq. (C.6) are about two times higher than those obtained from Eq, (C.7).

Gabor et al. (1980) experimentally studied natural convection in internally heated hemispherical pools with free surface. The surface of the hemispherical containers was cooled and the surface served both as a heat transfer surface and as one of the electrodes. A copper disc in the center, placed near the pool free surface, served as a second electrode. This arrangement of electrodes led to non-uniformity in the heating process. In the experiments, Z_nSO_4 - H_2O pools were formed in three sizes of hemispherical copper containers and pool depth was varied parametrically. No attempt was made in the experiments to calculate the variation of heat transfer

coefficient along the curved surface. The average heat transfer coefficient data for $2 \times 10^{10} \leq \text{Ra} \leq 2 \times 10^{11}$ and $0.5 \leq H/R \leq 1.0$ were correlated as

$$Nu = 0.55\ \text{Ra}^{0.15}(H/R)^{1.1} \qquad (C.9)$$

The Nusselt and Rayleigh numbers were defined based on the radius of the curvature. It was noted that the maximum temperature occurred in the middle of the upper pool surface, which was open to the atmosphere.

A comparison of Eq. (C.9) of Gabor et al. for $H/R = 1.0$ and Eq. (C.6) of Mayinger et al. shows that heat transfer coefficients predicted from the correlation of Mayinger et al. at high Rayleigh numbers are much higher. The difference between the two increases as the Rayleigh number becomes large. For nuclear reactor applications Rayleigh numbers of interest are on the order of 10^{17}. If the results of Mayinger et al. and Gabor et al. are extended for Rayleigh number of 10^{17}, the average heat transfer coefficient predicted from Mayinger is about ten times higher than that obtained from the correlation of Gabor .

Frantz and Dhir (1992) have reported results of natural convection heat transfer in volumetrically heated spherical cavities cooled from outside. Micro-wave heating was used in the experiments and it was concluded that a large variation in heat transfer coefficients existed along the vessel wall.

More recently Kymäläinen et al. (1993) have performed large scale natural convection experiments in a two dimensional slice of torospherical lower head of VVER 440 reactor. Joule heating was used to produce thermal energy in the liquid and Rayleigh numbers (based on the height of the curved portion of the pool) of the order of 1.8×10^{13} were obtained. It was concluded that the data compared well with the correlation of Mayinger et al. (1976) for circular segments. Local heat transfer coefficient data showed a linear dependence on angular position as opposed to a very rapid increase in heat transfer coefficient near the equator found in the experiments of Frantz and Dhir (1992).

As an extension of the work of Frantz and Dhir (1992), Asfia, Frantz and Dhir (1994) conducted natural convection experiments in volumetrically heated spherical pools with free surface. Similar to the Frantz and Dhir experiments, the pool was heated with Micro-wave and was cooled from the outside with water. The range of Rayleigh numbers for the data was $2 \times 10^{10} \leq \text{Ra} \leq 1.1 \times 10^{14}$. They also found the existence of a large variation in heat transfer coefficients along the vessel wall. The local heat transfer coefficients along the hemispherical wall were correlated as

$$\frac{\bar{h}(\theta)}{\bar{h}_{av}} = C_1 sin\Theta - C_2 cos\Theta \qquad (C.10)$$

$$C_1 = -1.25cos\phi + 2.6 \qquad \text{for} \qquad 0.75 < \frac{\theta}{\phi} \leq 1$$

$$C_2 = -2.65cos\phi + 3.6$$

and

$$\frac{\bar{h}(\theta)}{\bar{h}_{av}} = 1.17sin^4\Theta + 0.23 \qquad \text{for} \qquad 0 < \frac{\theta}{\phi} \leq 0.75$$

Nusselt number based on average heat transfer coefficient for $2 \times 10^{10} \leq \text{Ra} \leq 1.1 \times 10^{14}$ was obtained as

$$Nu = 0.54(Ra)^{0.2}(H/R_e)^{0.25} \qquad (C.11)$$

The Nusselt and Rayleigh numbers were defined as

$$\text{Nu} = \frac{\bar{h}_{av}H}{k_p} \qquad (C.12)$$

$$\text{Ra} = \frac{g\beta Q_v H^5}{k_p \nu_p \alpha_p} \qquad (C.13)$$

For $H/R_e = 1.0$ the average heat transfer coefficients predicted from Eq. (C.8) are comparable to those obtained from Eq. (C.6). The present work is a continuation of the work of Asfia, Frantz and Dhir and the objective the work is to experimentally study the role played by the following boundary conditions on local and average natural convection heat transfer coefficients in volumetrically heated pools:

(i) insulated rigid wall boundary condition on the pool surface

(ii) cooled rigid wall boundary condition on the pool surface.

C.2 EXPERIMENTS

The apparatus used in this work consists of a rigid box which serves as a tank for subcooled water as well as a support for a glass bell jar containing the test fluid. Figure C.1 shows the test setup. The box is a 3-layer water-tight container made of plywood and polyurethane foam. The outer and inner layers are made of 0.635 cm thick plywood. The middle is a 7.62 cm thick layer of Hathane 1680-11 (11 lb/ft^3 density) polyurethane foam. The outer and inner dimensions of the box are 0.927m×0.927m×0.762m and 0.762m×0.762m×0.686m, respectively. Two different sizes of Pyrex were used in the experiments. Bell jar 1 is 59.44 cm in length (from the top edge down to the center of the spherical bottom), 43.65 cm in diameter (inner) and has a thickness of 1.1 cm in the cylindrical portion. Bell jar 2 is 59.55 cm in length, 60.1 cm in diameter and has a

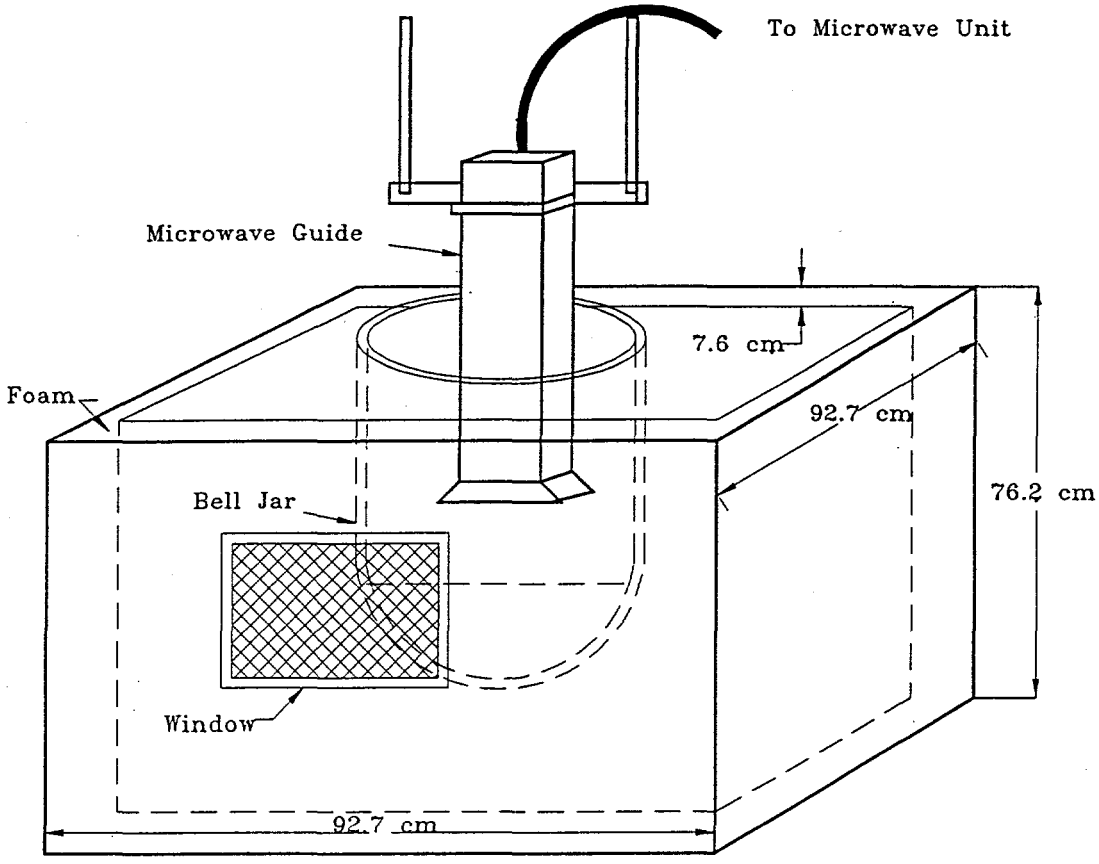

Figure C.1. Experimental apparatus.

wall thickness of 1.17 cm. Two double-paned 0.25m×0.18m wooden picture windows are built into the opposite sides of the box to allow viewing of the lower portion of the vessel. The fluid inside the vessel is heated uniformly with a 750 Watt magnetron, the power to which is controlled with a conventional microwave oven. The magnetron is attached to a 10.2 cm diameter copper tube serving as a waveguide for the microwaves. This device is suspended by steel rods and aluminum clamps above the vessel. To control radiation from the microwave, bronze screens are placed along each inner wall of the large plywood box prior to pouring of the polyurethane foam. The screen is connected to ground in order to short out the electromagnetic charge. A lucite lid was made to cover the opening of the vessel. A square opening with dimensions 11.4cm×11.4cm is cut in the center of the lid to allow the waveguide to be lowered into the bell jar. To impose rigid wall condition on the pool surface, a second lid was fabricated from plexiglass sheets. The lid is made of two 0.31 cm thick discs separated by 0.95 cm air gap. The diameter of these plates are 42.7 cm for bell jar 1 and 59.3 cm for bell jar 2. A rubber strip is used to hold these two plates. Thirty-four 4 mm diameter holes are drilled through the plates. Through these holes,

4 mm diameter Pyrex tubes each containing chromel-alumel thermocouple wires in the lid are inserted. Thermocouples are located in two perpendicular plates. The location of thermocouples in each plate (1/2 a plate) is shown in Figure C.2. Three more thermocouples are placed on the face of the lid touching the pool surface. The diameter of this lid is changed for smaller pool depths. To impose the cooled rigid wall condition on the pool surface, a third lid was made. Similar to the second lid, a rubber strip is used to hold the two discs 0.95 cm apart. The lid is cooled by passing cold air in the passage. The passage is divided in six sections so that air is distributed uniformly. Two 1.9 cm diameter holes are drilled into the upper plate and fitted with two 1.9 cm diameter (outer) and 58 cm length plexiglas tubes for inflow and outflow of cold air. Thirty-four chromel-alumel thermocouples each located in a 4 mm diameter Pyrex tube are used to measure the pool temperature at different locations. On the two sides of the lower plexiglass plate which touches the pool surface, three sets of thermocouples are attached. To cool the air, compressed air is allowed to pass through a copper coil placed in an ice bath. Air flowrate is measured with a float type flowmeter, and the inlet and outlet air temperatures are measured with two chromel alumel thermocouples. Figure C.3 shows the sketch of the lid used for imposing a cooled rigid wall boundary condition. Seven additional thermocouples are attached to the inner wall and seven more are added to the outer wall of the vessel using Omegabond 101 epoxy. Readings from the thermocouples are taken with an Acro 900 Data Acquisition System. The data are stored and later plotted using computer graphics.

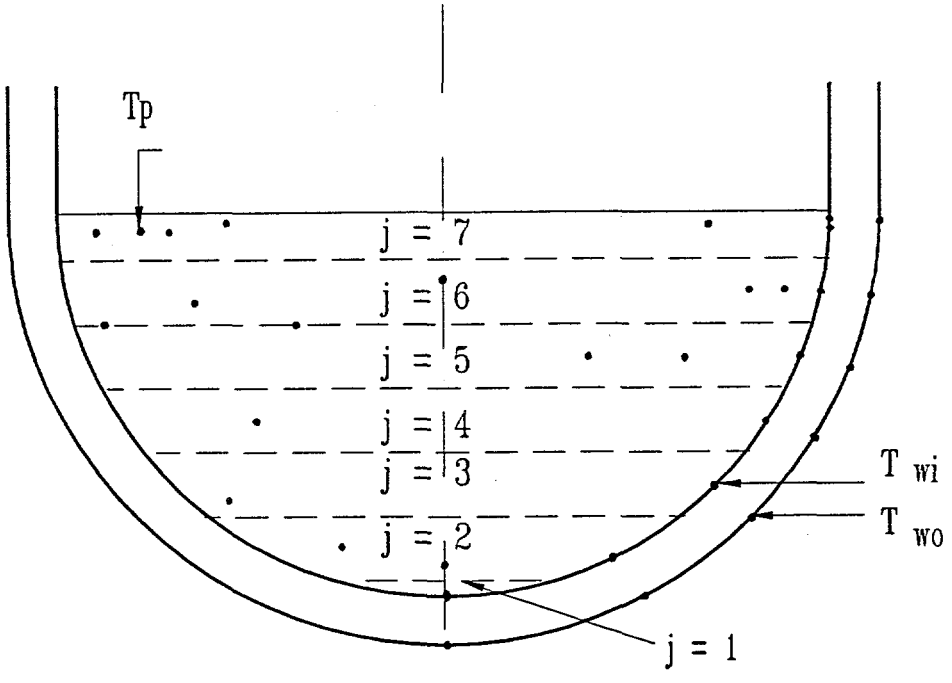

Figure C.2. Location of thermocouples in the pool and on the wall, $H/R_e = 1.0$.

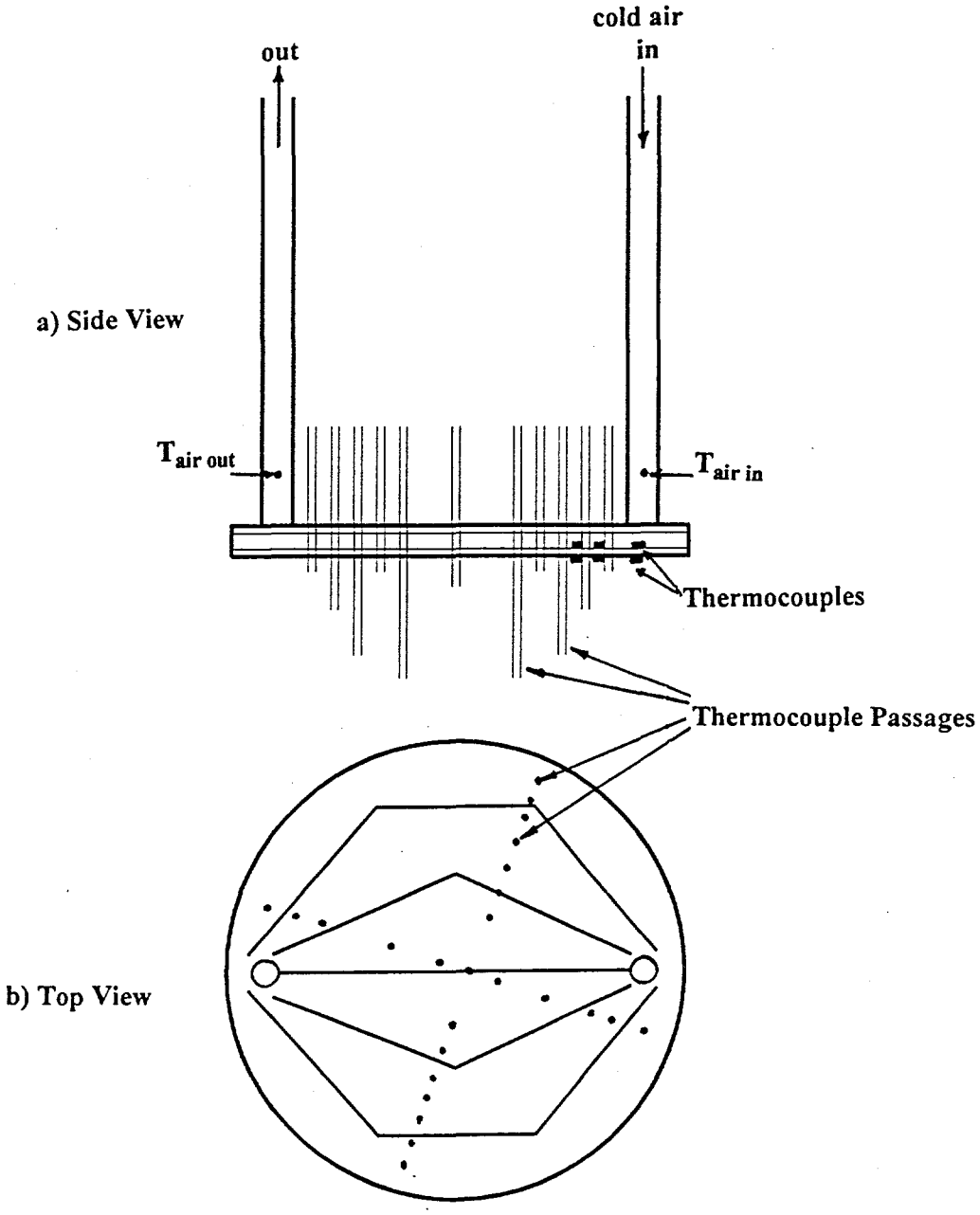

Figure C.3. Schematic diagram of the lid used to impose cold rigid wall boundary conditions.

A water cooling system is used to maintain the temperature of water surrounding the vessel nearly constant with time. A 2.5 cm hole is drilled into the bottom of the box and fitted with a copper pipe and flange to serve as both a water inlet and a drain when a particular experiment is completed. Water is removed from the upper surface of the pool. It is then passed through a copper coil, around which there is a continuous flow of cold water. Water exiting the heat exchanger is returned back to the bottom of the pool. In the experiments, the free surface of the water was generally kept 6-9 cm above the free surface of R-113 in the test vessel.

C.2.1 Procedure

Before the actual experiment was run, each thermocouple was calibrated. All thermocouples were individually submerged sequentially in an icebath, a pool of boiling Freon-113, and a pool of boiling water. The thermocouple outputs were compared with the temperature reading from a separate thermometer. Using these data, calibration curves were drawn for each thermocouple. From these curves, relative error in reading from a particular thermocouple could be determined. Once every thermocouple was properly calibrated, all of the thermocouples were placed in their designated spots.

Prior to every test run, the test liquid was pumped into the vessel to the desired pool volume. With lids in place and all of the thermocouples checked, the waveguide was lowered and fastened in place. Before adding water to the tank, a calibration run for heat generation rate in the fluid (lasting approx. 25-30 min.) was made. This was done in order to calculate the power output from the microwave and to determine the uniformity of heat generation rate in the test liquid. The data from these runs were plotted and the slopes of the temperature vs. time plots were used to calculate the heat input into the pool. Figure C.4 shows a typical rate of rise of fluid temperature at three locations in the pool when R-113 was used as the test liquid. The heat generation rate at different locations in the pool for all experiments was found to be within $\pm 7\%$.

After the calibration for heat input to the test liquid was performed, the tank was filled with water and the cooling system was activated. For cold rigid wall boundary condition experiments, the air cooling system was also started. After assuring that everything was properly running, the microwave was turned on again, and the pool was allowed to heat up. After approximately one hour, the pool acquired a nearly steady state temperature. The entire test run was carried out for about six hours. The Acro Data Acquisition System was adjusted to record the temperature every 15 seconds. It took almost 50 ms for the system to read the input of each thermocouple. Because of the inevitable interference from the microwave, proper thermocouple readings could not be obtained unless power was shut off. To avoid this problem, thermocouple readings were taken

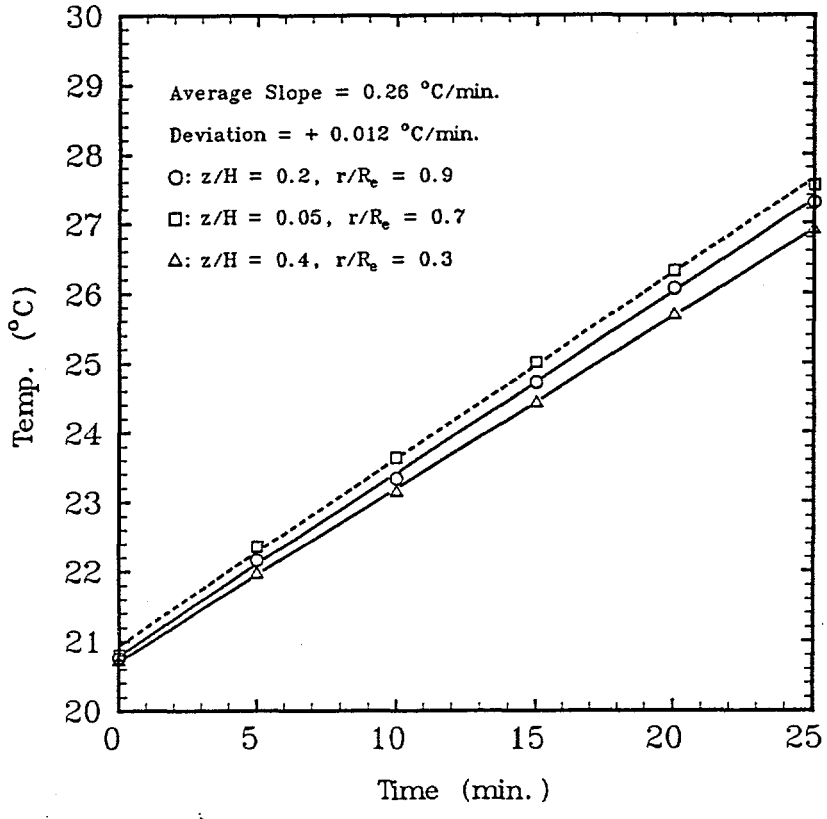

Figure C.4. Heat generation rate at different locations in the pool.

at 10 minute intervals. Thus, after every 575 seconds, power was cut off for twenty five seconds and two sets of thermocouple readings were taken (at 585 seconds and at 600 seconds) . After recording the second set, power was immediately restored. These short power interruptions appeared to have no effect on the temperature behavior of the pool over the duration of the experiment.

C.3 RESULTS AND DISCUSSION

One of the important considerations in the experiments conducted with internally heated pools is uniformity of the heat generation rate. Heating rates in various liquids, such as water, ethanol, olive oil, silicone oil, and R-113, using the microwave guide arrangement as shown in Figure C.1 were determined. A large difference in the heating rates near the pool free surface and at the bottom of the pool were found to exist in all liquids except R-113. As noted earlier with R-113, the rate of temperature rise at any location in the pool did not differ by more than $\pm 7\%$ from the mean value. Our lack of success in finding other liquids which could be heated uniformly with microwaves limited the number of data points that could be obtained.

Prior to conducting the experiments, the equivalent radii, R_e, of the vessel were obtained by noting the volume of liquid needed to fill the jar to a certain height. Table C.1 gives the equivalent radii along with other data.

Table C.1. Heat Transfer Rate for Each Experiment

Pool Surface Condition	R_e cm	H/R_e	Ra	dT/dt deg C/sec	Q_{in} W	Q_l W	Q_{out} W
Insulated	21.83	1.0	3.23×10^{13}	$4.31\times10^{-3}\pm4.5\%$	134.2	1.5	117.7
Rigid	23.5	0.57	2.9×10^{12}	$4.05\times10^{-3}\pm6\%$	66.7	1.2	65.2
Surface	22.7	0.43	4.7×10^{11}	$4\times10^{-3}\pm5.5\%$	36.6	0.8	36.1
	30.8	1.0	7.8×10^{13}	$2.03\times10^{-3}\pm7\%$	176.4	2.33	168.5
Cooled	21.83	1.0	3.03×10^{13}	$4.07\times10^{-3}\pm4\%$	134.3	21.2	103.6
Rigid Surface	22.7	0.43	5×10^{11}	$3.53\times10^{-3}\pm4.5\%$	32.3	7.3	25.8
	30.8	1.0	8×10^{13}	$2.06\times10^{-3}\pm3\%$	177.4	30.7	126.8

Because of the spherical geometry of the pool, the heat transfer area changes significantly with the angular position measured from the lower stagnation point. To determine the area supported by each of the thermocouples located discretely on the bell jar surface, the angle between any two neighboring thermocouples was determined. Half of this angle on either side of a given thermocouple was assigned to that thermocouple. By knowing the total subtended angle and the equivalent radius, the surface area and pool volume assigned to a given surface thermocouple could be determined.

Figure C.2 shows how the strips are defined in the pool. From the thickness, δ, and thermal conductivity, k, of the bell jar, measured time averaged maximum temperature, T_{pmax}, in the pool and the time averaged inside, T_{wi}, and outside, T_{wo}, wall temperatures, local time averaged heat transfer coefficient could be determined as

$$\bar{h}_j = \frac{k(\bar{T}_{wi} - \bar{T}_{wo})}{\delta(\bar{T}_{pmax} - \bar{T}_{wi})} \qquad (C.14)$$

Average heat transfer coefficient for the spherical segment is obtained as

$$\bar{h}_{av} = \frac{\sum_{j=1}^{j=N} \bar{h}_j \Delta A_j}{\sum_{j=1}^{j=N} \Delta A_j} \qquad (C.15)$$

The uncertainty in local heat transfer coefficient is found to range from $\pm 9\%$ to $\pm 25\%$. The highest uncertainty in the heat transfer coefficient occurred at the lower portions of the bell jar where the difference between the inside and outside wall temperatures was found to have the smallest value.

Heat transfer rate for each section was determined by knowing the surface area for each strip as:

$$\Delta Q_j = (\Delta A_j) k/\delta (T_{wi} - T_{wo}). \qquad (C.16)$$

The above equation is written under the assumption that heat transfer across the vessel wall is one dimensional. The assumption is realistic everywhere except for two locations, near the pool surface and the lower stagnation point. Two dimensional conduction analysis were performed to calculate the heat losses through the vessel wall at the top and bottom strips. The total heat transfer rate to the water is the sum of heat transfer rate for each section, $\sum \Delta Q_j$. Aside from the heat transfer across the vessel wall, the other contributor to the heat loss is conductive heat transfer through the rigid wall bounding the pool surface. Due to the air gap, the heat conducted through rigid walls in the absence of air flow is relatively small. By knowing the inner surface and ambient temperatures, this heat loss can be determined from

$$Q_l = \frac{A_{r.w.}(T_{r.w.} - T_{amb.})}{2\delta_1/k_1 + \delta_2/k_2 + 1/h_c} \qquad (C.17)$$

Where k_1 and δ_1 are the thermal conductivity and thickness of the two plexiglass plates ,k_2 and δ_2 are the thermal conductivity and thickness of the air gap, and h_c is the natural convection heat transfer coefficient for air. The heat loss for the cold rigid surface was determined by knowing the air flowrate,m_a and inlet and outlet temperatures of air passing through the air passage as

$$Q_l = m_a C_{pa}(T_{oa} - T_{ia}) \qquad (C.18)$$

Table C.1 gives the heat generation rate, Q_{in}, heat loss through the rigid wall on the pool surface, and heat transferred, Q_{out}, across the curved surface.

C.3.1 Rigid Nearly Insulated Pool Surface

Figure C.5 shows the ratio of the local to average heat transfer coefficient as a function of angular position measured from the lower stagnation point. The plotted data are for $H/R_e = 1.0$ and 0.43 for bell jar 1. Heat transfer coefficient is lowest at the stagnation point and increases along the periphery of the spherical segment except at the location very close to the rigid surface. At the location near the rigid surface the ratio decreases rapidly. Similar behavior in the ratio

of local to average heat transfer coefficient has been observed for other pool heights. Except at the location near the pool surface, the obtained data for local heat transfer coefficient could be correlated within ±20% with the correlation developed for free surface pools, Eq. (C.10). Figure C.6 shows the isotherms obtained by linear interpolation of temperatures obtained from thermocouples placed at different locations in the pool. Isotherms are not exactly symmetrical in the azimuthal direction. Stratification in the lower part of the middle section of the pool is much stronger than in the upper part. A comparison of these isotherms with the free pool surface case reported by Asfia, Frantz and Dhir reveals that presence of a rigid wall tends to limit the circulatory motion in the upper region leading to a relatively larger stratification in the upper region.

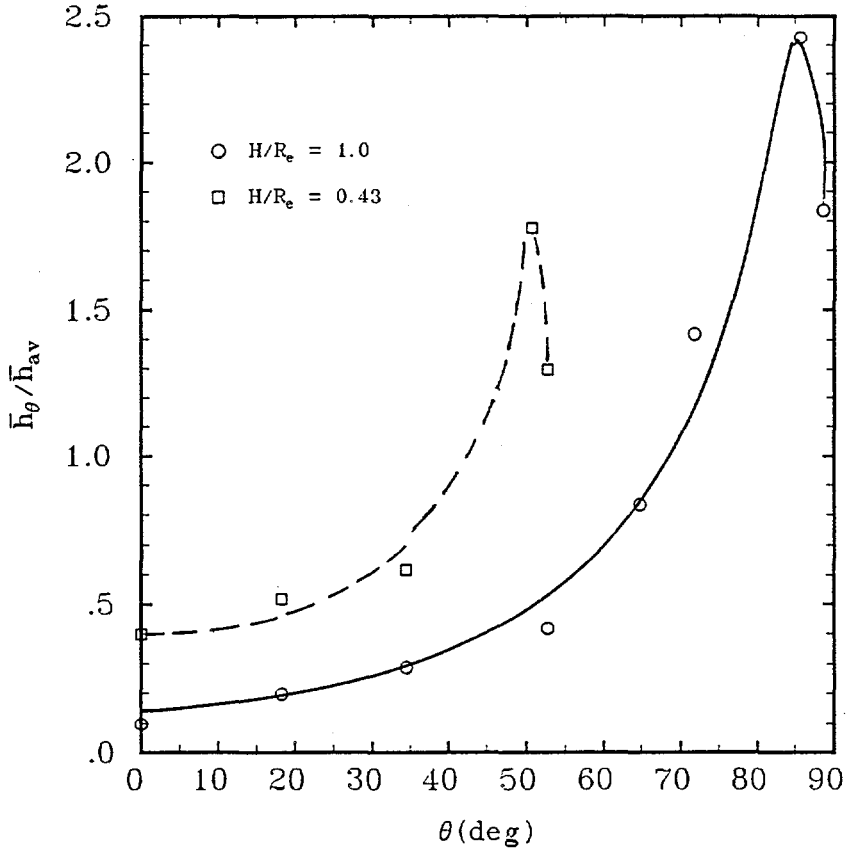

Figure C.5. Ratio of local to average heat transfer coefficient with respect to angle for insulated rigid wall for bell jar 1.

After initial heating of the pool, liquid and wall temperatures were observed to oscillate with time. For $H/R_e = 1.0$, Figure C.7 shows as a function of time the temperature output of one of the thermocouples located near the surface of the pool but closer to the cooled curved surface of the bell jar. The period, amplitude and time for onset of oscillations are given in Table C.2. It

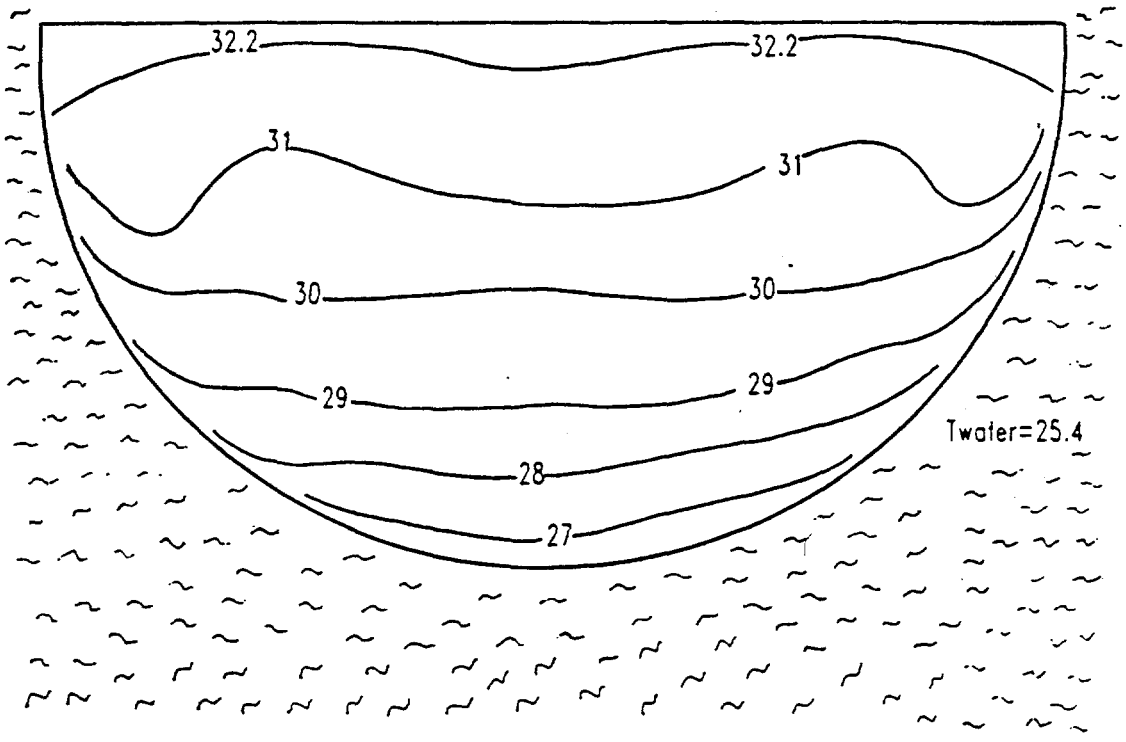

Figure C.6. Isotherm patterns for bell jar 1 for insulated rigid surface, $H/R_e = 1.0$. (All temperatures are in Celsius.)

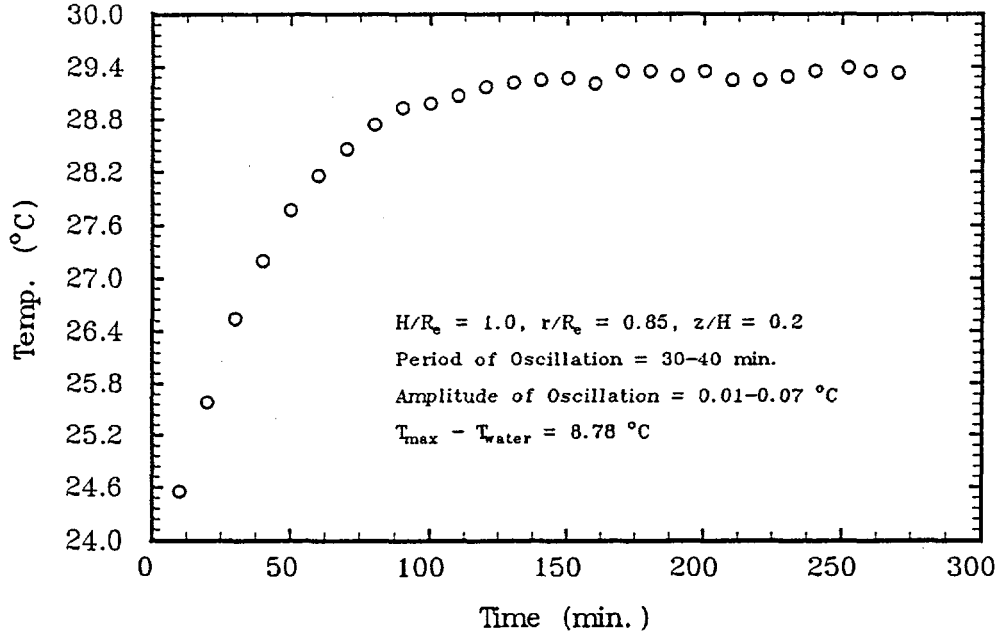

Figure C.7. Variation of temperature respect to time for one of the thermocouples located in the pool with insulated rigid wall.

Table C.2. Temperature Oscillations for Insulated Rigid Surface

	H/R_e	Position	$q_v(W/m^3)$, T_{pmax} $T_W(°C)$	Start min	Period min	Amplitude °C
	1.0	r/R_e=0.85, z/H=0.20	6443,	150	30-40	0.01-0.07
	1.0	r/R_e=0.75,z/H=0.05	8.78	170	30-40	0.04-0.1
	1.0	r/R_e=0.95,z/H=0.2		130	20-50	0.01-0.07
	1.0	T_{wi},z/H=0.07		180	20-40	0.05-0.11
	1.0	T_{wi},z/H=0.2		180	30-50	0.025-0.045
Bell jar	0.57	r/R_e=0.85,z/H=0.32	6100,	160	20-40	0.05-0.14
1	0.57	r/R_e=0.67,z/H=0.08	8.51	160	20-40	0.1-0.18
	0.57	r/R_e=0.75,z/H=0.32		160	30-50	0.025-0.14
	0.57	T_{wi},z/H=0.1		190	50	0.2
	0.57	T_{wi},z/H=0.32		190	40	0.1-0.13
	0.43	r/R_e=0.0,z/H=0.1	6000,	120	30-60	0.02-0.15
	0.43	r/R_e=0.2,z/H=0.68	7.9	120	20-60	0.06-0.1
	0.43	r/R_e=0.7,z/H=0.1		140	30-50	0.035-0.17
	0.43	T_{wi},z/H=0.1		120	30-50	0.02-0.2
	0.43	T_{wi},z/H=0.8		120	50	0.02-0.2
	1.0	r/R_e=0.9, z/H=0.03	3031.2,	230	20-40	0.1
Bell jar	1.0	r/R_e=0.65,z/H=0.55	7.65	210	20-40	0.05-0.1
2	1.0	r/R_e=0.5,z/H=0.80		150	20-40	0.05-0.1
	1.0	T_{wi},z/H=0.03		230	20-30	0.04-0.15
	1.0	T_{wi},z/H=0.48		210	20-40	0.08-0.12

generally took longer for pool temperature oscillations to develop near the cooled bell jar wall. In the lower portion, the temperature began to oscillate somewhat earlier. The largest values for the frequency and amplitude of oscillations also occur near the cooled walls. In comparison with the free surface pool case (Asfia, Frantz and Dhir (1994)), it took longer for the temperature oscillations to develop for pools with a rigid top surface. It was observed that the temperature oscillations for symmetrical locations across the pool are not symmetrical, even though the values for their time period and their amplitude are almost similar. The difference between the

maximum pool temperature and the water temperature is also given in Table C.2.The amplitude of oscillations is generally about 1% of the temperature difference. Generally, oscillation time periods varying from 20–60 minutes were found. No clear effect of change in pool height on the above observations was noted.

C.3.2 Rigid Cooled Pool Surface

Figure C.8 shows the variation of local heat transfer coefficient along the curved and flat walls bounding the pool for $H/R_e = 1.0$. The heat transfer coefficient has been normalized with the average heat transfer coefficients on the curved surface. The data beyond the angle of 90° are for the locations on the rigid wall. In plotting the rigid wall data, X is defined as the distance of each thermocouple from the bell jar wall. Except for the location near the pool surface, the obtained data for local heat transfer coefficients for the curved wall are again correlated within $\pm 20\%$ with correlation developed for free surface pools, Eq. (C.10). The maximum heat transfer coefficient occurs below the pool upper surface. From this location the heat transfer coefficient decreases both on the curved wall as well as on the rigid wall. Isotherms in the pool with cold rigid wall on the top are shown in Figure C.9. A layer of fluid adjacent to the rigid wall has a temperature slightly less than the maximum temperature. Some circulatory motion in the upper region appears to have re-emerged and the propensity of stratification is weakened in comparison to a pool with the rigid insulated wall. Again, stratification in the lower part of the middle section of the pool is much stronger than in the upper part.

Similar to the insulated rigid wall case, after the initial heating of the pool, temperatures oscillated with time for the cold rigid wall. For $H/R_e = 1.0$, Figure C.10 shows as a function of time the temperature output of one of the thermocouples located near the surface of the pool but closer to the cooled surface of the bell jar. The period, amplitude and time for onset of oscillation are given in Table C.3. The behavior of the temperature oscillations for cold rigid wall pools is similar to that for the insulated rigid wall.

The data for the Nusselt number based on heat transfer coefficient averaged over the curved surface of the pool are plotted in Figure C.11 as a function of Rayleigh number. The plotted data are for $H/R_e = 0.43$, 0.57, and 1.0 for the insulated rigid wall and 0.43, and 1.0 for the cooled rigid wall when bell jar 1 was used. In this figure, $H/R_e = 1.0$ for both cases insulated rigid wall and cooled rigid wall for bell jar 2 are also plotted, Nusselt and Rayleigh number are defined by Eqs. (C.12) and (C.13). The heat transfer data have been correlated within $\pm 15\%$ with the correlation developed by Asfia, Frantz and Dhir (1994) for free surface pools, Eq. (C.11). This correlation, Eq. (C.11), for two different pool heights, $H/R_e = 1.0$ and 0.2, has also been shown in Figure C.11.

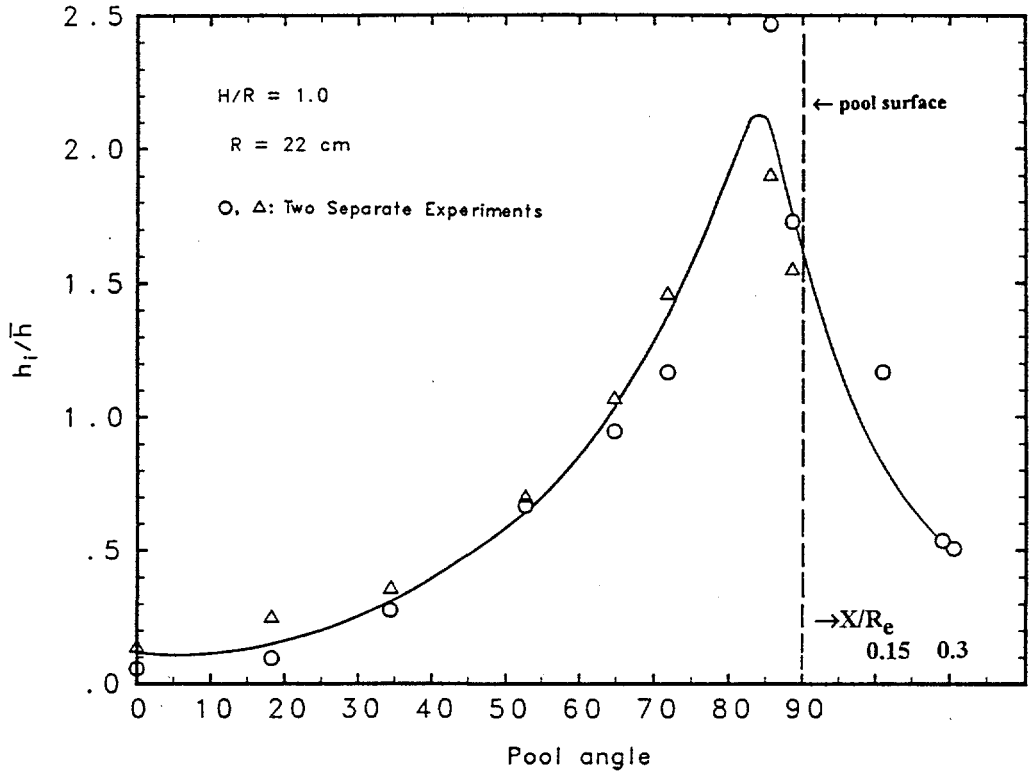

Figure C.8. Ratio of local to average heat transfer coefficient with respect to angle for cooled rigid wall for bell jar 1.

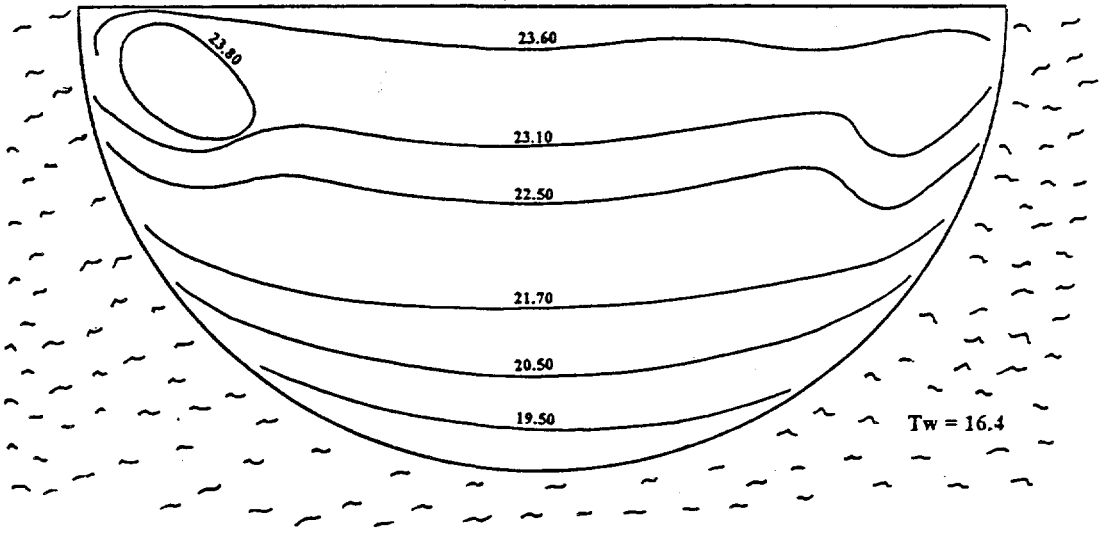

Figure C.9. Isotherm patterns for bell jar 1 for cold rigid surface, $H/R_e = 1.0$. (All temperatures are in Celsius.)

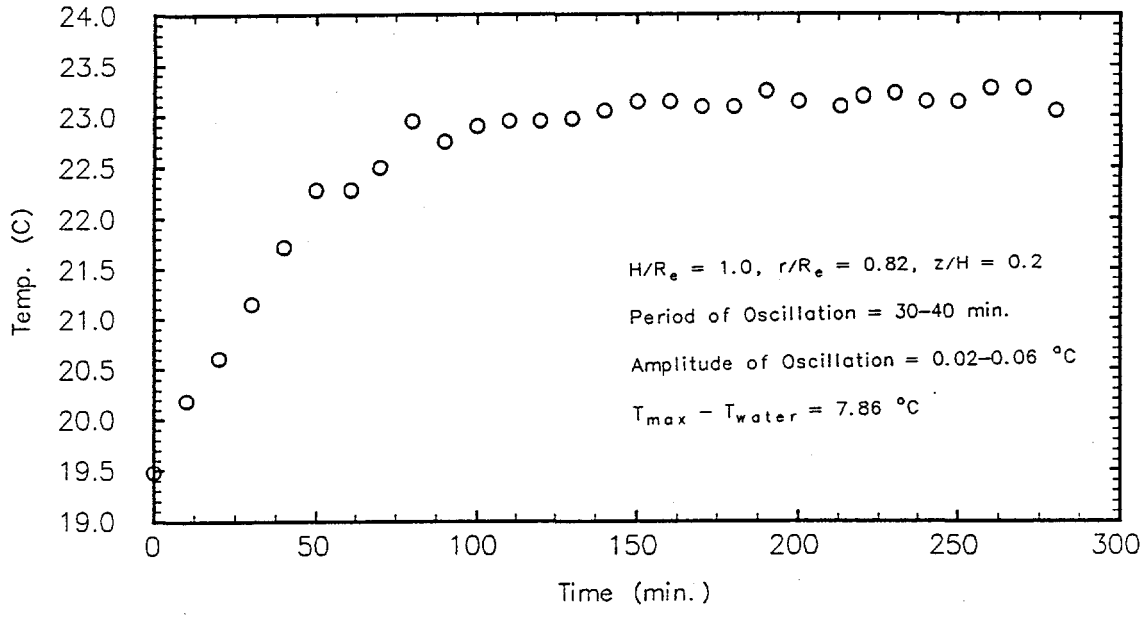

Figure C.10. Variation of temperature respect to time for one of the thermocouples located in the pool with cooled rigid wall.

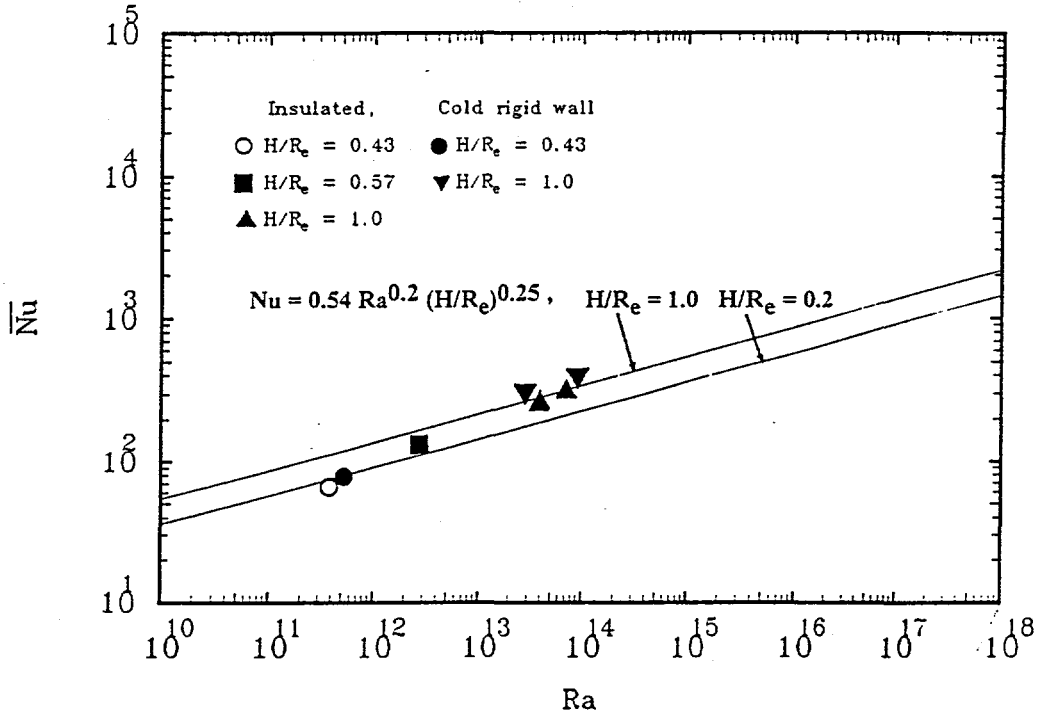

Figure 11. Comparison of the present data with the correlation developed for the pool with free surface.

Table C.3. Temperature Oscillations for Cold Rigid Surface

	H/R_e	Position	$q_v(W/m^3)$, T_{pmax} $T_W(°C)$	Start min	Period min	Amplitude °C
	1.0	r/R_e=0.82, z/H=0.20	6103,	140	30-40	0.02-0.06
	1.0	r/R_e=0.75,z/H=0.05	7.86	140	40-50	0.06-0.12
	1.0	r/R_e=0.9,z/H=0.20		120	20-40	0.025-0.06
	1.0	r/R_e=0.65,z/H=0.4		120	40-50	0.06
Bell jar	1.0	T_{wi},z/H=0.07		120	20-30	0.05-0.11
1	1.0	T_{wi},z/H=0.2		140	50	0.025-0.045
	0.43	r/R_e=0.25,z/H=0.78	5293.2,	70	50	0.02-0.15
	0.43	r/R_e=0.9,z/H=0.1	6.16	90	30-60	0.05-0.09
	0.43	r/R_e=0.7,z/H=0.1		90	30-60	0.05-0.06
	0.43	T_{wi},z/H=0.1		110	20-50	0.06-0.12
	0.43	T_{wi},z/H=0.8		110	20-30	0.04-0.1
	1.0	r/R_e=0.8, z/H=0.07	3070,	160	20-40	0.02-0.08
Bell jar	1.0	r/R_e=0.65,z/Z=0.58	5.27	140	20-50	0.01-0.06
2	1.0	r/R_e=0.5,z/H=0.78		130	20-50	0.01-0.06
	1.0	T_{wi},z/H=0.06		150	30-40	0.06
	1.0	T_{wi},z/H=0.48		150	30-40	0.06-0.08

By knowing the inside and outside temperatures for the lower plexiglas plate which touches the pool surface, local heat transfer coefficient on the cooled rigid wall could be determined. The measured heat transfer coefficients were averaged over the area where thermocouples were attached to the plexiglas plate. This area was about 50% of the total surface area for $H/R_e = 1.0$ and 33% for $H/R_e = 0.43$. The data for Nusselt number based on average heat transfer coefficient for the upper cooled rigid wall are plotted in Figure C.12 as a function of Rayleigh number. The Nusselt number and Rayleigh numbers for the cooled rigid wall are defined based on the depth of the pool, H. The prediction from the correlation developed by Kulacki and Emara for the upper surface is also shown in Figure C.12. It is seen that the present data compare favorably with predictions from the correlation of Kulacki and Emara (Eq. C.2).

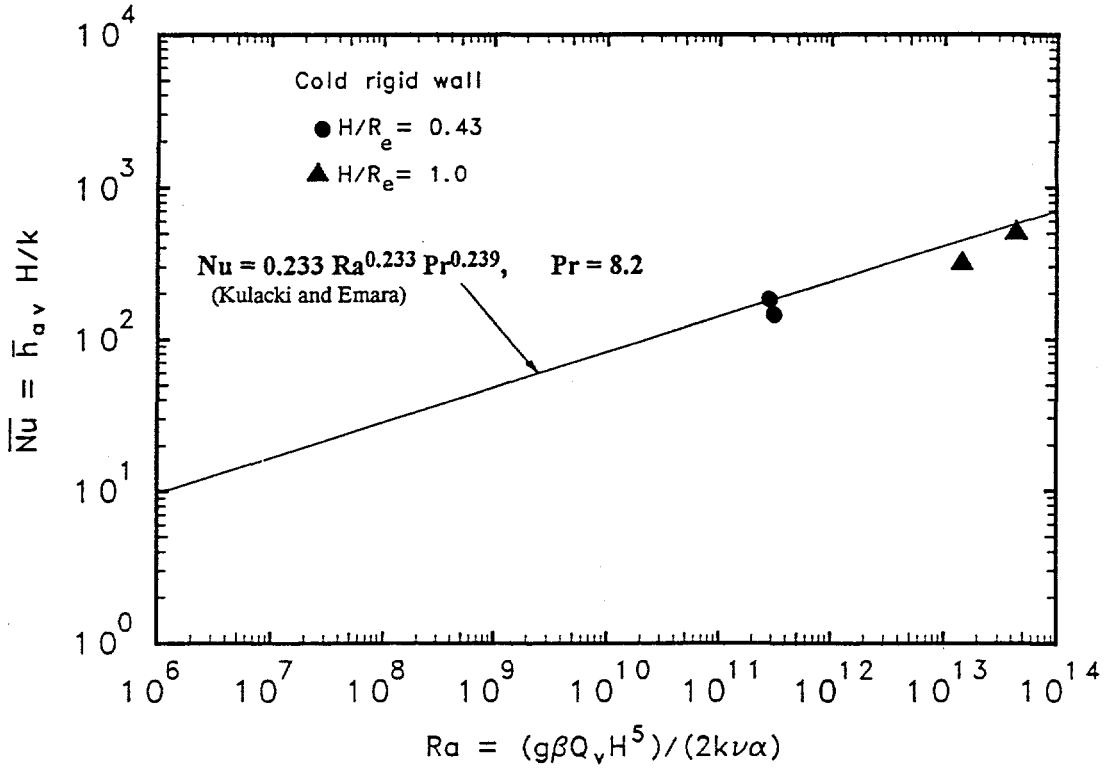

Figure C.12. Comparison of the present data for cooled rigid wall bounding the pool surface with the correlation developed by Kulacki and Emara (1975).

C.4 CONCLUSIONS

1. Using R-113 as the test liquid, natural convection heat transfer in internally heated pools contained in spherical segments cooled from outside have been obtained. Both insulated rigid wall and cooled rigid wall at the pool surface have been studied.

2. Nusselt numbers data obtained in this work compare favorably with the prediction from the correlation of Asfia, Frantz and Dhir (1994).

3. Heat transfer coefficient is lowest at the stagnation point and increases along the spherical segment except at the location near the pool surface. Maximum heat transfer coefficient occurs slightly below the pool surface.

4. Different boundary conditions in the pool surface (free surface, insulated rigid surface or cooled rigid surface) make only a slight difference in the average heat transfer coefficients.

5. Average heat transfer coefficients on the cold rigid wall bounding the pool surface appears to compare favorably with the correlation of Kulacki and Emara (1975).

C.5 NOMENCLATURE

A = wetted surface area (m^2)

c_p = specific heat (kJ/kgK)

g = gravitational acceleration (m/s^2)

H = dool depth (m)

$h(\theta)$ = local heat transfer coefficient (W/m^2 K)

$\bar{h}$ = time averaged heat transfer coefficient(W/m^2K)

$\bar{h}_{av}$ = time and area averaged heat coefficient (W/m^2K)

k = thermal conductivity (W/mK)

Nu = Nusselt number ($Q_{gen}R$)/ ($Ak\Delta T$)

Pr = Prandtl Number

Q = rate of heat transfer (W)

Q_{gen} = heat generation rate (W)

$\dot{Q}_v$ = volumetric heat generation (W/m^3)

Q_{in} = input heat (W)

Q_{out} = heat transfer rate across the curved surface (W)

Q_l = heat transfer rate across the rigid surface(W)

q = heat flux (W/m^2)

Ra = Rayleigh number ($Ra = g\beta Q_v R^5/k\nu\alpha$)

R = inner radius of vessel lower head (m)

R_e = equivalent radius corresponding to pool volume (m)

r = radial distance (m)

T = temperature (K)

t = time (sec)

V = volume

z = axial distance from the surface

X = radial distance from the edge on the surface

m = flowrate

Greek Letters

ϕ = pool angle (deg)

θ = angle along the vessel wall (deg)

Θ = $(\theta/\phi)(\pi/2)$

ρ = density

α = thermal diffusivity

β = coefficient of thermal expansion (1/K)

ν = kinematic viscosity

δ = thickness

Superscripts

- = time average

Subscripts

av = average

j = indices

max = maximum

p = pool

wi = inside wall

wo = outside wall

W = water

a = air

$r.w.$ = Rigid wall

$amb.$ = ambient

C.6 REFERENCES

1. Asfia, F.J., B. Frantz, and V.K. Dhir, 1994, "Experimental Investigation of Natural Convection in Volumetrically Heated Spherical Segments," Submitted to *Journal of Heat Transfer.*

2. Frantz, B., and V.K. Dhir, 1992, "Experimental Investigation of Natural Convection in Spherical Segments of Volumetrically Heated Pools," Proc. 1992 National Heat Transfer Conference, San Diego HTD Vol. 192, pp. 69-76.

3. Gabor, J.D., P.G. Ellison, and J.C. Cassulo, 1980, "Heat Transfer from Internally Heated Hemispherical Pools," Presented at the 19th National Heat Transfer Conference, Orlando, FL.

4. Jahn, M. and H.H. Reineke, 1974, "Free Convection Heat Transfer with Internal Heat Sources," Proceedings of the Fifth International Heat Transfer Conference, Vol. 3, p.74.

5. Kulacki, F.A., and A.A. Emara, 1975, "High Rayleigh Number Convection in Enclosed Fluid Layers with Internal Heat Sources," U.S. Nuclear Regulatory Commission Report NUREG-75/065.

6. Kulacki, F.A., and R.J. Goldstein, 1972, "Thermal Convection in a Horizontal Fluid Layer with Uniform Volumetric Energy Sources," Journal of Fluid Mechanics, Vol. 55, Part 2, pp. 271-287.

7. Kymäläinen, O., H. Tuomisto, O. Hongisto, and T.G. Theofanous, 1993, "Heat Flux Distribution From a Volumetrically Heated Pool With High Rayleigh Number," Proceedings of Sixth International Topical Meeting on Nuclear Reactor Thermal Hydraulic Grenoble 1993 Vol. 1, pp. 47-53.

8. Mayinger, F., M. Jahn, H. Reineke, and V. Steinbrenner, 1976, "Examination of Thermohydraulic Processes and Heat Transfer in a Core Melt," BMFT RS 48/1. Institute fur Verfanhrenstechnic der T.U., Hanover, Germany.

9. Min, J.H., and F.A. Kulacki, 1978, "An Experimental Study of Thermal Convection with Volumetric Energy Sources in a Fluid Layer Bounded from Below by a Segment of a Sphere," Presented at the 6th International Heat Transfer Conference, Toronto, Canada.

10. Park, H., and V.K. Dhir, 1991, "Steady State Analysis of External Cooling of a PWR Vessel Lower Head," AIChE Symposium Series, No. 283, Vol. 87, pp. 1-12.

11. Reineke, H. H., 1979, "Numerische Untersuchung der thermohydraulischen Vorgange und des Warmeuberganges in einer Kernschmeize bei kugelsegmentförmiger Geometrie und bei zuflie βendem Material von oben," BMFT RS 166-79-05, Band II A1.

12. Sonnenkalb, M, 1994, "Summary of Previous German Research Activities and Status of GRS Program on In-Vessel Molten Pool Behaviour and Ex-Vessel Coolability," Presented at the OECD Conference on Large Molten Pool Heat Transfer, Grenoble, France.

13. Suo-Antilla, F.A. and I. Catton, 1976, "An Experimental Study of a Horizontal Layer of Fluid with Volumetric Heating and Unequal Surface Temperatures," 10th National Heat Transfer Conference, St. Louis.

APPENDIX D

THE MINI-ACOPO EXPERIMENTS

Natural Convection in Hemispherical Enclosures at Internal Rayleigh Numbers up to 7×10^{14}

APPENDIX D

NATURAL CONVECTION IN HEMISPHERICAL ENCLOSURES AT INTERNAL RAYLEIGH NUMBERS UP TO 7×10^{14}

T.G. Theofanous, C. Liu, J. Scott, D. Williams, and T. Salmassi

Center for Risk Studies and Safety
University of California, Santa Barbara, CA 93106

D.1. INTRODUCTION

This appendix has been prepared under the assumption that it will be read in conjunction with Chapter 5. [Figure 5.1 containing the basic nomenclature is reproduced here as Figure D.1 for convenience.] Therein one can find the background on this subject, and the specific motivation for this experimental work. The experiment is called ACOPO (for Axisymmetric COPO), and mini-ACOPO is a small version of it, built to demonstrate the concept while at the same time allowing to fill in most of the data needs in a time frame consistent with the overall schedule for completing this report. The ACOPO is a 1/2-scale model of the AP600 lower head, it is presently under construction, and the data generated from it are expected to be confirmatory of the conclusions reached here (see Appendix V-2). The mini-ACOPO is an 1/8-scale model, and it constitutes the subject of this appendix. Although construction details are different between the two experiments, the design, operation, and instrumentation are precisely parallel, so the large experiment needs no further discussion here. The capabilities of these two experiments in relation to other existing experiments can be found in Table 5.1 (Chapter 5).

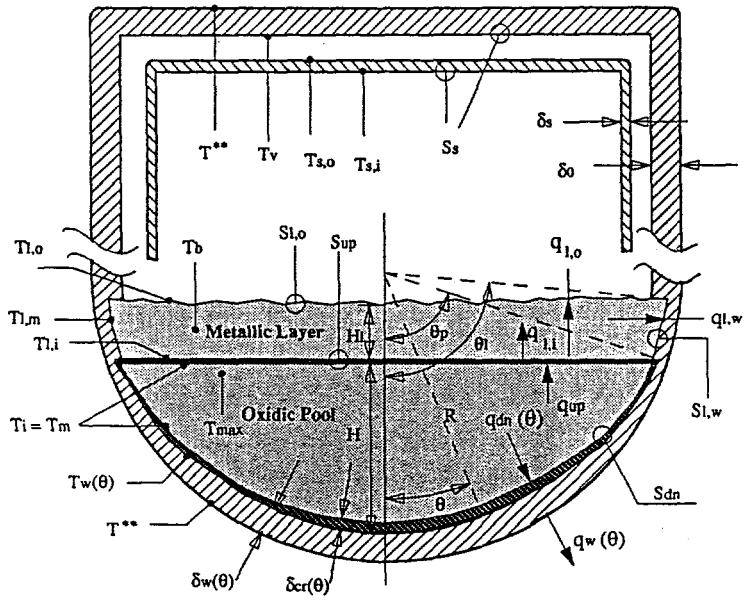

Figure D.1. Schematic of the in-vessel retention phenomenology and basic nomenclature used to describe it.

The basic concept is to sidestep the heating "problem" (discussed in Chapter 5) by not insisting in a true steady-state operation. Rather, the idea is to use detailed data from a transient cooldown, which for a large enough volume should be slow enough to allow the process to pass through a sequence of quasi-steady states that approximate corresponding steady-states with heating rates equal to the instantaneous cooling rates in the experiment. In other words, we use the heat capacity of the fluid as the "source" of heat that is being extracted at the boundaries.

Some additional background on the genesis of the ACOPO concept, and the description of the mini-ACOPO experiment are given in section D.2. The measurements, related instrumentation and experimental error are discussed in Section D.3. An overview of the experimental program is provided in Section D.4. The results are presented and discussed in Section D.5, and the appendix concludes with a summary of the findings in Section D.6.

D.2 THE ACOPO CONCEPT AND THE MINI-ACOPO EXPERIMENT

As clearly illustrated by the interferograms of Jahn (Mayinger, et al., 1975) the key aspects of the natural convection process include:

1. Inverted plumes (thermals) descending from the upper boundary, creating a relatively uniform and turbulent upper pool region,
2. A thin/steep boundary layer descending down, and all around, along the curved walls, and
3. A stratified lower pool portion, the size and structure of which would seem to be affected by the magnitude of the Ra' number.

For the very high Ra' numbers and isothermal pool boundaries of interest here, we expect that the uniform upper region will occupy a significant fraction of the pool volume and that the remaining stratified portion will reach a largely self-similar behavior as found, for example, in enclosures with buoyant plumes. In the present case the wall-plume will decelerate as it enters the stratified region not only because of a continuously diminishing body force, but also because of the increasingly more inclined (to the vertical) boundary, and the cylindrical convergence (creating a buildup). The self-similarity is created by the entrainment processes in these wall-plumes, which, therefore, also dominate the global circulation patterns (the turnover)–see Figure D.2. Our conjecture then is that instantaneous heat transfer rates at any of the quasi-steady states traversed during a cooldown transient are adequately close to the steady state, obtainable (in principle) from it if the cooldown was to be interrupted and volumetric heat was supplied to exactly balance these instantaneous losses. The mini-ACOPO has demonstrated that this is the case, and for the ACOPO with its much larger time constant, this will be even more so. Moreover, as we will see below, the ACOPO concept provides the experimental flexibility to

address transient effects, especially effects due to adjustment of the internal stratification patterns, as well as other complicating aspects (i.e., non-uniform wall temperatures) that add important depth in understanding the behavior in the reactor.

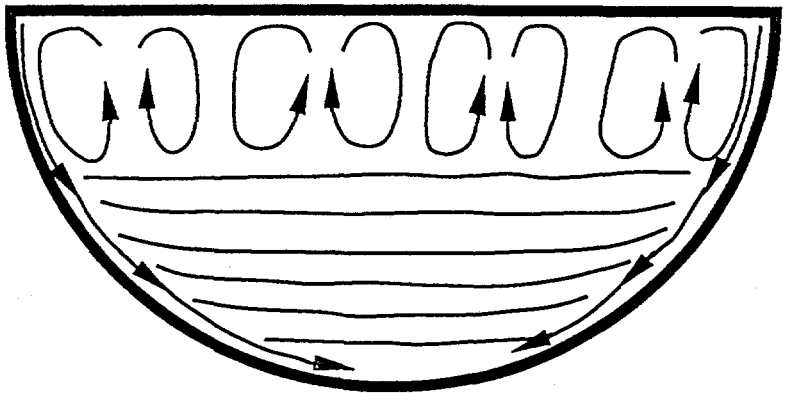

Figure D.2. Conceptual model of natural convection processes in a hemispherical enclosure at high Rayleigh numbers.

A schematic of the mini-ACOPO test apparatus is shown in Figure D.3. It has been constructed from 1/4-inch copper tubing coiled, brazed into shape, and filled in on the inside crevices with low-melting solder to create smooth internal boundaries of a complete hemisphere (0.44 m in diameter). The tubing was separated into nine separate circuits, each having its own inlet and outlet. As shown in the detail, the circuits were insulated from each other along all their interfacing areas. Each wall region corresponding to each circuit can be heated or cooled to any desired temperature by simply connecting the circuit to an appropriate coolant bath (water is used as the heating/cooling medium). In this way, either isothermal conditions or any desired degree of initial stratification can be created prior to starting a cooldown transient. The enclosure is filled/drained from the bottom, and the expansion volume is provided to accommodate specific volume changes of the fluid in the enclosure during operation.

The expansion volume provides the means also for ensuring removal of all gas/vapor bubbles after filling the enclosure and prior to commencing an experiment. After filling the enclosure, hot water is circulated in all the coils until the fluid in the hemisphere is brought slowly to within a few degrees of the boiling point, and this is continued for a sufficient time to ensure removal of any gases initially present within by the escaping vapor. The vapors are brought to a condenser for recovery.

Just prior to the experiment the expansion volume is switched to another one that contains the appropriate quantities and temperature of liquids that will be sucked back into the enclosure during the cooldown test period. This inflow is gradual and of a small quantity, so that its effects can be made negligible by choosing for it a temperature within the range of the upper

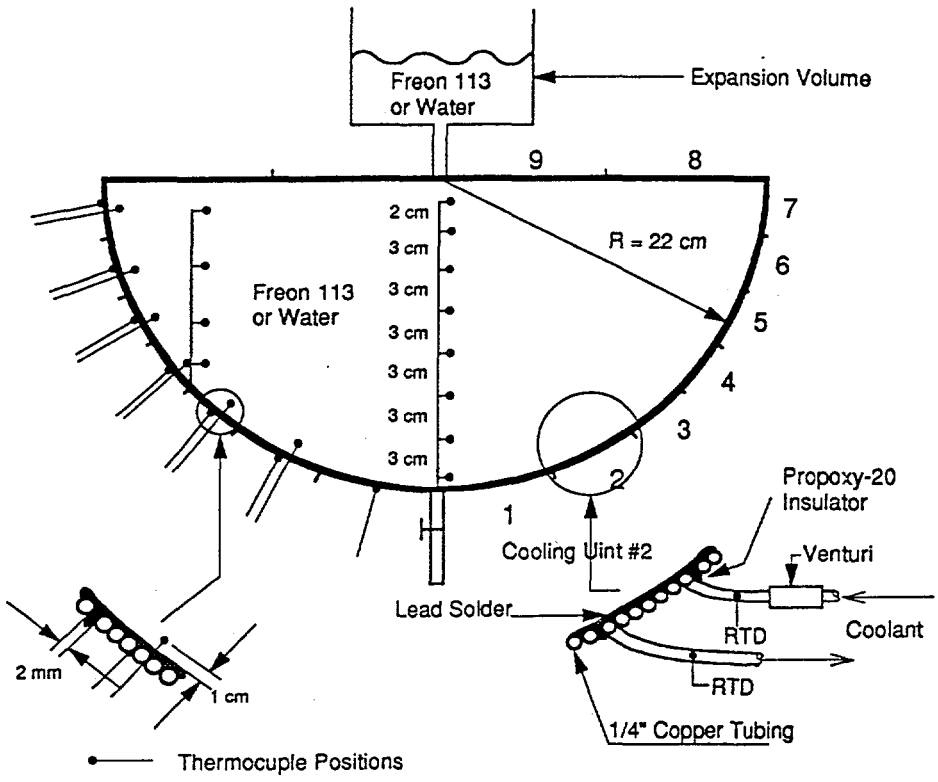

Figure D.3. Schematic of the mini-ACOPO experiment including the key construction details and instrumentation.

pool temperatures during a run. By choosing it to be at a much lower temperature the effect of such drain-flow can be determined. By choosing the fluid to be part water and part freon, a predetermined thickness of water layer can be deposited, very smoothly, on top of the freon pool within the enclosure. These special options have not been exercised in the experimental program reported herein.

An actual experimental run commences when, after some settling time, the coolant circuits are switched to take suction from a cold water pool, usually maintained at $\sim 0\,^{\circ}C$ (with ice) for runs with an isothermal boundary. Separate baths for each cooling unit circuit are used if a non-isothermal boundary is required.

The above-described apparatus was designed primarily for use with Freon-113, i.e., maximum pool temperature of $\sim$ 40° C, and it is called mini-ACOPO A. An essentially duplicate apparatus, the mini-ACOPO B, was built for operation with water at temperatures up to 100° C (or even higher using other fluids) to pursue a special investigation on Prandtl number effects.

In this second apparatus, not being interested in local behavior, we simplified the design, and improved the structural stability for the considerably larger temperatures necessary, by employing a shell-within-a-shell concept. The two shells were made of copper such as to fit, one inside the other, with a spacer coil in between, to create the flow channel necessary for cooling to a uniform temperature. The top was built from two copper plates built in a similar fashion. The hemisphere was closed with a flanged connection and adequate insulation in between to ensure that the two cooling circuits could operate completely isolated from each other.

After carrying out most runs in mini-ACOPO A, it became apparent that the useful data range could be extended by minimizing the duration of the initial transient by rapidly cooling down the boundary to the desired temperature. This was accomplished by incorporating high flow circuits to each cooling unit. These are called bypass flows, because they bypass the instrumentation, as at such high flows the temperature change is insufficient for accurate measurement of the heat transfer rates. The procedure then was to first apply the bypass flow for 1 to 2 minutes, until the boundary structural material could cool to the desired temperature, and switch to the normal cooling circuits, for data acquisition, during the remaining of the transient. All runs with the mini-ACOPO B (B1 to B3) were performed in this fashion. Also, run A16 was performed similarly, and more specifically in this run, having established the accuracy of our measurement systems and observance of the energy balance [between loss infered from pool thermocouples and energy convected out by the cooling circuits], the high bypass flow in the upper boundary circuits was left on for the duration of the run.

D.3. MEASUREMENTS AND INSTRUMENTATION

The basic measurements in this experiment are for temperature and flow. Temperatures are measured with K-type thermocouples which, calibrated and operated with a high resolution data acquisition board, are good to within $\pm 0.5\,^{\circ}C$. This is quite adequate for all pool and wall temperature measurements (see Figure D.3). For the coolant streams the requirement is more stringent because we cannot allow a temperature rise of more than $\sim 1\,^{\circ}C$ (to maintain an isothermal boundary), while at the same time this rise must be measured accurately enough for the intended energy balance (that gives the local heat flux). Thus we use RTDs which allow an accuracy of $\pm 0.01\,^{\circ}C$. Similarly, the flows must be measured very accurately. We use venturi meters and orifices carefully and repeatedly calibrated, such that these measurements are good to within $\pm 5\%$. All data are recorded during a run at 1 Hz and analyzed immediately after.

The apparatus and all lines were meticulously insulated and several key tests of accuracy have been and continued to be periodically performed during the experimental program.

(a) *Total Heat Gain from the Environment.* With the enclosure empty (filled with air) and isolated from the atmosphere, ice water at 2 °C was circulated through all cooling units at the highest and lowest rates typical during an experiment. We found an average rise of 0.04 °C at the highest rate, and of 0.08 °C at a flow of one-half this value. This translated to a total heat gain, which is only 2 to 3% of the thermal load in the high Rayleigh number range (at the beginning of a run, employing the maximum attainable temperature difference between the pool and the wall). Near the end of a run, the heat fluxes from the pool become low enough for this correction to be significant. In any case, it is accounted for in the data analysis by using the circuit-specific values measured.

(b) *Circuit-to-Circuit Heat Transfer.* Such a heat transfer can affect the local shape of the thermal load, rather than values averaged over the upper and lower boundaries. Tests were carried out in an empty vessel as above, but with a lower grouping of the cooling circuits run about 5 °C lower temperature than the rest of them. By repeating this process with different groupings of the cooling circuits, all interfaces were examined. The heat transfer thus measured could be reduced to a limiting conduction resistance between the circuits that corresponds well with the characteristics of the insulation material ($k \sim 1$ W/m K) and the thickness (2 mm) used in the construction of the facility. Under a circuit-to-circuit temperature difference of less than 2 °C, this mechanism was estimated to cause an error of less than 3% in the measured heat loads, in the local sense. Again, this is negligible, but the correction was used in the data analysis.

(c) *Total Energy Balance.* The data are reduced by a 50-second, sliding time-average during which heat loss from the pool and total heat picked up by the cooling circuits at the boundaries are calculated. Accounting also for the small corrections due to heat transfer from the environment [item (a) above] and the makeup fluid from the expansion volume, the overall energy balance was found to be satisfied to a remarkable degree (see details in Section D.5). This is consistent with the individual measurement error described above and the interpretation of pool energy in terms of the temperature measurements at nine positions.

D.4. EXPERIMENTAL PROGRAM

The experimental program carried out so far is summarized in Table D.1. Each experimental run involves a transient cooldown from some initial state, until the pool-to-wall temperature difference and corresponding heat fluxes are too low for reliable measurements. Using Freon-113, the maximum pool temperature was ~40 °C, and with ice water for cooling, the minimum wall temperature was ~3°C. With this maximum ΔT, cooldowns of up to 25 minutes could be carried out, to cover a Rayleigh number range of $2 \cdot 10^{13}$ to $7 \cdot 10^{14}$. The data are recorded at 1

Table D.1. Overview of the Experimental Program in the mini-ACOPO Facility			
A Runs with Freon-113, B Runs with water			
Run #	Initial Pool Temperature (°C)	Wall Temperature (°C)	Purpose
A2	37 Uniform	~3 Uniform	Test concept and instrumentation
A3	37 Uniform	~3 Uniform	Check Reproducibility
A4	40–19 Self-similar shape	~3 Uniform	Immediate approach to self-similar stratification
A5	40–19 Self-similar shape	~3 Uniform	Check reproducibility
A7	30–5 Self-similar shape	~3 Uniform	Check data trend in early portion of the transient
A10	40 Uniform	8 to 3 Linear	Check effect of wall temperature non-uniformity
A6	40 Uniform	~3 Upper boundary not cooled	Check effect on flux shape
A16	40 Uniform	~3 Uniform	To extend the Ra′ number range by making use of the earliest portion of the transient
B1	95 Uniform	~26 Uniform	Check Pr number effects
B2	100 Uniform	~66 Uniform	Check Pr number effects
B3	100 Uniform	~3 Uniform	Check Pr number effects

Hz and analyzed using a 50-second-wide sliding time average, at the same rate of 1 Hz. Thus, up to 1500 data points covering the Rayleigh number quoted above are generated from each run; because of their proximity, the data actually look as continuous lines traversing the Ra′ number space.

The first two runs (A2 and A3) were carried out with a uniform pool initial temperature and an imposed isothermal boundary. The purpose was to test the experimental concept and especially the approach to self-similar stratification and the performance of the measurement and data analysis approach. With these established, the next two runs (A4 and A5) were aimed at further exploring the evolution of stratification by imposing the self-similar stratification pattern, as determined in the previous two runs, right from the start. As expected, no significant changes in the pool stratification shape during the run were observed. These runs established that the pool suffers no major internal adjustments during the cooldown, such that the quasi-static approximation is valid throughout the cooldown transient, to a high degree of accuracy.

The fifth run (A7) was carried out with a lower pool initial temperature, such that the initial Rayleigh number was only $2 \cdot 10^{14}$. The purpose was to check the behavior in the initial period of the transient by direct comparison to all four previous runs in which this Rayleigh number was reached after ~5 minutes.

The next two runs (A10 and A6) were oriented to non-isothermal boundary effects. Specifically, run A6 was carried out without top cooling and an isothermal, cooled lower boundary; and run A10, with an imposed linearly increasing wall temperature. These runs introduced important insights about the heat flux distribution.

The final run with mini-ACOPO A was A16, and it was carried out with the bypass flow explained in the previous section. It allowed the collection of data for Ra′ numbers up to $\sim 7 \cdot 10^{14}$.

Finally three runs (B1, B2, and B3) were carried out in mini-ACOPO B with water as the working fluid to explore separate Prandtl number effects. With initial water temperatures at ~100 °C and cooling circuits operated to maintain wall temperatures at 3, 26, or 66 °C, these experiments could cover the ranges $2.5 < \mathrm{Pr} < 11.0$ and $10^{12} < \mathrm{Ra}' < 3 \cdot 10^{13}$.

D.5. EXPERIMENTAL RESULTS AND DISCUSSION

The key point about the validity of the experimental concept is the establishment of a self-similar stratification pattern in the pool during the cooldown. This was demonstrated by defining

a local dimensionless temperature

$$\Theta = \frac{T - T_b}{T_{\max} - T_b} \qquad (D.1)$$

where T_b is the "bulk" (volume-averaged) pool temperature, and plotting it against vertical position in the pool. The thermocouples in Figure D.3 show that lateral temperature gradients in the pool are always negligible [[less than 5% of the overall ΔT, $\Delta T = T_{max} - T_i$]], so the bulk temperature could be quite accurately estimated by volume averaging the temperatures from the central thermocouple tree, each corresponding to the corresponding horizontal slice of the hemisphere. [Data in the first 3-4 minutes are not shown in these figures, as this time was required to eliminate the effects of the initial transient, as described in the next two paragraphs.] The results from run A2, and from all A runs (with isothermal boundaries) put together, are shown in Figures D.4 and D.5 respectively. The choice of the ordinate is such that it reflects the volume of fluid associated with each portion of the pool stratification pattern. From these figures we see that only the very bottom (less than 10%) of the pool volume undergoes any significant change or departure from self-similarity during an experimental run. These figures also show that about one-half (the upper) of the pool volume is essentially at a uniform temperature ($T_{\max}$), and that a well-defined, self-similar temperature gradient exists in the intermediate 10% to 50% of the pool volume. It is clear that the large, uniform temperature layer on top is reflective of the agitation created due to the strong cooling on the top boundary (and the associated descending plumes).

The other key point, as in any experiment, is the accuracy of the experimental measurements and data reduction techniques. Aside from the individual instrument accuracy, and quantification of corrections due to non-perfect insulation effects, as discussed in Section D.3, an overall energy balance provides an important means for verification. This was affected by comparing the energy loss from computing the energy change in the pool (as deduced from thermocouple measurements), to the energy loss obtained by summing up the measured energy losses at the pool boundaries (to the nine cooling circuits). Because of the importance of this verification measure, the results from all runs are shown in Figures D.6(a) through D.6(j). In all but the last three of these figures, the times at which some flow rate was changed in any of the cooling circuits is also marked — such changes were necessary to make during the course of a run, in order to maintain the measurement accuracy as the heat fluxes continually decrease as a result of the pool cooling down. We can see that, not unexpectedly, such changes cause short-duration, and marked departures from the energy balance, while for all the rest of the time the balance is observed to be within $\pm$ 10% (much less most of the time). The data during these short time periods of departure have been discarded from further use.

In the same light, the first 3-4 minutes in each run were discarded. It is interesting to note that within the same time frame the internal stratification pattern stabilized to the self-similar long

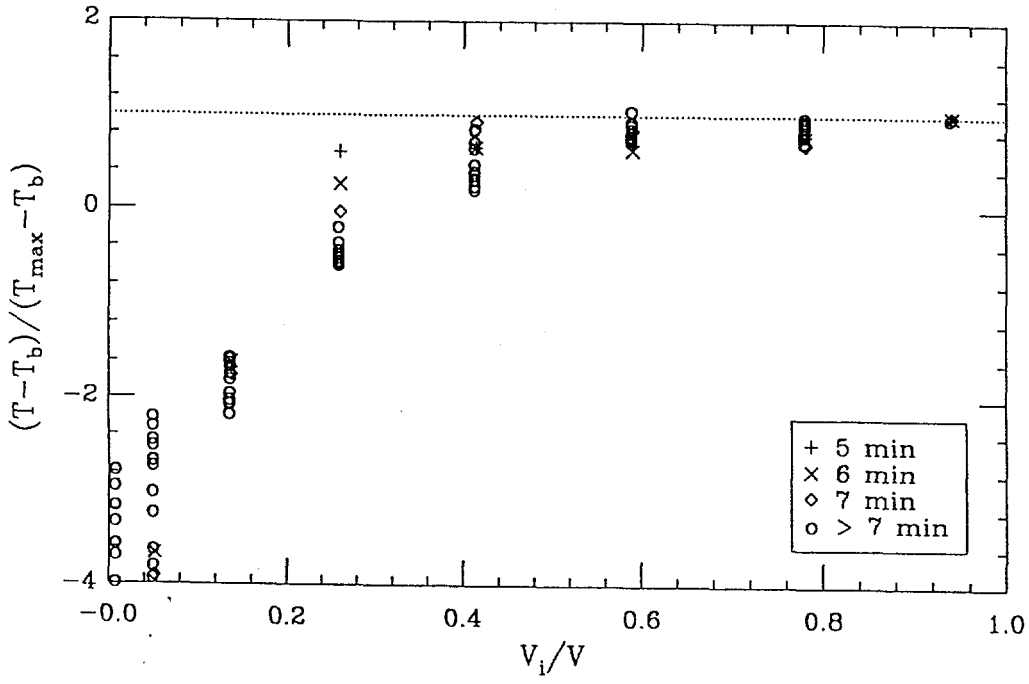

Figure D.4. Dimensionless pool stratification pattern obtained in run A2. V_i/V is the fractional pool volume below the pool elevation in question.

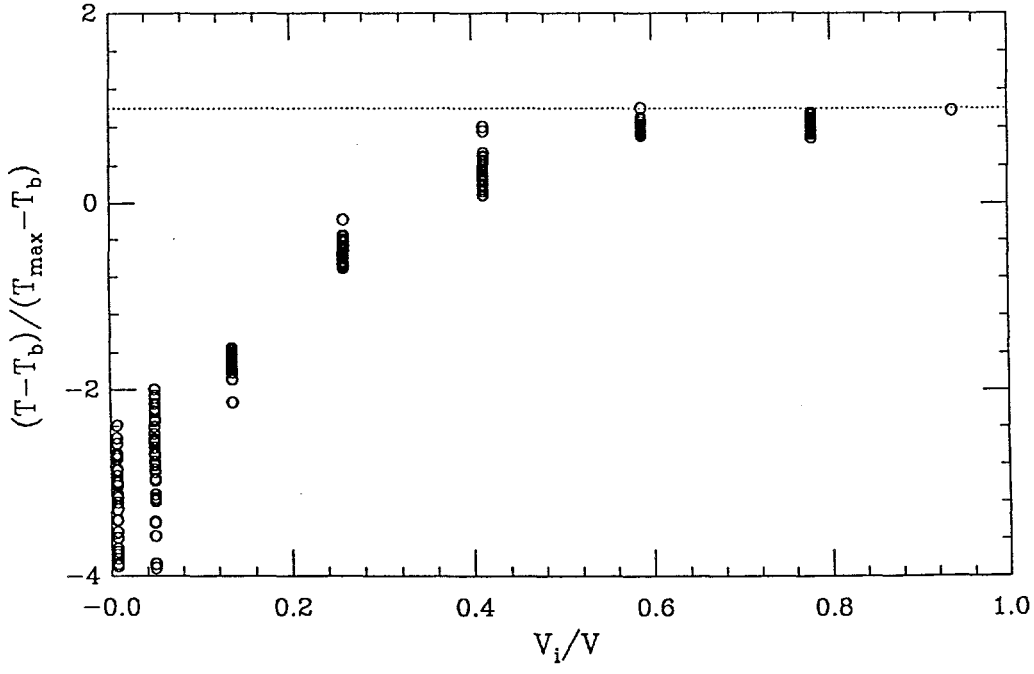

Figure D.5. Dimensionless pool stratification data from all runs with isothermal pool boundaries (A2, A3, A4, A5, and A7). V_i/V is the fractional pool volume below the pool elevation in question.

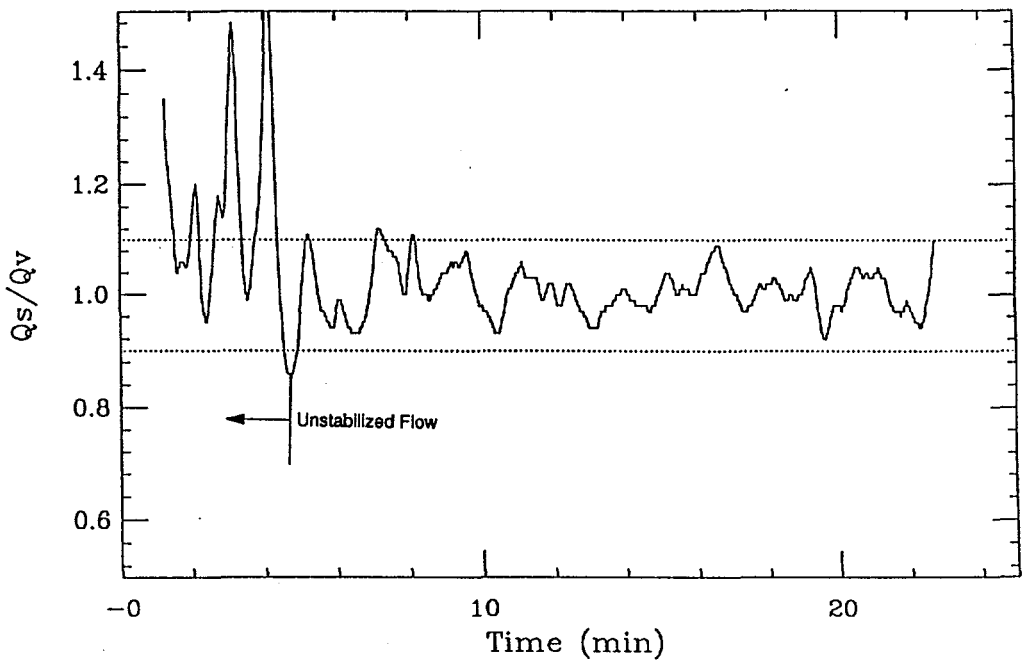

Figure D.6(a). The energy balance obtained in run A2. In this and all subsequent D.6 figures, "unstabilized flow" means a period of initial adjustments in cooling unit flow rates, as well as a transient associated with the thermal inertia masses associated with the cooling circuits themselves.

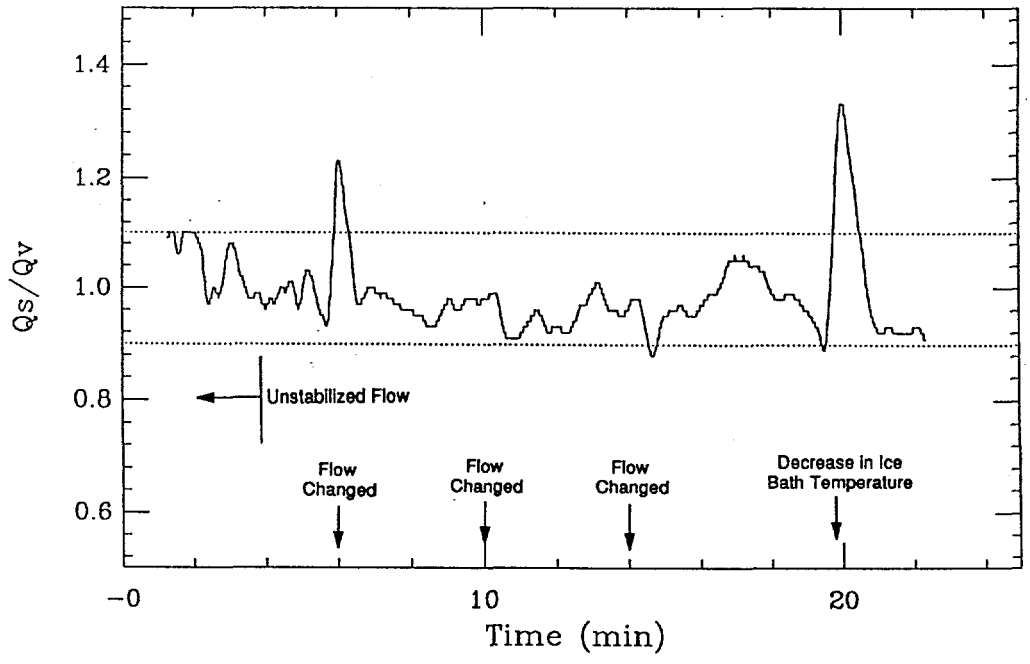

Figure D.6(b). The energy balance obtained in run A3.

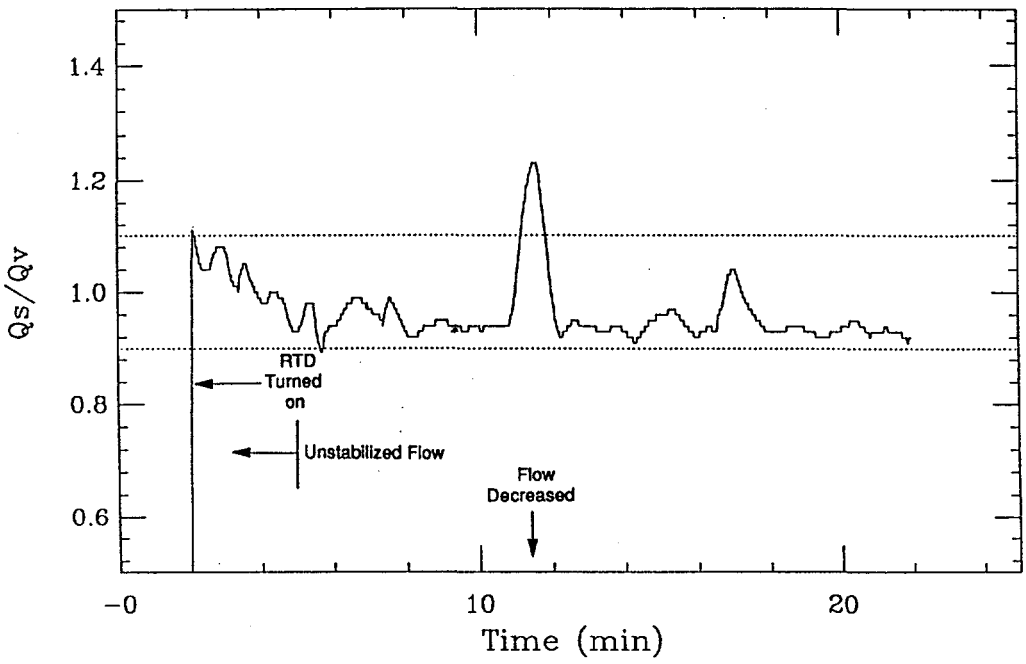

Figure D.6(c). The energy balance obtained in run A4.

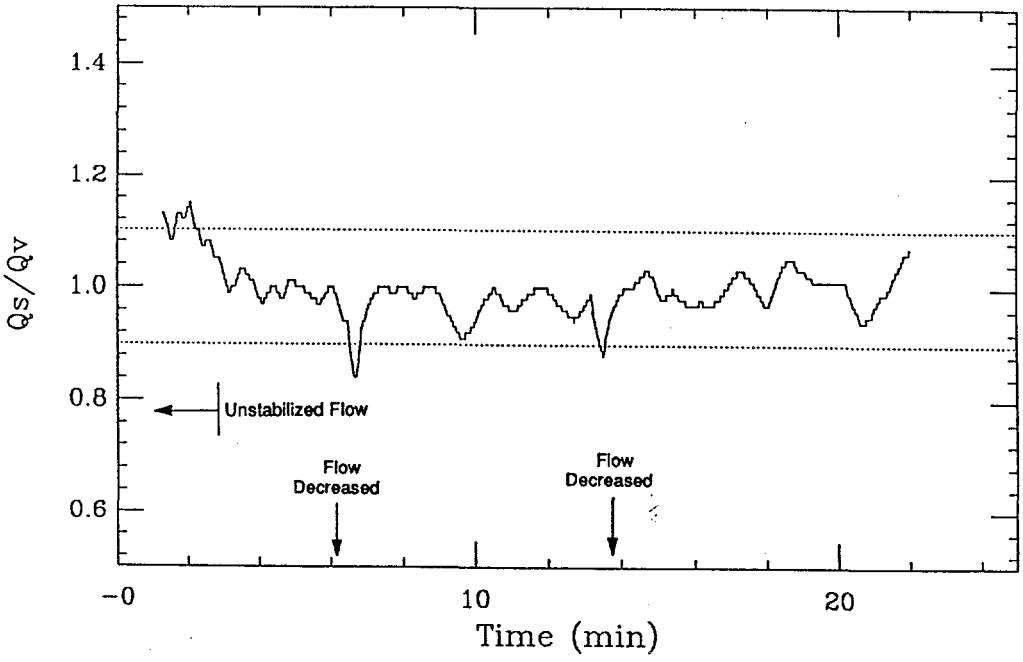

Figure D.6(d). The energy balance obtained in run A5.

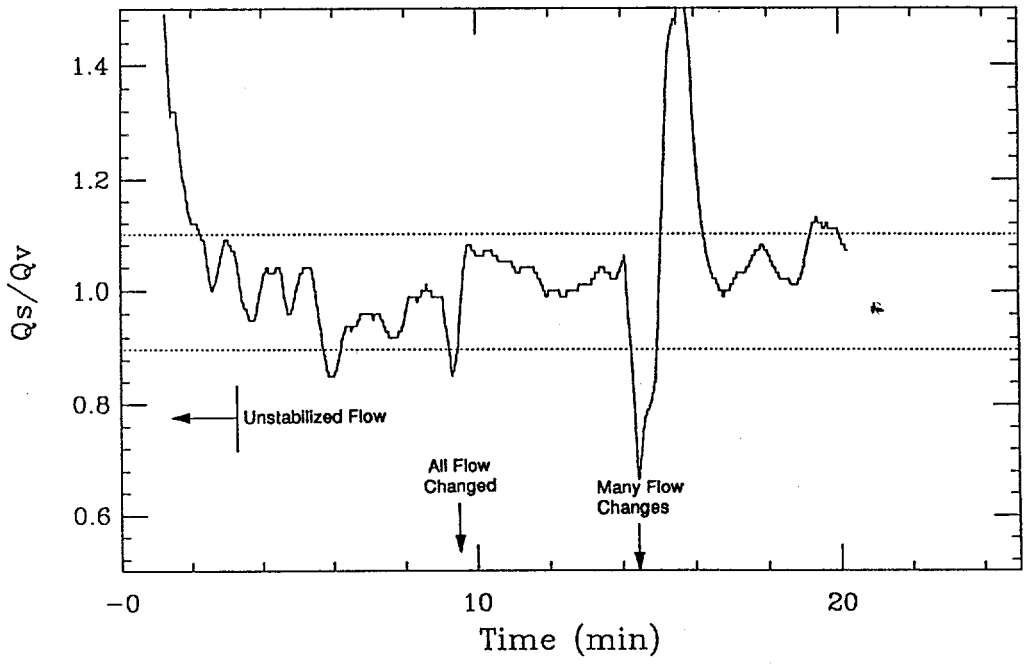

Figure D.6(e). The energy balance obtained in run A7.

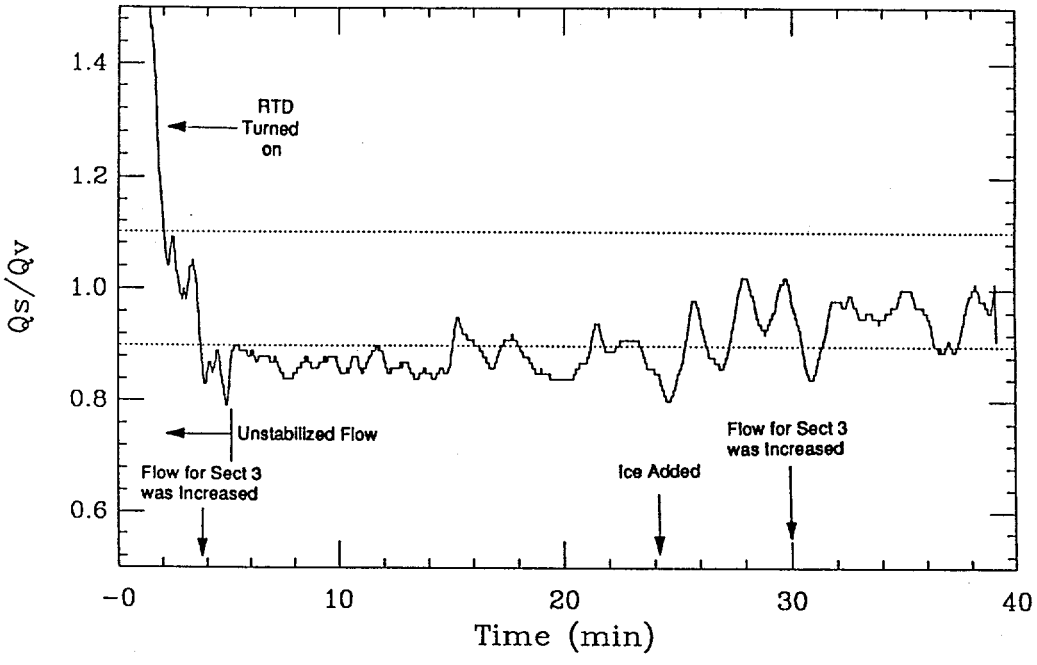

Figure D.6(f). The energy balance obtained in run A6.

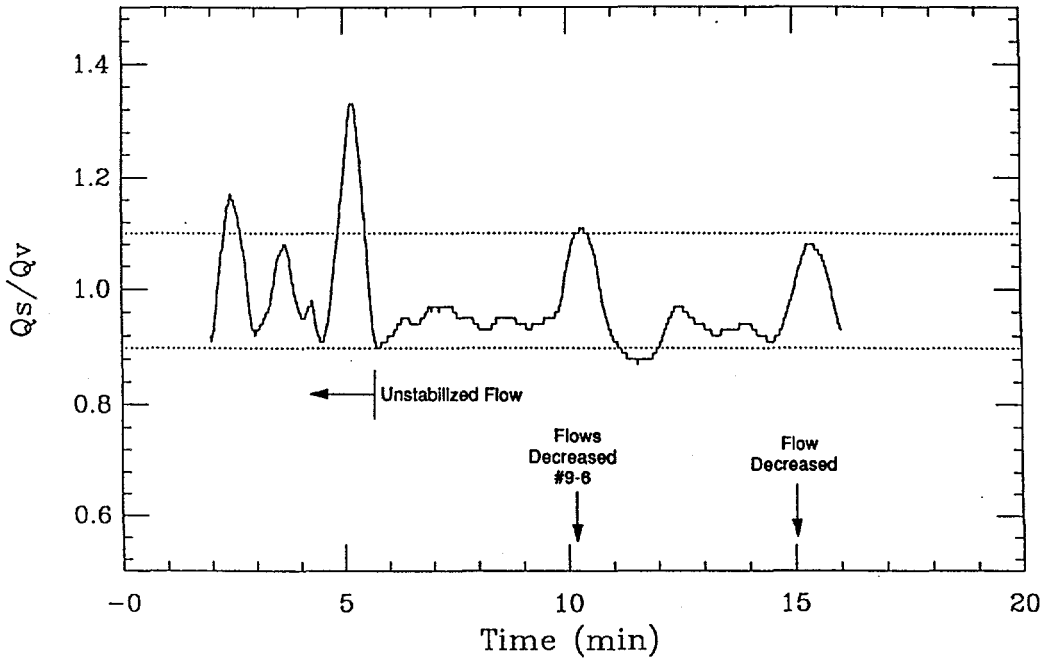

Figure D.6(g). The energy balance obtained in run A10.

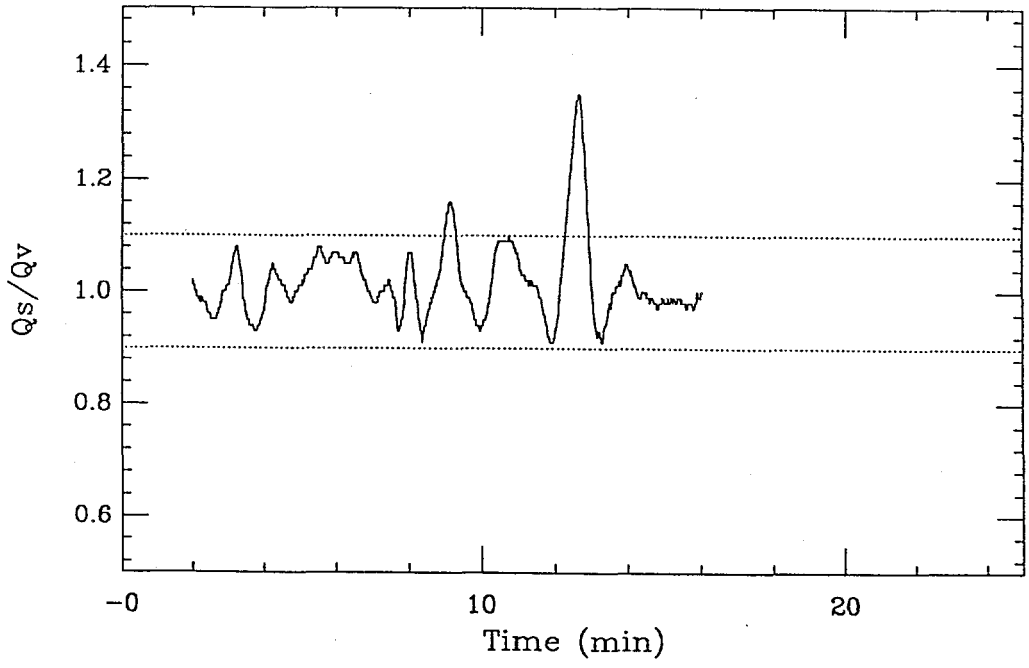

Figure D.6(h). The energy balance obtained in run B1.

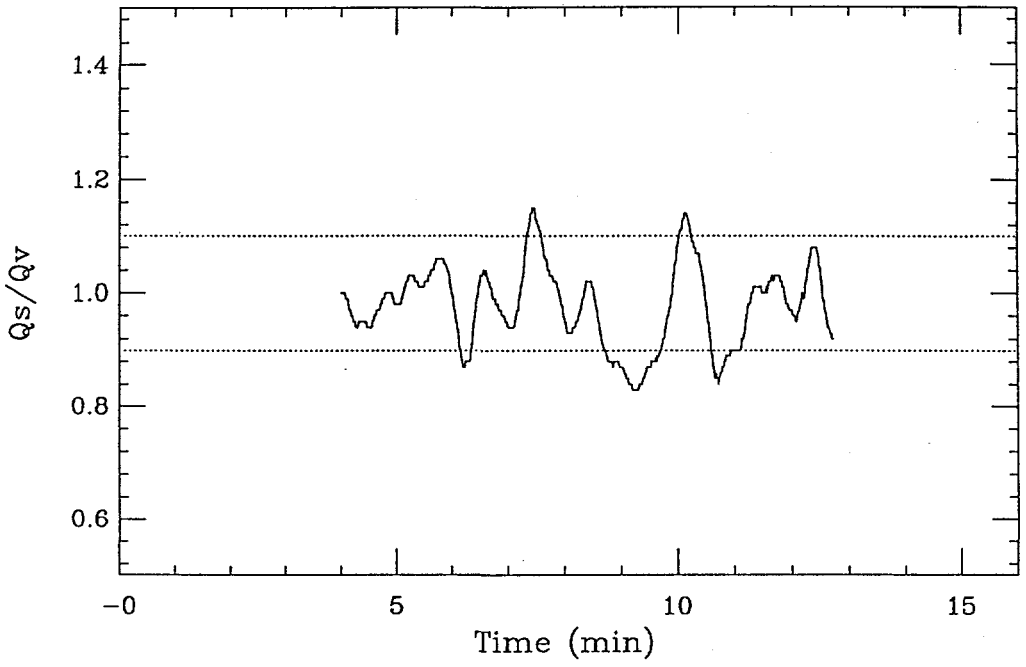

Figure D.6(i). The energy balance obtained in run B2.

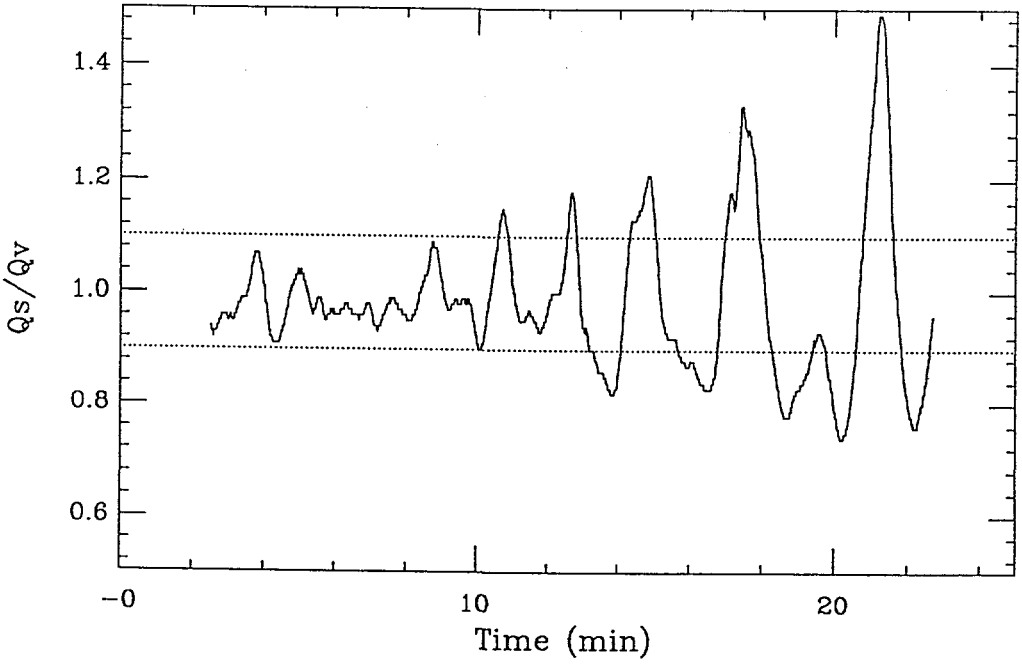

Figure D.6(j). The energy balance obtained in run B3.

term behavior. While these more esoteric aspects may be of some interest in verification studies of detailed numerical simulations (such as those mentioned in Chapter 5), they are peripheral to our present purposes and will not be discussed here any further. Rather, we focus on the average heat transfer results and the flux distribution on the curved boundary, only during the quasi-steady portion of the transients. The Steinberner and Reineke (1978) and the Mayinger et al. (1975) correlations discussed in Chapter 5 were found to be in good agreement with these data [for upward and downward heat transfer, respectively] so they are included in the figures that present them. Also shown on these figures are the $\pm$ 15% intervals around these correlations. The results of the series B runs, addressing Prandtl number effects, are given directly in Chapter 5. So, without further reference, in the following we will be discussing the A series of runs only.

The results for upward heat transfer are shown in Figures D.7, D.8 and D.9. Figure D.7 contains the data from all isothermal boundary runs, except run A16, which is given separately in Figure D.8. This special status is assigned to this run because it represents the culmination of perfecting the experimental techniques, including the bypass flow and hence the largest coverage in the Ra' number. In Figure D.9 we can see that the flux distribution in the upper boundary (the central portion occupies ~50% of the area) is very nearly uniform, and this is typical of all runs.

The results for downward heat transfer are shown in Figures D.10, D.11 and D.12. Figure D.10 contains the data from all the runs, except run A16, which is shown in Figure D.11. In Figure D.12 we have collected the local fluxes, normalized to the average flux, from all the mini-ACOPO experiments. On the same figure we show the line that represents the experimental trends (Eqs. D.2 and D.3 shown below), and also the UCLA correlation from Appendix C. A generally good agreement is seen, except for the higher peaking exhibited by the UCLA correlation for $\theta > 80°$. This, however, must be tempered by recognizing that our values are averaged over the width of the cooling units—the values shown at ~84° really correspond to an average over $78° < \theta < 90°$. On the other hand, it is also interesting to note that the UCLA experiment exhibits a somewhat broader stratification pattern, i.e., almost absence of an upper well-mixed portion (see Figure D.13 in comparison to Figure D.4).

Runs A10 and A6 were carried out for exploring further these aspects. In run A10 we imposed a non-uniform wall temperature, as illustrated in Figure D.14. It did not appear to make any significant difference on the stratification pattern, the downward heat flux, or even the heat flux distribution, as illustrated in Figures D.15, D.16 and D.17, although it should be noted that the degree of imposed non-uniformity was small in comparison to the bulk-to-wall temperature difference—this is especially so because as shown by all previous experiments the upper portion of the pool is dominated by the strong cooling from the upper boundary.

In run A6 we kept the upper boundary adiabatic, and this did have a profound effect. First, in Figure D.18 we see a totally different stratification pattern. As expected, we find an absence of a well-mixed upper pool portion, and an essentially linear variation over the whole depth of the pool (in the V_i/V coordinates). In Figure D.19 we see that the effect of this pattern is to produce an excessively strong peaking, with values reaching up to 4. Finally, in Figure D.20 we see that the downward heat transfer is perceptibly lower than that found in the uniform wall temperature runs, but interestingly enough, the sensitivity is not as great as perhaps might be expected.

The remarkable features of Figure D.12 are that the peak-to-average heat flux is below 2 and that the data depict two distinct regions (or trends) connected with an inflection (or transition) region. With reference to Figure D.4, it can be seen that these regions correspond exactly to the two regions of the stratification pattern. That is, an upper region, $65 < \theta < 90°$, which corresponds to $0.40 < V_i/V < 1.0$ and the lower remaining volume. The flux shape is rather curved over the lower region, but is proceeds with an abrupt reduction in slope and in essentially a linear fashion (on the average) into the upper region. It is remarkable that such a two-region trend can be discerned at the lower Rayleigh number data of Jahn (Mayinger et al., 1975) obtained at $\mathrm{Ra}' = 1.2 \cdot 10^{10}$ in a semicircular (slice) geometry (see Figure 5.8 in Chapter 5). In this case, the peak-to-average flux ratio was ~1.6. With the help of these considerations we arrive at a proposed correlation for the flux shape given by

$$\frac{\mathrm{Nu}_{dn}(\theta)}{\mathrm{Nu}_{dn}} = 0.1 + 1.08\left(\frac{\theta}{90°}\right) - 4.5\left(\frac{\theta}{90°}\right)^2 + 8.6\left(\frac{\theta}{90°}\right)^3 \quad \text{for} \quad 0.1 \leq \frac{\theta}{90°} \leq 0.6 \quad (D.2)$$

and

$$\frac{\mathrm{Nu}_{dn}(\theta)}{\mathrm{Nu}_{dn}} = 0.41 + 0.35\left(\frac{\theta}{90°}\right) + \left(\frac{\theta}{90°}\right)^2 \quad \text{for} \quad 0.6 < \frac{\theta}{90°} \leq 1.0 \quad (D.3)$$

This correlation is normalized to unity and is shown in relation to the data in Figure D.12. In applications where local peaking is of interest, we recommend that a reasonable upper bound can be obtained from

$$\frac{\mathrm{Nu}_{\max}}{\mathrm{Nu}} = 2.0 \quad (D.4)$$

As a final point we would like to observe that the heat fluxes found at the outer portion of the horizontal boundary and the upper edge of the curved boundary are close to each other. This can be seen quite readily by applying the peaking factors from Figure D.12 (1.5 to ~2.0) to the results in Figure D.11, and compare with Figure D.8. For example, at $\mathrm{Ra}' = 3 \cdot 10^{14}$, from Figure D.11 we read $\mathrm{Nu}_{dn} \sim 420$; applying the peaking factors we get 630 to 840, and from Figure D.8 we read $\mathrm{Nu}'_{up} \sim 750$.

D.6. CONCLUSIONS

A new experimental approach to the problem of heat transfer from volumetrically heated enclosures has been proposed and verified. The approach is especially important in making feasible experimentation at the very high Rayleigh number range (10^{15} to 10^{17}) that is found in practical applications of severe accident management in certain nuclear power reactors (in-vessel retention). While a 1/2-scale experiment (the ACOPO) is in preparation, results obtained from a proof-of-concept, 1/8-scale experiment (the mini-ACOPO), verify and extend the Steinberner–Reineke (1978) and Mayinger et al., (1975) correlations for upward and downward heat transfer respectively, to the already relevant Rayleigh numbers of up to $7 \cdot 10^{14}$. This is complimentary to the UCLA work (Appendix C) that already reached these conclusions for Ra' numbers up to $9 \cdot 10^{13}$. In addition, these data demonstrate that the pool is characterized by a stable (self-similar) stratification pattern, in which the upper half of the pool volume is at a uniform temperature, and that the heat flux distribution along the lower boundary can be expressed by Eqs. (D.2) and (D.3). To bound the heat flux peaking at the upper edge of the curved boundary a value of 2 is recommended. This is somewhat lower than the 2.4 value found in the UCLA-experiments, and it may be worthy of further clarification. Finally, in the Series B runs covering the range $2.5 < \mathrm{Pr} < 11.0$, no independent Prandtl number effects were found (see Chapter 5).

D.7. REFERENCES

1. Mayinger, F., M. Jahn, H. Reineke, and U. Steinberner (1975) "Examination of Thermo-hydraulic Processes and Heat Transfer in a Core Melt," Final Report BMFT RS 48/1. Technical University, Hannover, W. Germany. As reviewed by F.A. Kulacki, Ohio State University, for the US NRC, march 31, 1976.

2. Steinberner, U. and H.-H. Reineke (1978) "Turbulent buoyancy convection heat tansfer with internal heat sources," Proc. Sixth International Heat Transfer Conf., Toronto, Canada, Aug 1978.

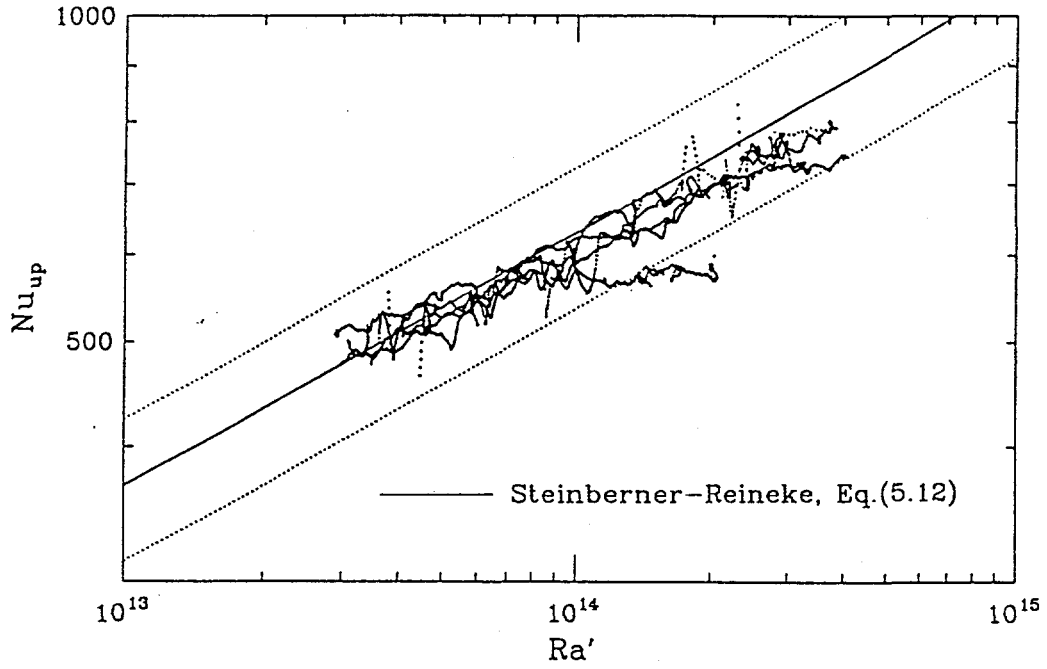

Figure D.7. The upward heat transfer obtained from all mini-ACOPO runs with isothermal boundary, except run A16.

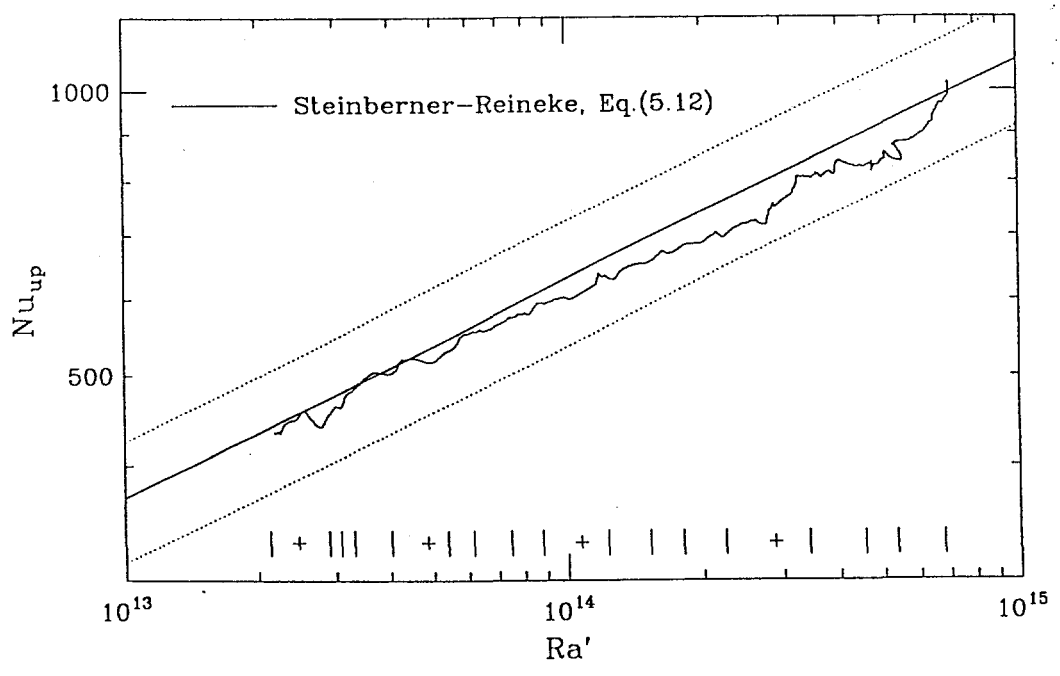

Figure D.8. The upward heat transfer obtained in mini-ACOPO run A16. The lines and plus signs at the bottom show incrementally 1 minute intervals during the cooling transient.

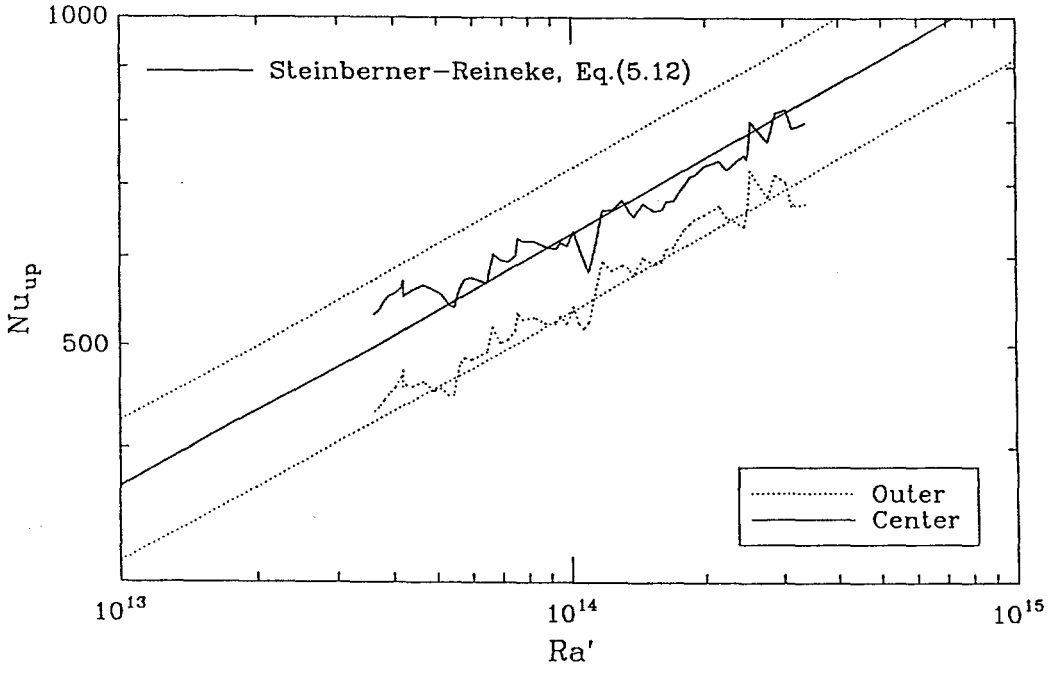

Figure D.9. The heat flux distribution in the upper boundary for run A3. The outer ring represents 50% of the area.

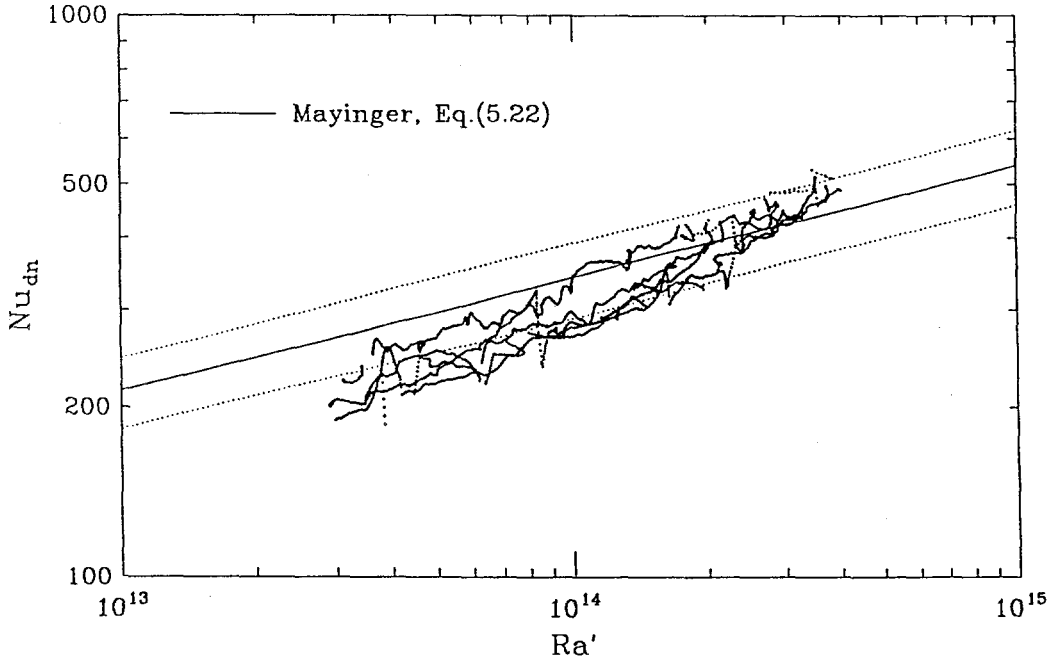

Figure D.10. The downward heat transfer obtained from all mini-ACOPO runs with isothermal boundary, except run A16.

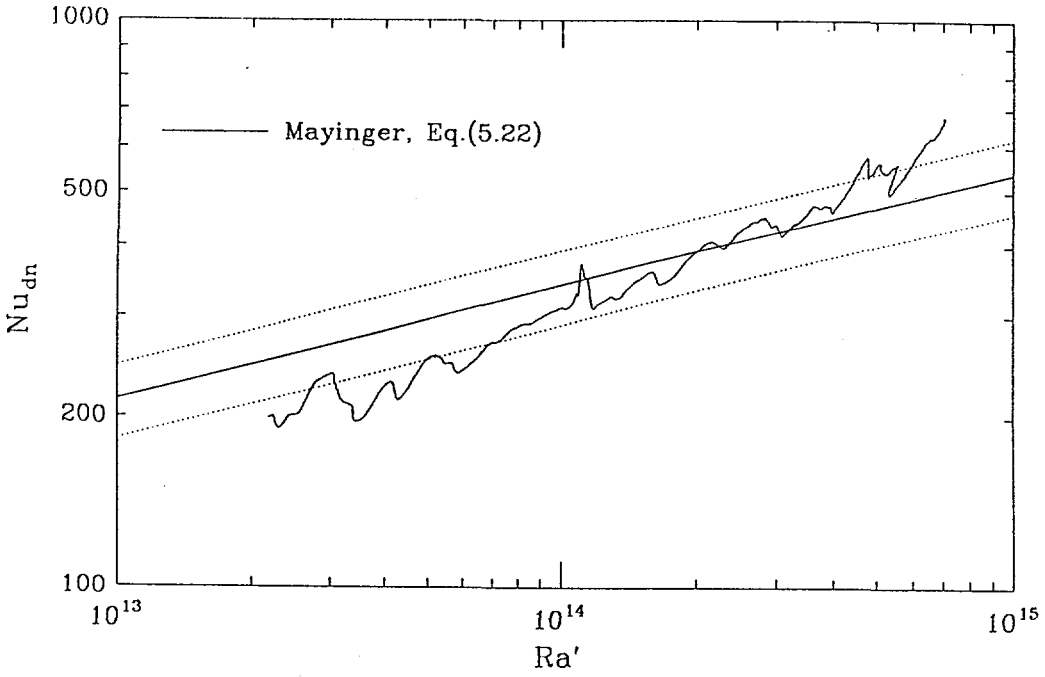

Figure D.11. The downward heat transfer obtained in mini-ACOPO run A16.

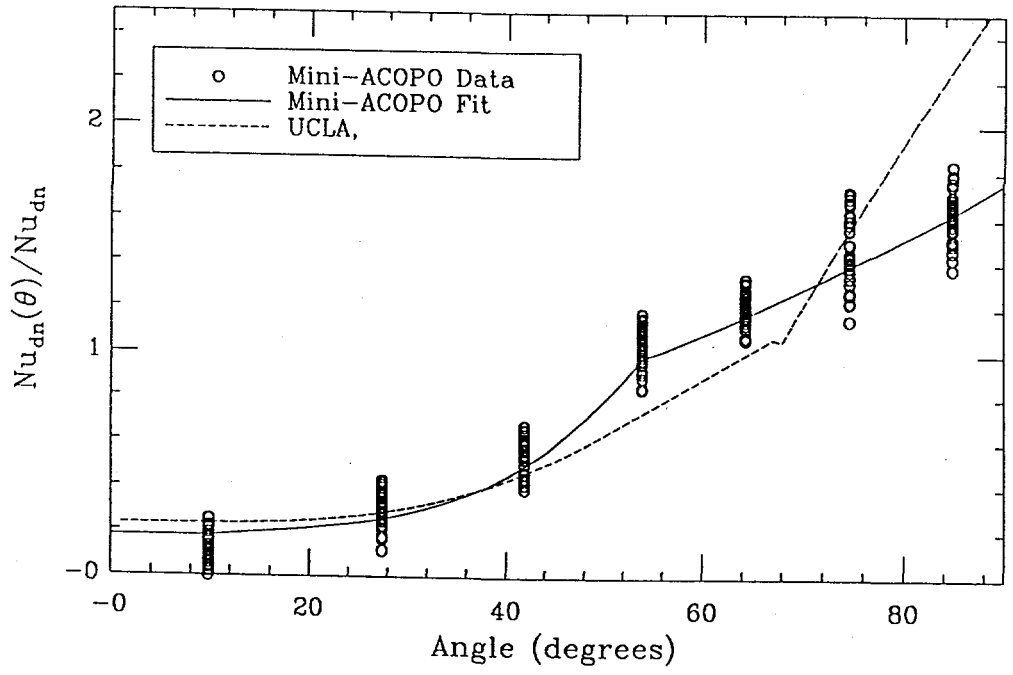

Figure D.12. The heat flux distribution over the lower boundary obtained in all mini-ACOPO runs with an isothermal boundary. Also included are the UCLA correlation (Appendix C), and a line through the mini-ACOPO data (Eqs. D.2 and D.3). The points are placed at the center of the arc covered by the respective cooling circuits.

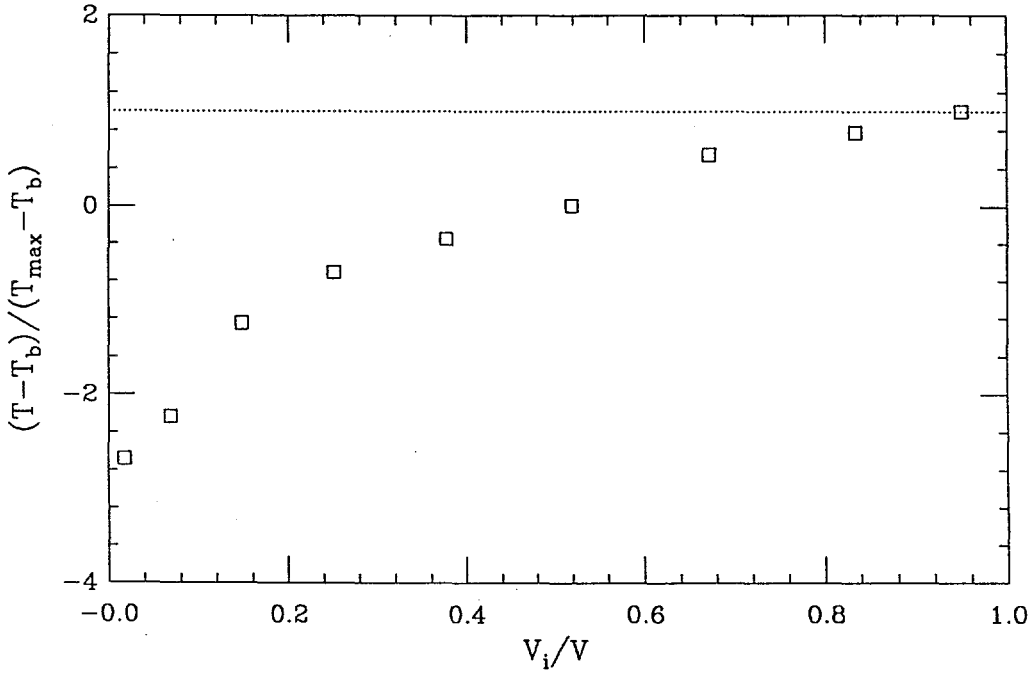

Figure D.13. The stratification pattern in the UCLA run at $Ra' = 9 \cdot 10^{13}$.

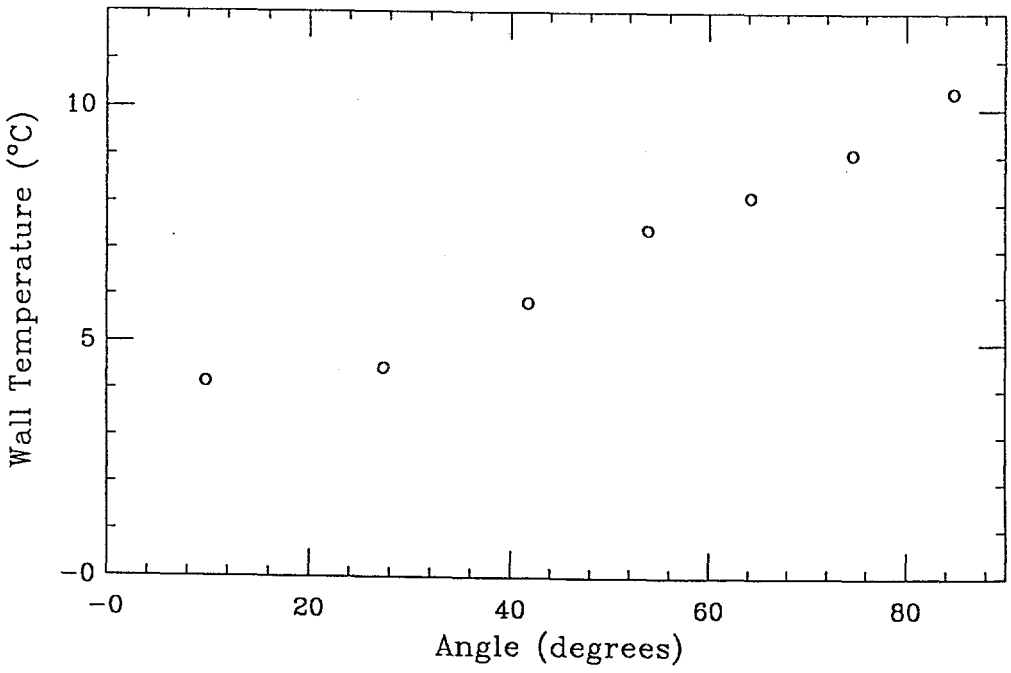

Figure D.14. The temperature distribution imposed on the curved boundary of run A10.

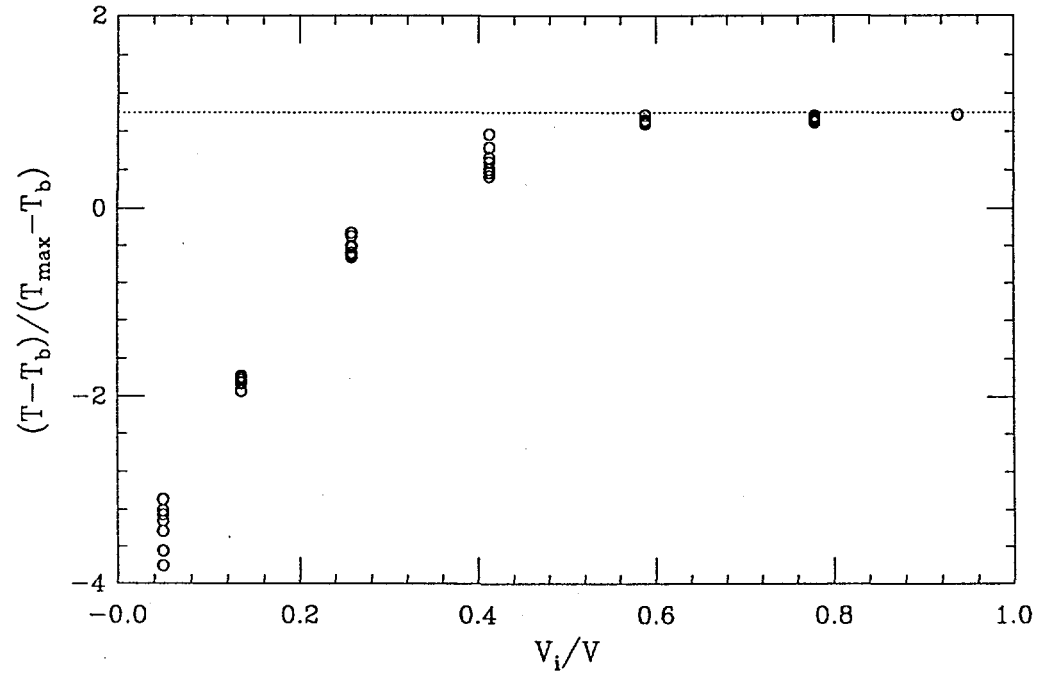

Figure D.15. The dimensionless pool stratification pattern obtained in run A10.

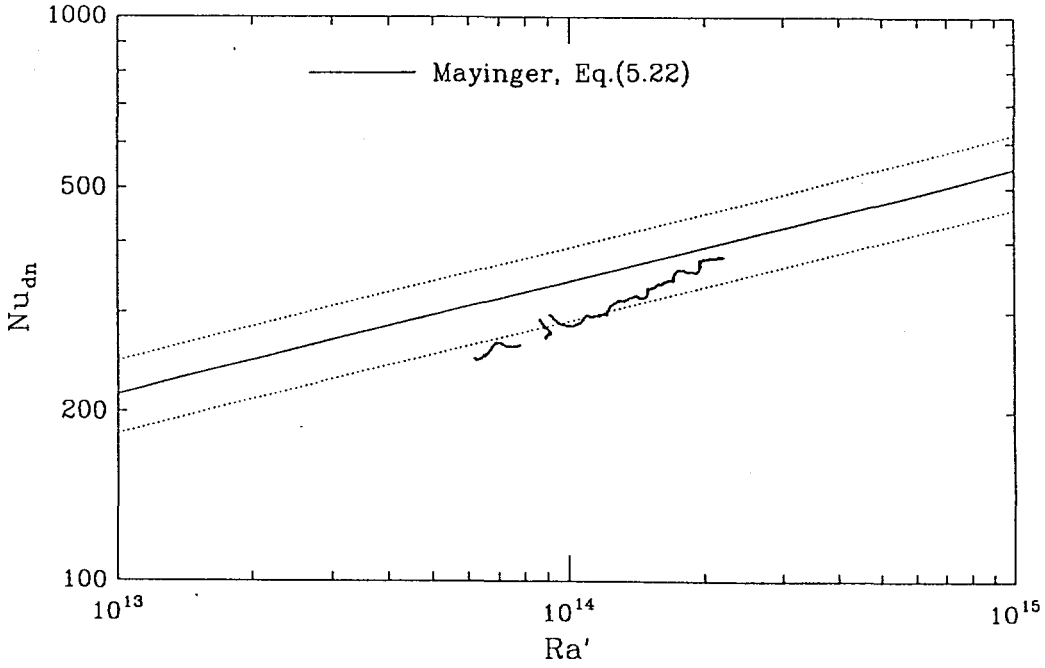

Figure D.16. The downward heat transfer obtained in mini-ACOPO run A10.

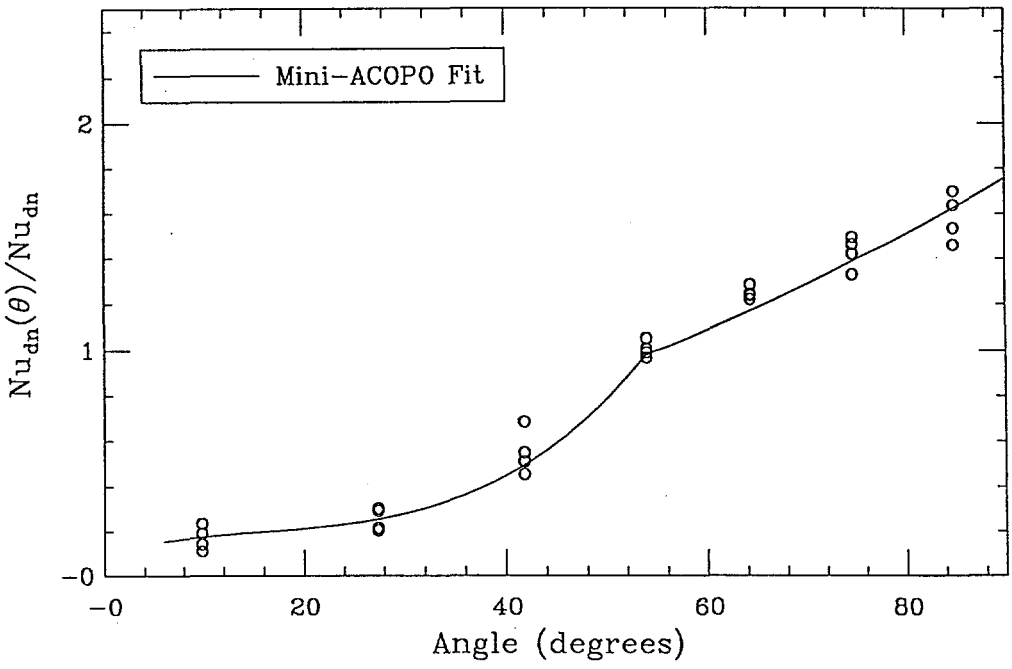

Figure D.17. The heat flux distribution found in run A10.

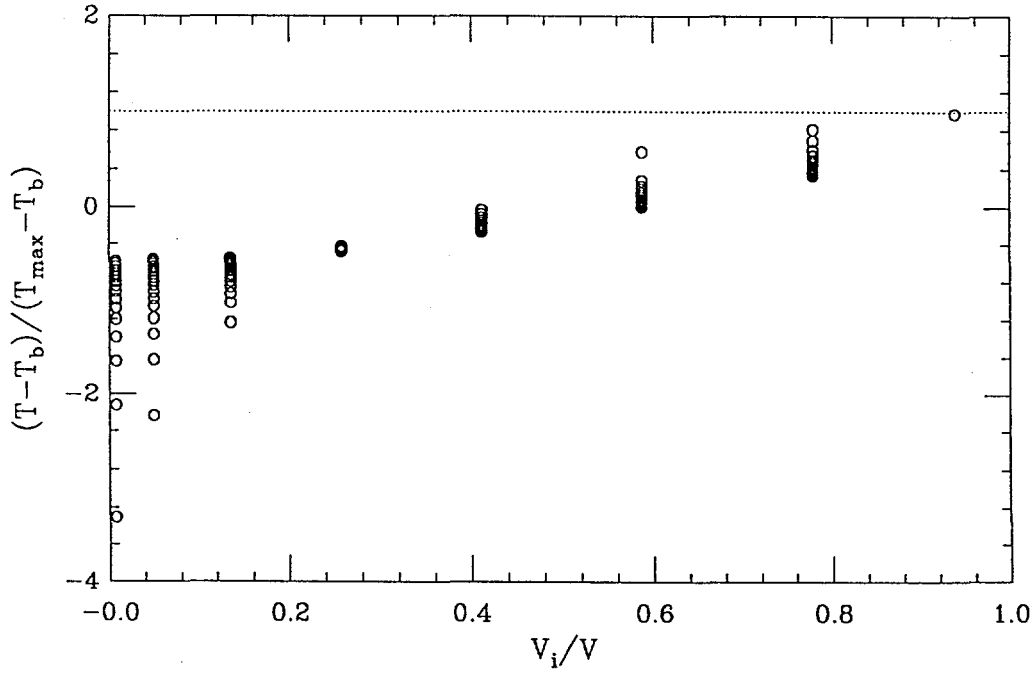

Figure D.18. The dimensionless pool stratification pattern obtained in run A6.

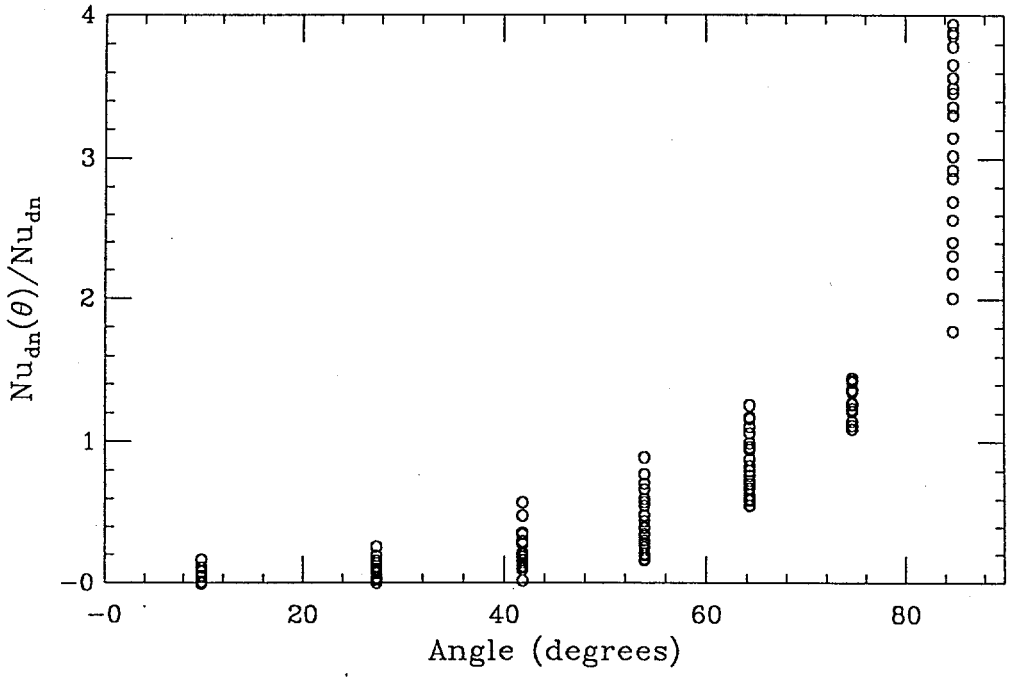

Figure D.19. The heat flux distribution found in run A6.

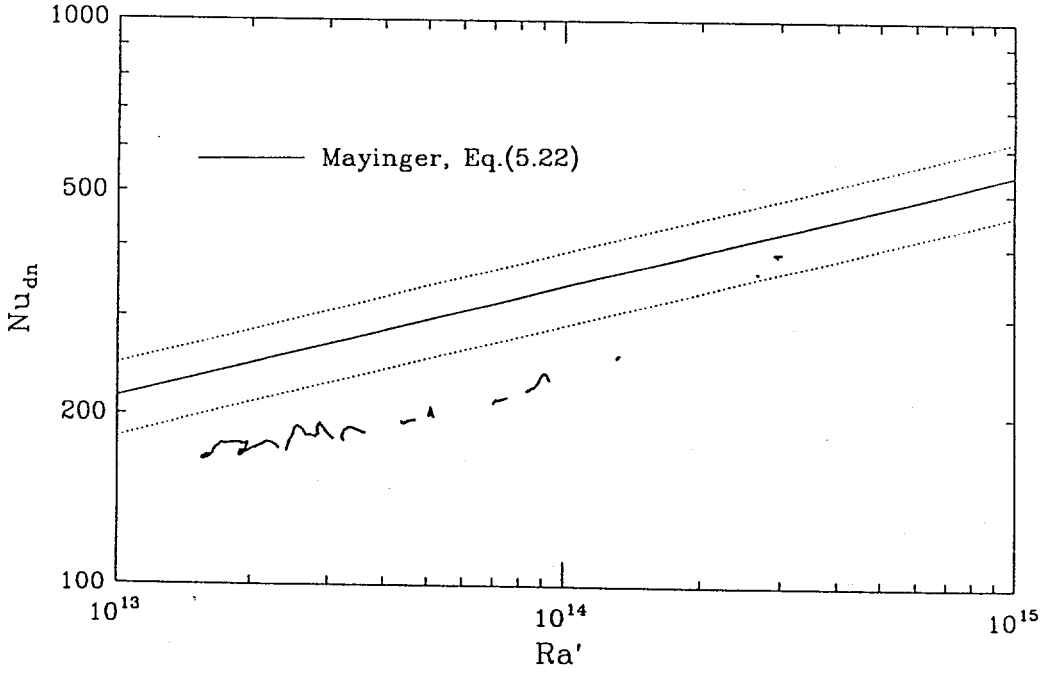

Figure D.20. The downward heat transfer obtained in mini-ACOPO run A6.

[[ADDENDUM TO APPENDIX D]]

The purpose of this addendum is to present more detail on the development, with time, of the pool stratification pattern, and heat flux distributions, in mini-ACOPO.

As explained already, mini-ACOPO A16 was run such as to minimize the duration of the initial transient; thus it also provides the best information on the development of the pool stratification pattern. This development is shown in Figure D.21, and indicates much more rapid approach (within 1 or 2 minutes) to the self-similar shape, than the other runs (see, for example, Figure D.4). This time is consistent also with that required for a few residence times of the fluid descending within the thermal boundary layers over the curved surface (path length ~40 cm, velocity ~1 cm/s, adjusted from the values measured by Steinberner and Reineke, 1978, for turbulent boundary layers at somewhat lower Ra′ numbers).

The measured evolution of heat flux shapes with time, for runs A3, A4, A5, A7, A10, and A6 are shown in Figures D.22 through D.27 respectively. We note that with only the exception of the data in position 40° at late times (15 to 19 minutes) in run A4, shapes are consistently regular and evolve gradually, and to a small degree, flattening out somewhat, especially near the very end of the cooldown (this represents the low end of the Ra′ numbers covered—see for example Figure D.8). It is noted again that the run with the adiabatic upper boundary (A6) is interesting for understanding certain aspects, as discussed already, but it is not relevant to the reactor situation of interest here.

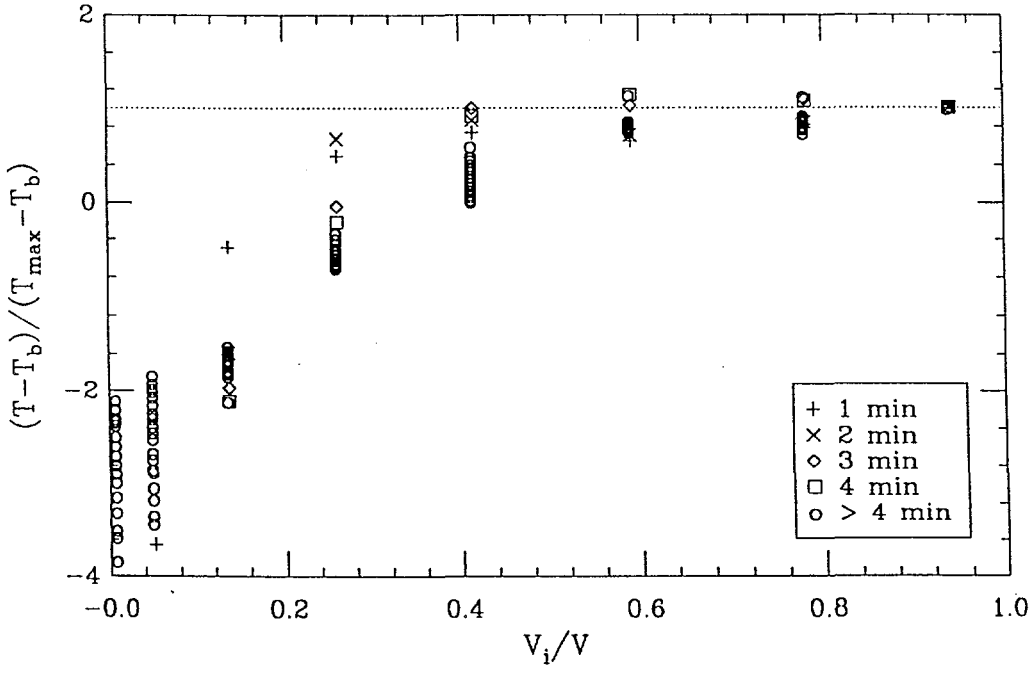

Figure D.21. Evolution of pool stratification patterns with time for run A16.

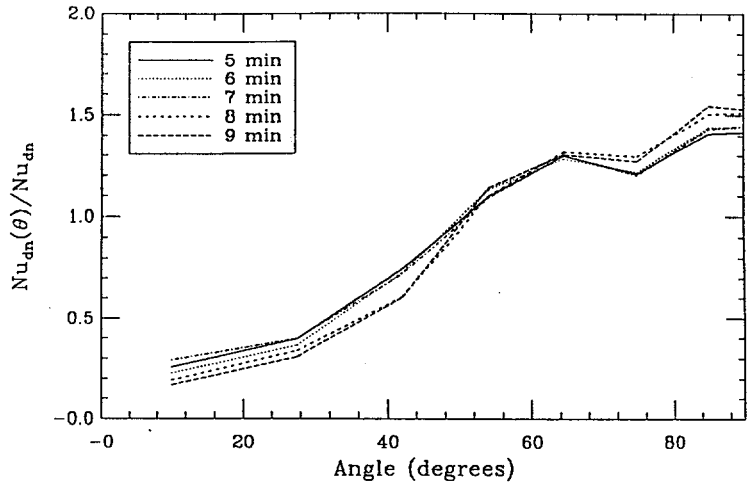

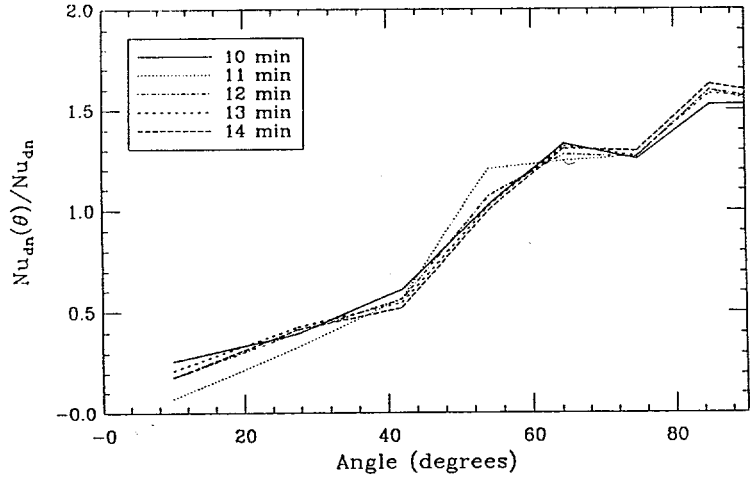

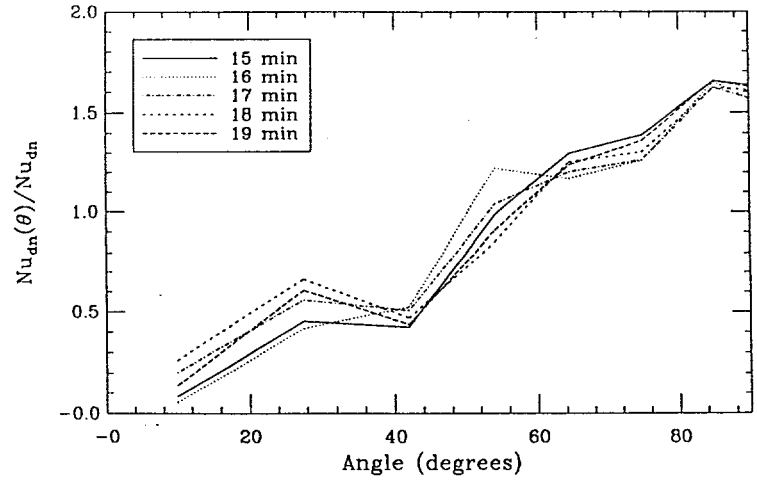

Figure D.22. Evolution of heat flux shapes with time for run A3.

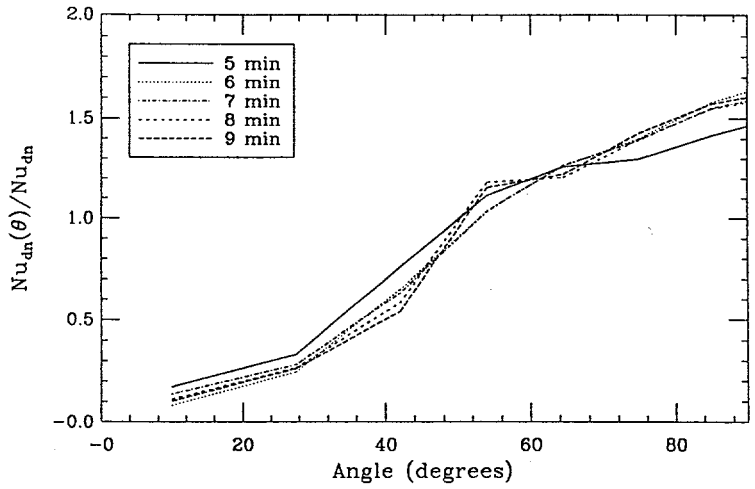

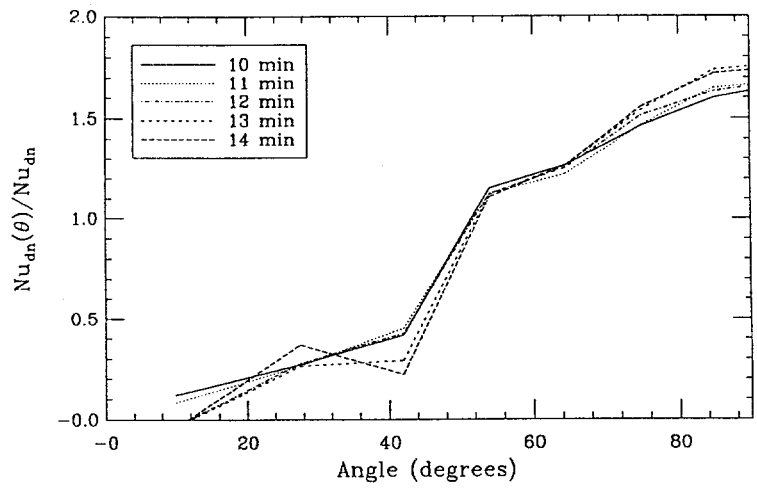

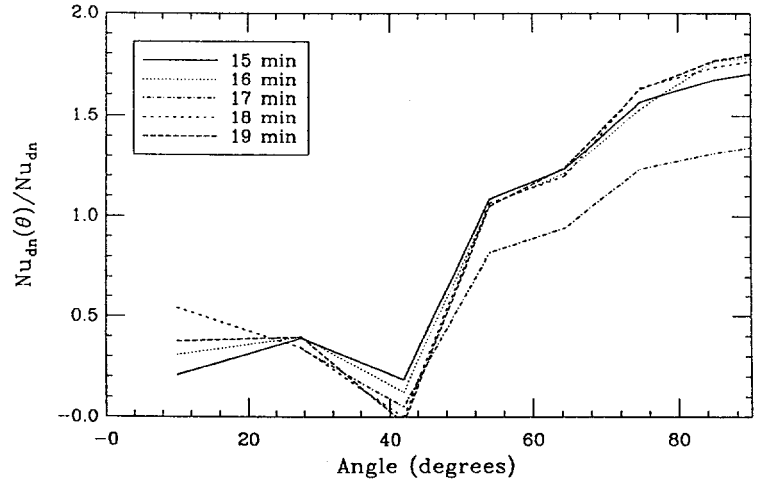

Figure D.23. Evolution of heat flux shapes with time for run A4.

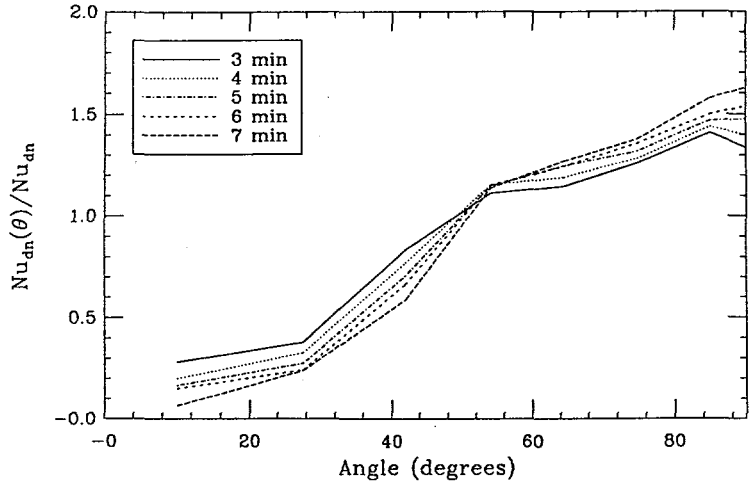

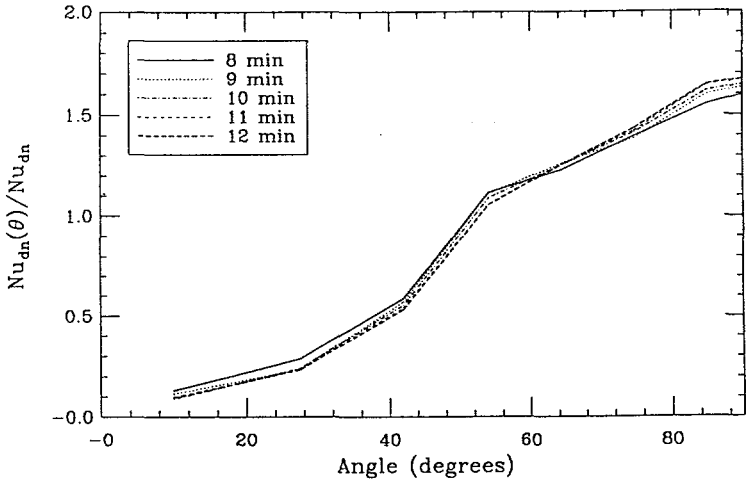

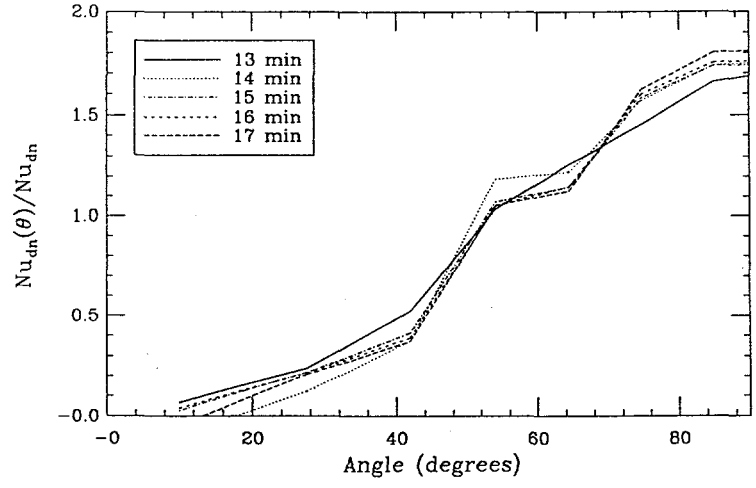

Figure D.24. Evolution of heat flux shapes with time for run A5.

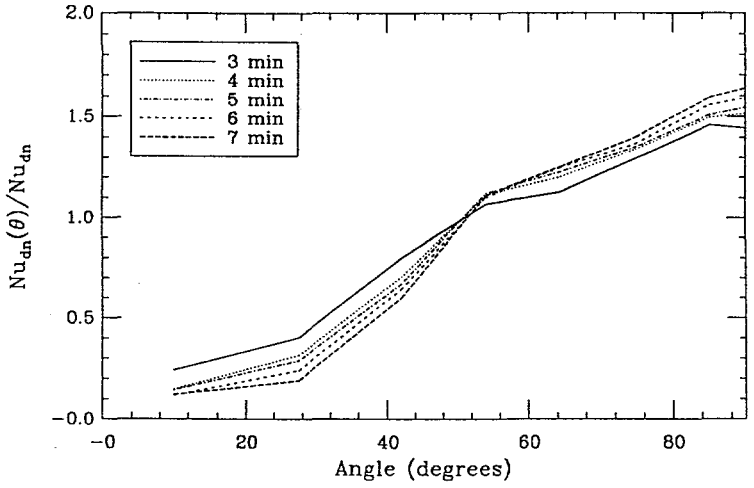

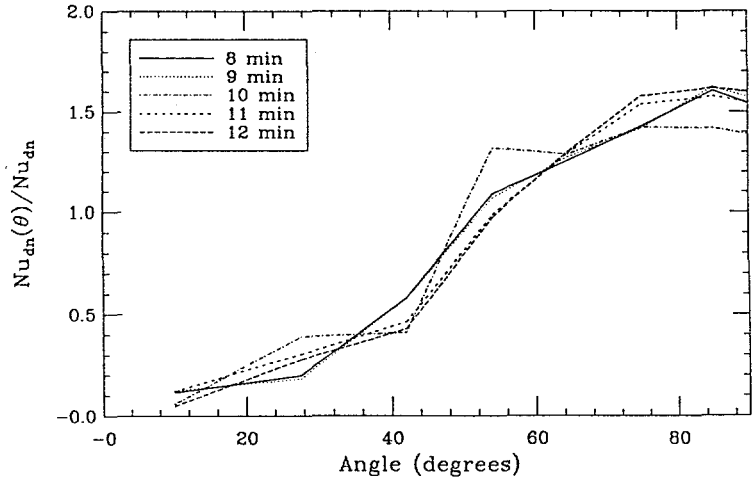

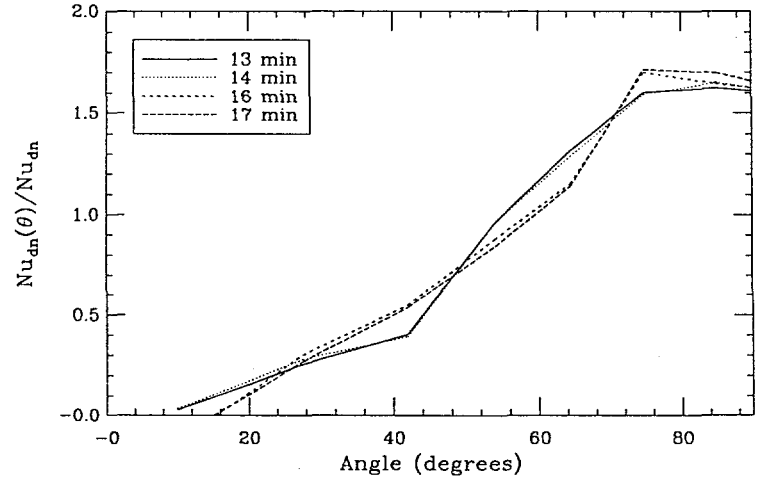

Figure D.25. Evolution of heat flux shapes with time for run A7.

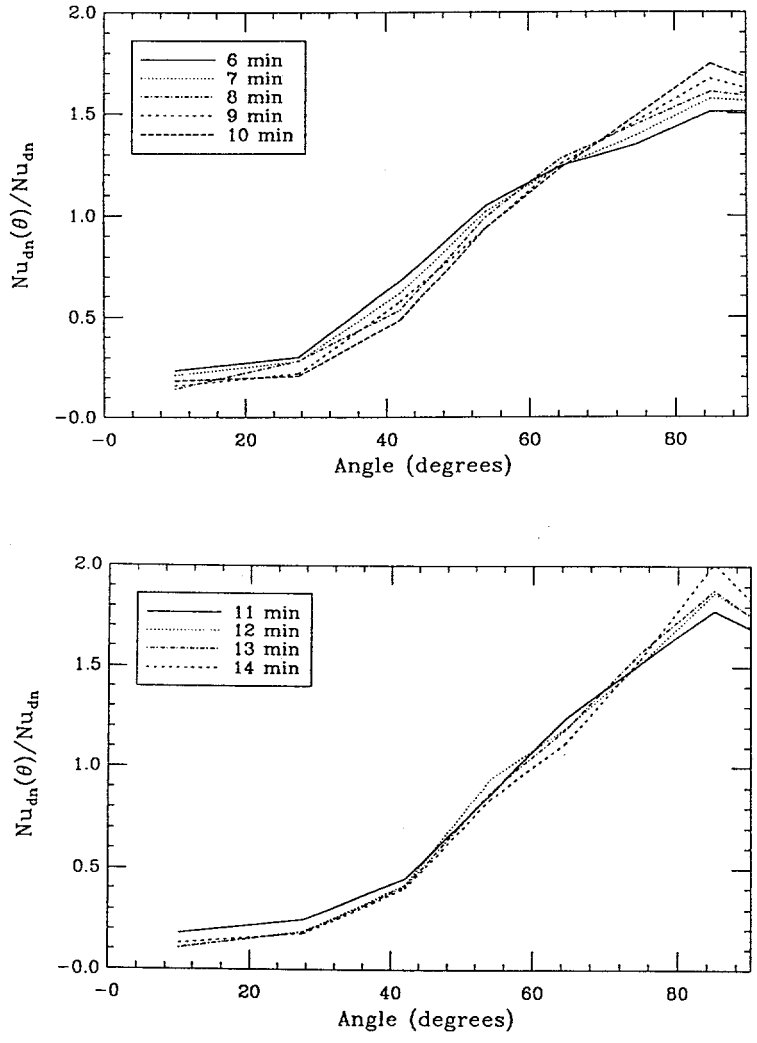

Figure D.26. Evolution of heat flux shapes with time for run A10.

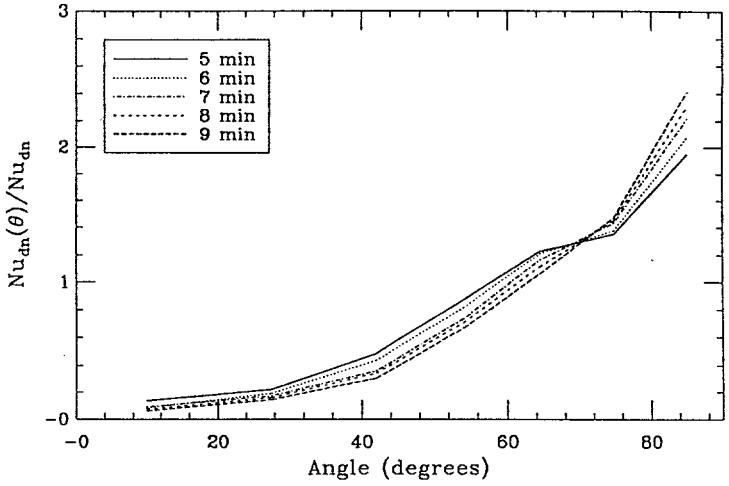

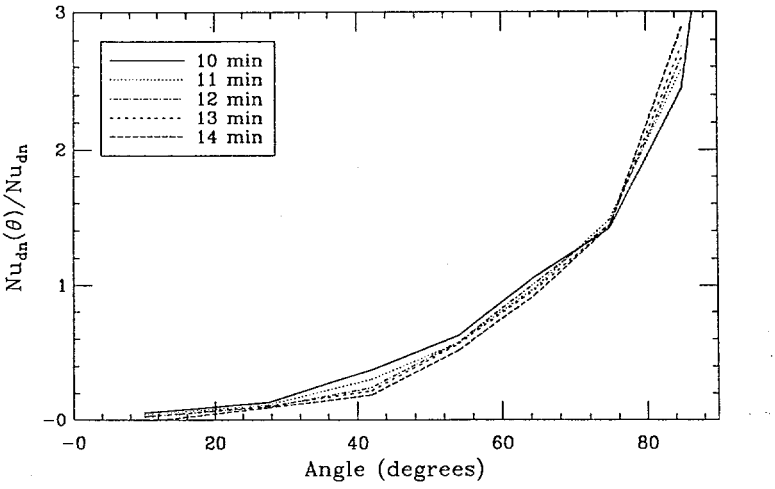

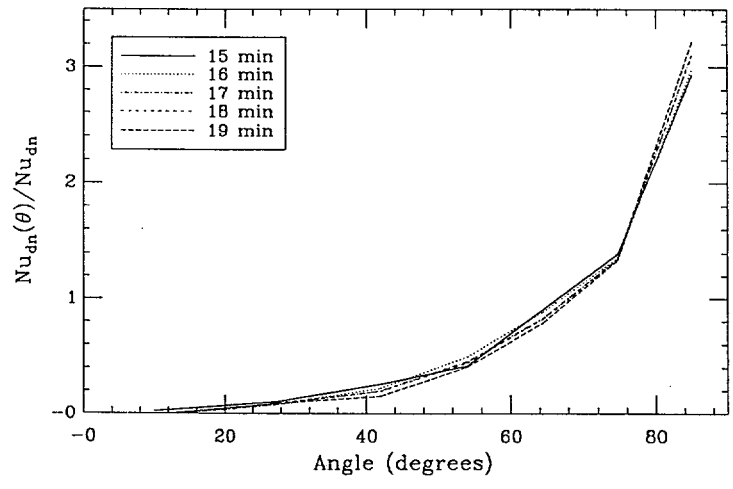

Figure D.27. Evolution of heat flux shapes with time for run A6.

APPENDIX E

THE ULPU EXPERIMENTS

This appendix consists of four parts, as follows:

E.1. Critical Heat Flux Through Curved, Downward Facing, Thick Walls

Nuclear Engineering and Design **151**, 247-258, 1994

and

E.2. The Coolability Limits of a Lower Reactor Pressure Vessel Head

Proceedings, NURETH-7
Saratoga Springs, New York, September 10–15, 1995
NUREG/CP-0142, Vol. 1, 627–647.

and

**[[E.3. Critical Heat Flux Sensitivity to Flux Shapes and]]
Recirculation Flow Rates**

and

[[E.4. ULPU Configuration III Results]]

OVERVIEW

The purpose of this appendix is to present the experimental data obtained in the ULPU-2000 facility. This facility is a large-scale upgrade of the original ULPU, built to investigate critical heat flux on extended vertical, thick walls under flow conditions relevant to the Loviisa "in-vessel retention" accident management scheme. The present ULPU-2000 facility is oriented to the curved portion of a hemispherical lower head, as in the AP600 design. The basic concept in this design is to use power shaping to effect an essentially full-scale simulation of critical heat flux (under the appropriate flow condition) in a 2-D slice; that is, a full-length quarter-circle geometry. The full elevation of the flow path, and flow phenomena in the annular space between the cavity wall and the reactor pressure vessel (the "riser"), are also simulated (in a 1-D approximation). The facility is capable of fluxes up to 2000 kW/m^2, easy recovery from film boiling without damaging the heater (that is, experiments can be run back-to-back within only a few minutes), and it allows easy visualization of the flow regimes on the heater surface and in the riser.

Experiments reported here cover two facility configurations. Configuration I is focused on the lower-most portion of the lower head, $-30° < \theta < 30°$, in a conservative representation of the coolant condition — saturated pool boiling. Configuration II is oriented to full simulation; that is, including natural convection flow and local subcooling (due to the gravity head), and the full heater arc, $0° < \theta < 90°$. While Configuration II involves an "open" access to the lower head, there are provisions also for future Configuration III testing, intended to simulate any reactor-specific vessel insulation or other reactor-specific geometric features. This appendix, then, consists of two parts,[a] corresponding to the two configurations just mentioned. The details of the experimental concept, the power shaping principle, the facility description, and the measurement techniques can be found in the early portion of the first part (E.1). The main conclusions can be summarized as follows:

With the completion of the Configuration II experiments reported here, we have established a firm estimate for the coolability limits of the lower head of a reactor vessel submerged in water and heated internally. The scale of the experiment, and the power shaping principle, ensure that these data, and resulting correlation, are directly applicable to the reactor. The correlation reveals a two-region behavior,

$$q_{cr}(\theta) = 500 + 13.3\ \theta \quad \text{kW/m}^2 \qquad \text{for} \quad \theta < 15° \tag{E.1}$$

$$q_{cr}(\theta) = 540 + 10.7\ \theta \quad \text{kW/m}^2 \qquad \text{for} \quad 15° < \theta < 90° \tag{E.2}$$

[a] [[Appendices E.3 and E.4, addressing sensitivities to recirculation flow rates and flux shapes,and reactor conditions respectively, were provided subsequently, in the course of the review.]]

which has been related to the different flow regimes observed in the two-phase boundary layer in the respective regions. The data can be equally well fit by a single equation

$$q_{cr}(\theta) = 490 + 30.2\ \theta - 8.88 \cdot 10^{-1}\theta^2 + 1.35 \cdot 10^{-2}\theta^3 - 6.65 \cdot 10^{-5}\theta^4 \quad \text{kW/m}^2 \qquad (E.3)$$

which has been used in Chapter 3 of the report.

Application of these generic results to reactor situations should consider specific aspects of the geometry and surface conditions as follows:

(a) **Geometry.** As a modifier to the Configuration II geometry, this refers to the presence of insulation, the natural circulation flow path (especially water inflow toward the lower head surface, and any restrictions to the venting of vapor), and the presence of any obstacles within the two-phase boundary layer (either mounted on the vessel as, for example, for loose part monitoring purposes, or externally imposed by something else coming to rest against the lower head during an accident). Any significant deviations from the Configuration II examined should be tested prior to using the present results. However, the Configuration I results

$$q_{cr} = 300 \quad \text{kW/m}^2 \qquad \text{for} \quad \theta < 5^\circ \qquad (E.4)$$

$$q_{cr} = 310 + 12.6\ \theta \quad \text{kW/m}^2 \qquad \text{for} \quad 5^\circ < \theta < 30^\circ \qquad (E.5)$$

provide another perspective, possibly useful if one was interested in a minimum bound realized under saturated pool boiling.

(b) **Surface Conditions.** The AP600 lower head is made of carbon steel, and the external surface is machined (to 250 rms), primed, and painted over after installation. According to the paint supplier, this coating is unstable in boiling water and would be expected to flake off soon in such an environment, exposing the as-machined metal surface. From a point of view of water wetability, we expect this surface to behave as the fully-aged copper surface tested so far in ULPU-2000. However, a prototypic piece of steel is now ready to be installed in ULPU, and we expect to fully illucidate this point within the first quarter of 1995.

[[This appendix also contains two addenda prepared simultaneously and as a part of the responses to the first round of the reviewers' comments. The first addendum is Appendix E.3. It covers the results of an extended experimental matrix in Configuration II with flux shapes that include those found in the sensitivity/parametric studies as well as variations thereof, and arbitrary variations of recirculation flow rates, obtained by throttling the inlet, to 50% of the normal ($\sim$130 gpm) flow rate, and to full stagnation. The results indicate that Eq. (E.3) is a robust conservative estimate appropriate for the evaluations performed in this report. The second addendum is Appendix E.4. It covers Configuration III experiments, built in accordance with the thermal insulation design just completed by Westinghouse (see Appendix K). In addition, this set of experiments included the effect of a prototypic heating surface, i.e., reactor vessel grade steel with and without the normally employed paint. The results once more demonstrate the roubustness of Eq. (E.3) and its applicability for our purposes.]]

APPENDIX E.1

CRITICAL HEAT FLUX THROUGH CURVED, DOWNWARD FACING, THICK WALLS

Nuclear Engineering and Design 151, 247-258, 1994.

APPENDIX E.1

CRITICAL HEAT FLUX THROUGH CURVED, DOWNWARD FACING, THICK WALLS

T.G. Theofanous*, Sanna Syri and Tony Salmassi***
Olli Kymäläinen and Harri Tuomisto****

*Center for Risk Studies and Safety
Department of Chemical and Nuclear Engineering
University of California, Santa Barbara
Santa Barbara, CA 93106, USA

**IVO International Ltd.
01019 IVO, Finland

ABSTRACT

Experimental data are presented that provide a lower envelope on the critical heat flux distribution over the external surface of a hemisphere submerged in water. The experiment was designed and run so as to provide an essentially full-scale simulation of a reactor pressure vessel lower head. Thus the data, and the correlation derived from them, can be applied directly, and they are supportive of the important severe accident management idea of retaining the core debris in the reactor vessel by external flooding ("in-vessel melt retention").

E.1 INTRODUCTION

The purpose of this paper is to make available the first experimental data directly relevant to establishing the coolability limits (critical heat flux) of reactor-scale hemispheres submerged in water and heated internally. The situation arises in the management of severe accidents, and a relatively recent idea that the relocation of molten corium could be arrested at the lower head of a reactor pressure vessel by external flooding, as illustrated in Figure E.1 (Theofanous et al., 1994). For this idea to work, it is necessary that the thermal load created by natural convection of the heat-generating pool on the inside be below what could cause a boiling crisis (BC) on the outside.

In relation to previous work on critical heat flux (CHF), the present situation involves two unique and important aspects. One is that the vapor generated by boiling remains confined by gravity within a two-phase boundary layer all along the heating surface. Flow velocities and phase distribution within this boundary layer depend very much on the local surface orientation to the gravity vector, and on the cumulative quantities of steam generated in all upstream positions. The other unique aspect is that the heating surface, typically up to 15 cm thick, has a very

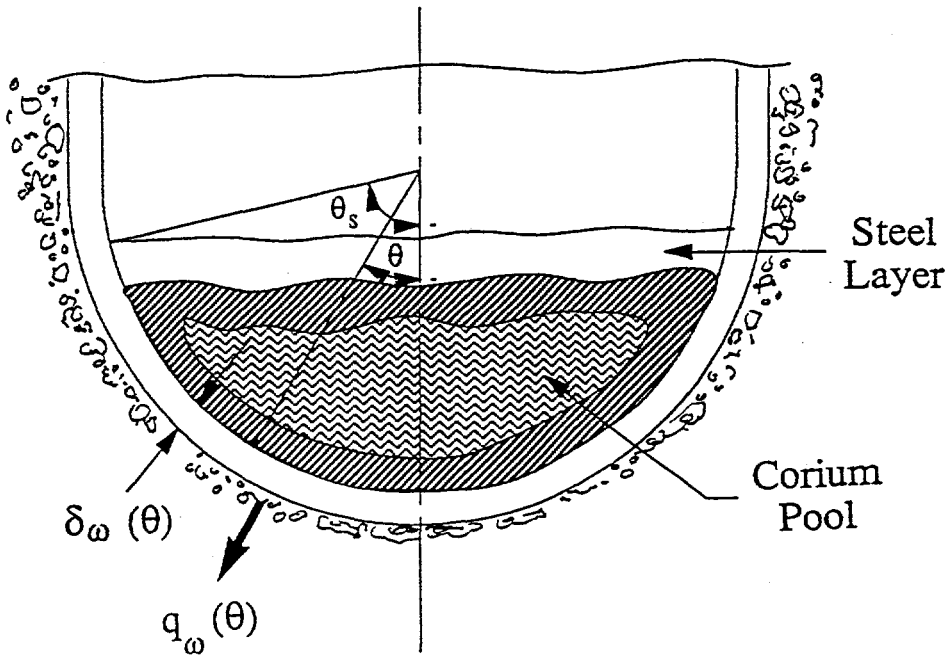

Figure E.1. Schematic of the in-vessel retention phenomenology and basic nomenclature used to describe it.

large thermal inertia. It is clear that both the hydrodynamic ("repulsive") mechanisms and the surface-thermal contributions to it (capillary-wetting effects, susceptibility to temporary/local dryouts) (Bui and Dhir, 1985) can in the present situation be significantly different from anything examined in the past—however, the initial efforts by Henry and Fauske (1993) and Chu et al. (1994) are noted.

Accordingly, we have adopted an experimental approach that is to evolve gradually from overall parametric studies and simulations (of the reactor conditions of interest), to detailed investigation of local phenomena, and thus eventually to identification of the crisis mechanism and, hopefully, to an analytical model. The emphasis on simulations in the early part of this program derives from two reasons. One is to afford an early identification and focus on the particular flow and heat transfer regimes relevant to the problem of practical interest. The other, and perhaps more important one, is that the practical need for reasonably robust estimates of CHF is imminent as reactor-specific accident management schemes are now up against key decision points and regulatory scrutiny (AP600, Loviisa). The results presented in this paper are intended to fulfill this immediate need. In addition, these results provide an initial perspective on mechanisms as a starting point for the more detailed investigations of the phenomena at the local level. It should also be noted that both of these reactors have lower heads with no penetrations, so the effects of such complications in geometry are left for future studies.

The experimental work is carried out in the ULPU facility, and the overall program involves this facility in three significantly different configurations. The overall strategy in the design of this experiment and its three configurations is given in the next section, while the details can be found in Section E.3. Experimental procedures and the test program are summarized in Section E.4. The experimental results are presented and discussed in Section E.5, and concluding remarks are provided in Section E.6.

E.2 EXPERIMENT CONCEPT

Not surprisingly, the basic concept for this experiment was derived from the unique features of the practical problem considered, as mentioned in the Introduction; namely, the thick wall and the two-phase boundary layer. The thick wall consideration is straightforward, easy to satisfy and, in fact, it leads to certain important conveniences (in comparison to thin walls) in both the construction and experimentation, as described in the following two sections. For the two-phase boundary layer, we wish to match, in the experiment, its local structure and dynamics to the local surface inclination, as they are to be found in the prototype, all along the vertical arc length from $\theta = 0°$ to $\theta \sim 90°$. This cannot be accomplished in sub-scale models, while a full-scale representation (in an experiment with prototypic heat flux at all locations) is clearly impractical, if not impossible.[a] The approach used takes advantage of the axial symmetry in the prototype, in combination with a power-shaping approach in the experiment. The axial symmetry allows a "pie" segment representation of the hemisphere, but this is still, for a variety of reasons, a formidable experimental geometry to work with. By power-shaping we can effectively represent the flow behavior in such a pie segment with a uniform (in thickness) vertical slice, which, as it turns out, is experimentally feasible. We call this a "full-length" representation. A key conclusion of this paper is that this representation affords an essentially perfect full-scale simulation.

Our task is to conduct simulation experiments that allow the determination of the critical heat flux $q_{p,cr}$, in the reactor, as a function of the angular position θ under the constraint of a specified power shape, say $q_p(\theta)$. Our approach is to make this determination for a discrete set θ_{mi} $i = 1 \ldots n$ of values of the angular position, by a corresponding set of experiments, each simulating the prototype for the particular angular position considered. *For this we set*

$$q_{p,cr}(\theta_m) = q_{e,cr}(\theta_m) \qquad (E.1)$$

[a] A full scale test with a torospherical lower head, in the CYBL facility, demonstrated a nucleate boiling condition for uniform heat fluxes up to 200 kW/m^2 (under subcooling corresponding to the gravity head).

and require (i) that the superficial vapor velocities (expressed as volumetric flow rate per unit width) match up with those of the prototype for all $\theta > \theta_m$, and (ii) that for $\theta < \theta_m$ the vapor flow rates build up gradually, so as to smoothly approach the value required at $\theta = \theta_m$, while allowing a "natural" development of the boundary layer in all of the upstream region. By satisfying these requirements, we ensure that the two-phase boundary layer is properly driven in a broad neighborhood of the location under consideration (θ_m) as well as all of the downstream region.

The situation is somewhat complicated by the presence of subcooling and the dynamic aspects of vapor production and (partial) collapse. In the following, the derivation is limited for convenience to saturated and steady conditions. It can be easily seen that that the same results can be obtained under moderate subcoolings, as in the case of interest here, if one considers the total energy (sensible plus latent) flow per unit width, which, in turn, provides a more generalized similarity criterion, reflecting the fact that the convected sensible heat is also important in the local behavior of the two-phase boundary layer.

The relation of the constant-width test section to the pie-segment geometry is illustrated in Figure E.2. Let the superficial vapor velocity, at position θ, be denoted by $J(\theta)$. One possible way of meeting the above requirements is by selecting, in the upstream region:

$$q_e(\theta) = q_p(\theta)\frac{W(\theta)}{W(\theta_m)} = q_p(\theta)\frac{\sin\theta}{\sin\theta_m} \qquad \text{for } \theta \leq \theta_m \tag{E.2}$$

For saturated conditions (no condensation), the superficial velocities can thus be written as:

$$J_e(\theta) = R'\int_0^\theta q_p(\theta')\frac{\sin\theta'}{\sin\theta_m}d\theta' \tag{E.3}$$

$$J_p(\theta) = R'\frac{W_m}{W(\theta)}\int_0^\theta q_p(\theta')\frac{\sin\theta'}{\sin\theta_m}d\theta' \tag{E.4}$$

and their relative deviation can be derived to be:

$$\frac{\Delta J(\theta)}{J_p(\theta)} \equiv \frac{J_p(\theta) - J_e(\theta)}{J_p(\theta)} = 1 - \frac{\sin\theta}{\sin\theta_m} \tag{E.5}$$

This relation is shown in Figure E.3, which also includes the upstream lengths within which the "distortion" in the superficial vapor velocity is less than 10% or 20%. For θ_m as small as 10°, the simulation is deemed to be acceptable, and it improves drastically as θ_m increases, especially beyond 40°. Interestingly enough, it is this outer region, $40° < \theta < 90°$, in which cumulative vapor flow can be expected to be the most important.

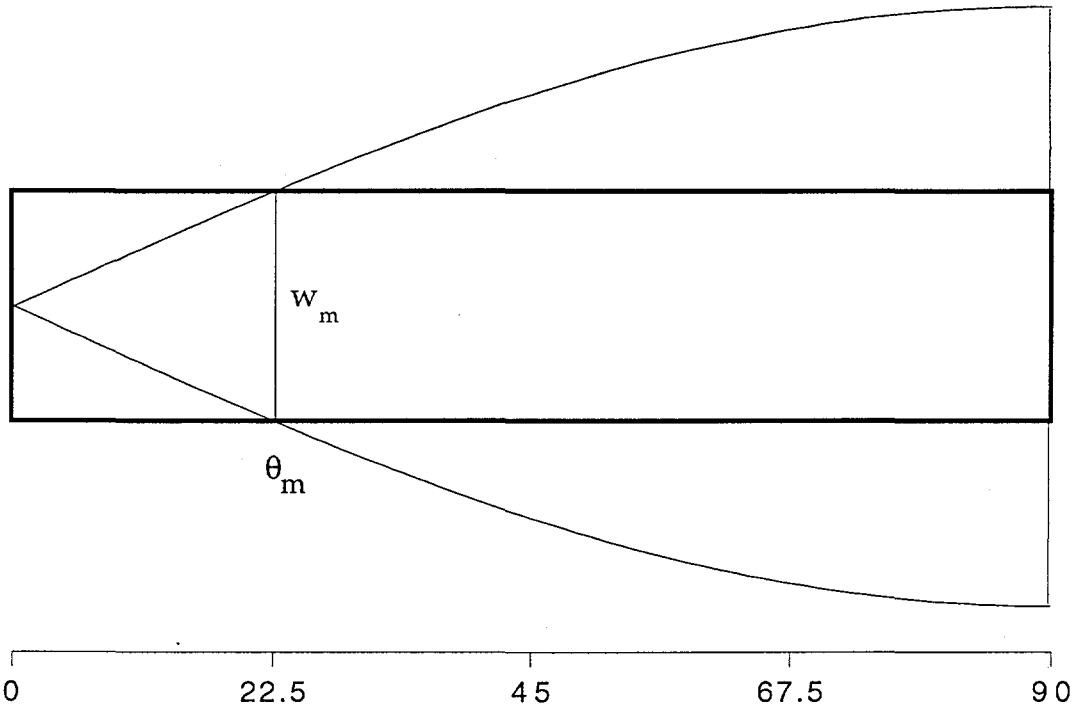

Figure E.2. Geometric relationship between the constant-width test section in ULPU and the pie-segment geometry, deduced from axial symmetry, for simulation. Both are shown unfolded, and θ_m is the position at which the CHF is simulated.

The inner region, $0° < \theta < 10°$, can also be approached from a flux-matching standpoint alone; that is, by applying a uniform heat flux and setting

$$q_{p,cr}(0) = q_{e,cr}(0) \tag{E.6}$$

is negligible and the most limiting CHF position is at $\theta \sim 0°$. We do not expect cumulative vapor flow effects to be important here, but it can be readily shown that now

$$\frac{\Delta J}{J_p} = \frac{1 - \cos\theta - \theta \sin\theta}{1 - \cos\theta} \sim -1 \qquad \text{for } 0° < \theta < 10° \tag{E.7}$$

and if anything, this strategy should provide a conservatively biased simulation for this region.

For the downstream region, the similarity of local superficial velocities requires that, for any position $\theta > \theta_m$,

$$J_p(\theta_m)\frac{W(\theta_m)}{W(\theta)} + \int_{\theta_m}^{\theta} q_p(\theta')\frac{W(\theta')}{W(\theta)}R'd(\theta') = J_p(\theta_m) + \int_{\theta_m}^{\theta} q_e(\theta')R'd\theta' \tag{E.8}$$

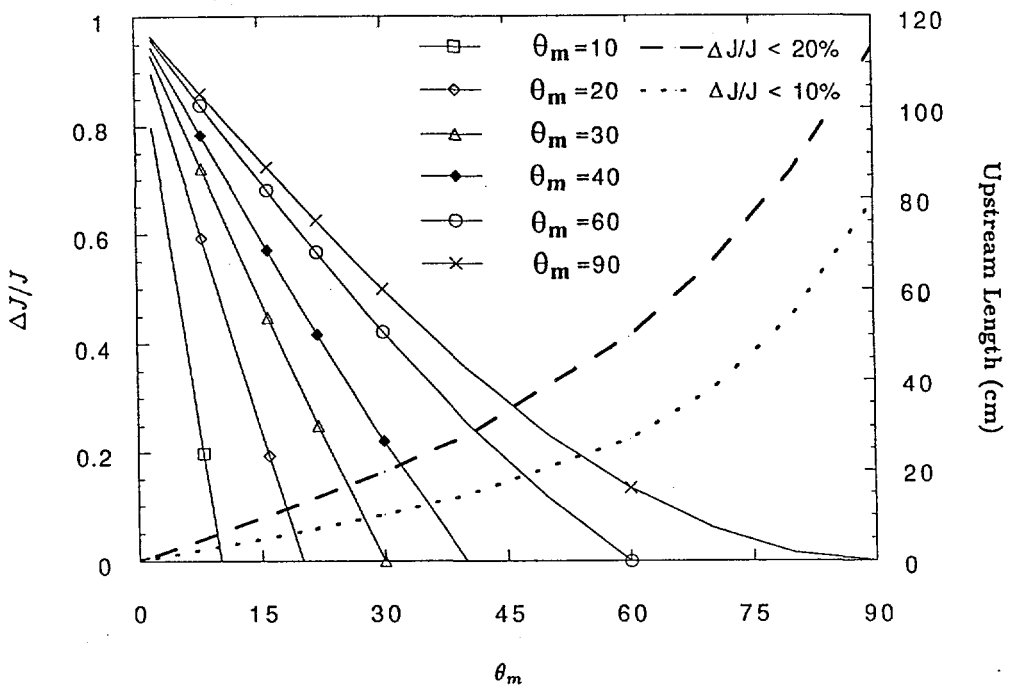

Figure E.3. Illustration of the distortion $\Delta J/J_p$ in superficial vapor velocity, as a function of upstream position, for various matching positions, θ_m. Also shown are the upstream lengths within which the distortion is less than 10% or 20%.

which can also be written somewhat more explicitly as

$$\int_{\theta_m}^{\theta} q_e(\theta')d\theta' = \bar{\bar{q}}_p\,(1-\cos\theta_m)\left\{\frac{1}{\sin\theta}-\frac{1}{\sin\theta_m}\right\}+\frac{1}{\sin\theta}\int_{\theta_m}^{\theta} q_p(\theta')\,\sin\theta' d\theta' \qquad (E.9)$$

where $\bar{\bar{q}}_p$ is an "average" flux over $0 < \theta < \theta_m$ defined by

$$\bar{\bar{q}}_p = \frac{\sin\theta_m}{W_m(1-\cos\theta_m)}\int_0^{\theta_m} q_p(\theta')W(\theta')d\theta' \qquad (E.10)$$

In the region $0° < \theta_m < \theta < 30°$, which is of interest in the experiments presented here, and the relatively uniform $q_p(\theta)$ within it (see below), Eq. (E.9) can be shown to reduce to the simple result

$$q_e(\theta) \sim \frac{1}{2}q_p(\theta) \qquad \theta_m < \theta < 30° \qquad (E.11)$$

and it is interesting to note that this creates a discontinuity with Eq. (E.1) at $\theta = \theta_m$. This discontinuity arises because of the requirement to match the superficial velocity as well as the critical heat flux at θ_m, and the need for choosing something like Eq. (E.2) for doing so. As we will see in Section E.4, this discontinuity can be represented in the heater design selected,

exactly at $\theta = 30°$ or $60°$, and approximately at all other positions. Moreover, the importance of satisfying the downstream conditions can be checked by means of sensitivity runs around the result of Eq. (E.9).

Local subcooling and vapor condensation effects clearly enhance the critical heat flux. To understand this behavior, we follow a two-pronged approach. One prong is to obtain a lower bound by running experiments at saturated, pool boiling conditions. The other prong is to allow for a natural convection flow loop in which the downcomer fluid, while saturated at the top of the facility, attains a subcooling equivalent to the gravitational head at the bottom of the test section. An important condition for this second set of experiments is to simulate the vertical void fraction profile over the entire length of the reactor vessel; it depends on the vapor supplied due to direct heating through the lower head, plus the vapor created all along the vertical vessel walls which are radiatively heated from the top of the molten corium pool (see Figure E.1). An important object of these experiments is to determine the radial distributions (distance from the wall) of local subcooling and their evolution from $\theta = 0°$ to $\theta = 90°$.

Based on the above considerations, we arrive at the conceptual design, involving three distinct experiment configurations, as illustrated in Figures E.4 and E.5. Configuration I (to be denoted by C (I)) is for studying saturated, pool boiling in $-30° < \theta < 30°$, and especially in the region around $\theta \sim 0°$, which is not as well represented in the other configurations. Configuration II (C (II)) is for simulating the complete geometry (a full one-quarter circle) under both loop flow (including the effects of subcooling) or pool boiling (saturated) conditions. As seen in Figure E.5, this configuration is to represent an open-to-the-cavity geometry. A channel geometry, as it might arise from particular thermal insulation designs with an inlet at the very bottom ($\theta \sim 0°$), can be created by introducing a baffle, as illustrated in Figure E.5, to obtain Configuration III (C (III)). In this paper we present data from Configuration I only.

E.3 DETAILED DESCRIPTION OFTHE EXPERIMENT

The experiment (ULPU-2000) and the related technology in building the heater blocks evolved from the original ULPU work which was aimed at the vertical (side) wall of the reactor vessel and the exit restriction of the natural convection path in the Loviisa reactor (Kymäläinen et al., 1992). In that experiment the heater was limited both by design and available power to 1400 kW/m^2, and CHF could not be reached for the range of conditions investigated. In the present experiment, both the power and the heater design were upgraded to allow a peak flux of 2000 kW/m^2, hence the name ULPU-2000. Another important requirement in the present experiment, as explained in the previous section, was to have control of the power shape over the whole extent of the heater surface, which is to cover, in Configurations II and III, the region

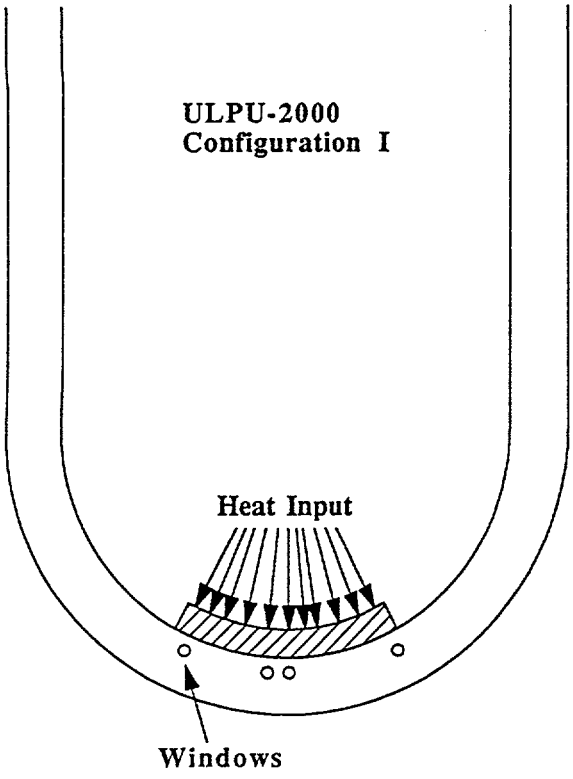

Figure E.4. Schematic of Configuration I in ULPU-2000. The heater blocks extend over the region $-30° < \theta < 30°$.

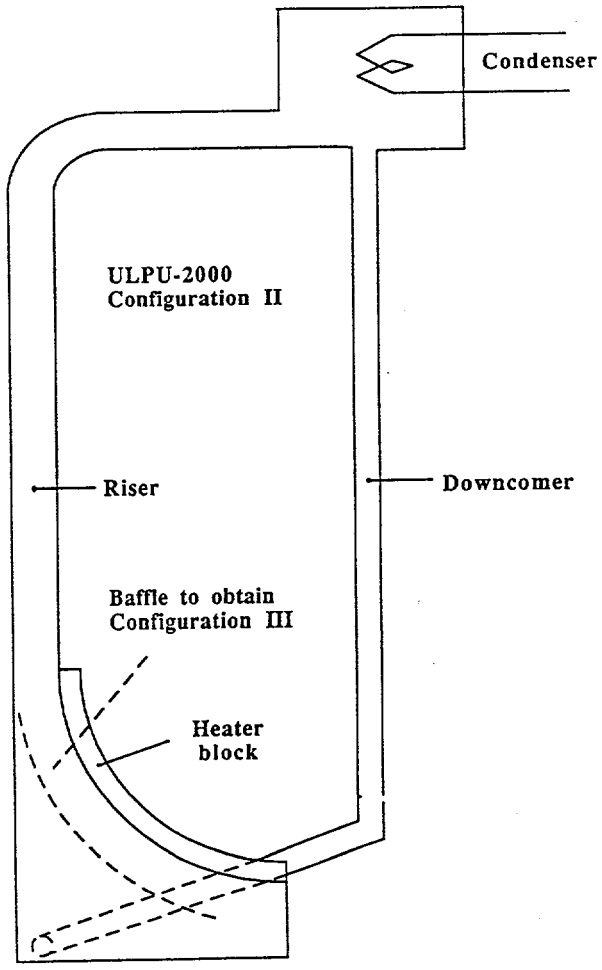

Figure E.5. Schematic of Configurations II and III in ULPU-2000. The heater blocks extend over the region $0° < \theta < 90°$.

$0° < \theta < 90°$; that is, a much larger physical dimension than in the original ULPU. Finally, certain important improvements in the installation of the heater blocks were made to essentially eliminate lateral losses and hence any departures from the desired 1-D behavior (i.e., heat flux and temperatures varying only with angle θ).

Three heater blocks were built, each covering, nominally, a 30°arc of a circle, with a radius of curvature of 1.76 m, which is well within the range of typical reactor dimensions. The actual arc is 27°, for a total length of 0.83 m. The block height and width were chosen as 7.6 cm and 15 cm, respectively, such as to ensure sufficient thermal inertia and to minimize side-wall effects. One such block is illustrated in Figure E.6, and in a photograph, prior to assembly, in Figure E.7. The holes are 9.5 mm in diameter and allow two cartridge heaters (per hole) to be inserted, one from each side. The "fit" must be very good, while precision machining is also required in the accurate positioning of the holes, the 1.5 mm in diameter holes needed for the thermocouples, and the forming at the smooth, curved faces. Copper stock was selected as the raw material. Voltage (217 V) is supplied to the cartridge heaters through 32 relays which are individually computer controlled to cycle in the "on-off" positions so as to obtain any desired power distribution on the heater block.[b] The total power obtained by summing the calculated power of each cartridge (from the voltage applied, the known resistivity, and the fractional "on"-time), agreed to within 1% of the total power supplied by the power generator. In Configuration I, we have used two heater blocks (Figure E.4), which allows up to 16 power zones on each block. In fact, such fine resolution is unnecessary, and we use only eight power zones (i.e., 3.375° arc each). Temperatures are measured at eight corresponding positions along the length of each block.

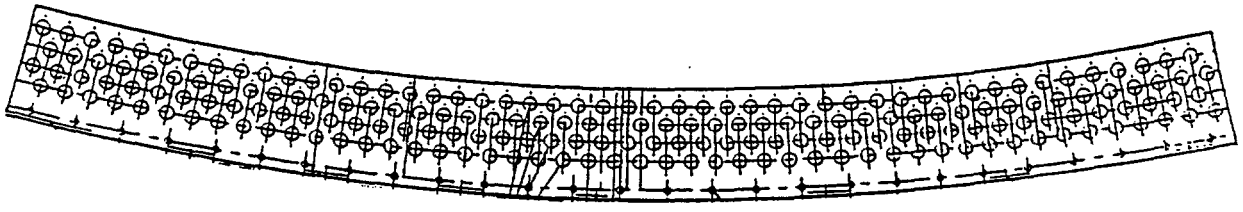

Figure E.6. Heater block design, showing the holes for the cartridge heaters and the thermocouples.

[b] In all experiments the cycling time was 3.52 s, which is small when compared to the conduction time constant of the copper block (58 s).

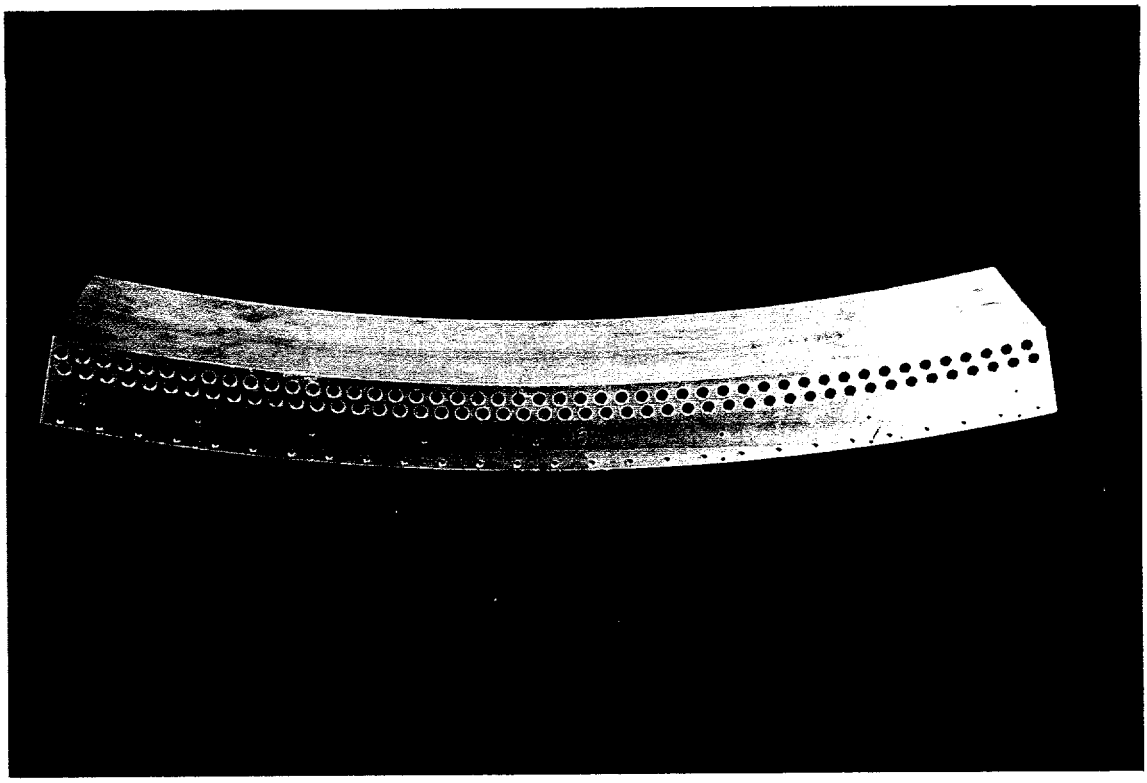

Figure E.7. One of the heater blocks immediately after machining.

In Configuration I, each heater block fits onto the one (open) side of a similarly curved channel of a rectangular cross-section (15 cm on the side), as illustrated in Figure E.8. During operation, the blocks and channels are well insulated, and relative losses to the outside have been estimated to be negligible. On the sides the blocks overlap with the 2.5 mm stainless steel channel walls by approximately 13 mm, with a rubber gasket in between. Absence of steep temperature gradients in this region assures that any "bypass" losses to water are also negligible, and this is confirmed by the near-perfect agreement of the four thermocouples placed along the width of the heater block at each of the eight "axial" positions. As seen in Figure E.4, the channels are equipped with windows, for visualization. Also, the channels are equipped with thermocouple "trees" arranged at various key positions ($\theta = 0°$, $\theta = 30°$, etc.) to measure water temperatures. The overall experiment in Configuration I is shown in Figure E.9. At the ends of the U-tube [[15 cm each leg inside diameter]], we have installed condenser coils so that the facility can be operated open to the atmosphere without significant loss of steam (reflux mode operation).

The exact positioning of the thermocouples, the heating zones, and the related nomenclatures used in the subsequent discussions are given in Figure E.10.

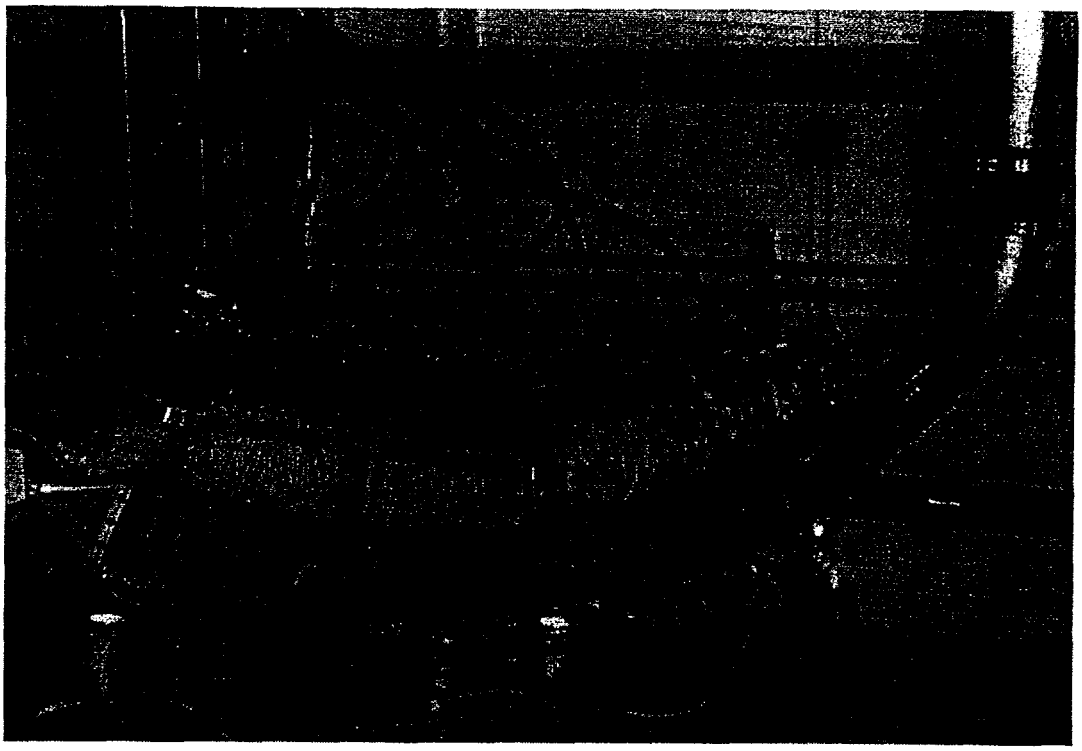

Figure E.8. The test section of Configuration I.

E.4 PROCEDURES AND TEST PROGRAM FOR CONFIGURATION I

An approach to the boiling crisis can be recognized quite easily by sporadic, small (in both amplitude and duration) departures of thermocouple signals; usually following a small increase in power level, a steady excursion indicating boiling crisis is observed. In taking data the aim is to bracket the CHF between a value where BC occurs and a value which can be sustained for a sufficiently long time (see next section). The power, power shape, and all thermocouple signals are recorded (at 0.5 Hz) so that a complete documentation of each run is retained.

Video records before, during, and after BC are also obtained. This is possible because of the high heater thermal inertia which allows operation well past the BC. The temperature excursion can be arrested at will (by reducing the power); rewetting can easily be established; and experimental runs basically can be made back-to-back. This greatly facilitates the search for narrowing the range between the CHFs and the fluxes at which nucleate boiling persists.

All experiments but one in the Configuration I program were run with saturated water at a height of between 1.2 and 1.8 m in the U-tube, measured above the heater surface at $\theta = 0°$. The one "other" run was made under transient subcooling conditions; that is, starting with a water temperature of 20 °C and holding the power constant so as to deliver a uniform heat flux

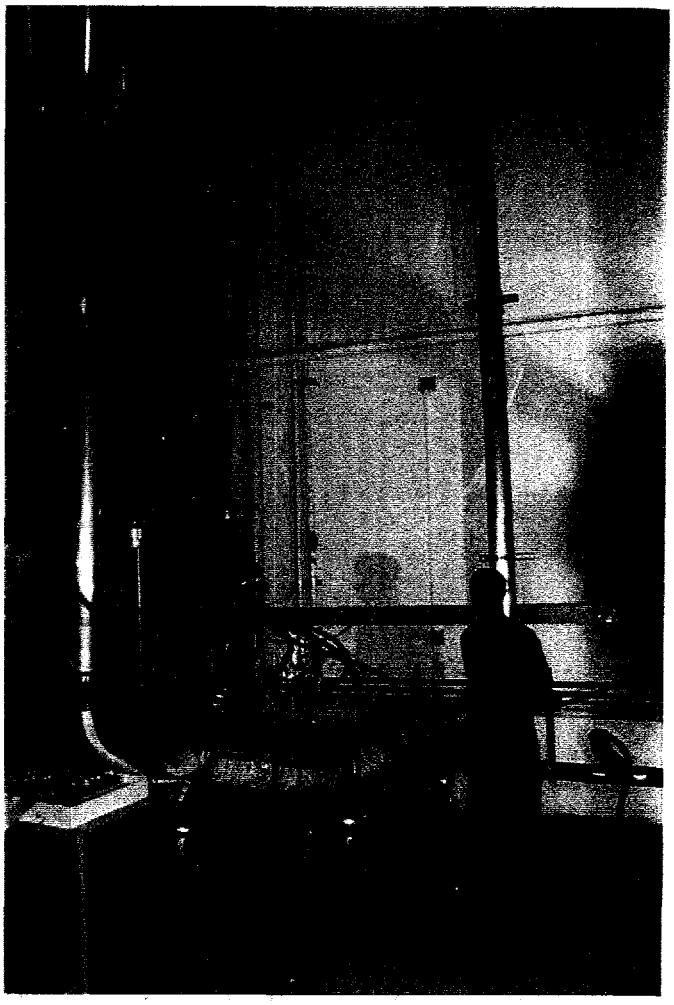

Figure E.9. An overall view of ULPU-2000 in Configuration I.

of 400 kW/m^2. The saturated water runs can be distinguished by the power shape employed. One group involves a simulated flux shape, as discussed in Section E.2, and consists of three subgroups, corresponding to CHF "matching" at zones 1, 3, and 5. These runs are denoted by the heating zone at which the matching condition is specified. That is, run SF-3 means a flux shape simulating CHF at heating zone 3 ($18.75° < \theta < 22.5°$). The other group is aimed at the region $\theta \sim 0°$ (zone 8), and it was approached in three different ways, all employing a uniform flux around $\theta \sim 0°$, but with different shapes in the downstream region. These runs are indicated by the last included zone of the uniform power segment, and the fractional power applied to the downstream region. Thus, run UF-6-50% means a uniform flux in the region of zones 8, 7, and

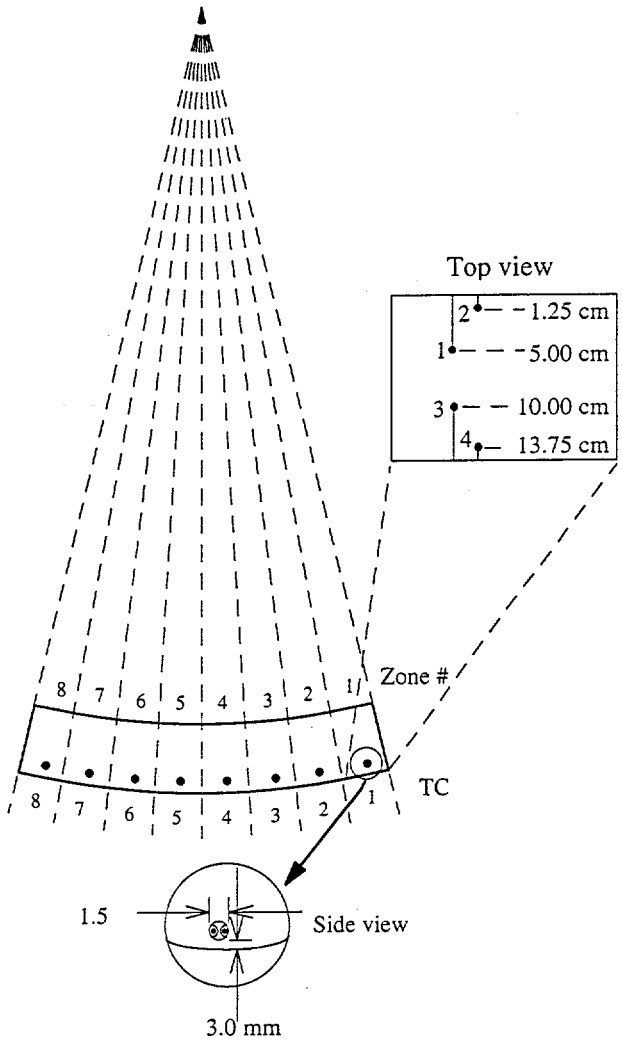

Figure E.10. The heating zones and thermocouple positions on a heating block. In Configuration I zone 8 of each heating block is adjacent to $\theta = 0°$, and zone 1 at $\pm 30°$.

6 ($-11.25° < \theta < 11.25°$) and 50% of this flux applied to the remainder of the heater blocks. Repeat runs are shown by the number in parenthesis at the end as, for example, by SF-3 (1), UF-6-50% (3), etc. The whole experimental program in Configuration I is summarized in Table E.1.

The reference reactor power shape (Theofanous et al., 1994) and the shape used in the simulations are shown in Figure E.11 — the flat portion is due to the steel layer on top of the corium pool. Clearly, in the absence of the $30° < \theta < 90°$ regions, these are only partial simulations; however, within the context of the Configuration I program, they are believed to be appropriate. The calculations were carried out with Eq. (E.9), and the resulting "wanted" flux shapes for runs SF–5, SF–3, and SF–1 are shown in Figures E.12, E.13, and E.14, respectively. These figures also show the fluxes delivered to each of the heating zones, and the resulting,

Table E.1. Summary of the Experimental Program in Configuration I, ULPU-2000, and Related Nomenclature

Group	Subgroup	Remarks
SF	SF–5	4 runs
	SF–3	4 runs
	SF–1	4 runs
UF	UF–1–0%	4 runs
	UF–5–0%	1 run
	UF–6–0%	2 runs
	UF–7–0%	2 runs
	UF–5–50%	1 run
	UF–6–50%	4 runs
	UF–7–50%	1 run

actual, fluxes following the "smoothing" effect of axial conduction. The latter were obtained by numerical simulations of 2-D conduction in the heater blocks using the boundary conditions determined in the respective experiments. From these figures, we obtain the correction factors of 0.85, 0.89, and 0.95 for converting peak input to actually delivered peak fluxes for the three cases respectively. (The data reported in the next section incorporate this correction.) These figures also show the discontinuity at $\theta = \theta_m$ mentioned in Section E.2. Because the heater blocks can be insulated from each other, it is easy to see that the discontinuity can be represented exactly at 30° and 60° (in Configuration II or III, of course). In all interior points the discontinuity can be represented approximately (because of axial conduction), but it is noted that Figures E.12 and E.13 are only illustrative of the experimental capability — no special efforts were made to represent the discontinuity quantitatively in these partial simulations in Configuration I. That is, the delivered "discontinuity" can be improved by suppressing even further the downstream power levels to the test section, as illustrated, for example, in Figure E.15, made to show the behavior in the UF-series of runs. (Here the position $\theta = 0°$ is of interest, and as seen in the figure, the correction due to axial conduction is negligible in all cases.) Returning to the internal discontinuity, it may be of interest to note that the "wanted" fluxes in Figures E.12 and E.13 do not appear to exactly follow Eq. (E.11). This is because of the finite discretization combined with the increasing trend of the prototypic flux shape (see Figure E.11), especially for $\theta > 15°$.

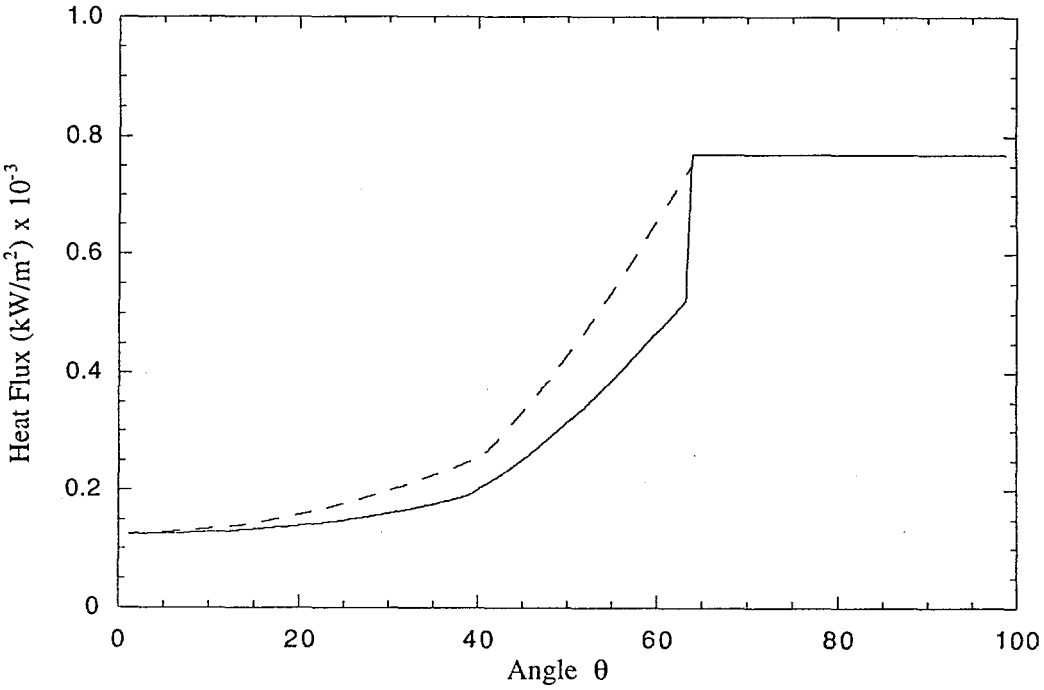

Figure E.11. The reference reactor heat flux shape (——) (from Theofanous et al., 1994), and the shape used in the simulations (– – –).

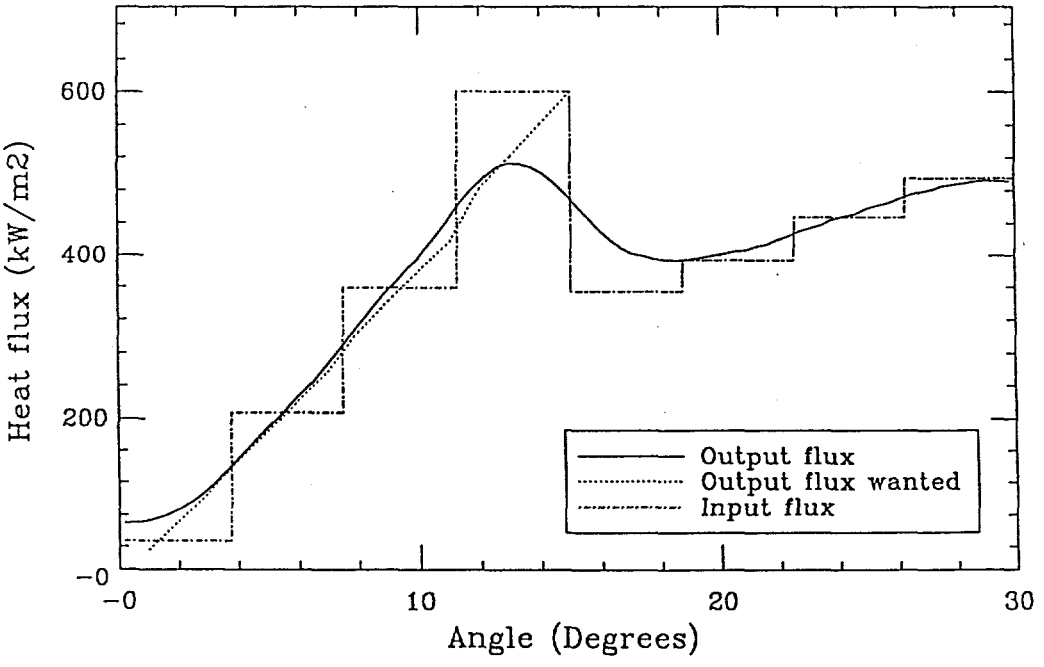

Figure E.12. The wanted, input-equivalent, and the actual heat fluxes for runs SF-5.

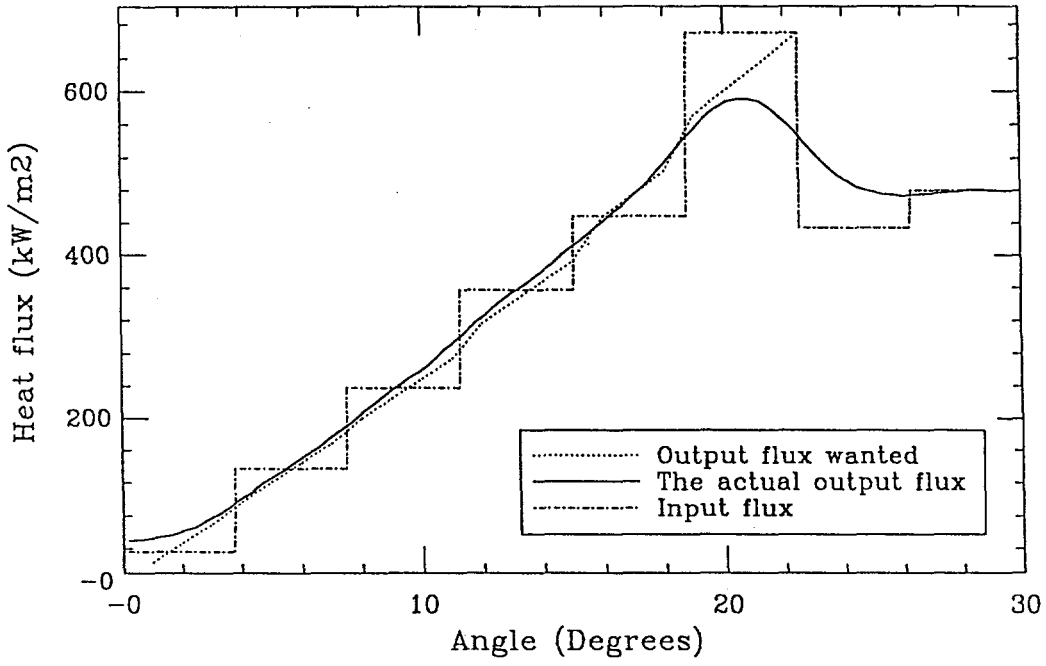

Figure E.13. The wanted, input-equivalent, and the actual heat fluxes for runs SF-3.

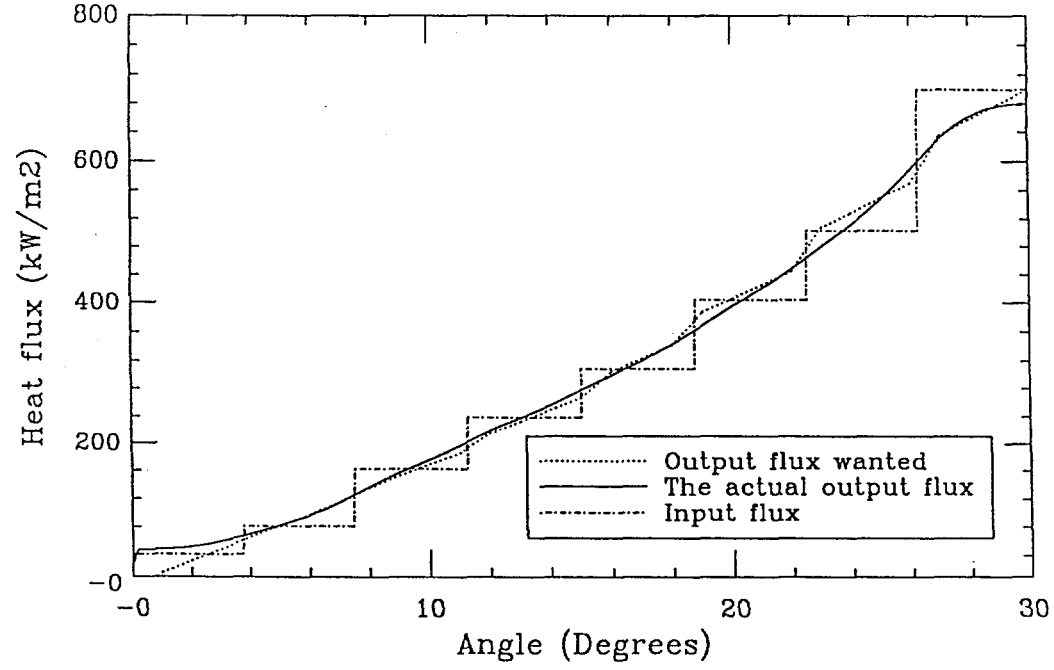

Figure E.14. The wanted, input-equivalent, and the actual heat fluxes for runs SF-1.

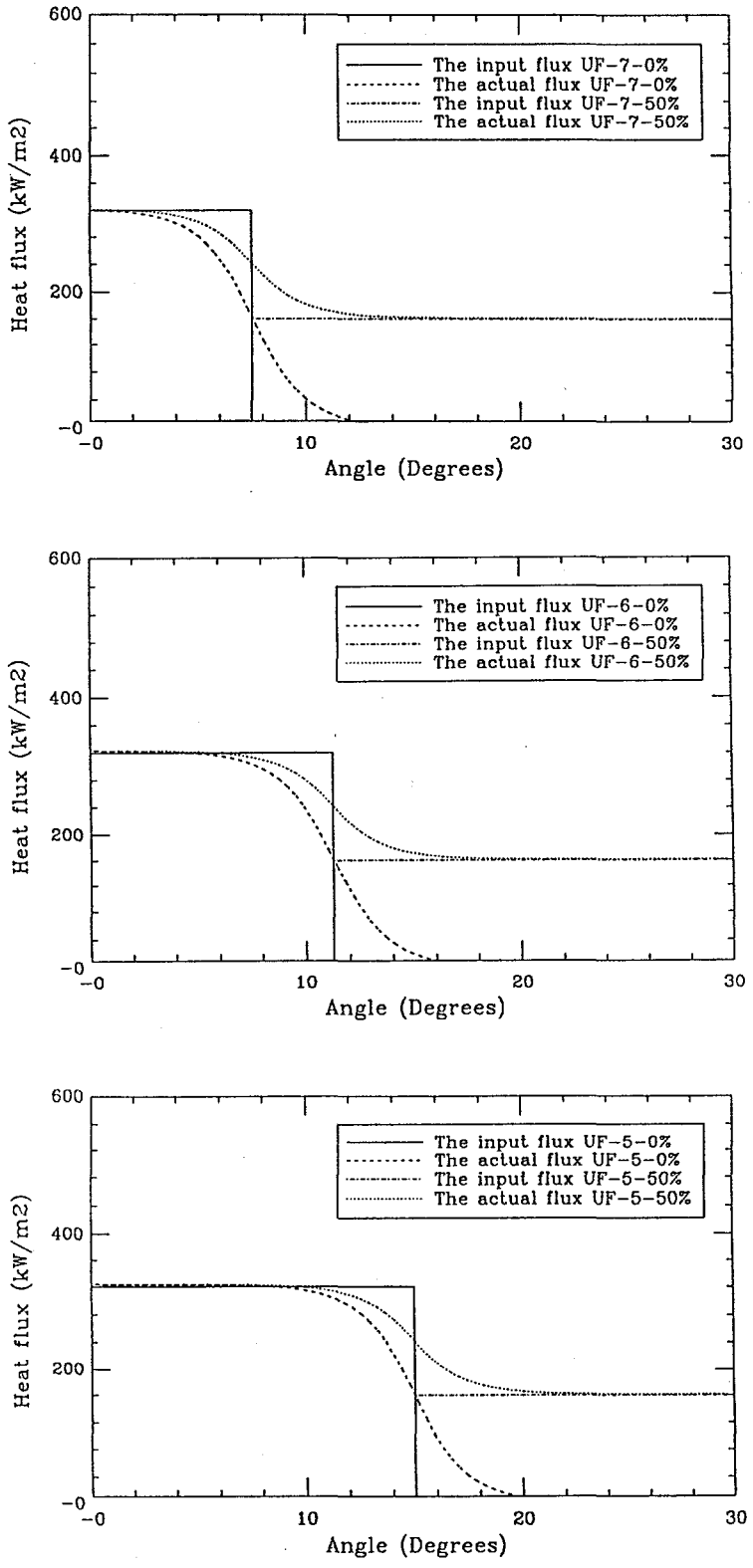

Figure E.15. The input-equivalent and actual heat fluxes delivered in all UF-series of runs. (a) Runs UF–7–0% and UF–7–50%, (b) runs UF–6–0% and UF–6–50%, (c) runs UF–5–0% and UF–5–50%.

E.5 EXPERIMENTAL RESULTS AND DISCUSSION

In the early shakedown experiments we saw successively increasing values of CHF over a period of one week. Having started with a clean, polished heater surface, this was due to the expected aging effects. Eventually this behavior stabilized, and since our interest is for a fully-aged carbon steel surface, only then did we enter the the actual test program described in the previous section.

The thermocouple behavior during the approach to CHF and beyond its occurrence is illustrated for a typical case in Figure E.16. In each run we approached CHF from above, or from below, seeking the lowest flux yielding CHF and the highest flux at which nucleate boiling would persist indefinitely. Quite soon it became apparent that the behavior is asymptotic. That is, small reductions in power below some level produce increasingly delayed BCs, as illustrated for the case of a series of UF–6–50% runs in Figure E.17. On this basis the nucleate boiling data points were obtained after a 50 min wait in nucleate boiling, and they may be taken to represent a reasonably conservative lower bound for CHF. In addition, a set of 120 min wait runs were made, at the end, to provide a more definitive lower bound. One might think of these latter data as corresponding to deterministically impossible CHF. The delay time may provide important clues on the mechanisms, but quantitatively it is not so important in that it spans a less than 10% effect on the magnitude of CHF.

The data from all runs performed are summarized in Figure E.18 and in Table E.2. The most important and interesting observation is that the simulation runs at positions 5, 3, and 1 line up well among themselves and also with the lower bound of the UF runs at $\theta \sim 0°$. The other key point is that even with rather wide variations in the downstream flux shape in the UF-series of runs, a reasonably consistent behavior, and lower bound of approximately 300 kW/m^2 in CHF is quite evident. The boundaries for the two CHF bounds defined above, as determined from the respective data sets, are shown in Figure E.18, and they can be described by:

conservative bound

$$\begin{aligned} q_{cr}(\theta) &= 300 \text{ kW/m}^2 \quad \theta < 5° \\ &= 300 + 12.6\theta° \text{ kW/m}^2 \quad 5° < \theta < 30° \end{aligned} \tag{E.12}$$

deterministic bound

$$\begin{aligned} q_{cr}(\theta) &= 276 \text{ kW/m}^2 \quad \theta < 5° \\ &= 276 + 12.6\theta° \text{ kW/m}^2 \quad 5° < \theta < 30° \end{aligned} \tag{E.13}$$

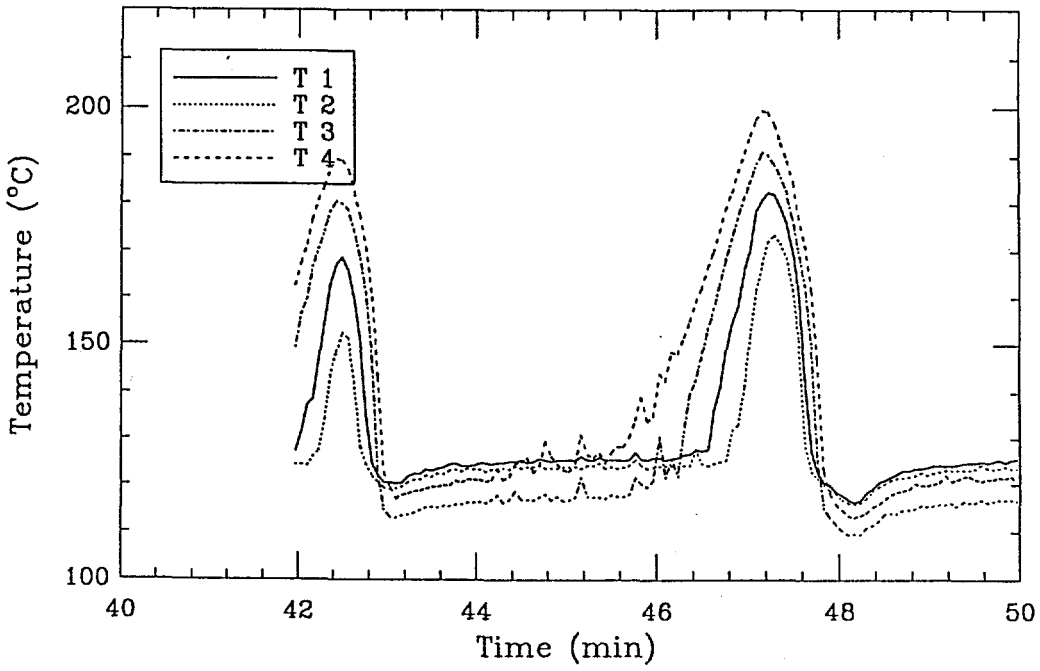

Figure E.16. Heater surface temperature behavior as critical heat flux is approached, and the excursion associated with its occurrence. Test SF–3 (1), zone 3, thermocouple position as shown in Figure E.10.

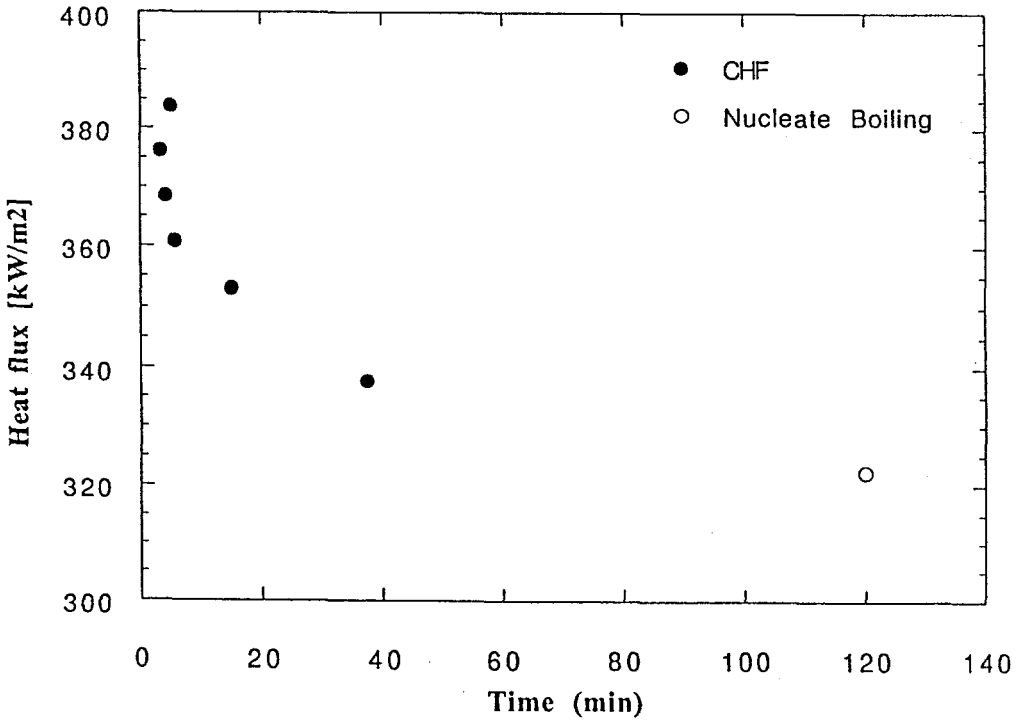

Figure E.17. Illustration of the asymptotic CHF delay time behavior, in the UF–6–50% series of tests.

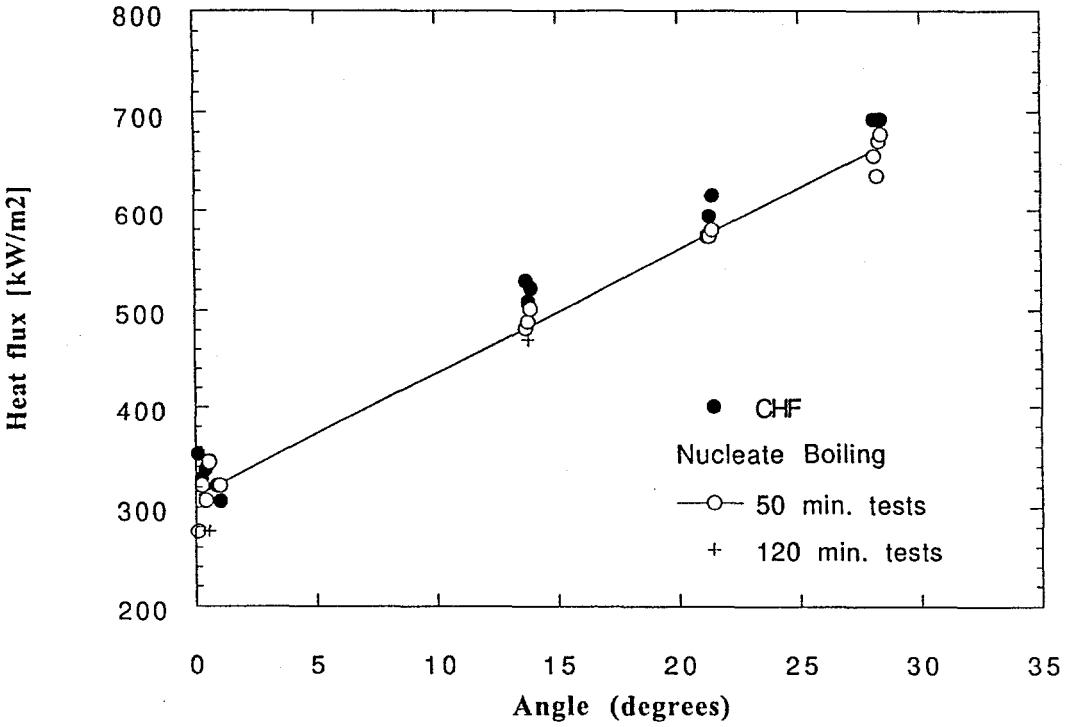

Figure E.18. Summary of all the data obtained in Configuration I. Solid symbols denote occurrence of BC; open circles denote persistence of nucleate boiling for approximately 50 min; crosses show persistence of nucleate boiling for 2 h. (At 0° angle, runs UF–6–0 and UF–5–0 are not shown.)

E.6 CONCLUDING REMARKS

Full-scale simulations of the critical heat flux distribution on the lower head of a reactor vessel submerged in water are possible in the ULPU-2000 facility. In this paper we have presented data from Configuration I, representing the lowermost ($-30° < \theta < 30°$) spherical segment conservatively in saturated pool boiling. These data are enveloped by Eqs. (E.12) or (E.13) which can be applied directly as conservative bounds to the reactor case. In future testing (Configurations II and III) the effects of full geometry ($0° < \theta < 90°$), natural convection, subcooling, and flow path geometry are to be considered, and detailed investigations of the local phenomena and mechanisms are to be carried out.

As noted in Section E.4, a preliminary investigation of the effect of subcooling was carried out in Configuration I. The heat flux was set at a uniform value of 400 kW/m^2 (over the whole $-30° < \theta < 30°$ region) and the experiment was started with water at 20 ° C (and the same level as all other runs reported in this paper). As the experiment continued, the water heated up gradually, leading to several distinct condensation regimes, both in terms of the intensity of the resulting vibrations as well as in terms of the observed two-phase flow phenomena near the heating surface. Nucleate boiling persisted throughout. The heatup transient and CHF occurred

Table E.2. Listing of the Experimental Runs Performed in ULPU-2000 Configuration I, Heat Fluxes, and Respective Waiting Times

Test	Nucleate Boiling		Boiling Crisis	
	Flux (kW/m^2)	Time (min)	CHF (kW/m^2)	Time (min)
UF–7–0	322	20	353	3
	322	44	337	7
UF–6–0	384	18	407	6
	376	40	391	22
UF-5–0	422	24	437	2
UF–1–0	322	30	329	12
	—		346	10
	—		338	6
	307	20	322	4
UF–7–50	322	40	337	11
UF–6–50	322	41	337	9
	—		307	75
	276	120	—	
	322	120	337	38
UF–5–50	345	30	353	3
SF–1	656	21	693	2
	635	50	693	3
	671	44	693	2
	678	42	693	23
SF–3	580	50	615	3
	574	20	595	7
	—		574	14
	—		568	100
SF–5	483	50	529	1
	490	16	509	13
	502	42	522	5
	470	120	—	

(at $\theta = 0°$) within some tens of seconds after reaching saturation. This is consistent with Figure E.17 and demonstrates the important effect of subcooling to increase the CHF.

At this time we also have a preliminary result from Configuration III with one heated block at position $60° < \theta < 90°$ (see Figure E.4). In this experiment the flow channel used was as in Configuration I in pool boiling at saturation. Boiling crisis was obtained with flux levels around

1000 kW/m^2, and the point of inception could be made to move across the length of the block by relatively small changes (less than 20%) in the power shape.

Finally, returning to the application, a perspective on the above results can be obtained with a reference to Figure E.11, indicating the predicted thermal loads distribution in the reactor. It can be seen that near the bottom the available margins are of the order of 200%. From the preliminary information presented here on the upper region, however, it appears that the margins could be of the order of a few tens of per cent. While experiments in Configurations II and III will clarify this point, it is already clear that contrary to the generally held opinion that the region $\theta \sim 0°$ is limiting, the real limitation may actually be around $\theta \sim 90°$.

E.7 ACKNOWLEDGMENTS

Support for this work was provided by IVO International Ltd and the Argonne National Laboratories, for DOE's ARSAP Program under contract no. 23572401. Mr. Sergio Angelini's collaboration in working out the similarity criteria, and Mr. Stephen Additon's help with many aspects of this work are also gratefully acknowledged.

E.8 NOMENCLATURE

J	superficial vapor velocity
q	heat flux
R'	radius of curvature divided by the latent heat per unit volume of vapor
W	width

Greek

θ	angle of surface inclination from horizontal

Subscripts

cr	critical
e	experiment
m	matching point for experiment and prototype
p	prototype (reactor)

E.9 REFERENCES

1. Bui, T.D. and V.K. Dhir (1985) "Transition Boiling Heat Transfer on a Vertical Surface," Trans. ASME, Vol. 107, 756–763.

2. Chu, T.Y., B.L. Bainbridge, J.H. Bentz and T.B. Simpson (1994) "Observations of Quenching of Downward-Facing Surfaces," Rep. SAND93-0688, Sandia National Laboratories.

3. Henry, R.E. and H.K. Fauske (1993) "External Cooling of Reactor Vessel Under Severe Accident Conditions," Nucl. Eng. and Des. **139**, 31-43.

4. Kymäläinen, O., H. Tuomisto and T.G. Theofanous (1992) "Critical Heat Flux on Thick Walls of Large, Naturally Convecting Loops," ANS Proc. 1992 National Heat Transfer Conf., San Diego, CA, August 9-12, 1992, Vol. 6, 44–50, (and in more complete form in IVO International Ltd. Rep. LO1-GT1-59).

5. Theofanous, T.G., C. Liu, S. Angelini, O. Kymäläinen, H. Tuomisto and S. Additon (1994) "Experience from the First Two Integrated Approaches to In-Vessel Retention Through External Cooling," OECD/CSNI/NEA Workshop on Large Molten Pool Heat Transfer, Grenoble, France, March 9-11.

APPENDIX E.2

THE COOLABILITY LIMITS OF A LOWER REACTOR PRESURE VESSEL HEAD

Proceedings, NURETH-7
Saratoga Springs, New York, September 10–15, 1995
NUREG/CP-0142, Vol. 1, 627–647.

APPENDIX E.2

THE COOLABILITY LIMITS OF A LOWER REACTOR PRESSURE VESSEL HEAD

T.G. Theofanous* and S. Syri**

*Center for Risk Studies and Safety
Department of Chemical and Nuclear Engineering
University of California, Santa Barbara, CA 93106

**IVO International Ltd.
01019 IVO, Finland

E.1 INTRODUCTION

This second part of Appendix E is written as a sequel to, and in conjunction with, the paper given as the first part, reporting on the Configuration I experiments. The experiment concept, simulation approach, experimental facilities, and measurement techniques have already been described therein. Thus, here we enter directly into the detailed aspects of the Configuration II facility and test program—Sections E.2 and E.3 respectively. The experimental results are presented and discussed in Section E.4, and the conclusions from the work on both configurations are given in Section E.5.

E.2. CONFIGURATION II FACILITY

The overall geometry of the experiment and related terminology are shown in Figure E.1. The three heater blocks (the primary heater) are fit (in the same manner as in Configuration I) on top of a two-dimensional chamber (15 cm wide) with a shape (in the other two dimensions) as shown. This chamber simulates an open lower cavity geometry (no reactor vessel insulation); it is 2 m wide (at the base) and 0.5 m in height at the short end. The chamber is made of stainless steel sheet, 2.5 mm thick, and it is reinforced externally over the flat areas to sustain the substantial hydrostatic forces without any significant distortion. This test section stands bolted on shock absorbers capable of carrying 3000 kg, which in turn are anchored to the floor. The riser and downcomer are assembled from glass piping 6 m long and 15.2 cm and 7.6 cm in diameter respectively. The riser is equipped with a cable heater (referred to as the secondary heater) extending essentially over the whole length, and operating at a fixed power level of 24 kW. The purpose of this heater is to simulate the radiative power from the melt delivered through the wall of the reactor pressure vessel to the water in the annular space between the cavity wall and the reactor vessel. (The riser in the experiment corresponds to this space.) Finally, the

condensor at the top is to minimize coolant losses and allow operation with saturated water at the inlet to the downcomer. In Configuration II runs this was accomplished by direct contact condensation; that is, a fine spray of demineralized, room temperature water injected at rates sufficient to make up the steam loss to the environment (let out through a permanently open vent line). The condenser was also equipped with a safety relief valve which, however, did not ever have to energize.

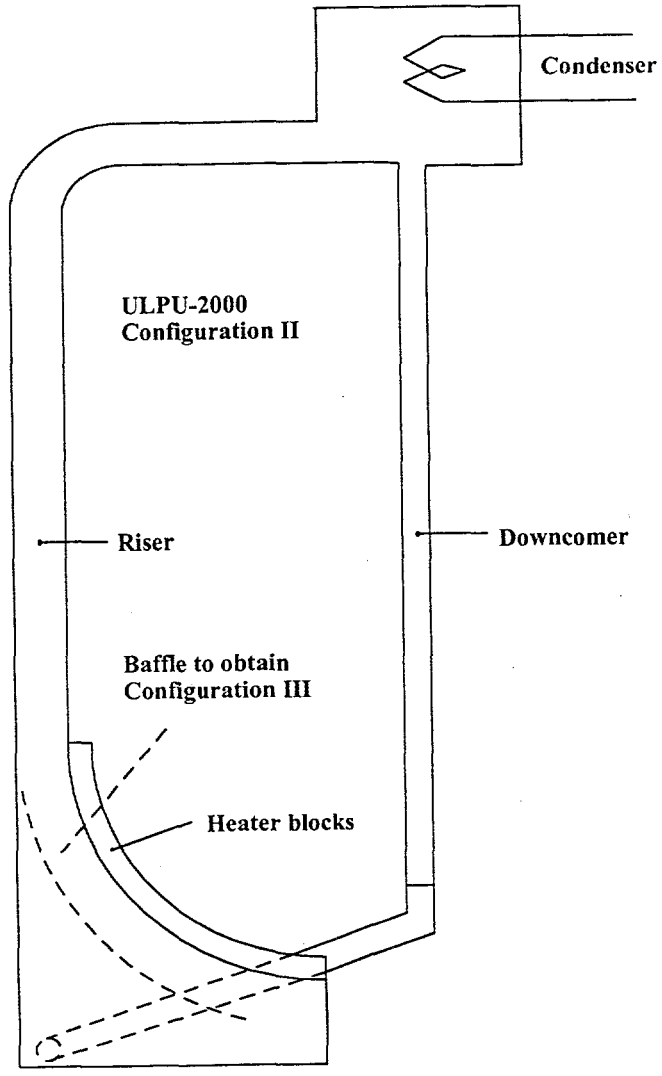

Figure E.1. Schematic of the experiment arrangement in Configuration II.

In addition to the instrumentation employed in Configuration I (heater block thermocouples, thermocouple trees in water opposite the heater surface, and windows/video for visualization), in Configuration II we also had an electromagnetic flow meter for instant flow measurement in the downcomer, and pressure transducers for pressure drop measurements in the riser for the overall void fraction in the upper and lower halves of its length.

In keeping with Configuration I, we assigned 8 heating zones per block, and counting from the upper end of the heater ($\theta = 90°$) as zone #1, we had a total of 24 zones. [In fact, because the upper block had twice as many heaters — 4 rows as compared to 2 rows of the other two — it was assigned 16 relays for power control, but with coupled operations in pairs such as to produce 8 heating zones.] Because the heater blocks were insulated from each other, it was possible to represent especially well the discontinuities dictated by the power shaping criteria (for similarity) of positions 30 and 60°.

The whole facility, in operation, is shown in the photos of Figures E.2 and E.3.

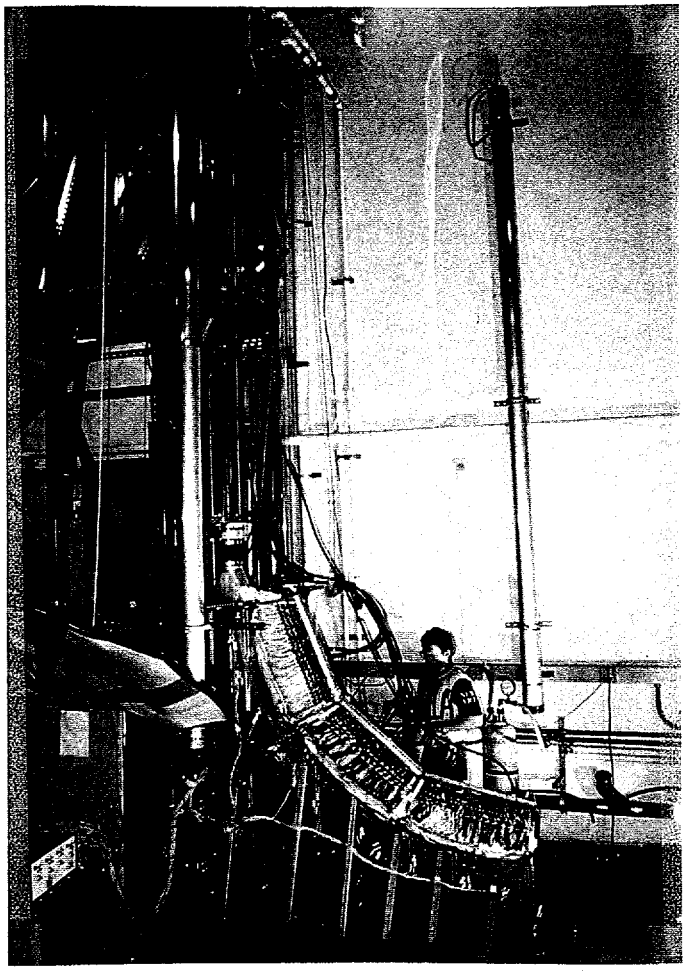

Figure E.2. The ULPU-2000 Configuration II in operation.

E.3 OVERVIEW OF THE TEST PROGRAM

All experimental and data acquisition and reduction techniques were the same as in Configuration I. Again, we found an aging affect, from the initial, polished copper surfaces, with CHF increasing and then leveling off when the surface was fully oxidized. The data reported here are those obtained with the surface in this fully-aged state. We expect this to provide a good

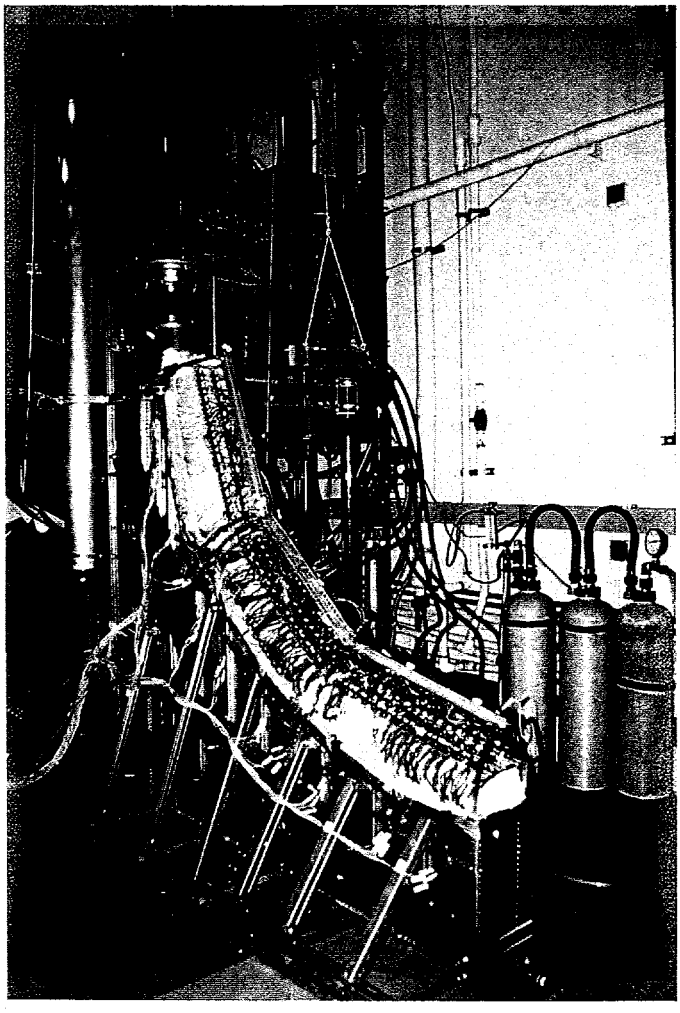

Figure E.3. The ULPU-2000 Configuration II test section.

simulation for the aged, carbon steel reactor pressure vessel surface; however, an exact duplicate of this material has been secured (from one of the prospective manufacturers) and is planned to be tested, by replacing one of the current copper blocks, for confirmation.

All runs in Configuration II were carried out with sufficient water in the loop to close the natural circulation path. Thus, there was a relatively strong flow, depending on the total power level (typically $\sim$ 80 kg/s) and subcooling at the base, corresponding to the gravity head ($\sim$10 K). Although the flow regimes near the heater surface in these runs were qualitatively similar to those observed in Configuration I, here the CHF would occur typically within a few minutes or not at all. It appears that the present conditions (flow, subcooling) do not favor a CHF-delay-time behavior, as found in Configuration I. Thus, zeroing in the CHF was now much easier; starting from the high end, the power was reduced after successive occurrences of boiling crisis (BC) (each of those runs being only a few minutes long), until the last reduction (typically by a few percent) where the heater remained in nucleate boiling. Once it was established that the delay time was not a significant factor here, this nucleate boiling condition was allowed to continue,

for most runs, for 10 to 30 minutes. A grouping of several successive BCs and a final period in nucleate boiling is referred to as one experimental run.

Regarding the power shape, two types of runs were carried out: "uniform flux" (UF) runs, involving a number of zones around $\theta = 0°$ at a uniform power (that is, simulating heat flux at $\theta \sim 0°$) while the remaining two blocks were powered according to the power shaping principle; and "shaped flux" (SF) runs, powered according to the power shaping principle, to simulate CHF at specific locations ($\theta \neq 0°$) along the test section. The reference power shape used here is the same as that employed in Configuration I, and it is shown in Figure E.4. However, certain modifiers from these general descriptions are necessary:

(a) Because of the strong peaking in the reference shape, simply elevating the power level always produces CHF at $\theta = 90°$; that is, under reactor conditions, the position $\theta \sim 90°$ is by far more limiting than the very bottom of the lower head. Thus, to obtain the CHF at $\theta \sim 0°$ we had to reduce the downstream power very significantly. This was done, up to whatever degree was necessary, while maintaining the shape, however. That is, the highest power in the downstream (to the uniform flux section) region is still at 90°. [This power level was denoted in the run identification number as a percentage of the uniform flux level imposed at $\theta = 0°$).] An example of what has been described above is given in Figure E.5.

(b) For SF runs, the same "compromise," for the same reason described above, was necessary for forcing CHF anywhere on the lower block ($0 < \theta < 30°$).

(c) For CHF in the upper block ($60° < \theta < 90°$), an essentially exact simulation could be obtained for the lower end of it ($\theta \simeq 67.5°$); but in order to force CHF at 90°, the upstream power profile within the third block had to be reduced somewhat. The reason for this is that in this upper region the reactor flux is rather flat, which translates to a rather uniform shape also according to the power shaping principle, thus yielding CHF at $\theta < 90°$.

About naming, we follow the same procedure employed in Configuration I. That is, we use a prefix, UF or SF, to denote uniform and shaped flux respectively. Following this there is a numerical index that for UF runs indicates the number of zones subject to the uniform flux, while for SF runs indicates the zone at which CHF is simulated. Uniform flux runs are only employed to simulate CHF at the bottom end of the test section ($\theta \simeq 0°$). Then, there is a third numerical index for UF runs only, indicating the percentage of increase in power at the upper end of the test section ($\theta = 90°$) in relation to that on the uniform flux portion. Finally, the number in parenthesis at the end indicates the order in which repeat runs (if any) were performed; however, repeat runs were not run consecutively, but rather were intermingled among the various runs.

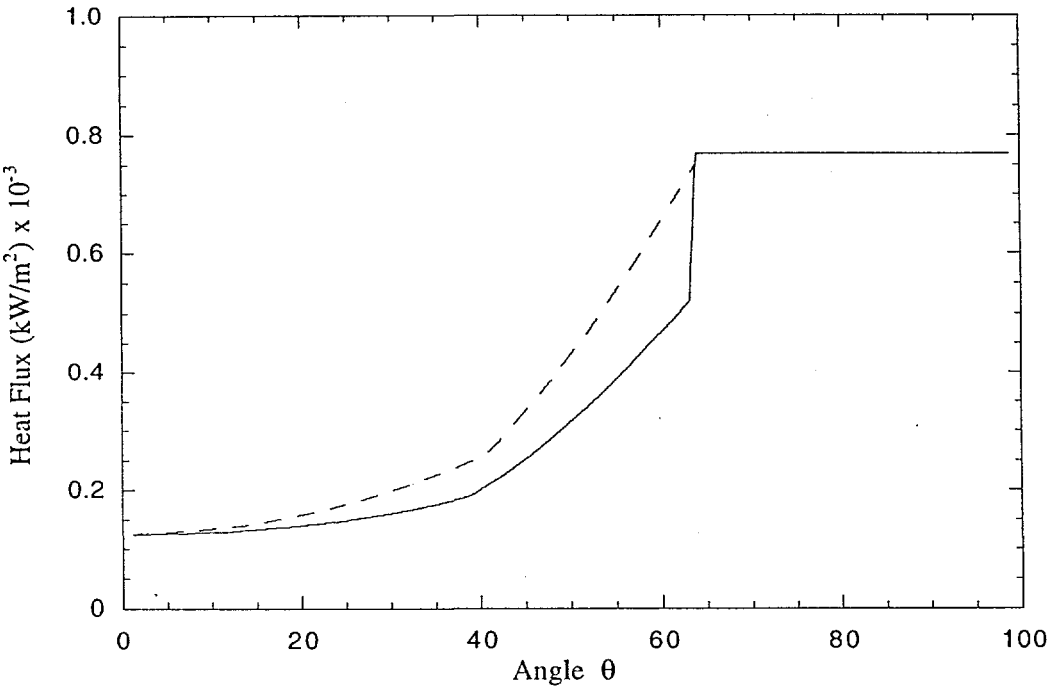

Figure E.4. The reference reactor heat flux shape (——) (from Theofanous et al., 1994), and the shape used in the simulations (– – –).

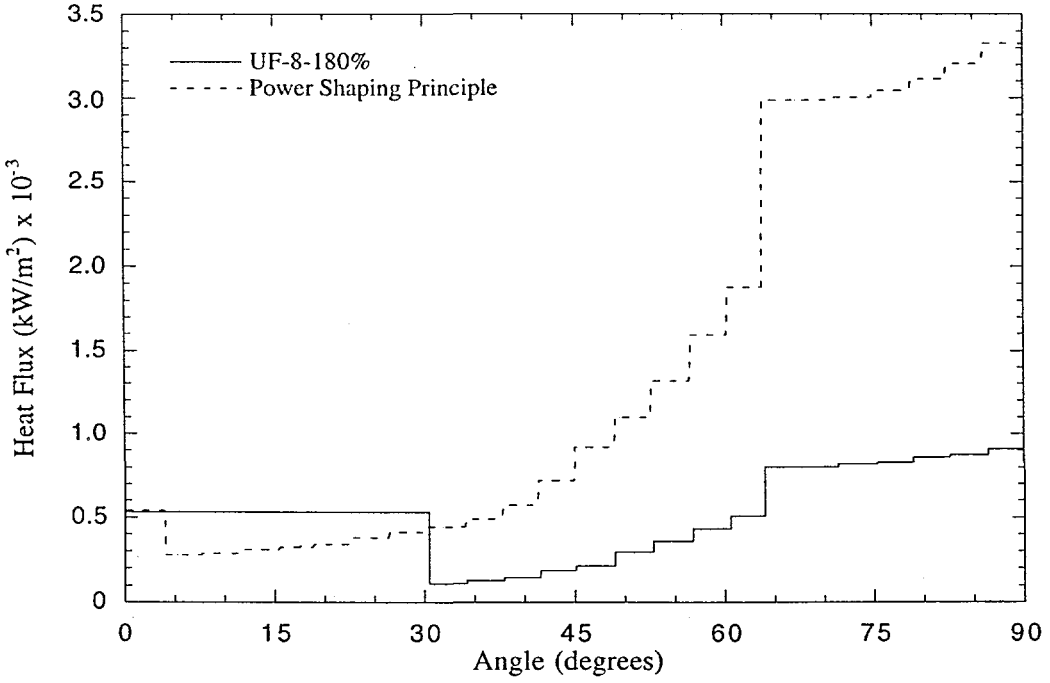

Figure E.5. Illustration of the power shape "compromise" necessary to *force* CHF at $\theta = 0°$.

To illustrate the above,

UF-8-145%(2)

means: (a) a uniform flux run, simulating CHF at $\theta \sim 0°$, with all 8 zones of the lower block (i.e., zones 17 to 24) at the same power; (b)middle and upper blocks powered according to the power shaping principle (as discussed above) and such that the power level at the upper end (90°) is 145% of that at $\theta = 0°$; and (c) this is the second run carried out under these conditions, while

SF-7(4)

means: (a) a run simulating CHF in zone #7 ($\theta \sim 67°$); (b) run with a heat flux distribution according to the power shaping principle; and (c) this is the fourth run carried out under these conditions.

A listing of all runs carried out in Configuration II is given in Table E.1. The flux shapes employed in each case are shown in relation to those dictated by the power shaping principle in Figures E.5, E.6, and E.7(a) through E.10(a). The conduction correction for UF runs is negligible (see Configuration I), and for the SF runs the actual fluxes delivered are shown in Figures E.7(b) through E.10(b). The corrections involved are summarized in Table E.2. These small corrections have been applied already to the data reported.

E.4 EXPERIMENTAL RESULTS AND DISCUSSION

A rough idea of the surface aging effect on CHF is given in Figure E.11. In it, we see that the effect is measurable even after ~4 hours of operation, but it is clearly leveled out, compared to the very initial value of 450 kW/m^2. Also, for $\theta = 90°$, the initial value was ~1.2 MW/m^2, as compared to the fully-aged value of ~1.6 MW/m^2. As noted already, this work is focused on the fully-aged surface condition, and these are the results reported and discussed below.

The results from all experimental runs are shown in Figure E.12, and in tabular form in Table E.3. In Figure E.12, we also show the results from Configuration I. The following observations and comments can be made:

1. Configuration II exhibits a significantly higher tolerance to boiling crisis as compared to Configuration I. These are clearly the effects of flow and subcooling, and they amount to about 50% increase.

2. For Configuration II, the variation of CHF with angular position seems to be composed of two, remarkably linear, regions. We believe these to be reflective of the significantly different flow regimes observed in the respective regions.

3. The CHF level at the upper end (1.6 MW/m^2) is remarkably higher than anything observed previously — under *any* orientation. This is contrary to the "conventional wisdom" that flat plate (horizontal) CHF is generally applicable.

Further, it should be noted that: (i) the nucleate boiling point shown for $\theta = 45°$ was obtained at the maximum available power in the middle block at the time. Now, a third row of heaters has been added to it, and we expect to carry out experiments in this area shortly — and to confirm that the results lie on the same linear trend for this "upper" region; (ii) in Table E.3 we find three runs in which CHF occurred after a few minutes; however, note that all three cases were for the lowermost region ($0° < \theta < 15°$), and that the differences were rather small (2–4%). This again is another indication, or symptom, of a different mechanism in the lower region identified in the data trends (Figure E.12). The lower envelope for the Configuration II data in Figure E.12 can be expressed by:

$$q_{cr}(\theta) = 500 + 13.3\theta \ \text{kW/m}^2 \quad \text{for} \quad \theta < 15° \qquad (E.1)$$

$$q_{cr}(\theta) = 540 + 10.7\theta \ \text{kW/m}^2 \quad \text{for} \quad 15° < \theta < 90° \qquad (E.2)$$

However, the data can be fit equally well with one equation:

$$q_{cr}(\theta) = 490 + 30.2\theta - 8.88 \cdot 10^{-1}\theta^2 + 1.35 \cdot 10^{-2}\theta^3 - 6.65 \cdot 10^{-5}\theta^4 \ \text{kW/m}^2 \qquad (E.3)$$

This line is shown in Figure E.12.

E.5 CONCLUSIONS

With the completion of the Configuration II experiments reported here, we have established a firm estimate for the coolability limits of the lower head of a reactor vessel submerged in water and heated internally. The scale of the experiment, and the power shaping principle, ensure that these data, and resulting correlation, are directly applicable to the reactor. The correlation reveals a two region behavior [Eqs. (E.1) and (E.2)] which has been related to the different flow regimes observed in the two-phase boundary layer in the respective regions.

E.6 ACKNOWLEDGMENTS

This work was funded by IVO International Ltd. (supporting S. Syri) and the U.S. Department of Energy's Advanced Reactor Severe Accident Program (ARSAP) through ANL subcontract No. 23572401. We are also grateful to Sergio Angelini, Tony Salmassi, and Mitch Frey, for help with design and construction of Configuration II, and to Jeff Smith, for helping with the construction, running of the latest portion of the experiments, and helping with the data reductions. Mr. Stephen Additon (TENERA) played a key role in programmatically supporting this project.

Table E.1. Listing of Runs Carried Out in Configuration II		
Group	Subgroup	Remarks
SF	SF–1 SF–7 SF–17 SF–21	3 Tests 3 Tests 3 Tests 2 Tests
UF	UF–3–180% UF–3–220% UF–8–145% UF–8–180%	1 Test 1 Test 2 Tests 1 Test

Table E.2. Heat Flux Correction to the Input Flux due to Axial Conduction		
Run #	CHF Position	Correction Factor
All UF	0°	1
SF-21	15°	0.965
SF-17	30°	0.992
SF-7 (4)	67.5°	0.947
SF-7 (3)	67.5°	0.985
SF-7 (2)	67.5°	0.962
SF-7 (1)	67.5°	0.94
SF-1	90°	0.998

Table E.3. Listing of the Experimental Runs Performed in ULPU-2000 Configuration II, Heat Fluxes, and Respective Waiting Times.

Test	Nucleate Boiling		CHF Boiling	B.C Time
	Flux (kW/m^2)	Time (min)	(kW/m^2)	(min)
UF–3–180%	461	15	517	2.5
			498	3.5
			479	14
UF–3–220%	479	15		
UF–8–145% (1)			545	1.5
			526	3.5
			508	47
UF–8–145% (2)	527	120	573	1.5
			564	1
			555	2
			536	3
UF–8–180%	498	15		
SF–1 (1)	1485	10		
SF–1 (2)	1504	30	1617	1
			1579	2
SF–1 (3)	1579	10	1617	2.5
SF–7 (1)	1231	30		
SF–7 (2)	1246	30		
SF–7 (3)	1282	10		
SF–7 (4)	1299	60	1335	2
			1317	1.5
			1335	1
SF–17 (1)	932	10		
SF–17 (2)	914	30	932	2.5
SF–17 (3)	914	30		
SF–21 (1)	789	30	862	1
			843	2
			816	2
SF–21 (2)	762	30	789	13

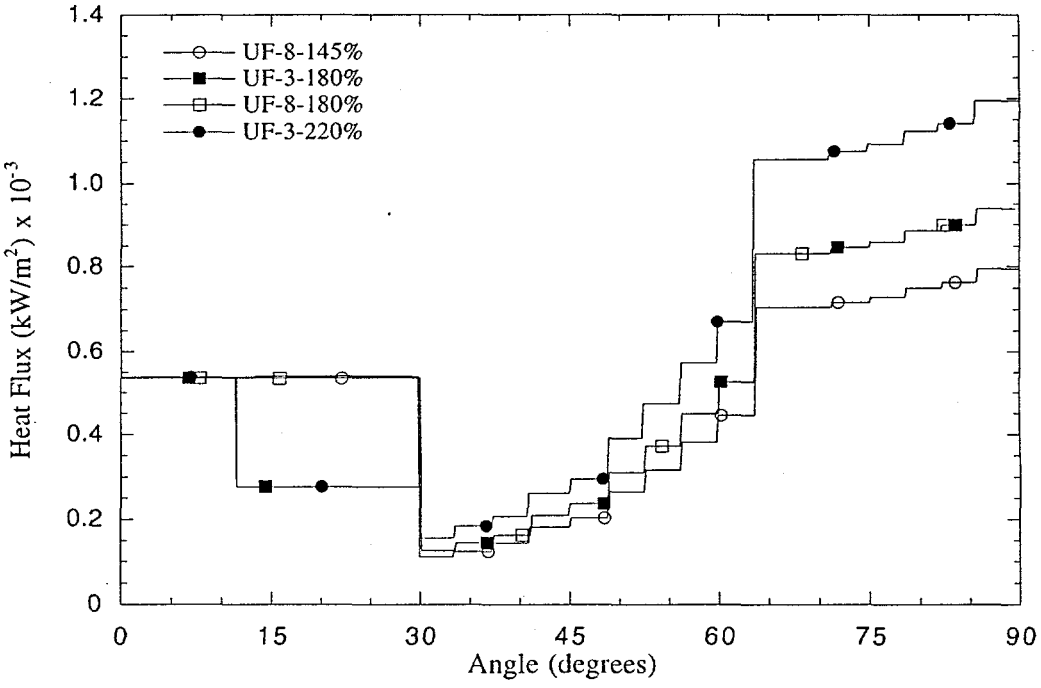

Figure E.6. Heat flux profiles imposed on UF-type runs. The shape required for "simulation" for these runs is shown in Figure E.5.

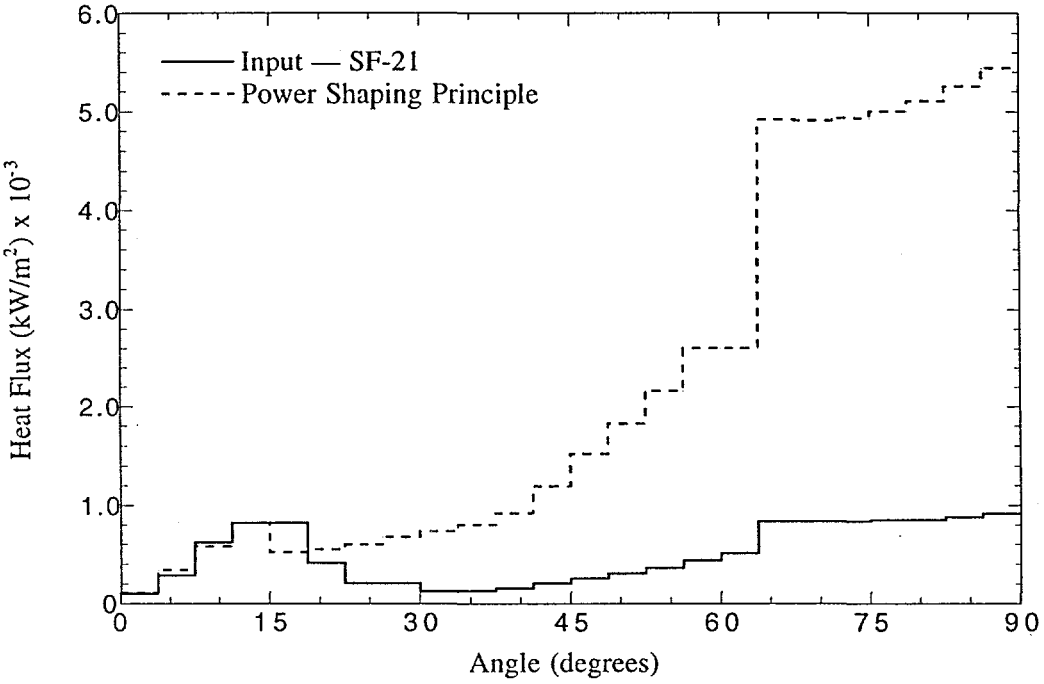

Figure E.7(a). The actual power shape for run SF-21 compared to that derived from the power shaping principle.

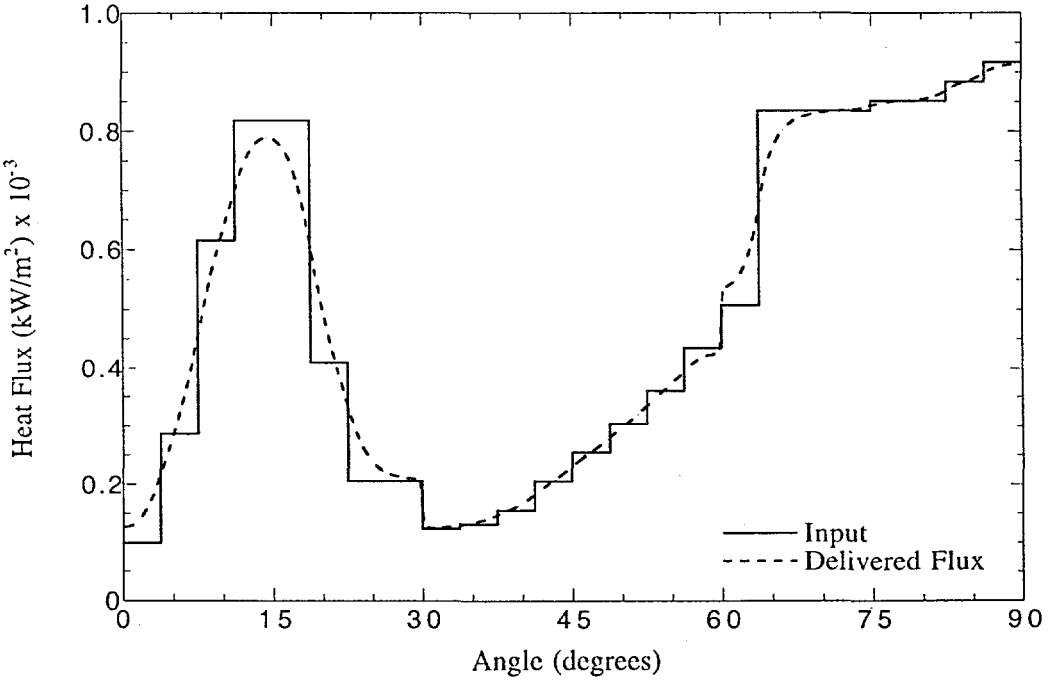

Figure E.7(b). The effect of axial conduction in the heater block in modifying the input flux shape for run SF-21.

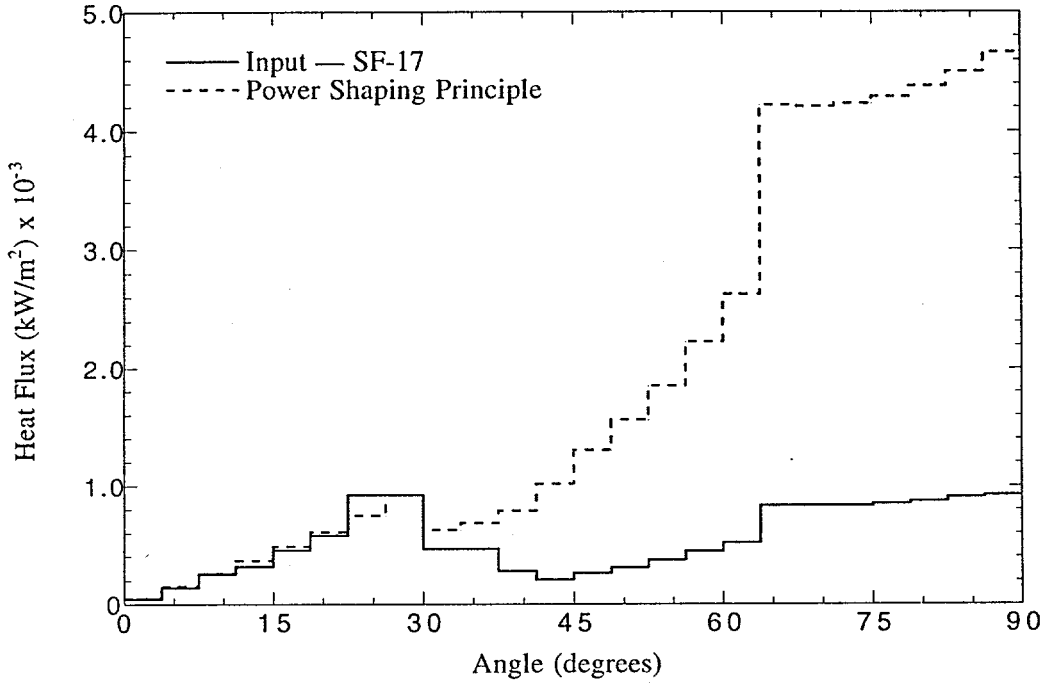

Figure E.8(a). The actual power shape for run SF-17 compared to that derived from the power shaping principle.

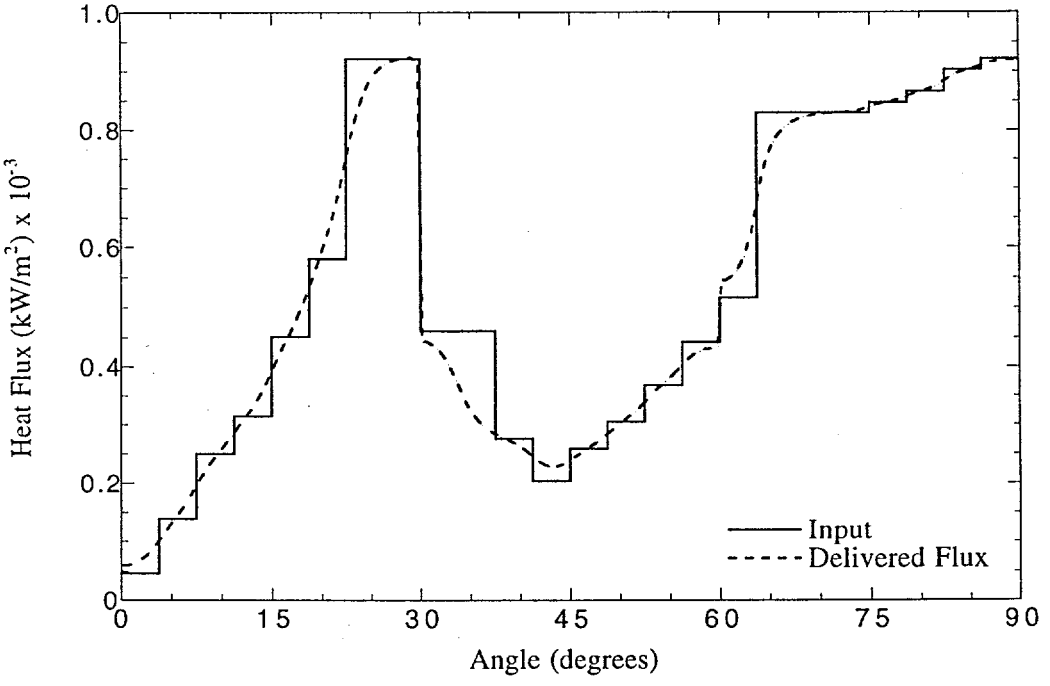

Figure E.8(b). The effect of axial conduction in the heater block in modifying the input flux shape for run SF-17.

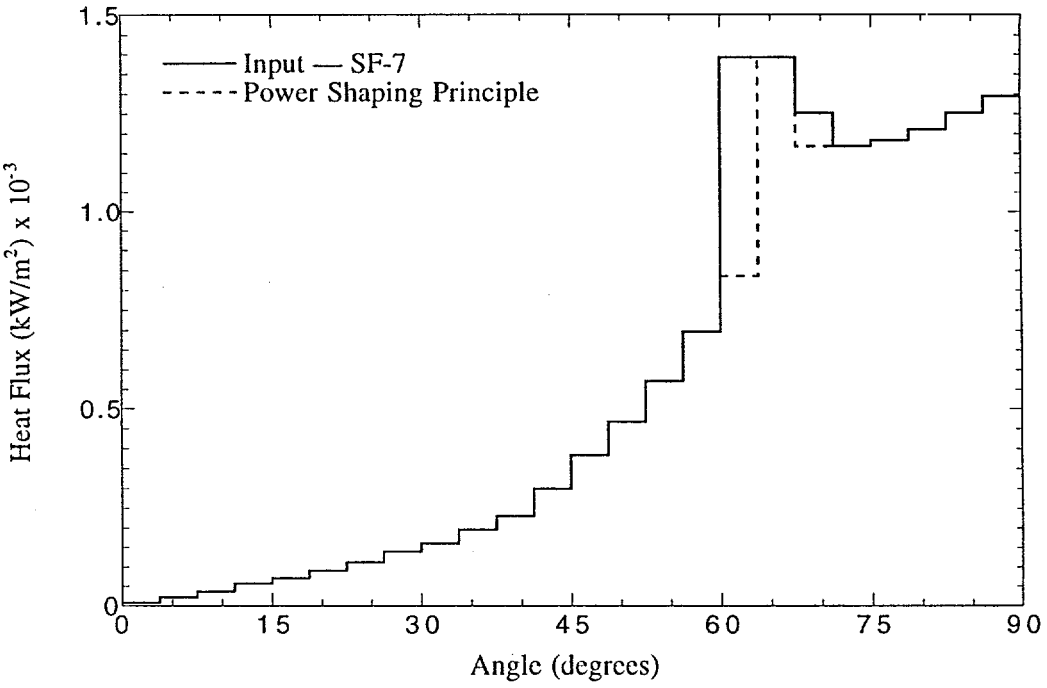

Figure E.9(a). The heat flux profile according to the power shaping principle for CHF at $\theta = 67.5°$ and effect of axial conduction.

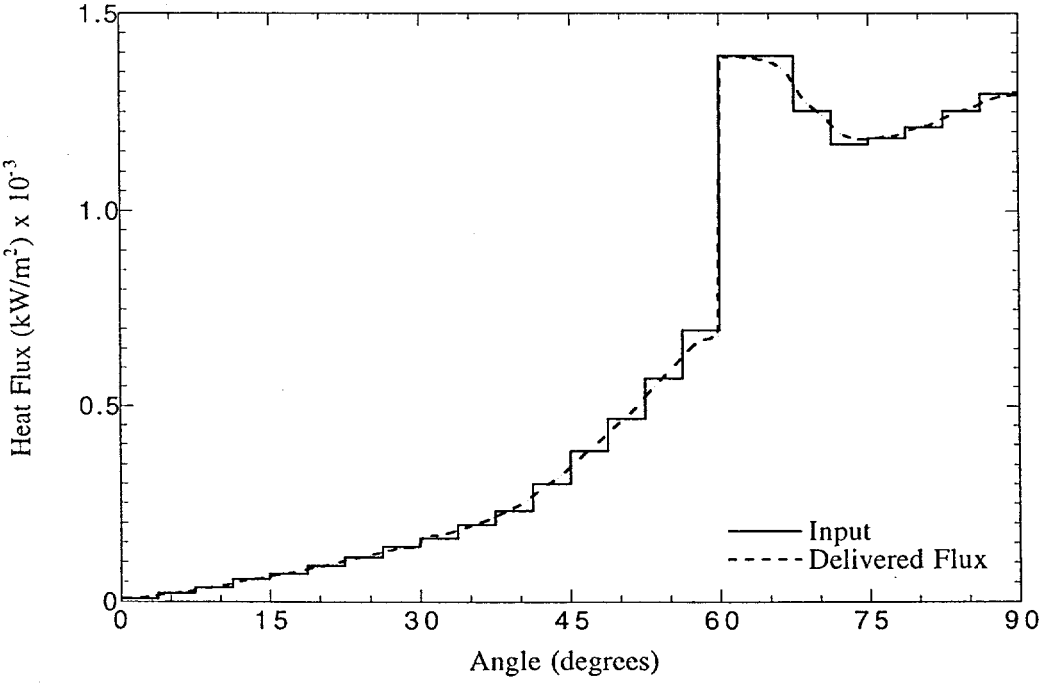

Figure E.9(b). The effect of axial conduction in the heater block in modifying the input flux shape for run SF-7.

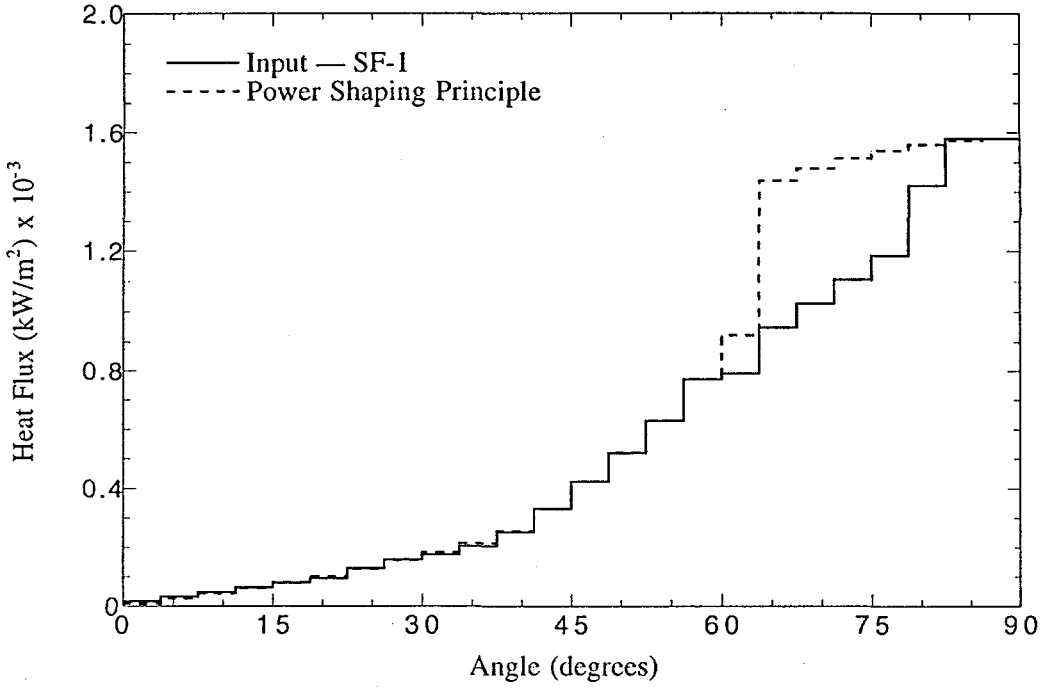

Figure E.10(a). The actual power shape for run SF-1 compared to that derived from the power shaping principle.

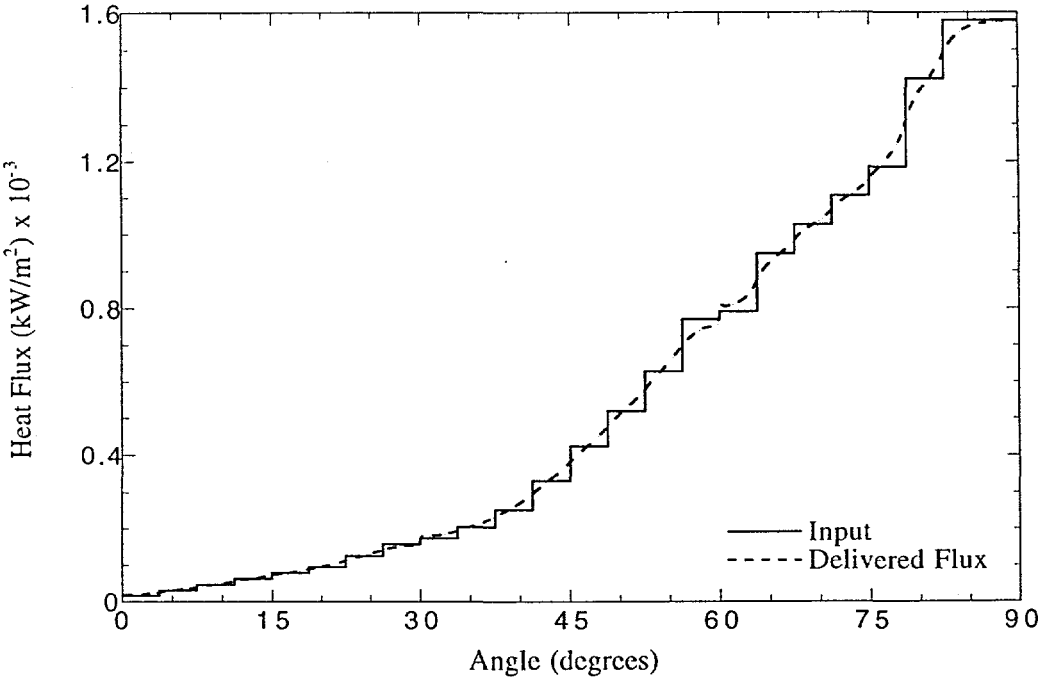

Figure E.10(b). The effect of axial conduction in the heater block in modifying the input flux shape for run SF-1.

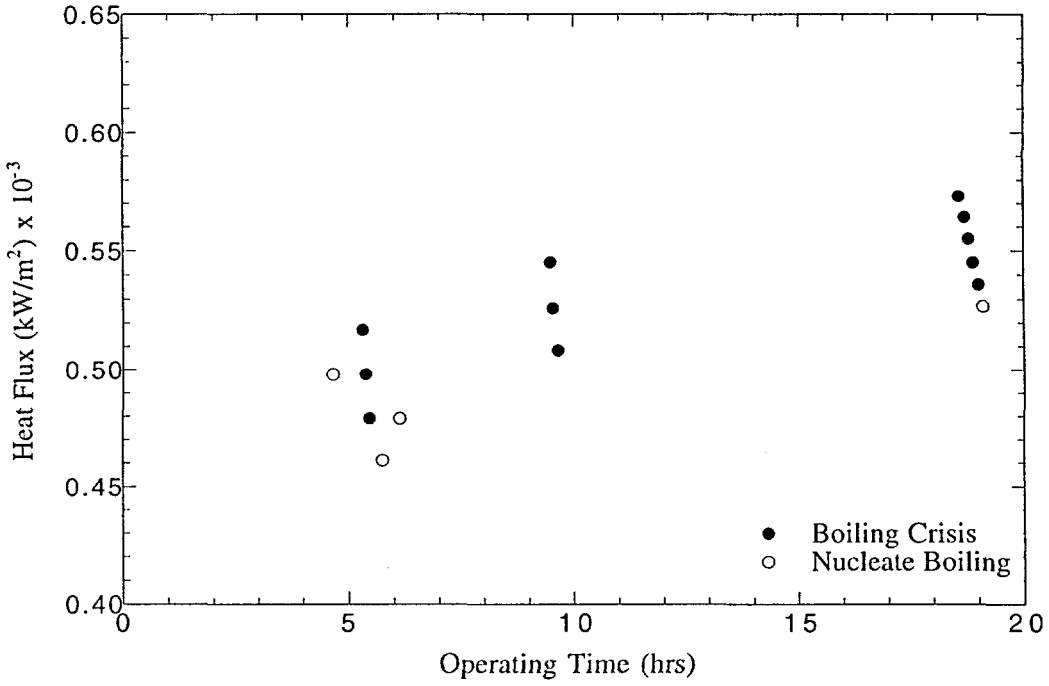

Figure E.11. Illustration of the surface aging effect in Configuration II, for times greater than 4 hrs. [Data for earlier times are not shown.] All data refer to boiling crisis at $\theta = 0°$.

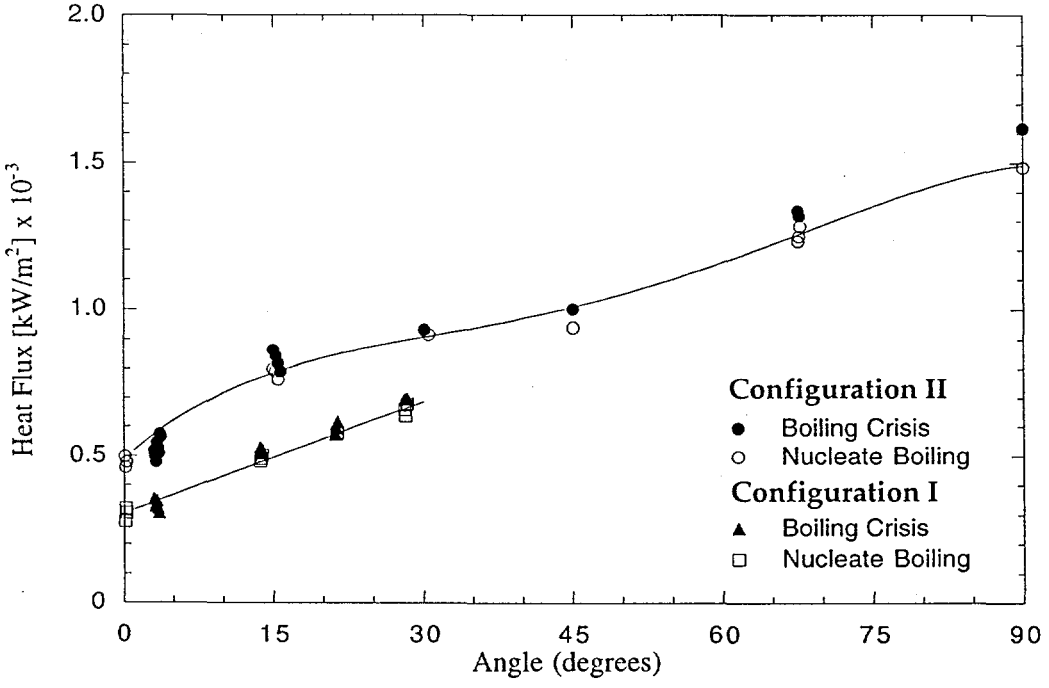

Figure E.12. Collective presentation of all critical heat flux data in both Configuration I and Configuration II experiments in ULPU-2000. The line shown for Configuration II is Eq. (E.3). The B.C. points at $\theta \sim 0°$ have been displaced to the right for clarity of presentation.

APPENDIX E.3

CRITICAL HEAT FLUX SENSITIVITY TO FLUX SHAPES AND RECIRCULATION FLOW RATES

APPENDIX E.3

CRITICAL HEAT FLUX SENSITIVITY TO FLUX SHAPES AND RECIRCULATION FLOW RATES

A new series of experiments was carried out in ULPU, to examine sensitivity of the critical heat fluxes to the flux shape and the natural circulation flow rates. The experimental facilitity was in Configuration II, as described in Appendix E.2, except for increasing the power control resolution (by adding relays to the control circuit) to 48 zones. In the runs described here each zone corresponds to an arc length of 1.875°. We have also changed the nomenclature; now, the zone numbers begin at 0° and increase with angular position, so that zone 0 is over $0° < \theta < 1.875°$ and zone 48 over $88.125° < \theta < 90°$.

Flux shape sensitivity is examined using, besides the base case flux shape shown in Figure E.1 (note that it is somewhat different from the shape used in Appendix E.2, as illustrated in the same figure as the "old shape"), several variations around it, as well as shapes associated with the parametric cases considered for the reactor. Flow rate sensitivity studies were carried out by throttling the downcomer so as to obtain about 60 gpm, or about half the flow normally obtained (~130 gpm) with the flow path completely open. In addition, the case of zero flow was examined by letting the level drop sufficiently so as to interrupt the natural circulation flow path.

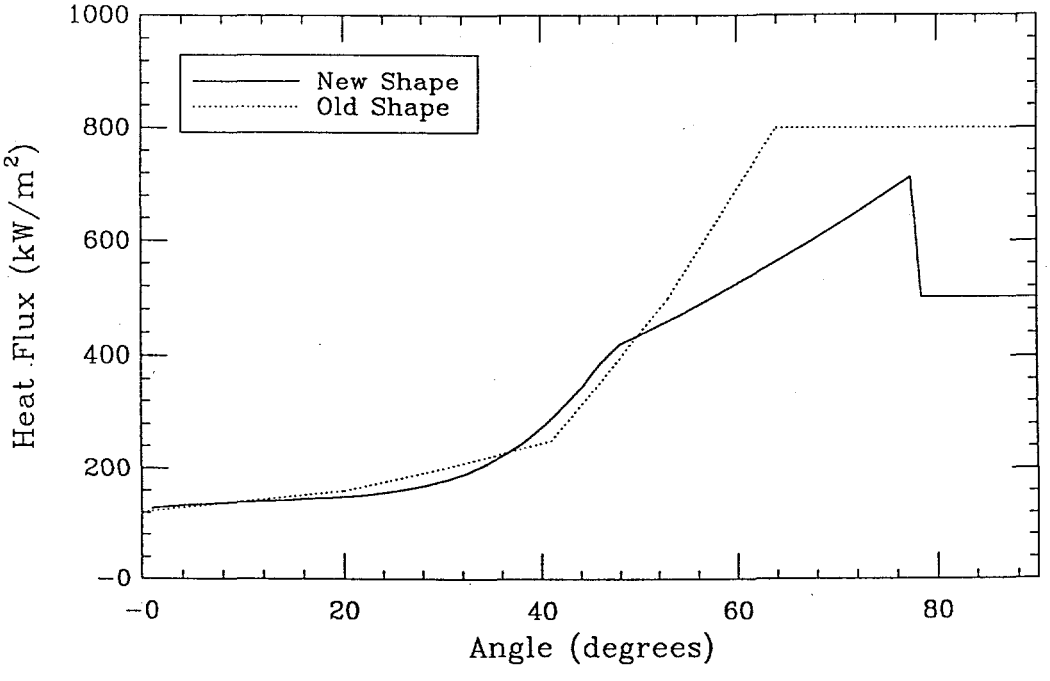

Figure E.1. The presently used base case flux shape in relation to that used in Appendix E.2.

The experimental matrix is summarized in Table E.1, together with the resulting CHF values. The second column indicates the origin of the reference flux shape used in each case. The actual flux shapes used are shown, together with the shapes that would be required according to the power shaping principle, in Figures E.2 through E.19.

The results are shown in graphical form in Figures E.20 and E.21. Figure E.20 contains the comparison between all present full-flow data with the CHF correlation obtained in Appendix E.2. This figure shows that the correlation represents a robust lower envelope even under some not insignificant variations of the heat flux shapes. But this figure also shows that there is a significant additional tolerance to CHF under a strongly peaked heat flux at the top. The sensitivity to the flow rate can be seen in Figure E.21. It is very interesting that the zero flow case produces a negative effect only near the top and even then, it is only a $\sim$20% reduction. Note that the zero flow case in effect eliminates the cavity subcooling as it is operated under a significantly lower water level ($\sim$2.0 m vs 5.6 m from the bottom of the lower head). *These results indicate that simply immersing the lower head of the AP600 would be sufficient to remove the thermal loads from a base-case-like scenario with very significant margins.*

Table E.1. Summary Of The ULPU (Configuration II) Experimental Program on Flux Shape and Recirculation Flow Effects

ID Number[b]	Reference[a] Shape	Maximum Flow CHF (kW/m^2)	Medium Flow CHF (kW/m^2)	No Flow CHF (kW/m^2)	Angular Position (Actual)[c] (°)
Z00A	Figure Q.1	508	545		0
		564			0
				658	0
(Z00B)			498		0(6)
			564		0
(Z00C)		602			0
Z08B	Figure Q.1	718	649		15
		770			15
Z14A	Figure Q.1	902	866		26
		902			26
Z19B	Figure Q.1	1125	1005		37
		1139			37
		1072			37
(Z19C)		1072	991		37
Z24A	Figure Q.1	1205	1096		45
		1191	1083		45
		1151			45
				1042	45
(Z24B)		1179			45
(Z24C)		1228			45
Z30A	Figure Q.1	1116	1064		56
		1104			56
Z35A	Figure Q.1	1263	1190		66
		1263			66
		1255			66
Z35C	Figure 7.16	1340			66
(Z40A)		1186			75(90)
		1318			75(80)
		1340			75
Z40B	Figure Q.1	1489	1370		75
(Z40C)		1310			75(85)
Z42A	Figure 7.15	1523			78
48A	Eq. (5.30)	1480	1263		90
		1622			90
				1118	90
Z48B	Eq.(5.30) with cut	1353			90

[a]Flux shapes based on calculated reactor shapes, as follows:

- Normal print number. Base case calculation as in Figure Q.1.
- Number in parenthesis. Sensitivity variations around the base case.
- Number in bold print. Parametric cases examined for the reactor.

[b]The number indicates the zone number at which CHF is being simulated. Total 48 equal size zones starting with zone 0 at 0° and ending with zone 48 at 90°.

[c]The actual boiling crisis position is shown in parenthesis when it is different from the expected one.

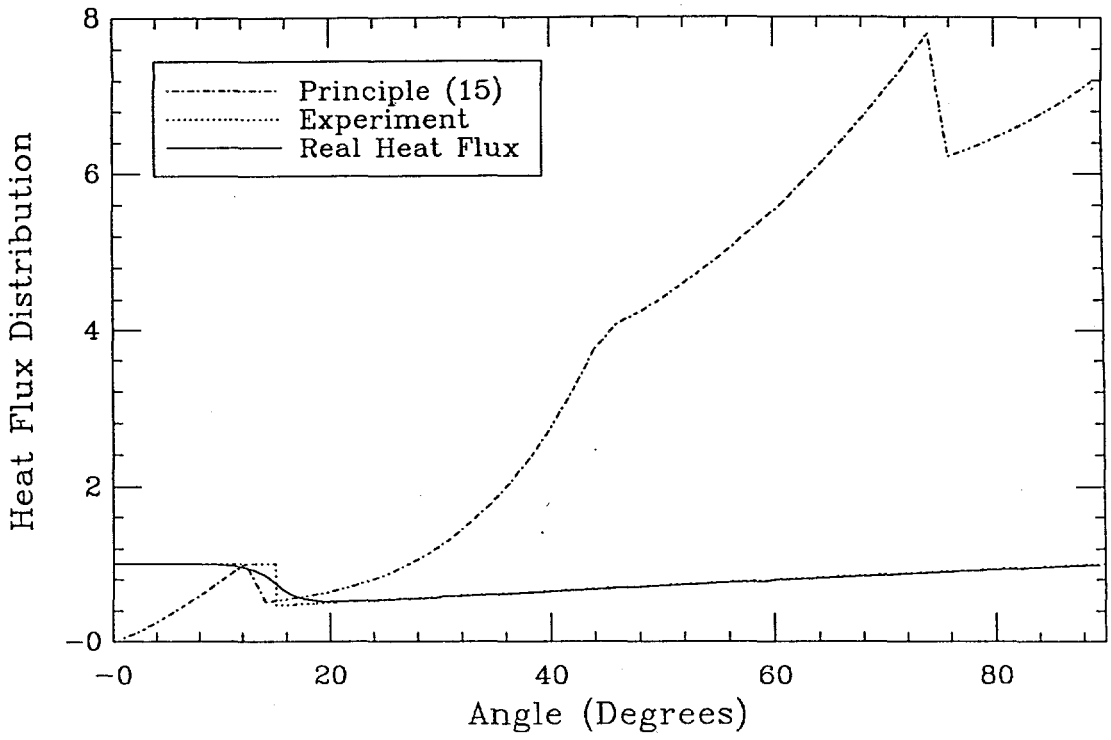

Figure E.2. The actual input and delivered flux shapes in comparison to that obtained from the power shaping principle for run Z00A.

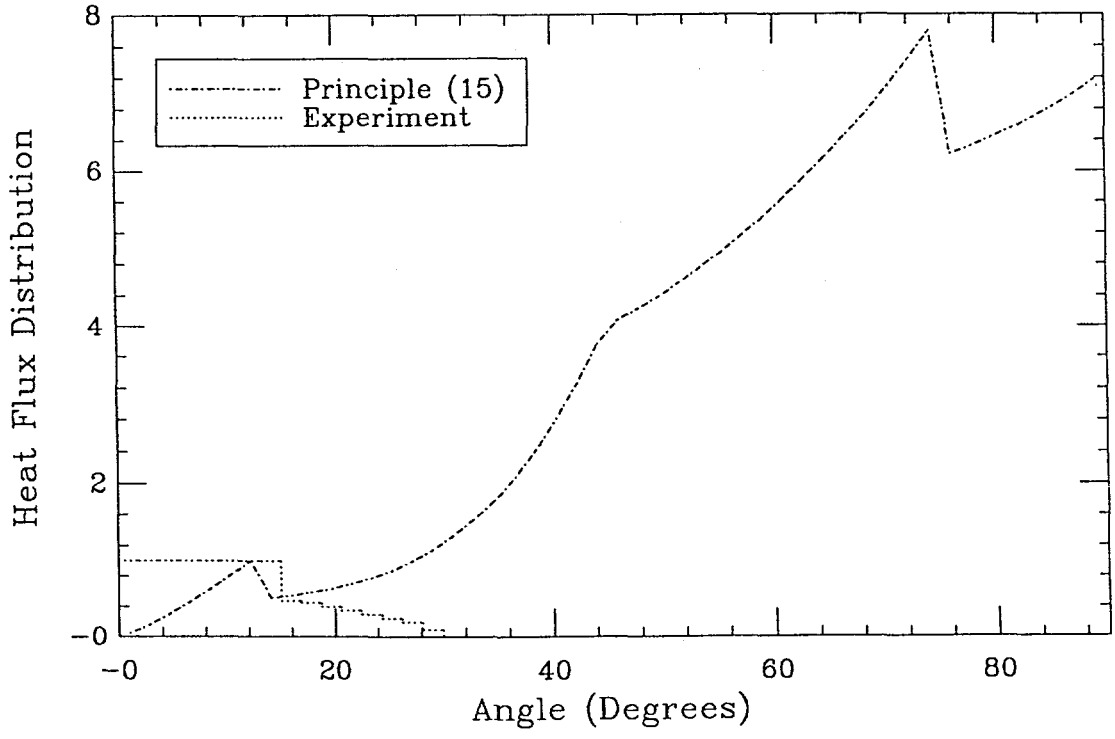

Figure E.3. The actual input and delivered flux shapes in comparison to that obtained from the power shaping principle for run Z00B.

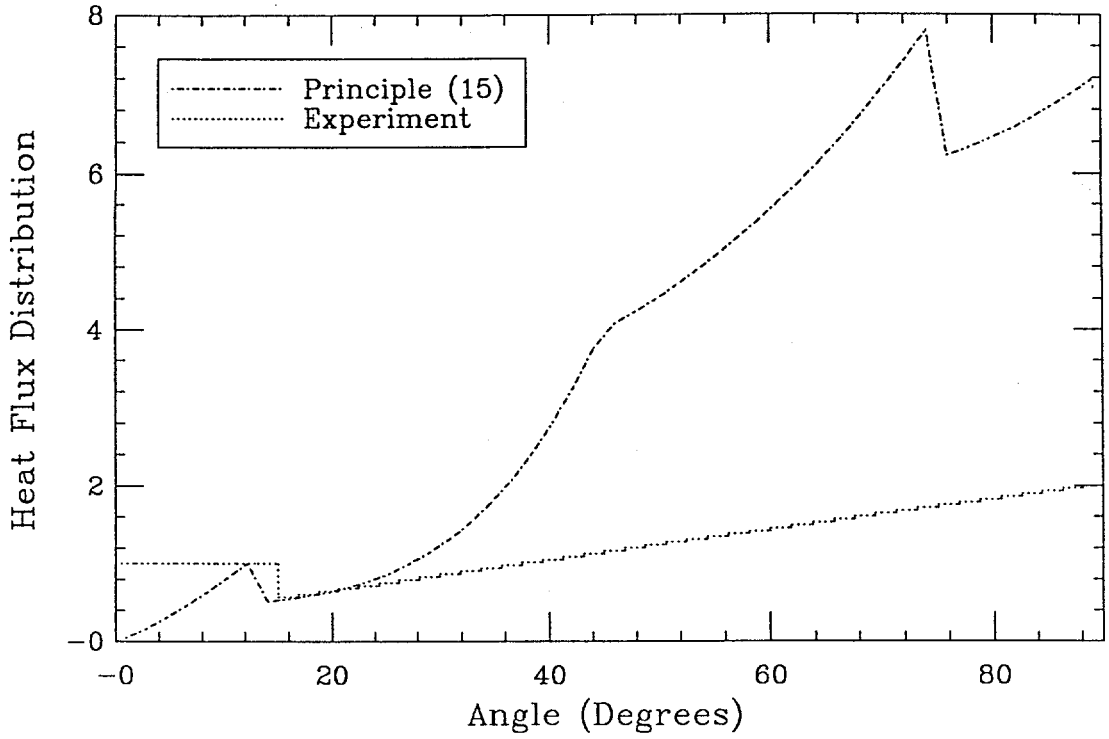

Figure E.4. The actual input and delivered flux shapes in comparison to that obtained from the power shaping principle for run Z00C.

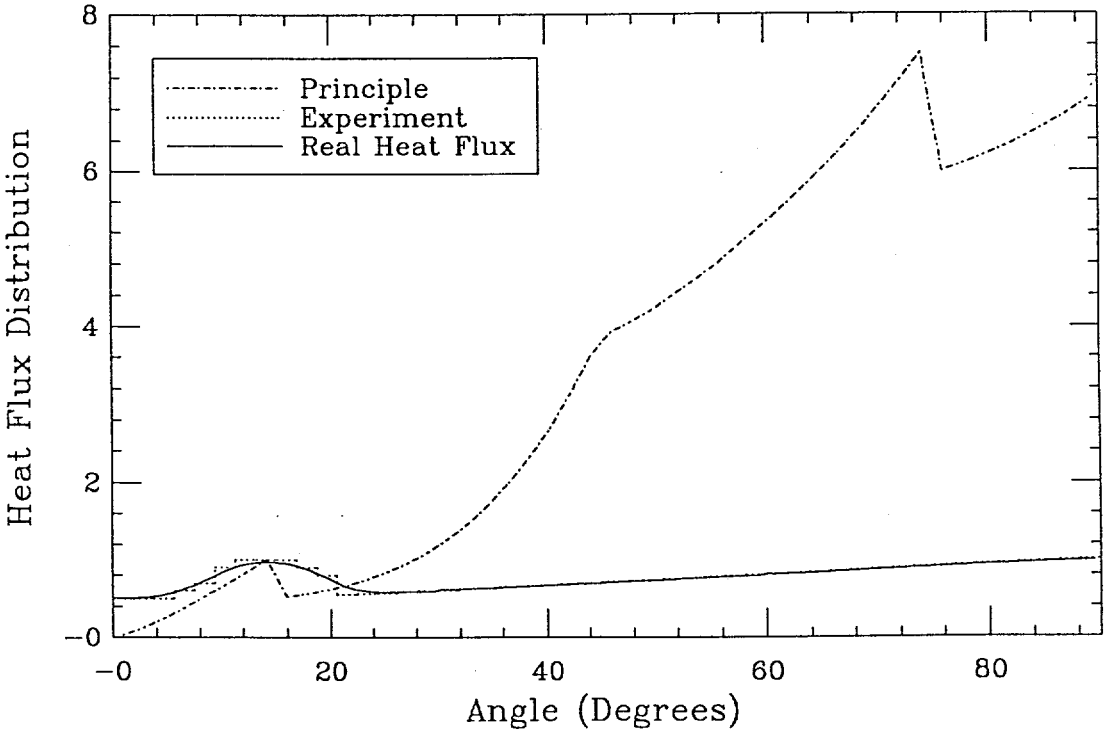

Figure E.5 The actual input and delivered flux shapes in comparison to that obtained from the power shaping principle for run Z08B.

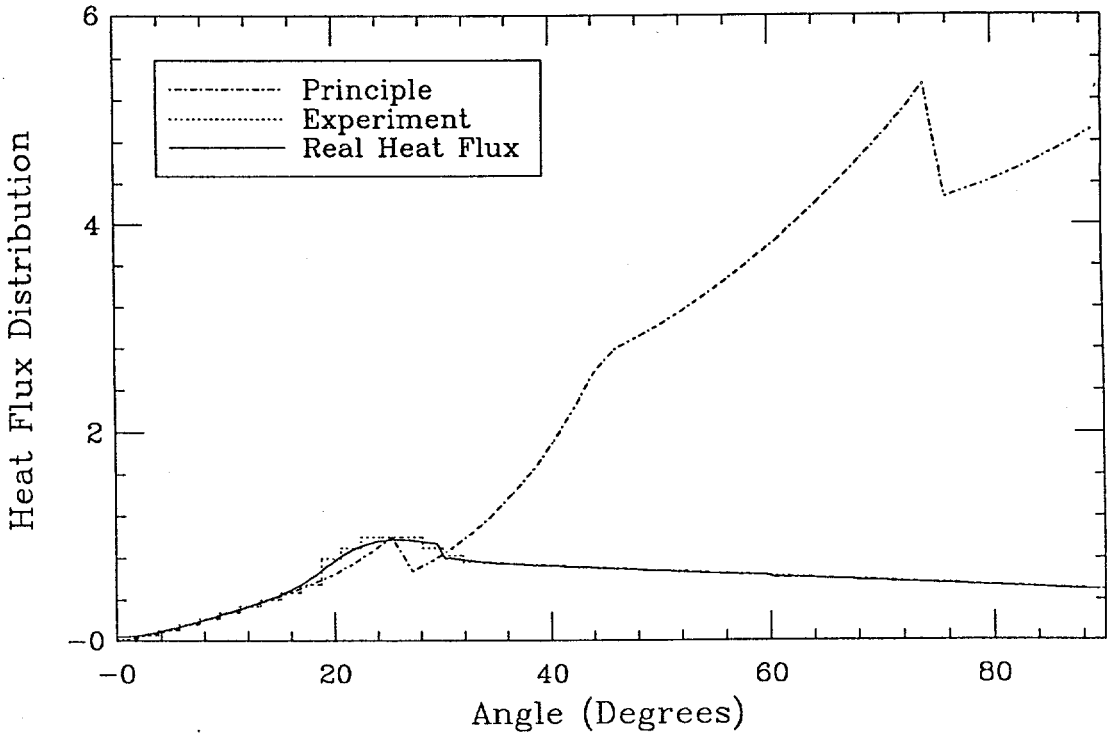

Figure E.6. The actual input and delivered flux shapes in comparison to that obtained from the power shaping principle for run Z14A.

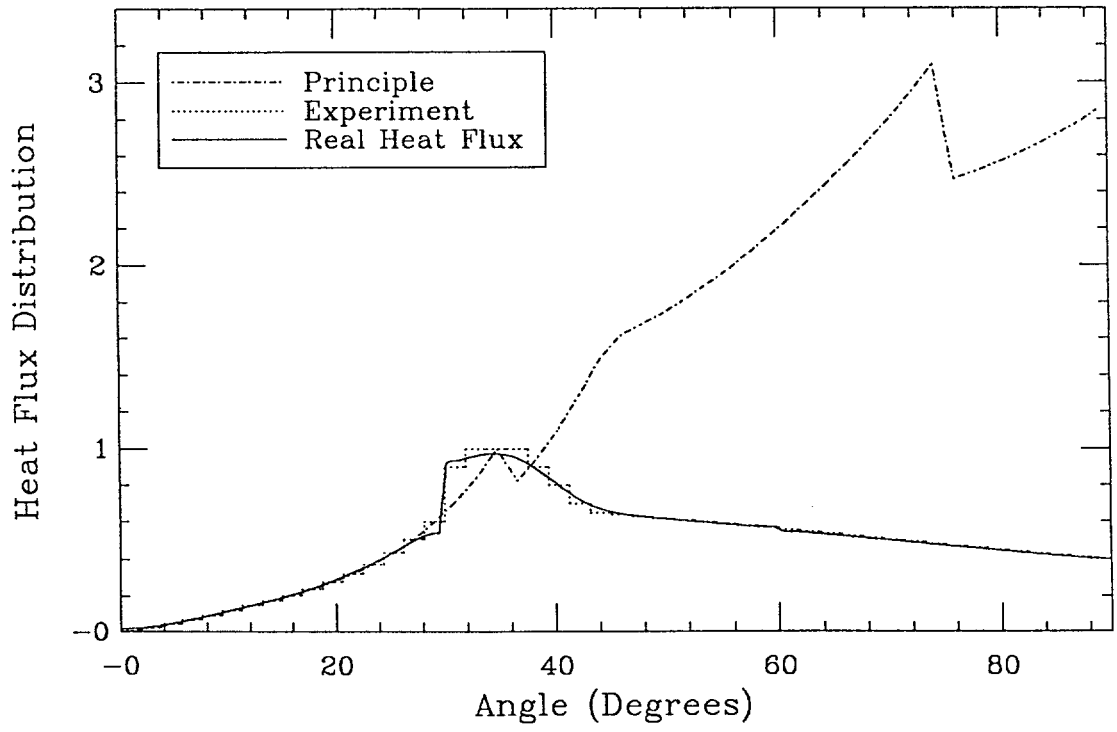

Figure E.7. The actual input and delivered flux shapes in comparison to that obtained from the power shaping principle for run Z19C.

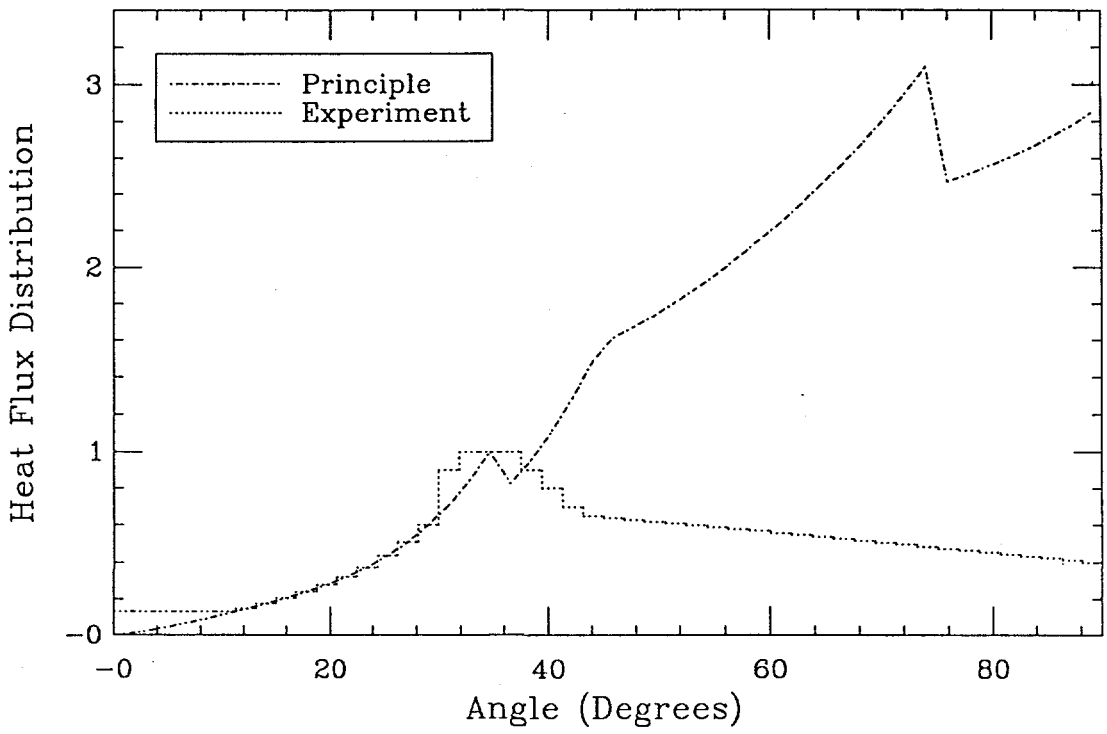

Figure E.8. The actual input and delivered flux shapes in comparison to that obtained from the power shaping principle for run Z19B.

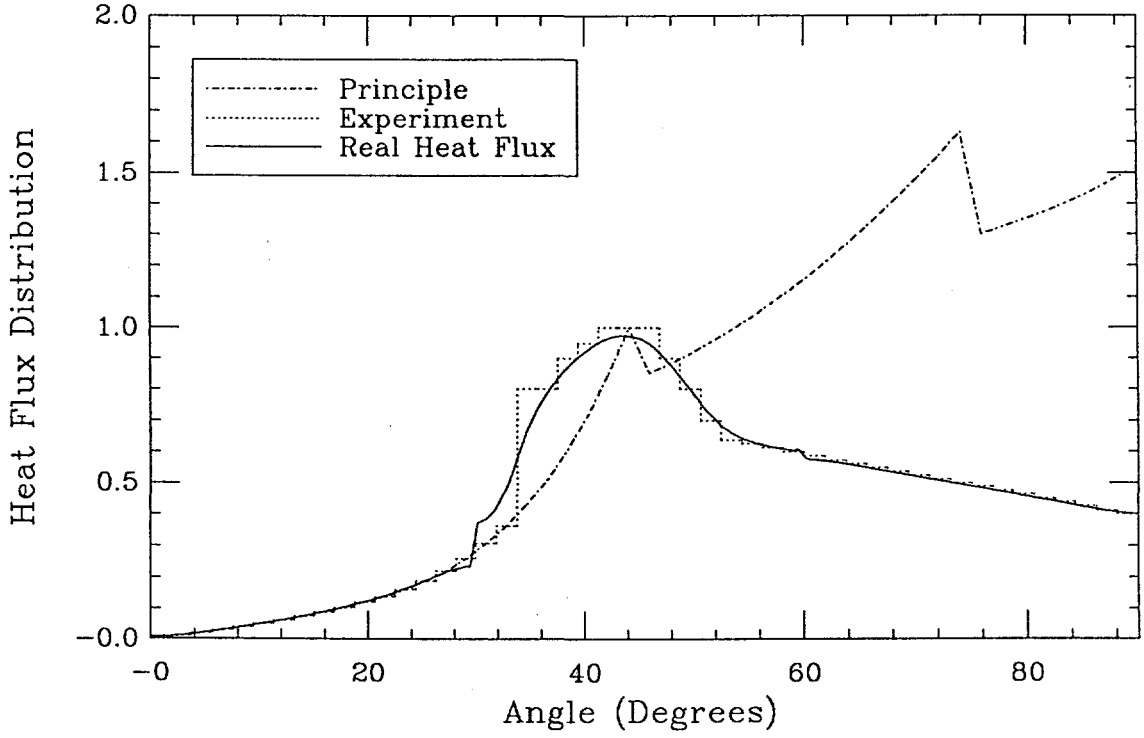

Figure E.9. The actual input and delivered flux shapes in comparison to that obtained from the power shaping principle for run Z24A.

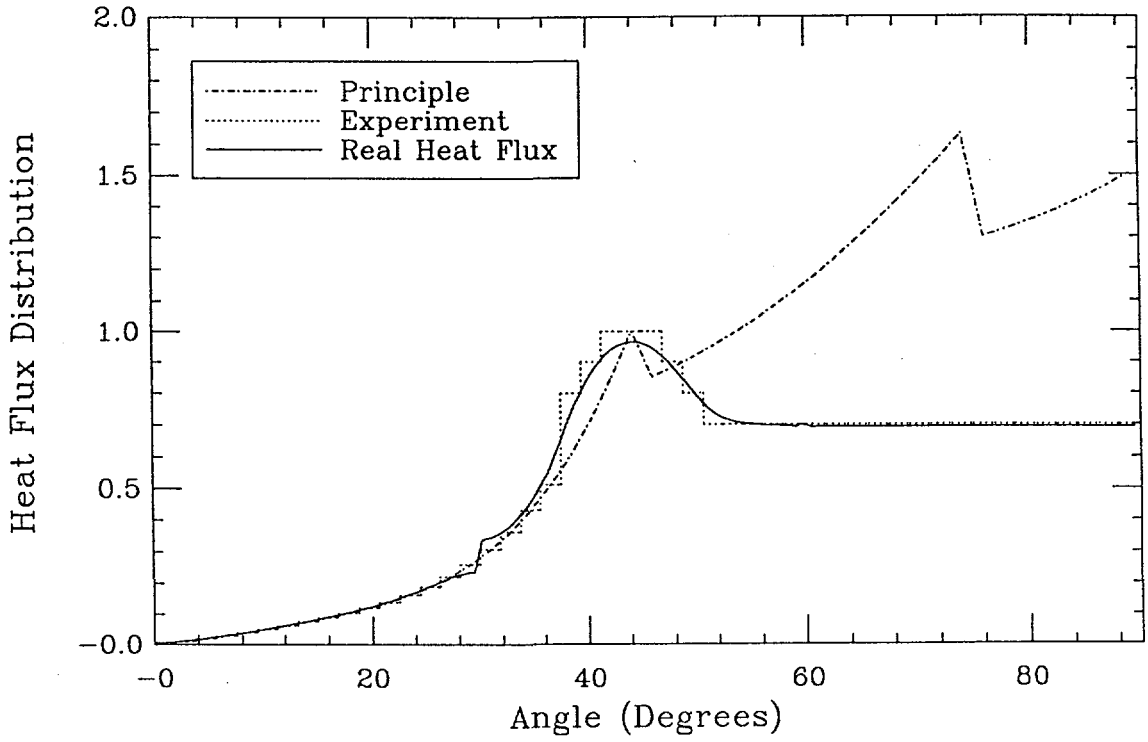

Figure E.10. The actual input and delivered flux shapes in comparison to that obtained from the power shaping principle for run Z24B.

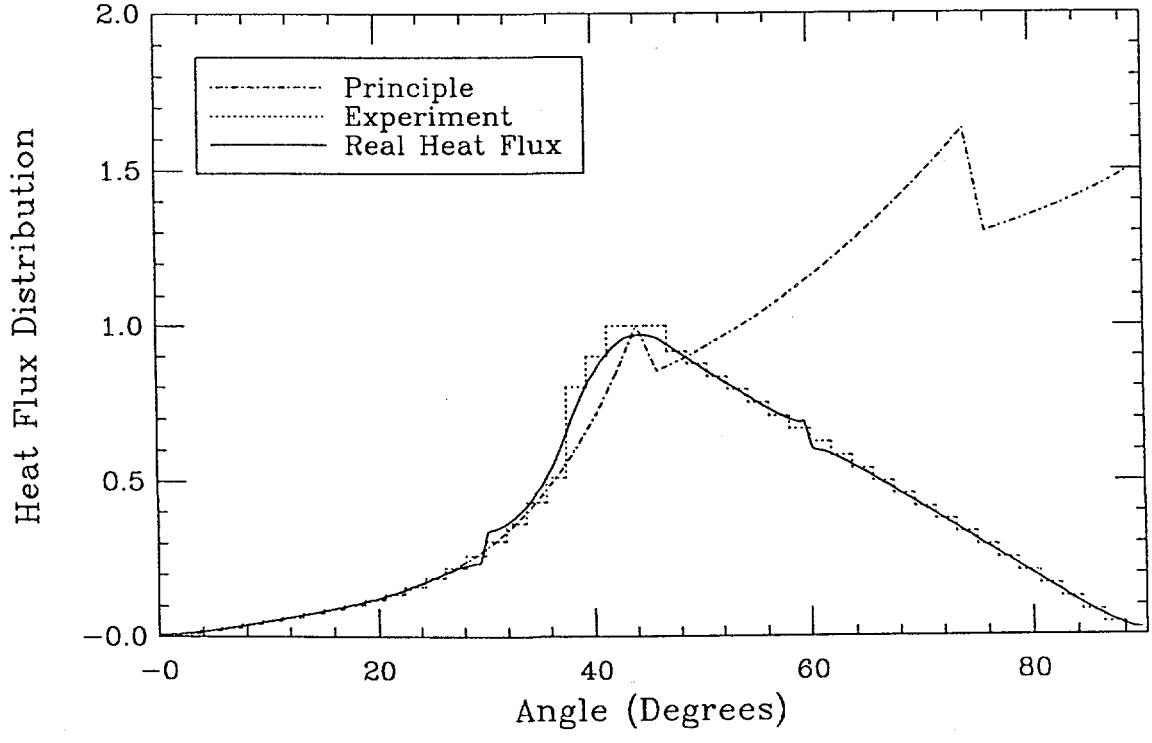

Figure E.11. The actual input and delivered flux shapes in comparison to that obtained from the power shaping principle for run Z24C.

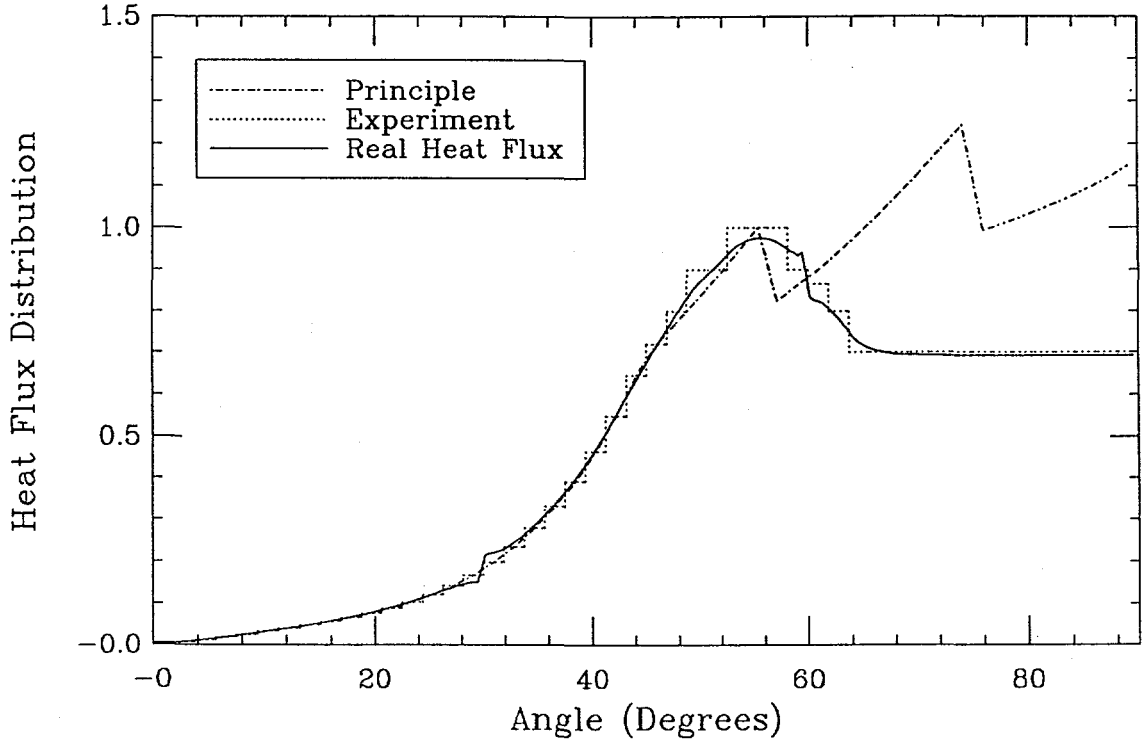

Figure E.12. The actual input and delivered flux shapes in comparison to that obtained from the power shaping principle for run Z30A.

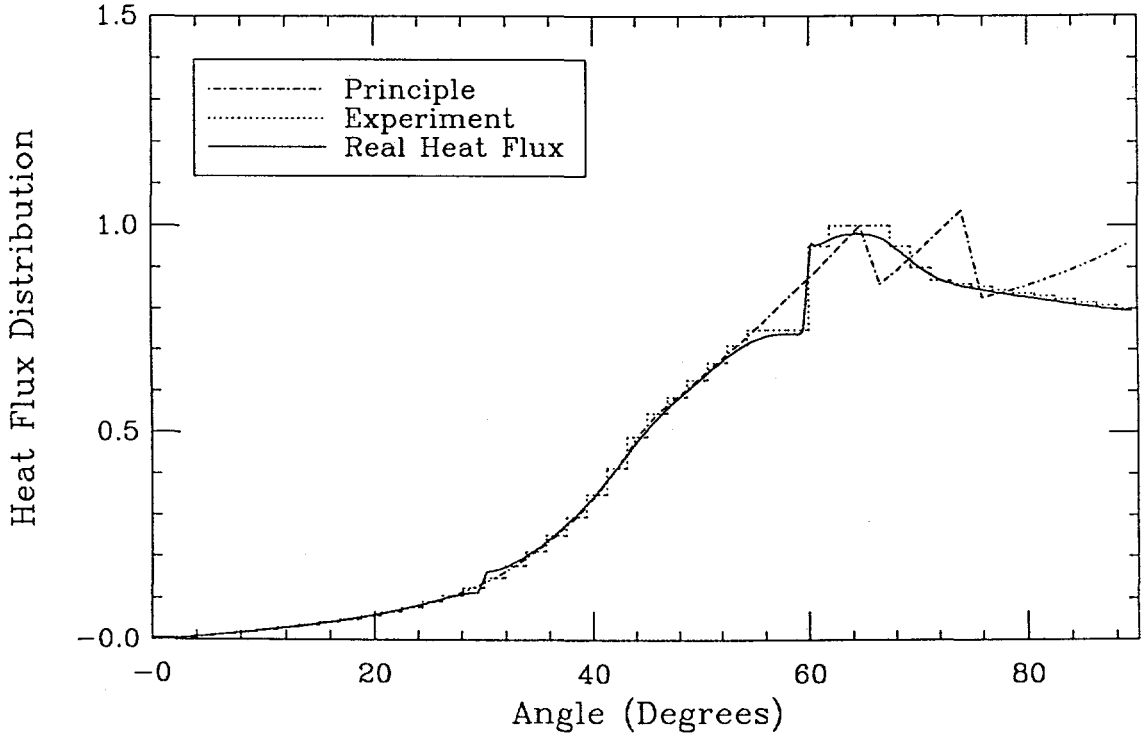

Figure E.13. The actual input and delivered flux shapes in comparison to that obtained from the power shaping principle for run Z35A.

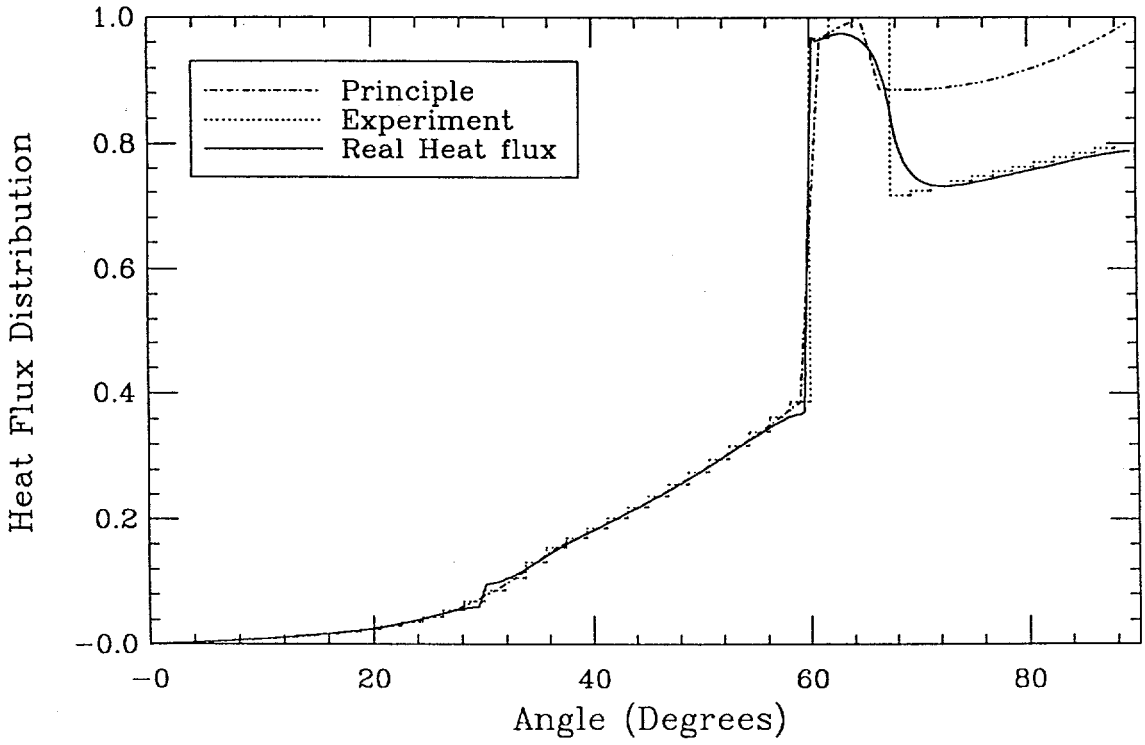

Figure E.14. The actual input and delivered flux shapes in comparison to that obtained from the power shaping principle for run Z35C.

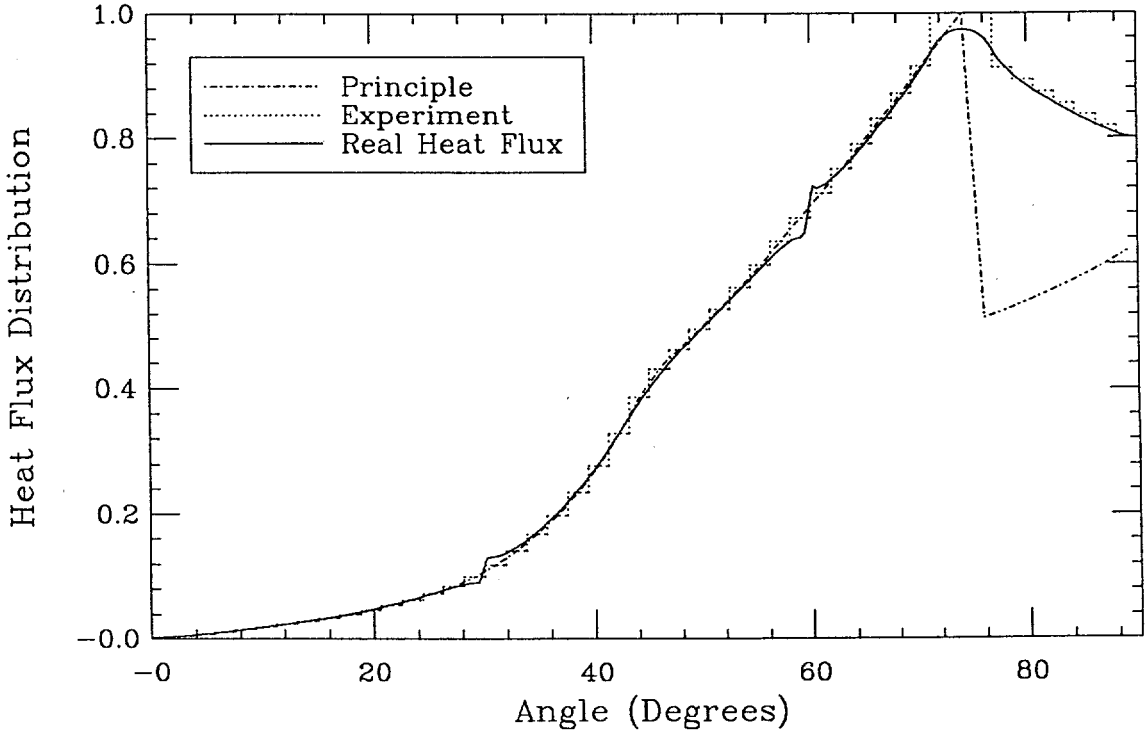

Figure E.15. The actual input and delivered flux shapes in comparison to that obtained from the power shaping principle for run Z40A.

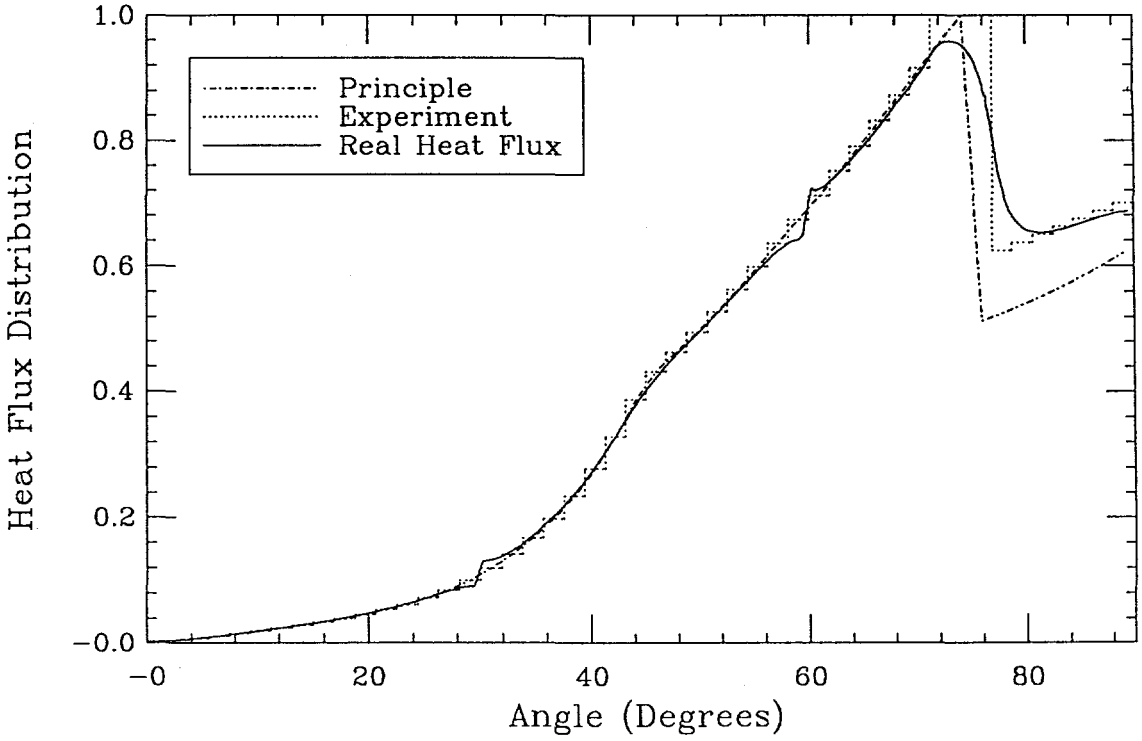

Figure E.16. The actual input and delivered flux shapes in comparison to that obtained from the power shaping principle for run Z40B.

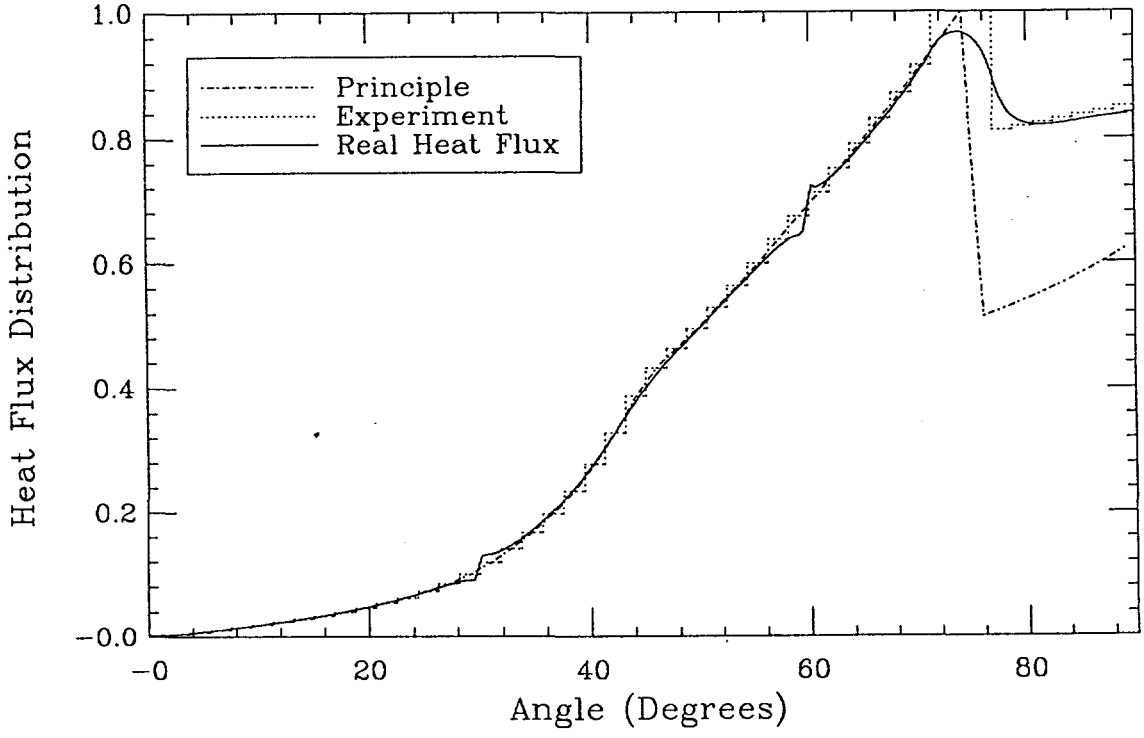

Figure E.17. The actual input and delivered flux shapes in comparison to that obtained from the power shaping principle for run Z40C.

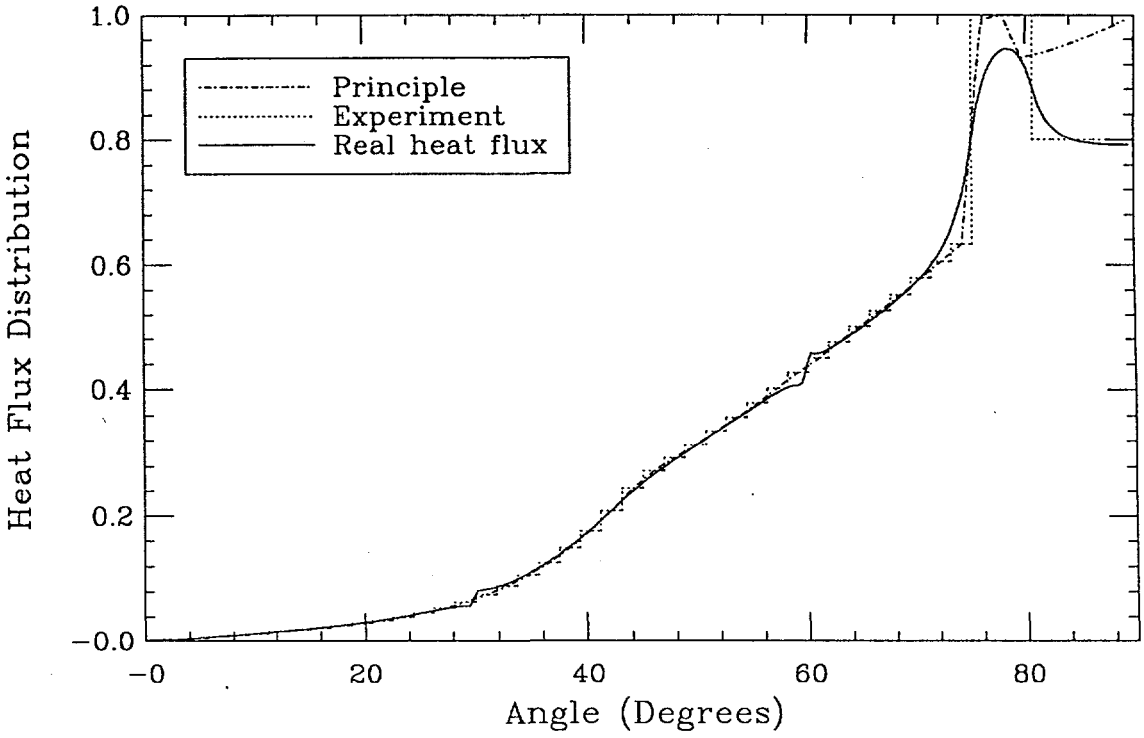

Figure E.18. The actual input and delivered flux shapes in comparison to that obtained from the power shaping principle for run Z42A.

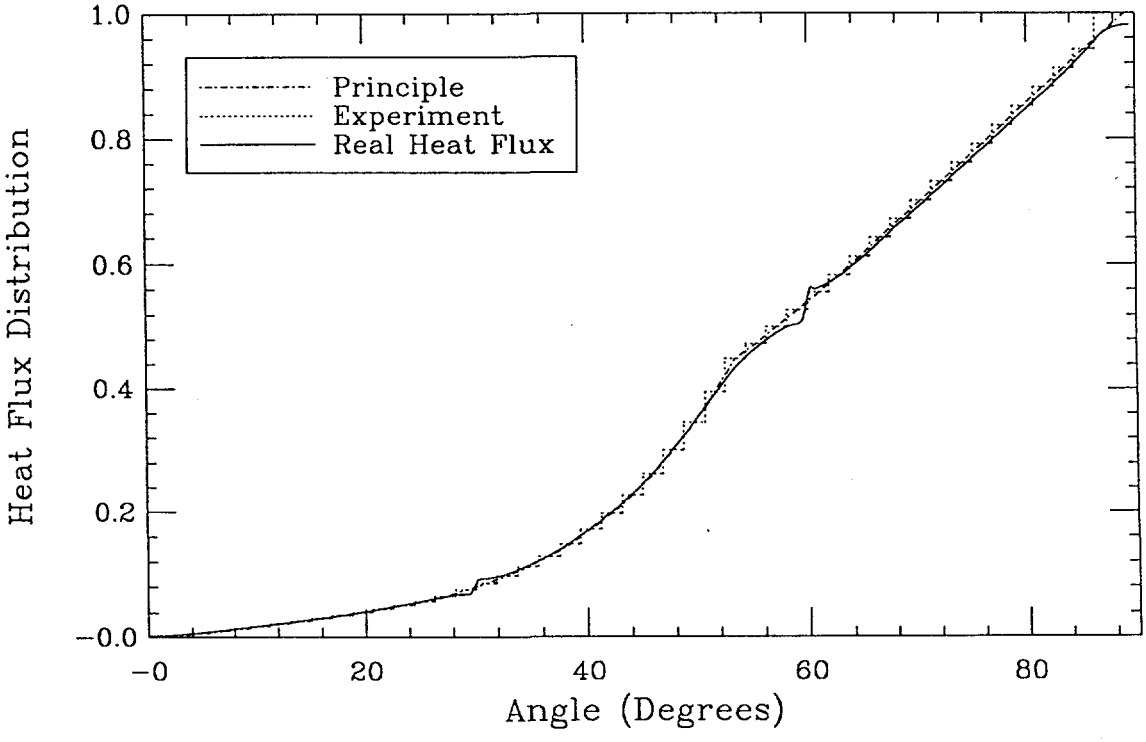

Figure E.19. The actual input and delivered flux shapes in comparison to that obtained from the power shaping principle for run Z48A.

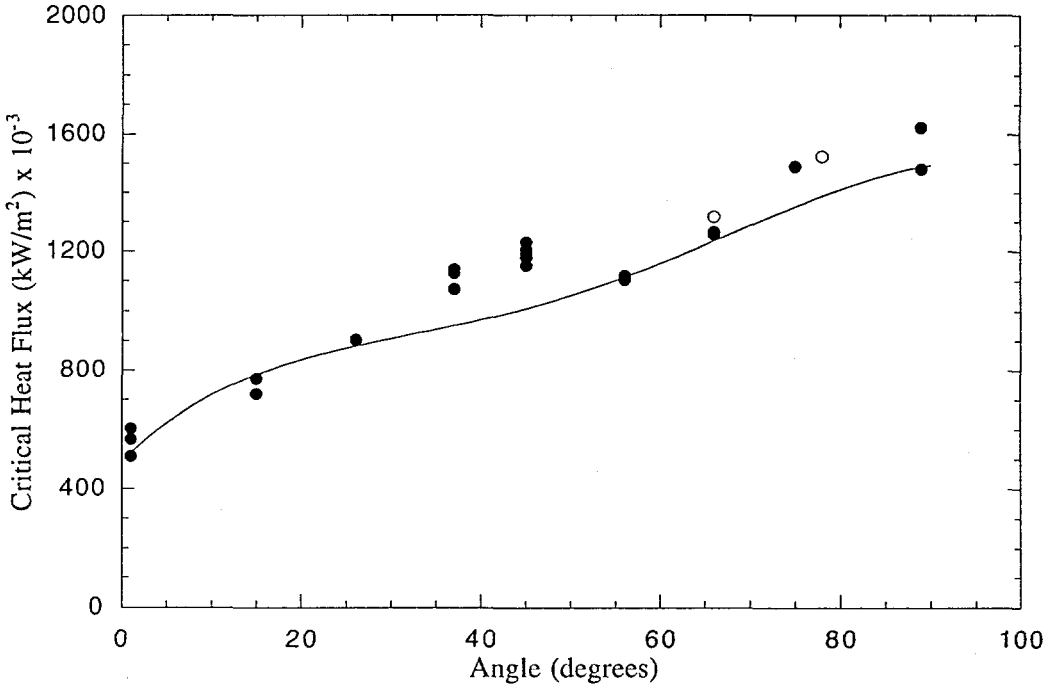

Figure E.20. Comparison of all present full flow data with the correlation in Appendix E.2. The open circles are for flux, with a shape representative of the Extreme Parametric (discontinuous, high peak at the top).

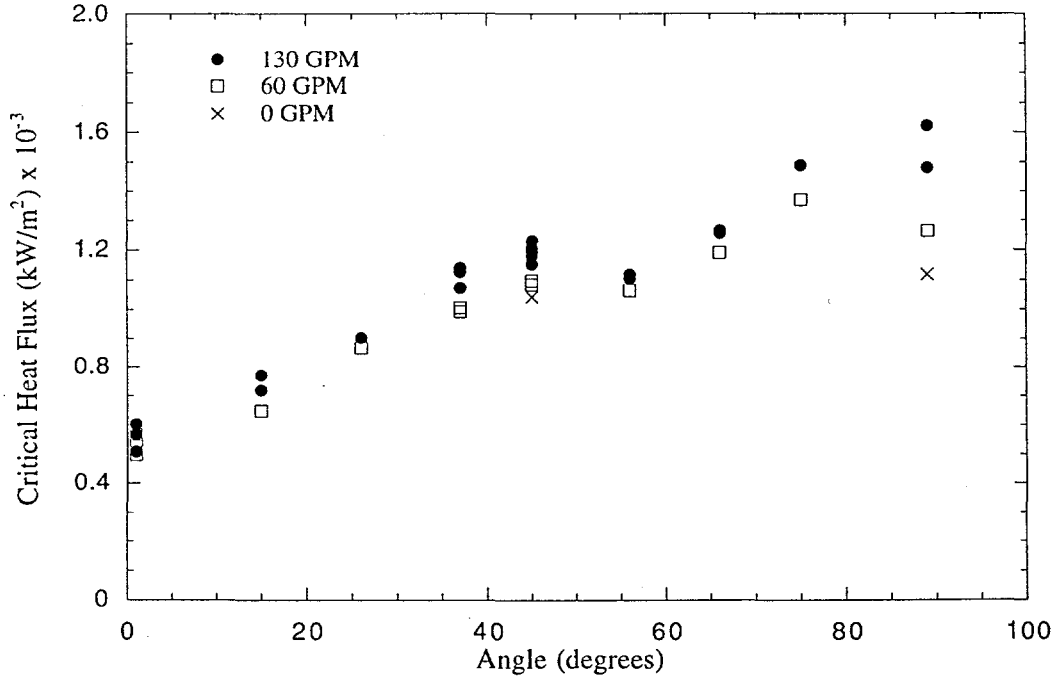

Figure E.21. Sensitivity of measured CHF on natural circulation flow rate.

[[APPENDIX E.4]]
ULPU CONFIGURATION III RESULTS

[[APPENDIX E.4]]
ULPU CONFIGURATION III RESULTS

The Configuration III specifications as shown in Figure E.1 were obtained from Figure K.3a. The baffle simulating the lower part of the reflective insulation was introduced such as to allow the minimum clearance of 9″ (22.86 cm) at an angular position of 30°. The riser is 15.24 cm in diameter as compared to the 15 cm annular gap allowed around the reactor vessel by the insulation. Finally, an exit restriction (10 cm diameter) was introduced as shown to reduce the flow area down to ~40% of that available in the riser (as in the case for the reactor). These riser and restriction dimensions correspond well to the prorated values based on the minimum simulated circumferential fraction in ULPU. This minimum is obtained for a matching angle of 90° and corresponds to 1.2% of the reactor circumference. The riser and restriction areas then become 220 cm^2 and 84 cm^2 respectively, with equivalent diameters of 16.7 cm and 10 cm respectively.

Two sets of experiments were performed: the first focusing on the effect of changes in flow geometry (baffle and exit restriction), and the second on the combined affect (of this change) with heater material and surface. In particular, for the second set the heater block was constructed from prototypic A508 ASTM standard class 3 steel, purchased from one of the potential suppliers of the AP600 reactor vessel (Japan Steel Works, Hokkaido). Half of the block surface was left as bare steel, while the other half ($15° < \theta < 30°$) was painted with the paint normally employed to protect the vessel material (a Carboline G6504L paint employed at a thickness of 0.002 ± 0.001 inch or $0.05 \text{ mm} \pm 0.025$ mm). The paint was cured at 450 °F (232 °C) for 3 to 4 hrs, prior to installation. Contrary to what we were able to learn prior to the actual use of it, this paint appears to bond very well, creating a highly tenacious coating even under prolonged boiling and successive boiling crisis events. Sample microphotographs of the surfaces of all three materials—copper, steel, and Carboline paint on steel, after use in ULPU—are shown in Figures E.2 through E.4. The results are compared to Eq. (E.1) — This is Eq. (E.3) of Appendix E.2) — in Figure E.5.

$$q_{cr}(\theta) = 490 + 30.2\theta - 8.88 \cdot 10^{-1}\theta^2 + 1.35 \cdot 10^{-2}\theta^3 - 6.65 \cdot 10^{-5}\theta^4 \text{ kW/m}^2 \qquad (E.1)$$

The copper data were obtained with the first heater block ($0° < \theta < 30°$) in a "fresh" condition (cleaned to a fine polish), while the other two blocks were fully aged from the experiments reported in Appendix E.3. The power shapes were based on the base case simulations as described in Appendix E.3. The new geometry can be seen to clearly enhance the CHF

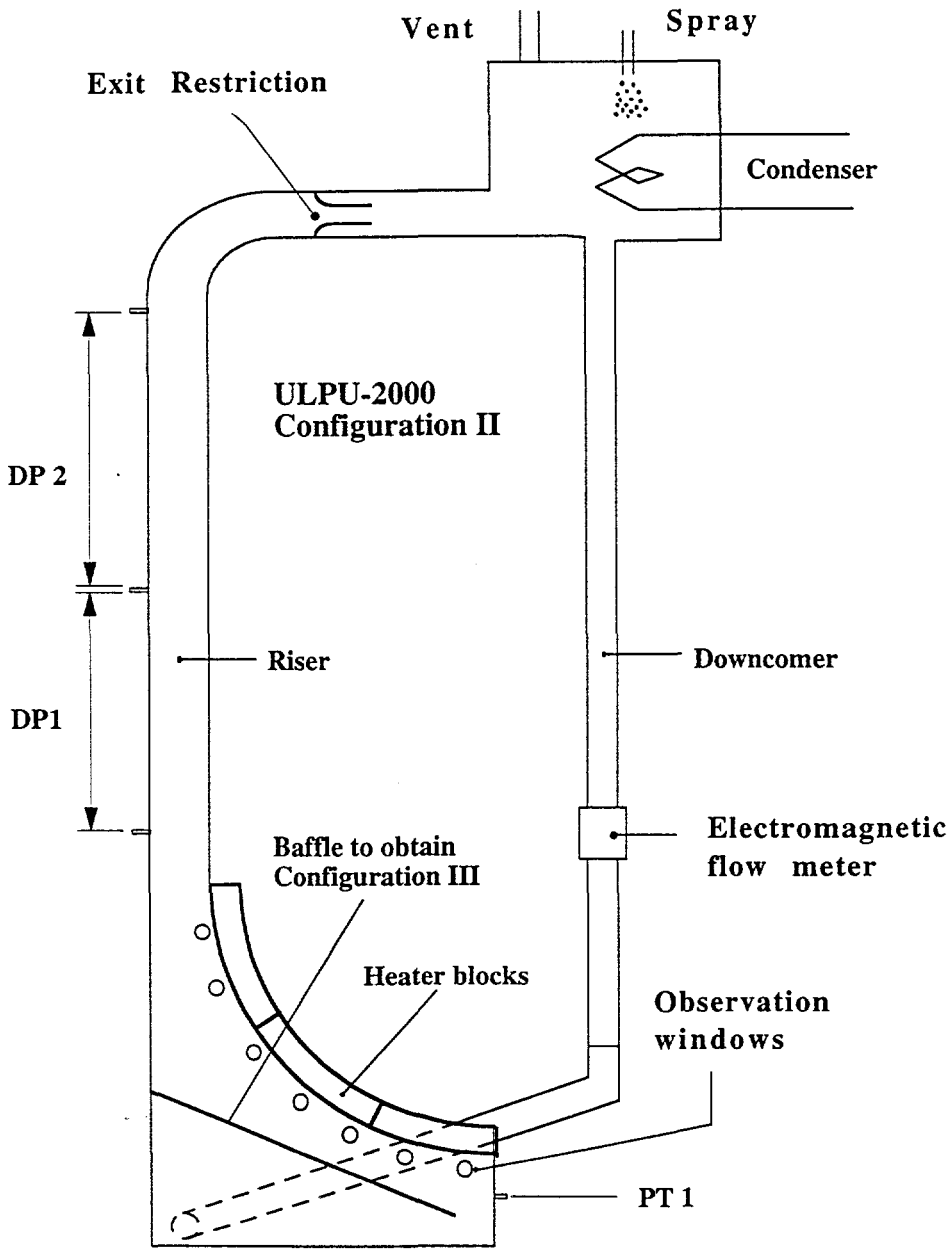

Figure E.1. Schematic of the Configuration III ULPU facility

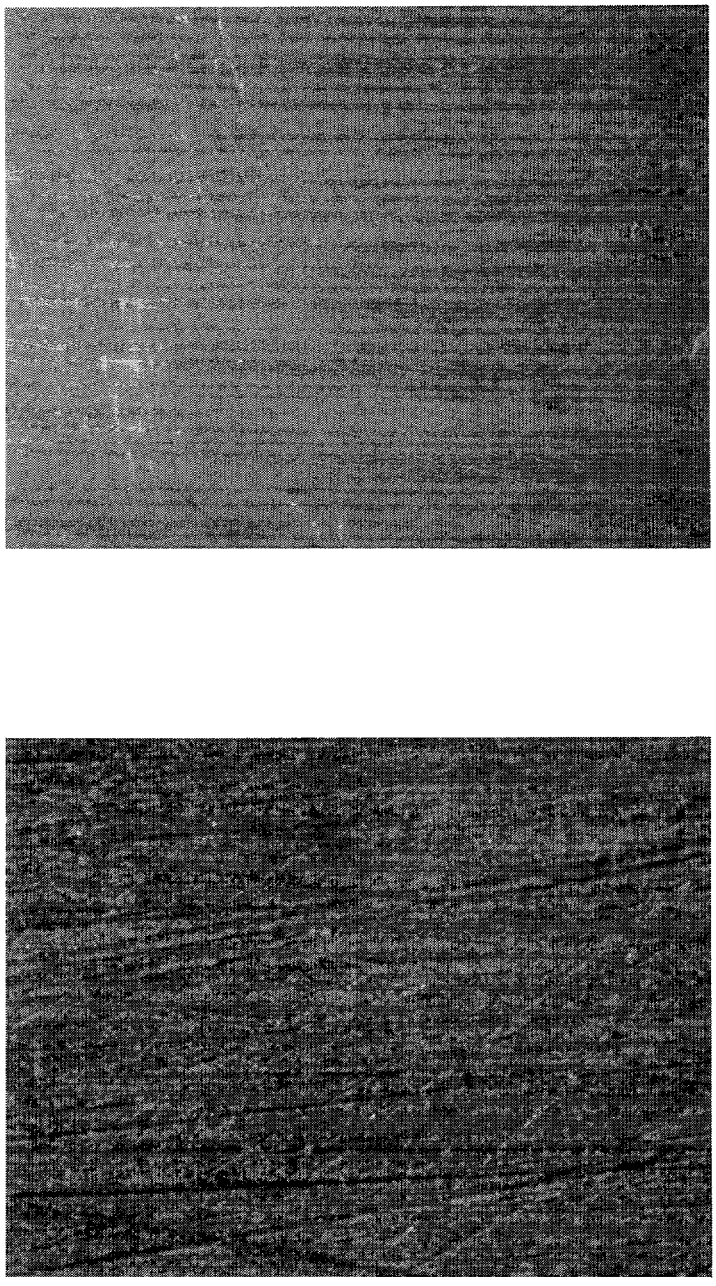

Figure E.2. Microphotographs of the copper heater surface, after exposure in the ULPU tests described in this appendix. Magnifications of 10X and 63X at top and bottom respectively.

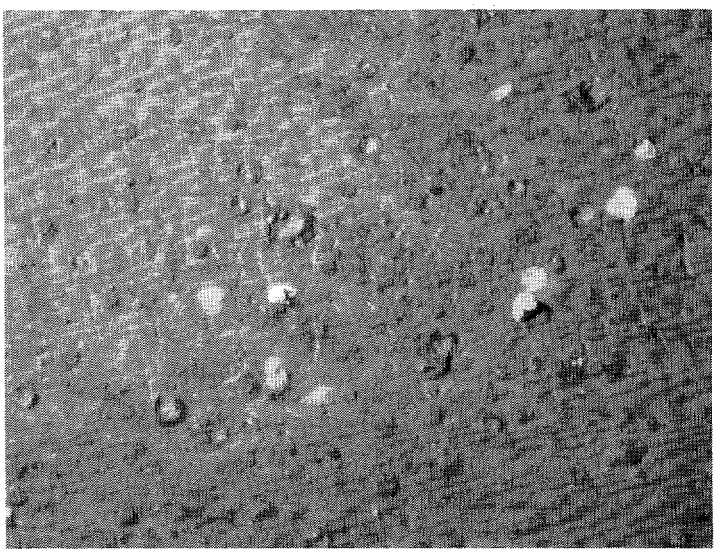

Figure E.3. Microphotographs of the steel heater surface, after exposure in the ULPU tests described in this appendix. Magnifications of 10X and 63X at top and bottom respectively.

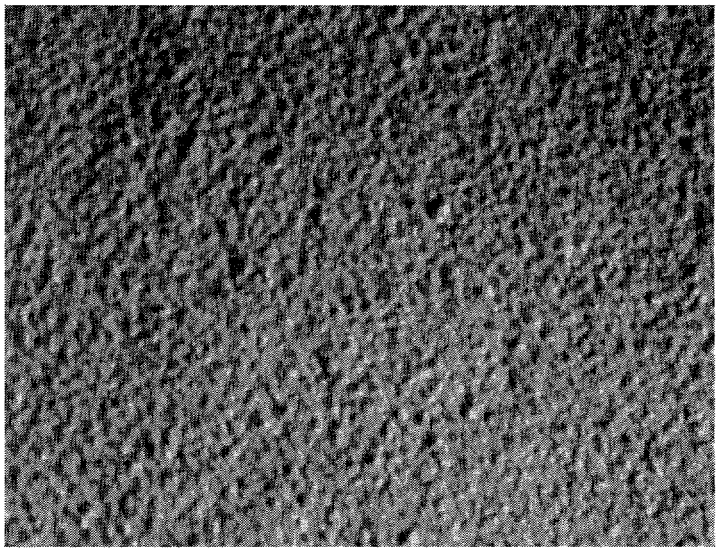

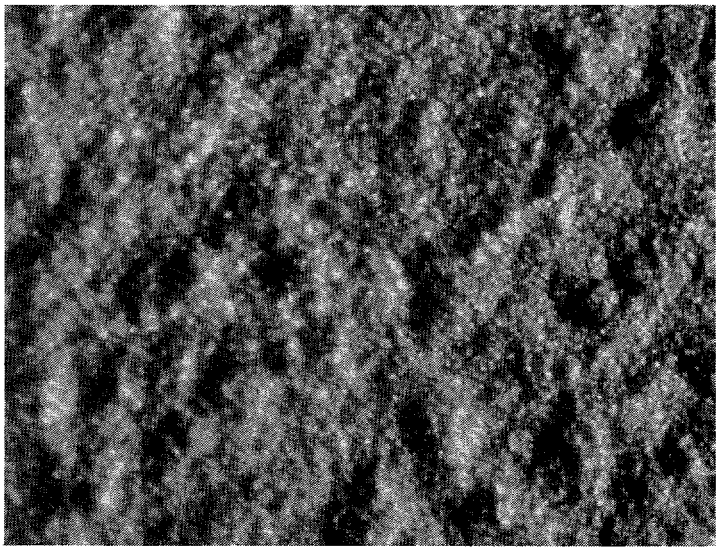

Figure E.4. Microphotographs of the Carboline paint on the steel heater surface, after exposure in the ULPU tests described in this appendix. Magnifications of 10X and 63X at top and bottom respectively.

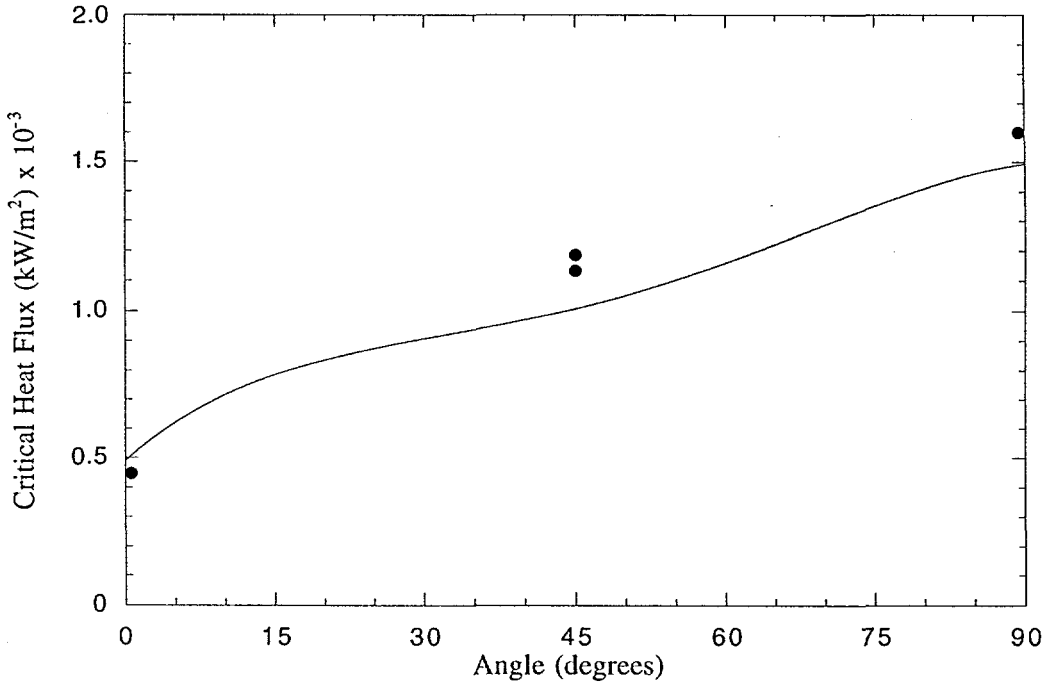

Figure E.5. Summary of Configuration III results in ULPU.

performance. For position $\theta = 0°$ the enhancement is in that the geometry effect is seen to just about compensate for the fresh surface effect, which for copper, as explained in Appendix E.2, is rather significant.

The steel data were obtained with the steel heater block at the low position ($0° < \theta < 30°$), as it is here that surface/material effects would appear first, if at all. All three data points in Figure E.5 are shown as nucleate boiling fluxes, because boiling crisis was not obtained for any of them. The reason is experimental difficulties due to the relatively lower thermal conductivity of steel compared to copper; at high fluxes this causes problems with gasket integrity. This will be overcome in the future, but it did provide a limitation within the tight schedule of completing this appendix in the course of the review. Thus, we began with position $\theta = 0°$ (flux shape shown in Figure E.2 of Appendix E.3), and stopped the power ascension (to conserve the gaskets) as soon as the confirmatory level of heat flux (compared to Eq. E.1) was reached. We then moved to position $\theta = 22° < \theta < 28°$ with the flux shape shown in Figure E.6 of Appendix E.3. Power was increased until the gaskets failed, at which point we had to abandon the test. Fortunately, as seen in Figure E.5, this occurred quite close to the target values (Eq. E.1), thus the confirmatory nature of this test can be considered basically completed. Further elaboration can be expected from our ongoing experimental and analytical efforts aimed at the fundamental mechanism and prediction.

APPENDIX F

THE CYBL EXPERIMENTS

Ex-Vessel Boiling Experiments— Laboratory and Reactor Scale Testing of the Flooded Cavity Concept for In-Vessel Core Retention

Part I: Observations of Quenching of Downward-Facing Surfaces

Part II: Reactor-Scale Boiling Experiments of the Flooded Cavity Concept for In-Vessel Core Retention

Proceedings, Workshop on Large Molten Pool Heat Transfer
Grenoble, France, 9-11 March 1994

APPENDIX F

Ex-Vessel Boiling Experiments— Laboratory and Reactor Scale Testing of the Flooded Cavity Concept for In-Vessel Core Retention

Part I:

Observations of Quenching of Downward-Facing Surfaces

T.Y. Chu, B.L. Bainbridge, R.B. Simpson, and J.H. Bentz
Sandia National Laboratories
Albuquerque, New Mexico

Part II:

Reactor-Scale Boiling Experiments of the Flooded Cavity Concept for In-Vessel Core Retention

T. Y. Chu, J. H. Bentz, and S. E. Slezak
Sandia National Laboratories
and
Walter F. Pasedag, USDOE

ABSTRACT

Flooding a reactor cavity and immersing the reactor pressure vessel in water to extract decay heat from core debris following a severe accident is appealing as a safety feature. A flooded cavity is an accident management concept currently under consideration for advanced light water reactors (ALWRs) as well as for existing light water reactors (LWRs). It was also implemented in the design of the now deferred Heavy Water New Production Reactor (HWR-NPR). One of the uncertainties in the evaluation of the flooded cavity concept arises from the uncertainties in the boiling heat transfer outside of the reactor pressure vessel (RPV) bottom head. Because of the upside-down geometry, the vapor generated in boiling cannot readily move away from the hot surface; rather, it must flow along the surface to the edge before it is released into the bulk liquid. Based on two-phase boundary analysis, it can be shown that the heat transfer process could be scale dependent. The present paper presents the results of two experimental studies of the ex-vessel boiling process. The first experiment, presented in part I, Observations of Quenching of Downward-Facing Surfaces, summarizes the results of a series of quenching experiments to examine the boiling curve of relative large (comparing to existing experimental studies) downward-facing surfaces. The critical heat flux was found to be approximately 50 W/cm^2. The nucleate boiling precess was found to be cyclic in nature. The second experiment, presented in Part II,

Reactor-Scale Boiling Experiments of the Flooded Cavity Concept for In- Vessel Core Retention, summarizes results of reactor-scale ex-vessel boiling experiments performed in the CYBL facility. Experiments with uniform and edge-peaked heat flux distributions up to 20 W/cm^2 across the vessel bottom were performed. Boiling outside the reactor vessel was found to be subcooled nucleate boiling. The subcooling is mainly due to the gravity head which results from flooding the sides of the reactor vessel. The boiling process exhibits a cyclic pattern with four distinct phases: direct liquid/solid contact, bubble nucleation and growth, coalescence, and vapor mass dispersion (ejection). The results suggest that under prototypic heat load and heat flux distributions, the flooded cavity in a passive pressurized water reactor like the AP-600 should be capable of cooling the reactor pressure vessel in the central region of the lower head that is addressed by these tests.

PART I:
OBSERVATIONS OF QUENCHING OF DOWNWARD-FACING SURFACES

T.Y. Chu, B.L. Bainbridge, R.B. Simpson and J.H. Bentz

F.1.0 INTRODUCTION

The design of the Heavy Water New Production Reactor (HWR NPR) as well as the Advanced Light Water Reactor (ALWR) incorporate a flooded reactor cavity as an accident management feature to prevent melt-through of the reactor vessel in the event of a core meltdown accident. It is expected that boiling heat transfer on the outer surface of the bottom head will remove the decay heat from the molten core. One of the uncertainties in the evaluation of the flooded cavity concept arises from the uncertainties in the boiling heat transfer outside of the reactor pressure vessel (RPV) bottom head. Because of the upside-down geometry, the vapor generated in boiling cannot readily move away from the hot surface; rather, it must flow along the surface to the edge before it is released into the bulk liquid.

There is experimental evidence that the boiling process depends on both surface inclination (Nishikawa et al., 1984; Guo and El-Genk, 1991) and scale (Babin et al., 1990). According to the classical study of Nishikawa et al. (1984), at low heat fluxes (< 7 W/cm^2) increasing (toward horizontal) surface inclination was found to increase the effectiveness of heat transfer, but the surface inclination effect diminishes at high heat fluxes (> 17 W/cm^2). Other studies tend to confirm this general trend (Chen, 1978; Guo and El-Genk, 1991).

Despite the observed near independence of nucleate boiling from inclination for downward-facing surfaces at high heat fluxes, critical heat flux (CHF) was found to decrease monotonically with inclination (Guo and El-Genk, 1991, Vishnev et al., 1976; Beduz et al., 1988). The deterioration of CHF accelerates as the surface inclination approaches horizontally downward-facing. Anderson and Bova (1971) obtained boiling curves for downward-facing circular disks with diameters ranging from 5 cm to 30 cm in saturated R-11. They found that the critical heat flux varied inversely with the disk diameter.

While the above mentioned small scale experiments show some alarming trends, recent experiments give rather encouraging results. The integral experiments of Henry et al. (1993a) demonstrated that for highly subcooled water, nucleate boiling heat flux from a 30 cm diameter curved surface exceeds 100 W/cm^2. Steady state experiments by Theofanous et al. (1994), using a section of a two-dimensional slice of an AP-600 like reactor vessel, showed that the critical

heat flux from downward-facing surfaces in saturated water is in the range of 30 W/cm^2. This value is quite favorable compared to the heat dissipation requirement of 10-20 W/cm^2 for in-vessel core retention estimated by Henry et al. (1993a,b).

In the present study, quenching experiments have been performed to examine the boiling processes from downward-facing surfaces using two 61-centimeter diameter test masses, one with a flat test surface and one with a curved test surface having a radius of curvature of 335 cm, matching that of the Cylindrical Boiling (CYBL, See Part II) facility test vessel. The scale of the experiments is between that of reactor-scale and typical centimeter-scale bench experiments (Chu, et al., 1992, 1993), but it is by far the largest experiment of boiling from downward-facing surfaces. Boiling curves were obtained for both test surfaces facing horizontally downward. The boiling process showed some unique features not observed in boiling from upward-facing surfaces.

F.2.0 EXPERIMENTS

A series of intermediate-scale quenching experiments was performed to examine the boiling processes from downward-facing axisymmetric surfaces. These experiments were performed as a presurser to the reactor-scale experiments that have recently been performed in Sandia's Cylindrical Boiling (CYBL) facility.

Two test masses made of 6061 aluminum were used. They were made from 61 cm (24 in.) diameter stock approximately 10 cm (4 in.) thick. The first mass was a simple upright cylinder with a flat bottom (Figure F.1). The second mass was similar to the first, except that the bottom surface had a radius of curvature of 335 cm (132 in.) (Figure F.1), matching the crown radius of the CYBL test vessel. The experimental masses were heated to an elevated temperature between 160°C and 330°C, and then plunged into a pool of water at saturation. The vertical surfaces and the top of the experimental masses were insulated to limit the boiling to only the downward-facing surfaces. Figure F.2 shows how the masses were machined such that the Visilox^R silicone rubber insulating layers were set into the surface so that the test surface extended all the way to the edge of the test mass, and the two-phase flow across the test surface would not encounter an abrupt obstruction or change of material.

The test masses were instrumented with seven pairs of near-surface thermocouples. Each pair consisted of a thermocouple at a depth of 0.64 cm (0.25 in) and one at a depth at 1.27 cm (0.5 in). The near-surface thermocouples were located at radii 1.27 cm (0.5 in) to 27.94 cm (11 in) as shown in Figures F.1 and F.2. The thermocouples used were type K, 1.6 mm (1/16 in.) diameter stainless steel sheathed thermocouples with grounded junctions. These thermocouples

were chosen because they will be used in the reactor-scale CYBL experiments. For ease of installation, the near-surface thermocouples were installed from the water side. Observations during the quenching experiments indicated that the presence of the thermocouples did not cause significant disturbance to the overall characteristics of the boiling process. There were also three thermocouples 1.27 cm (0.5 in) below the top surface of the test mass for interior temperature measurements.

The test surface was machined to a No. 32 finish and then brushed with a fine steel brush. Figure F.3 shows the typical surface texture as machined and after brushing. To ensure identical starting conditions for each experiment, the surface finish was renewed before each experiment by brushing. Each mass was supported from above by a rod screwed into the top. The other end of the rod was connected to an air cylinder that allowed for vertical motion.

The sample was first heated by six two-kilowatt cartridge heaters to the desired initial temperature. After a brief waiting period, when the temperatures were observed to equilibrate, the experiment was initiated by extending the air cylinder and plunging the mass into a test vessel filled with water. The test vessel was a Lexan^R box, 91 cm on each side. The box was filled with de-ionized water to a depth of 60 cm, and the test surface was immersed approximately 15 cm below the water surface. Two auxiliary heaters were used to keep the water at saturation. The quenching process was videotaped through windows in the bottom and the side of the Lexan^R tank. A Hewlett Packard model 3852, 5-1/2 digit integrating analog-to-digital converter was used for data acquisition. The sampling interval was slightly under 0.5 seconds.

F.3.0 EXPERIMENTAL OBSERVATIONS

As a test mass is quenched from an elevated temperature it goes through film boiling, transition boiling, critical heat flux, and finally nucleate boiling.

The liquid/vapor interface during film boiling appears to be relatively stable. The surface can best be described as a visually smooth film with superimposed small amplitude waves, as shown in Figure F.4. The initiation of transition boiling from film boiling is signaled by the appearance of groups of bulges in the vapor film moving around the edge of the test surface. Eventually, the number and locations of bulges around the edge increase, and the bulges move inward to extend across the entire surface.

Transition boiling is characterized by intermittent direct liquid/solid contacts and a liquid/vapor interface with growing and receding bulges, as shown in Figures F.4 and F.5. Over time, the interface appears to have a rather uniform appearance. The typical dimension of bulges is of the order of 1 cm. The intermittent solid/liquid contacts appear as swirling clouds moving

around the surface. The cloudy appearance is probably associated with the rapid vaporization at the contact sites.

As the mass cools further, the critical heat flux (CHF) is reached. The CHF regime is characterized by cyclic explosive vaporization. Shown in Figure F.6 is one such cycle. The cycle starts with a surface covered completely with a vapor film. A small indentation appears in the film probably leading to direct liquid/solid contact. This initial disturbance results in an ever expanding circular region of intense vaporization. As the circular region expands, the vapor film outside of the circle is pushed beyond the edge and released into the bulk liquid. As shown in the side-view in Figure F.7, the vapor mass extends as much as five centimeters away from the surface. The periods of this cyclic event for the flat specimen and the curved specimen are 0.29 and 0.27 seconds, respectively. In time, the explosions become less intense and less far-reaching. While the vapor film thickness still undulates, the amplitude becomes much less. Subsequently, the mass enters the nucleate boiling regime.

Visual observation indicates that nucleate boiling from downward-facing surfaces is a cyclic process. Starting with direct liquid/solid contact, bubbles nucleate at various sites. These bubbles grow and coalesce into larger bubbles (Figures F.4 and F.8). For the flat surface at high heat fluxes ($q > 10$ W/cm^2), the coalescence phase ends with nearly the entire surface covered with one single vapor mass.

At high heat fluxes, the ejection phase is vigorous and chaotic. The large single vapor mass may break into several pieces and slide off the surface in several directions or shed away as a single entity. However, over time, the process appears to be quite rhythmic and the directions in which the vapor masses leave appear to be random. At high heat fluxes, nucleation takes place immediately at the freshly exposed surfaces left by the shedding fragments of the large vapor mass. Therefore, the ejection phase of the first cycle and the growth phase of the second cycle actually overlap in time; the surface is partly covered by large retreating vapor masses of the first generation and the new bubbles of the second generation nucleating and growing in between the retreating large vapor masses (Figure F.9). At intermediate heat fluxes (3 W/cm^2 $< q <$ 10 W/cm^2) bubbles do not always grow to cover the entire surface before the ejection phase (Figure F.10). For low heat fluxes ($q < 3$ W/cm^2), the nucleation sites become far apart and bubble coalescence becomes increasingly local in scale. Eventually, at lower heat fluxes, the surface is covered with a few growing bubbles lumbering toward the edge of the surface with a significant portion of the surface in direct contact with the bulk liquid. For the curved surface, the cyclic process still applies. However, as a result of the geometry the shedding of the vapor masses from the surface is more regular, always taking a more or less radial direction, especially at lower heat fluxes. It is also interesting to note, for the curved surface at low heat fluxes, the

bubbles take a crescent shape as they move toward the edge of the surface, as shown in Figure F.10.

The thermocouple data are processed with an inverse conduction code SODDIT (Blackwell et al., 1987) to obtain boiling curves. SODDIT is a finite difference code that can be used to solve one and quasi-two-dimensional direct and inverse heat conduction problems. When solving inverse problems, the unknown surface heat flux is calculated by minimization of the squared error between the temperatures measured at specified locations and the corresponding computed temperatures. In addition, more than one future time can be used in the heat flux calculation to reduce the effect of measurement error and noise.

During preliminary experiments, it was discovered that while the cooling rates over the test surface were reasonably uniform during film boiling; the rates started to diverge considerably as transition boiling approached. Transition boiling occurred first near the edge of the test surface and moved inward. Therefore, the heat transfer within the mass became multi-dimensional. As a result, different locations on the surface underwent critical heat flux at different times, making it highly inaccurate to use the SODDIT code to calculate the surface flux. However, if the initial temperature were in the range of transition boiling, the temperature response over the surface became nearly uniform. This is probably related to the nearly uniform appearance of the surface during transition boiling (Figure F.5). Therefore, two sets of experiments were performed. High temperature quench from 330°C was used to obtain the film boiling to transition boiling portion of the boiling curve, and low temperature quench from 160°C to 170°C was used to obtain the transition boiling to nucleate boiling portion of the curve.

A composite boiling curve for the flat specimen from three low temperature quench experiments and one high temperature quench experiment is shown in Figure F.11. The critical heat flux is found to be between 40–60 W/cm^2; the corresponding superheat is approximately 30°C. The spread of the data represents an experimental uncertainty of approximately ±20%. This critical heat flux is higher than those reported for previous experiments using 15-m test masses (Chu et al., 1992b). We feel that the previous results are in error because data rates were too low, and the quenching curve failed to resolve the high cooling rates associated with the critical heat flux. The present CHF values are also higher than those obtained by Guo and El-Genk (1991) quenching a 50 mm copper disk. We believe the Guo and El-Genk CHF value is low because of the effect of the insulation rim around their quenching specimen. As shown in Ishigai et al. (1961) experiments, the CHF value decreases by almost a factor of two with the size of the insulating rim around the Guo and El-Genk test specimen.

The 10°C superheat corresponding 10 W/cm^2 is in good agreement with previous quenching experiments (Chu et al., 1992b) as well as the results of Nishikawa et al. (1984) and Guo and

El-Genk (1991). A boiling curve is also calculated for the curved specimen (Figure F.12). The critical heat flux is essentially the same as that for the flat surface. The nucleate boiling portion of the curve is slightly below that for the flat surface. This is consistent with previously observed trends of the effects (Nishikawa, et al., 1984, Guo and El-Genk 1991) of surface inclination.

It is interesting to note that there appears to be a rather distinct change of slope of the boiling curve near 10 W/cm^2. This transition is analogous to the transition from the isolated bubble regime to that of slugs and columns for upward-facing surfaces, as first pointed out by Lienhard (1985). As described earlier, for heat flux less than 10 W/cm^2, the bubbles do not always grow large enough to coalesce into a large vapor mass to cover the entire surface before the ejection phase. But for higher heat fluxes, the ejection phase is always associated with a surface-size vapor mass. There are also changes in the rhythmic/cyclic behavior of the boiling process associated with the transition. The general trend is for the cycle period to increase (as well as the nucleation site density to decrease) with decreasing heat flux. Between critical heat flux and 10 W/cm^2, the cycle time increased by about 17%. Whereas, between 10 W/cm^2 and 5 W/cm^2, the cycle time increased by more than 30%.

F.4.0 CONCLUDING REMARKS

Quenching experiments have been performed to examine the boiling processes from downward-facing surfaces using two 61-centimeter diameter test masses, one with a flat test surface and one with a curved test surface having a radius of curvature of 335 cm. Boiling curves were obtained for both test surfaces facing horizontally downward. The critical heat flux was found to be essentially the same, having an average value of approximately 50 W/cm^2. This value, while smaller than the accepted value of CHF for upward-facing surfaces (typically 100-130 W/cm^2), is larger than those obtained from correlations derived from smaller scale experiments (Guo and El-Genk, 1991; Vishnev et al., 1976). The critical heat flux is significantly higher than the estimated heat fluxes required for in-vessel core retention for the HWR NPR (Jedruch, 1992) and for light water reactors (Henry, et al., 1993a,b); those values are 16 W/cm^2 and 20 W/cm^2, respectively.

The liquid/vapor interface during film boiling appears to be relatively stable. The traveling bubble pattern observed by Bui and Dhir (1985) on vertical surfaces was not observed. The liquid/vapor interface can best be described as a visually smooth film with superimposed small amplitude waves.

Transition boiling is characterized by intermittent direct liquid/solid contacts and a liquid/vapor interface with growing and receding bulges. Over time, the interface appears to have a rather uniform appearance. The typical dimension of bulges is of the order of 1 cm.

The critical heat flux regime is characterized by cyclic explosive vaporization with circular expansion patterns. The periods of this cyclic event for the flat specimen and the curved specimen are 0.29 and 0.27 seconds, respectively.

The nucleate boiling process is found to be cyclic with four relatively distinct phases: direct liquid/solid contact, nucleation and growth of bubbles, coalescence, and ejection. The general trend is for the cycle time to increase with decreasing heat flux.

Traditionally, experiments aimed at investigating basic mechanisms of boiling and theoretical treatments of boiling have concentrated on upward-facing flat surfaces. Other geometries have been treated as extensions of upward-facing surfaces. However, the current experiments reveal rather unique flow patterns compared to those observed from upward-facing surfaces. While there are similarities in the initial nucleation and growth of bubbles, there appear to be substantial differences in the mechanisms of late-phase growth, coalescence and detachment of vapor masses in the nucleate boiling regime, and in the appearance of near surface two-phase flow, approaching CHF. Although many of the key mechanisms of the current hydrodynamic stability based theory of CHF are not operational in downward-facing boiling, both boiling processes generate the characteristic boiling curve. It is appropriate to recall a recent lecture by Bergles (1992): "nucleate boiling still defies accurate prediction [and] ... there is a lack of agreement on the mechanism of critical heat flux." The present observations, although qualitative, suggest that perhaps by examining upward-facing and downward-facing boiling in parallel experiments, it would be possible to single out a common set of mechanisms that give rise to the boiling curve. These mechanisms can then be considered necessary and sufficient to build a mechanistic model of boiling.

F.5.0 REFERENCES

Anderson, R. P., and L. Bova, 1971, "The Role of Dowfacing Burnout in Post-Accident Heat Removal," Trans. Am. Nucl. Soc., Vol. 14, p. 294.

Babin, B. R., W. Linear, and G. P. Peterson, (1990), "Cooling Electronic Component with Thermosyphons," Thermal Modeling and Design of Electronic Systems and Devices, HTD-vol. 153, ASME, New York, N.Y., pp. 89-94.

Beduz, C., R. G. Scurlock, and A. J. Sousa, 1988, "Angular Dependence of Boiling Heat Transfer Mechanisms in Liquid Nitrogen," Advances in Cryogenic Engineering, Vol. 33, pp. 363-370.

Bergles, A. E., 1992, "What are the Real Mechanisms in Pool Boiling?" Pool and External Flow Boiling, Eds., V. K. Dhir and A. E. Bergles, ASME, New York, NY.

Blackwell, B. F., R. W. Douglass, and H. Wolf, 1987, A User's Manual for the Sandia One-Dimensional Direct and Inverse Thermal (SODDIT) Code, SAND85-2478, Sandia National Laboratories, Albuquerque, NM.

Bui, T. D., and V. K. Dhir, 1985, "Film Boiling Heat Transfer on an Isothermal Vertical Surface," J. Heat Trans., Vol. 107, pp. 764-771.

Chu, T. Y., R. C. Dykhuizen, and C. E. Hickox, 1993, Scoping Studies of Boiling Phenomena Associated with the Flooded Cavity Design of the Heavy Water New Production Reactor, SAND 91-2383, NPRW-SA91-7, Sandia National Laboratories, Albuquerque, NM.

Chu, T. Y., R. C. Dykhuizen, and C. E. Hickox and B. L. Bainbridge, 1992, "Boiling from Downward Facing Surfaces with Applications to the Flooded Cavity Concept," ANS Proceedings, 1992 National Heat Transfer Conference, San Diego, CA, HTC-Vol. 6, pp. 367-375.

Guo, Z., and M. S. El-Genk, 1991, "An Experimental Study of the Effect of Surface Orientation on Boiling Heat Transfer During Quenching," Proceedings ASME Winter Annual Meeting, Atlanta, GA, Dec. 2-5.

Henry, R. E., J. P. Burelbach, R. T. Hammersley, C. E. Henry and G. T. Klopp, 1993a, "Cooling of Core Debris within the Reactor Vessel Lower Head," Nuclear Technology, Vol. 101, pp. 385-399.

Henry, R. E., H. K. Fauske, 1993b, "External Cooling of a Reactor Vessel Under Severe Accident Conditions," Nuclear Engineering and Design, Vol. 139, pp. 31-43.

Ishigai, S., K. Inoue, Z. Kiwaki, and T. Inai, 1961, "Boiling Heat Transfer from a Flat Surface Facing Downward," Proceedings of International Heat Transfer Conference, Boulder, Colorado, 1961, p. 224-229.

Jedruch, J., 1992, Post-Melt Heat Flux Estimate in 670 MWt NPR Lower RV Head, EBASCO Services Inc. Report, New York, NY.

Lienhard, J. H., 1985, "On the Two Regimes of Nucleate Boiling", J. Heat Trans., Vol. 107, pp. 262-264.

Nishikawa, K., Y. Fujita, S. Uchida, and H. Ohta, 1984, "Effect of Configuration on Nucleate Boiling Heat Transfer," Int. J. Heat Mass Transfer, Vol. 27, pp. 1559-1571.

Theofanous, T.G., S. Syri, T. Salmassi, O. Kymäläinen, and H. Tuomisto, 1994, "Critical Heat Flux Through Curved, Downward Facing, Thick Walls," Proceedings, OECD/CSNI/NEA Workshop on Large Molten Pool Heat Transfer, Nuclear Research Center, Grenoble, France, March, 1994.

Vishnev, I. P., I. A. Filatov, Y. A. G. Vinokur, V. V. Gorokhov, and V. V. Svalov, 1976, "Study of Heat Transfer in Boiling of Helium on Surfaces With Various Orientations," Heat Transfer – Soviet Research, Vol. 8, No. 4, pp. 194-108.

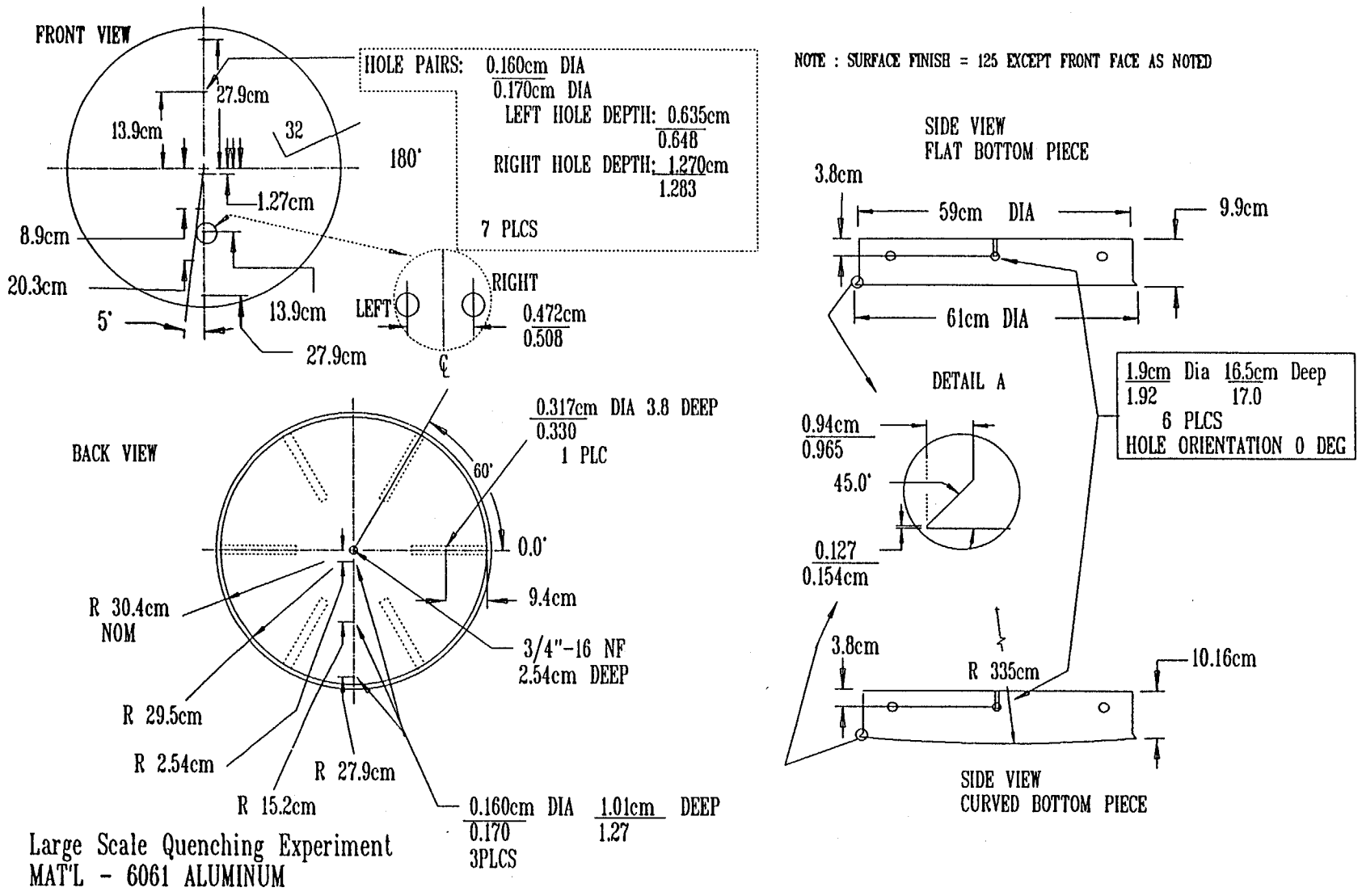

Figure 1. Design of Test Specimens

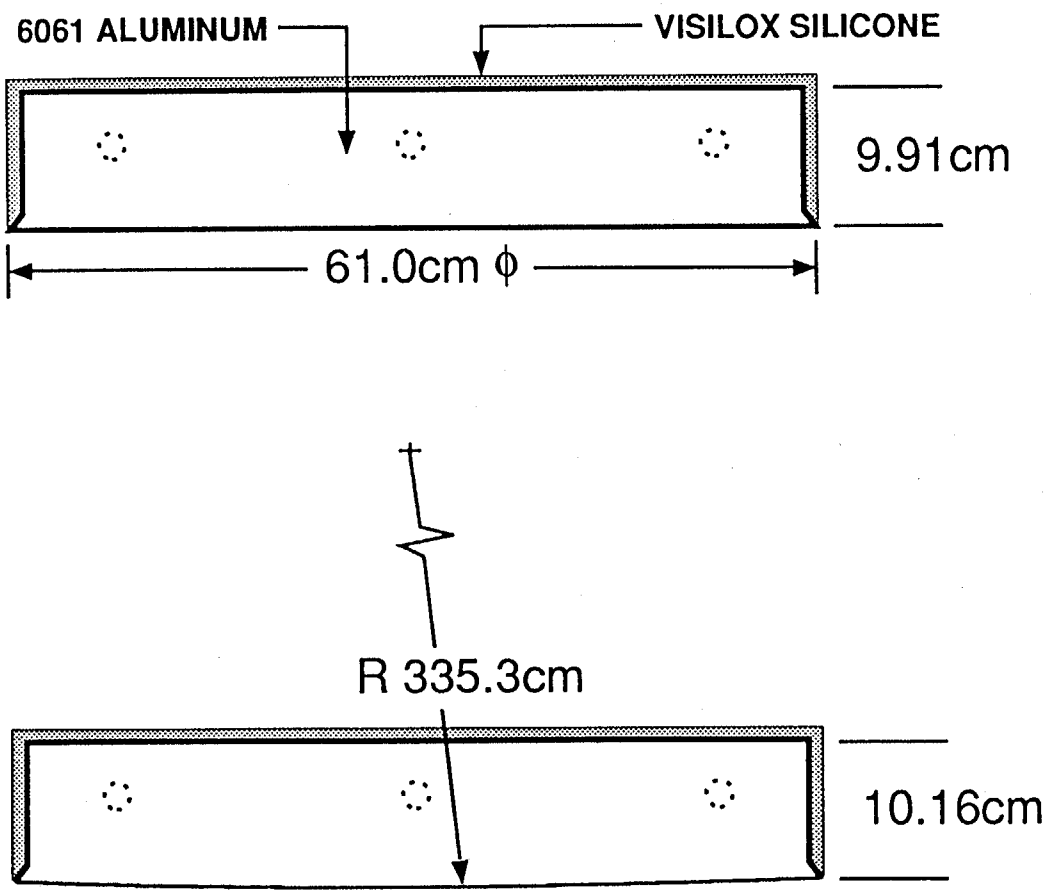

Figure 2. Design of Test Specimen Insulation

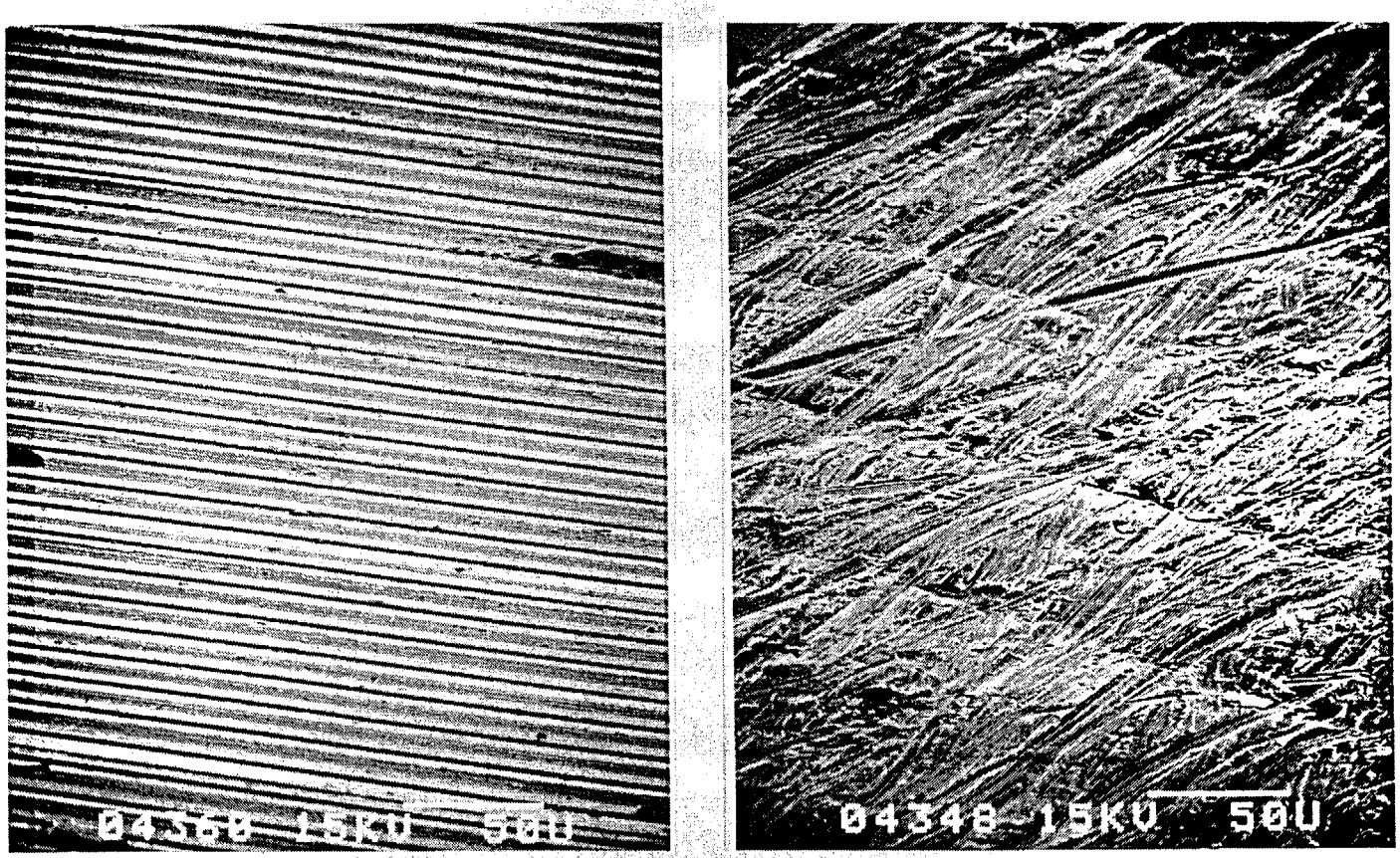

Figure 3. Scanning Electron Micrograph of Test Surface, 400X and 70° Viewing Angle

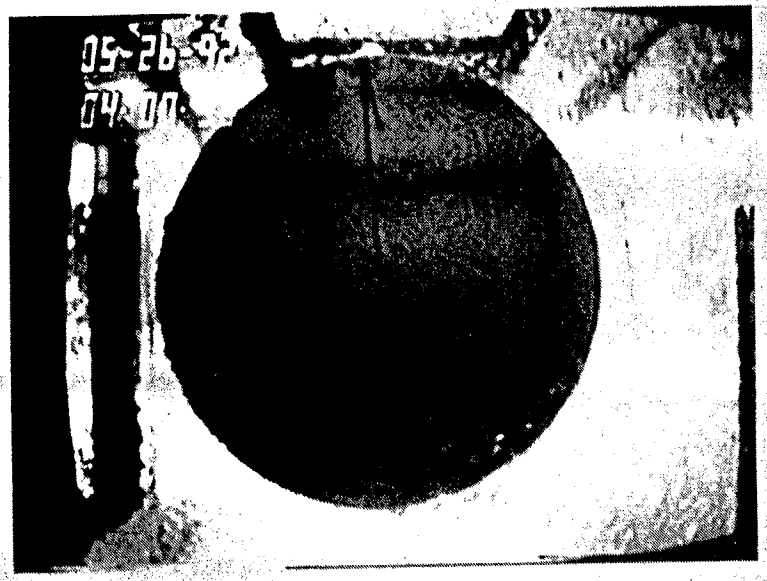

Film Boiling

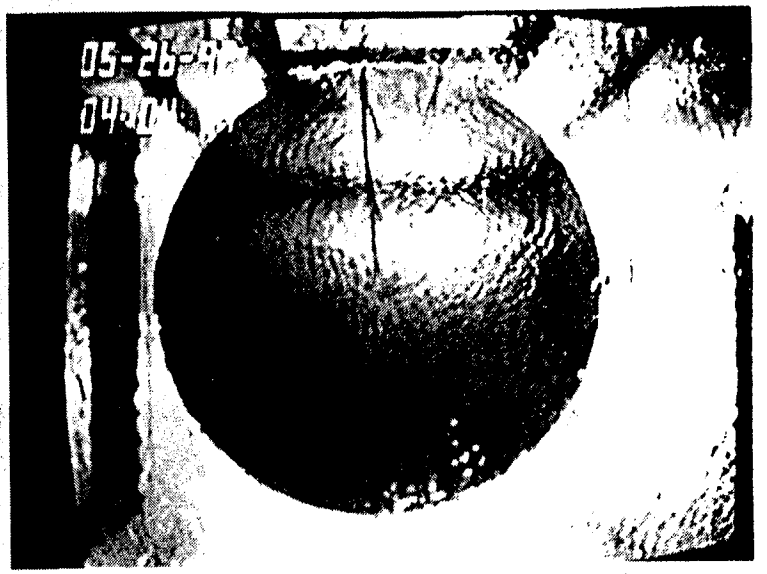

Film Boiling Instability

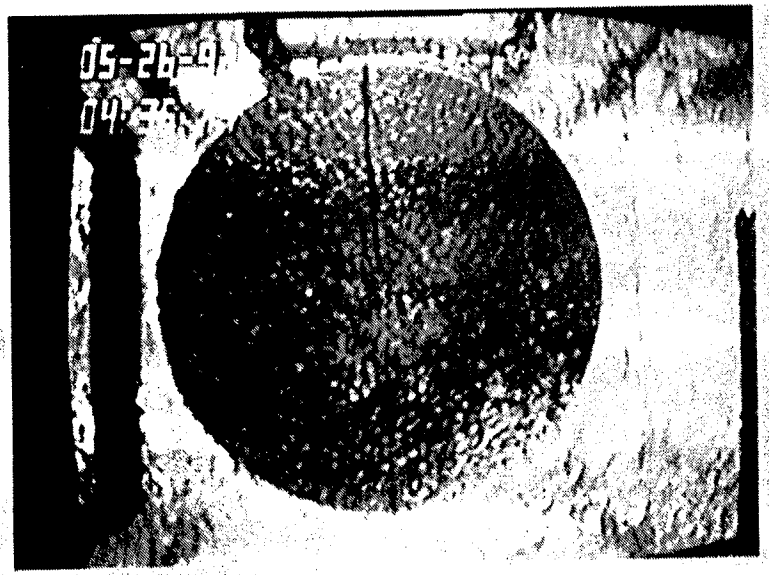

Transition Boiling

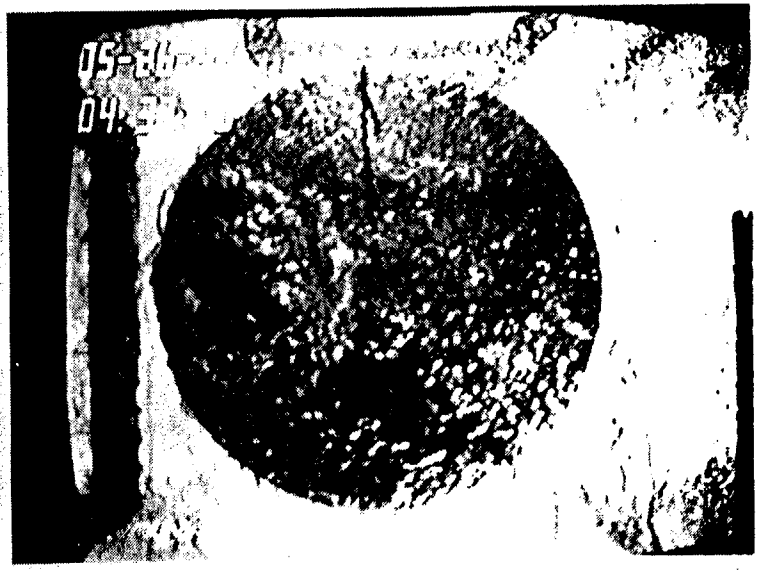

Nucleate Boiling (High Heat Flux)

Figure 4. Video Frames of the General Appearance of Liquid/Vapor Interface for Different Boiling Regimes.

Figure 5. Photograph of the Liquid/Vapor Interface in Transition Boiling

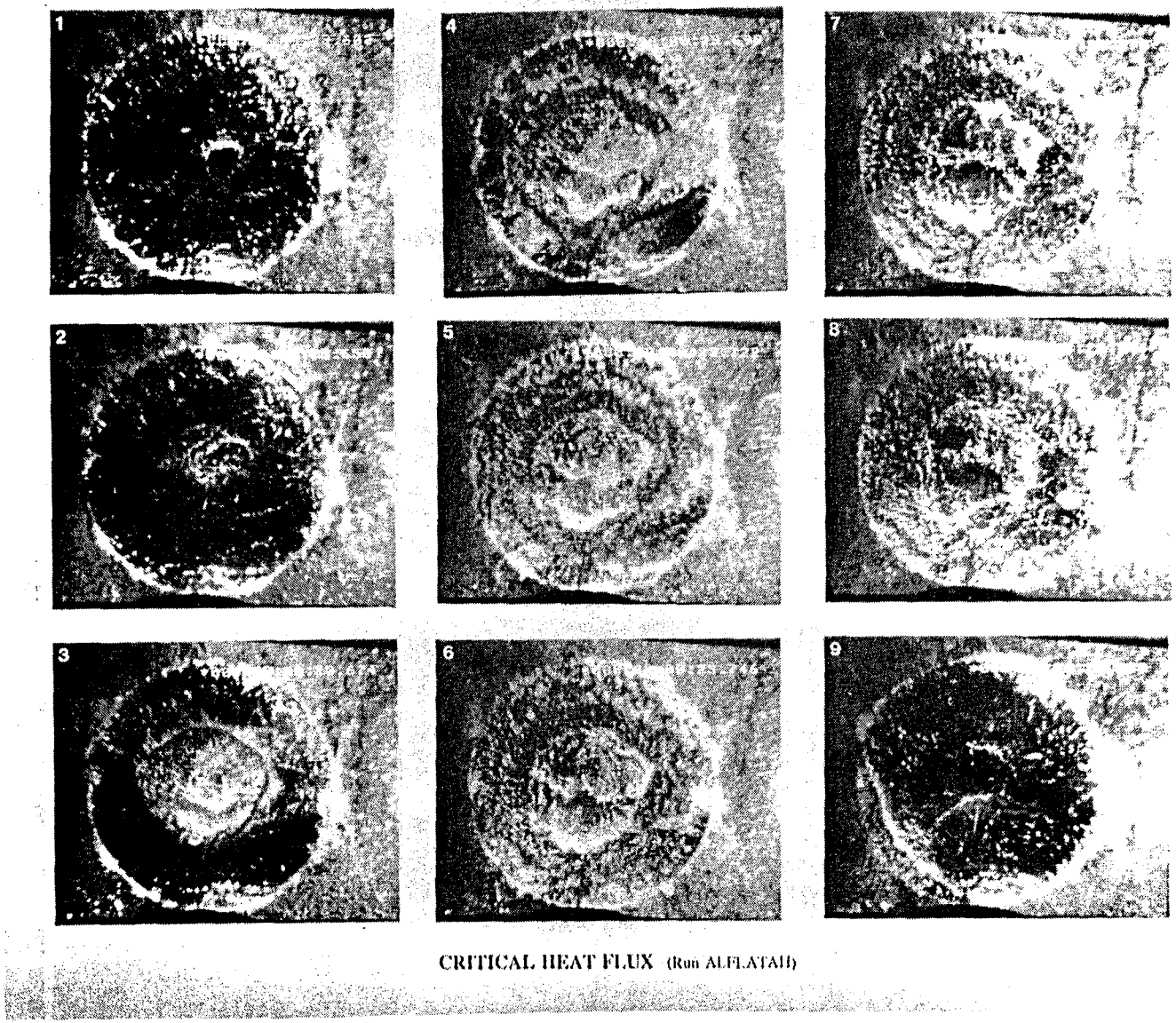

Figure 6. Video Frames of a Cycle of Explosive Vapor Formation at CHF, Bottom View

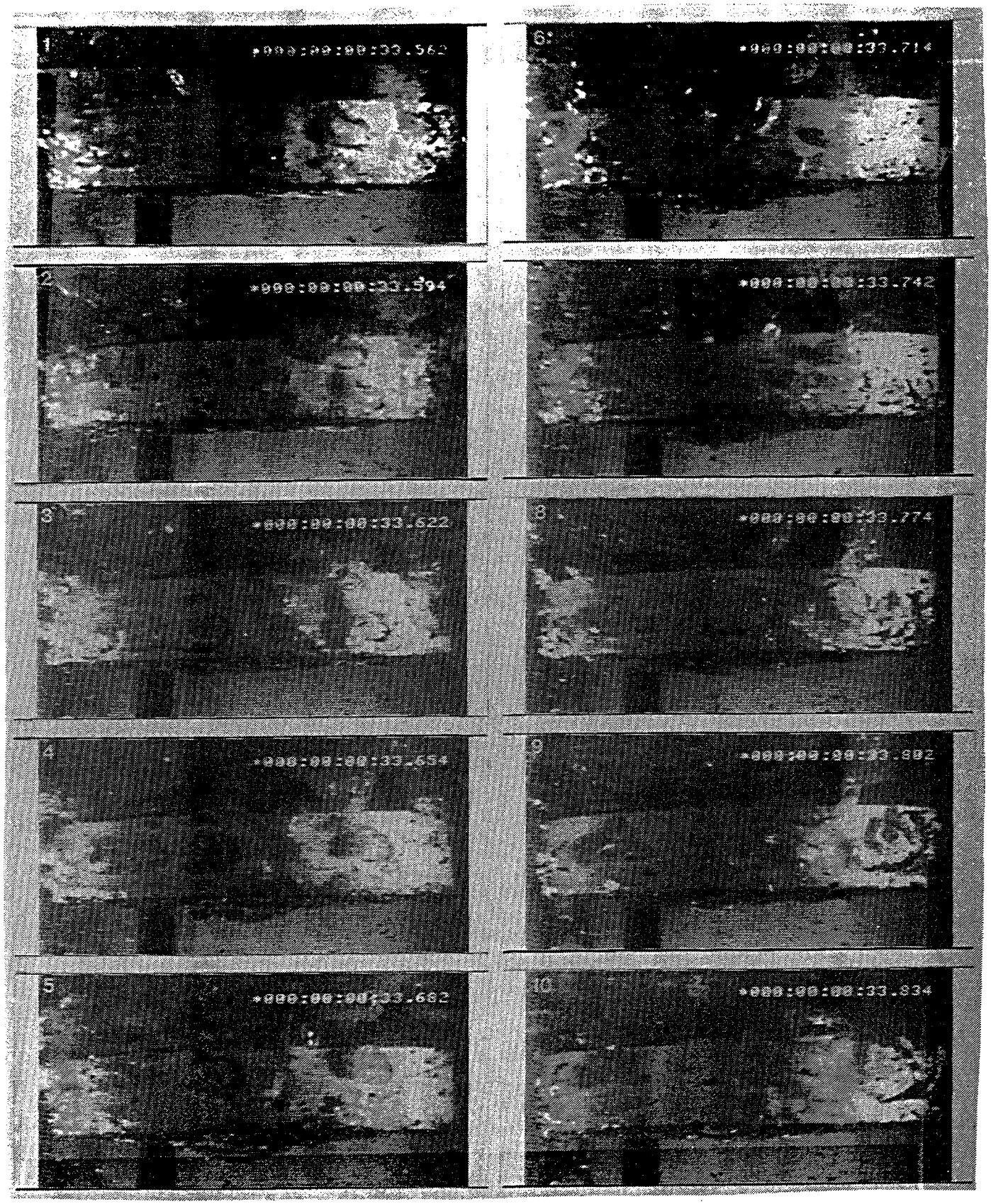

Figure 7. Video Frames of a Cycle of Explosive Vapor Formation at CHF, Side View

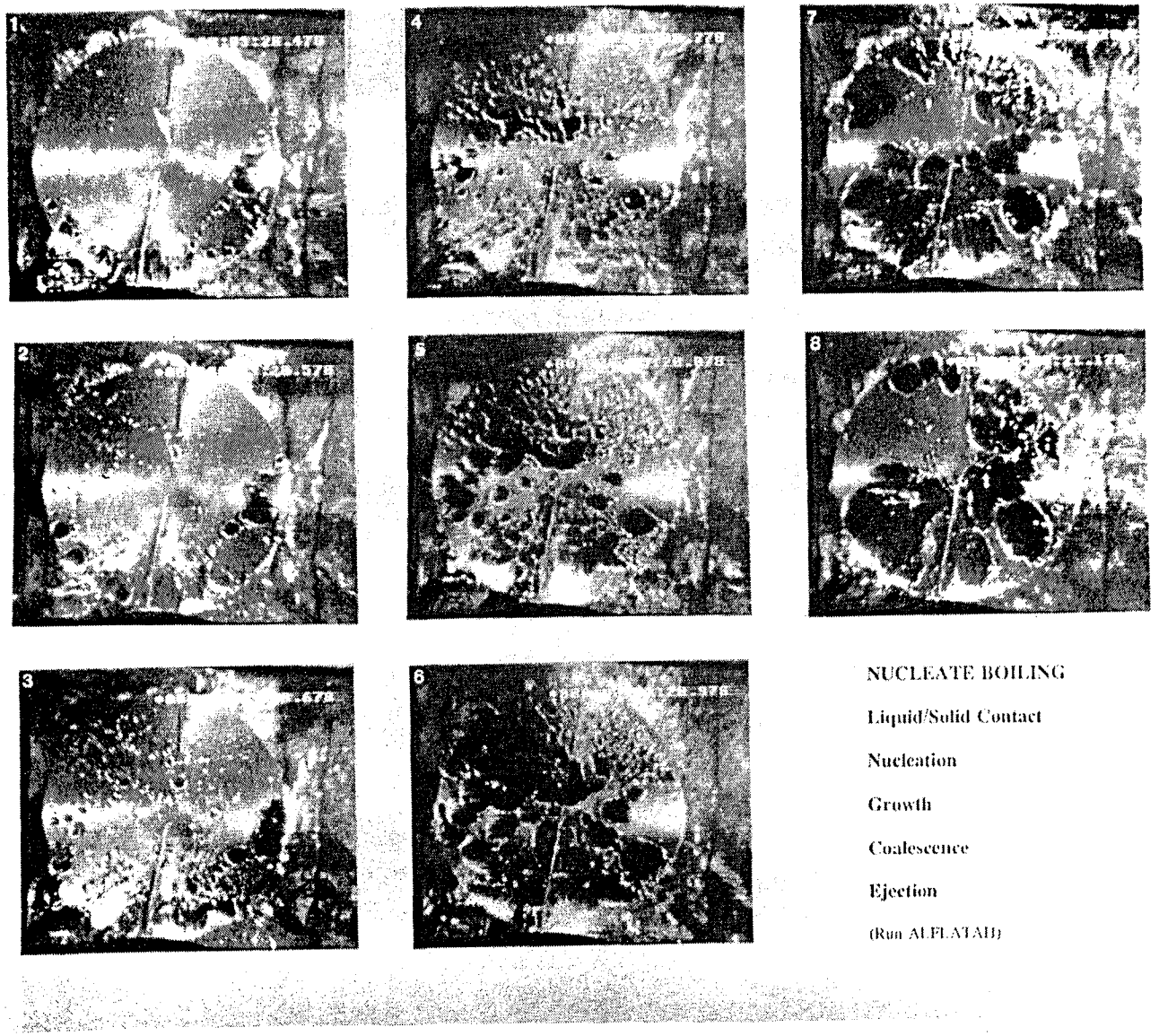

Figure 8. Video Frames of Nucleate Boiling at Intermediate Heat Fluxes

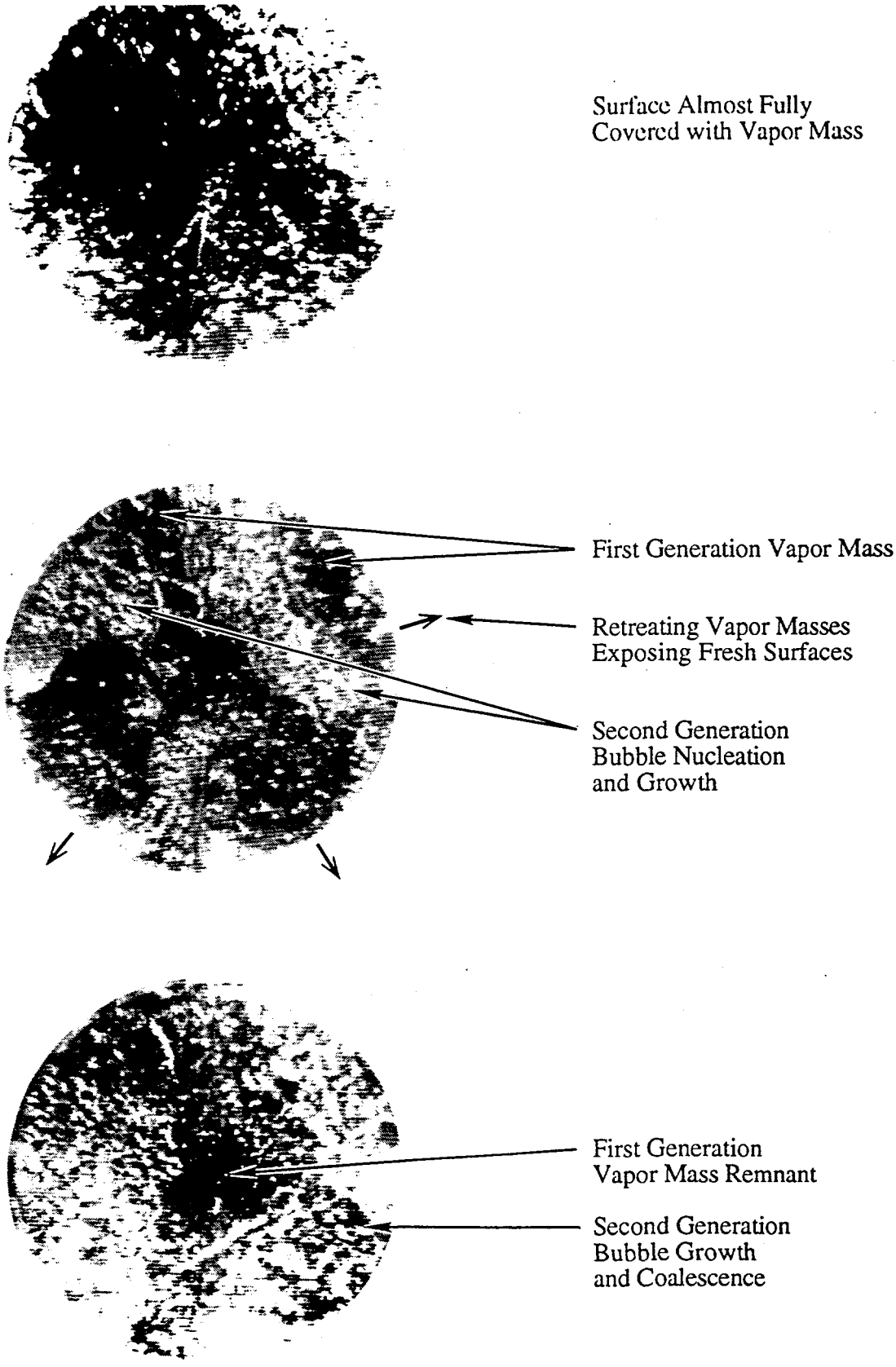

Figure 9. Video Frames of Nucleate Boiling at High Heat Fluxes

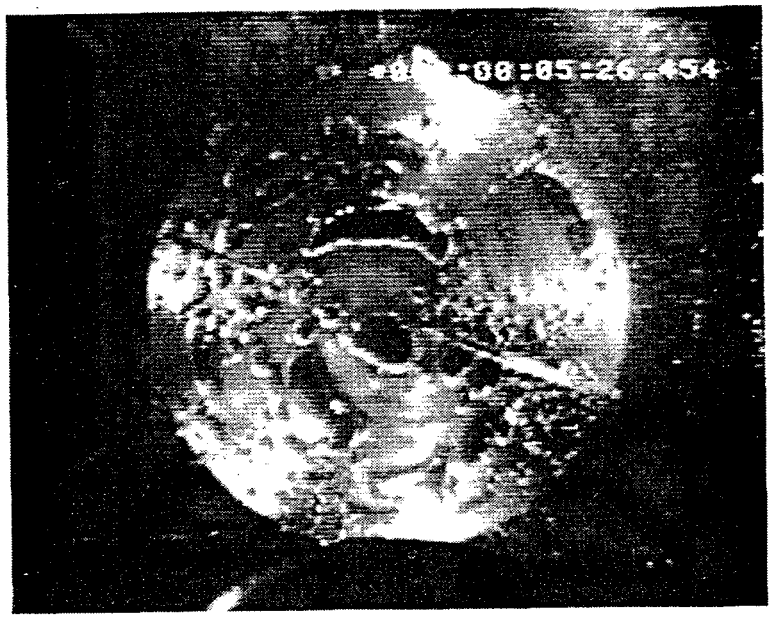

Figure 10. Video Frames of Nucleate Boiling at Low Heat Fluxes on the Curved Bottom Test Specimen

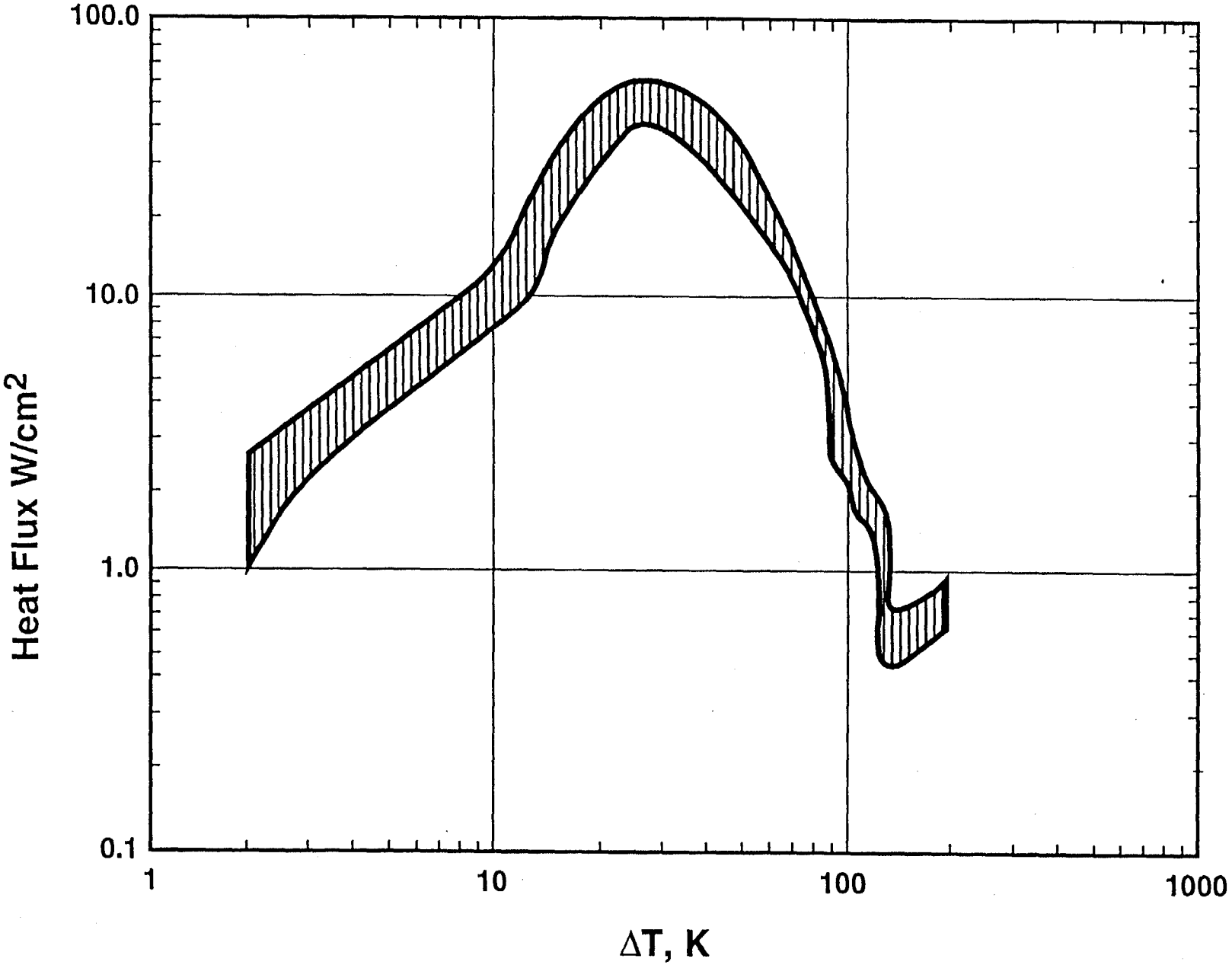

Figure 11. Boiling Curve from Flat Test Specimen

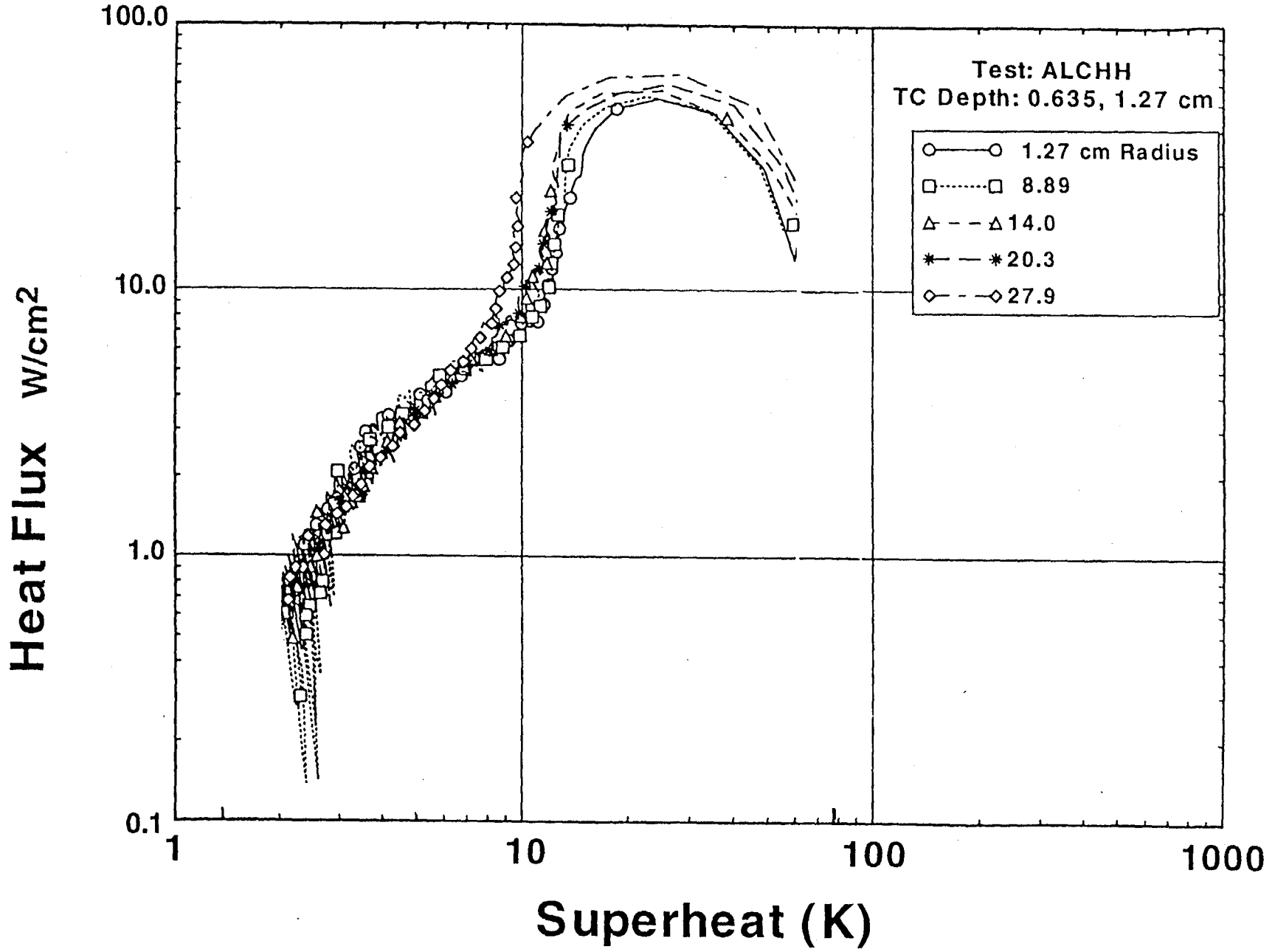

Figure 12. Boiling Curve from Curved Test Specimen

PART II:
REACTOR-SCALE BOILING EXPERIMENTS OF THE FLOODED CAVITY CONCEPT FOR IN-VESSEL CORE RETENTION

T.Y. Chu, J.H. Bentz, S.E. Slezak and Walter F. Pasedag

F.1.0 INTRODUCTION

The success or failure of in-vessel core retention has a profound effect on the progression of severe accidents, and because engineering the capability to flood the reactor cavity can have a significant impact on plant design, it is essential that there be a solid technical understanding of reactor-scale, downward-facing boiling heat transfer before risk assessments or safety qualifications can credit a flooded cavity with ensuring in-vessel core retention (Okkonen, 1994, Rouge and Seiler, 1994). But with only small scale downward-facing boiling data (Chen, 1978, Nishikawa, et al., 1984 Beduz, et al., 1987, and Guo and El-Genk, 1991) and without a validated analytical model to extrapolate existing data, reactor-scale testing is the only viable means for confirming the required heat transfer capability. For this reason, the Department of Energy (DOE) New Production Reactor (NPR) Program funded Sandia National Laboratories to develop a reactor-scale facility and to perform confirmatory testing of the effectiveness of boiling heat transfer of the flooded cavity design for the Heavy Water New Production Reactor (HWR-NPR). The facility is named CYBL, short for CYlindrical BoiLing (facility). Despite the indefinite deferral of the HWR-NPR program, DOE continues to sponsor the CYBL testing program through the Office of Nuclear Energy (DOE-NE) because of the value of a reactor-scale vessel cooling demonstration for Advanced Light Water Reactor (ALWR) applications.

Sandia has recently completed a series of tests for DOE-NE in support of the Advanced Reactor Severe Accident Program. The objectives of the present testing program are to conduct tests which demonstrate the required cooling capability for the central, most downward-facing region of the passive PWR lower head.

Part II of the paper presents results of ex-vessel boiling experiments performed in the CYBL facility. CYBL was developed as a reactor-scale facility for confirmatory research of the flooded cavity concept for accident management. CYBL has a tank-within-a-tank design; the inner tank simulates the reactor vessel and the outer tank simulates the reactor cavity. Because the facility was initially developed for the NPR program, the test vessel head is torispherical rather than hemispherical, to conform to the NPR design. Experiments with uniform and edge-peaked heat flux distributions up to 20 W/cm^2 across the vessel bottom were performed. The edge-peaked heat flux distribution experiments are designed to examine the sensitivity of the

ex- vessel boiling process to a non-uniform heat flux distribution similar to the predicted edge-peaked distribution resulting from melt convection (O'Brien and Hawkes, 1991, Kymäläinen et al., 1993, and Asfia and Dhir, 1994). The current estimated range of cooling requirements for the AP-600 reactor is 10-20 W/cm^2 (Henry et al., 1993a,b). The target heat flux of 20 W/cm^2 for the tests is based on providing data at prototypic heat flux levels covering the uncertainty within the current cooling requirement estimates. The test planning included an evaluation of the fact that the CYBL vessel is flatter at the bottom than the hemispherical bottom head typical of many U.S. reactors. The general consensus from a workshop of experts held at Sandia in July 1993 is that CYBL results would be conservative when applied to surfaces with steeper angles of inclination (i.e., hemispherical heads will be more efficient in ex-vessel boiling as they curve upward more rapidly).

Heat transfer results including heat flux, surface temperature and bulk water temperature as well as observations of the characteristics of ex-vessel boiling are reported. The results suggest that under prototypic heat load and heat flux distributions, the flooded cavity in a passive pressurized water reactor like the AP-600 should be capable of cooling the reactor pressure vessel in the central region of the lower head that is addressed by these tests.

F.2.0 EXPERIMENT

CYBL has a tank-within-a-tank design; the inner tank simulates the reactor pressure vessel, the outer tank simulates the reactor cavity (Figures F.1a and F.1b). The inner tank, made of 1.6-cm- thick 316 L stainless steel, is 3.7 m in diameter and 6.8 m high. The outer tank is 5.1 m in diameter and 8.4 m high, made of 0.95-cm-thick 316 L stainless steel. At present, the inner test tank has a torispherical head, but the test fixture is designed to accept a test vessel of any configuration with a diameter of 3.7 m or less. The present torispherical bottom has a crown radius of 3.35 m and a knuckle radius of 0.66 m.

The energy deposition on the bottom head is accomplished with an array of twenty radiant lamp panels. Each panel measures 0.3 m by 1.2 m, and consists of a flat aluminum reflector and two bus bars for installing up to sixty-three 480 V, 6 kW linear quartz lamps. The reflector and the bus bars are water cooled. The panels are organized into twelve individually controlled heating zones (Figure F.2). Each numbered zone has two panels except the four panels (1, 9, 6, and 12) on the outer rim of the array. By adjusting the power input to each zone, the density of lamps of each heating panel, and the three dimensional configuration of the panel array, the heat flux distribution can be customized to the needs of the experimenter. The maximum total power available is 4.3 MW from a 6 MW supply with the limitation based on the present connecting cables between the substation and the power supply.

For uniform heat flux tests, the double-panel heating zones (2, 3, 4, 5, 7, 8, 10, and 11 zones in Figure F.2) are all operated at the same power and the four single-panel heating zones (1, 6, 9, and 12) are operated at 75% of the power of the double-panel zones. Therefore, the power density at panels 1, 6, 9, and 12 is 1.5 times that of the other panels. For an edge-to-center heat flux ratio of 2, the center four panels (zones 3 and 4) are off and the rest of the zones are powered at 120% of the power required for uniform heat flux tests to achieve the same maximum heat flux. The maximum achievable heat flux was determined from system design experiments to be about 40 W/cm^2.

The CYBL test fixture is installed over an observation pit. The 51 viewing windows, ranging from 30 to 60 cm in diameter on the side and bottom of the outer vessel, allow the boiling process to be observed from a variety of directions. Nearly three-hundred data channels are used to monitor vessel and surface temperatures as well as water temperatures. Temperature gradients from in-depth and surface temperature measurements are used to calculate local heat fluxes. A map of thermocouple array placement and thermocouple locations on the bottom head is shown in Figure F.3. Arrays A and B are 7.5° on either side of the 0° axis and arrays E and F are 7.5° on either side of the 90° axis. Arrays C and D are along the 30° and 60° axes respectively. Five thermocouples located 15 cm away from the surface, following the contour of the bottom head, are used to measure the bulk water temperature. A thermocouple tree monitors the temperature of the water as well as the steam temperature at fifteen vertical locations over the entire height of the outer vessel. All except the surface thermocouples are 1.6 mm (1/16 in) stainless steel sheathed thermocouples with grounded junctions. The surface thermocouples are intrinsic thermocouples made from the same 1.6 mm sheathed thermocouples with the last 2.5 cm stripped to bare thermocouple wires. The two bare wires are welded individually onto the test surface; the distance between the wires is typically 2-3 mm. This installation lessen the effect of the presence of thermocouples on the surface and the temperature reading represents a locally (3 mm) averaged surface temperature.

A ten-camera video system is used to view and record the boiling process. Additional cameras are used to monitor key systems in the facility. The data acquisition and control system plots selected heat transfer data as well as operating parameters in real time. The system is also used to "scram" the test power, should thermocouples detect conditions that indicate departure from nucleate boiling. Also monitored for operational safety are the cooling water flow rates and temperatures for all the cooling water circuits.

F.3.0 EXPERIMENTAL RESULTS

A total of three test series have been completed in the CYBL facility: the NPR series under the DOE-NPR program, and the NE1 and NE2 series under the DOE-NE program. A summary of all the tests is given below:

Test	Heat Flux* W/cm^2	Flux Distribution
NPR-A	16	uniform
NPR-B	16	edge-peaked
NE1-UA	16	uniform
NE1-UB	18	uniform
NE1-UC	20	uniform
NE2-A	8	edge-peaked
NE2-B	16	edge-peaked
NE2-C	17	edge-peaked
NE2-D	18	edge-peaked
NE2-E	20	uniform
*Peak heat flux for edge-peaked tests.		

For all the experiments performed, the water level is 5 meters above the bottom center of the test vessel. Because of the 5 meters of gravity head, the bulk condition near the bottom head area was subcooled, and in all cases, the entire bottom head was in subcooled nucleate boiling. The purpose of the present paper is to report the main observations of the experiments and results that have direct impact in the evaluation of the flooded cavity design. Representative heat flux and surface temperature distributions are reported here to illustrate the general trend of the data. Detailed heat transfer analysis as well as correlation/modeling of the heat transfer process will be reported in the future.

The heat flux distribution from two uniform heat flux tests (NE1-UA, 16 W/cm^2 and NE2-E, 20 W/cm^2) and one non-uniform heat flux test (NE2-B) are shown in Figure F.4. Arrays A/B and E/F are two orthogonal arrays on the bottom head, Figure F.3. Arc distances from 0 cm to 146 cm correspond to the crown region and the knuckle region extends from 146 cm to 218 cm. The edge of the crown region has a surface inclination of 25.7°; surface inclination reaches 90° at the edge of the knuckle region. Within each region, the surface inclination increases linearly with arc distance. The heat fluxes are calculated from temperature gradients given by in-depth thermocouples at 0.95 cm into the surface and the surface thermocouples. Temperatures and

temperature gradients used are averaged over a 200-500 second interval. For the uniform heat flux tests, NE1-UA and NE2-E, the heat flux over the entire surface is constant to within about 10% to an arc distance of 168 cm. Along the 0°-180° and 90°-270° axes, there is a gradual drop of about 20% to a distance of 213 cm and a sharp drop to zero at 229 cm. The drop off is slightly faster along the 30° and 60° axes (as well as symmetrical directions in the other quadrants), by about 25% at 213 cm. For the non-uniform heat flux case, the heat flux peaks around 168 cm from the bottom-center location. The peak is relatively broad; the heat flux is within 90% of the peak value 30 cm on either side of the peak.

Surface temperature excess (over saturation temperature) as measured by arrays A/B and E/F are shown in Figure F.5. Because there is a 90 cm change in elevation along the surface (from bottom center to the rim of the bottom head), there is a corresponding change in local saturation temperature of approximately 2 K. Therefore it is more appropriate to examine the surface temperature excess over local saturation temperature. It is interesting to note that in all cases, including the non-uniform heat flux experiment (NE2-B) where the heat flux is lowest at the bottom center, the surface temperature excess is still highest at the bottom center location. This suggests that the bottom center area is least effective in heat dissipation. The heat transfer data from the CYBL experiments are compared with the result from the quenching experiment in Figure F.6. There appears to be general agreement between the two experiments, although, the surface temperature excess at CYBL bottom center for 20 W/cm^2 is approximately 2.5 K higher than the surface temperature of the quenching specimen. There is not enough data to judge if this is a scale effect.

The effectiveness of boiling heat transfer can be examined quantitatively using the data of the NE2-E experiment. Shown in Figure F.7 is the heat transfer coefficient based on temperature excess over local saturation temperature as a function of surface location. While the applied heat flux is essentially constant over the surface (between arc distance 0 and 168 cm) the heat transfer coefficient increase monotonically with arc distance. The heat transfer coefficients obtained by Nishikawa et al. (1984) for 20 W/cm^2 is 1.3 W/cm^2-K in their laboratory-scale experiments; this value is higher than the heat transfer coefficient for the bottom center area, but lower than the values in the knuckle area. This comparison suggests that scale and geometry do have an effect on the heat transfer coefficient.

The effect of heat flux distribution on heat transfer can be examined by comparing experiments NE1-UA and NE2-B. The peak heat flux is approximately 16 W/cm^2 for both experiments but NE1-UA has uniform heat flux and NE2-B has edge-peaked heat flux with an edge-to-center heat flux ratio of approximately 2, Figure F.4. The surface temperature excess is slightly less near the bottom center area for NE2-B as a result of lower heat flux near the center. The heat

transfer coefficients for the two experiments are compared in Figure F.8. It is interesting to note that in the region between arc distance 137 cm and 183 cm where the heat fluxes for both experiments are comparable, the heat transfer coefficients for both experiments are quite close (increasing from 1.4 W/cm^2-K to 1.6 W/cm^2-K). The result suggests that for the present range of heat fluxes, the local heat transfer coefficient is not a strong function of the shape of the surface heat flux distribution. In other words, the heat transfer coefficient near the outer radius of the vessel appears not to be strongly effected by the net heat input (vapor generation) upstream (close to the vessel center). As we will see in the next section, this is a direct consequence of the general phenomenology of the ex-vessel boiling process.

F.4.0 PHENOMENOLOGY OF EX-VESSEL BOILING

The ex-vessel boiling process is best described as subcooled nucleate boiling. Visual observations indicate that the boiling process near the bottom center is cyclic in nature and has four distinct phases: direct liquid/solid contact, bubble nucleation and growth, coalescence, and vapor mass dispersion (ejection). Because of the axi-symmetrical configuration, the flow patterns are axi-symmetric. The general direction of flow is in the radial direction. This radial flow gives rise to an orderly progression of the four phases as a function of radius from the bottom center of the test vessel. The progression of flow patterns has the appearance of waves of vapor emanating from the bottom center of the test vessel, although vapor is actually produced over the entire surface. Two sequences of video frames illustrating this cyclic progression for heat fluxes of 8 W/cm^2 and 14 W/cm^2 are shown in Figures F.9 and F.10, respectively. The field of view is approximately 2 meters.

The frequency of the cyclic/pulsating pattern in the bottom center region increases with heat flux but the rate of increase decreases with heat flux (i.e., the frequency only increases very slightly at high heat fluxes). The cyclic/pulsating pattern is much more regular temporally and spatially at higher heat fluxes. There is not sufficient data to determine the demarcation between high and low heat fluxes but it is above 8 W/cm^2 and less than 10 W/cm^2. It is interesting to note that this demarcation is near the heat flux where the boiling curves from the quenching experiments changes slope (see Figures F.11 and F.12, Part I). Furthermore, the general trend of the variation of cycle frequency and heat flux is also observed in the quenching experiments. The frequency is approximately 2 Hz for heat fluxes above 10 W/cm^2. Each cycle starts with nucleation near the bottom center region; in time, bubble nucleation progresses outward from the bottom center. The growth of the bubbles eventually results in a coalesced circular vapor mass of as large as one meter in diameter, Figure F.10. Similar to the trend in frequency, the size of the vapor mass increases rapidly with increasing heat flux for low heat fluxes, but only increases

slightly at higher heat fluxes. For the range of heat fluxes tested, the maximum thickness of the central vapor mass varies approximately from one to three centimeters.

The vapor mass disperses in the form of an expanding flat ring rising along the surface (Figure F.10). However, eventually the configuration becomes unstable and the ring thickens and breaks into smaller arc segments. The broken vapor segments condense in the surrounding subcooled water leaving essentially no trace. The radial location of this condensation zone is quite well defined; the corresponding radius increases with heat flux. As a result, the boiling process beyond the condensation zone is to a large degree decoupled from the cyclic pulsation of the center bottom and is observed to be essentially steady in nature. This is probably the reason that the heat transfer coefficient is not influenced significantly by the upstream heat flux distribution, Figure F.8.

The vapor in the outer region also condenses in the bulk water a very short distance beyond/above the bottom head region. While the subcoling corresponding to the 5-meter gravity head is approximately 12 K; the actual observed subcooling of the bulk water near the bottom center is in the range of 9-10 K. The amount of subcooling decreases with heat flux. This reduction in subcoling is probably the result of condensation and convective mixing. Figure F.11 is a plot of the vertical temperature distribution of the bulk water for test NE2-E. The rim of the bottom head corresponds to 0 on the distance axis and the bottom center of the vessel head is at -91 cm. The water steam interface is at 409 cm. Note the temperature bulge near the rim of the bottom head (0 cm location) due to vapor condensation. Locations above the rim of the bottom head are essentially occupied by single phase subcooled liquid until within approximately 60 cm of the interface. Intense vaporization takes place in the top 30 cm of the water. Figure F.12 is a schematic of all the important physical mechanisms of the ex-vessel boiling process. There appears to be no qualitative difference in the boiling process between the non-uniform heat flux and uniform heat flux cases. The bottom center region still exhibits the typical cyclic pattern. There is still a well-defined condensation zone separating the cyclic central region and the steady two-phase outer region. In a "real" accident, the vertical portion of the reactor vessel wall is heated by radiation and convection. The condensation zone near the bottom head rim would certainly be modified.

F.5 CONCLUDING REMARKS

The ex-vessel boiling process is best described as subcooled nucleate boiling. The boiling pattern is divided into two regions: a cyclic/pulsating bottom center region and an outer steady two-phase boundary layer region. Condensation takes place at the edge of both regions. The bulk of the water in the annular space between the reactor vessel and the cavity wall is single- phase

liquid. Intense vaporization takes place near the top surface of the water. The subcooling is mainly due to the gravity head of the water flooding the simulated reactor cavity. But the degree of subcooling is modified by the complex ex-vessel boiling pattern. Because of condensation, the outer rim of the bottom head is to a large degree decoupled from the cyclic pulsation of the bottom center area, the heat transfer coefficient is found not to be significantly influenced by the upstream heat flux distribution.

The results of three CYBL test series and the critical heat flux study of Theofanous et al. (1994) suggest that under prototypic heat load and heat flux distributions, the AP-600 flooded cavity should be capable of cooling the reactor pressure vessel in the central region of the lower head that is addressed by these tests.

There is general agreement between the heat transfer results of the quenching experiments and the CYBL experiments. It is interesting to note that the quenching experiments also exhibit similar cyclic behavior in the nucleate boiling regime but the temperol and spatial regularity certainly could not have been predicted from the quenching experiments. The comparison with the Nishikawa et al. (1984) results suggests that geometry and scale does influence the ex-vessel boiling process. The CYBL experiments demonstrated that the ex-vessel boiling process is dominated by spatial structures of meters in scale. Therefore, the reactor-scale tests performed in CYBL should prove valuable for an accurate assessment of the potential of ex-vessel boiling for in-vessel core retention.

The CYBL facility can be used in the future to investigate reactor-scale vessel coolability issues not addressed by the current test series. Issues that could be addressed include: the coolability of a hemispherical vessel head; the impact of vessel penetrations or vessel insulation; the effect of an only partially flooded cavity; characterization of the two-phase boundary layer; sensitivity to higher heat flux levels; and the effect of water subcooling and recirculating flow on vessel coolability.

F.6.0 ACKNOWLEDGEMENTS

The authors would like to thank Steve Additon of TENERA for many insightful comments and suggestions. This work was performed at Sandia National Laboratories and supported by the U.S. Department of Energy under Contract No. DE-AC04-76DP00789.

F.7.0 REFERENCES

Beduz, C., R. G. Scurlock, and A. J. Sousa, 1988, "Angular Dependence of Boiling Heat Transfer Mechanisms in Liquid Nitrogen," Advances in Cryogenic Engineering, Vol. 33, pp. 363-370.

Chen, L. T., 1978, "Heat Transfer to Pool-Boiling Freon from Inclined Heating Plate," Lett. Heat Mass Transfer, Vol. 5, pp. 111-120.

Chu, T. Y., J. H. Bainbridge, J. H. Bentz, and R. B. Simpson, 1994, Observations of Quenching of Downward-Facing Surfaces, SAND93-0688, Sandia National Laboratories, Albuquerque, NM.

Chu, T. Y., R. C. Dykhuizen, and C. E. Hickox, 1992, Scoping Studies of Boiling Phenomena Associated with the Flooded Cavity Design of the Heavy Water New Production Reactor, NPRW-SA92-2, Sandia National Laboratories, Albuquerque, NM.

Guo, Z., and M. S. El-Genk, 1991, "An Experimental Study of the Effect of Surface Orientation on Boiling Heat Transfer During Quenching," ASME Winter Annual Meeting, Atlanta, GA, Dec. 2-5, 1993.

Henry, R. E., J. P. Burelbach, R. J. Hammersley, and C. E. Henry, 1993a, "Cooling of Core Debris Within the Reactor Vessel Lower Head," Nuclear Technology, Vol. 101, pp. 385-399.

Henry, R. E., H. K. Fauske, 1993b, "External Cooling of a Reactor Vessel Under Severe Accident Conditions," Nuclear Engineering and Design, Vol. 139, pp. 31-43.

Kymäläinen, O., H. Tuomisto, O. Hongisto, and T. G. Theofanous, 1993 "Heat Flux Distribution from a Volumetrically Heated Pool with High Rayleigh Number," Proceedings, NURETH 6, Grenoble, France, October 5-8, 1993., pp. 47-53.

Nishikawa, K., Y. Fujita, S. Uchida, and H. Ohta, 1984, "Effect of Configuration on Nucleate Boiling Heat Transfer," Int. J. Heat Mass Transfer, Vol. 27, pp. 1559-1571.

O'Brien, J. E., and G. L. Hawkes, 1991, "Thermal Analysis of a Reactor Lower Head with Core Relocation and External Heat Transfer," AIChE symposium Series 283, Vol. 87, pp. 159- 176, National Heat Transfer Conference, July 28-31, 1991, Minneapolis, MN.

Okkonen, T., 1994, "In-vessel Core Debris Cooling through External Flooding of the Reactor Pressure Vessel," Proceedings, OECD/CSNI/NEA Workshop on Large Molten Pool Heat Transfer, Nuclear Research Center, Grenoble, France, March, 1994.

Rouge S., and J. M. Seiler, 1994, "Core Debris Cooling with Flooded Vessel or Core Catcher Heat Exchange Coefficients under Natural Convection," OECD/CSNI/NEA Workshop on Large Molten Pool Heat Transfer, Nuclear Research Center, Grenoble, France, March, 1994.

Theofanous, T. G., S. Syri, T. Salmassi, O. Kymäläinen, and H. Tuomisto, 1994, "Critical Heat Flux Through Curved, Downward Facing, Thick Walls," Proceedings, OECD/CSNI/NEA Workshop on Large Molten Pool Heat Transfer, Nuclear Research Center, Grenoble, France, March, 1994.

CYBL

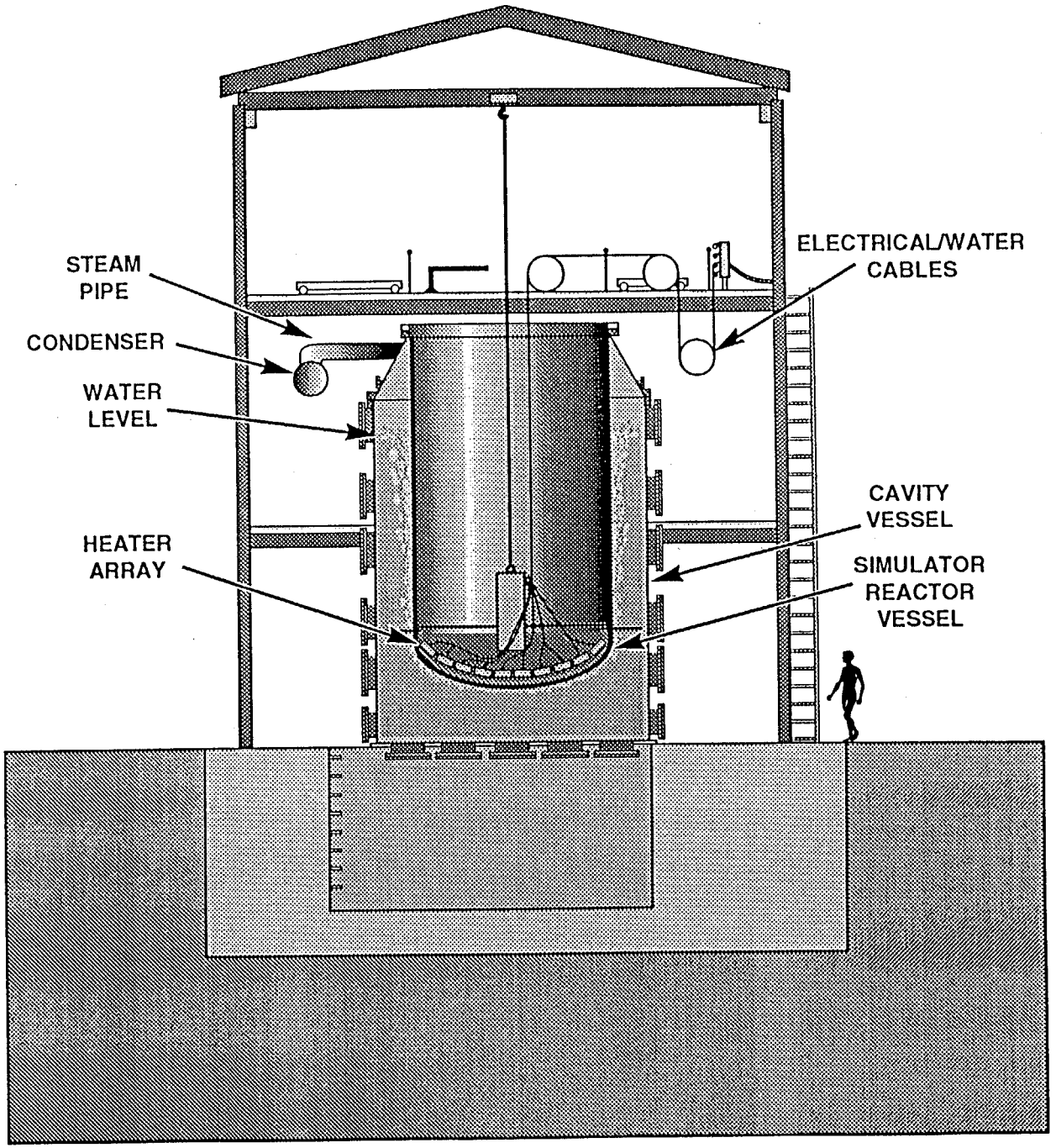

Figure 1a. Schematic of the CYBL Facility

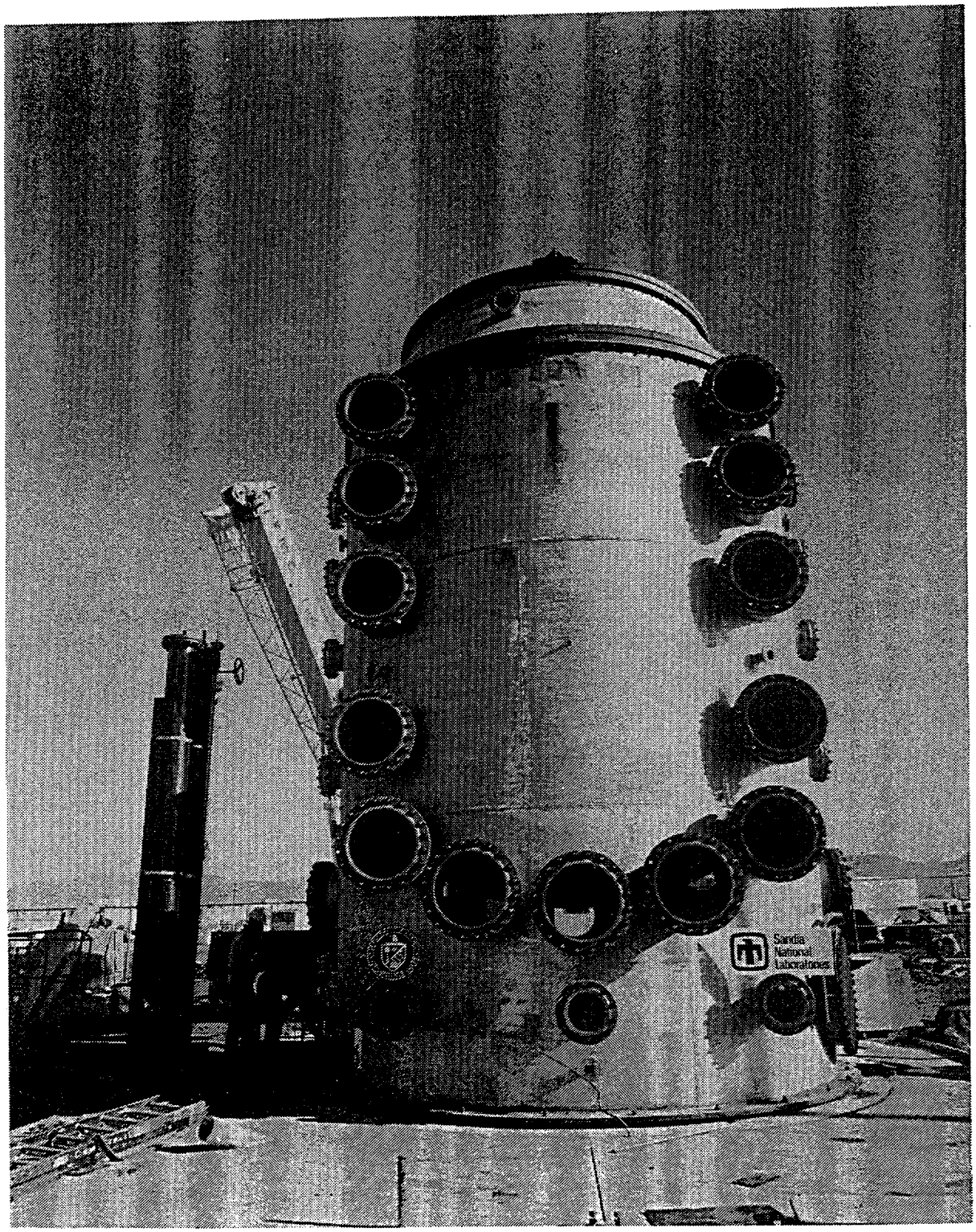

Figure 1b. CYBL Facility Before Construction of the Test Enclosure Building

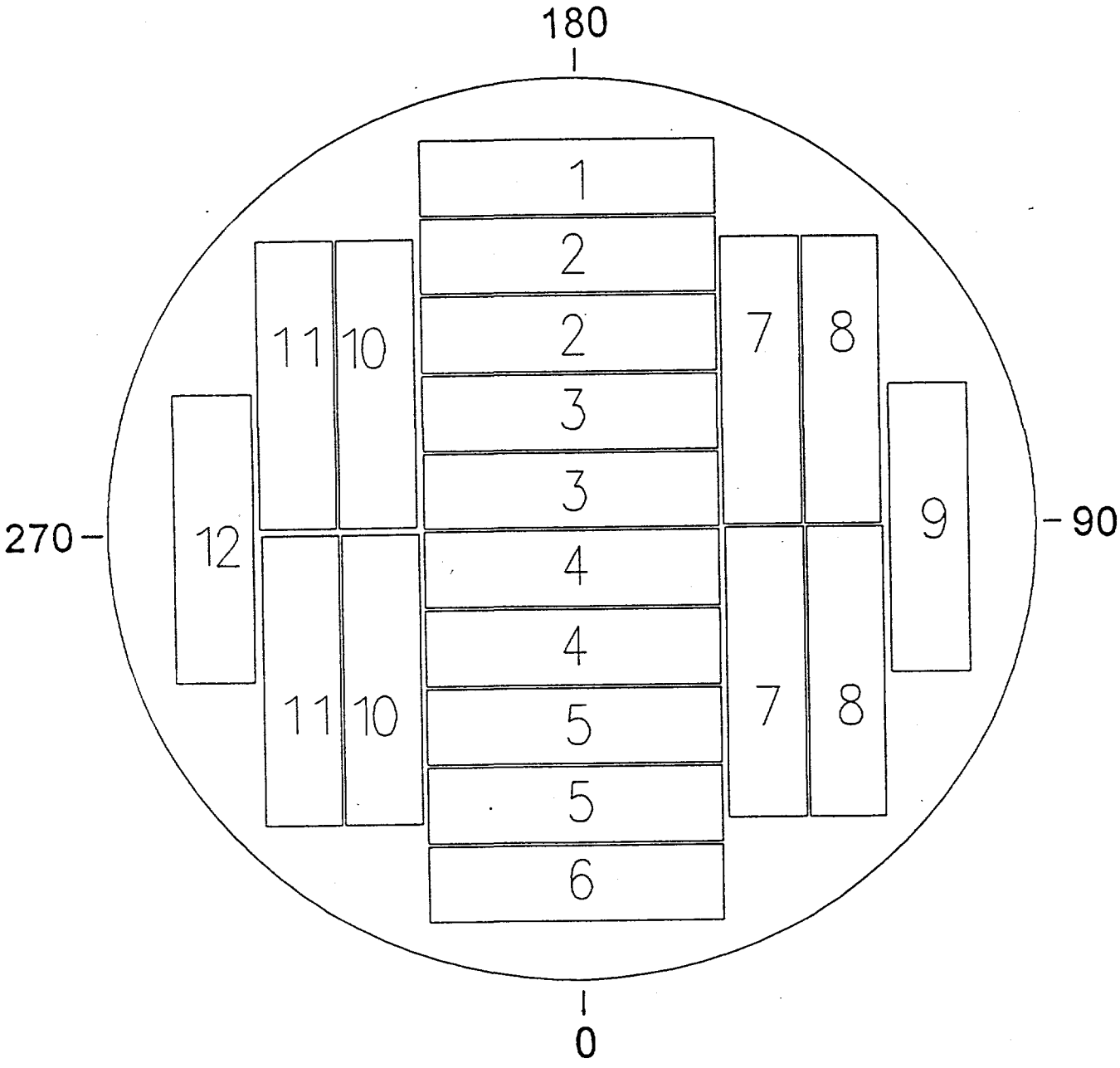

Figure 2. Schematic of the Heater Array Design

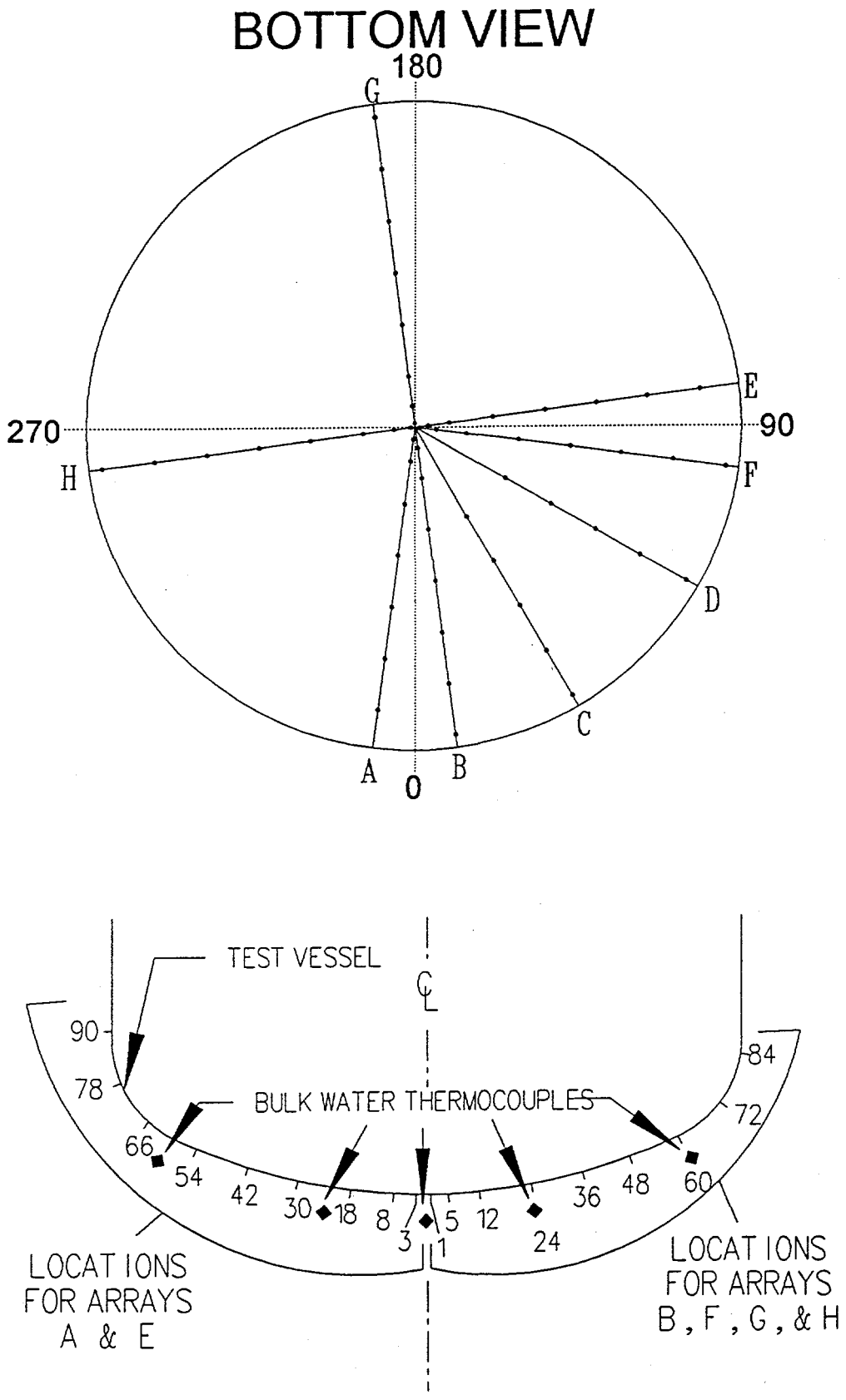

Figure 3. Schematic of Thermocouple Locations on the Bottom Head

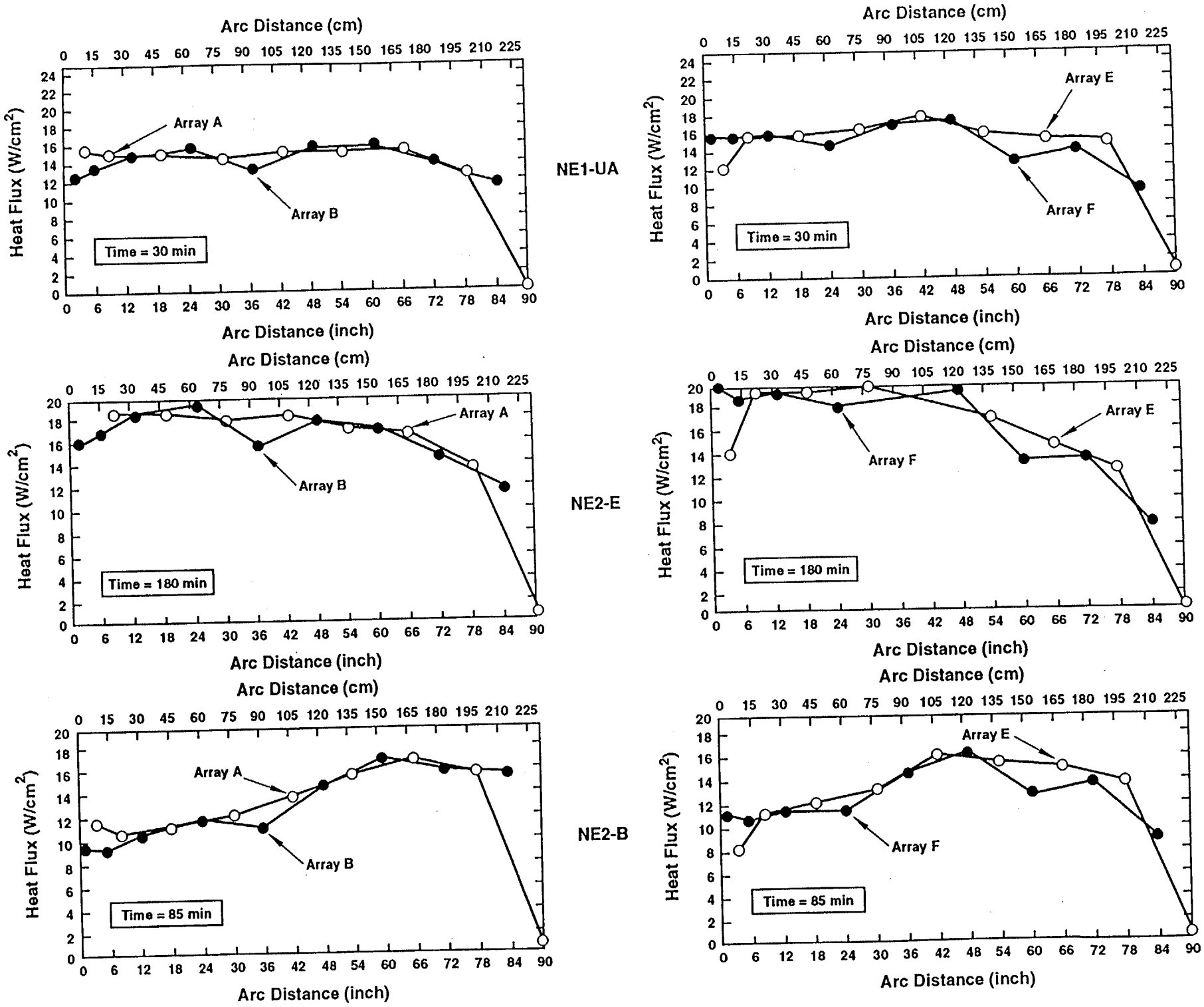

Figure 4. Heat Flux Distribution for NE1-UA, NE2-E, and NE2-B

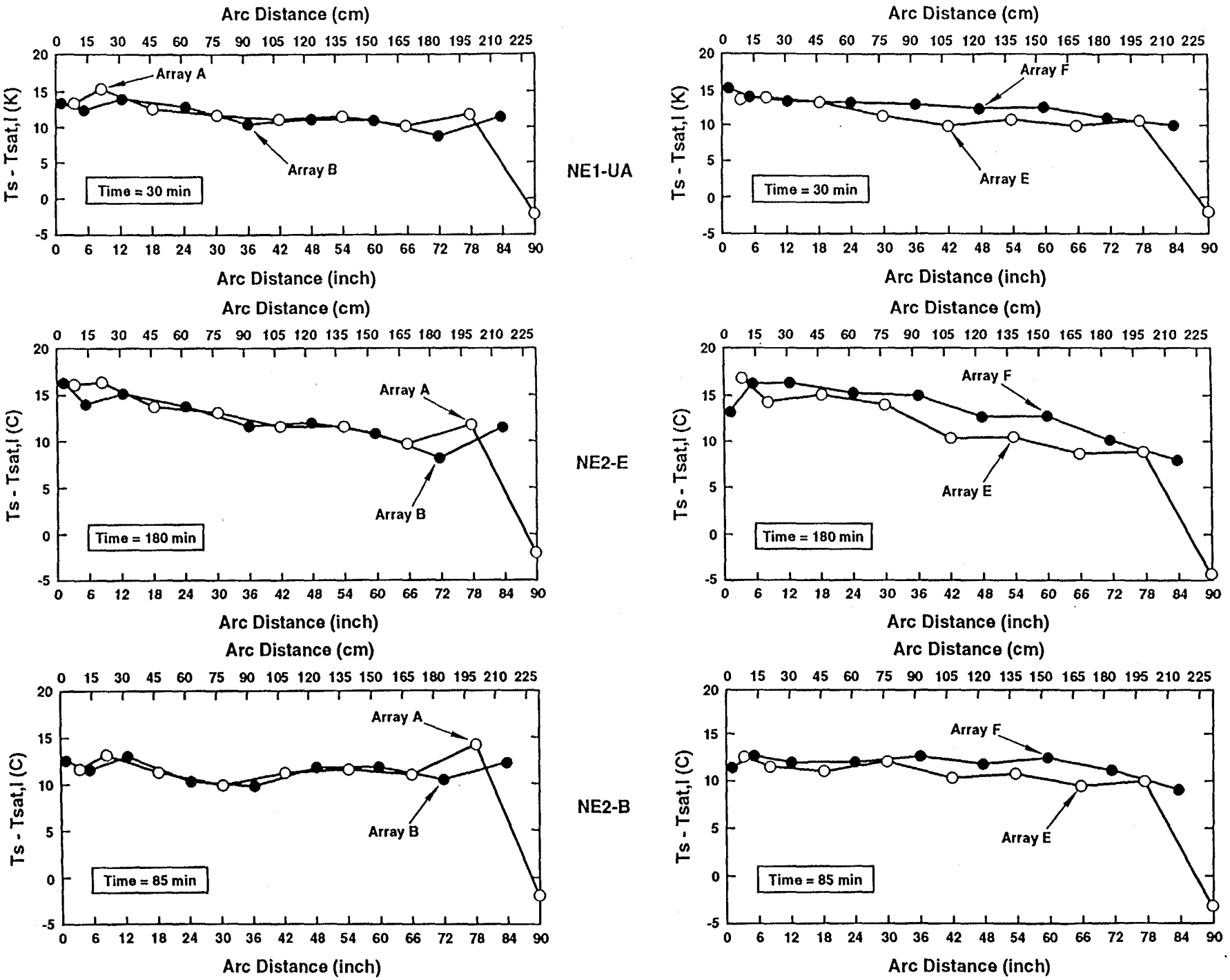

Figure 5. Distribution of Surface Temperature Excess for NE1-UA, NE2-E, and NE2-B

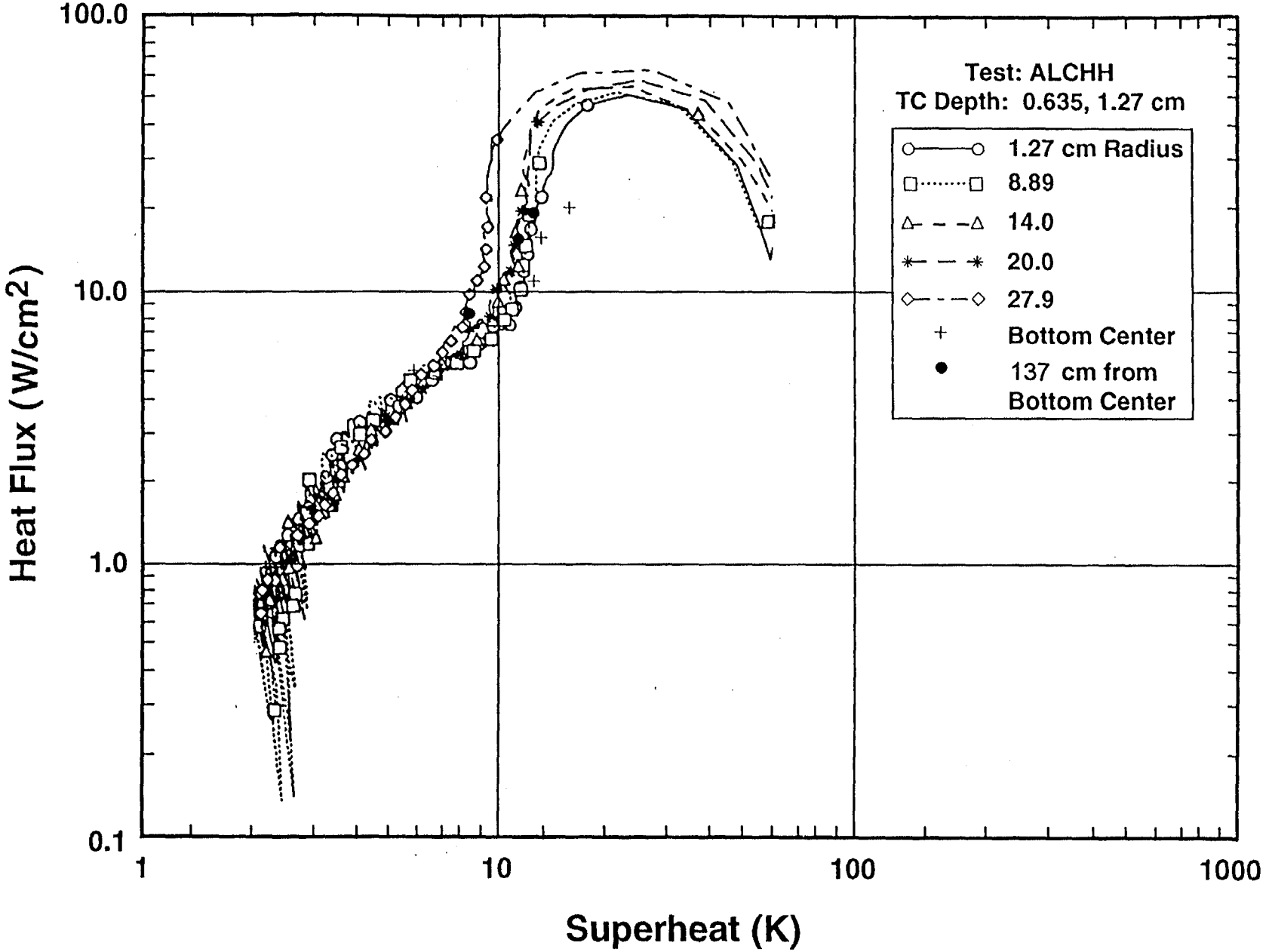

Figure 6. Comparison Between the CYBL Experiment and the Quenching Experiment

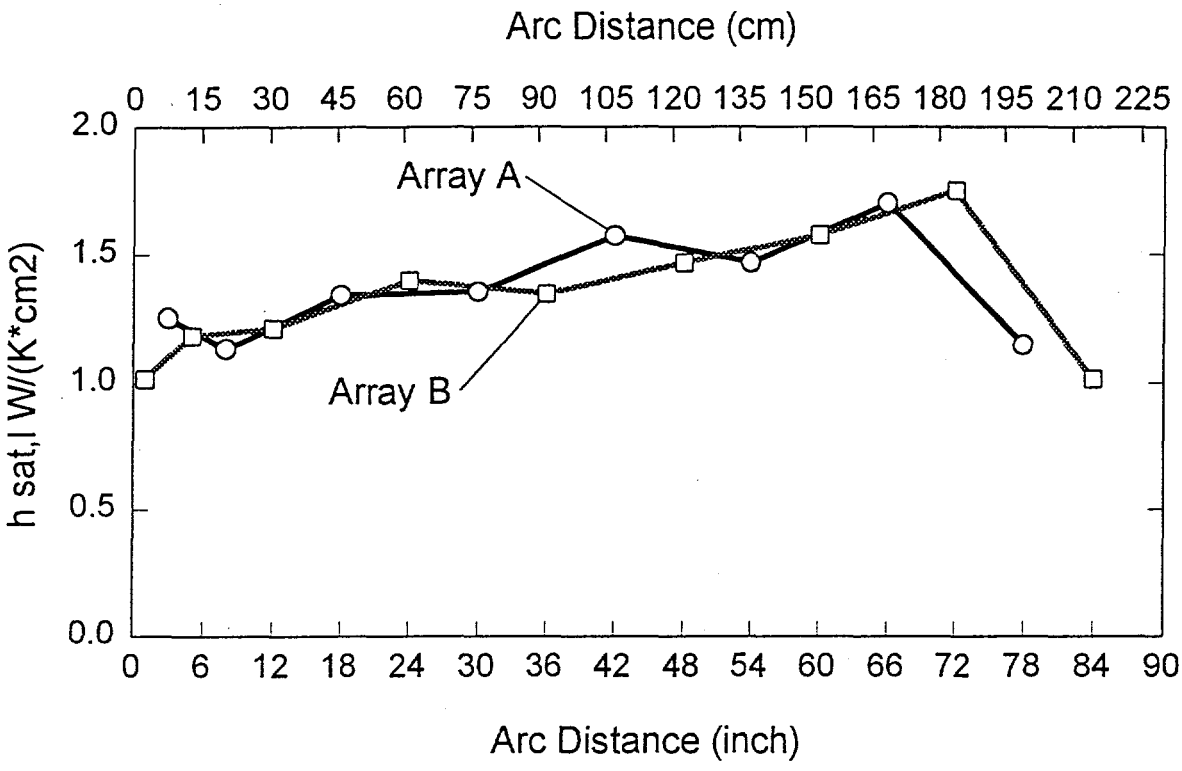

Figure 7. Heat Transfer Coefficient for NE2-E

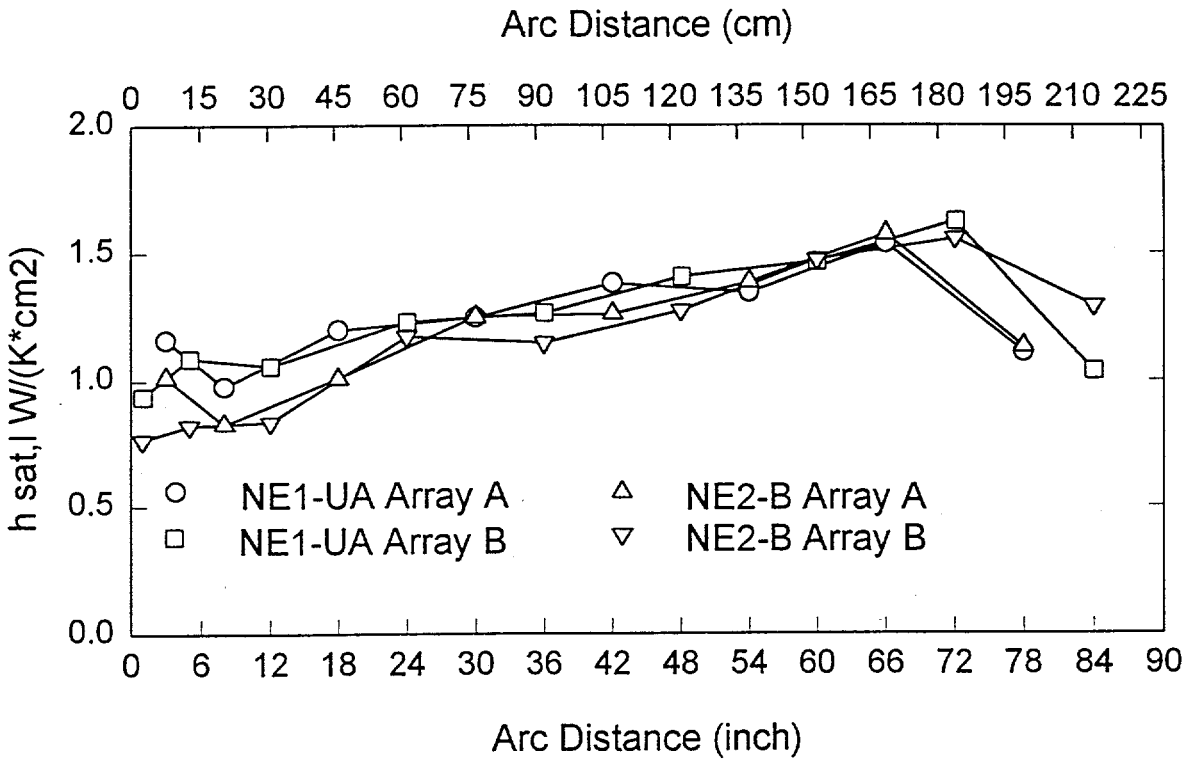

Figure 8. Heat Transfer Coefficient for NE1-UA and NE2-B

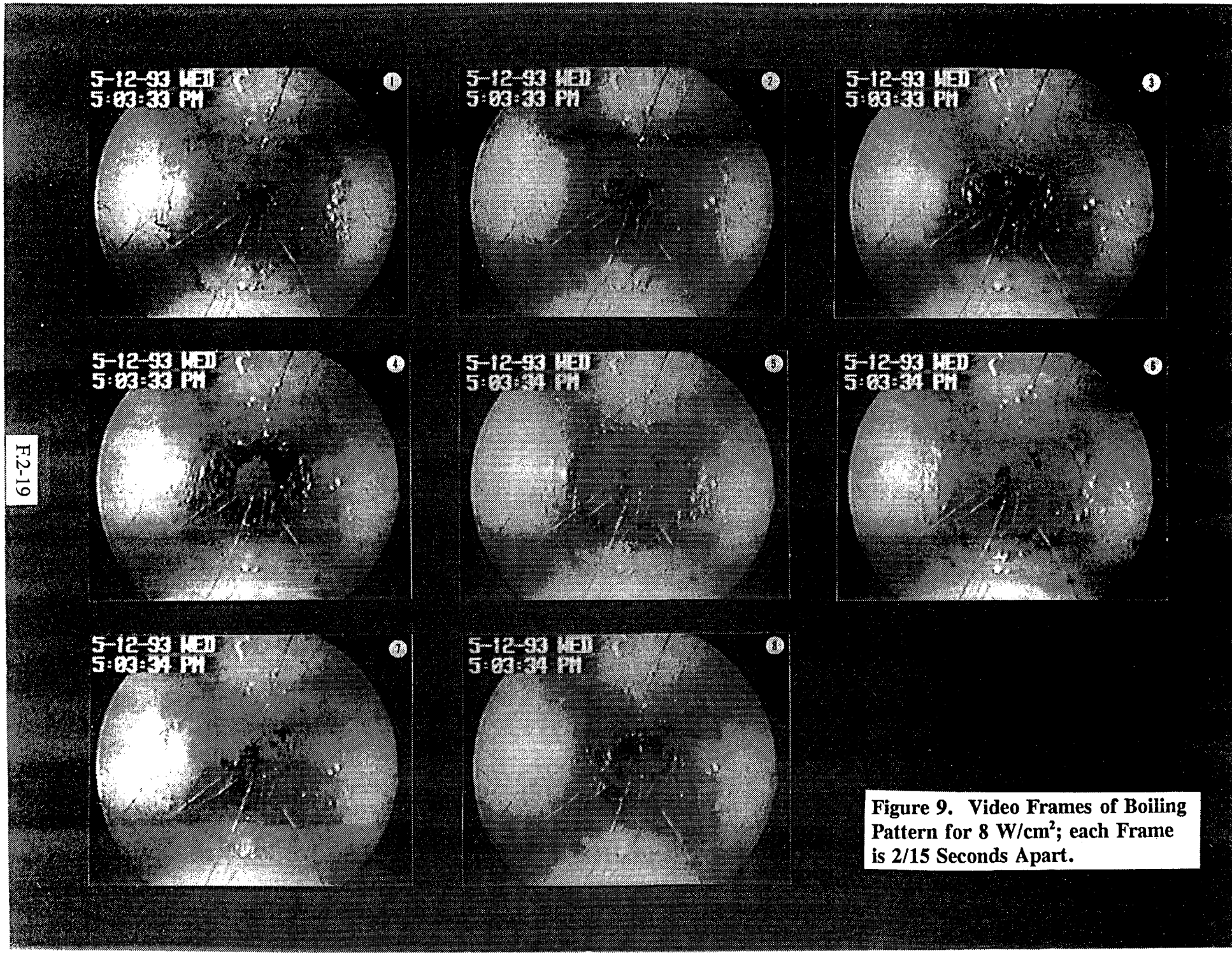

Figure 9. Video Frames of Boiling Pattern for 8 W/cm^2; each Frame is 2/15 Seconds Apart.

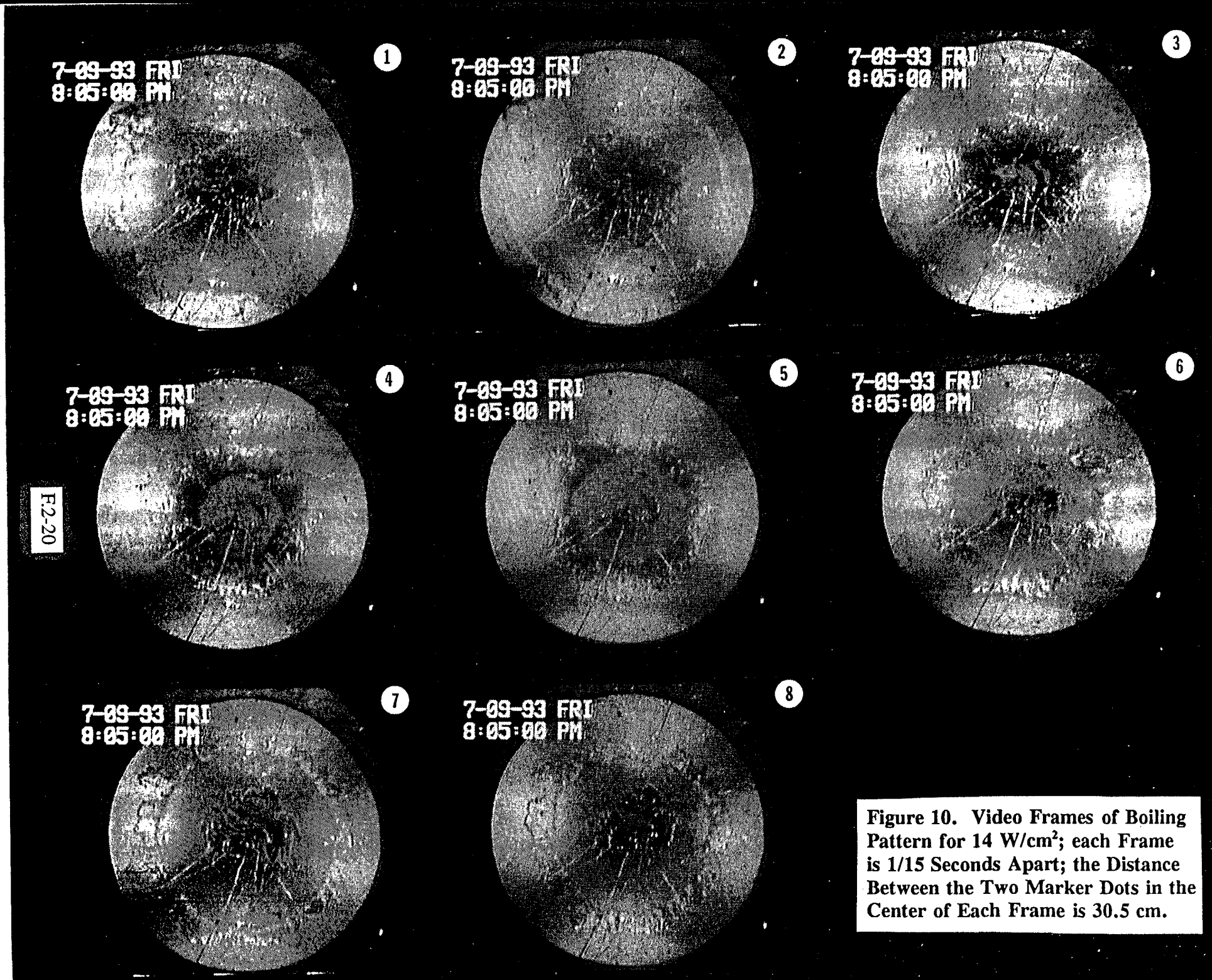

Figure 10. Video Frames of Boiling Pattern for 14 W/cm^2; each Frame is 1/15 Seconds Apart; the Distance Between the Two Marker Dots in the Center of Each Frame is 30.5 cm.

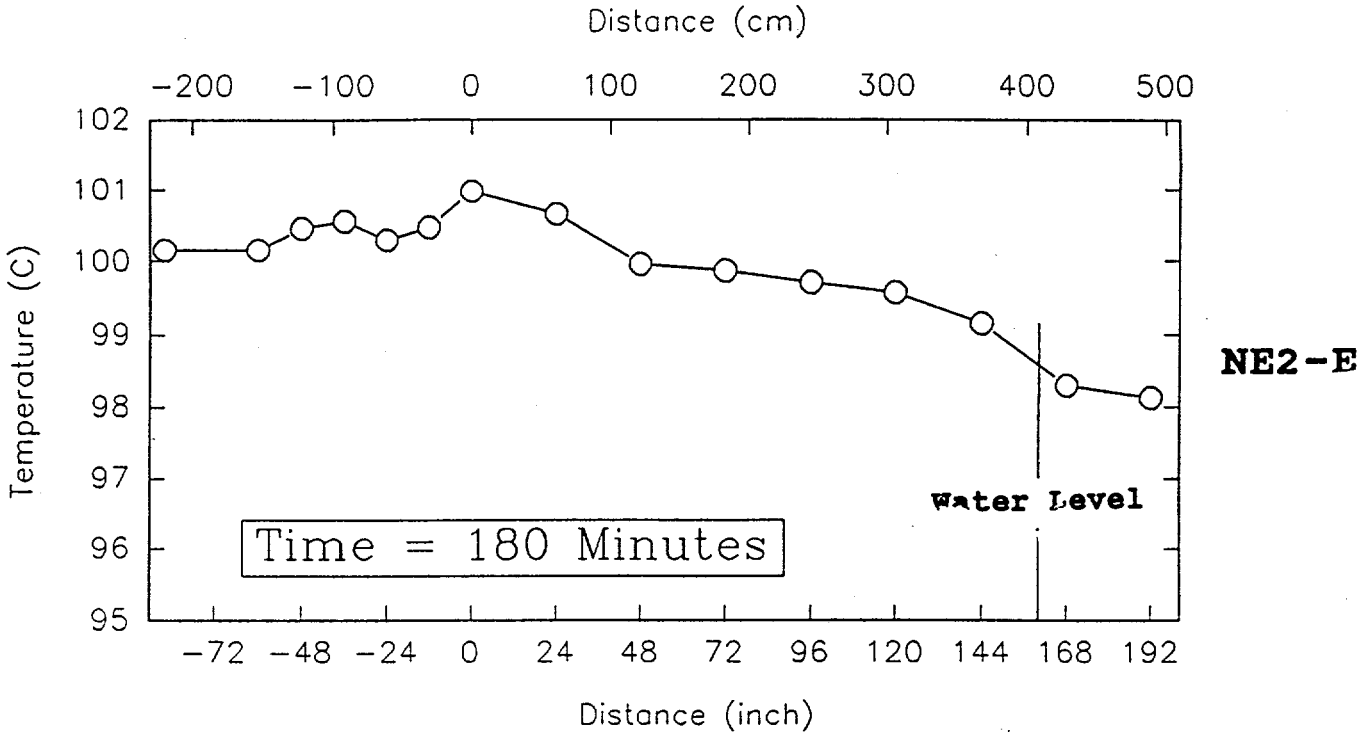

Figure 11. Vertical Bulk Temperature Distribution, NE2-E

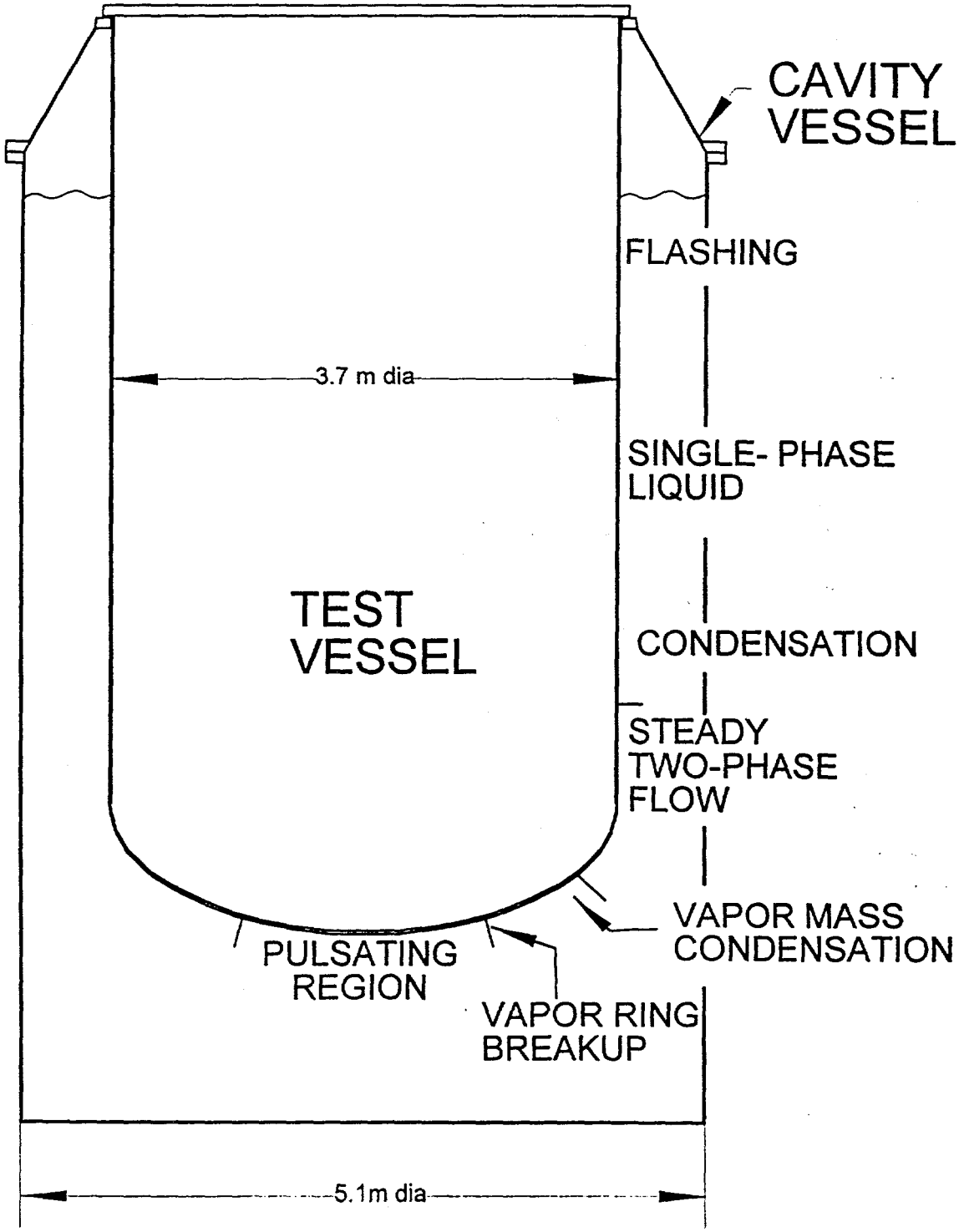

Figure 12. Schematic of Ex-Vessel Boiling Phenomenology

APPENDIX G

CREEP CONSIDERATIONS FOR THE LOWER HEAD

APPENDIX G

CREEP CONSIDERATIONS FOR THE LOWER HEAD

J. Rashid

ANATECH Research Corporation
6432 Oberline Drive, San Diego, CA 92121

The purpose of this appendix is to illustrate how creep on the inside high temperature portion of the lower head thickness acts to relieve stresses that otherwise would have been imposed on the outer, colder portions. The creep calculations presented here demonstrate that the first-principles analysis of structural failure in Chapter 4 is indeed conservative. Moreover, the analysis results provide an indication of the margin of conservatism. To help fully assess the implications of the analysis results it is necessary to describe the analysis bases including material data, constitutive model and failure criteria.

Under the loading conditions considered in this study, the creep behavior of the vessel lower head requires detailed finite-element-based finite-strain time dependent analysis. For this one needs high-temperature material properties and creep data, a properly formulated constitutive model and failure criteria. A constitutive model has been developed using material properties and creep data developed by Idaho National Engineering Laboratory for SA533 pressure vessel steel (Rempe et al., 1990). The material properties data provided elastic modulus, yield strength and ultimate strength as functions of temperature up to 1200 °C. The creep data was obtained for temperature and stress combinations that gave rupture times ranging from a few minutes to hundreds of hours. The highest test temperature for creep was 1100 °C.

With regards to failure criteria, the well known Larson-Miller Parameter (LMP) correlation (Larson and Miller, 1952) provides the best known measure for estimating creep rupture life of tension structures. For simple structures whose response is predominantly one-dimensional under constant temperature, the LMP criterion gives a fairly reliable estimate of the creep rupture life without resorting to complicated creep calculations. For the present analysis, however, it is necessary to extend the LMP criterion from its original basis of uniaxial constant load and constant uniform temperature to time varying multi-dimensional stresses and variable temperatures. This is accomplished using the concept of cumulative incremental damage, and by further replacing the nominal stress by the true stress, a strain-based criterion is developed as an additional necessary condition for failure.

Material Data

A creep law, shown in Eq. (G.1), is used to fit the data referenced above where, ε_{cn} is the nominal (engineering) creep strain, σ_0 is the applied initial stress in ksi, and t is the time in hours.

$$\varepsilon_{cn} = A\sigma_0^r t^s \qquad (G.1)$$

The creep strain rate is obtained by differentiating Eq. (G.1),

$$\dot{\varepsilon}_{cn} = As\sigma_0^r t^{s-1} \qquad (G.2)$$

The logarithmic creep strain ε_c is related to the measured nominal creep strain by

$$e^{\varepsilon_c} = \varepsilon_{cn} + 1 \qquad (G.3)$$

The parameters A, r, and s are dependent on temperature but independent of stress. These parameters were obtained through least-square fit of the data obtained by digitizing the creep curves in Rempe et al., 1990. The resulting values for A, r and s are shown in Table G.1. Selected creep curves for temperatures below and above the transition temperatures are shown in Figures G.1 and G.2 respectively. Note that the model uses the solid lines for primary and secondary creep and the dotted lines for the tertiary creep. Figure G.3 shows the yield strength and elastic modulus as function of temperature.

Table G.1. Creep Power Law Constants Determined by Least Square Approximation

$e_c = A\,s^r\,t^s$	Primary/Secondary Creep Power Law Constants			Tertiary Creep Power Law Constants		
Temperature (°F)	A	r	s	A	r	s
750	3.17E-16	7.01	0.243	—	—	—
900	3.76E-10	3.83	0.405	—	—	—
1050	4.90E-9	3.96	0.624	—	—	—
1160	1.06E-6	2.83	0.836	2.18E-11	5.93	1.69
1200	2.64E-5	1.76	0.564	—	—	—
1340	1.25E-3	1.77	0.678	1.05E-4	2.55	1.75
1430	6.62E-4	2.66	0.704	6.52E-7	6.75	1.53
1610	1.08E-3	3.00	0.788	5.82E-5	4.73	1.38
1790	8.56E-3	3.67	0.536	1.20E-4	11.1	1.57
2012	0.236	4.74	0.714	0.748	11.6	1.82

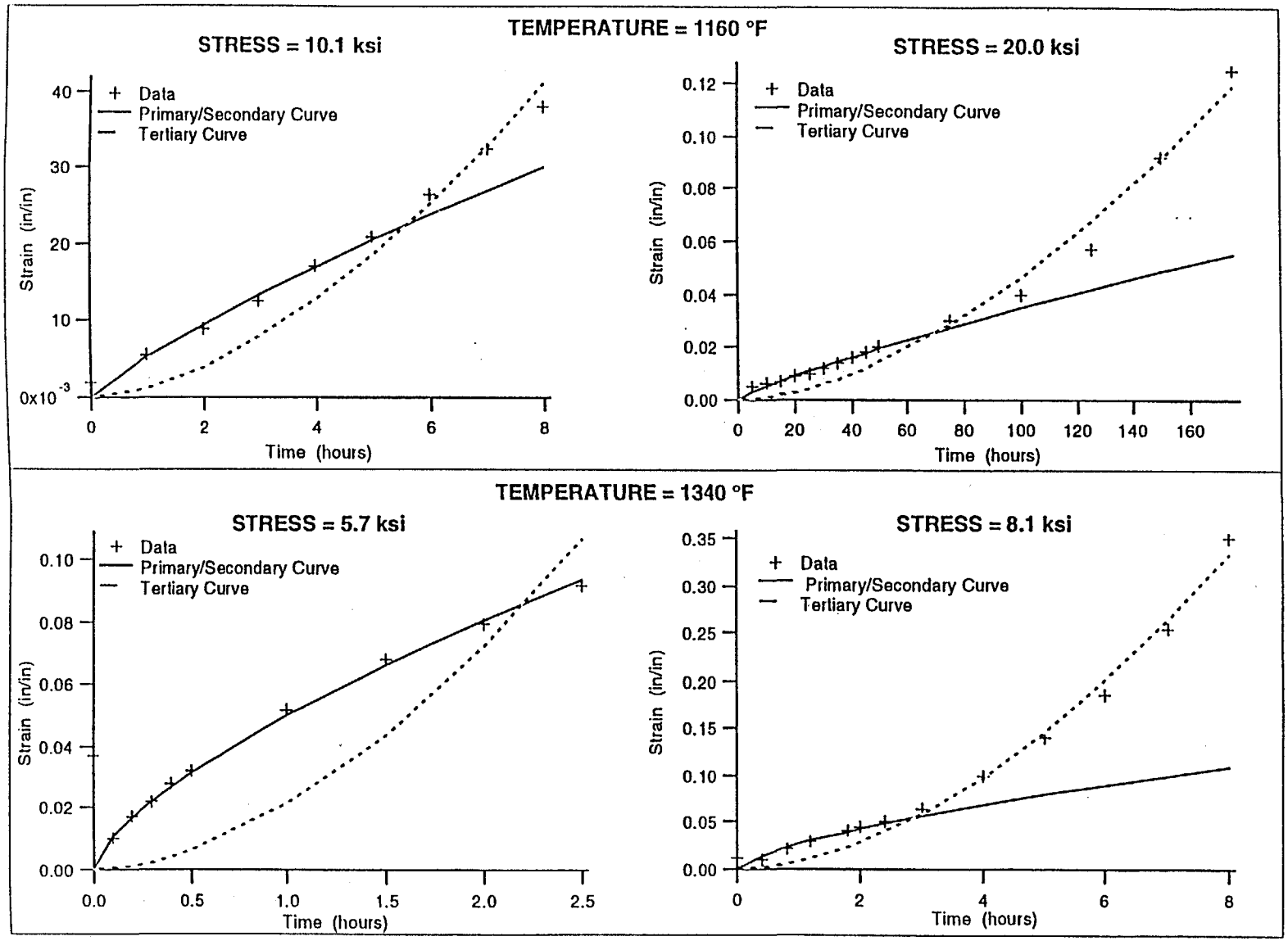

Figure G.1. Creep data for temperatures 1160° and 1340° F.

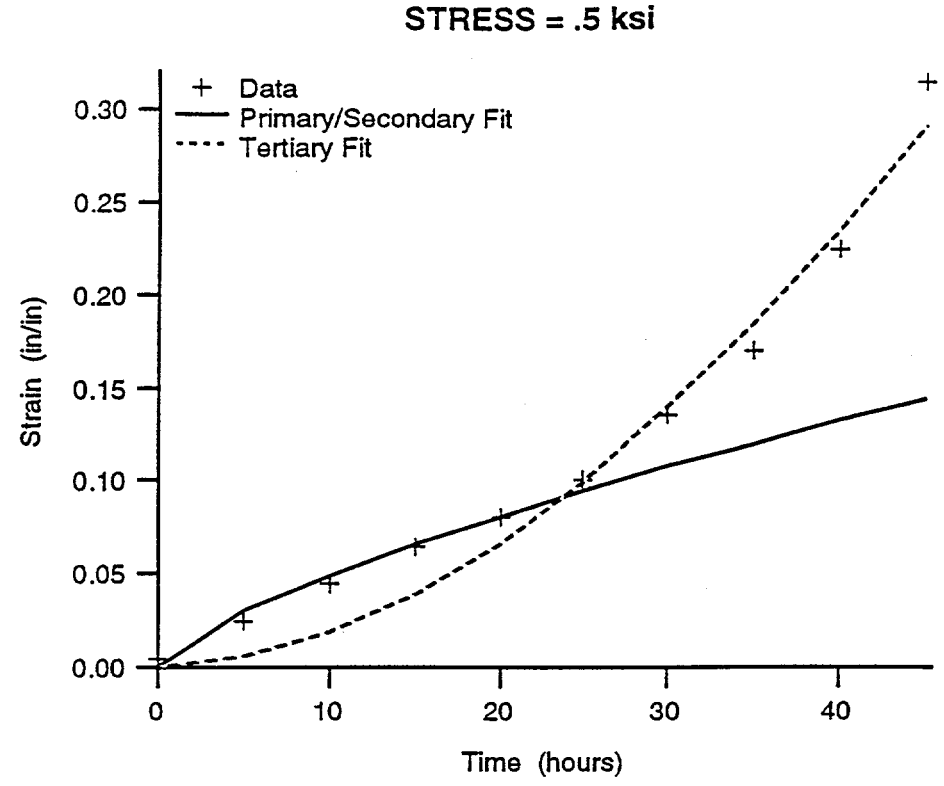

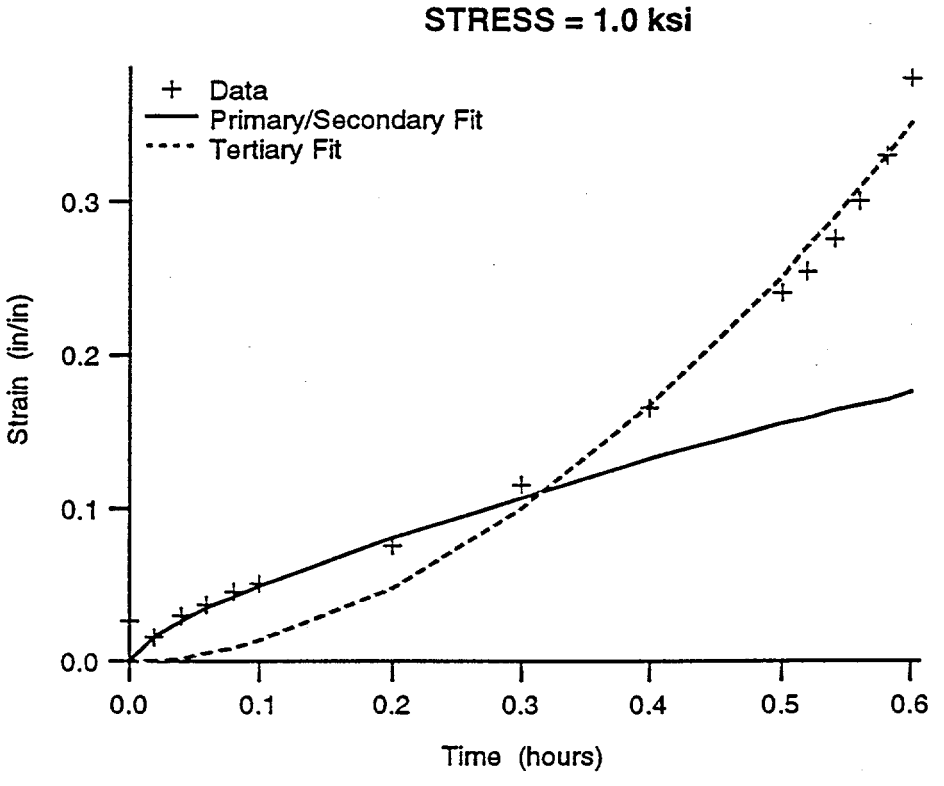

Figure G.2. Creep data for 2012 °F.

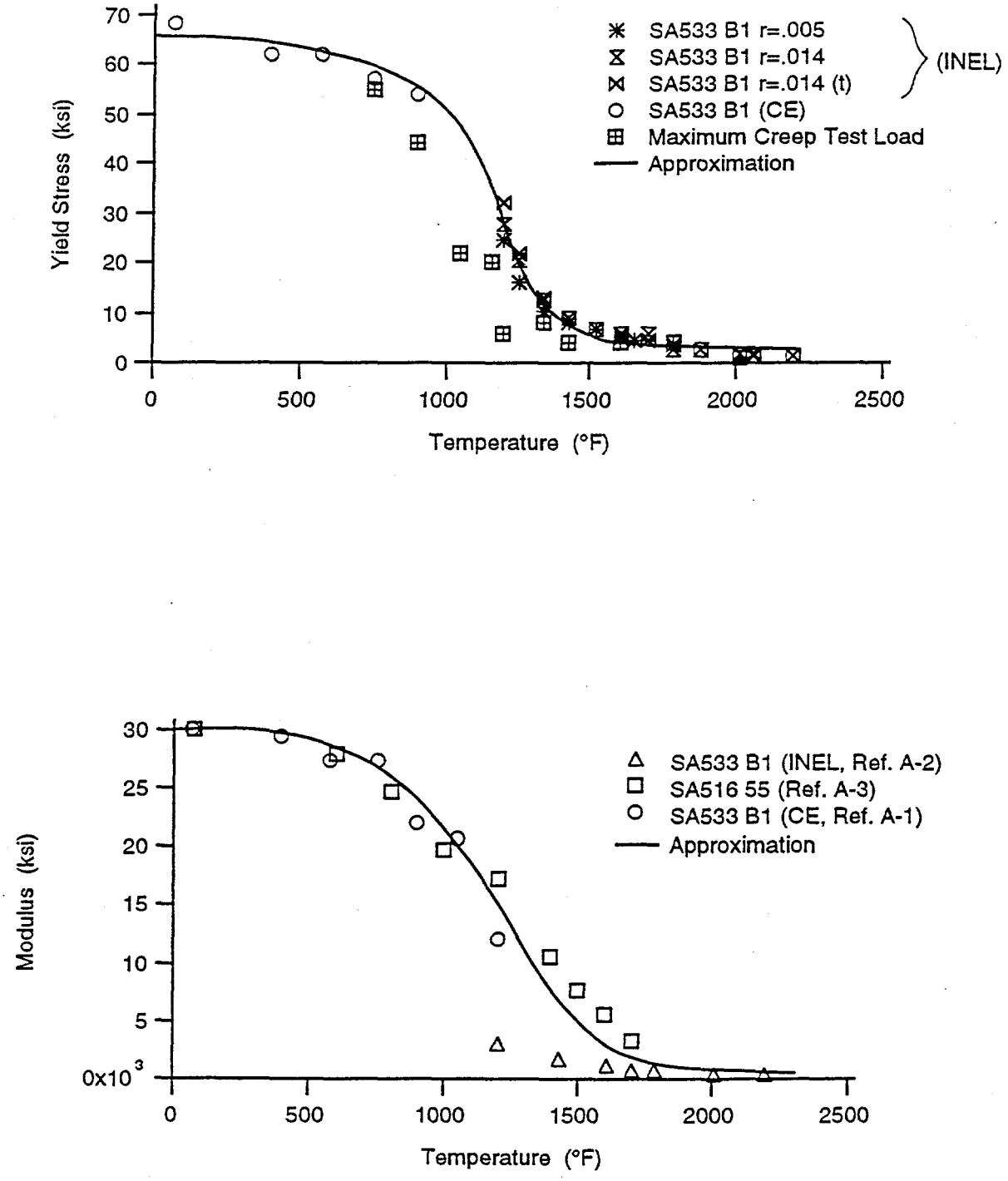

Figure G.3. Yield stress and modulus dependence on temperature.

Uniaxial Constitutive Model

A rate-dependent uniaxial material response is expressed as follows:

$$\sigma = K\varepsilon n \left(\frac{\dot{\varepsilon}}{\dot{\varepsilon}_r}\right)^m \qquad (G.4)$$

where

σ:	True or cauchy stress
ε:	Logarithmic strain
$\dot{\varepsilon}$:	Logarithmic strain rate
$\dot{\varepsilon}_r$:	Reference strain rate
K:	Strength coefficient, function of temperature and has units of stress
n:	Hardness coefficient, function of temperature
m:	Strain-rate sensitivity coefficient, function of temperature

The true stress is related to the initial (nominal) stress σ_0 by the equation

$$\sigma = \sigma_0 e^{\varepsilon} \qquad (G.5)$$

Using Eqs. (G.4) and (G.5), we obtain the strain rate equation as follows:

$$\dot{\varepsilon} = \dot{\varepsilon}_r \left(\frac{\sigma_0}{K}\right)^{\frac{1}{m}} \left(e^{-\varepsilon_c} \varepsilon_c^{-n}\right)^{\frac{1}{m}} \qquad (G.6)$$

where

$\dot{\varepsilon}_c$:	Logarithmic creep strain rate at time t
ε_c:	Integrated logarithmic creep strain
σ_0:	Initial applied stress

The model parameters K, m and n are expressed in terms of the material parameters A, r and s as follows:

$$K = (s^s A)^{\frac{1}{r}}, \quad n = \frac{1-s}{r}, \quad m = \frac{s}{r} \qquad (G.7)$$

A three-dimensional constitutive model and computer program were developed using the material data and equations described above. This computer program was then utilized as a user subroutine in the ABAQUS general purpose finite element program (Hibbitt, Karlsson, and Sorenson, Inc., 1989), which was then used for the creep analyses included in this appendix. For a detailed description of the three-dimensional constitutive model see Theofanous et al. (1993).

Creep-Rupture Model

The creep-rupture model used in the present study is based on the Larson-Miller Parameter and the cumulative damage concept. As mentioned earlier, INEL reported creep rupture times for the SA533 steel at temperatures ranging from 1160 °F (627 °C) to 2012 °F (1100 °C) (Rempe et al., 1990). The LMP correlation is given by

$$LMP = .001(20.0 + \log_{10} t_r)T \qquad (G.8)$$

where t_r is the time to rupture in hours and T is the temperature in Rankine. Figure G.4 shows the data and best fit curves for the applied stress as function of LMP.

$$LMP = b\ell n\frac{\sigma_0}{a}; \qquad a = 5,272.0, \qquad b = -5.7241 \qquad (G.9)$$

where σ_0 is the initial stress (ksi).

Table G.2 shows the data plotted in Figure G.4.

Table G.2. Summary of the SA533B1 Material Creep Tests

Temperature (°F)	Applied Stress (KSI)	Time to Rupture (hours)	Larson Miller Parameter
1160	10.1	190	36.08
1160	20.0	11.3	34.10
1340	5.7	8.9	37.70
1340	8.1	4.6	37.19
1430	2.0	264	42.37
1430	3.8	18.9	40.21
1610	1.8	54.7	44.99
1610	3.8	4.1	42.66
1790	1.2	61.2	49.01
1790	1.8	2.2	45.76
1790	3.8	.045	41.96
2012	0.5	46.9	53.56
2012	1.0	0.65	48.97

For a stress σ and a temperature T applied for a time duration Δt, The incremental damage is defined as follows:

$$\Delta D = \Delta t / t_r(\sigma, T) \qquad (G.10)$$

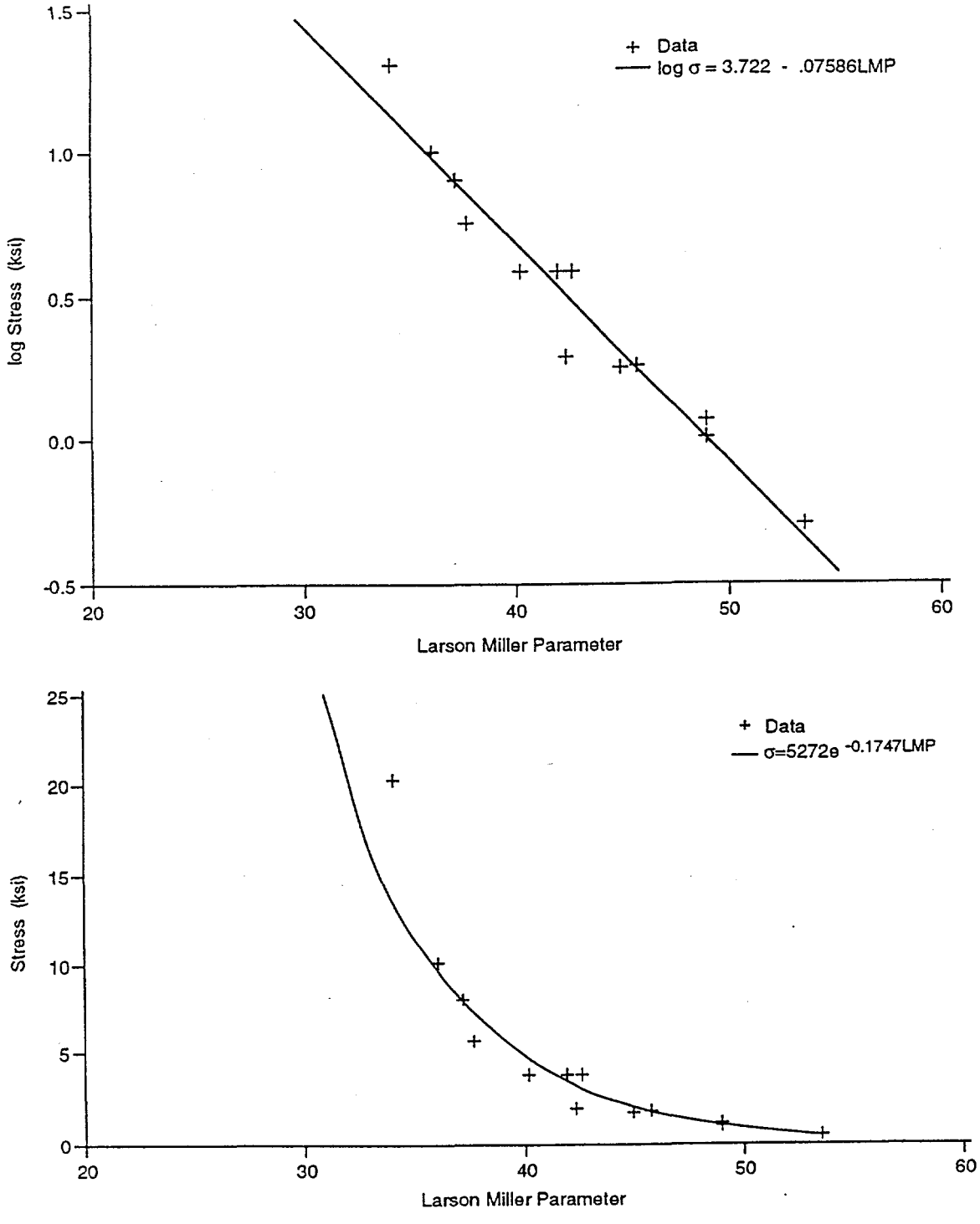

Figure G.4. Stress dependence on Larson-Miller parameter.

where t_r is the rupture time determined from a constant-load creep-rupture test. By re-arranging Eq. (G.8), the time-to-rupture t_r can be determined by

$$t_r = e^{2.303[(LMP/.001T)-20.0]} \qquad (G.11)$$

The total damage at any given time is given by the sum of the incremental damages as follows:

$$D = \sum \Delta t/t_r \qquad (G.12)$$

Thus, failure by creep rupture is indicated when $D \geq 1.0$. Equation (G.10) indicates that ΔD is computed using the current true stress σ and the current temperature T. It is therefore necessary to convert the calculated stress σ to σ_o through Eq. (G.5) before it is used to calculate LMP.

It should be mentioned that experience has shown that the incremental damage procedure described above can significantly underestimate the rupture strain. A strain-based failure criterion would avoid this problem. To develop such a criterion we make use of two sets of creep experiments (Sturm, 1992) conducted under constant load and constant stress conditions as shown in Figure G.5. Comparing the rupture times for these two sets of tests, it is seen that the rupture times differ by a factor of 10. This implies that σ vs LMP curve for the constant load test can be shifted to the right to obtain the curve for the constant stress test. We can then write from Eqs. (G.8) and (G.9).

$$\Delta LMP = 0.001T = b\left(\ell n\frac{\sigma_o}{\alpha} - \ell n\frac{\sigma}{\alpha}\right) \qquad (G.13)$$

Substituting Eq. (G.5) into Eq. (G.13) gives the following expression for the uniaxial rupture strain:

$$\varepsilon_r = 1.747 \times 10^{-4}T \qquad (G.14)$$

where T is in °Rankine. Equation (G.14) is shown in Figure G.6 compared to elongation data, converted to logarithmic strains.

Using this expression for rupture strain and a biaxiality coefficient of 2, we state the creep ductility-exhaustion criterion for the pressure vessel head as follows:

$$\varepsilon_{eff} \geq 0.874 \times 10^{-4}T \qquad (G.15)$$

Condition G.15 and G.8, satisfied simultaneously within the bounds of uncertainty, are necessary and sufficient conditions for the lower head rupture.

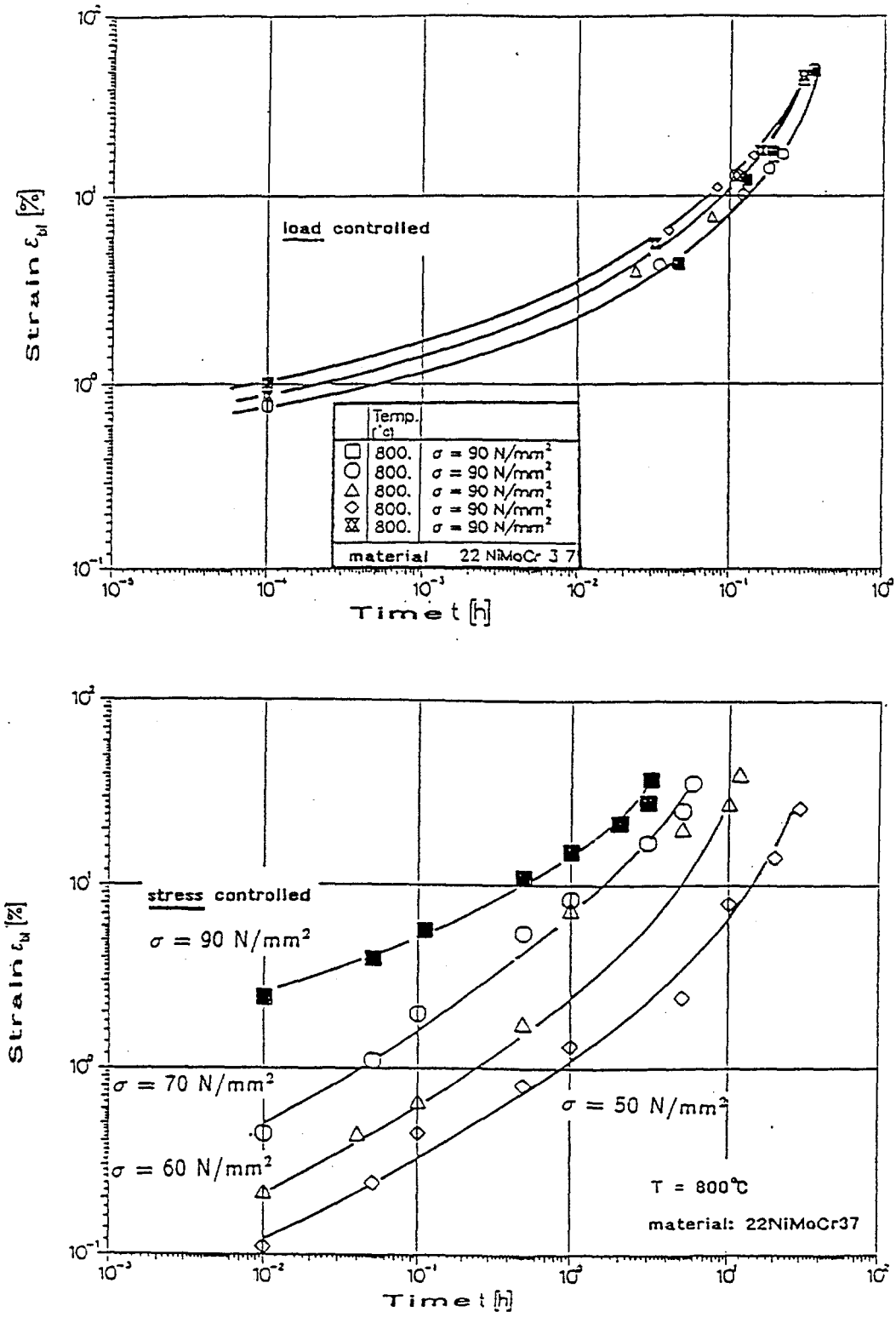

Figure G.5. Creep experiments under constant load and constant stress conditions.

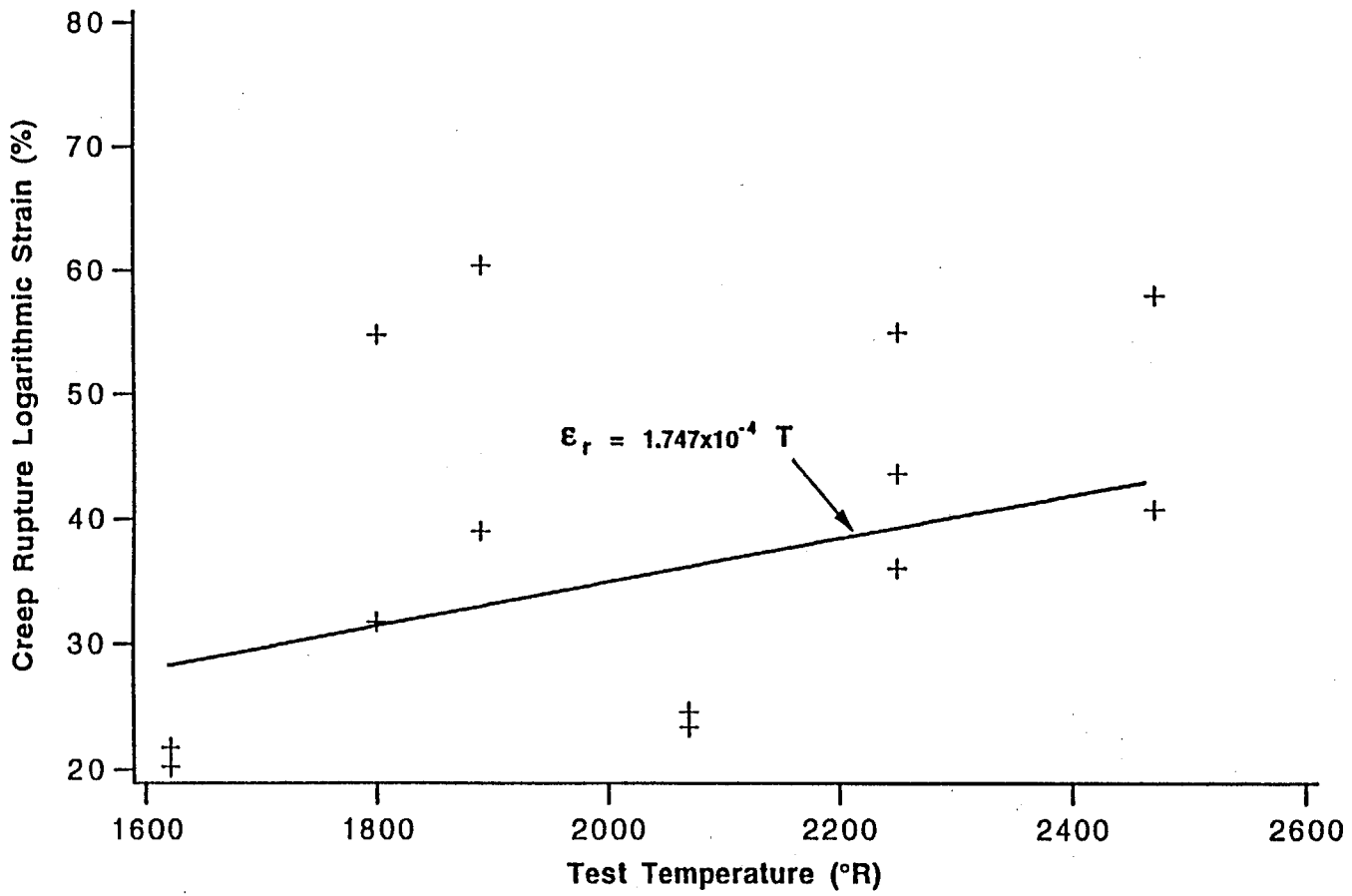

Figure G.6. Creep rupture ductility developed from the Larson-Miller parameter data for SA533 B1 steel.

Analysis Results

The calculations considered a hemispherical head, of 5 cm wall thickness, containing an internal pressure of 400 psi. The inside temperature was ramped to the steel melting point (1550 °C) over a period of 1 hour, while the outside boundary was kept at 100 °C (nucleate boiling).

The calculated hoop stress and von Mises stress distributions are as shown in Figures G.7 and G.8 respectively. It is clear from these figures that the compressive thermal stress over the inner region does little to stress the outer region because of creep, even at 1 hour, and it is further relaxed at later times. Also, it is clear that the outer 1-cm thick layer carries the whole load comfortably and without being subjected to any significant strain, as shown in Figures G.9 and G.10 for hoop strain and effective plastic strain respectively. The hoop stress distribution in Figures G.7 shows a 1-cm-thick compressively stressed region (that has not accumulated any damage) and the point of zero and surrounding area of low stress levels discussed in Chapter 5. The strain-based damage index is illustrated in Figure G.11, where it can be seen that for more than half of the wall (the outer half) the damage index is below 0.1. Therefore, it can be easily seen that the structure can take the 400 psi load without danger of failure. This amount of pressure is equivalent to about 5000 metric tons of material, implying that the outer 1 cm thick is capable of carrying the entire content of the vessel as dead weight.

REFERENCES

1. Hibbitt, Karlsson, and Sorenson, Inc. (1989) "ABAQUS Users Manual Version 4.9," Providence, RI.

2. Larson, F.R., and J. Miller (1952) "A Time-Temperature Relationship for Rupture and Creep Stresses," *Transactions of the ASME*, July 1952, pp. 756-775.

3. Rempe, J.L., G.L. Thinnes, and C.M. Allison (1990) "Light Water Reactor Lower Head Failure Analysis," NUREG/CR-5642, U.S. Nuclear Regulatory Commission.

4. Sturm, D. (1992) University of Stuttgart, Private Communication, May 25, 1992.

5. Theofanous, et al. (1993) "The Probability of Mark-I Containment Failure by Melt-Attack of the Liner," NUREG/CR-6025, U.S. Nuclear Regulatory Commission.

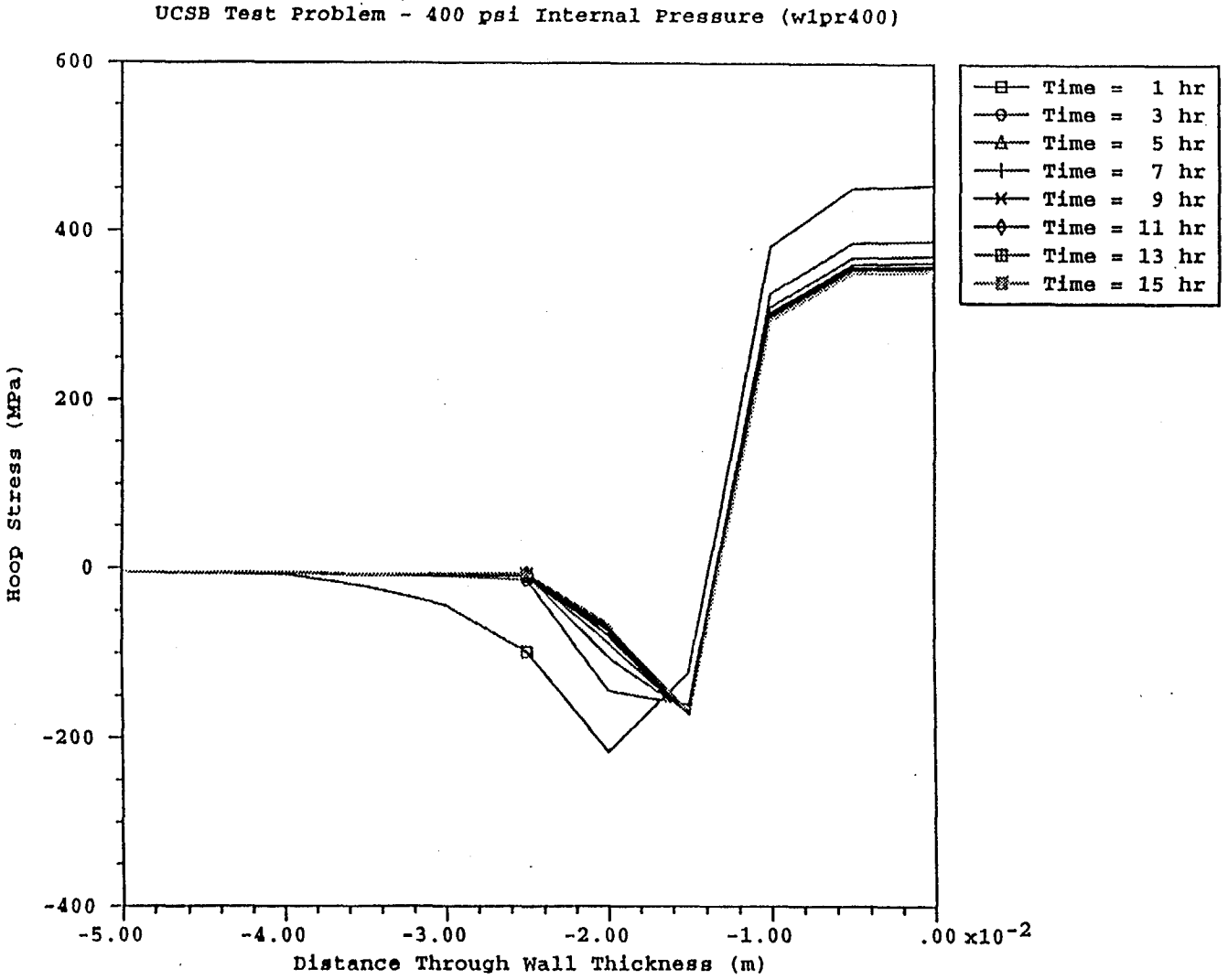

Figure G.7. The calculated hoop stress.

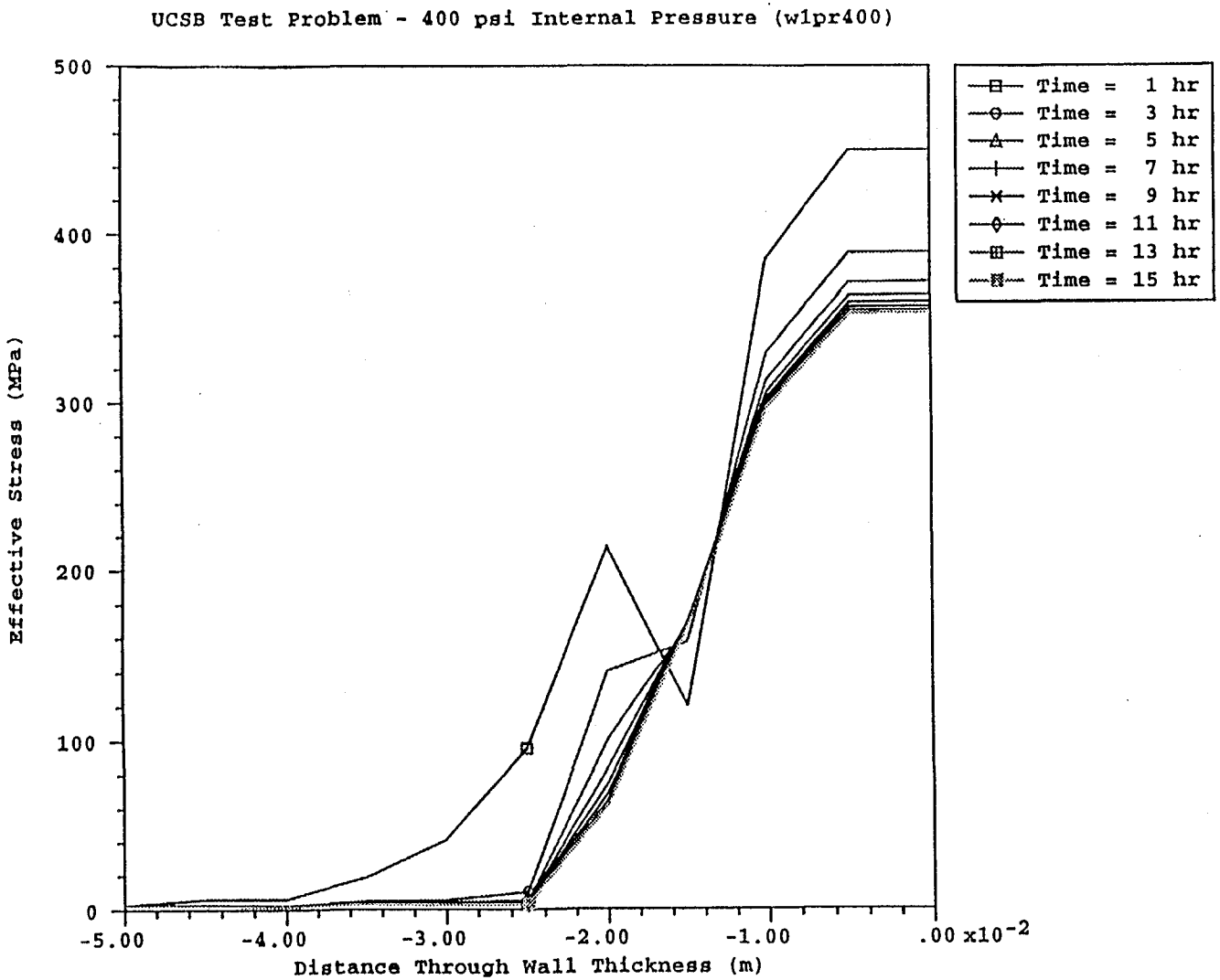

Figure G.8. The calculated von Mises stress distribution.

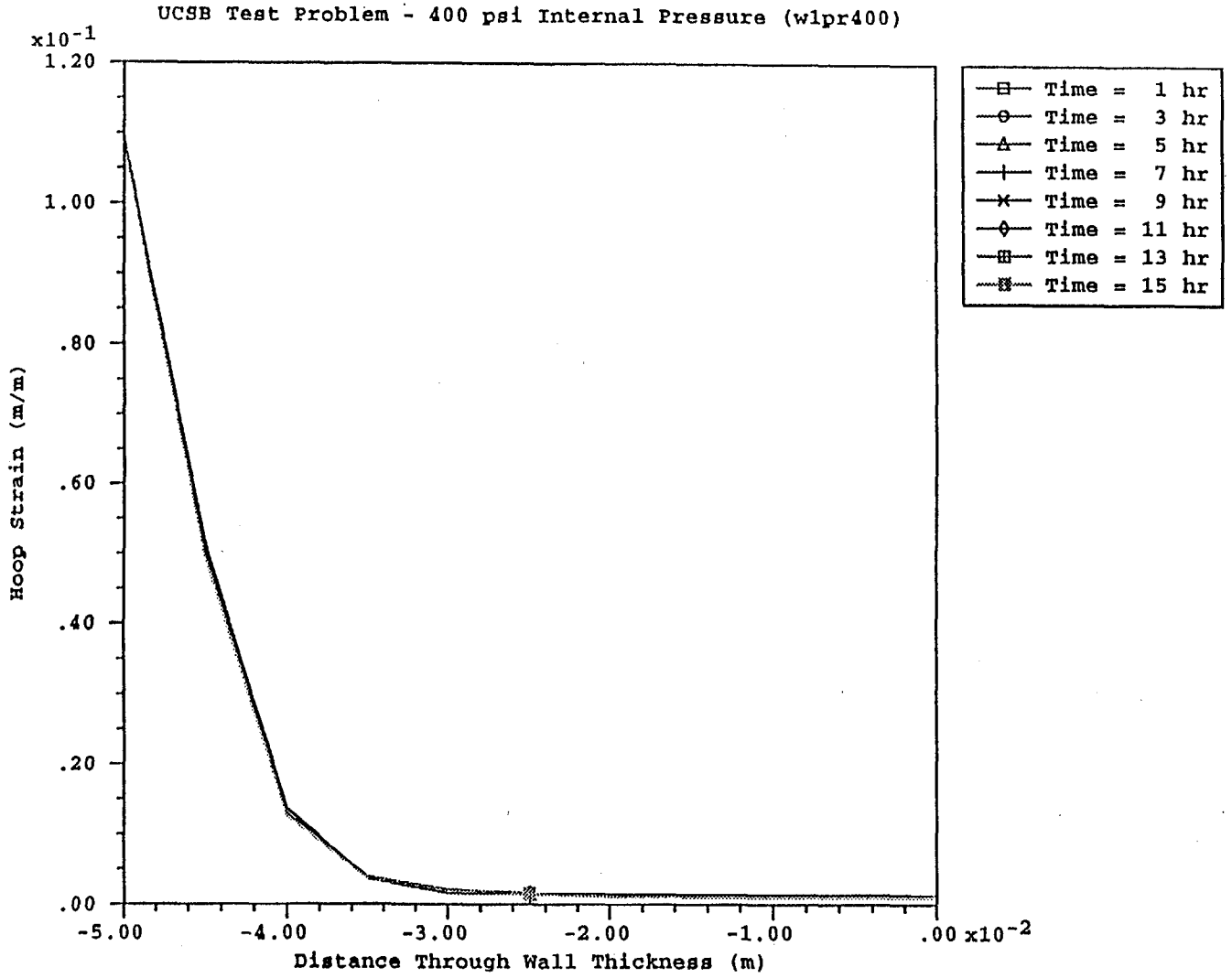

Figure G.9. The calculated hoop strain distribution through wall thickness.

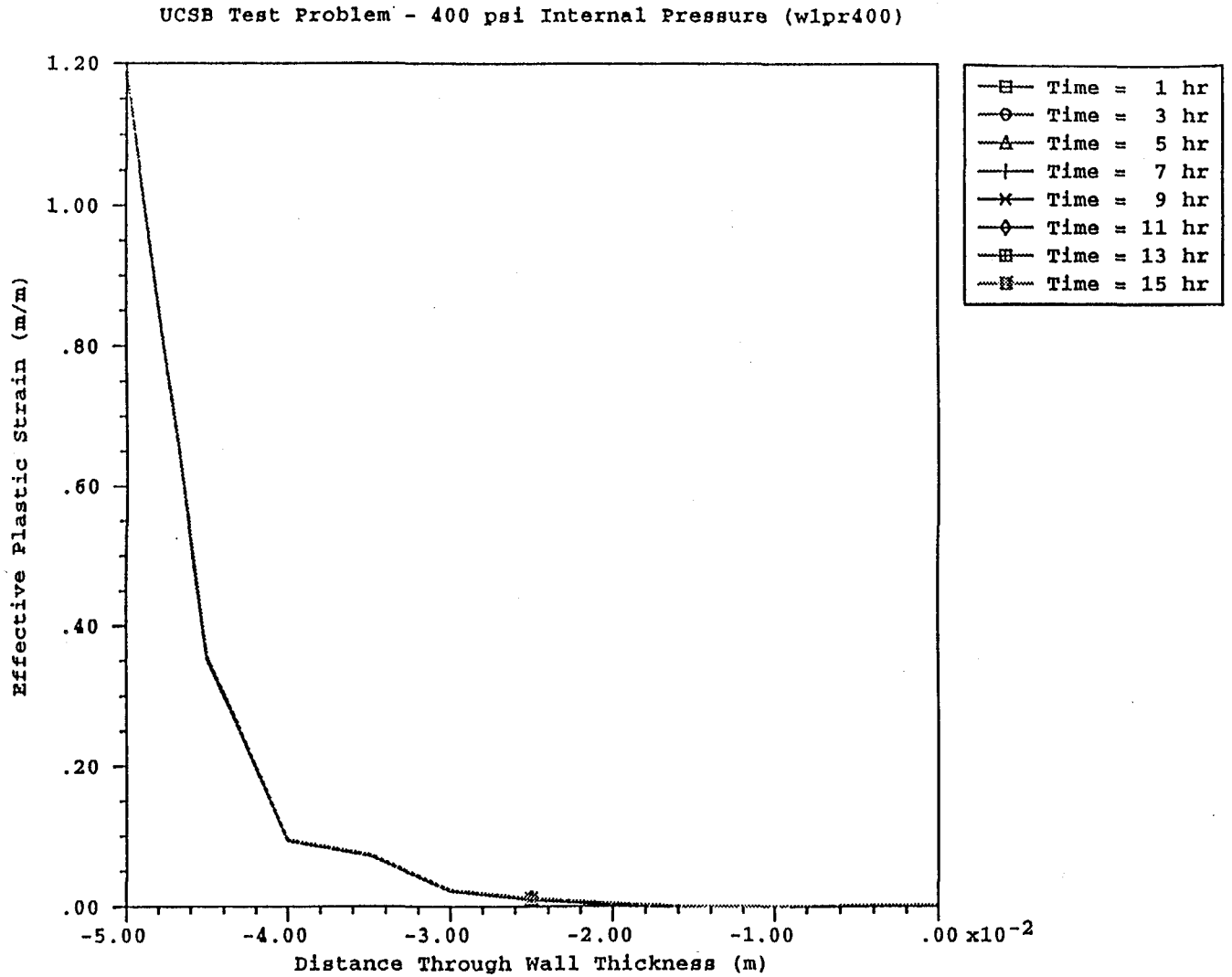

Figure G.10. The calculated plastic strain distribution through the wall thickness.

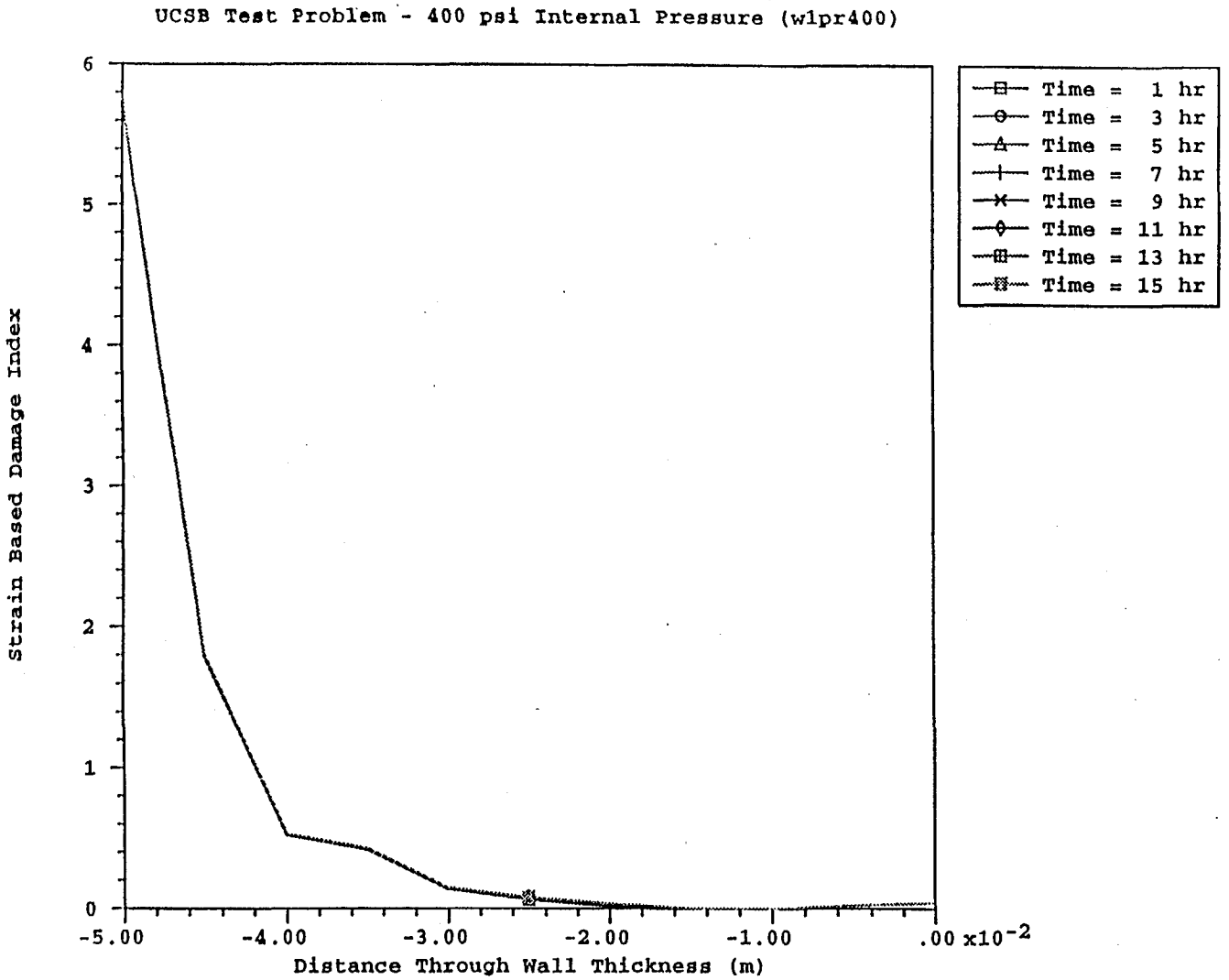

Figure G.11. The predicted strain-based damage index distribution through the wall thickness.

APPENDIX H

INDEPENDENT ANALYSIS OF MELT IMPINGENT

APPENDIX H

MELT IMPINGEMENT THERMAL ATTACK UPON THE LOWER HEAD DURING DOWNWARD CORE RELOCATION[a]

J. J. Sienicki

Engineering Development Laboratories
Reactor Engineering Division
Argonne National Laboratory, Argonne, IL 60439

This appendix provides a more mechanistic basis for the analyses presented in Chapter 8. The approach consists of a bounding calculation of the thickness of the lower head wall that is eroded; the calculation incorporates a number of conservative assumptions that are known to give rise to an overprediction of the eroded thickness. The failure location is assumed to involve either: i) the edge of the bottom blockage near the reflector; or ii) the reflector itself near the bottom blockage. The oxide melt is assumed to have a molten superheat of 165 degrees Kelvin. The released melt will collect locally upon the 36 centimeter thick core support plate and flow into the lower plenum through one or more of the plate flow holes. The bottom diameter of each flow hole is 4.8 centimeters (1.9 inch). For a hole filled with melt, the melt velocity exiting the bottom of the hole will be at least as large as

$$U_{hole} = (2gL_{csp})^{1/2} \qquad (H.1)$$

where

U_{hole} = velocity at bottom of flow hole,
g = gravitational acceleration,
L_{csp} = core support plate thickness,

which provides an exit velocity of 2.6 meters per second. The corresponding mass flowrate,

$$G_{hole} = \rho U_{hole} \frac{\pi}{4} D_{hole}^2, \qquad (H.2)$$

equals 39 Kilograms per second. The presence of a thin layer of melt atop the core support plate would not be expected to increase the overall distance from the top of the melt to the bottom of the hole by a significant amount due to the large plate thickness. Thus, the flowrate for melt drainage through each hole is not expected to differ significantly from the 39 Kilograms per second value. It follows that for the bounding downward release conditions of Reference 1, the

[a] Work sponsored by the United States Department of Energy Advanced Reactor Severe Accident Program.

time dependent melt release rate may be accommodated by flow through from one to ten flow holes.

Equation (H.1) is most appropriate for situations in which melt drains from the plate upper surface into the hole. However, if a hole is located directly in the path of melt released from the failure site in the pool lower boundary, then it is possible for melt to follow a straight shot pathway through the flow hole. In this case, the velocity exiting the bottom of the hole will be representative of free-fall from the failure site to the bottom of the plate,

$$U_{hole} = [2g(h_{fall} + L_{csp})]^{1/2} \qquad (H.3)$$

where

h_{fall} = fall height from failure site to top of core support plate.

The core melt pool configuration in Reference 1 was based upon the results of a MAAP 4.0 calculation. At the edge of the core, the melt release location could be as high as 91 centimeters above the core support plate. In Reference 1, an initial release velocity of 3.6 meters per second was calculated. It follows that the melt velocity exiting the bottom of the core support plate could be as high as 6.1 meters per second.

At the edge of the core, the vertical distance from the bottom of the core support plate to the lower head is about 83 centimeters. The lower head will be filled with water at the onset of relocation. It is interesting to compare the melt release conditions with the melt entry conditions in the Argonne CCM-5 and CCM-6 experiments.[2,3] The tests involved the release of about 11 Kilograms of melt through openings 5.08 centimeter in diameter into pools of water 1.07 meter deep. The experiments were conducted at near atmospheric pressure; the water was initially subcooled by 49 degrees Kelvin in CCM-5 and 2.5 degrees Kelvin in CCM- 6. The fall height from the melt vessel to the water surface was 0.34 meter. In CCM-5, melt is estimated to have entered the water at velocities that decreased from 2.9 to 2.6 meters per second and diameters that decreased from 3.4 to 0.4 centimeters.[4] The melt entry velocity in CCM-6 is estimated to have decreased from 5.7 to 3.7 meters per second while the diameter decreased from 4.8 to 4.3 centimeters.[4] In both experiments, all of the corium collected as particulate at the bottom of the water pool. The melt stream in CCM-5 penetrated no more than about halfway into the water. The stream leading edge penetration calculated with THIRMAL-1 is in good agreement with the thermocouple data. In CCM-6, the stream leading edge was calculated by THIRMAL-1 to penetrate to the base of the pool early in time and recede thereafter such that only 2 percent of the mass impinged as a stream. Interaction of the melt streams with water will cause a portion of the melt to break up and freeze prior to reaching the lower head.

The first assessment integrating together analyses of the melt relocation mode, lower head structure effects, melt stream breakup, stream impingement conditions, and impingement-induced lower head heatup was performed by Argonne for the TMI-2 core relocation event.[5,6] That work included calculations with the THIRMAL-0 code. Calculations of impingement conditions accounting for water and structure effects utilizing THIRMAL-0 were later carried out for other operating LWR lower head configurations.[7] Based upon the results of recent THIRMAL-1 calculations, impingement of a significant part of the melt in a stream mode is still expected in the present situation because of the shallow water depth of 83 centimeters. In the present analysis, a significant conservatism is introduced by completely neglecting the effects of the water in the lower head.

Neglecting the effects of water, the stream impingement conditions are obtained accounting for the free-fall acceleration of the stream between the core support plate bottom and the lower head,

$$U_{imp} = (U_{hole}^2 + 2gh_{LH})^{1/2}, \qquad (H.4)$$

where

h_{LH} = fall height from bottom of core support plate to lower head.

The impingement heat flux,

$$q_{imp} = h_{imp}\Delta T_{sup}, \qquad (H.5)$$

where

q_{imp} = impingement heat flux,
h_{imp} = impingement heat transfer coefficient,
ΔT_{sup} = melt superheat,

reflects the presence of solid oxide crusts between the eroding steel and the flowing melt. The heat transfer coefficient is taken to be that for impingement of a laminar stream given by Swedish et al.,[9]

$$h_{imp} = \frac{Nu_{imp}k}{D_{imp}} \qquad (H.6)$$

$$Nu_{imp} = 2^{1/2}\ \mathrm{Re}^{1/2} 0.553\ \mathrm{Pr}^{1/3}, \qquad (H.7)$$

k = melt thermal conductivity,
Re = $\frac{\rho U_{imp} D_{imp}}{\mu}$,
Pr = $\frac{c\mu}{k}$,
ρ = melt density,

μ = melt viscosity,

c = melt specific heat.

Equation (H.7) applies to normal impingement and thus overestimates the initial heat transfer to the sloped inner surface of the lower head below the edge of the core.

The lower head steel erosion rate is approximated with the one-dimensional expression,

$$\frac{d\delta}{dt} = \frac{q_{imp}}{\rho_s(e_{s,liquidus} - e_{s,o})}, \qquad (H.8)$$

where

δ = steel thickness eroded,

t = time,

ρ_s = initial steel density,

$e_{s,liquidus}$ = specific enthalpy of steel at liquidus,

$e_{s,o}$ = specific enthalpy of steel at initial temperature.

The use of Eq. (H.8) introduces a number of significant conservatisms. First, Eq. (H.8) is a one-dimensional formula and thus applies in the limit where the plate thickness is less than or similar to the impinging stream diameter. In the present case, the stream diameter is significantly less than the lower head thickness. As a result, the use of Eq. (H.8) neglects the heat sink effects of steel surrounding the impingement zone in which Eq. (H.7) holds. The heat transfer coefficient increases as the stream diameter decreases. However, this does not mean that the erosion rate continues to increase with decreasing diameter. To the contrary, when the stream diameter becomes sufficiently small compared to the head thickness, then multidimensional conduction effects inside the steel will enhance the fraction of energy transferred to the steel that is conducted into the surrounding solid thereby reducing the erosion rate below that given by Eq. (H.8).

Another major conservatism inherent in Eq. (H.8) is that when the stream diameter is sufficiently small relative to the head thickness, then a layer of melted head steel will collect inside the eroded cavity tending to insulate the underlying eroding solid. This effect will further reduce the erosion rate below that given by Equation (H.8).[10]

In addition, Eq. (H.8) ignores any heat removal from the lower head outer surface due to boiling heat transfer to water inside the cavity.

While the melt collecting upon the core support plate flows through a number of flow holes that may vary with time, the flow through one of the holes will likely continue throughout the duration of the sudden massive release. The cumulative erosion associated with the impingement of this particular stream thus bounds the local erosion of the lower head. Table H.1 shows the

thermophysical properties assumed for the impinging oxidic melt. Table H.2 shows the conditions and results of the bounding erosion calculation carried out for the two extremes of velocity of melt exiting a core support plate flow hole. The assumption of an unvarying exit velocity of 6.1 meters per second is another conservatism in that the velocity of release from the core pool actually decreases with time.

The cumulative thickness of steel eroded is observed to be bounded by 12 to 14 centimeters over the range of melt velocity exiting the flow hole. This is less than the 15.24 centimeter (6.0 inch) thickness of the lower head. Due to the conservatisms inherent in the calculation, the erosion is expected to be significantly less than the bounding values in Table H.2. Thus, a sudden massive downward release of oxidic melt from the core will not result in lower head meltthrough due to melt stream impingement thermal attack.

Table 1. Thermophysical Properties Assumed in Lower Head Erosion Analysis

Melt density, Kg/m^3	8120
Melt specific heat, KJ/(Kg·K)	0.579
Melt thermal conductivity, W/(m·K)	2.9
Melt viscosity, Kg/(m·s)	5.4×10^{-3}
Initial steel temperature, K	398
Steel initial density, Kg/m^3	7840
Steel liquidus specific enthalpy, MJ/Kg	1.29
Steel initial specific enthalpy, MJ/Kg	0.049

Table 2. Conditions and Results of Bounding Lower Head Erosion Analysis

Melt mass released, Kg	47000	47000
Melt stream velocity at bottom of core support plate, m/s	2.6	6.1
Melt stream velocity impinging upon lower head, m/s	4.8	7.3
Melt stream diameter at bottom of core support plate, cm	4.8	4.8
Melt stream diameter impinging upon lower head, cm	3.6	4.4
Melt superheat, K	165	165
Reynolds number	260000	480000
Prandtl number	1.0	1.0
Impingement Nusselt number	410	560
Impingement heat transfer coefficient, $KW/(m^2 \cdot K)$	33	37
Impingement heat flux, MW/m^2	5.4	6.0
Steel erosion rate, cm/s	0.056	0.062
Melt impingement time, s	220	220
Cumulative steel erosion, cm	12.4	13.7

REFERENCES

1. J. J. Sienicki and C. C. Chu, "ANL Contribution to the Draft Report on In- Vessel Retention/In-Vessel Explosions (Draft)," Argonne National Laboratory, Reactor Engineering Division (June 1994).

2. B. W. Spencer, S. K. Wang, C. A. Blomquist, L. M. McUmber, and J. P. Schneider, "Fragmentation and Quench Behavior of Corium Melt Streams in Water," NUREG/CR-6133, ANL-93/32, U. S. Nuclear Regulatory Commission (February 1994).

3. S. K. Wang, C. A. Blomquist, B. W. Spencer, L. M. McUmber, and J. P. Schneider, "Experimental Study of the Fragmentation and Quench Behavior of Corium Melts in Water," *Fifth Proceedings of Nuclear Thermal Hydraulics*, ANS 1989 Winter Meeting, San Francisco, CA, November 26-30, 1989, p. 120, American Nuclear Society, LaGrange Park, IL (1989).

4. C. C. Chu, J. J. Sienicki, and B. W. Spencer, "Comparison of the THIRMAL-1 Melt-Water Interaction Code with the Results of the FARO Scoping and Quench Tests Plus the CCM-5 and CCM-6 Experiments," ANL/RE/LWR 94-2, Argonne National Laboratory, Reactor Engineering Division (September 1994).

5. S. K. Wang, J. J. Sienicki, and B. W. Spencer, "Assessment of the Integrity of the TMI-2 Lower Head Instrument Penetration Weldments," ANL/RAS-GPU-1, Argonne National Laboratory, Reactor Analysis and Safety Division (August 1988).

6. S. K. Wang, J. J. Sienicki, and B. W. Spencer, "Heatup of the TMI-2 Lower Head During Core Relocation," *Fifth Proceedings of Nuclear Thermal Hydraulics*, ANL 1989 Winter Meeting, San Francisco, CA, November 26-30, 1989, p. 136, American Nuclear Society, LaGrange Park, IL (1989).

7. J. J. Sienicki, S. K. Wang, and B. W. Spencer, "Analysis of Melt Arrival Conditions on the Lower Head in U. S. LWR Configurations," *Proceedings of the Fifth International Topical Meeting on Reactor Thermal Hydraulics NURETH-5*, Salt Lake City, UT, September 21-24, 1992, Vol. II, p. 450, American Nuclear Society, LaGrange Park, IL (1992).

8. J. J. Sienicki and B. W. Spencer, "Analysis of Reactor Material Experiments Investigating Corium Crust Stability and Heat Transfer in Jet Impingement Flow," *ANS Proceedings 1985 National Heat Transfer Conference*, Denver, CO, August 4-7, 1985, p. 255, American Nuclear Society, LaGrange Park, IL (1985).

9. M. J. Swedish, M. Epstein, J. H. Linehan, G. A. Lambert, G. M. Hauser, and L. J. Stachyra, "Surface Ablation in the Impingement Region of a Liquid Jet," *AICHE Journal*, **25**, No. 4, p. 630 (1979).

10. A. Furutani, S. Imahori, K. Sato, and M. Saito, "Erosion Behavior of a Solid Plate by a Liquid Jet-Effect of Molten Layer," *Nuclear Engineering and Design*, **132**, p. 153 (1991).

APPENDIX I

THE EMISSIVITY OF THE STEEL LAYER

APPENDIX I

THE EMISSIVITY OF THE STEEL LAYER

T.G. Theofanous, G. Wang and X. Chen

Center for Risk Studies and Safety
University of California, Santa Barbara, CA 93106

Although we could find anecdotal evidence (from those with experience in the steel industry) that molten steel should have an emissivity "around 0.4," hard data seem to be limited to only one reference [VD1-Wärmeatlas, 1991] that cites an emissivity of 0.45 for molten iron at 1770 °C. Given the importance of this parameter it became clear to us that it would be worthwhile to undertake its measurement, especially in relation to effects of temperature and composition variations found in the application considered here. In particular, this includes the presence of components found in stainless steel and of zirconium.

The experimental approach was based on pyrometer (total radiance) and temperature measurements of small, ~10 g sample sizes, of metal, inductively heated in an inert atmosphere. The sample was held in a ceramic crucible (~1 cm internal diameter and ~2 cm deep). A C-type thermocouple was positioned to protrude from the crucible bottom by ~3 mm, and it was coated with zirconia. With two pyrometers focusing on the upper surface of the sample, the surface temperature (measured with the two-color pyrometer) and radiation intensity (measured with the pyrometer) were obtained simultaneously. The total emissivity was determined by comparing the radiation intensity with that of a black body at the same temperature. For an ϵ-slope of 1.06 (expected to be applicable to a fully molten steel sample), this upper surface temperature was found to be about 90 °C lower than the thermocouple indication at the insulated bottom of the sample [for a temperature level of ~1700 °C]. By using analog readouts thermocouple measurements were possible even under power operation—the voltmeter and pyrometer readings were recorded continuously on a videotape and were later manually analyzed. The overall experimental arrangement is shown in Figure I.1. The molten sample in the crucible during one of the runs in shown in Figure I.2.

The emissivity of a sample of carbon steel was first measured through a heatup and cooldown cycle up to a temperature of 1700 °C. The results, as shown in Figure I.3, give an essentially constant value of 0.43, which is in excellent agreement with the previously available information as summarized at the beginning of this appendix. After cooldown ~1 g of stainless steel was added to the solidified sample and data were obtained for another heatup and cooldown cycle again to a peak temperature of 1700 °C. These results are shown in Figure I.4, and again exhibit

a constant value of 0.43. In both cases, after cooldown the sample surface was found to be perfectly smooth (concave upward) and free of any contamination (shining).

The emissivity data deduced for the solid steel material (prior to melting) are shown in Figure I.5. Early on the emissivity is ~1, which is expected for the basically preoxidized sample used. Gradually, however, it is seen to drop toward the 0.43 value—we suspect by some surface melting and gradual clearing up of the oxide contamination by surface tension forces, pulling it to the sides of the crucible where it was indeed found at the end of the experiment. To elucidate the temporary "dip" of the emissivity seen between 1450 and 1500 °C, the measured temperature transients by the thermocouple and the two-color pyrometer are shown in Figure I.6. Note that the area in question is from 150 to 300 seconds, and it may be a consequence of a temporary change in the ϵ-slope as the surface itself melts. Also note that the dip in the pyrometer reading from 300 to 400 seconds is due to surface "cleaning" as impurities are pulled up to the sides by surface tension forces—from this point on the emissivity remains at 0.43 including the whole cooldown (not shown). It should also be noted that in other experiments in our lab involving heating of stainless steel spheres to ~1200 °C in film boiling, an emissivity value of 0.8 was deduced (Liu et al., 1993).

For the next test, an ~1 g piece of zirconium was added on top of the solidified sample from the previous experiment, and the process was repeated. In this test both pyrometers were focused on the zirconium piece. In this case the appropriate ϵ-slope of the two-color pyrometer was also found to be 1.06, and the deduced emissivities are shown in Figure I.7. In this case melting occurred by eutectic formation, as expected, well below the zirconium melting point (~1900 °C). This melt was able to cause crucible failure at ~1800 °C. The high emissivities seen in Figure I.7 would appear to be the consequence of preexisting oxides on the zirconium piece, which, however, instead of pulling away from the melt surface, remained there, apparently aided by the concave upward (wetting the crucible walls) configuration.

REFERENCES

1 Liu, C., T.G. Theofanous and W. Yuen (1'992) "Film Boiling from Spheres in Single- and Two-Phase Flow," ANS Proceedings1992 National Heat Transfer Conference, San Diego, CA, Aug. 9-12, 1992, Vol. 6, 211–218.

2 VDI-Wärmeatlas (1991) "Berechnungsblätter für den Wämeübergang, Sechste Auflage, VDI-Verlag, Düsseldorf.

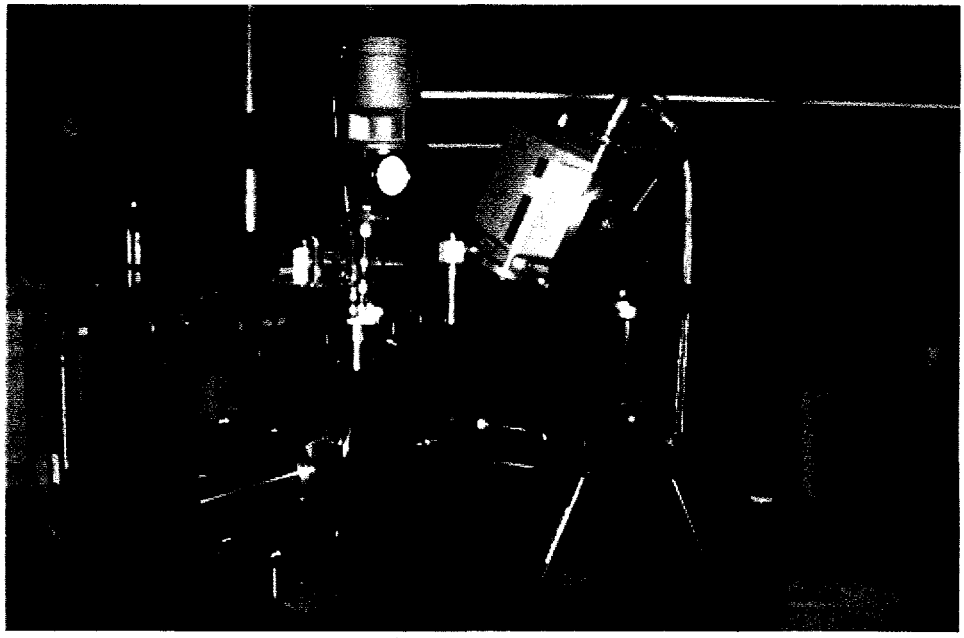

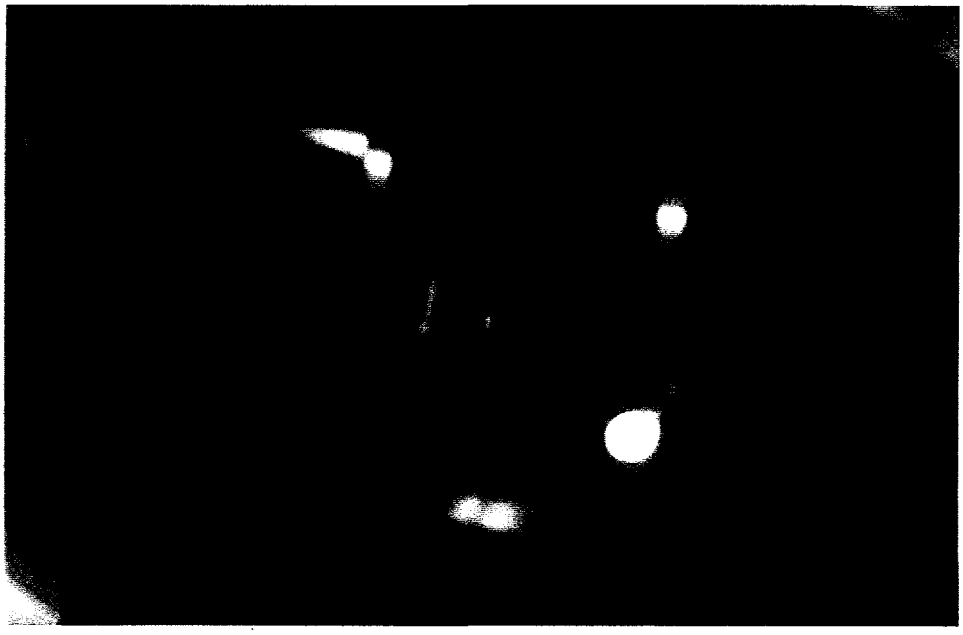

Figure I.1. The overall experimental setup for the emissivity measurement.

Figure I.2. A molten steel sample in the crucible surrounded by the induction coils, as viewed from a window of the inerted chamber.

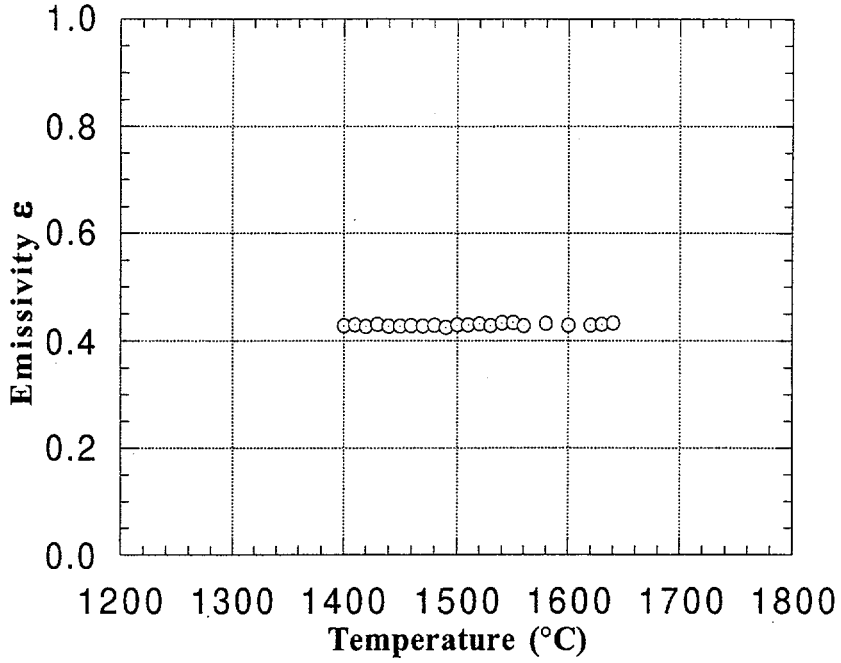

Figure I.3. The emissivity of molten steel as a function of sample surface temperature (during colling down) as deduced from pyrometer measurements.

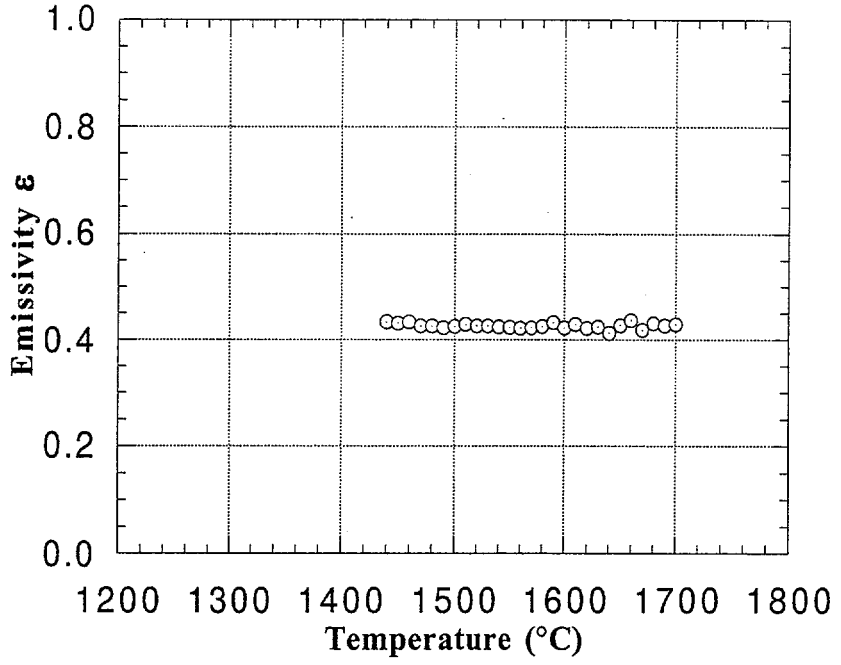

Figure I.4. The emissivity of molten steel, containing ~10% stainless steel by weight, as a function of sample surface temperature as deduced from pyrometer measurements.

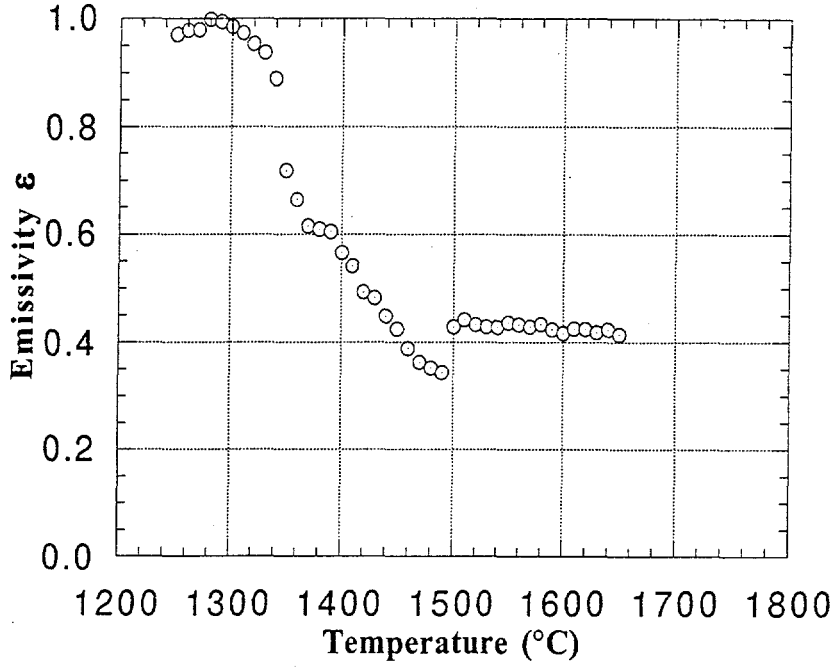

Figure I.5. The emissivity of the steel sample as a function of sample surface temperatures (during heating up) as deduced from pyrometer measurements.

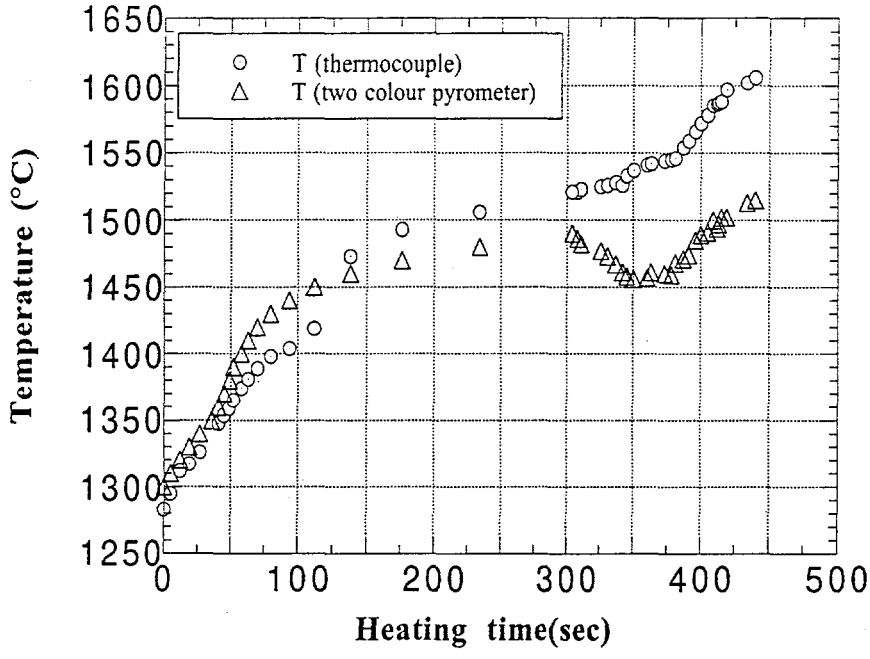

Figure I.6. Temperature transients during melting of a stainless steel sample.

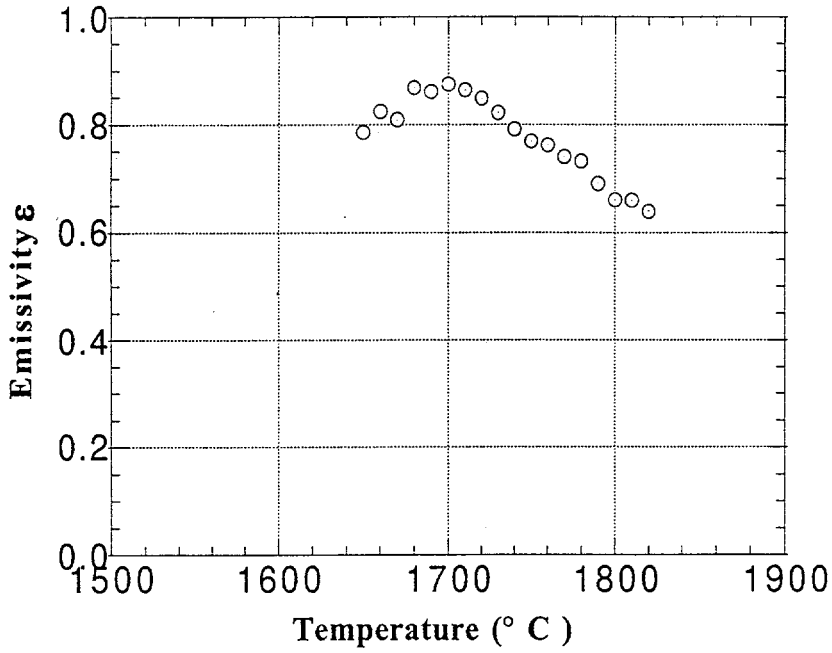

Figure I.7. The emissivity of molten steel, containing 10% stainless steel and 10% zirconium as a function of sample surface temperature as deduced from pyrometer measurements.

APPENDIX J

CHEMICAL REACTIVITY TESTS

APPENDIX J

CHEMICAL REACTIVITY TESTS

T. Salmassi, X. Chen and T.G. Theofanous

Department of Chemical and Nuclear Engineering
Center for Risk Studies and Safety
University of California, Santa Barbara, CA 93106

Even though the iron-zirconium chemical interaction phase behavior are well understood, we used an already available apparatus from another experiment, to gain some working familiarity of this important aspect of our present effort. The apparatus called HITEC (for High Temperature Crucible) is designed to heat small samples of any material to high temperatures under an inert (Ar) atmosphere. The design is showing schematically in Figure J.1. Thermal power is generated in a graphite structural element (including the crucible shown) supplied by a low voltage, high current transformer. In the present experiment samples of well-mixed Fe-Zr powders, contained in steel a crucible (1.5 cm in diameter, 2 cm in height, 0.2 cm wall thickness) were heated by placing inside the graphite crucible. The temperature was monitored by means of a K-type thermocouple imbedded into the steel crucible wall. Radiated energy could be removed by the water-cooled coil, shown in the figure, so that experiments could be run on a time scale of tens of minutes. The power is sufficient to raise the temperature to over 1,000° within ~100 seconds, and by manually controlling the voltage the temperature could be stabilized at any desired level.

Our interest is for iron-rich mixtures, so we worked with 90% Fe, 10% Zr by weight samples. The transfer of the zirconium powder was done under water, and mixing with iron was carried out under methanol to avoid oxidation. After placing the crucible in the apparatus high vacuum was applied in combination with inerting and slight heating to completely dry the methanol, then flow of Argon gas (itself properly purified from trace humidity in the supply cylinder) was established to maintain a slight pressure above the ambient (atmospheric), and the sample was brought quickly to the desired temperature, where it was maintained for the desired length of time. The sample was then allowed to cool and then visually examined.

Three transients were carried out by successively heating, and letting cool, a sample to higher and higher temperatures until meltdown of a steel crucible was obtained. The temperature transients are shown in Figures J.2, J.3 and J.4 for the three runs respectively, where it can be seen that failure finally occurred at $1250°C < T < 1270°C$. The failure occurred suddenly and completely 10 minutes after the sample was heated to ~1250 °C, as melt was released from a hole at the bottom of the graphite crucible. Upon examination, all the lower portion of the steel crucible in contact with the Fe/Zr mixture was found to be melted away. The observed failure temperature is only slightly lower than the expected 1330°C (see Figure 6.1) value and is considered confirmatory for the demonstration purposes of this experiment.

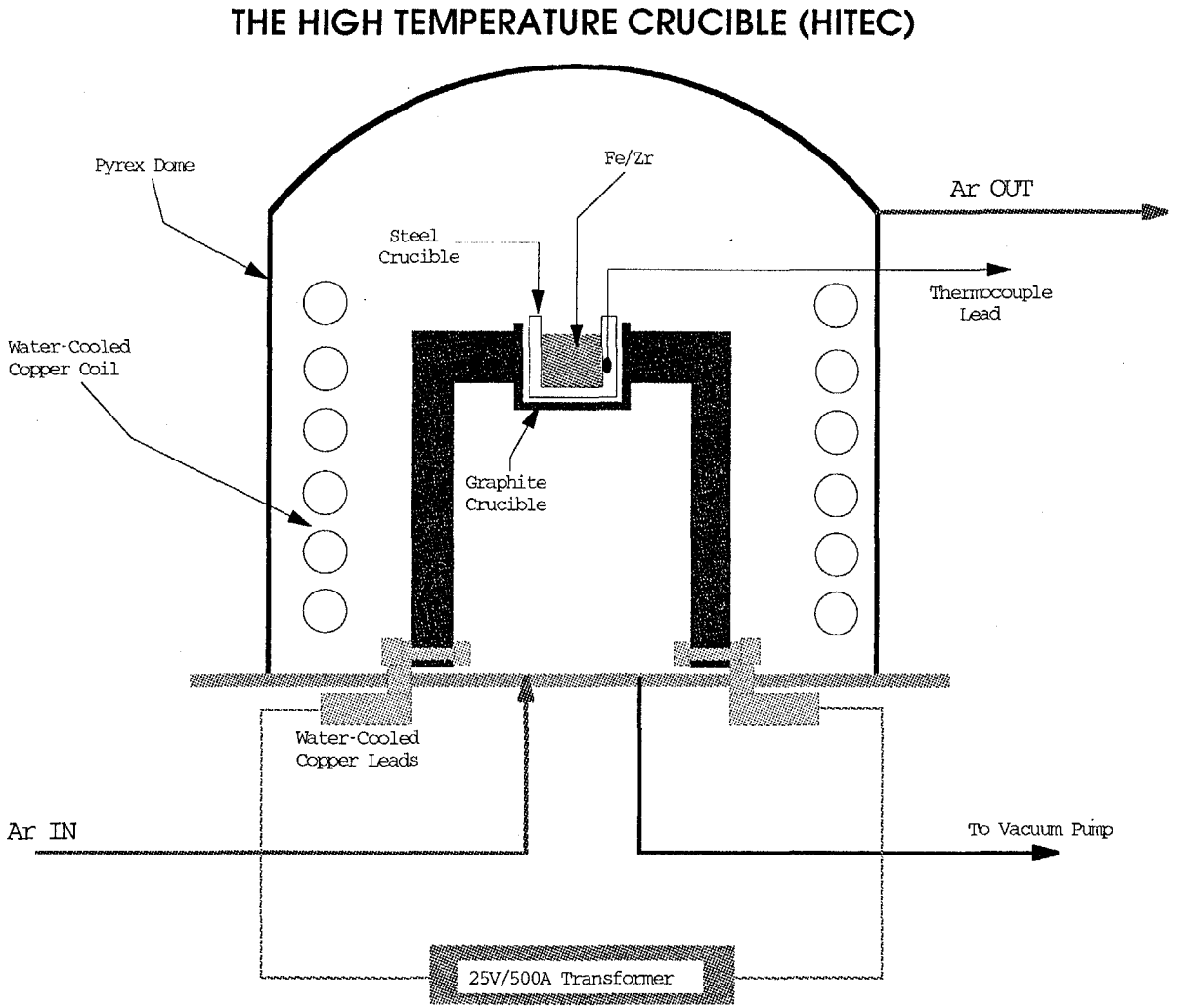

Figure J.1. Schematic of the HITEC experiment design.

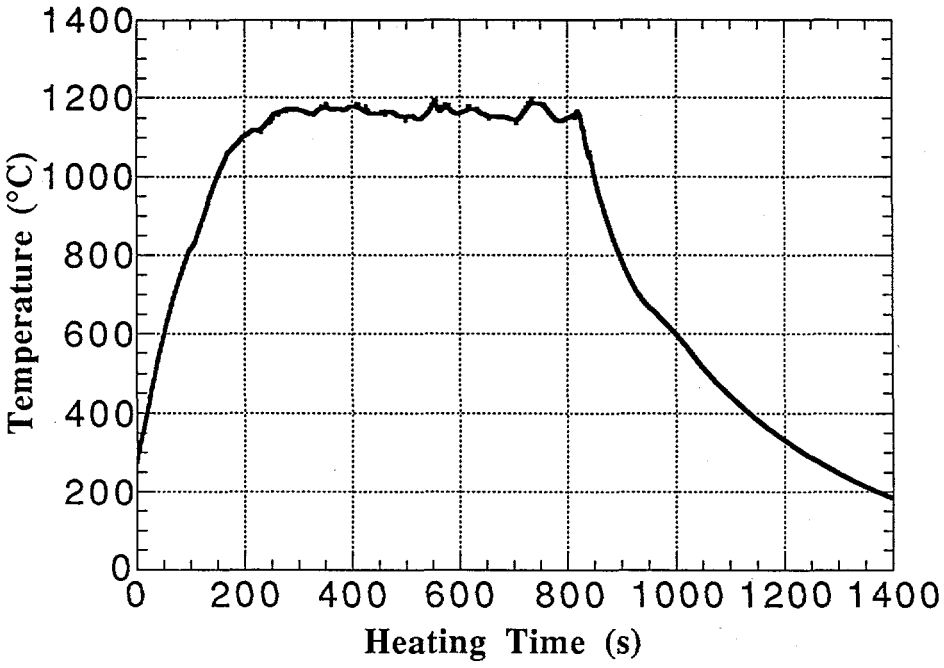

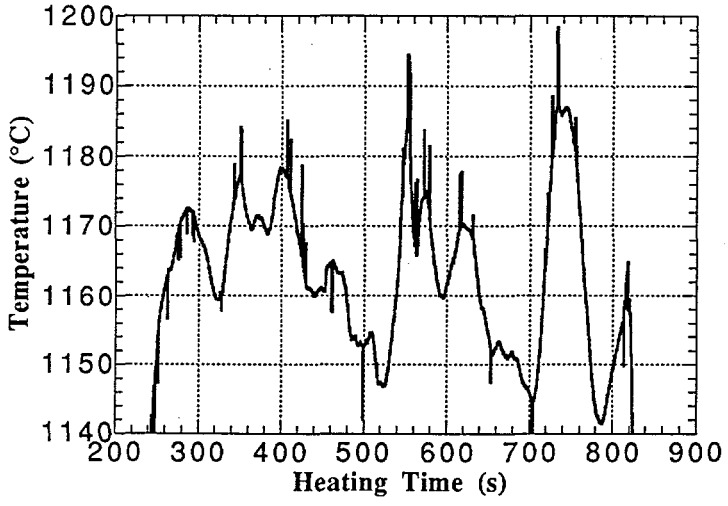

Figure J.2. The temperature transients in the wall of the steel crucible during the first heating of an 90% Fe – 10% Zr sample.

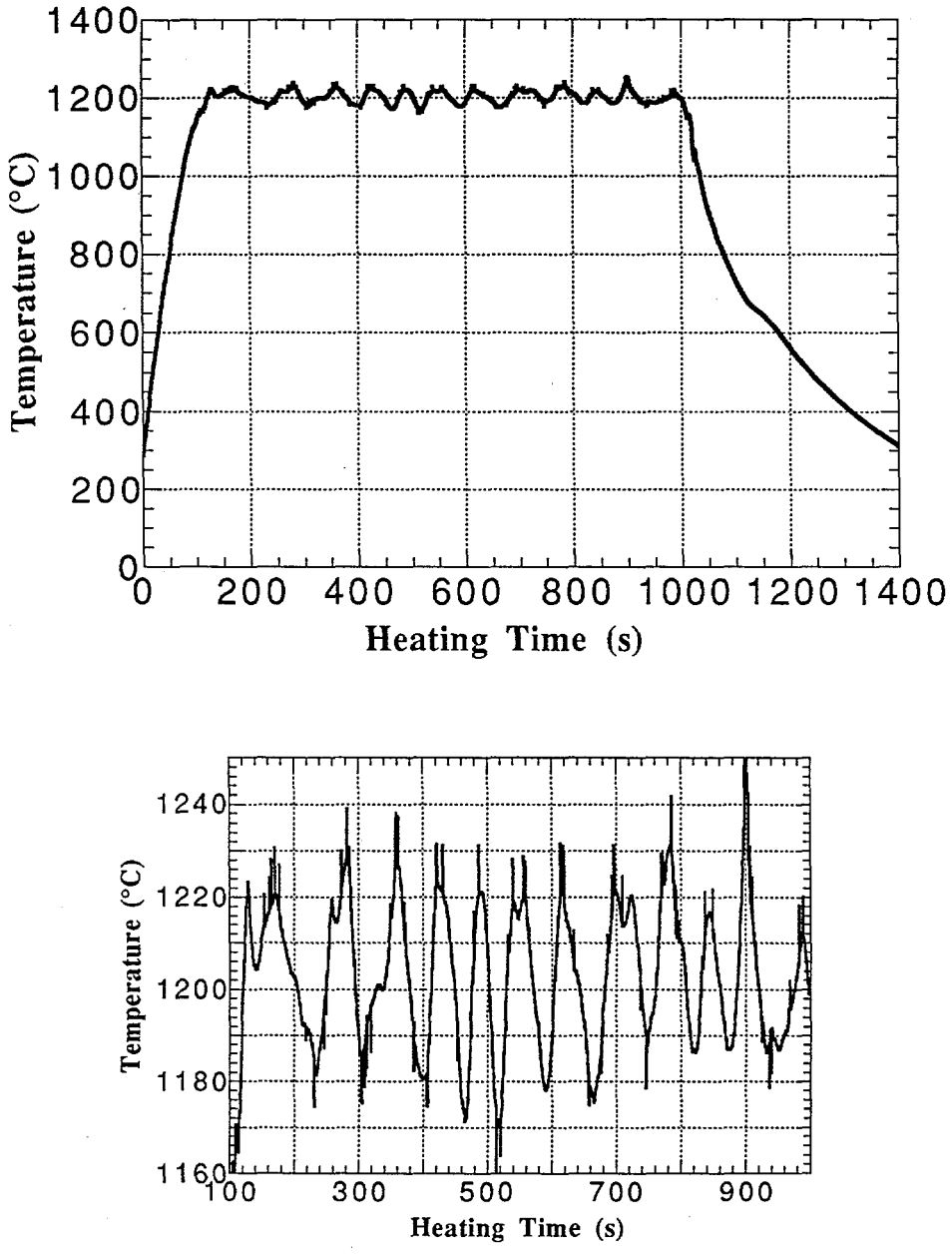

Figure J.3. The temperature transients in the wall of the steel crucible during the second heating of an 90% Fe – 10% Zr sample.

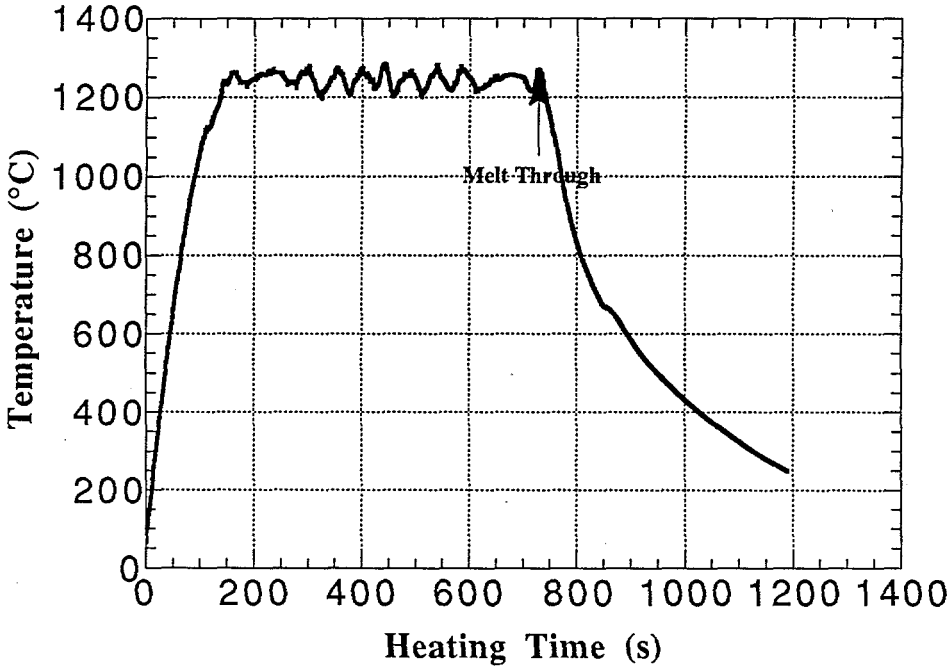

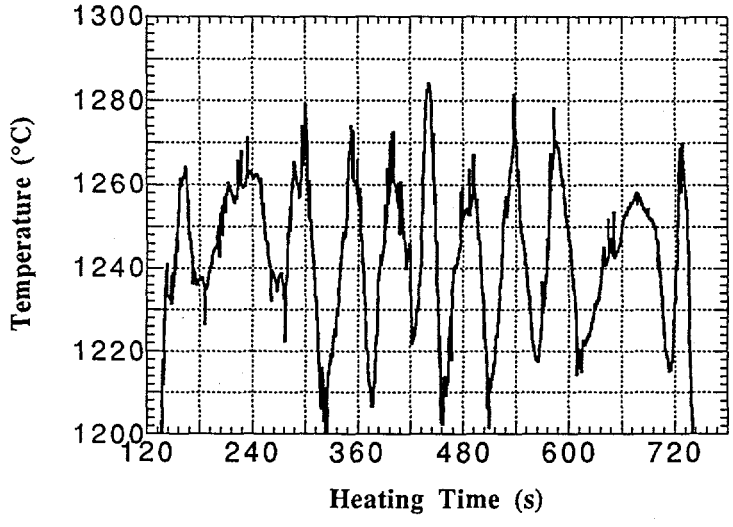

Figure J.4. The temperature transients in the wall of the steel crucible during the third heating of an 90% Fe – 10% Zr sample.

[[ADDENDUM TO APPENDIX J]]

X. Chen, Mark Maguire, and T. Salmassi

Here, we pursue the investigation described in Appendix J, to obtain a better understanding of wall attack under eutectic Fe/Zr composition, including the effect of silver, and for prolonged time periods.

A new HITEC apparatus was developed for this purpose, as illustrated in Figure J.5. It employs induction heating, and a completely closed graphite crucible as the heating element, to overcome the Curie point barrier at 760 °C. Prior to operation, the chamber was evacuated for 20 minutes, and then continuously purged with Argon to maintain an inert atmosphere during operation. The effectiveness of inerting was confirmed by the absence of oxidation in post-test examination of the metallic specimens, after operating times as long as ~5 hours.

Inside the heating element, we place the steel test element (or crucible)—a simple cylindrical container charged with the desired Fe/Zr mixture in powder form. This mixture is measured and transferred under water to prevent oxidation of the highly reactive zirconium metal powder. The heatup is very gradual, over ~1 to 2 hours, to avoid the development of internal temperature gradients. The temperature is measured with a type C thermocouple, imbedded in the wall of the test element. This measurement is supported by a type K thermocouple, which is more accurate, but fails at ~1350 °C, and by a two-color pyrometer, focused on the top of the graphite crucible. The uncertainty in our temperature measurement is estimated at ±10 °C.

Several shakedown tests were carried out, to develop the experimental techniques, and to determine the optimal choice of dimensions of the test element. As an experimental objective, we wanted to obtain complete melting of the charge but maintain test element integrity for prolonged time periods. This, of course, is not possible under the isothermal conditions of the experiment, unless there is enough wall material to melt and alter the liquid composition so it can come to a new equilibrium state with the wall at the imposed temperature prior to melting through. Thus we employed thick-wall steel test elements. The choice of inner diameter is also interesting. In early tests we used 6 mm, and found this dimension to be too small to allow release of the internal voids formed as the powder melts and compacts locally. One such test is described below. With subsequent testing, we determined that an internal diameter of 12.7 mm allows the formation of a fully compacted melt pool at the bottom of the test element. One such test is also described below. The respective steel element dimensions for these two tests are shown in Figure J.6.

Crucible A was used, with a charge of 3.20 g of Fe/Zr powder, 4.8% Zr mole fraction, and a small quantity of Ag (~1% weight fraction). The Fe/Zr liquidus at this composition is 1425 °C. Crucible B was used, with a charge of 12.58 g of Fe/Zr powder, at the eutectic composition of 8.8% Zr mole fraction, the eutectic temperature being 1335 °C. The test with crucible A was run for ~4 hours, at a temperature of 1355 °C, and with crucible B for ~3.5 hours, at a temperature of 1410 °C. The temperature histories of both runs are shown in Figure J.7. In both tests, the test elements survived. The internal morphology was determined by sectioning along one or more vertical planes, obtained by gradually machining the mass away. The photographic records thus obtained are shown in Figures J.8 and J.9 for test elements A and B respectively.

In Figure J.8, we can see that the charge was fully molten. Also, we see the internal "large" voids mentioned above. After careful examination at the melt-crucible boundaries, we could not identify any melt attack. In Figure J.9, we can see that the charge was fully molten and that melt attack actually occurred. The cross section at 6.97 (just touched by melt) indicates a radial attack by 0.62 mm. This is consistent with the width of the attacked region shown at radial position 6.45. The amount of steel mass that was thus incorporated in the melt is estimated as 2.06 g, and the corresponding change in composition is from 8.8% to 7.5% Zr mole fraction. The change in liquidus is from 1335 °C to 1350 °C. Clearly, a driving force of more than 50°C appears to have been insufficient to rapidly erode the wall — this, of course, was in the absence of mixing mechanisms. It is also interesting to note in the photographs that part of the melt remained as "thick" film on the vertical walls of the cricible.

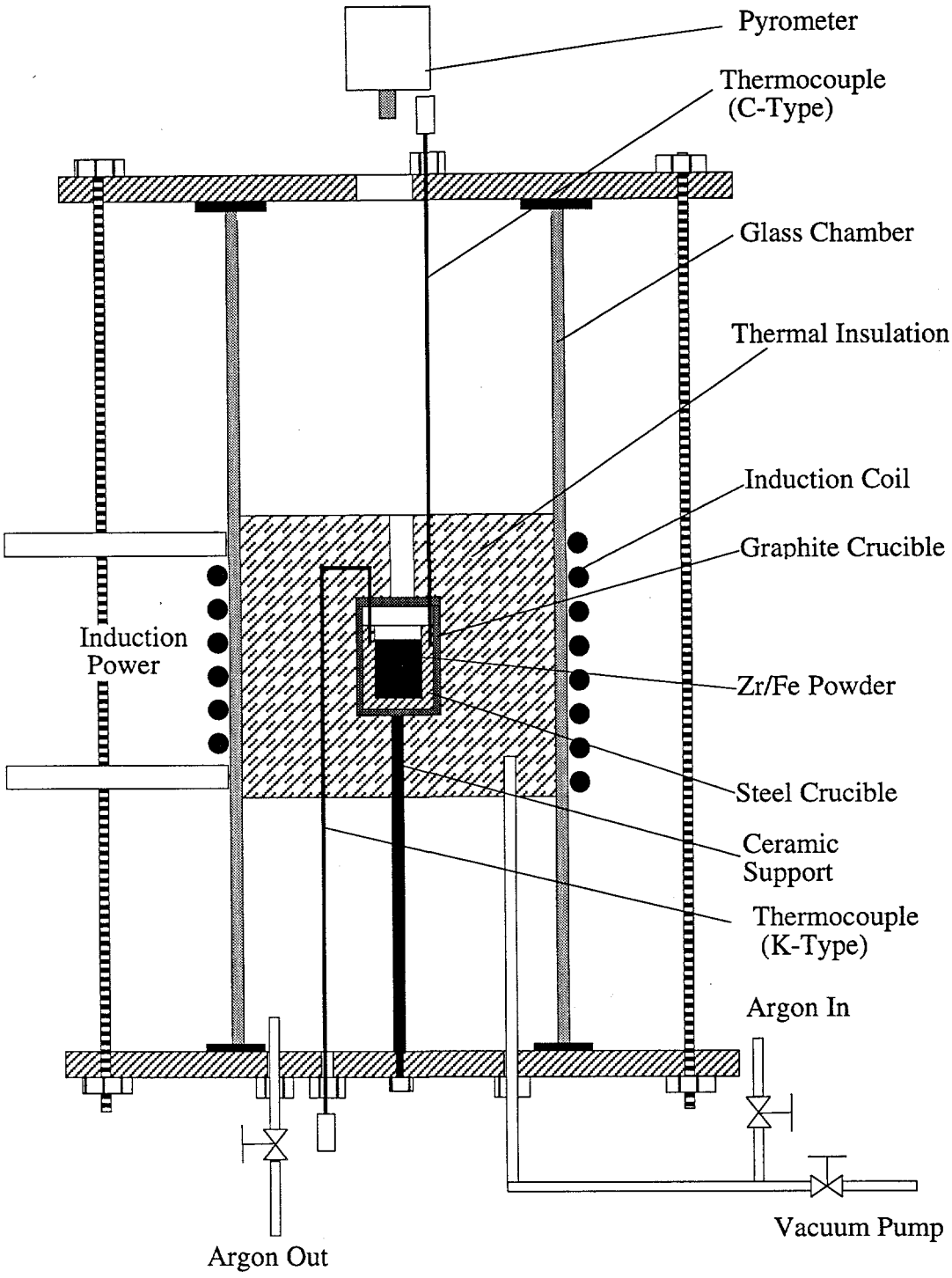

Figure J.5. Schematic of the new HITEC design.

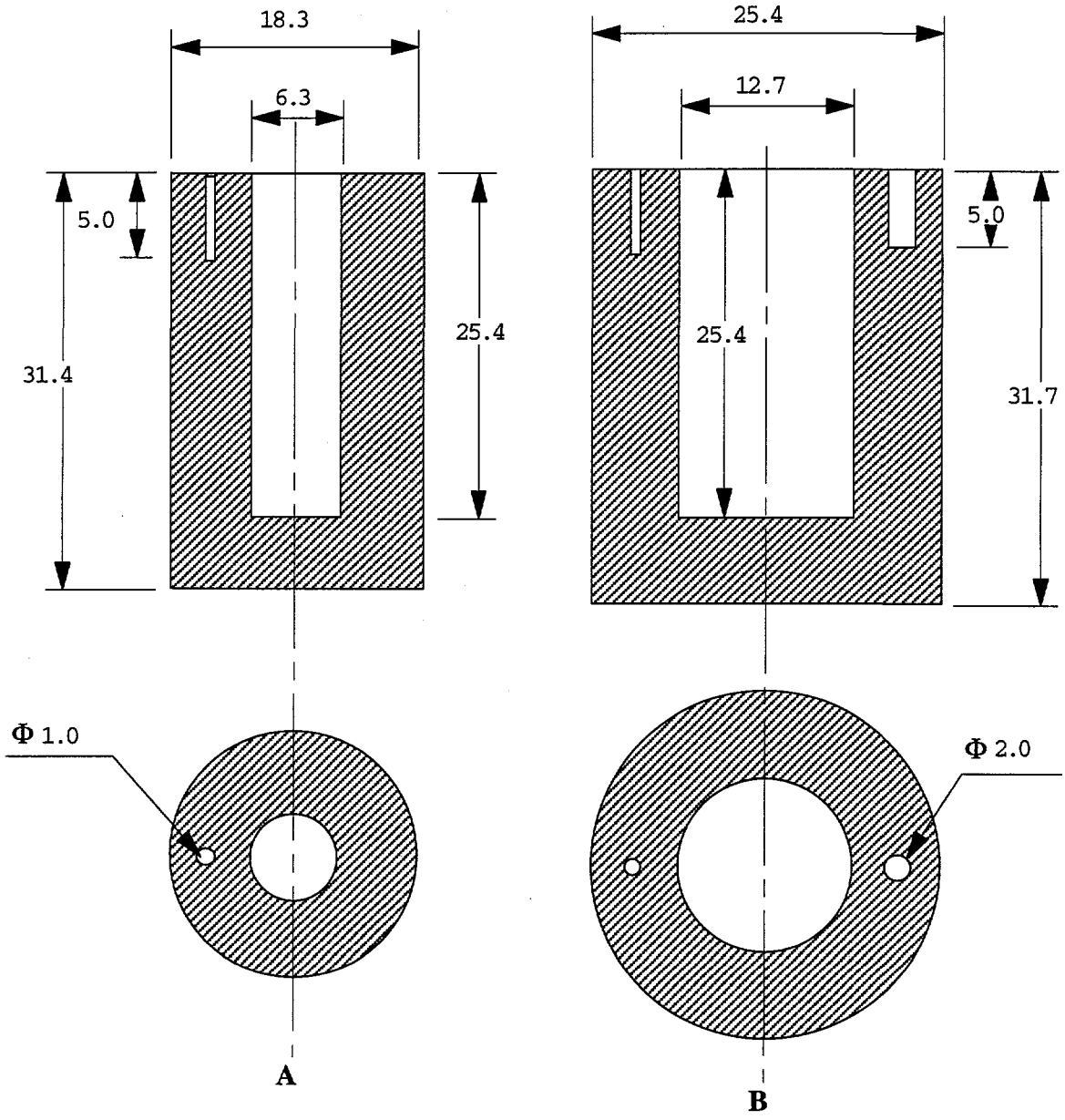

Figure J.6. Dimensions of the two steel test elements. All dimensions in mm.

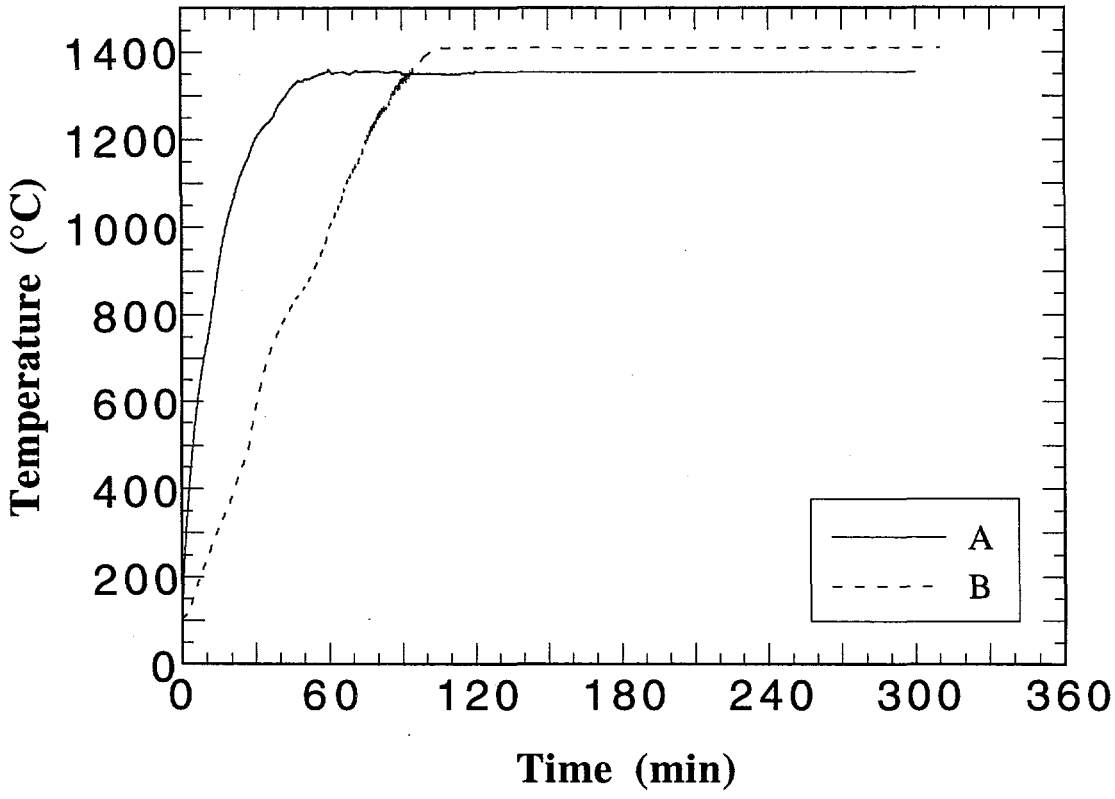

Figure J.7. Thermal history of the test elements A and B.

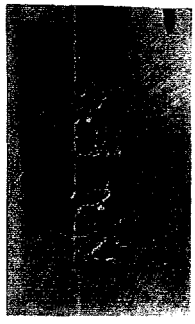

Figure J.8. Internal configuration of test element A through a vertical central section.

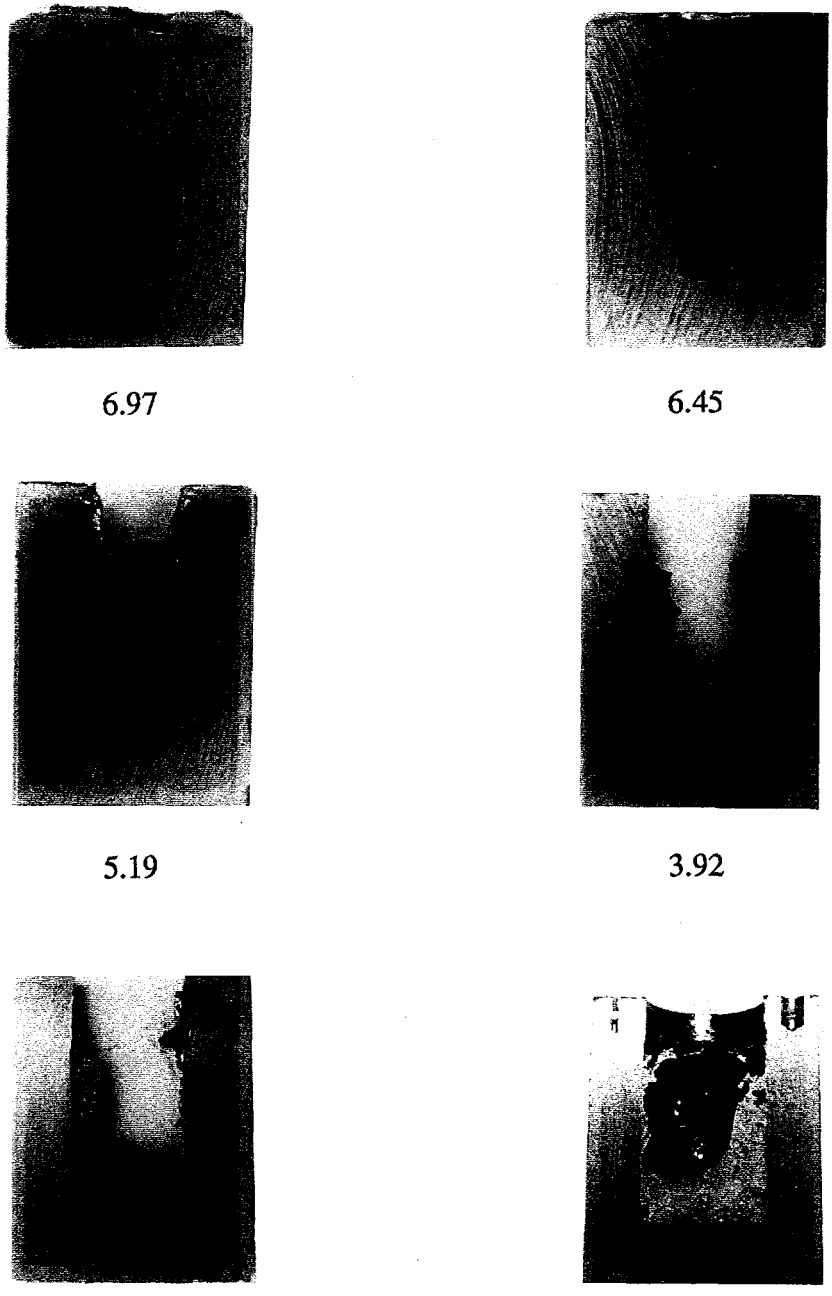

Figure J.9. Internal configuration of test element B through successive vertical sections. The numbers below each photo indicate the radial distance of the respective section from the center line.

APPENDIX K

THERMAL INSULATION DESIGN OPTIONS

APPENDIX K

THERMAL INSULATION DESIGN OPTIONS

Stephen Additon* and T.G. Theofanous**

*TENERA, L.P.
1901 Research Boulevard, Suite 100
Rockville, MD 20850-3164

**Department of Chemical and Nuclear Engineering
Center for Risk Studies and Safety
University of California, Santa Barbara, CA 93106

The purpose of this appendix is to examine the potential flow path configuration in the AP600 reactor cavity as it might be affected by the particular design of the insulation "structures" around the reactor pressure vessel (and of the related geometric features, such as supports, etc.) and to discuss respective CHF implications. For in-vessel retention to succeed, the insulation design must admit cooling water near the bottom of the lower head, vent the steam generated cooling the lower head and vessel wall, and permit relatively stable flow without excessive pressure drops along the flow path to the ultimate heat sink (the containment dome). The following describes the design concept for the AP600 insulation system and then addresses the expected performance of the system during in-vessel retention and reactor-specific design options which must be considered to ensure its success.

DESIGN CONCEPT FOR AP600 REACTOR INSULATION SYSTEM

Detailed design for the AP600 insulation system has not yet been performed. The design concept (see Figure K.1) was not based on severe accident considerations and therefore does not address the particular demands of an in-vessel cooling strategy directly. The key features of the design concept include:

- The reactor cavity is octagonal in shape and the flat insulation panels along the sides of the vessel are hung from the walls with a 5 cm outside clearance that allows for normal ventilation to cool the concrete during plant operation. The inside clearance is a minimum of about 23 cm where the flat panels are most nearly tangent to the cylindrical vessel and larger in the corners of the octagon. The inside clearance is required for inspection access to the vessel from above.
- The lower head is also covered with flat insulation panel segments, but the required, so far, inside clearance is only about 2.5 cm to accommodate the expected vessel growth upon heatup to operating temperature.

- All of these flat insulation panels are about 10 cm thick and consist of stainless steel reflective insulation with air gaps between relatively thin sheets of metal. The panels are sized to permit easy lifting by one person. While the metal is thin, the panels are encased in a module designed to support a persons weight without damage. The panels are supported from a frame structure to which they are attached along the vessel sides, but the lower head panels are held in place by their weight alone.
- Where the vessel emerges from the octagonal cavity, a transition in insulation design is needed to accommodate: the change from octagonal to circular geometry, the increase in vessel thickness in the nozzle region, the lack of a nearby wall for support, and the need for access to the inner annulus for vessel inspection. These transition modules will conceptually be designed to pop-off into the open space beneath the nozzles at a pressure no greater than about two feet of water.
- Minimum clearances for steam flow discharge in this design are about 2.8 m^2 around the hot and cold leg nozzle penetrations to the steam generator compartments and 1.7 m^2 assuming the larger vessel diameter is inside the intact octagonal insulation after the transition pieces pop off (this is a conservative estimate since more clearance is needed to provide the desired access for inspection).
- The preferred pathway for the return of condensate to the reactor cavity in the AP600 involves entrance at the elevation of the top of the lower head through a tunnel from the steam generator compartment (see Appendix M). Hence, counter flow is not expected when the IRWST drain valves are actuated. Passive reflux to the cavity would enter in the outlet nozzle region and drain down through the octagonal portion of the cavity. [[However, the approach here is based on the high reliability of the cavity flooding system that places passive reflux at or below screening frequency levels and, as a consequence, no special consideration is given to the implied counter-current flow regime.]]

EXPECTED PERFORMANCE AND REACTOR-SPECIFIC DESIGN OPTIONS

Experiments in the ULPU facility demonstrated that the in-vessel retention flow patterns are highly dynamic, involving flow oscillations, major flow surges in combination with geysering, and condensation shocks. For the AP600 design concept, the insulation panels may or may not remain in position under these conditions. Dislocated panels might facilitate water entry and steam discharge, but they also might accumulate in positions where they would contact the reactor vessel, impeding local cooling. The flat panel design bounds the potentially affected area given the continuous curvature of the vessel and such local effects are not expected to alter the conclusions of this study.

Water entry for the AP600 might occur through seams at the insulation panel boundaries (these seams are not taped or sealed). Assuming, as expected,that the panels are not buoyant, they

would not be lifted out of position during flooding. This should be verified as buoyancy would increase their potential to interfere with the heat transfer process. Since the bottom insulation needs to be lowered from the position of near tangency to the vessel shown in Figure K.1, water entry might be assured at the same time with a concept like the one shown in Figure K.2 which affords radiative heat transfer shielding. There are no known constraints on such use of the space under the vessel.

A specific design for the insulation transition pieces is needed to perform calculations or tests that would verify their pop-up or blow-out characteristic. Assuming the conceptual capability is achievable (blow-out at less than two feet of water differential pressure), the insulation and the remaining clearances should not significantly retard the steam flow, but this remains to be verified. If there is an impact on the flow, or flow dynamic behavior, sensitivity tests in ULPU would be appropriate to verify that there is no unacceptably deleterious impact on CHF.

CONCLUSION

The AP600 conceptual cavity insulation design affords features which may serve to provide for water ingress and steam egress needed to establish in-vessel retention. A few remaining issues can only be resolved by the final detailed design which is not yet performed (by Westinghouse) or scheduled. The available information supports a conclusion that acceptable performance of the insulation system is feasible and can be achieved for this plant design.

[[ADDENDUM TO APPENDIX K]]

THERMAL INSULATION DESIGN

The design concept for the AP600 insulation system has recently been revised to address the severe accident considerations pertinent to in-vessel core debris retention. This update to the original Appendix K describes the revised design concept.

As previsously noted, for in-vessel retention to succeed, the insulation design must admit cooling water near the bottom of the lower head, vent the two-phase flow generated by cooling the lower head and vessel wall, and permit relatively stable flow without excessive pressure drops along the flow path to the ultimate heat sink (the containment dome). The revised design concept for the AP600 insulation system addresses these severe accident requirements, together

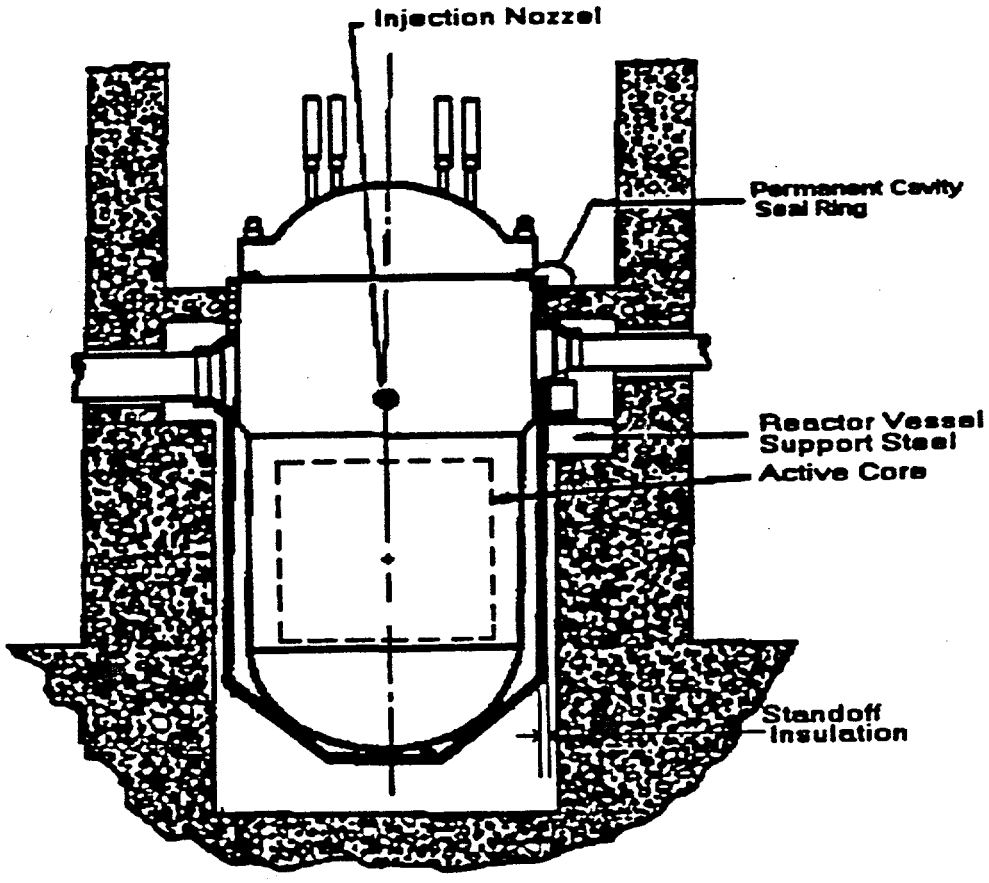

Figure K.1. AP600 reactor vessel standoff insulation concept.

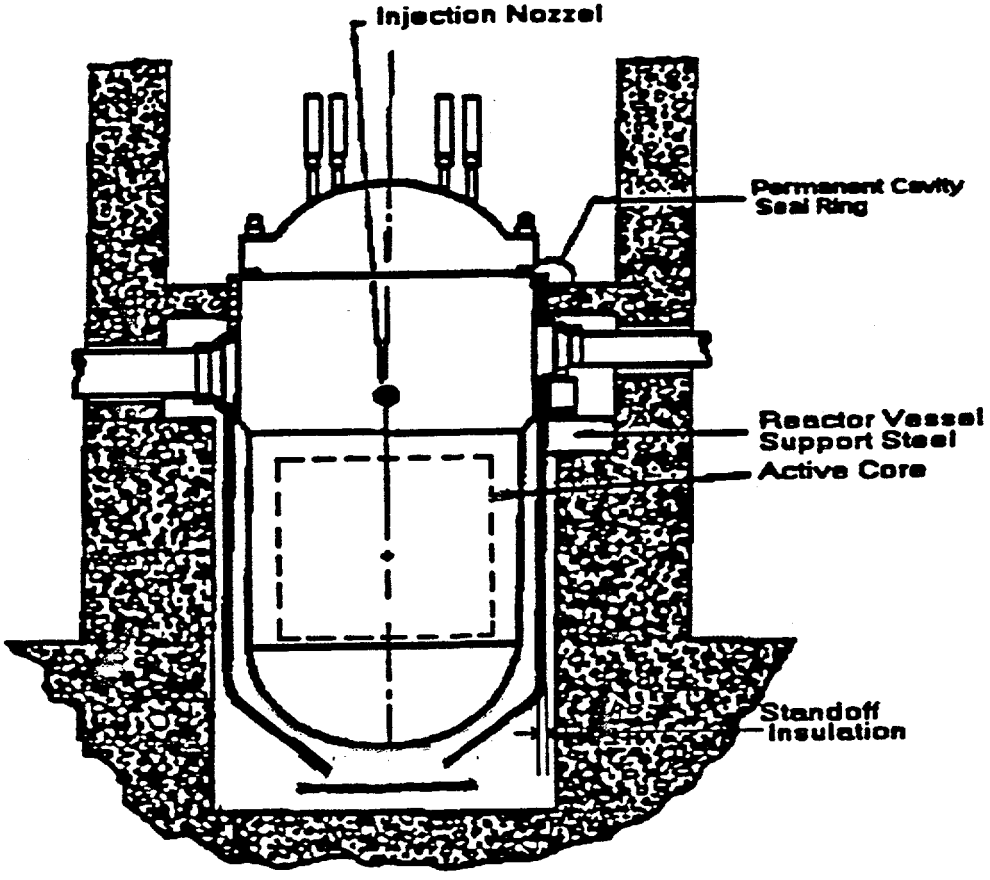

Figure K.2. Alternative vessel insulation concept. [[The position of the tunnel connecting the cavity to the steam generator compartment, not shown on this figure, can be found in Figure 3.1.]]

with other design requirements pertinent to successful operation of the facility. The other design considerations include: neutron shielding to prevent streaming from the cavity region; ex-core flux detectors; normal HVAC with provisions for cooling of the cavity concrete, neutron shielding, ex-core dectectors, and reactor vessel supports during operation; and provisions for access to the vessel exterior surface for unplanned inspection. Aspects of the new design concept have been deemed patentable by the AP600 designers.

Revised Design Concept for AP600 Reactor Insulation System

The revised design concept for the AP600 insulation system is illustrated in Figures K.3 and K.4. The key features of this design concept include:

- Within the octagonal reactor cavity, eight rugged tubes are permanently mounted to the walls. These tubes will contain the ex-core detectors which are inserted into the tubes from below. Frame sections to support the insulation are engineered with collars that provide support from these ex-core detector tubes, permitting the insulation panel segments to be raised into position from below or lowered, if necessary, for vessel inspection. The frame sections make a transition from the octagonal cavity shape to circular insulation. A 5 cm outside clearance (between frame sections and wall) allows for normal ventilation to cool the concrete, ex-core detectors, shielding blocks, and vessel supports during plant operation. The inside clearance (between insulation and vessel) is specified as a minimum of 15 cm to provide the path for upward water and steam flow along the vessel in the in-vessel retention mode of operation.

- The lower head is also covered with insulation panel segments. The minimum required inside clearance is specified as about 23 cm to accommodate in-vessel retention in this lower-head region where the highest heat fluxes may exist.

- The curved insulation panels along the vessel walls are about 10 cm thick and consist of stainless steel reflective insulation with air gaps between relatively thin sheets of metal. Fibrous insulation is used only inside the shield blocks (where design constraints preclude the use of metallic insulation) in order to minimize the risk that critical clearances might become obstructed should the insulation become detached from the vessel.

- The design includes a special water-inlet module designed to provide a seal sufficient to prevent any streaming of cold air from the HVAC system to the vessel during normal operation, while also assuring an open flow path for water to enter the insulation package during the in-vessel retention mode of operation. The concept utilizes buoyant steel balls in "cages" to effect the change from blocked air flow during normal operation to unimpeded

water flow for in-vessel retention (see Figure K.3b. The inlet shown in Figure K.3 does not reflect the relative size to be used in the plant. The inlet can actually be up to 1.6 meters in diameter (much larger than the scale shown). The actual size will be chosen to ensure that the inlet pressure drop is not significant relative to the buoyant head along the in-vessel retention flow path.

- The outlet flow path at the top of the reactor vessel requires some careful explanation, which will be done with the help of Figures K.5 through K.8. Figure K.5 shows that shield blocks (boro-silicone) seal the flow area of four (alternate) sides of the octagon, such as to allow the HVAC air to flow through the slots (cooling duty) in the steel blocks that support the reactor vessel from the four inlet nozzles. Figure K.6 shows a specially designed damper system, on the other four sides of the octagon that upon opening would allow flow through clearances around the shield blocks, as illustrated in Figure K.8. On the other hand, Figure K.7 shows that on the sides of the octagon under the cold leg nozzles the thermal insulation closes off (no dampers) The seals (shown in both Figures K.7 and K.8) at the very top are to create the flow path for the HVAC air, circulating *outside* the thermal insulation, through the vertical slots in the supports. The damper detail is shown in Figure K.8. It is free to flip open due to forces from the upwelling two-phase flow, during IVR, while it is heavy enough to resist the gravitational head difference due to temperature gradients in the air during normal operation. Both the minimum clearances around the shield blocks and the slots through the vessel supports allow venting areas of 0.7 m^2. This represents a small restriction in the flow path — 37% of the 1.88 m^2 available in the annulus.

- The preferred pathway for the return of condensate to the reactor cavity in the AP600 involves entrance at the elevation of the top of the lower head through a tunnel from the steam generator compartment (see Appendix M). Hence, counter flow is not expected as long as the IRWST drain valves are actuated. While passive reflux to the cavity may occur even without cavity flooding, credit is not taken for this mode of operation in evaluating the in-vessel retention capability of the design.

- The designers have evaluated typical dynamic pressure variations observed in ULPU testing and have concluded that the insulation and supports might deform outward to contact the wall (see Figure K.9), but would not deform inward given the circular shape. Thus, the flow path for in-vessel retention would not be impeded.

Conclusion

The revised design concept for the AP600 cavity insulation affords features which appear to address the requirements for in-vessel retention. Specific provisions are made for water ingress,

steam egress, and the clearances needed in between in order to establish and maintain in-vessel retention. The available information now supports a firm conclusion that acceptable performance of the insulation system is feasible and can be achieved for this plant design.

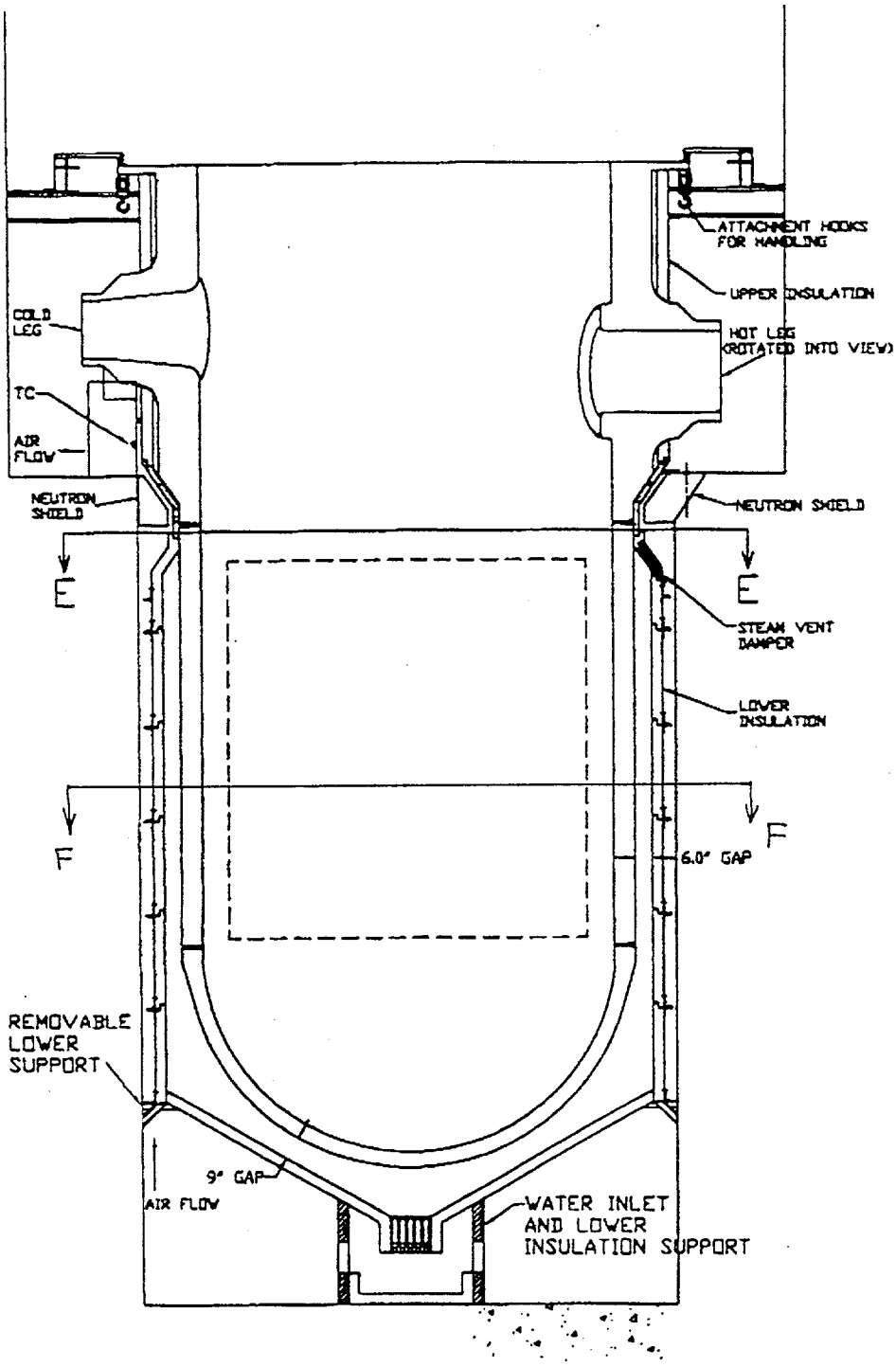

Figure K.3a. AP600 reactor cavity insulation and shielding.

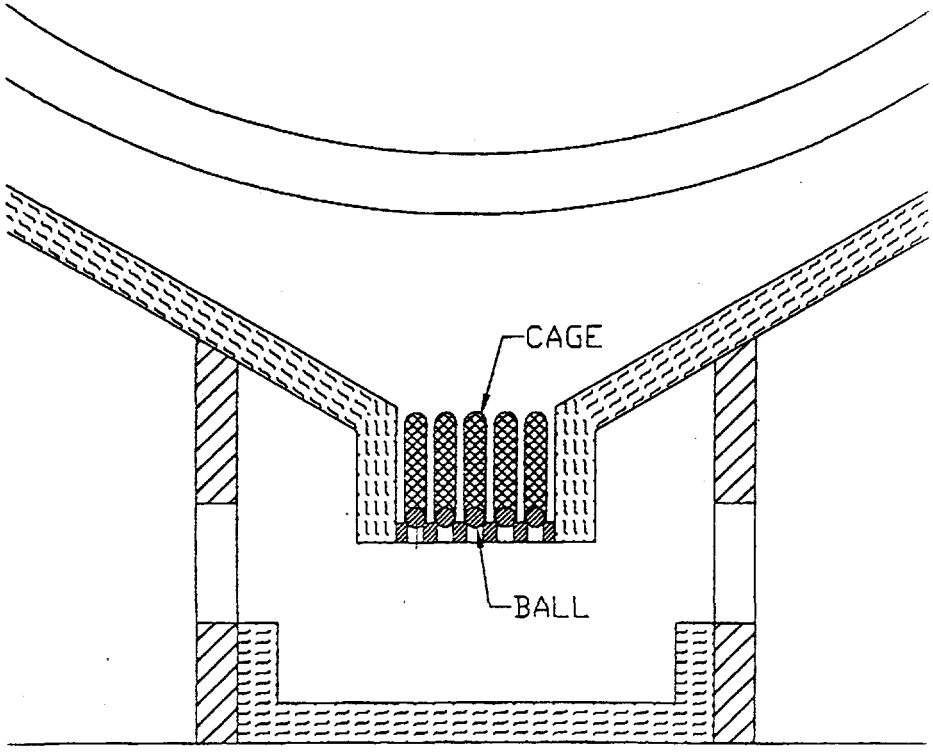

Figure K.3b. Detail of the ball-and-cage design.

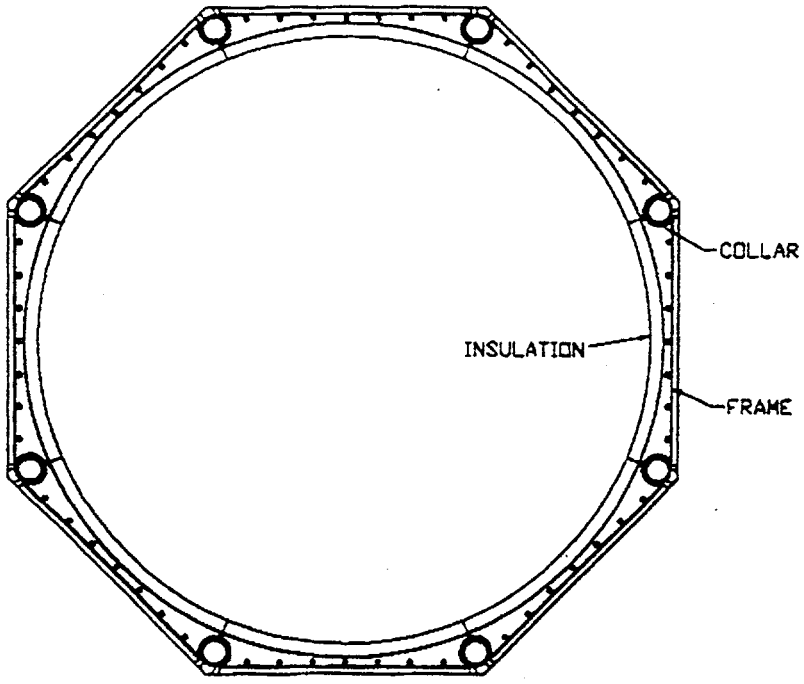

Figure K.4. Section F-F in Figure K.3a.

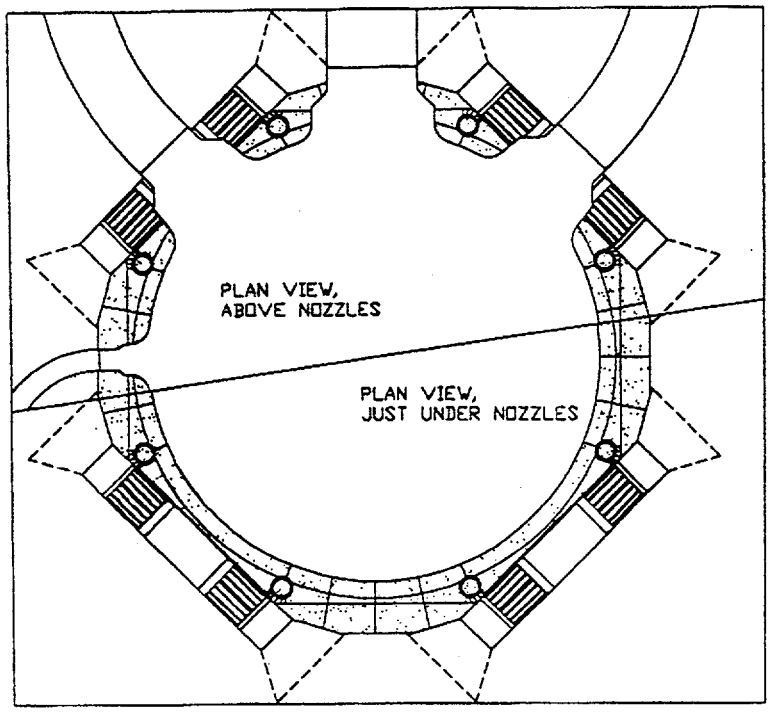

Figure K.5. Illustration of shield segments and reactor vessel supports.

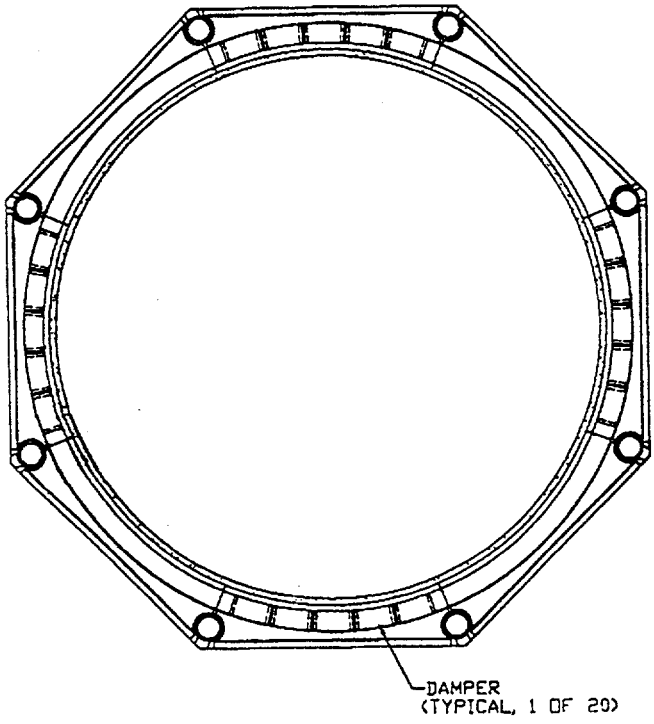

Figure K.6. Section E-E in Figure K.3a.

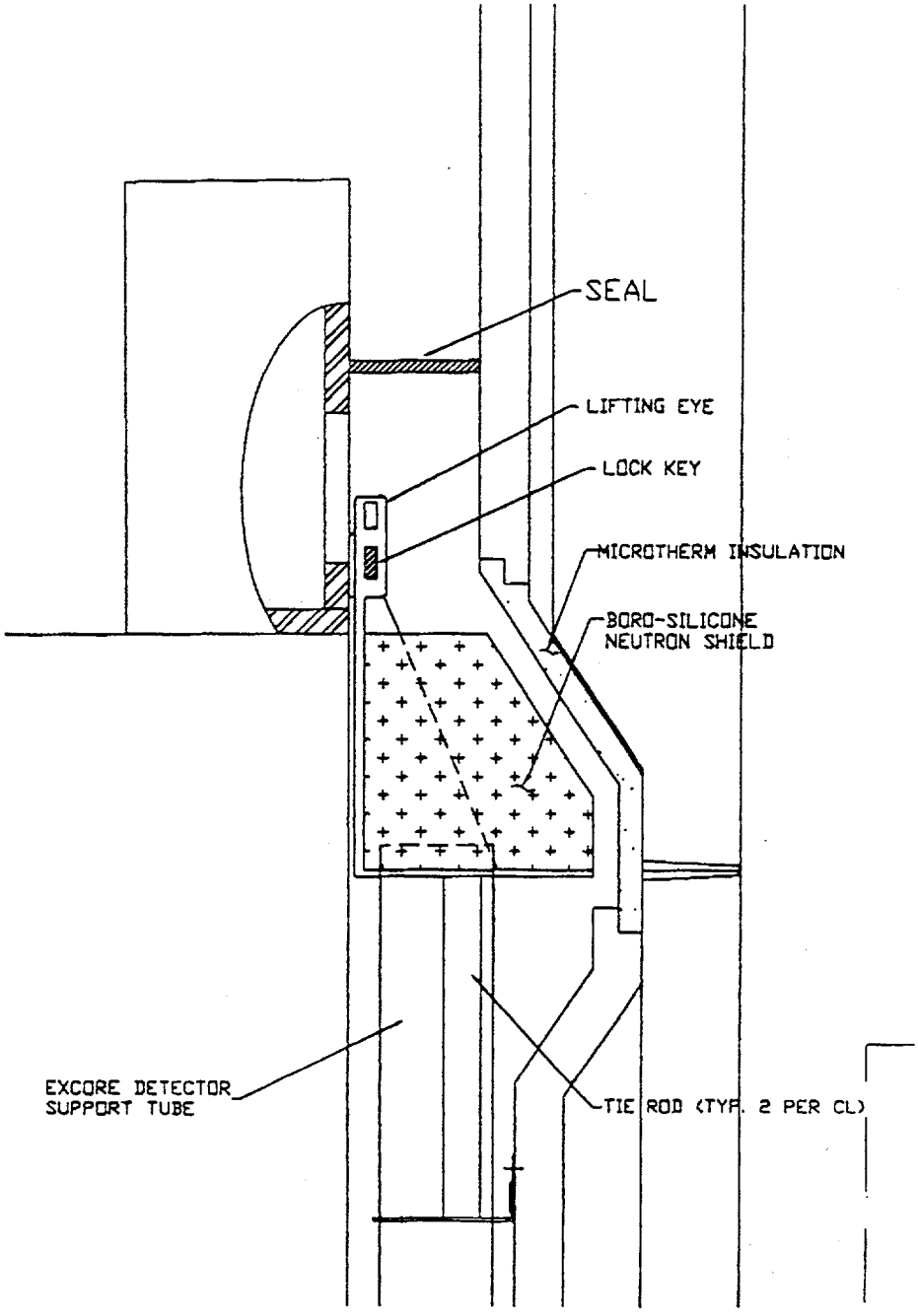

Figure K.7. Detail under inlet nozzles.

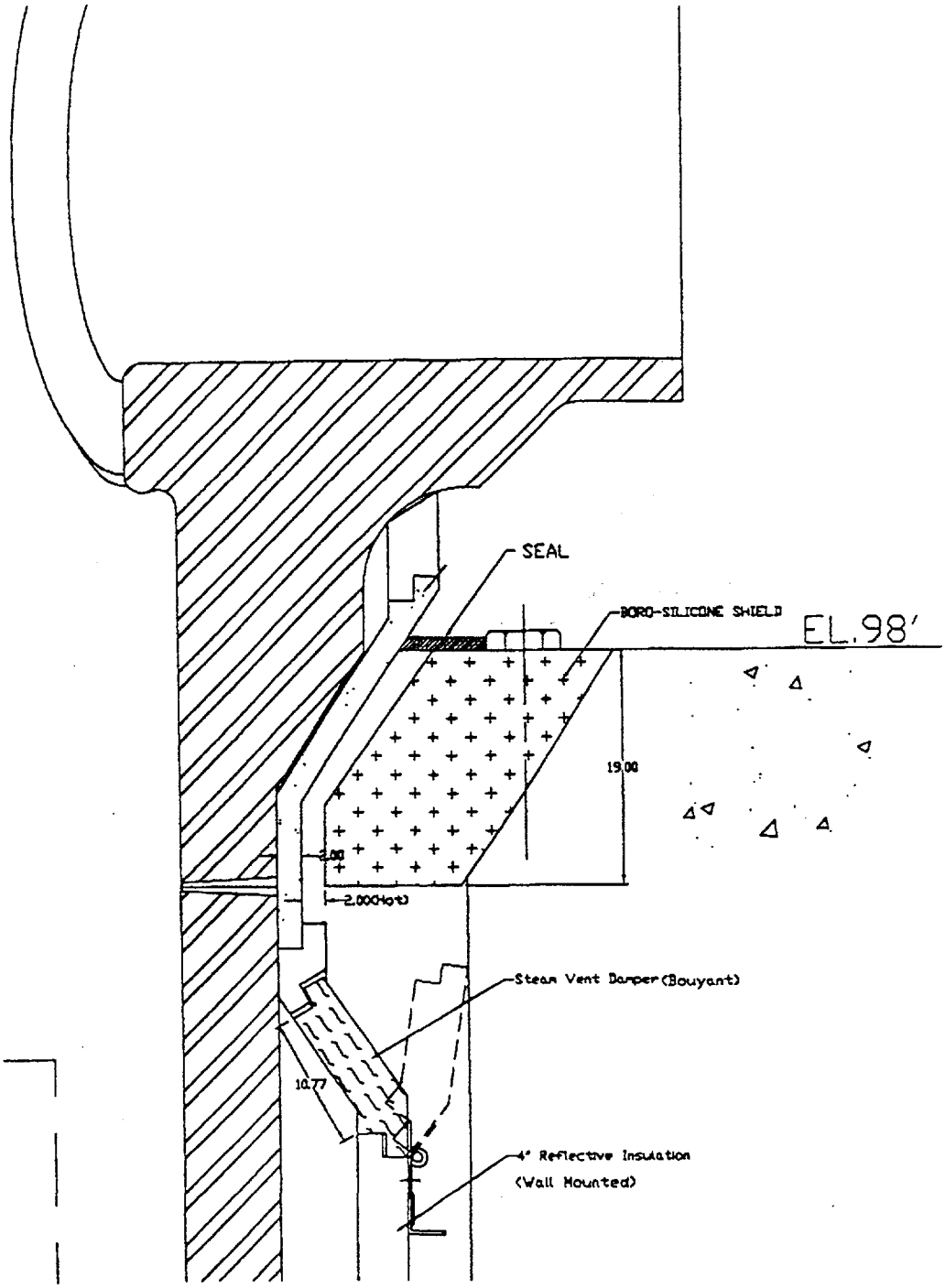

Figure K.8. Detail under outlet nozzles and DVI nozzles.

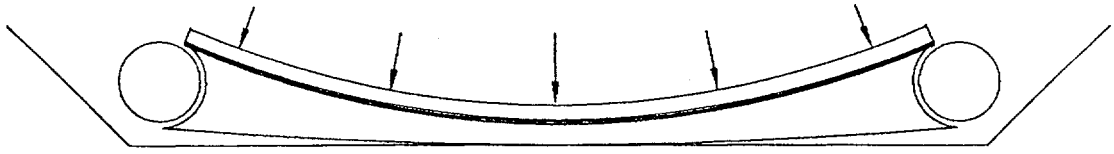

Figure K.9. Frame deflection.

APPENDIX L

THERMAL-PHYSICAL PROPERTIES AND UNCERTAINTIES

APPENDIX L

UNCERTAINTY ANALYSIS FOR THERMOPHYSICAL PROPERTIES USED IN IN-VESSEL RETENTION ANALYSES

C. C. Chu, J. J. Sienicki, and L. Baker, Jr.

Engineering Development Laboratories
Reactor Engineering Division
Argonne National Laboratory

L.1 INTRODUCTION

This appendix provides an assessment of the uncertainties inherent in the thermophysical properties that enter into the in-vessel retention analyses. In general, much property data is available for individual constituents such as UO_2 or ZrO_2 but data is lacking for the oxide and metal mixtures comprising the molten oxide pool and the overlying metal layer. Consequently, it is necessary to estimate properties for the oxide and metal mixtures. Therefore, there are two sources of uncertainties: i) uncertainties in the properties of individual constituents; and ii) uncertainties in the methods used to estimate mixture properties. Both sources of uncertainty are treated in the present work. For each property, a best estimate value and uncertainty range are provided. The steps by which these are arrived at are discussed for each property on a case by case basis. Only those specific properties that enter into the in-vessel retention analyses are addressed.

L.2 MOLTEN OXIDE

It is assumed that the composition range of the molten oxide corresponds to 8.5 m^3 UO_2 and a volume range of 1.0 to 3.0 m^3 ZrO_2.

L.2.1 Density and Volume Thermal Expansion Coefficient of Molten Oxide

The expression used to calculate the liquid mixture density is derived by assuming that each mixture component contributes a volume equal to the volume that the component would have as a free substance. The liquid mixture density is thus the total mass divided by the total volume,

$$\overline{\rho} = \frac{\sum_i V_i \rho_i}{\sum_i V_i} \qquad (L.1)$$

where

$\overline{\rho}$ = density of liquid mixture (Kg/m^3),
ρ_i = density of the pure component i in liquid state (Kg/m^3),
V_i = volume of component i (m^3).

The volumes of most liquid mixtures are actually linear functions of composition. While many liquid mixtures show small deviations from the linear superposition relationship of component density (Equation L.1), maximum values of the difference between the actual liquid mixture volume and the predicted liquid mixture volume generally lie within $\pm 3\%$, and more usually within $\pm 2\%$ (Iida and Guthrie, 1993). Therefore, an uncertainty of $\pm 2\%$ for the linear superposition of liquid densities in Equation L.1 is assumed.

The density of UO_2 is calculated by using room temperature data and data for the temperature dependent thermal expansion. The general relation is

$$\rho_{UO_2} = \frac{\rho_0}{(1+\varepsilon_o)^3} \qquad (L.2)$$

where

ρ_{UO_2} = density of UO_2 (Kg/m^3),
ρ_0 = room-temperature density of UO_2 = 10,970 (Kg/m^3),
ε_0 = linear thermal expansion of UO_2.

The room temperature density, 10,970 Kg/m^3, is taken from Christensen (1963) and the uncertainty for this density is $\pm 1\%$ (11 Kg/m^3) (Fink, 1981). Christensen (1963) determined that UO_2 experiences a linear thermal expansion of 0.043 on melting with considerable scatter. The experiments of Christensen on UO_2 produced the only data available and a least square fit to his limited data yields (Fink, 1981)

$$\varepsilon_0 = 7.87 \times 10^{-2} + 3.78 \times 10^{-5}(T - T_{m,UO_2}) \qquad (L.3)$$

where

T_{m,UO_2} = melting temperature of UO_2, 3120 K,
T = temperature of UO_2, K.

The estimated errors are those associated with the thermal expansion data and not with the polynomial fit to the calculated results. This reflects a standard error of approximately 10% of the value calculated by Equation L.3 found from the Christensen UO_2 data set (Fink, 1981).

Thus, the value of the density of liquid UO_2 and the uncertainty in this value at the melting point calculated by Equations G.2 and G.3 is recommended as:

$$\rho_{UO_2} = 8740 \pm 200 \text{ Kg/m}^3.$$

For liquid zirconium oxide, the expression for the linear thermal expansion is (Hagrman, 1990)

$$\varepsilon_0 = -1.1 \times 10^{-2} \qquad \text{for} \quad T \geq T_{m,ZrO_2} \tag{L.4}$$

where T_{m,ZrO_2} is the melting temperature of ZrO_2, 2973 degrees Kelvin. The expected standard error of the linear thermal expansion in Equation L.4 is $\pm 50\%$ of the predicted value (Hagrman, 1990). The reference density is the value of 5800 Kg/m^3 at 300 degrees Kelvin reported by Gilchrist (Hagrman, 1990). Thus, the recommended value of the density of liquid ZrO_2 and the uncertainty in this value calculated by Equations G.2 and G.4 is

$$\rho_{ZrO_2} = 5990 \pm 100 \text{ Kg/m}^3 \quad \text{for } T \geq T_{m,ZrO_2}.$$

The values of the density and the uncertainties in these values for a liquid oxide mixture made up of 8.5 m^3 UO_2 and 1.0 to 3.0 m^3 ZrO_2 at the melting temperature of $(T_{m,ox})$ is

$$\overline{\rho}_{ox} = 8450 \pm 350 \text{ Kg/m}^3, \qquad \text{for 8.5 m}^3 \text{ UO}_2 \text{ and 1.0 m}^3\text{ZrO}_2,$$

and

$$\overline{\rho}_{ox} = 8020 \pm 330 \text{ Kg/m}^3, \qquad \text{for 8.5 m}^3 \text{ UO}_2 \text{ and 3.0 m}^3\text{ZrO}_2.$$

The melting temperature of the oxide phase mixture is 2973 degrees Kelvin for a mixture made up of 8.5 m^3 and 1.0 m^3 ZrO_2 and is 2923 degrees Kelvin for a mixture made up of 8.3 m^3 UO_2 and 3.0 m^3 ZrO_2 (Lambertson and Mueller, 1953). The recommended values and associated uncertainties of the density for each component (i.e., UO_2 and ZrO_2) and their liquid mixture are listed in Tables L.1 and L.2, respectively.

The expression used to calculate mixture volume thermal expansion coefficient is derived by assuming that the mixture is made up of components which produce independent thermal expansions. The mixture thermal expansion coefficient is

$$\overline{\alpha} = \frac{\sum_i V_i \alpha_i}{\sum_i V_i} \tag{L.5}$$

Table L.1. Recommended Values and Their Uncertainties for Constituent Properties

	UO_2	ZrO_2	Zr	Fe
Atomic Weight	270.03	123.22	91.22	55.84
Melting temperature, (K)	3120	2973	2098	1811
Density[a] (Kg/m^3)	8740 ± 200	5990 ± 100	6130 ± 180	7020 ± 90
Thermal conductivity (W/K·m)	5.6 ± 1.1	3.25 ± 1.85	36 ± 5	24.1 ± 4.8
Specific heat (J/Kg·K)	485 ± 5	815 ± 16	458 ± 14	835 ± 25
Viscosity[a] $\times 10^{-3}$(Pa·s)	5.7 ± 1.9	4.9 ± 1.6	4.5 ± 0.5	5.4 ± 0.8
Viscosity $\times 10^{-4}$ (Pa·s)	$(1.61 \pm 0.54)\times$ $\exp\left[\frac{11130}{T}\right]$	$(1.5 \pm 0.5)\times$ $\exp\left[\frac{10430}{T}\right]$	$(2.0 \pm 0.2)\times$ $\exp\left[\frac{6620}{T}\right]$	$(2.21 \pm 0.33)\times$ $\exp\left[\frac{5776}{T}\right]$
Volume Thermal Expansion Coefficient $\times 10^{-4}$ (K^{-1})	1.05 ± 0.1	1.05 ± 0.1	0.54 ± 0.11	1.2 ± 0.17

[a] At melting temperature.

Table L.2. Molten Pool Properties

Composition	Oxide Phase		Metallic Phase	
	8.5 m^3 UO_2+ 1.0 m^3 ZrO_2	8.5 m^3 UO_2+ 3.0 m^3 ZrO_2	90 at % Fe + 10 at % Zr	35 at % Fe + 65 at % Zr
Melting temperature, K	2973	2923	1600	1600
Density,[a] Kg/m^3	8450 ± 350	8020 ± 330	6890 ± 240	6380 ± 280
Thermal conductivity, (W/K·m)				
Li method, (Equation (L.9))	5.3 ± 1.5	4.9 ± 1.7	25.5 ± 6.3	32.8 ± 50
Filippov eq. (Equation (L.8))	5.3 ± 1.6	4.9 ± 1.6	24.8 ± 6.3	31.4 ± 50
Hagrman-Hohorst correlation (Equation (L.7))	5.2 ± 1.5	4.7 ± 1.7		
Viscosity[a] (Pa·s) $\times 10^{-3}$	5.35 ± 2.50	5.25 ± 2.45	4.2 ± 1.1	4.0 ± 1.1
Specific heat (J/Kg·K)	510 ± 6	550 ± 7	778 ± 24	552 ± 17
Volume thermal expansion coefficient (K^{-1})	$(1.05 \pm 0.12) \times 10^{-4}$	$(1.05 \pm 0.12) 10^{-4}$	$(1.10 \pm 0.18) 10^{-4}$	$(0.69 \pm 0.13) 10^{-4}$

[a] At melting temperature.

where

$\overline{\alpha}$ = volume thermal expansion coefficient of liquid mixture (K^{-1}),

α_i = volume thermal expansion coefficient of the pure component i in liquid state (K^{-1}).

As discussed above, an uncertainty of ±2% is assumed for the linear superposition of liquid mixture thermal expansion coefficients in Equation L.5.

The volume thermal expansion coefficient is equal to three times the linear thermal expansion coefficient. The volume thermal expansion coefficient for liquid UO_2 is derived as (Fink, 1981)

$$\alpha_{UO_2} = \frac{1.05 \times 10^{-4}}{1 + 3.5 \times 10^{-5}(T - 3120)} (K^{-1}). \qquad (L.6)$$

Equation L.6 is valid for liquid UO_2 in the temperature range 3120 to 3420 degrees Kelvin. The recommended function for the liquid UO_2 range, 3120 to 3420 degrees Kelvin, has an estimated uncertainty of a standard error (1 σ) of ±9% (Fink, 1981).

For liquid ZrO_2, although the thermal expansion of Equation L.4 is constant implying that the thermal expansion coefficient of liquid ZrO_2 is zero, it is assumed that the thermal expansion coefficient of liquid ZrO_2 is equal to that for liquid UO_2. The resulting expression for the volume thermal expansion coefficient and the uncertainty in this value for the molten oxide is

$$\overline{\alpha}_{ox} \simeq (1.05 \pm 0.12) \times 10^{-4} (K^{-1}).$$

L.2.2 Thermal Conductivity of Molten Oxide

The molten oxide thermal conductivities are usually less than those predicted by either a mole (or weight) fraction average. Three correlation methods for the molten oxide thermal conductivity are used here. They are described separately below:

1) Hagrman-Hohorst correlation (Hagrman and Hohorst, 1990)

This correlation was obtained by fitting the thermal conductivity data of a $UO_2 - ZrO_2$ solid mixture. The expression is only used for predicting the oxide phase thermal conductivity,

$$k_{ox} = \chi_{UO_2} k_{UO_2} + \chi_{ZrO_2} k_{ZrO_2} - 0.4 \chi_{UO_2} \chi_{ZrO_2}, \qquad (L.7)$$

where

k_{ox} = thermal conductivity of oxide phase (W/m·K),
k_{UO_2} = thermal conductivity of UO_2 (W/m·K),
k_{ZrO_2} = thermal conductivity of ZrO_2 (W/m·K),
χ_{UO_2} = mole fraction of UO_2,
χ_{ZrO_2} = mole fraction of ZrO_2.

Equation L.7 is an atomic fraction-weighted average of the thermal conductivity of UO_2 and ZrO_2 modified to include cross products. The coefficient of the cross product was obtained by requiring Equation L.7 to reproduce a thermal conductivity of 1.44 W/m·K at 2073 K for a composition of 31.5 at % UO_2 and 68.5 at % ZrO_2.

2) Filippov Equation (Reid, Prausnitz and Poling, 1987)

This correlation has been extensively tested on many types of mixtures. The expression for a binary system of components denoted by the subscripts, 1 and 2, is

$$k = W_1 k_1 + W_2 k_2 - 0.72\, W_1 W_2 \mid k_1 - k_2 \mid \qquad (L.8)$$

where

k = thermal conductivity of mixture (W/m·K),
W_1 = weight fraction of component 1,
W_2 = weight fraction of component 2,
k_1 = thermal conductivity of component 1 (W/m·K),
k_2 = thermal conductivity of component 2 (W/m·K).

The constant 0.72 may be replaced by an adjustable parameter if binary mixture data are available. The technique is not suitable for more than two components.

3) Li method (Reid, Prausnitz and Poling, 1987)

Li proposed a technique developed for multicomponent systems. For a binary system of components 1 and 2, the expression of the mixture thermal conductivity is

$$k = f_1^2 k_1 + 4 f_1 f_2 \left(k_1^{-1} + k_2^{-1}\right)^{-1} + f_2^2 k_2 \qquad (L.9)$$

where

f_1 = superficial volume fraction of component 1,

$$= \frac{\chi_1 V_1}{\chi_1 V_1 + \chi_2 V_2}, \qquad (L.10)$$

$$f_2 = \text{ superficial volume fraction of component 2,}$$
$$= \frac{\chi_2 V_2}{\chi_1 V_1 + \chi_2 V_2} \qquad (L.11)$$

The Filippov and Li methods for estimating mixture thermal conductivity described above have been extensively tested by using binary mixture data and all show approximately the same average error. One can use these relations to estimate a liquid mixture thermal conductivity with the expectation that errors will rarely exceed 5 percent (Reid, Prausnitz and Poling, 1987). The Hagrman-Hohorst correlation was obtained from solid $UO_2 - ZrO_2$ mixture data. However, all three methods used for estimating the molten oxide thermal conductivity show approximately the same results. It is suggested that a standard error of $\pm 5\%$ of the value predicted by all three methods is expected.

The thermal conductivity of liquid UO_2 was first measured by Kim et. al. (1977) and found to be about 4 to 5 times greater than that of the solid at the melting point. A constant of 11.0 W/(m·K) with an uncertainty of ± 3.3 W/(m·K) was estimated from the measured data. Two other measurements by Tasman et. al., (1983) and Otter and Damien (1984) of the thermal conductivity of liquid UO_2 were reported. Tasman et. al., reported a thermal conductivity for liquid UO_2 near the melting point of 2.2 ± 1.0 W/(m·K) which is about 65% of the extrapolated value of the solid at the melting point. Otter and Damien reported a thermal conductivity for liquid UO_2 of 8.5 ± 1.7 W/(m·K). An analysis was performed of the three exiting measurements of the thermal conductivity of molten uranium oxide (Fink, 1985). A transient heat transfer code (THTB) was used for this analysis. A much smaller range of values for the thermal conductivity than originally reported was found. The original values range from 2.2 to 11 W/(m·K) with a mean of 7.3 W/(m·K) whereas the recalculated values range from 4.5 to 6.75 W/(m·K), with a mean of 5.6 W/(m·K). Table L.1 summarizes the recommended values for the thermal conductivity of liquid UO_2 calculated from the THTB models for these experiments. The recommended value for the thermal conductivity of liquid UO_2 is the mean of the THTB calculated values from the three experiments, namely 5.6 W/(m·K) with an estimated standard error of ± 1.1 W/(m·K) (Fink, 1985).

For liquid ZrO_2, Hagrman (1990) assumed that the thermal conductivity is approximately 1.4 W/(m·K) which is the value of the thermal conductivity data for "black oxide" at the melting temperature of solid ZrO_2. However, the thermal conductivity of solid ZrO_2 extrapolated from Adams data is approximately 2.75 W/(m·K) (Hagrman, 1990). A standard error of $\pm 5\%$ of the data of Adams is reported (Touloukian et. al., 1979). An increased standard error of $\pm 10\%$ of the extrapolated thermal conductivity of 2.75 W/(m-K) for solid ZrO_2 at the melting point is assumed. Thermal conductivity data for ZrO_2 could be obtained only for solid ZrO_2. In view

of lack of liquid ZrO_2 data together with the low proportion of liquid ZrO_2 in the molten oxide mixture, a high upper limit of the liquid ZrO_2 thermal conductivity in terms of the relationship of the thermal conductivity between solid and liquid UO_2 is assumed in order to bound the effects of the thermal conductivity of liquid ZrO_2 in the molten oxide mixture. Considering the thermal conductivity of liquid UO_2 to be about two times greater than that of solid UO_2 at the melting point, it is assumed that the upper limit of the thermal conductivity of liquid ZrO_2 in the UO_2–ZrO_2 mixture is also about two times greater than that of solid ZrO_2 at the melting point. Thus, a much wider range of the thermal conductivity of liquid ZrO_2 from 1.4 to 5.0 W/(m·K) with a mean of 3.25 W/(m·K) is obtained.

All three methods for estimating the mixture thermal conductivity described above (Equation L.7 through L.9) have been used to calculate the thermal conductivity and uncertainties in the calculated thermal conductivity for the oxide mixture. All show approximately the same values and uncertainties as shown in Table L.2.

L.2.3 Viscosity of Molten Oxide

Two methods are used to estimate the viscosity of liquid mixtures. First, Hirai (1993) reported that the viscosity of liquid metals could be estimated using temperatures of the liquidus of the corresponding phase diagram. This approach was stimulated by the study of Andrade (1934) who derived a formula for viscosity of pure liquid at their melting points based on the quasi-crystalline theory. The Andrade formula (Equations L.12 and L.13) has been found to be very successful in predicting the viscosity of pure liquid metals in the neighborhood of their melting points. Hirai extended Andrade's equations suggesting that the viscosity of liquid alloys could be calculated by the following equations:

$$\mu(T) = A \exp\left[\frac{B}{RT}\right], \qquad (L.12)$$

$$A = \frac{(5.7 \pm 10\%) \times 10^{-5} \left(T_m \overline{M}\right)^{1/2}}{\exp\left[\frac{B}{RT_m}\right] V_m^{2/3}} \text{ (Pa·s)}, \qquad (L.13)$$

$$\begin{aligned} B &= \text{activation energy}, \\ &= 2.65 T_m^{1.27} (J/\text{mole}), \end{aligned} \qquad (L.14)$$

where

$\mu(T)$ = viscosity of liquid mixture at temperature T (Pa·s),
T_m = melting temperature of liquid mixture (K),

$\overline{M}$ = molecular weight of the liquid mixture (g-mole),

$$= \sum \chi_i M_i, \qquad (L.15)$$

χ_i = mole fraction of component i,

M_i = molecular weight of component i (g-mole),

V_m = molecular volume at melting temperature (cm^3),

$$= \overline{M}/\overline{\rho}_m, \qquad (L.16)$$

R = gas constant, 8.3143 J/(mole·K),

$\overline{\rho}_m$ = density of liquid mixture at melting point obtained from Eq. (L.1) (g/cm^3),

m = subscript denotes melting point.

It has shown that for pure liquid, a value of 5.7×10^{-5} gives melting point viscosities within $\pm 10\%$ of experimental values (Beer, 1972). The application of this method to the calculation of the viscosities of several binary systems at temperatures above the melting temperature shows reasonable agreement between the calculated and experimental results with an expected standard error of $\pm 10\%$ of the calculated value (Seetharaman and Sichen, 1994).

The second method for estimating of the viscosity of liquid mixture is similar to Hirai's method (Andrade's formula) but the pure component activation energy, B, is based on the correlation recommended by Strauss (1962) and the coefficient of A is based on the value recommended by Nazare et. al. (1977),

$$A = \frac{(6.12 \pm 10\%) \times 10^{-5} \left(T_m \overline{M}\right)^{1/2}}{\exp\left[\frac{B}{RT_m}\right] V_m^{2/3}} \text{ (Pa·s)}, \qquad (G.17)$$

where

$$B = 1.8033\, T_m^{1.348} (J/\text{mole}), \qquad (L.18)$$

and the mixture molecular volume is based on the parameters suggested by Teja and Rice (1981),

$$V_m = \chi_1^2 V_1 + \chi_2^2 V_2 + \chi_1 \chi_2 \frac{\left(V_1^{1/3} + V_2^{1/3}\right)^3}{4} \qquad (L.19)$$

Equations L.17 and L.18 have been recommended by Nazare, Ondracek, and Schultz (1977) for calculating the viscosity of liquid corium. A standard error of $\pm 10\%$ of the value calculated has been assumed in Equation L.17.

A simple linear correlation instead of a traditional Arrhenius relation (Equation L.12) has been proposed for the viscosity of liquid UO_2 by Watson and Hagrman (1990),

$$\mu_{UO_2} = 1.23 \times 10^{-2} - 2.09 \times 10^{-6}\ T. \qquad (L.20)$$

This correlation for viscosity of liquid UO_2 was obtained from the data of Tsai and Olander (1972) and the data of Woodley (1974). Figure L.1 illustrates the viscosities calculated with the Equation L.20 and the experiment data. The dashed lines are the upper and lower uncertainty limits obtained by adding $\pm 1/3$ of the predicted viscosity. However, applying Equations L.12 and L.17 at the melting point of UO_2, the Andrade's formula (1934) for liquid viscosity, the viscosity of liquid UO_2 at the melting point is approximately 5.70×10^{-3} (Pa·s) which is close to the value of 5.79×10^{-3} (Pa·s) shown in Figure L.1. Also, using Equations L.12, L.17 and L.18 for temperatures above the melting temperature of UO_2, the calculated results of the viscosity of liquid UO_2 reflect a difference of less than 5% from the values calculated by Equation L.20. Therefore, it is suggested that the viscosity of liquid UO_2 can be calculated by Equations L.12, L.17, and L.18 with an uncertainty of $\pm 33\%$ of the calculated value to obtain

$$\mu_{UO_2} = (5.7 \pm 1.9) \times 10^{-3}\ \text{(Pa·s)} \qquad (L.21)$$

at the melting temperature of UO_2 and

$$\mu_{UO_2} = (1.61 \pm 0.54) \times 10^{-4} \exp\left[\frac{11130}{T}\right]\ \text{(Pa·s)} \qquad (L.22)$$

at temperatures above the melting temperature. The uncertainties of the viscosity of liquid UO_2 in Equations L.21 and L.22 are the greater of the uncertainty estimated from the equations used or $\pm 33\%$ of the calculated value based on the uncertainty of the UO_2 data.

The viscosity of liquid ZrO_2 are also calculated with Equations L.12, L.17, and L.18 and its uncertainties are also assumed to be $\pm 33\%$ of the calculated value,

$$\mu_{ZrO_2} = (4.9 \pm 1.6) \times 10^{-3}\ \text{(Pa·s)} \qquad (L.23)$$

at the melting temperature of ZrO_2 (2973 K) and

$$\mu_{ZrO_2} = (1.5 \pm 0.5) \times 10^{-4} \exp\left[\frac{10430}{T}\right]\ \text{(Pa·s)} \qquad (L.24)$$

at temperatures greater than the melting temperature.

Both the Hirai (i.e., Equations L.13, L.15 and L.16) and Teja and Rice (i.e., Equations L.15, L.17 and L.19) methods for estimating liquid mixture viscosity at the melting temperature

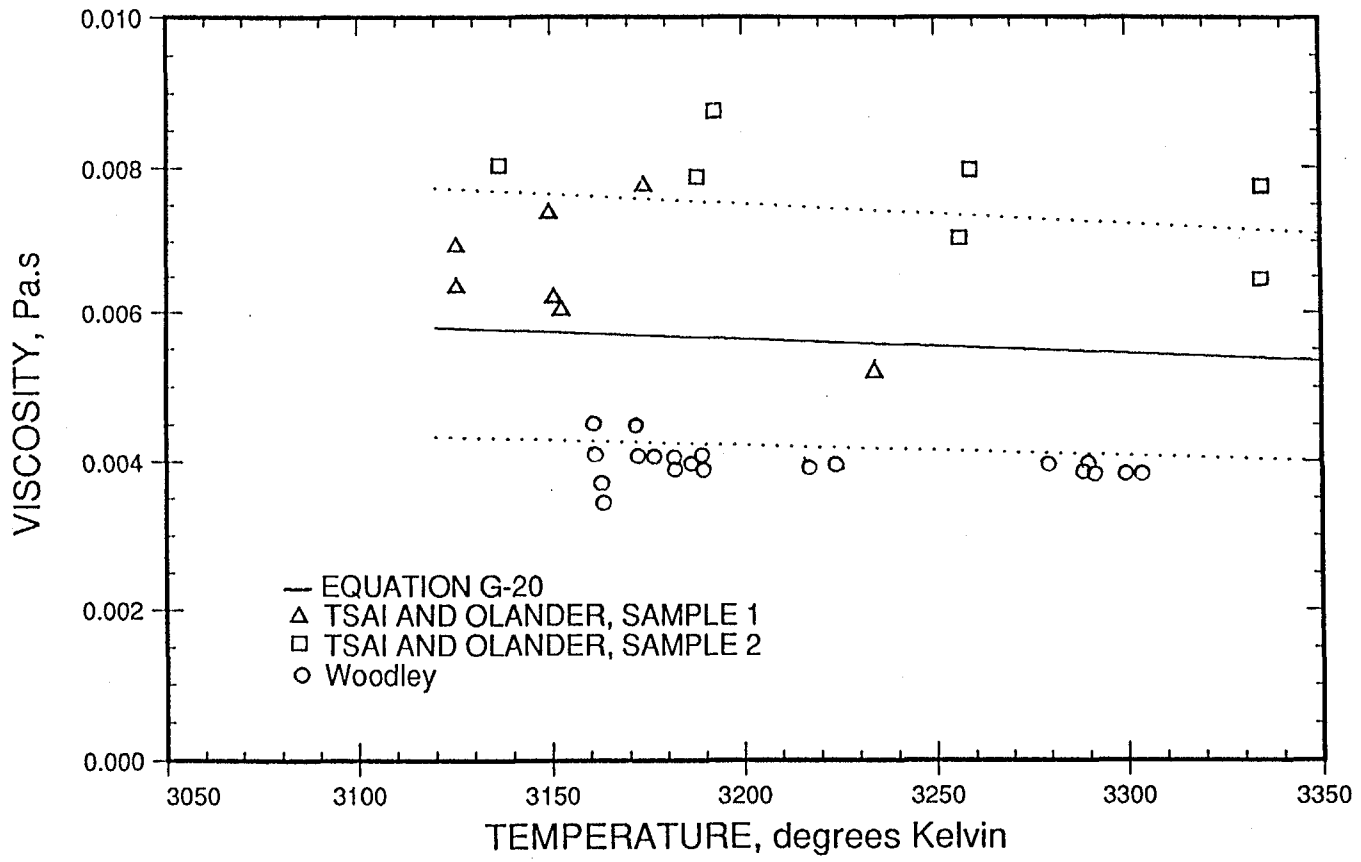

Figure L.1. Viscosities of UO_2 calculated with Eq. (L.20) (solid line) and upper and lower uncertainty estimates (dashed lines) compared with data (Watson and Hagrman, 1990).

described above have been used to calculate the viscosity and its associated uncertainties for the UO_2–ZrO_2 mixture. It is noted that the uncertainties of viscosity of the UO_2–ZrO_2 mixture have included the uncertainty of ±33% in the viscosity of individual constituents (UO_2 and ZrO_2) and the uncertainties of ±10% in the equations (Equations L.13 and L.17) used to estimate the viscosity of the UO_2–ZrO_2 mixture. The ranges of the values calculated are presented in Table L.2.

L.2.4 Specific Heat of Molten Oxide

The expression used to calculate the specific heat is a weight fraction average of the specific heats for UO_2 and ZrO_2,

$$C_p = \frac{\sum_i C_{p_i} W_i}{\sum_i W_i}, \qquad (L.25)$$

where

C_p	=	specific heat of the mixture, (J/Kg·K),
C_{p_i}	=	specific heat of the pure components i (J/Kg·K),
W_i	=	weight-fraction of pure component i in the mixture.

For liquid UO_2, the constant value obtained for the specific heat is (Fink, 1981)

$$C_{p_{UO_2}} = 485 \text{ (J/Kg·K)} \qquad (L.26)$$

with a standard error of ±1%.

For liquid ZrO_2, the specific heat is obtained from the measurement of Hammer (1967),

$$C_{p_{ZrO_2}} = 815 \text{ (J/Kg·K)}. \qquad (L.27)$$

It is believed that the specific heat of ZrO_2 is accurate to several percent (Hohorst, 1990). Therefore, it is assumed that the expected standard error of the specific heat for ZrO_2 is ±2% of the value.

The specific heat and its uncertainty for the molten oxide made up of 8.5 m^3 UO_2 and 1.0 to 3.0 m^3 ZrO_2 is calculated using Equations L.25 through L.27. The ranges of the values calculated are presented in Table L.2.

L.3 MOLTEN METAL

It is assumed that the composition ranges of the molten metal are 90 at % Fe - 10 at % Zr and 35 at % Fe - 65 at % Zr. The first composition of the molten metal is chosen on the iron

rich liquidus curve, namely, the eutectic point at 90 at % Fe and 1600 degrees Kelvin from the Fe–Zr phase diagram (Arias and Abriata, 1988). One point on the Zr-rich liquidus curve is also chosen, namely giving the same melting temperature but different composition of the molten metal (65 at % Zr and 1600 K).

L.3.1 Density and Volume Thermal Expansion Coefficient of Molten Metal

For liquid Zr at the melting temperature of 2098 degrees Kelvin, the linear thermal expansion is 1.86×10^{-2} with a standard error of $\pm 50\%$ (Reymann, 1990). Iida and Guthrie (1993) provide a range of estimated values for the thermal expansion coefficients of high melting point liquid metals from 0.45×10^{-4} K^{-1} (α_{Re}) to 0.54×10^{-4} K^{-1} (α_{Zr}). It is assumed that a standard error of $\pm 20\%$ of the estimated values for the liquid Zr thermal expansion coefficient based on the ranges estimated. The expressions for the linear thermal expansion in liquid Zr ($T \geq 2098K$) are thus

$$\varepsilon_o = (1.86 \pm 50\%) \times 10^{-2} + (5.4 \pm 20\%) \times 10^{-5} \ (T - 2098). \qquad (L.28)$$

The reference density, ρ_o, for Zr is 6500 Kg/m^3 at 300 degrees Kelvin (Brandes, 1983). Thus, the density of liquid Zr at the melting temperature can be calculated using Equations L.2 and L.28 as

$$\rho_{Zr}(T = 2098 \text{ K}) = 6130 \pm 180 \text{ (Kg/m}^3\text{)}. \qquad (L.29)$$

The density of liquid Fe at the melting temperature of 1811 degrees Kelvin, ρ_{Fe} (1811 K), and a range of reported values of the thermal expansion coefficient, α_{Fe}, are obtained from Steinberg (1974). The density of liquid Fe at the melting temperature is 7030 Kg/m^3. The thermal expansion coefficient of liquid Fe is $(1.2 \pm 0.17) \times 10^{-4} K^{-1}$. The density and thermal expansion coefficient for liquid Fe can be also taken from Beer (1972). The liquid iron density at the melting point is 7010 Kg/m^3 and the liquid thermal expansion coefficient is $1.2 \times 10^{-4} K^{-1}$. The reference density, ρ_o, for Fe is 7867 Kg/m^3 (Brandes, 1983). Thus, the linear thermal expansion of liquid Fe at the melting temperature is 3.63×10^{-2}. It is assumed that the uncertainty in this value is about $\pm 10\%$ which is the same as that recommended for solid Fe (Touloukian and Ho, 1970) . Thus, the density of liquid Fe and its uncertainty at the melting temperature are

$$\rho_{Fe}(T = 1811 \text{ K}) = 7020 \pm 90 \text{ (Kg/m}^3\text{)} \qquad (L.30)$$

and the thermal expansion coefficient and its uncertainty for liquid Fe are

$$\alpha_{Fe}(T \geq 1811 \text{ K}) = (1.2 \pm 0.17) \times 10^{-4} (K^{-1}). \qquad (L.31)$$

The density and thermal expansion coefficient of the Zr-Fe metallic pool and its uncertainty calculated using Equations(L.1, L.5 and L.29 through L.31 for a mixture made up of 90 at % Fe and 10 at % Zr are

$$\rho_{\text{Zr-Fe}} = 6890 \pm 240 \text{ (Kg/m}^3\text{)}$$

and

$$\alpha_{\text{Zr-Fe}} = (1.10 \pm 0.18) \times 10^{-4} \text{ (K}^{-1}\text{)}$$

while for a mixture made up of 35 at % Fe and 65 at % Zr they are

$$\rho_{\text{Zr-Fe}} = 6380 \pm 280 \text{ (Kg/m}^3\text{)}$$

and

$$\alpha_{\text{Zr-Fe}} = (0.69 \pm 0.13) \times 10^{-4} \text{ (K}^{-1}\text{)}.$$

The recommended values and uncertainties for the density and volume thermal expansion coefficient for the liquid Zr-Fe mixture are listed in Table L.2.

L.3.2 Thermal Conductivity of Molten Metal

The thermal conductivities of liquid Zr and Fe are assumed equal to the values in the solid-state at the melting temperature divided by a factor of 1.6 ± 0.2 for metals like Zr and Fe with eight nearest neighbor atoms (Nazare et. al., 1977). Since the solid state thermal conductivity of Zr is 58 ± 1 W/m·K, the liquid state thermal conductivity of Zr should be about 36 ± 5 W/m·K (Hohorst, 1990). The solid state thermal conductivity of Fe is reported to be 38.6 W/m·K with a standard error of $\pm 5\%$ in the value (Touloukian and Ho, 1981). The thermal conductivity of liquid Fe should therefore be about 24.1 ± 4.8 W/m·K.

The thermal conductivity of the molten metal and the uncertainty calculated by both the Filippov equation (Equation L.8) and the Li method (Equation L.9) are presented in Table L.2.

L.3.3 Viscosity of Molten Metal

The viscosity of liquid Zr and the uncertainty in this value can be calculated with Eqs. (L.17) and (L.18)

$$\mu_{\text{Zr}} = (4.5 \pm 0.5) \times 10^{-3} \text{ (Pa·s)} \qquad (L.32)$$

for $T = T_{m,\text{Zr}}$(2098 K), and

$$\mu_{\text{Zr}} = (2.0 \pm 0.2) \times 10^{-4} \exp\left[\frac{6620}{T}\right] \text{ (Pa·s)} \qquad (L.33)$$

for $T \geq T_{m,\text{Zr}}$.

There are over 100 references available for the viscosity of molten iron. The available experiment data cover the temperature range from 1730 to 2110 degrees Kelvin showing a considerable spread of the data as shown in Figure L.2. The values for the viscosity of liquid Fe recommended by Touloukian and Ho (1981) can be represented approximately by the Arrhenius-type relation,

$$\mu_{Fe} = (2.21 \pm 0.33) \times 10^{-4} \exp\left[\frac{5776}{T}\right] \text{ (Pa·s)}. \qquad (L.34)$$

The uncertainty in the recommended function is believed to be within ±15%. For comparison, the viscosity of liquid Fe is also calculated by Eqs. (L.12), (L.17) and (L.18) and reflects a difference of less than ±10% from the recommended function.

Both the Hirai (Equations L.13, L.15 and L.16) and Teja and Rice (Equations L.15, L.17 through L.19) methods for estimating liquid mixture viscosity at the melting point have been used to calculate the viscosity and the uncertainties for the molten metal mixtures. The uncertainties of the calculated values have also included the uncertainties associated with the equations used and the uncertainty in the viscosity of individual constituent (Zr and Fe). The ranges of the values calculated are presented in Table L.2.

L.3.4 Specific Heat of Molten Metal

For liquid Zr, the value for the specific heat is obtained from the JANAF Thermochemical Tables (Chase et. al., 1986),

$$C_{p_{Zr}} = 458 \text{ (J/Kg·K)}, \qquad (L.35)$$

with an expected standard error of ±3% (14 J/Kg·K) in the value. The uncertainty in the value is estimated based on the expected standard error of enthalpy of liquid Zr from ±33% (at the melting temperature of 2098 degrees Kelvin) to ±50% (at temperature of 2657 degrees Kelvin) (Hagrman, 1990B).

A constant value of 835 J/Kg·K is recommended by Touloukian and Ho (1981) for the specific heat of iron in the molten state. This value agrees to within ±3% (25 J/Kg·K) with the experiment data. Also, another recommended value of 825 J/Kg·K is obtained from the JANAF Thermochemical Tables (Chase et. al., 1986). Thus, the value for the specific heat of liquid Fe is

$$C_{p_{Fe}} = 835 \text{ (J/Kg·K)} \qquad (L.36)$$

with an uncertainty of a standard error of ±25 J/Kg·K.

The specific heat and its uncertainty for the molten metal are presented in Table L.2.

L.4 THERMAL CONDUCTIVITY OF THE LOWER HEAD STEEL

The thermal conductivity of the lower head steel is calculated using properties for A508 Class 3 steel. This is a low carbon, low alloy steel for which the composition range is 0.25% max C, 1.20–1.50% Mn, 0.45–0.60% Mo, 0.40–1.00% Ni, 0.15–0.40% Si, 0.025% max P, 0.25% max Cr, 0.025% max S, and the remainder Fe (ASTM, 1992). Thermal conductivity data for A508 Class 3 steel could be identified only for low temperatures less than approximately 1100 degrees Kelvin. In view of lack of high temperature data together with the low proportions of alloying elements, the steel vessel thermal conductivity in the high temperature is described in terms of data for pure iron (Touloukian and Ho, 1981). The thermal conductivity below 1100 degrees Kelvin is assumed between that recommended for one representative Mn–Mo–Ni low alloy steel which the composition range is 0.25% max C, 1.15–1.5% Mn, 0.4–0.6% Mo, 0.15–0.3% Si and 0.75% Ni and another representative C–Mn–Si high manganese-silicon carbon steel which has nominal amount of Mn $>$ 1.0% and Si $>$ 0.15% (ASME, 1989). The uncertainties in the recommended value are assumed equal to that estimated for pure iron, namely 2% from 150 to 1300 degrees Kelvin and 5% above 1300 degrees Kelvin. The recommended values and their uncertainty estimates for the thermal conductivity of the steel are shown in Figure L.3. The thermal conductivity above 1100 degrees Kelvin is assumed to be equal the thermal conductivity for pure iron corrected by the difference between the recommended value and the pure iron data at the temperature of 1100 degrees Kelvin. To support this assumption, the steel thermal conductivity data up to a temperature of 1500 degrees Kelvin from three different compositions and above two representative compositions are presented in Figure L.4. The first one is high-manganese low carbon steel (0.23% C, 1.51% Mn, 0.12% Si, 0.04% Ni, and 0.025% Mo), the second one is Chromium-Molybdenum low alloy steel (0.3% C, 0.5% Mn, 0.3% Si, 0.95% Cr and 0.5% Mo), and the last one is low carbon plain steel (0.23% C and 0.64% Mn) (Cubberly et. al., 1978). It is found that these thermal conductivity data have a considerable spread for temperatures less than approximately 1000 degrees Kelvin but the high temperature data all show approximately the same values and are within the uncertainty estimates. It is believed that the recommended values and the uncertainty in these values in the high temperature regime shown in Figure L.3 should be accurate to represent the thermal conductivity of the lower head wall.

L.5 THERMAL CONDUCTIVITY OF THE CORIUM CRUST

The thermal conductivity of solid UO_2 from experiment data for specimens with densities in the range of 98% of theoretical density and model predictions are shown in Figure L.5 (Hagrman, 1990C). The recommended values and the uncertainty in these values at four different states, i.e., the liquid state, solid state, 2000 K, and 500 K, for UO_2 are listed in Table L.3. The standard

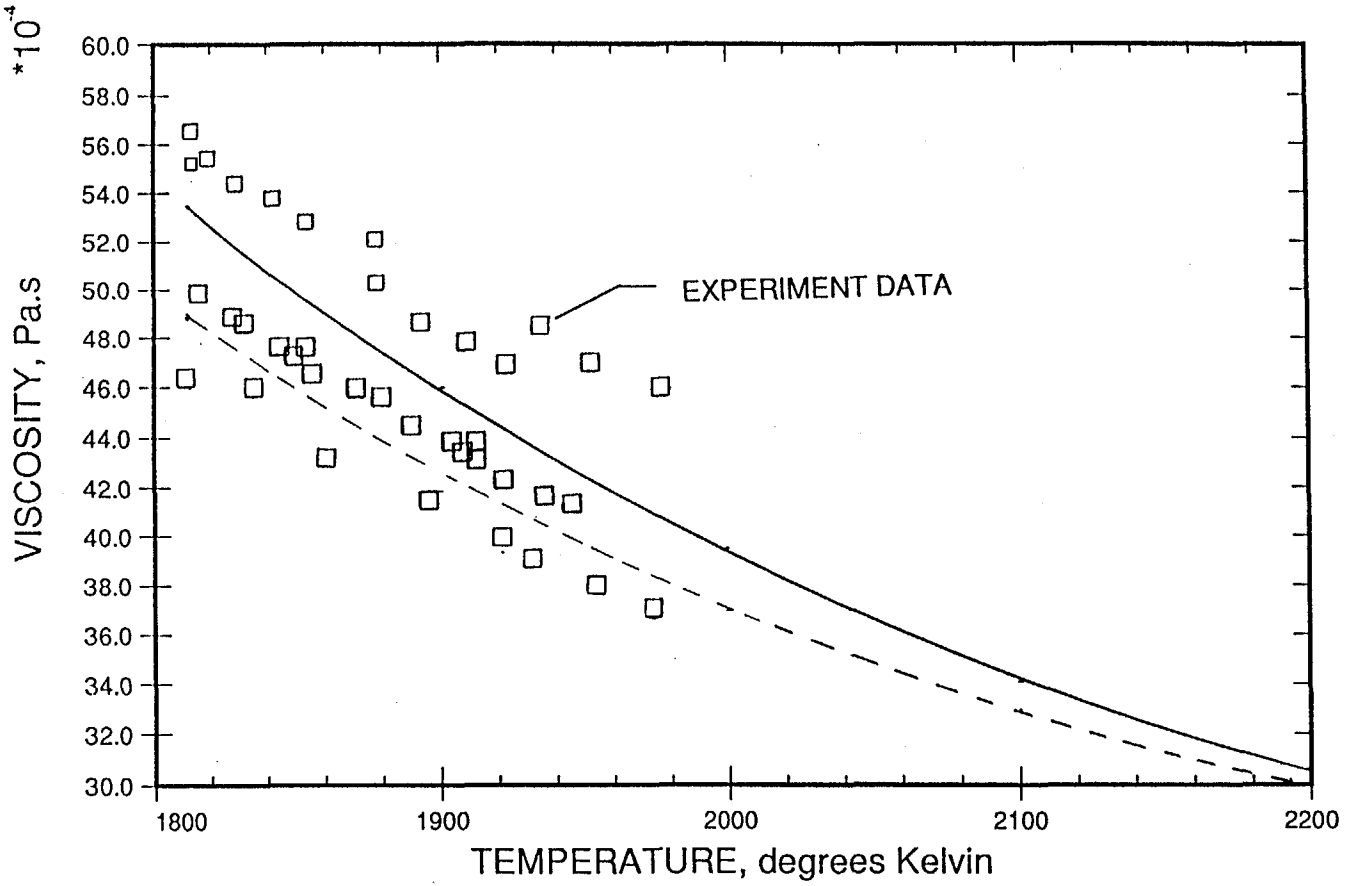

Figure L.2. Viscosities of iron calculated with Eq. (L.34) (solid line) and Eqs. (L.12), (L.17) and (L.19) (dashed lines) compared with data (Touloukian and Ho, 1981).

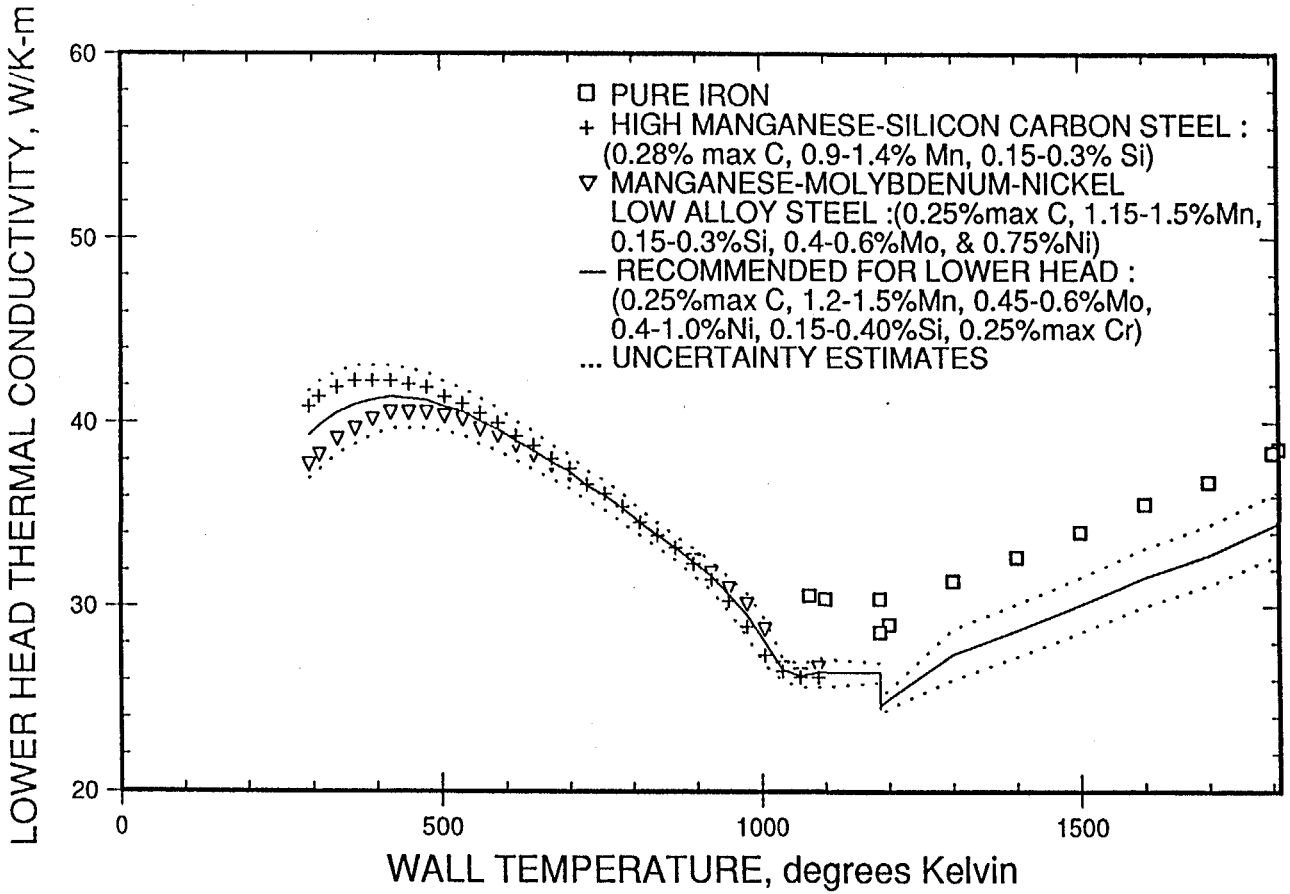

Figure L.3. Lower head steel thermal conductivity recommended (solid line) and upper and lower uncertainty estimates (dash lines).

error of the recommended values for thermal conductivity with respect to its solid UO_2 data base is ± 0.2 W/m·K. The standard error of the recommended values for the thermal conductivity for the UO_2 liquid-state is ± 1.1 W/m·K.

A simple linear equation has been fit to the data of Adams (Hagrman, 1990) for the thermal conductivity of solid ZrO_2,

$$k_{ZrO_2} = 1.67 + 3.62 \times 10^{-4} T \text{ (W/m·K)}. \qquad (L.37)$$

The data extends over a temperature range from 300 to 1550 degrees Kelvin. A standard error of $\pm 5\%$ of the data of Adams is reported (Touloukian et. al., 1970). It is assumed that the values of the thermal conductivity of solid ZrO_2 above the temperature range of Adam's data could be extrapolated from Equation L.37 with an increased standard error of $\pm 10\%$ of the extrapolated thermal conductivity. The recommended values and the uncertainties in these values are also listed in Table L.3.

Since all three methods for estimating the mixture thermal conductivity described above (Equation L.7 through L.9) provide approximately the same values and standard errors, the first method which based on solid UO_2-ZrO_2 mixture data is used here for the UO_2-ZrO_2 corium crust made up of 8.3 m^3 UO_2 and 1.0 to 3.0 m^3 ZrO_2 at four different states: liquidus, solidus, 2000 K and 500 K. The ranges of the calculated values at the four different states are presented in Table L.3.

L.6 ACKNOWLEDGEMENTS

This work was sponsored by the United States Department of Energy Advanced Reactor Severe Accident Program. The authors are indebted to S. W. Sorrell, ARSAP Program Manager, and S. L. Additon (TENERA). Argonne project management was provided by L. Baker, Jr. and B. W. Spencer. The manuscript was typed by L. J. Ondracek.

L.7 REFERENCES

1. E. N. C. da Andrade, Philos. Mag., Vol. 17, p. 497 (1934).
2. D. Arias and J. P. Abriata, Bull., Alloy Phase Diagrams, Vol. 9, p. 597 (1988).
3. ASME Standard: Boiler and Pressure Vessel Code, Section III, Division I - Appendices, American Society of Mechanical Engineers, New York (1989).
4. ASTM Standard: A 508/A 508M Standard Specification for Quenched and Tempered Vacuum-Treated Carbon and Alloy Steel Forgings for Pressure Vessels, Vol. 01.04, p. 308 (1993).

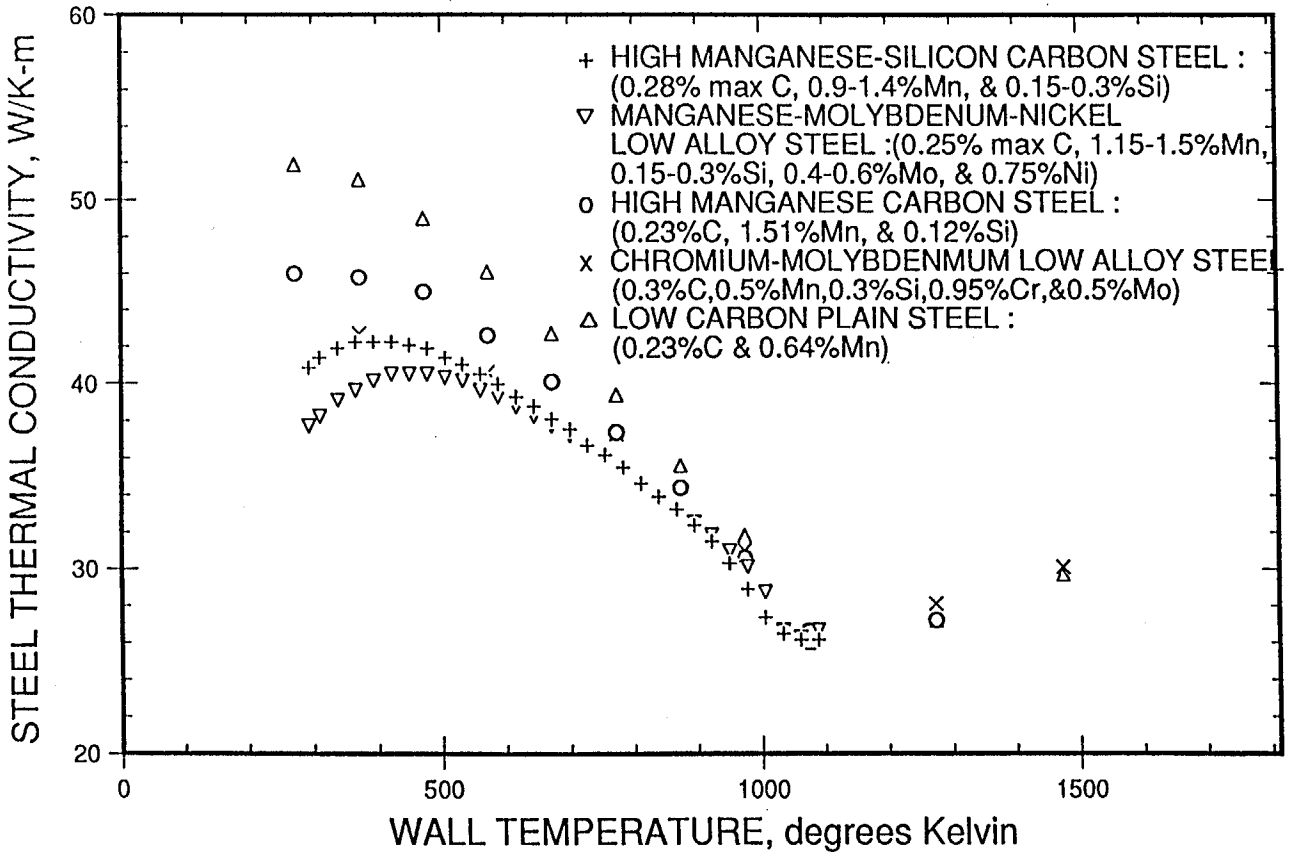

Figure L.4. Thermal Conductivity of carbon and low-alloy steel at various temperatures.

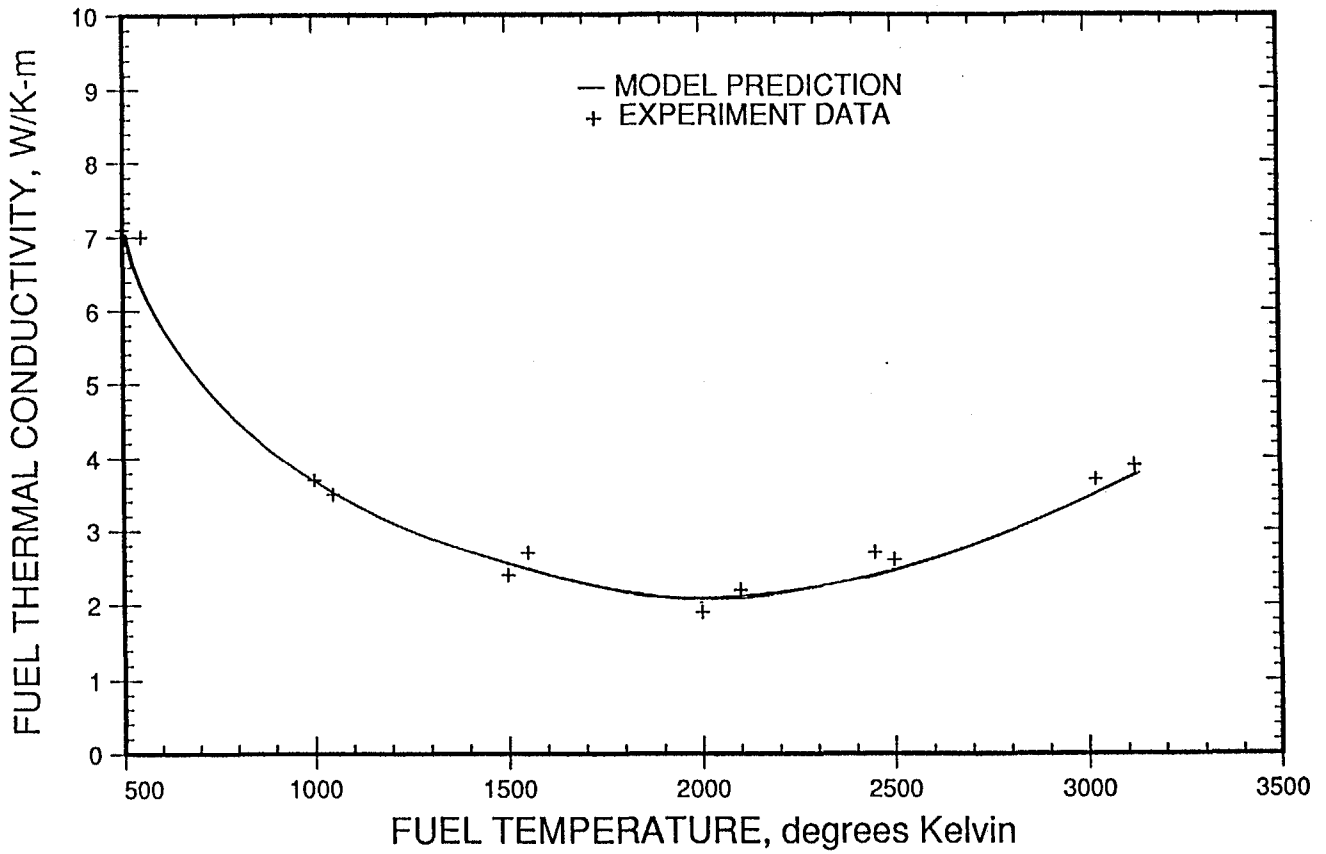

Figure L.5. Model prediction (Hagrman, 1990C) for thermal conductivity of 0.98 TD UO_2 compared to data from specimens with densities in the range 0.975 to 0.985 TD.

Table L.3. Thermal Conductivity of the Corium Crust

	UO_2	ZrO_2	8.5 m^3 UO_2 +1 m^3 ZrO_2	8.5 m^3 UO_2 +3 m^2 ZrO_2
Thermal conductivity (W/m·K)				
$T = T_\ell$ (liquidus state)	5.6 ± 1.1	3.25 ± 1.85	5.2 ± 1.05	4.7 ± 1.7
$T = T_s$ (solidus state)	3.8 ± 0.2	2.75 ± 0.28	3.6 ± 0.4	3.4 ± 0.4
$T = 2000$ K	2.0 ± 0.2	2.40 ± 0.24	2.0 ± 0.3	2.0 ± 0.3
$T = 500$ K	7.0 ± 0.2	1.85 ± 0.19	6.2 ± 0.5	5.4 ± 0.5

5. S. Z. Beer, Ed., Liquid Metals Chemistry and Physics, Marcel Dekker Inc., New York (1972).

6. E. A. Brandes, Ed., Smithells Metals Reference Book, Sixth Ed., Butterworths, Inc., London (1983).

7. M. W. Chase et. al., JANAF Thermochemical Tables, Third Edition, American Institute of Physics, New York (1986).

8. J. A. Christensen, "Thermal Expansion and Change in Volume of Uranium Dioxide on Melting," J. of the American Ceramic Society, Vol. 46, p. 607 (1963).

9. W. H. Cubberly et. al., Metals Handbook, Vol. 1: Properties and Selection: Irons and Steels, Ninth Edition, American Society for Metals, Metals Park, Ohio (1978).

10. J. K. Fink, M. G. Chasanov, and L. Leibowitz, "Thermodynamic Properties of Uranium Dioxide," ANL-CEN-RSD-80-3 (1981).

11. J. K. Fink and L. Leibowitz, "An Analysis of Measurements of the Thermal Conductivity of Liquid Urania," J. of High Temperature-High Pressure, Vol. 17, pp. 17-26 (1985).

12. D. L. Hagrman, "Zircaloy Oxides," SCDAP/RELAP5/MOD2 Code Manual, Vol. 4: MATPRO-A Library of Materials Properties for Light-Water-Reactor Accident Analysis, ed., J.K. Hohorst, NUREG/CR-5273, EGG-2555, p. 5-1 (1990).

13. D. L. Hagrman, "Cladding Specific Heat, the Effect of Hydride Solution on Cladding Specific Heat, and Enthalpy," SCDAP/RELAP5/MOD2 Code Manual, Vol. 4: MATPRO-A Library of Materials Properties for Light-Water-Reactor Accident Analysis, ed. J.K. Hohorst, NUREG/CR-5273, EGG-2555, p. 4.3-1 (1990B).

14. D. L. Hagrman, "Thermal Conductivity of Uranium Dioxide," SCDAP/RELAP5/MOD2 Code Manual, Vol. 4: MATPRO-A Library of Materials Properties for Light-Water-Reactor Accident Analysis, ed. J.K. Hohorst, NUREG/CR-5273, EGG-2555, p. 2.3-1 (1990C).

15. D. L. Hagrman and J. K. Hohorst, "Thermal Conductivity of Core Components," SCDAP/RELAP5/MOD2 Code Manual, Vol. 4: MATPRO-A Library of Materials Properties for Light-Water-Reactor Accident Analysis, ed. J.K. Hohorst, NUREG/CR-5273, EGG- 2555, p. 11.3-1 (1990).

16. R. R. Hammer, "Zircoloy-4, Uranium Dioxide, and Materials Formed by Their Interaction," IN-1093 (1967).

17. A. Hirai, Iron Steel Inst. Jpn. Int., Vol. 33, p. 251 (1993).

18. J. K. Hohorst, ed. "Specific Heat Capacity and Enthalpy of Zircaloy Oxide," SCDAP/RELAP5/MOD2 Code Manual, Vol. 4: MATPRO-A Library of Materials Properties for Light-Water-Reactor Accident Analysis, NUREG/CR-5273, EGG-2555, p. 5.2-1 (1990).

19. T. Iida and R. I. L. Guthrie, The Physical Properties of Liquid Metals, Clarendon Press, Oxford (1993).

20. C. S. Kim, R. A. Haley, J. Fischer, M. G. Chasanov, and L. Leibowitz, "Measurement of Thermal Conductivity of Molten UO2," Proc. Seventh Symp. on Thermophysical Properties, ed., A. Cezairliyan, ASME, New York, p. 338 (1977).

21. W. A. Lambertson and M. H. Mueller, "Uranium Oxide Phase Equilibrium Systems: III, UO2 - ZrO2," J. of the American Ceramic Society, Vol. 36, No. 11, p. 365, (1953).

22. C. Otter and D. Damien, High Temp.-High Pressures, Vol. 16, p. 1 (1984)

23. R. C. Reid, J. M. Prausnitz, and B. E. Poling, The Properties of Gases and Liquids, fourth edition, McGraw-Hill Book Company, New York (1987).

24. G. A. Reymann, "Thermal Expansion and Its Relation to Texture and Density of Zircaloy," SCDAP/RELAP5/MOD2 Code Manual, Vol. 4: MATPRO-A Library of Materials Properties for Light-Water-Reactor Accident Analysis, ed. J.K. Hohorst, NUREG/CR- 5273, EGG-2555, p. 4.5-1 (1990).

25. S. Seetharaman and Du Sichen, "Estimation of the Viscosities of Binary Metallic Melts Using Gibbs Energies of Mixing," Metallurgical and Materials Trans. B, Vol. 25B, p. 589 (1994).

26. D. J. Steinberg, Met. Trans., Vol. 5, p. 1341 (1974).

27. H. A. Tasman, D. Pel, J. Richter, H. E. Schmidt, High Temp.-High Pressures, Vol 15, p. 419 (1983).

28. Y. S. Touloukian, R. W. Powell, C. Y. Ho, and P. G. Klemens Eds., Thermophysical Properties of Matter, Thermal Conductivity Nonmetallic Solids, Vol. 2, IFI Plenum Press, New York (1970).

29. Y. S. Touloukian and C. Y. Ho, Eds., Properties of Selected Ferrous Alloying Elements, Vol. III-1 of McGraw-Hill/CINDAS Data Series on Material Properties, McGraw-Hill Book Company, New York (1981).

30. H. C. Tsai and D. R. Olander, "The viscosity of Molten Uranium Dioxide," J. of Nuclear Materials, Vol. 44, p. 83 (1972).

31. C. S. Watson and D. L. Hagrman, "Viscosity of Uranium of Dioxide," SCDAP/RELAP5/ MOD2 Code Manual, Vol. 4: MATPRO-A Library of Materials Properties for Light-Water-Reactor Accident Analysis, ed. J.K. Hohorst, NUREG/CR-5273, EGG-2555, p. 2.13-1 (1990).

32. R. E. Woodley, "The Viscosity of Molten Uranium Dioxide," J. of Nuclear Materials, Vol. 50, p. 103 (1974).

APPENDIX M

CAVITY FLOODING AND RELATED FLOW PATHS

APPENDIX M
CAVITY FLOODING CONSIDERATIONS

Stephen Additon

TENERA, L.P.
1901 Research Boulevard, Suite 100
Rockville, MD 20850-3164

The purpose of this appendix is to examine AP600 design features which govern both the flooding of the reactor cavity prior to significant debris relocation to the lower head and the maintenance of a sufficient inventory of water in the cavity to sustain in-vessel retention. Immersing the lower head prior to significant relocation of core debris to the lower head is taken as a reasonable early success condition, while recognizing that eventually deeper flooding is appropriate to protect the cylindrical walls of the vessel. Most scenarios which achieve and maintain immersion of the lower head do proceed to flood the entire cavity and substantial boil-up of the cold inventories evaluated here would occur in the interim extending cooling protection up the vessel wall. The following describes the flooding system for the AP600 and then addresses operational aspects.

The evaluation is based on the current status of the AP600 design which affords many, but not all, of the details required for a comprehensive assessment. The information available is judged sufficient to support a conclusion that it is feasible to ensure sufficient cavity flooding to maintain in-vessel retention for this design, that is, that the missing details can either be confirmed to be acceptable as the design is completed or can be made so without significantly impacting the design. Details to be confirmed are noted.

DESCRIPTION OF THE AP600 FLOODING SYSTEM

The AP600 design includes features (see Figure M.1) that aid cavity flooding including: a large in-containment coolant inventory; interconnection of compartments below the operating deck; a reactor vessel situated low in the reactor cavity, below other significant volumes that will also flood; and a passive containment cooling system that causes steam to condense on the inside of the containment shell and return through a gutter system to the In-containment Refueling Water Storage Tank (IRWST). The significance of the various containment volumes and interconnections to cavity flooding is illustrated in the schematic (Figure M.2). The inventories available for cavity flooding include the reactor coolant system inventory (~150 tons with the pressurizer), two accumulators (42 tons each), two core makeup tanks (56 tons each), and the

large in-containment refueling water storage tank (IRWST with 2,173 tons). Makeup from ex-containment is also possible. The vessel lower head itself is situated near the reactor cavity floor (< 1.5 m above it) and thus only 125 tons of water is needed to fully immerse the hemispherical lower head (2 m radius). A total of ~1060 tons is needed to reach the top of the active fuel elevation as shown in Figure M.3.

Clearly, the large IRWST inventory is most significant to successful deep cavity flooding. The IRWST is also important in that core damage is prevented if its passive coolant injection function succeeds and because the passive containment cooling system is designed to return the condensate to the IRWST. Thus, cavity flooding considerations focus on sequences in which the IRWST inventory is not injected to the reactor, perhaps due to multiple failures of check valves in the injection lines or sufficient residual pressure in the Reactor Coolant System (RCS) to prevent gravity driven flow from the IRWST.

To utilize the IRWST inventory for cavity flooding, the AP600 design affords two lines, each with two normally closed, [[actually, remote actuated, motor operated valves]] in series (one 25-cm line and one 10-cm line), either of which would cause the IRWST to drain to the lower volume in the containment when both valves in series are opened. The rates of cavity flooding afforded by these pathways are illustrated in Figure M.4. The 25-cm (10-inch) line rapidly immerses the lower head and the 10-cm (4-inch) line is capable of doing so within 1.5 hours which is sufficiently rapid (see further discussion below) for in-vessel retention provided the prescribed action is taken when core exit temperatures exceed 1090°C. Both lines discharge through a common tail pipe into a sump in the steam generator compartment. From there, the water spills onto the floor and drains into the reactor cavity through a tunnel at the compartment floor elevation which spills into the cavity at the elevation of the top of the lower head (see Figure M.2).

Some passive flooding of the reactor cavity will also occur in the AP600. Two cases must be considered:

A LOCA will spill much of the RCS, CMT and accumulator inventory to the steam generator compartments from which it will drain to the cavity and immerse the lower head. Once the water is boiled off, however, it will not return to the cavity until holdup volumes in the IRWST and refueling canal are accumulated (see next case). The minimum level before reflux of condensate is established may not be sufficient to protect the lower head. Thus, passive flooding can only be counted on for temporary protection of the vessel given a LOCA, but does lessen the need for manually-activated flooding.

In a transient event, where the RCS inventory is blown down to the IRWST, the IRWST overflows after expansion or added mass equivalent to about 110 tons, The IRWST overflow

spills through a 15-cm line to the refueling canal and from there to the cavity (after accumulating more than 150 tons) through another 15-cm line (see Figure M.2). These holdup volumes cannot be decreased as they are sized to prevent vessel damage in an inadvertent partial blowdown, facilitating rapid recovery and enhancing expected plant availability. The total mass available in such a case (from the RCS, CMTs, accumulators, and IRWST expansion) is more than sufficient to immerse the lower head. In this case, water boiled off would reflux via the IRWST to the cavity and the lower head would remain protected, but the vessel walls would not be immersed without manually-actuated flooding.

In the preceding evaluation the inventory holdup in the containment atmosphere with the passive containment cooling system operating is not significant. If external cooling water is unavailable, the atmospheric holdup does increase to establish equilibrium with less-effective external cooling.

OPERATIONAL ASPECTS

In a representative large loss of coolant accident, the LOCA passively floods the reactor cavity to a depth of about 4 m, immersing the lower head; the core exit temperatures exceed 1090°C at 2.1 hours into the event leading to manual action to open the valves; and the cavity is fully flooded (10 m water depth) by the time core debris relocation to the lower head is initiated (after 4 hours).

The available studies of flooding reliability are not sufficiently rigorous to support firm conclusions about the design. The AP600 PRA addresses cavity flooding in the updated Level II submittal (Revision 1, dated July 22, 1994). The PRA concludes that flooding was unsuccessful in 20% of the core damage cases. The failures were dominated by one sequence (17.7% of CDF) in which common mode failures of instrumentation and display systems were assumed to prevent operators from taking action to flood the cavity. Of the remaining 2% of CDF cases without successful flooding, the operators contributed about 40% and the failure of the hardware to respond on demand contributed about 60%.

The one dominant sequence will be the subject of further study as accident management is addressed for the design and it should prove possible to specify criteria that would ensure flooding even if such an instrument failure occurs. As part of this effort, the high pressure sequence involved also merits further accident management consideration which should lead to expectations of earlier depressurization which may affect the time available for cavity flooding.

The residual failure rates are also above the levels which ought to be achievable for such a manually-activated system of safety importance. Further study of the time window for operator response is warranted because the operator's unreliability should be below 10^{-3} with adequate

time and clear indications, provided that issues regarding expected reluctance to wet the reactor vessel are resolved. Similarly, better hardware performance should be achievable provided the required equipment (including DC-power supplies for the motor operated valves) is designed for reliability and evaluated for survivability under the potential severe accident conditions when the decision to flood would be made.

Additional studies appear to be warranted to verify that the long term flooding rate afforded by the 10-cm line is adequate to protect the upper vessel and maintain in-vessel retention. The provisions for assuring reliability of the normally-open overflow path from the refueling canal should be reviewed since it must be closed during refueling.

CONCLUSION

The AP600 design affords many features which serve to provide the capability for cavity flooding needed to establish in-vessel retention. The large coolant inventory in containment, the favorable geometry which transports water to the cavity and affords a minimal volume to immerse the lower head, and the provisions for manual action (even including makeup from ex-containment if necessary) are among the most significant features. Some details relating to sequence-dependent time margins and the reliability of flooding (human factors, equipment, and accident management) remain to be verified during the design certification process. The available information supports a conclusion that reliable cavity flooding is feasible and could be achieved for this plant design.

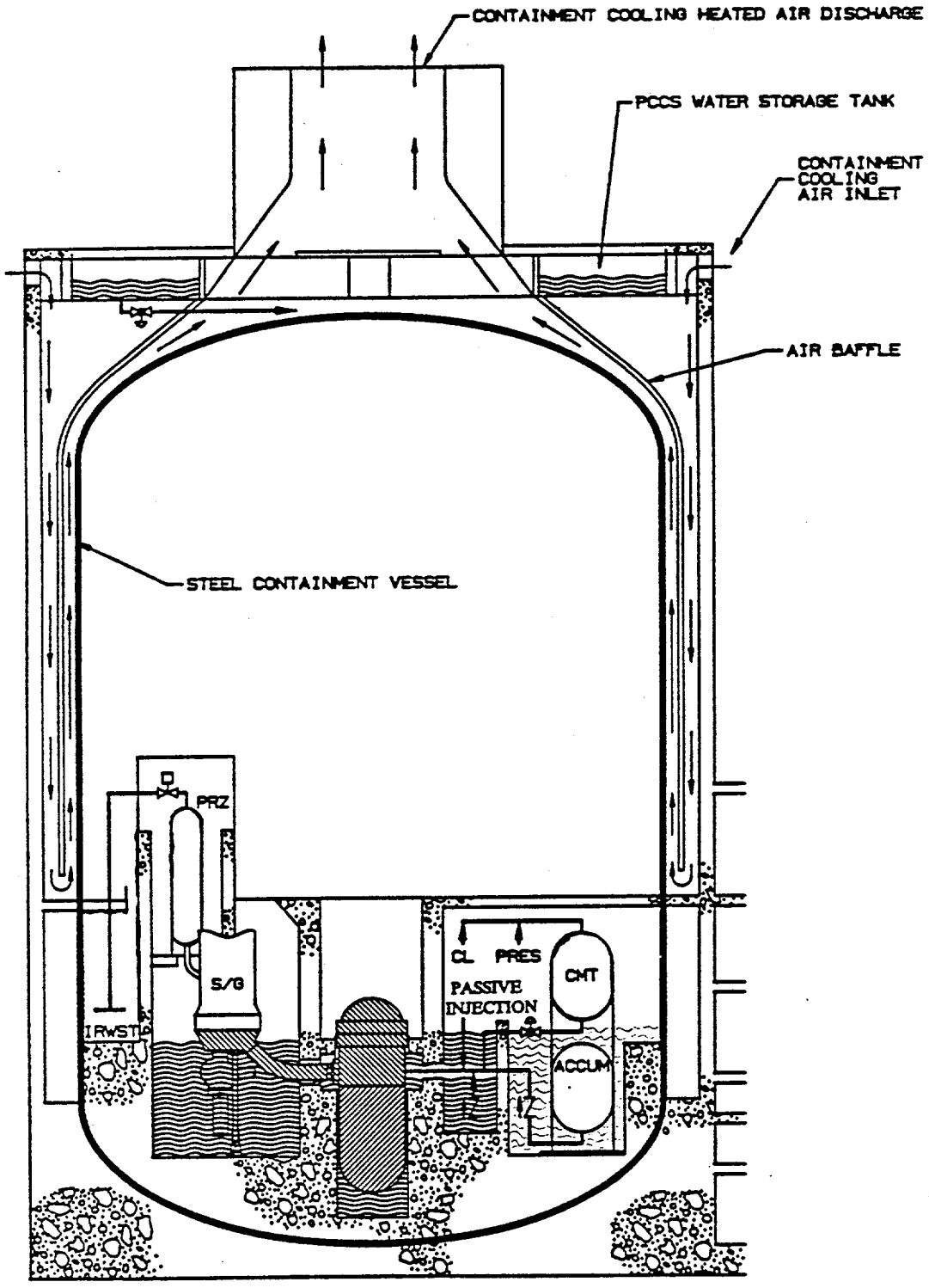

Figure M.1. Illustration of AP600 containment.

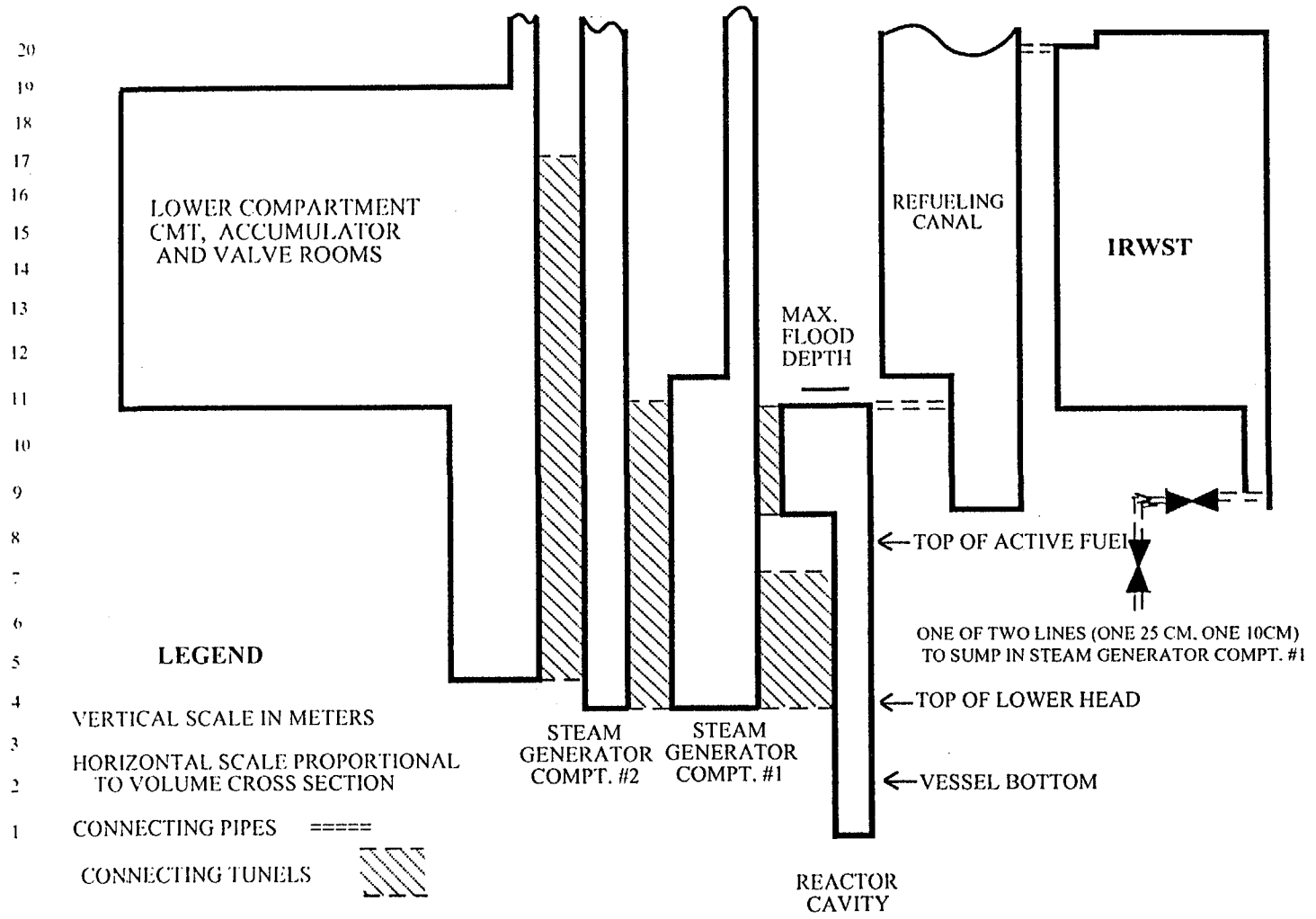

Figure M.2. Schematic of AP600 containment volume interconnections.

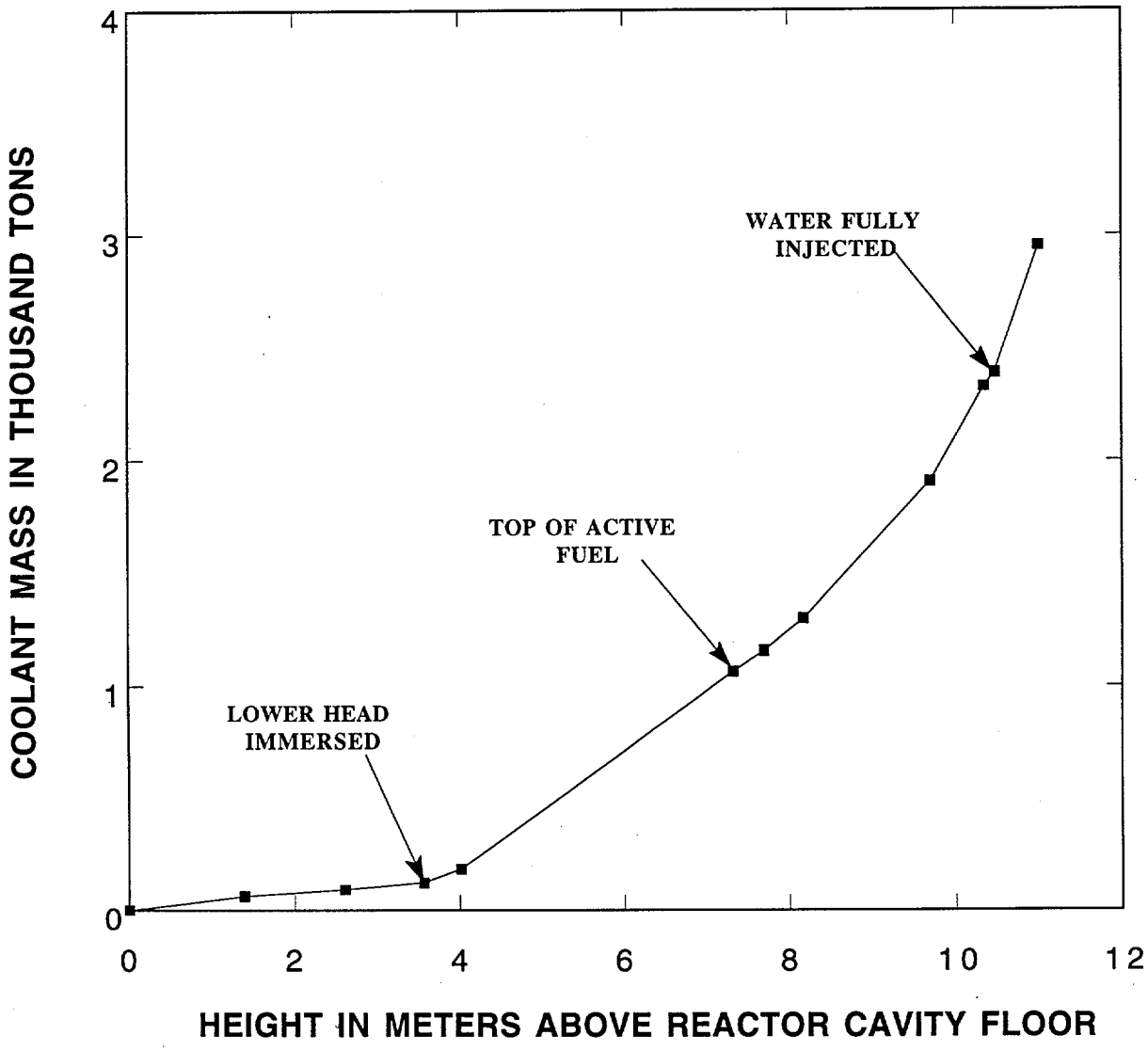

Figure M.3. Inventory required versus flood elevation.

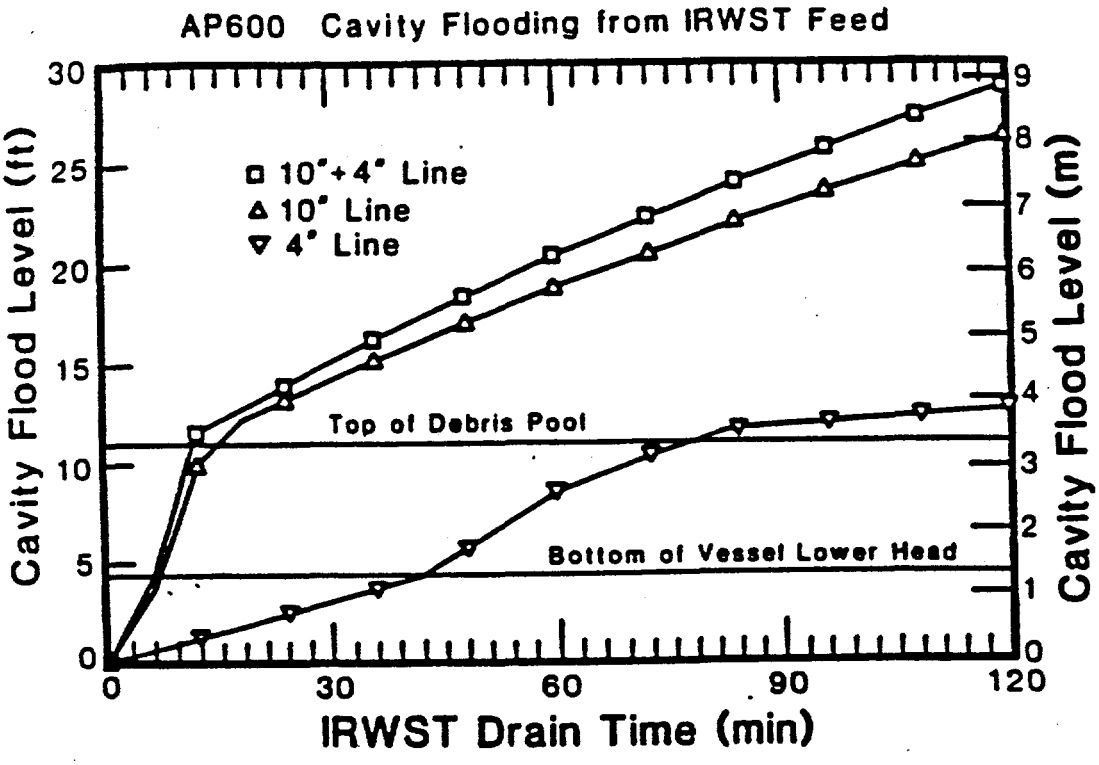

Figure M.4. Flooding from IRWST lines.

[[ADDENDUM TO APPENDIX M]]

UPDATED CAVITY FLOODING CONSIDERATIONS

The design for the AP600 has evolved and the PRA quantification has been updated in several respects that affect the evaluation of the timing and reliability of reactor cavity flooding. This update to the original Appendix M addresses these considerations.

The principal changes in the AP600 design and in its reliability quantification pertinent to reactor cavity flooding since the original report include:

- New diagrams are available to illustrate the cavity flooding flow path.
- The valve and line configuration for manually activated cavity flooding has been changed. The current design affords two 15-cm lines in place of the prior 25-cm and 10-cm lines addressed in the original Appendix M. The lines are now identical and each has one squib valve in series with one motor operated valve in place of the former two motor operated valves in series.
- The reliability of manual flooding has been recalculated and the previously significant common mode failure vulnerability (17.7% of core damage failure cases) was eliminated through more refined analyses of actual common features among the multiple trains of AP600 digital control logic. The evaluated unreliability of reactor cavity flooding ($\sim$0.7%) is based on conservative assumptions for generic hardware and procedures indicating that higher reliability can be expected when specific components are selected and corresponding emergency operating procedures are developed.

Each of these aspects is discussed more fully below.

Improved Illustration of Cavity Flow Path

Figures M.5a and M.5b provide exploded and assembled three dimensional views of the interconnected volumes in the AP600 containment that are pertinent to cavity flooding and the in-vessel retention flow paths. The lines from the IRWST connect to a sump in the steam generator compartment floor. The water draining from the IRWST spreads across the floor and spills into the volume labeled "reactor cavity volume". From there, it spreads across the floor and enters the region around the vessel which is labeled as "reactor shield wall volume". The upper portion of this volume (around the eight vessel nozzles) is actually square in plan view (see Addendum to Appendix K) and not round as shown here. The connection between the reactor cavity and the reactor shield wall volumes shown here may be obstructed by neutron shielding, but there is a redundant connection through an open HVAC tunnel, also flush with

the cavity floor, at the left of the illustrated interconnection. These drawings are provided to aid three-dimensional visualization of the flow path for the cavity flooding water.

Revised Valve and Line Configuration for Cavity Flooding

The AP600 designers have elected to change the valve configuration for the cavity flooding lines, from two mechanical (motor-operated) valves in series in each of the redundant lines, to one squib valve and one mechanical valve in each line. Further, the line sizes are now identical at 15-cm (6-inches) each, whereas the former line sizes were significantly different at 25-cm (10-inches) and 10-cm (4-inches). The identical line sizes make the squib valve application practical; the squib valves improve the reliability of these lines when used for core cooling suction, a function separate from their use for cavity flooding during in-vessel retention.

Two aspects of the design change require evaluation: the impact on possible flooding rates and the impact on flooding reliability (see next topic). The impact on flooding rates assuming none of the RCS inventory is available in the cavity (conservative for most severe accident sequences) is illustrated in Figure M.6. The two new lines flood the cavity somewhat more slowly than the single 25-cm line could in the prior design, but the difference in timing is not significant for in-vessel retention. More importantly, either new line alone is substantially faster than the old backup 10-cm line. The lower head can now be immersed (83-foot level of knee in curves on Figure M.6) in less than 20 minutes with only a single line available. In contrast, the 10-cm line required almost 50 minutes to reach this level.

While the remainder of the cavity fills more slowly, the thermal challenge in this region would also develop slowly. Further, the boiled up fluid level can be significantly higher than the indicated single phase flooding level. The proposed flooding criterion of 2000F at the core exit affords ample time for operator action and flooding to reach above the level of the lower head and thus precludes early failure from the prompt relocation thermal challenge. Further, the vessel wall can be protected effectively as well by the subsequent flooding even with only one of the 15-cm flooding lines available.

Reliability of Manual Flooding

The evaluated failure rate for manual flooding for a typical quantification of the fault tree in the updated PRA is 6.82×10^{-3}. Common cause mechanical failure contributes about 65% of the total, while human error contributes about 25%. The mechanical failure probability was evaluated based on the earlier design with four mechanical valves, but would not be expected to decrease significantly with the change to two squib valves as both valve types remain common mode. The failure rate data are generic values established by EPRI to represent new passive

designs conservatively and lower values would be expected if actual hardware characteristics were considered in the quantification. Similarly, the operator error rates are conservatively estimated based on generic considerations and unavailable procedures. Typical values for operating facilities are significantly lower. Thus, the estimated error rates are judged to be upper bound values that can be improved upon for an actual design.

Conclusion

The revised design for the AP600 flooding lines and the reliability reevaluation are judged to strengthen the earlier conclusion that reliable cavity flooding is feasible and could be achieved for this plant design.

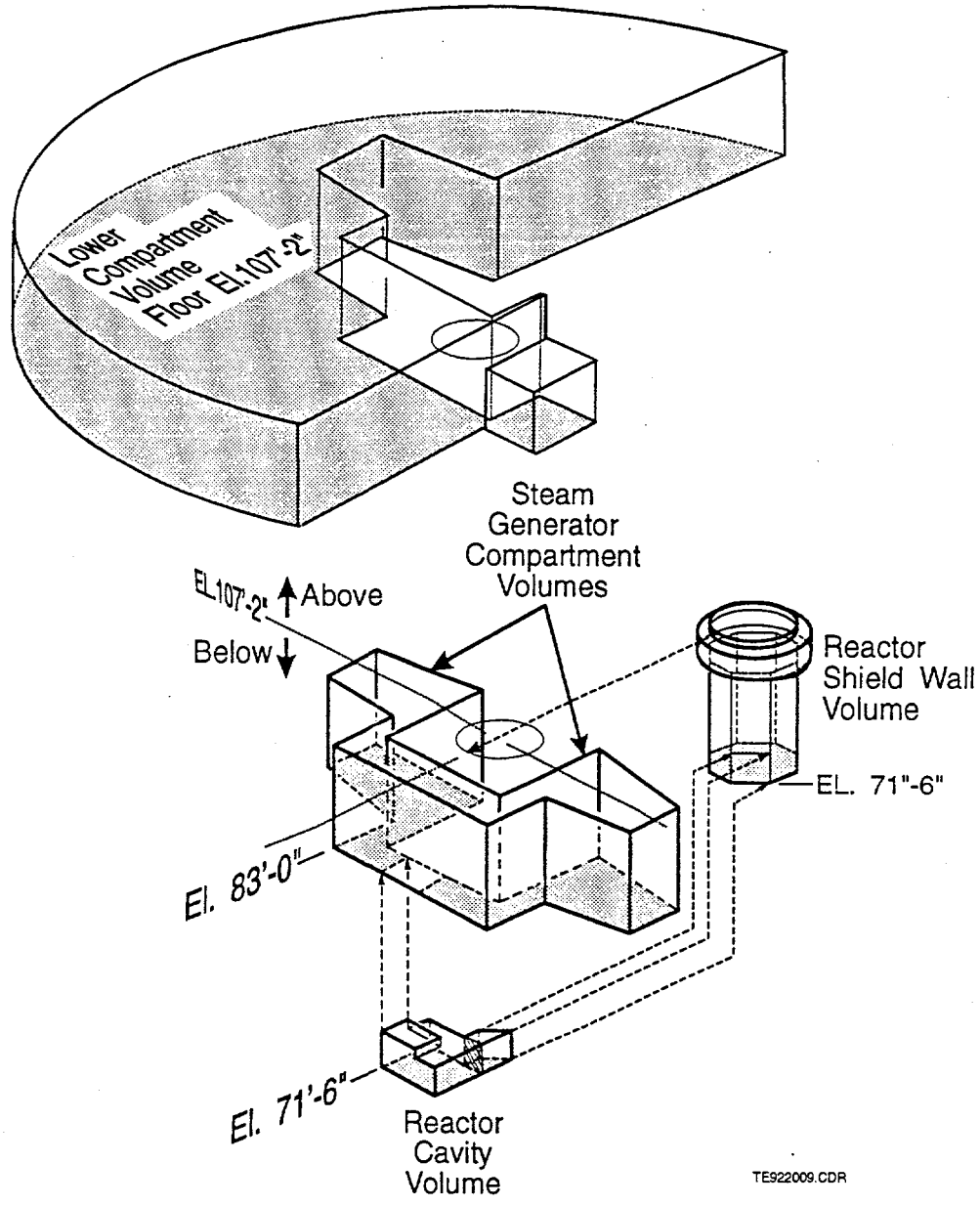

[Note: Reactor shield wall volume actually square in plan view, not round as shown]

Figure M.5a. AP600 key floodable volumes in containment — exploded view.

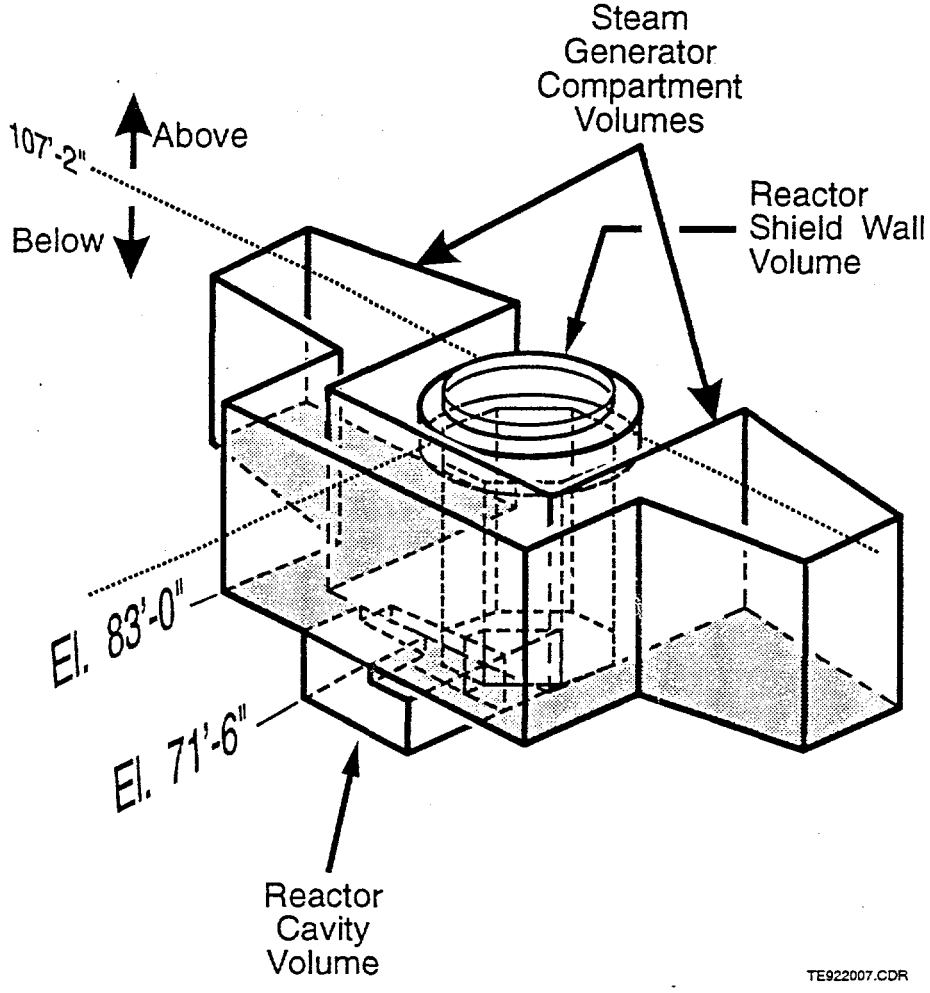

[Note: Reactor shield wall volume actually square in plan view, not round as shown]

Figure M.5b. AP600 key floodable volumes in containment — assembled view.

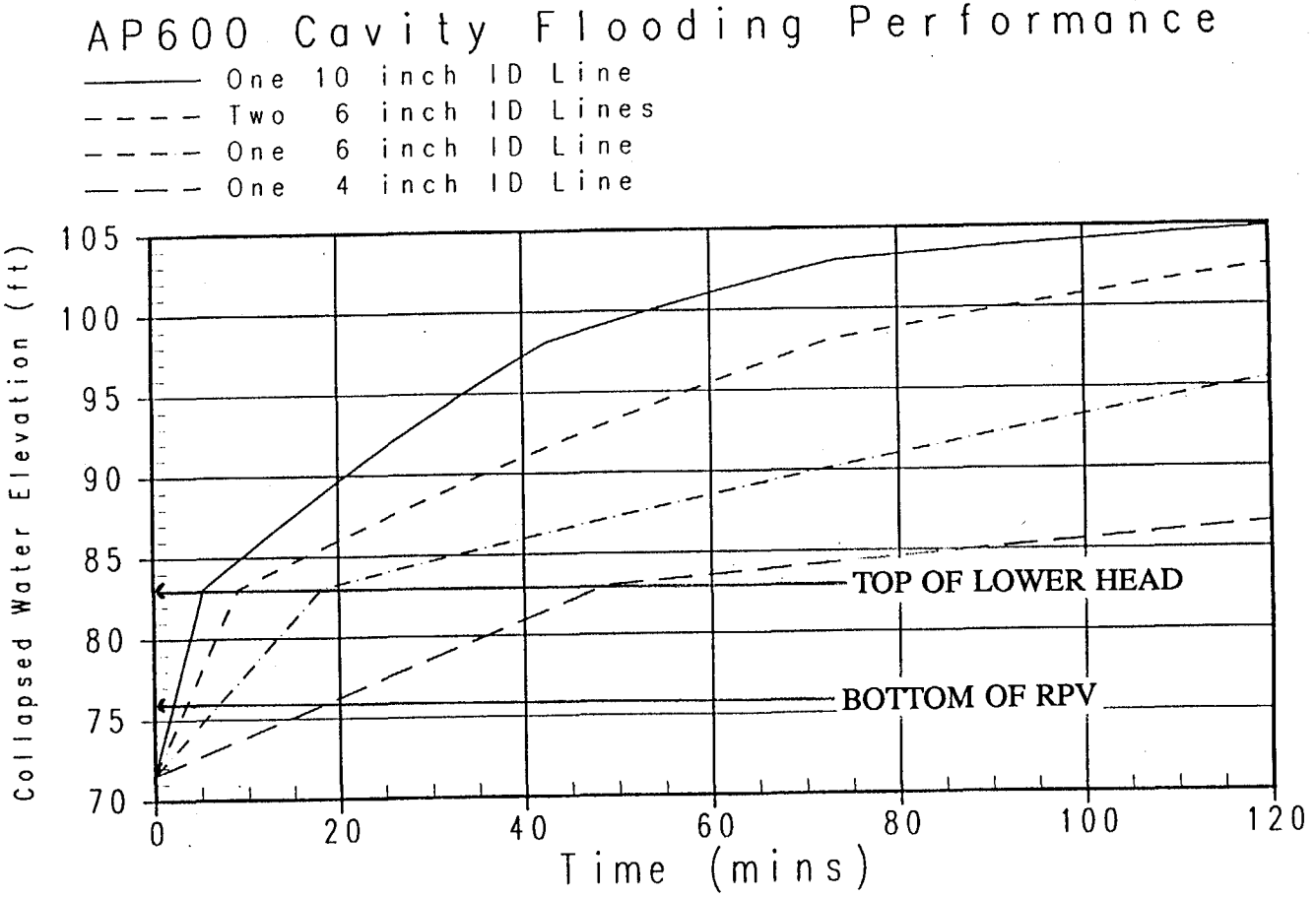

Figure M.6. Comparison of cavity flooding rates for old (10-inch and 4-inch lines) and new (two 6-inch lines) designs.

APPENDIX N

THE MELAD EXPERIMENT

APPENDIX N

THE MELAD EXPERIMENT

C. Liu and T.G. Theofanous

Department of Chemical and Nuclear Engineering
Center for Risk Studies and Safety
University of California, Santa Barbara, CA 93106

While the correlations concerning heat transfer at the top (bottom) and side boundaries are well established, as discussed in Chapter 5, we could not find any information about the simultaneous existence of both processes and the effect of their interaction. As discussed at the end of Chapter 5, this interaction is expected to occur in the bulk of the layer and manifest itself, for a sufficiently small aspect ratio, as a radial temperature gradient in the bulk. When this occurs, the assumption of a well-mixed bulk is conservative in producing higher thermal loads to the side. The purpose of the relatively simple experiment reported here was to demonstrate this effect.

The experimental apparatus, called the MELAD for Metal Layer Demonstration, is illustrated in Figure N.1. The test section consists of a rectangular box 50 cm long, 10 cm wide, and 10 cm in height. The top and one of the sides are cooled to desired temperatures; the other side is thermally insulated, and the bottom is heated by direct electrical current using a steel foil and a low voltage transformer. The front and back faces (in the picture) of the apparatus are insulated to create a 2-D behavior.

Both cooling plates are made from copper, with internal channels, and are equipped with several thermocouples to measure the plate surface temperatures. Flows are measured to an accuracy of 5%, and the RTDs measure the temperature rise between the inlet and exit streams to an accuracy of $\pm$ 0.02 °C. The steel foil temperature is measured with thermocouples fixed at the back of it. The water layer temperatures are measured with thermocouple "trees" positioned at various distances from the side cold plate. All temperature measurements are made to an accuracy of $\pm$0.5°C.

Two groups of experiments were carried out. The first involved only top cooling; the purpose was to understand better the performance of the Globe-Dropkin correlation, while shaking down the apparatus. The second group involved both top and side cooling and was oriented to the main purpose of this experiment–i.e., to determine the up-to-side energy flow split. A listing of all runs, experimental conditions, and other key information is given in Table N.1. The key results are summarized in Figures N.2 to N.5. Other details and discussion are provided below.

First, with reference to Table N.1 we observe that the energy balance is satisfied to a sufficient accuracy for the demonstration purposes of this experiment. The small systematic error is in the most part due to heat losses. On this basis, measured heat fluxes can be consider to be good to be within a few percent, and are used directly in comparison with predictions.

Runs B, were considered both by means of the Globe-Dropkin correlations, as well as by means of its adapation for "local" use as discussed in Chapter 5. The overall application is based on the temperature difference between the bottom and top plates, and a Ra number based on properties defined at the "average"' temperature. We call this the "bulk," Ra_b, Rayleigh number. In the past column of Table N.1 we show also the "local" Ra numbers for the bottom (ℓ, i) and to $(\ell, 0)$ boundary layers, based on the "film" properties. Here "film" temperatures were defined as the averages between the **measured** bulk temperature (T_b in Table N.1) and the bottom and top plate temperatures respectively. Note that there is a significant difference, indicating on the basis of the Globe-Dropkin correlation itself, an enhanced heat transfer across the bottom boundary layer, compared to the top, and hence an upwards bias of the bulk temperature. This trend is clearly evident in Table N.1 by comparing the T_b to $(T_{\ell,i} + T_{\ell,o})/2$ for the set B runs. [There is a Prandtl number effect also, but due to the 0.074 power it is rather small compared to the Ra number effect just discussed–however, in the calculation it is taken into account as well.] As seen in Figure N.2, the overall Globe-Dropkin correlation provides quite a good prediction, apparently being able to compensate between the "over" and "under" predictions at the top and bottom boundary layers respectively. It is interesting that it is able to do so by using a fictitious bulk temperature, the $(T_{\ell,i} + T_{\ell,o})/2$. For the local application of Globe-Dropkin we make use of Eq. (5.41) in an energy balance

$$q_{up} = 0.174\ \mathrm{Pr}_{\ell,i}^{0.074} \left\{ \frac{g\beta}{\alpha\nu} \right\}_{\ell,i}^{1/3} k_{\ell,i} (T_{\ell,i} - T_b)^{4/3} = 0.174\ \mathrm{Pr}_{\ell,o}^{0.074} \left\{ \frac{g\beta}{\alpha\nu} \right\}_{\ell,o}^{1/3} k_{\ell,o} (T_b - T_{\ell,o})^{4/3} \qquad (N.1)$$

and these two equations are solved for the two unknowns: $T_{\ell,i}$ and T_b. The results are shown in Figure N.3 in comparison with the measured values. The agreement is good, but note that the bulk temperature shift, towards the temperature of the bottom plate, discussed above is not fully accounted.

In a similar fashion we proceed now to the interpretation of set A runs. The model is along the lines of that used for the metallic layer [see Eqs. (6.9) to (6.11)] except for the difference in geometry and substituting for the radiation condition at the upper boundary the known upper plate temperature. Thus we have

$$q_{up} = q_{\ell,o} + 0.2 q_{\ell,w} \qquad (N.2)$$

where

$$q_{up} = 0.174\ \mathrm{Pr}_{\ell,i}^{0.174} \left\{ \frac{g\beta}{\alpha\nu} \right\}_{\ell,i}^{1/3} k_{\ell,i} (T_{\ell,i} - T_b) \qquad (N.3)$$

$$q_{\ell,o} = 0.174\ \mathrm{Pr}_{\ell,o}^{0.074} \left\{ \frac{g\beta}{\alpha\nu} \right\}^{1/3} k_{\ell,o} (T_b - T_{\ell,o})^{4/3} \qquad (N.4)$$

$$q_{\ell,w} = h_{\ell,m}(T_b - T_{\ell,m}) \qquad (N.5)$$

and h is obtained from Eq. (5.39), with properties evaluated at the film temperature of the side boundary layer and the Ra based on $(T_b - T_{\ell,m})$. For this system of two equations [[N.3 and N.4]] we supply q_{up}, $T_{\ell,0}$,$T_{\ell,m}$ for each run and compute T_b, and $T_{\ell,i}$. Knowing T_b, the top and side heat fluxes can be also computed. The results are shown against the measured values in Figures N.4 and N.5 for the fluxes and driving forces respectively. Both predictions are found to be in very good agreement with the data. In fact, there was a small temperature gradient measured in the bulk as well, resulting in a 2 to 3°C lower temperature (than the average value used in Figure N.5) at the edge of the side boundary layer, that would make the agreement even better. However, since this is not within the scope of the model, it must be considered fortuitous, and is not shown in Figure N.5. With a slight overprediction (conservative) of the heat flux to the side wall, this demonstrates that the local formulation of the Globe-Dropkin correlation combined with the Chu–Churchill correlation for the vertical wall are quite adequate for our purposes.

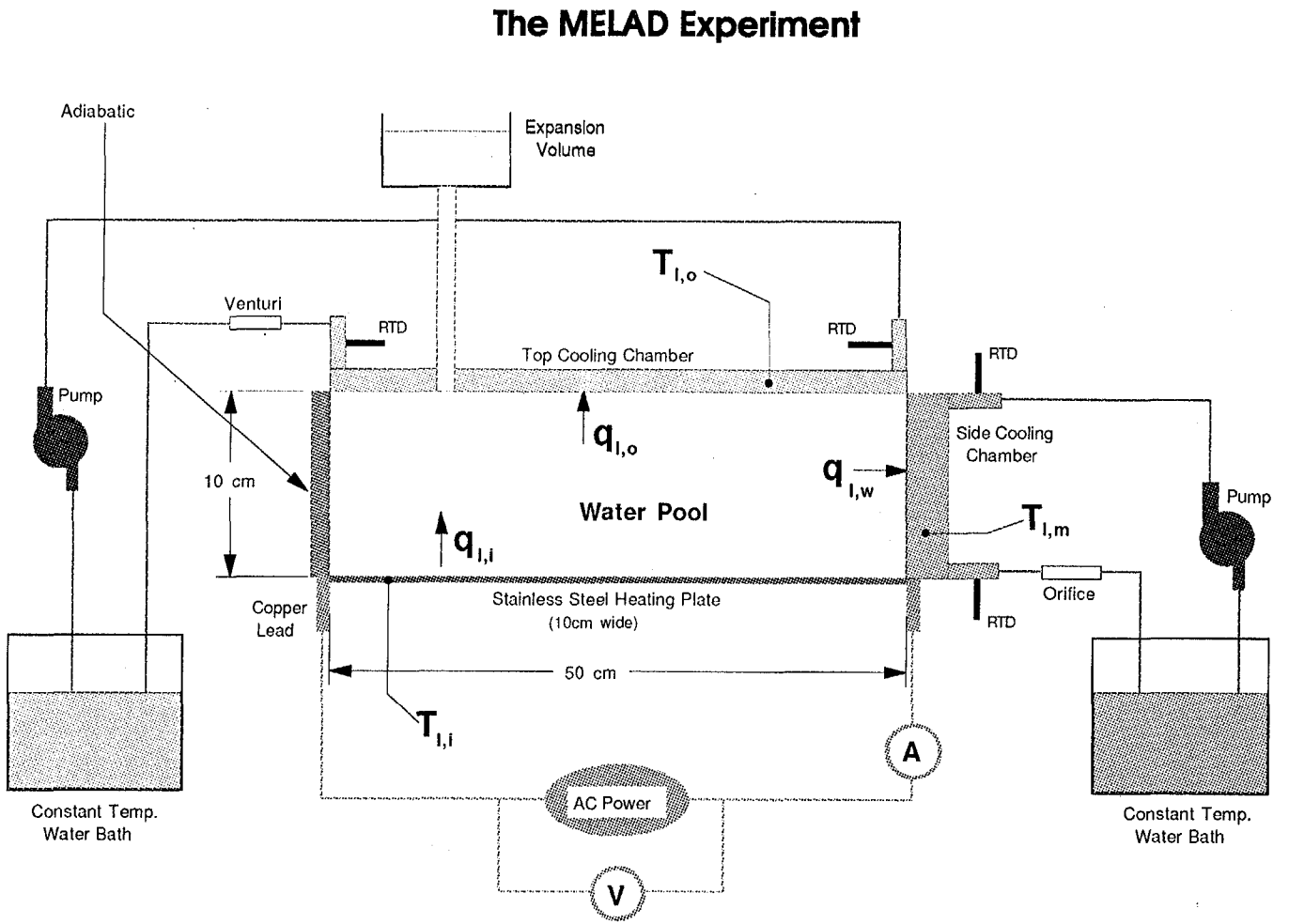

Figure N.1. Schematic of the MELAD experiment design.

Table N.1. The MELAD Experimental Program

Run I.D.	Power Input (kW/m^2)	Top Plate Power Out (kW/m^2)	Side Plate Power Out (kW/m^2)	Energy Balance $\frac{\text{In}-\text{Out}}{\text{In}}$ (%)	$T_{\ell,i}$ / $T_{\ell,o}$ / $T_{\ell,m}$ T_b / $\frac{T_{\ell,i}+T_{\ell,o}}{2}$ (°C)	Ra_b / $Ra_{\ell,i}$ / $Ra_{\ell,o}$ $\times 10^{-8}$
B-1	8.58	7.99	0	7	31.9 / 3.9 /– 21.8 / 17.9	3.3 / 2.1 / 1.2
B-2	13.4	12.1	0	9	41.3 / 5.2 / – 27.7 / 23.3	6.2 / 4.2 / 2.3
B-3	13.3	12.8	0	4	41.2 / 5.9 / – 28.5 / 23.6	6.2 / 3.9 / 2.5
B-4	24.4	21.9	0	10	58.8 / 8.8 / – 40.8 / 33.8	14.8 / 9.4 / 6.1
A-1	24.7	21.7	17.5	–2	59.1 / 8.7 / 4.7 37.5 / 33.9	15.0 / 11.0 / 4.9
A-2	40.6	33.2	28.1	4	75.6 / 11.3 / 5.1 47.5 / 43.5	28.0 / 20.0 / 8.9
A-3	24.2	19.5	16.0	6	57.2 / 7.9 / 3.7 35.9 / 32.6	14 / 10 / 4.4

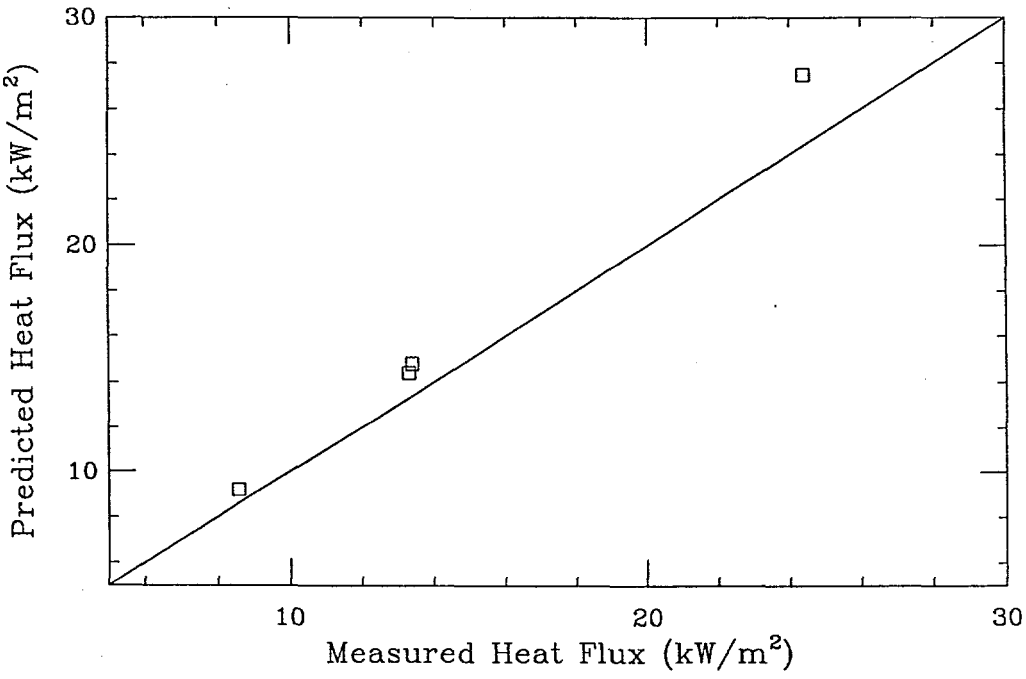

Figure N.2. Comparison of predicted heat fluxes using the Globe–Dropkin correlation to results from the set B MELAD experiments.

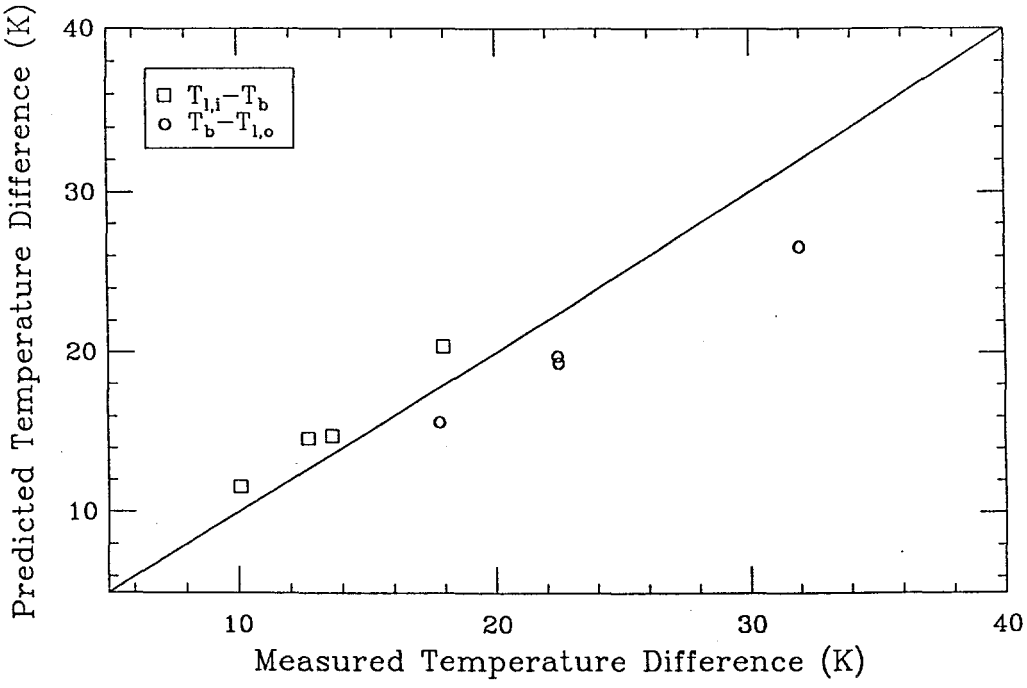

Figure N.3. Comparison of predicted temperature differences across the top and bottom boundary layers, from the local application of the Globe–Dropkin correlation, with values measured on the set B MELAD experiments.

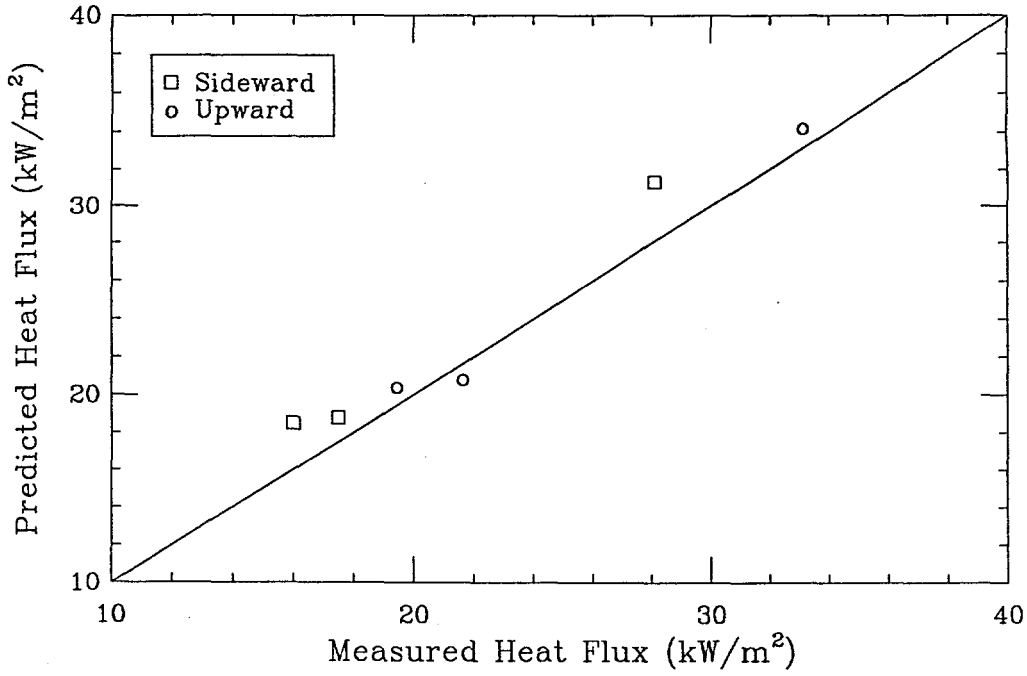

Figure N.4. Comparison of model predictions of top and side boundary heat fluxes with the results from the set A MELAD experiments.

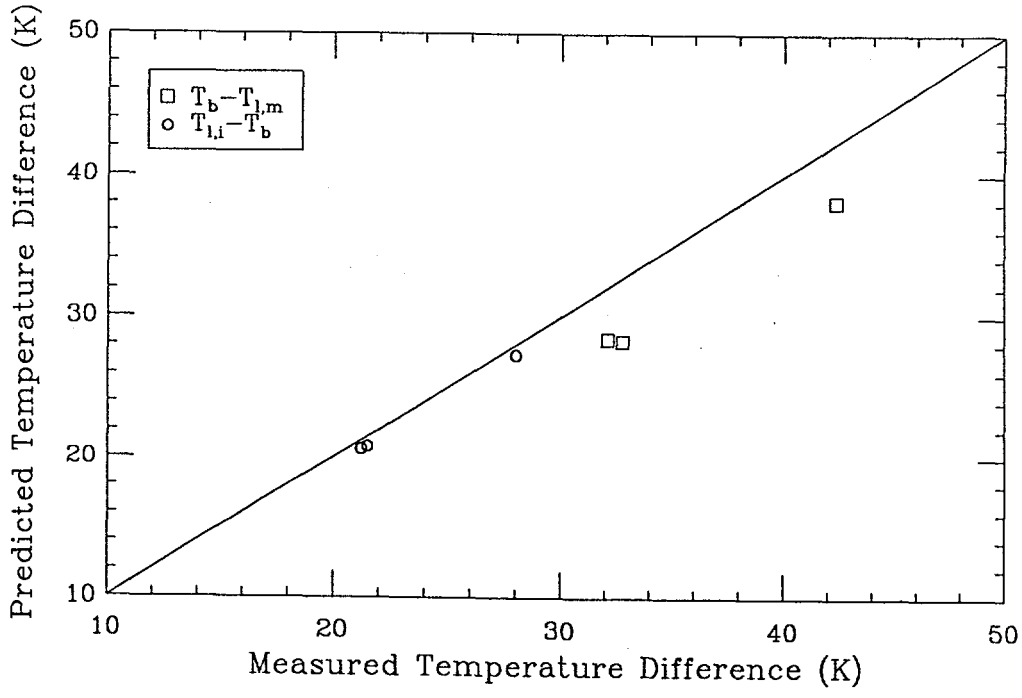

Figure N.5. Comparison of predicted temperature differences across the bottom and side boundary layers compared with measured values in the set A runs.